RECENT ADVANCES IN NATURAL METHANE SEEP AND GAS HYDRATE SYSTEMS

EDITED BY: Tamara Baumberger, Martin Scherwath, Ira Leifer and Samantha Joye

PUBLISHED IN: Frontiers in Earth Science

frontiers Research Topics

frontiers

ISSN 1664-8714
ISBN 978-2-88974-447-3
DOI 10.3389/978-2-88974-447-3

About Frontiers

Frontiers is more than just an open-access publisher of scholarly articles: it is a pioneering approach to the world of academia, radically improving the way scholarly research is managed. The grand vision of Frontiers is a world where all people have an equal opportunity to seek, share and generate knowledge. Frontiers provides immediate and permanent online open access to all its publications, but this alone is not enough to realize our grand goals.

Frontiers Journal Series

The Frontiers Journal Series is a multi-tier and interdisciplinary set of open-access, online journals, promising a paradigm shift from the current review, selection and dissemination processes in academic publishing. All Frontiers journals are driven by researchers for researchers; therefore, they constitute a service to the scholarly community. At the same time, the Frontiers Journal Series operates on a revolutionary invention, the tiered publishing system, initially addressing specific communities of scholars, and gradually climbing up to broader public understanding, thus serving the interests of the lay society, too.

Dedication to Quality

Each Frontiers article is a landmark of the highest quality, thanks to genuinely collaborative interactions between authors and review editors, who include some of the world's best academicians. Research must be certified by peers before entering a stream of knowledge that may eventually reach the public - and shape society; therefore, Frontiers only applies the most rigorous and unbiased reviews.
Frontiers revolutionizes research publishing by freely delivering the most outstanding research, evaluated with no bias from both the academic and social point of view. By applying the most advanced information technologies, Frontiers is catapulting scholarly publishing into a new generation.

What are Frontiers Research Topics?

Frontiers Research Topics are very popular trademarks of the Frontiers Journals Series: they are collections of at least ten articles, all centered on a particular subject. With their unique mix of varied contributions from Original Research to Review Articles, Frontiers Research Topics unify the most influential researchers, the latest key findings and historical advances in a hot research area! Find out more on how to host your own Frontiers Research Topic or contribute to one as an author by contacting the Frontiers Editorial Office: frontiersin.org/about/contact

RECENT ADVANCES IN NATURAL METHANE SEEP AND GAS HYDRATE SYSTEMS

Topic Editors:
Tamara Baumberger, Oregon State University, United States
Martin Scherwath, University of Victoria, Canada
Ira Leifer, Bubbleology Research Intnl
Samantha Joye, University of Georgia, United States

Citation: Baumberger, T., Scherwath, M., Leifer, I., Joye, S., eds. (2023). Recent Advances in Natural Methane Seep and Gas Hydrate Systems. Lausanne: Frontiers Media SA. doi: 10.3389/978-2-88974-447-3

Table of Contents

frontiers | Frontiers in Earth Science

EDITORIAL
published: 27 April 2022
doi: 10.3389/feart.2022.868609

Editorial: Recent Advances in Natural Methane Seep and Gas Hydrate Systems

Tamara Baumberger[1], *Ira Leifer*[2], *Martin Scherwath*[3]* *and Samantha Joye*[4]

[1]Oregon State University and NOAA Pacific Marine Laboratory, Hatfield Marine Science Center, Newport, OR, United States, [2]Bubbleology Research International, Goleta, CA, United States, [3]Ocean Networks Canada, University of Victoria, Victoria, BC, Canada, [4]Department of Marine Sciences, University of Georgia, Athens, GA, United States

Keywords: methane seeps, gas hydrates, brine seeps, gas venting, petroleum, hydrocarbon seepage, chemosymbiotic seep environments

Editorial on the Research Topic

Recent Advances in Natural Methane Seep and Gas Hydrate Systems

Marine hydrocarbon seep emissions of methane, oil, and other trace gases can profoundly impact the marine, regional, and global environment. Cold seeps arise from petroleum hydrocarbon fields (thermogenic), biogenic sources, and gas hydrates (thermogenic and biogenic). Deeply sourced, energy-laden fluids percolate through the sediment column, undergoing continual alteration (**Figure 1**). Seeps come in many flavors and varieties, ranging from highly active mud volcanoes to relict hardgrounds of authigenic carbonates (Joye, 2020). This global geological methane source is estimated to be 63–80 Tg CH_4 $year^{-1}$, with marine seepage contributing 20–30 Tg CH_4 $year^{-1}$ (Etiope et al., 2019) or 5–10 Tg CH_4 $year^{-1}$ (Saunois et al., 2020). An estimate of pre-industrial CH_4 emissions—which are not confounded with fossil fuel production emissions - from ice core $^{14}CH_4$ suggests an emission rate of 1.6 Tg CH_4 $year^{-1}$ (Hmiel et al., 2020). This lower estimate appears inconsistent with several recently published emissions from larger seep fields.

Underlying this debate is the paucity of quantitative studies, with challenges arising from the known spatial and temporal heterogeneity in seepage and the difficulty of doing seep science in some areas (e.g., the Arctic). Geological controls underlie these heterogeneities—particularly geological structures such as anticlines and faults that allow hydrocarbon accumulation and faults that allow migration to the seabed and atmosphere.

Another key question is what is the contribution of bioavailable chemosynthetic energy to higher trophic levels (Leifer et al., 2017). Methane seepage at the seafloor drives whole ecosystems through chemosynthetic primary production that is fueled by methane and sulfide oxidation and which induces authigenic carbonate formation (e.g., Levin et al., 2016). Although chemosynthetic production provides nutrition to a host of species at the bottom of the food chain, precipitated carbonate provides hardground for attachment and shelter. The extent of the seafloor and water-column ecosystem impacts of seepage remains unclear with further advances needed. It is timely to understand the full extent of seep ecosystem interactions as potential rises in their disturbance due to changes in the gas hydrate stability zone (GHSZ) become more common.

In this special issue, studies investigated the state and fate of methane from the sediments in the ocean and atmosphere (Becker et al., Chen et al., Grilli et al., Michel et al., and Meurer et al.). Others utilized seafloor mapping to quantify seepage and identify structural controls, and presented novel approaches (Ayoama and Maeda, Li et al., Merle et al., Riedel et al., Römer et al., and Vrolijk et al.). Several groups

OPEN ACCESS

Edited and reviewed by:
Timothy Ian Eglinton,
ETH Zürich, Switzerland

***Correspondence:**
Martin Scherwath
mscherwa@uvic.ca

Specialty section:
This article was submitted to Biogeoscience, a section of the journal Frontiers in Earth Science

Received: *03 February 2022*
Accepted: *25 March 2022*
Published: *27 April 2022*

Citation:
Baumberger T, Leifer I, Scherwath M and Joye S (2022) Editorial: Recent Advances in Natural Methane Seep and Gas Hydrate Systems. Front. Earth Sci. 10:868609. doi: 10.3389/feart.2022.868609

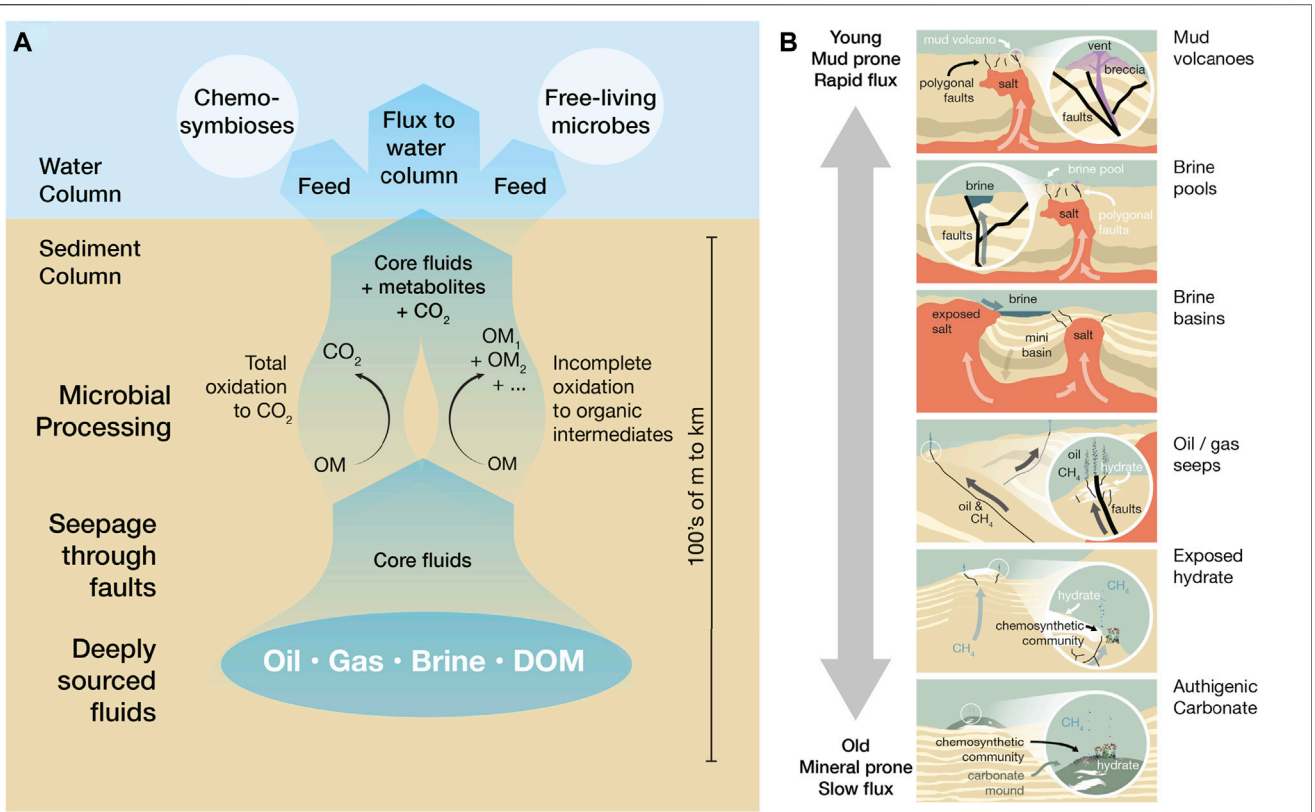

FIGURE 1 | (A) The fluids that fuel hydrocarbon seeps fall into four categories: oil, gas, brine, and dissolved organic matter (DOM), and are arranged like this: oil + gas and oil + gas + brine + DOM. During transit, fluids are altered by biotic and abiotic processes. Upon discharge, these organic rich substrates fuel activity free-living and chemosymbiotic associations. **(B)** A range of seep environments from mud-prone systems—including mud volcanoes, brine pools, and brine basins—to oil and gas seeps with gas hydrate and low flow systems dominated by authigenic carbonates. Adapted from Joye (2020).

studied environmental, geochemical, and biological impacts (Sert et al., Yao et al.). Below we describe these studies.

In recent years, the awareness of cold seeps along active and passive margins has grown due to better scientific tools for locating and quantifying seepage and its signatures. This is well illustrated in Merle et al. who used multibeam sonar to survey the seep spatial distribution along the U.S. Cascadia Margin. This elevated the known number of Cascadian seeps significantly and provided insights into the seep distribution along the whole margin from its southern to northern boundaries and from the coast to the base of the accretionary prism. Ayoama and Maeda propose a methodology to quantify the amount of methane seepage by understanding the correlation between plumes and originating seeps. Vrolijk et al. developed a decision-making tool to assist in seep exploration and evaluation, providing a methodical query structure to identify the required information needed to find and characterize a seep site.

Marine cold seep methane flux quantification remains uncertain because the underlying geological controls are poorly understood. Riedel et al. advance the knowledge on emission controls by combining an acoustic multibeam water column, bathymetry, backscatter, and sub-bottom profiler data to determine linkages between sub-seafloor structures, seafloor gas seeps, and gas discharge into the water column. They also classify depositional, erosional, and tectonic factors as mainly responsible for gas emission control. Li et al. show an example of tectonic controls wherein multiple gas emissions were identified near the fault complex along the western slope of the Mid-Okinawa Trough. They provide new evidence of the role tectonic stresses play in determining the sites of seepage. Furthermore, changing GHSZ boundaries also controls seafloor gas seepage. These new findings underscore these deposits' importance as a methane source with implications for habitat formation and energy sources. For example, Yao et al. present carbonate formation evidence through anaerobic methane oxidation during intense methane seepage likely associated with gas hydrate destabilization. Chen et al. shed light on the transition between gas hydrate and free gas occurrence and the zone where gas bubbles and hydrate crystals co-exist in the same aqueous solution. Becker et al. present 4 years of discrete and continuous temperature logging in an IODP hole on the Vancouver Margin accretionary prism that constrains possible pore-fluid flow in the prism associated with the bottom-simulating reflector and the base of the GHSZ.

Understanding methane's water column fate, including whether seep-derived methane reaches the sea surface and atmosphere, has become a pressing issue. Meurer et al. use a glider equipped for simultaneous measurements of currents and methane concentration to determine the dissolved plume spatial distribution and to quantify water column methane. The study

findings suggest biological seep impacts occur over longer distances than previously appreciated. Michel et al. and Grilli et al. demonstrate elevated methane concentrations throughout the whole water column at their study sites at the Cascadia Margin and the Western Black Sea and also observe areas of elevated dissolved methane concentrations at the surface, suggesting that these shallow seep sites contribute methane to the atmosphere. Similar observations were made by Römer et al. from shallow methane seepage related to salt diapirism in the German North Sea where bubble plumes reached close to the sea surface causing a slight methane oversaturation in surface waters, also indicating seabed seepage contributions to atmospheric methane inventories. Most of the methane dissolves into the shallow water column and provides bioavailable chemosynthetic energy. The extent of seep impacts on marine ecosystems remains poorly understood, addressed by Sert et al., who found that seep-related biogeochemical processes in Arctic seeps modify the composition of dissolved organic matter to higher diversity, but that distributions of nutrients, chlorophyll, and particulate matter were governed by the water-column hydrography and primary production.

These studies fill key knowledge gaps with respect to understanding the seep contribution to global methane budgets and thus climate change by introducing new survey tools, by identifying geological controls to enable more informed extrapolations, and by demonstration of conditions where transport to the atmosphere occurs. Unlike lower latitudes, the Arctic gas hydrates are sufficiently shallow to allow an atmospheric impact, with the magnitude of increases due to warming seabed and changes in the GHSZ very uncertain. Marine and terrestrial seepage currently are estimated to contribute ~14% of the natural (non-regulatable) budget (Saunois et al., 2020). This estimate has significant uncertainty and likely will increase as seep emissions that are co-mingled with production in oil fields, which predate the fields and will persist after oil fields become uneconomic and are eventually abandoned, are reassigned from production. Seep emissions will also increase as Arctic warming destabilizes submerged permafrost and hydrates. First evidence is from the Barents Sea, where methane concentration growth, sea ice retreat, and warming are the fastest on the globe (Yurganov et al., 2016; Yurganov et al., 2021). However, Arctic seepage processes, from hydrate and subsea permafrost destabilization, to seasonal sea ice, to mixed-layer depth changes and the resulting impacts on seep methane transport to the atmosphere remain poorly characterized. Given that current global estimates are from a handful of snapshot emissions of a highly dynamic process and extrapolation to vast geological settings (Leifer, 2019), the potential for significant budget mis-estimation argues for many more quantified studies, particularly in the Arctic.

AUTHOR CONTRIBUTIONS

The authors listed have made a substantial, direct, and intellectual contribution to the work and approved it for publication.

ACKNOWLEDGMENTS

The authors are immensely grateful to all the contributors and in particular the reviewers of the manuscripts, especially in light of the COVID-19 pandemic that suddenly emerged and impacted everyone and required additional patience with the entire process toward publication. This also extends to Frontiers Publishing who provided generous support and many necessary extensions of deadlines where required.

REFERENCES

Etiope, G., Ciotoli, G., Schwietzke, S., and Schoell, M. (2019). Gridded Maps of Geological Methane Emissions and Their Isotopic Signature. *Earth Syst. Sci. Data* 11 (1), 1–22. doi:10.5194/essd-11-1-2019

Hmiel, B., Petrenko, V. V., Dyonisius, M. N., Buizert, C., Smith, A. M., Place, P. F., et al. (2020). Preindustrial $^{14}CH_4$ Indicates Greater Anthropogenic Fossil CH_4 Emissions. *Nature* 578 (7795), 409–412. doi:10.1038/s41586-020-1991-8

Joye, S. B. (2020). The Geology and Biogeochemistry of Hydrocarbon Seeps. *Annu. Rev. Earth Planet. Sci.* 48, 205–231. doi:10.1146/annurev-earth-063016-020052

Leifer, I., Judd, A., and Hildebrand, J. A. (2017). Life Aquatic Chemosynthetic in the Photic Zone -Up the Food Chain? *Ocean. Fish. Open Access J.* 4, 555636. Under Review. doi:10.19080/OFOAJ.2017.04.555636

Leifer, I. (2019). A Synthesis Review of Emissions and Fates for the Coal Oil Point marine Hydrocarbon Seep Field and California marine Seepage. *Geofluids* 2019, 1–48. doi:10.1155/2019/4724587

Levin, L. A., Baco, A. R., Bowden, D. A., Colaco, A., Cordes, E. E., Cunha, M. R., et al. (2016). Hydrothermal Vents and Methane Seeps: Rethinking the Sphere of Influence. *Front. Mar. Sci.* 3, 72. doi:10.3389/fmars.2016.00072

Saunois, M., Stavert, A. R., Poulter, B., Bousquet, P., Canadell, J. G., Jackson, R. B., et al. (2020). The Global Methane Budget 2000-2017. *Earth Syst. Sci. Data* 12 (3), 1561–1623. doi:10.5194/essd-2019-128

Yurganov, L. N., Leifer, I., Leifer, I., and Lund Myhre, C. (2016). Seasonal and Interannual Variability of Atmospheric Methane over Arctic Ocean from Satellite Data. *Curr. Probl. Remote Sensing Earth Space* 13, 107–119. doi:10.21046/2070-7401-2016-13-2-107-119

Yurganov, L. N., Carrol, D., Pnyushkov, A., Polyakov, I. V., and Zhang, H. (2021). Ocean Stratification and Sea-Ice Cover in Barents and Kara Seas Modulate Sea-Air Methane Flux: Satellite Data. *Adv. Polar Sci.* 32, 118–140. doi:10.13679/j.1dvps.2021.0006

Conflict of Interest: Author IL is employed by Bubbleology Research International, which has no related commercial or financial interests that could be construed as a potential conflict of interest.

The remaining authors declare that the research was conducted in the absence of any commercial or financial relationships that could be construed as a potential conflict of interest.

Publisher's Note: All claims expressed in this article are solely those of the authors and do not necessarily represent those of their affiliated organizations, or those of the publisher, the editors and the reviewers. Any product that may be evaluated in this article, or claim that may be made by its manufacturer, is not guaranteed or endorsed by the publisher.

frontiers in Earth Science

ORIGINAL RESEARCH
published: 07 December 2020
doi: 10.3389/feart.2020.552731

Compositional Differences in Dissolved Organic Matter Between Arctic Cold Seeps Versus Non-Seep Sites at the Svalbard Continental Margin and the Barents Sea

Muhammed Fatih Sert[1], Juliana D'Andrilli[2], Friederike Gründger[1,3], Helge Niemann[1,4,5], Mats A. Granskog[6], Alexey K. Pavlov[7,8], Bénédicte Ferré[1] and Anna Silyakova[1]*

[1]CAGE - Centre for Arctic Gas Hydrate, Environment and Climate, Department of Geosciences, UiT the Arctic University of Norway, Tromsø, Norway, [2]Louisiana Universities Marine Consortium, Chauvin, LA, United States, [3]Arctic Research Centre, Department of Biology, Aarhus University, Aarhus, Denmark, [4]NIOZ Royal Institute for Sea Research, Department of Marine Microbiology and Biogeochemistry, and Utrecht University, Texel, Netherlands, [5]Department of Earth Sciences, Faculty of Geosciences, Utrecht University, Utrecht, Netherlands, [6]Norwegian Polar Institute, Fram Centre, Tromsø, Norway, [7]Institute of Oceanology, Polish Academy of Sciences, Sopot, Poland, [8]Akvaplan-niva, Fram Centre, Tromsø, Norway

OPEN ACCESS

Edited by:
Martin Scherwath,
University of Victoria, Canada

Reviewed by:
Kai Mangelsdorf,
Helmholtz Centre Potsdam, Germany
Dong Feng,
Shanghai Ocean University, China

***Correspondence:**
Muhammed Fatih Sert
Muhammed.f.sert@uit.no

Specialty section:
This article was submitted to Biogeoscience, a section of the journal Frontiers in Earth Science

Received: *16 April 2020*
Accepted: *09 November 2020*
Published: *07 December 2020*

Citation:
Sert MF, D'Andrilli J, Gründger F, Niemann H, Granskog MA, Pavlov AK, Ferré B and Silyakova A (2020) Compositional Differences in Dissolved Organic Matter Between Arctic Cold Seeps Versus Non-Seep Sites at the Svalbard Continental Margin and the Barents Sea. Front. Earth Sci. 8:552731. doi: 10.3389/feart.2020.552731

Dissociating gas hydrates, submerged permafrost, and gas bearing sediments release methane to the water column from a multitude of seeps in the Arctic Ocean. The seeping methane dissolves and supports the growth of aerobic methane oxidizing bacteria (MOB), but the effect of seepage and seep related biogeochemical processes on water column dissolved organic matter (DOM) dynamics is not well constrained. We compared dissolved methane, nutrients, chlorophyll, and particulate matter concentrations and methane oxidation (MOx) rates from previously characterized seep and non-seep areas at the continental margin of Svalbard and the Barents Sea in May and June 2017. DOM molecular composition was determined by Electrospray Ionization Fourier-transform ion cyclotron resonance mass spectrometry (FT-ICR MS). We found that the chemical diversity of DOM was 3 to 5% higher and constituted more protein- and lipid-like composition near methane seeps when compared to non-seep areas. Distributions of nutrients, chlorophyll, and particulate matter however, were essentially governed by the water column hydrography and primary production. We surmise that the organic intermediates directly derived from seepage or indirectly from seep-related biogeochemical processes, e.g., MOx, modifies the composition of DOM leading to distinct DOM molecular-level signatures in the water column at cold seeps.

Keywords: methane hydrate, methane oxidation, methane oxidizing bacteria, arctic ocean, Fourier-transform ion cyclotron resonance mass spectrometry, nutrients

INTRODUCTION

Dissolved organic matter (DOM) is the operationally defined mixture of organic compounds that passes through a 0.7 μm pore size filter (Repeta, 2015) and constitutes the largest reservoir of organic carbon in the oceans. Marine DOM has not been chemically characterized explicitly to date but 60–70% of the structural variability has been classified as major functional groups (Carlson and

Hansell, 2015). The distribution and the composition of DOM are mainly controlled by the bioavailability of these groups. The major part (humic acids, condensed aromatics, black carbon etc.) is considered refractory and remains in the water for years or even millennia (Williams and Druffel, 1987; Amon and Benner, 1994; Lechtenfeld et al., 2014). More biologically reactive DOM in the ocean, considered as bio-labile DOM (amino acids, sugars, proteins etc.), is available to heterotrophic microorganisms and rapidly remineralized by prokaryotes in the upper layers of the water column (Carlson et al., 1994; Carlson et al., 2010; Koch et al., 2014). Bio-labile DOM is produced and transformed by numerous biological processes including extracellular release, excretion, cell lysis, solubilisation and chemosynthetic processes (Carlson and Hansell, 2015).

DOM in the ocean is predominantly derived from biological processes, carrying a unique signature, which may comprise a fingerprint of the surrounding ecosystems. One distinct ecosystem of the Arctic Ocean involves cold seeps and methane bearing sediments in which methane emanates from seeps due to dissociation of methane hydrates (Westbrook et al., 2009; Ferré et al., 2012; Berndt et al., 2014; Sahling et al., 2014). Only a limited portion of the seeping methane reaches the atmosphere (Graves et al., 2015; Myhre et al., 2016; Steinle et al., 2016), while the major part remains in the water column as dissolved gas. Concentrations of methane may reach up to thousands times higher than background levels at seeps, yet decreases rapidly with the distance from the point source predominantly as a result of bacterial oxidation, lateral diffusion, and upward mixing (Graves et al., 2015; Silyakova et al., 2020). Microbial oxidation of methane (MOx), performed by methane oxidizing bacteria (MOB) which convert methane into methanol and formaldehyde, is the major removal mechanism of dissolved methane in ocean waters (Reeburgh, 2007; Murrell, 2010). Formaldehyde is then further used in the catabolism (i.e., oxidized to carbon dioxide to supply energy) or in the anabolism (i.e., incorporated into organic compounds to be used as building blocks for growth) (Hanson and Hanson, 1996). Previous culture experiments suggest that MOB produces a variety of organic acids and chemical products as intermediates (Kalyuzhnaya et al., 2013).

The contribution of cold seeps into marine DOM has never been documented despite its potential importance in waters receiving methane from seeps. The main objective of this study is to document the effect of methane seeps on DOM composition at cold seep sites at the continental margins of Svalbard and in the Barents Sea. Our main hypothesis is that methane-driven microbial processes such as MOx and/or seep-associated microbial modifications result in microbial discharge of metabolic intermediates that alter the molecular composition of DOM in the water column at cold seeps.

METHODS

Study Area

We collected samples near methane seepages with various hydrographic properties and bathymetric features during two research expeditions with R/V Helmer Hanssen between 16–29 May (CAGE-17-1) and 23–28 June 2017 (CAGE-17-2). Samples were collected at 18 stations at six different sites (**Figure 1** and **Table 1**) comprising two deep water stations at the Vestnesa Ridge (VR) and Yermak Plateau (YP), eight stations at the shallow shelf west of Prins Karls Forland (PKF), two stations at the southern end of Storfjordrenna (SS), three stations at Storfjordrenna pingos (SP) and three stations at the Olga Basin (OB) in the Barents Sea (**Figure 1**). At all sites, non-seepage stations were also sampled as a control that had similar water masses but only background methane concentrations. Active seeps were located with the ship-mounted EK60 single-beam echosounder. Based on echosounder data, we defined sampling stations that were literally located above active seeps. These stations are considered seep stations, while the others are considered non-seep stations (**Table 1**). The only exception was station PKF-1 which was not exactly located above seeps but surrounded by numerous seeps and located in the flow direction of many others (**Figure 1**).

Sampling and Storage

Seawater was sampled from discrete water depths (**Table 1**) during up-casts of a rosette sampler with 12 × 5 L PTFE lined Niskin bottles and a Sea-Bird 911 plus CTD (Conductivity Temperature Depth) with accuracies of 0.3 db, 0.001°C, and 0.002 for pressure, temperature and salinity, respectively. Dissolved oxygen data were collected using an SBE 43 oxygen sensor (calibrated by Winkler (1888) titration) attached to the CTD. Distribution of chlorophyll fluorescence and turbidity were determined at all stations by Setpoint sensors. All sensor measurements were averaged in 1 m depth bins. Methane and MOx samples were collected immediately after recovery of the rosette on-board. Samples for methane analysis were carefully filled (to prevent bubble formation) into 120 ml (1250 ml for non-seep surface samples) serum bottles amended with 1 M sodium hydroxide solution to stop microbial activity and crimped with butyl rubber septa. Samples were vigorously shaken and stored at 4°C until analysis.

For MOx rate measurements, 20 ml crimp top vials were filled bubble-free with seawater sample, capped with bromobutyl rubber stoppers that do not impede MOx activity (Niemann et al., 2015). Samples were processed immediately after sampling.

Samples for DOM, particulate matter, chlorophyll *a* (Chl *a*), and nutrients were collected in acid-washed (2% HCl) glass bottles (4 × 1000 ml) and stored at 4°C in the dark before processing. Samples were filtered within 6 hours after collection by applying low-pressure vacuum (50 mmHg). Triplicates of particulate matter and Chl *a* samples were collected on GF/F filters (Whatman) using 1 L of water for each sample. Particulate matterfilters were dried and stored at 25°C until X-ray fluorescence analysis. Chl *a* filters were folded twice in half, placed in 10 mL high density polyethylene tubes (HDPE), and stored at −80°C. The filtrate was collected into pre-rinsed 60 ml HDPE bottles, stored at −20°C, and used for the determination of the concentrations of nitrate, nitrite, phosphate, silicate, ammonia, dissolved organic carbon (DOC), total dissolved nitrogen, and total dissolved phosphorus.

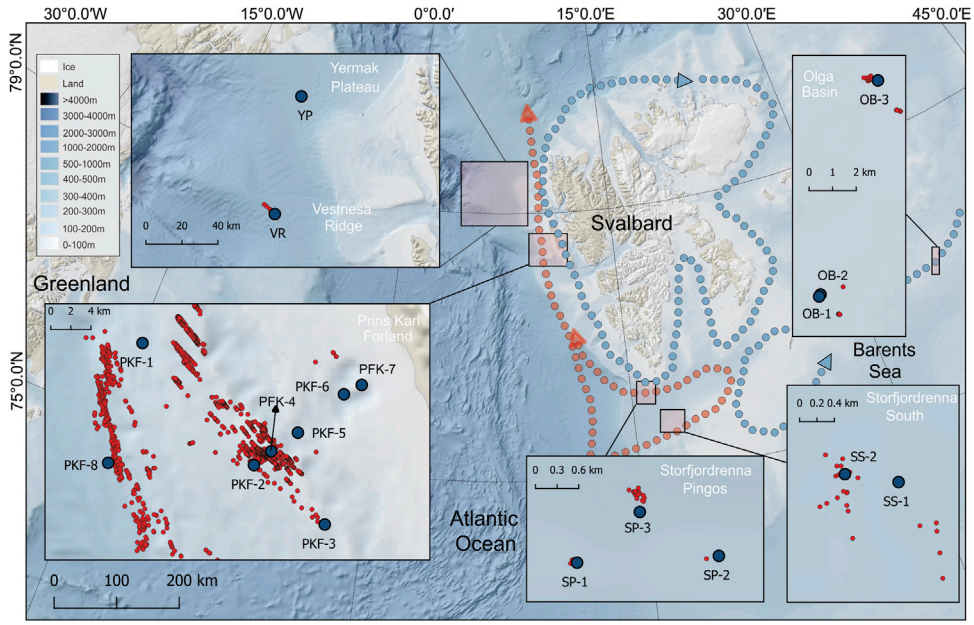

FIGURE 1 | Bathymetric map of sampling areas around Svalbard. Pale red and blue dotted lines show directions of the warm West Spitzbergen Current and cold polar currents, respectively. Five insets are shown to magnify the sampling areas with individual spatial scales along with known methane seeps indicated by the red dots. Sampling stations within the insets are indicated by the blue dots and further information is provided in **Table 1**.

For solid phase extraction DOM 1 L of filtrate was extracted on 500 mg styrene divinyl benzene polymer type cartridges (PPL, BondElut, Agilent Technologies) using a procedure modified from Dittmar et al. (2008). Briefly, filtrates were acidified to pH 2 by HCl (37% v/v, Merck) and transferred into pre-conditioned (6 ml methanol + 12 ml water) solid phase extraction cartridges. Next, 12 ml pH 2 water were flushed through the cartridge and cartridges were dried under air vacuum for 30 min. Concentrated DOM samples were eluted into combusted, Teflon capped amber glass vials by 2 ml methanol and stored at −20°C in the dark until FT-ICR MS analysis.

Biochemical Analyses

Nitrate + nitrite (further nitrate), silicate, phosphate, ammonium, total dissolved nitrogen and total dissolved phosphorus

TABLE 1 | Detailed information of the sampled stations listing sample regions, sampling stations, station location, methane seep characteristic, water depth, and sampling depth of water samples.

Region	Station	Latitude N	Longitude E	Methane seep	Water depth (m)	Sampling depths (m)
Prins Karls Forland	PKF-1	78° 40' 02''	09° 35' 33''	Yes	195	5, 25, 171, 192
	PKF-2	78° 33' 09''	10° 05' 53''	Yes	110	5, 25, 88, 108
	PKF-3	78° 29' 46''	10° 24' 53''	Yes	117	5, 25, 93, 113
	PKF-4	78° 33' 56''	10° 10' 33''	Yes	81	5, 25, 56, 78
	PKF-5	78° 34' 58''	10° 17' 48''	No	122	5, 25, 100, 120
	PKF-6	78° 37' 08''	10° 30' 21''	No	125	5, 25, 103, 123
	PKF-7	78° 37' 39''	10° 35' 13''	No	76	5, 26, 53, 73
	PKF-8	78° 33' 15''	09° 26' 31''	Yes	405	5, 25, 380, 402
Yermak Plateau	YP	79° 37' 33''	07° 30' 12''	No	822	5, 50,131,400,774,817
Vestnesa ridge	VR	79° 00' 05''	06° 56' 49''	Yes	1207	5, 50, 600, 1150, 1195
Storfjorrenna south	SS-1	75° 50' 20''	16° 38' 49''	No	345	5, 50, 170, 295, 340
	SS-2	75° 50' 25''	16° 37' 29''	Yes	350	5, 49, 170, 295, 347
Storfjordrenna pingos	SP-1	76° 06' 24''	15° 58' 05''	Yes	383	7.5, 28, 357, 375
	SP-2	76° 06' 21''	16° 02' 29''	No	386	5, 25, 363, 384
	SP-3	76° 06' 47''	16° 00' 12''	No	387	5, 25, 365, 384
Olga basin	OB-1	76° 46' 53''	35° 11' 28''	No	158	5, 25, 135, 155
	OB-2	76° 46' 51''	35° 11' 15''	No	159	5, 25, 60, 100, 135, 155
	OB-3	76° 51' 04''	35° 25' 57''	Yes	154	5, 25, 60, 130, 150

concentrations were measured colorimetrically (Grasshoff et al., 1999) by a segmented flow nutrient analyzer system (ALPKEM Flow Solution IV, OI Analytical). Dissolved organic nitrogen (DON) and dissolved organic phosphorus (DOP) concentrations were calculated by subtracting concentrations of nitrate + ammonium (DIN; dissolved inorganic nitrogen) from total dissolved nitrogen and phosphate from total dissolved phosphorus.

DOC concentrations were measured based on a high-temperature combustion technique (Qian and Mopper, 1996; Peterson et al., 2003). Unthawed samples were allowed to equilibrate at room temperature and acidified to pH 2 with HCl (37%). 15 ml of sample were then transferred into pre-combusted glass vials of the TOC analyzer (MQ-1001). Deep Ocean DOC samples (Hansell Laboratory, University of Miami) were used as reference material.

Particulate nutrient analyses were measured in triplicates using a method based on wavelength dispersive X-ray fluorescence with a detection limit < 0.1 µg per filter (Paulino et al., 2013) for particulate carbon C, nitrogen (N), and phosphorus (P).

The filters for Chl *a* concentration stored at −80°C were added to 10 ml methanol (Holm-Hansen and Riemann, 1978) and stored overnight at 4°C. Methanol extracted samples were transferred into pre-cleaned vials and maintained at room temperature. Fluorescence of the sample was measured against methanol blanks with recently calibrated Turner Design fluorometer at 440 nm before and after adding two drops of 5% HCl (Holm-Hansen et al., 1965). Final concentrations were determined using a calibration curve of Chl *a* standards.

Quantification of dissolved methane in seawater samples was conducted on-board using headspace gas chromatography (ThermoScientific, GC Trace 1310, FID detector, MSieve 5A column). 5 ml from the 120 ml (1250 ml for low concentration surface waters) sample bottles was replaced with high purity nitrogen and allowed to equilibrate at least for 24 hours. For Headspace GC measurement hydrogen was used as a carrier gas and oven temperature was set to 150°C (isothermal). 500 µl headspace was injected with a gas-tight syringe resulting in a detection limit of 1 ppm and 5% standard deviation. Dissolved methane concentration (nmol/L) was calculated using previously published solubility coefficients (Wiesenburg and Guinasso, 1979). Reproducibility of measurements was controlled with 2 ppm and 100 ppm methane containing air standards.

MOx rates was quantified by tritium labelled incubations (Niemann et al., 2015; Steinle et al., 2015) with modifications as described in Ferré et al. (2020). Briefly, hexaplicates of seawater samples were amended with trace amounts of ^{3}H-methane (10 µl gaseous $C^{3}H_4/N_2$, ~25 kBq, <50 pmol CH_4, American Radiolabeled Chemicals, United States) and incubated for 72 hours at *in situ* temperature in the dark. After following the procedure described in aforementioned publications, MOx rates were calculated from the fractional tracer turnover and *in situ* methane concentrations assuming first order reaction kinetics (Valentine et al., 2001; Reeburgh, 2007). All incubations were corrected for (insubstantial) tracer turnover in killed controls (Steinle et al., 2015).

Fourier-Transform Ion Cyclotron Resonance Mass Spectrometry Analysis and Molecular Formula Assignments

DOM mass spectra were obtained with a custom-built 9.4 T Fourier transform ion cyclotron resonance mass spectrometer (FT-ICR MS) instrument (National High Magnetic Field Laboratory [NHMFL], Tallahassee, Florida, United States). Mass spectra were generated in positive and negative ion electrospray ionization (ESI) mode with the following settings: flow rate 0.5 µL/min, needle voltage ± 2.5 kV, tube lens ± 250 V, heated metal capillary operated at 11.2 W, octopole frequency 2 MHz, frequency sweep rate of 50 Hz/ls and temperature 21.7°C. To generate mass spectra, 50 scans (time domain acquisitions) were co-added for each sample, Hanning apodized, and zero-filled once before fast Fourier transformation and magnitude calculation (Marshall and Verdun, 1990). NHMFL software was used to calibrate the data and generate peak lists for each sample prior to molecular formula assignment. Peak lists were generated with a signal to noise ratio threshold of 6x the baseline root mean square noise and internally calibrated with commonly known DOM methylene ($-CH_2$) compounds spanning across the 200–900 Da mass spectral range. DOM molecular compositions were assigned by PetroOrg (Corilo, 2014). Molecular formula assignments included all possible naturally occurring molecular combinations of C, H, N, O, and S within these ranges: $^{12}C_{1-100}$, $^{1}H_{1-200}$, $^{14}N_{0-2}$, $^{16}O_{1-50}$, and $^{34}S_{0-1}$. Formula confirmation was based on individual monoisotopic mass spectral peaks, error < 1 ppm, and homologous series inclusion, as has been conducted previously for manual composition assignments (D'Andrilli et al., 2015). Sodium and chlorine adducts were also considered during the molecular formula assignment procedure for positive and negative mode, respectively. Assigned molecular formulas were generated for each sample as negative and positive mode except samples PKF-1 at 195 m and SP-1 at 344 m which could not be calibrated in positive mode with acceptable error (<1 ppm). Positive and negative molecular assignments per sample were combined to analyze DOM composition and chemical characterization. For each sample containing duplicate molecular formulas in positive and negative mode, one was discarded from further analysis.

Chemical characterizations for the combined positive and negative formula lists of each sample were conducted to get percentages of 1) atomic heterogeneous contents – CHO, CHNO, CHOS, CHNOS – and 2) H:C and O:C atomic ratios and ranges on van Krevelen diagrams (Kim et al., 2003). Based on the elemental compositions of major biochemical compound groups, specific H:C and O:C ratio ranges were related to four compound classes: 1) lipid- & protein-like (LPD), 2) amino sugar- & carbohydrate-like (CAR), 3) unsaturated hydrocarbon- and condensed aromatic-like (UHC), and 4) lignin- & tannin-like (LGN), whose boundaries were obtained from Hockaday et al. (2009) and Hodgkins et al. (2016) (**Supplementary Table S1**). Samples were also interpreted by the percentages of the formulas above the molecular lability boundary (MLB_L; H:C ≥ 1.5) to compare more bioavailable DOM composition with less bioavailable material across all samples (D'Andrilli et al., 2015).

The aromaticity (or the aromatic fraction) of the samples were calculated using the equation given in Hockaday et al. (2009).

Statistical Analyses

Statistical analyses and data visualization were performed using R (R Core Team, 2018) with built-in functions and external packages: Vegan (Oksanen et al., 2018), FactoMineR (Lê et al., 2008), MASS (Venables and Ripley, 2002), and indicspecies (De Cáceres and Legendre, 2009).

Principal component analysis was applied on measured environmental variables to obtain multiple correlation between samples and variables.

Chemical diversity of the DOM molecular formulas for each sample was calculated by the 'diversity' function in R, which is analogue to biodiversity in ecology, i.e., the Shannon-Weaver index (Oksanen et al., 2018):

$$H = -\sum P_i * log_n(P_i)$$

where P is the relative abundance of formula i.

Non-metric multidimensional scaling (NMDS) analysis was applied in three steps on the molecular formula lists to determine the variation of DOM between samples. First, a presence/absence matrix was constructed (samples on rows and formulas on columns). Second, a dissimilarity matrix was calculated based on Jaccard formulation (Jaccard, 1912) on binary (0 or 1) data (e.g., *[A + B-2*J]/[A + B-J]* where *A* and *B* are number of formulas in two compared samples and *J* is the number of formulas that is common in both samples (Oksanen et al., 2018). Third, an NMDS ordination plot was depicted on two sets of scores in which the separation between the samples was largest. Distribution on the biplot states that closer samples are likely to be more similar than the ones further apart.

Permutational multivariate analysis of variance (PERMANOVA) was calculated on Jaccard distance matrices by using the 'adonis' function in the Vegan package in R (Oksanen et al., 2018). PERMANOVA was used to interpret how DOM compositions were influenced by categorical variables such as regional distribution, water masses and seep/non-seep association.

Indicator value indices (IndVal) of all detected formulas were calculated following a method developed by De Cáceres and Legendre (2009). IndVal is a product of two quantities (*A: group specificity; B: group fidelity*) that allow to define lists of formulas that associated to the predefined groups of sites. Statistical significance (p) of the group association were then tested by permutation test against the null hypothesis that a formula is not more frequently found at a group of sites than at sites not belonging to that group (De Cáceres and Legendre, 2009). A threshold of IndVal ≥ 0.7 and $p \leq 0.01$ were taken under 1000 permutations for group association.

RESULTS

Distribution of Water Masses and Environmental Variables

The studied sites were characterized by five main water masses (**Figure 2**). Three of them were classified within the window of σ_t density 27.70 and 27.97 kg/m^3 (Rudels et al. 2000), with the

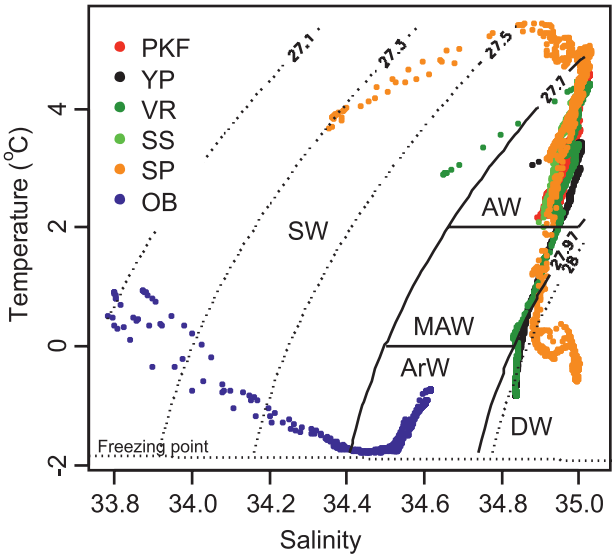

FIGURE 2 | Water mass definitions on temperature vs. salinity diagram from the CTD profiles. 27.70–27.97 kg/m^3 σ_t isoclines separate Surface water (SW) and Deep Water (DW) and 0–2°C horizontal temperature lines separate Atlantic Water (AW) and Arctic Water (ArW) from Modified Atlantic Water (MAW). Colored data points indicate the sample data for each region listed in **Table 1**.

temperature ranges of > 2°C (Atlantic Water; AW), 0–2°C (Modified Atlantic Water; MAW) and < 0°C (Arctic Water; ArW). Waters with $\sigma_t \leq 27.70$ kg/m^3 were considered as surface water (SW) with a wide range of temperature and salinity. Waters that have $\sigma_t > 27.97$ kg/m^3 were classified as Arctic deep water (DW). DW reveals two distinct influences depending on the site location (lower right corner in **Figure 2**). At VR and YP stations the water column was composed of DW that has formed in the polar region and sank below the AW layer. At the lower part of the SP, on the other hand, DW was characterized by higher salinity which were formed in Storfjorden and sank underneath the MAW layer at the southern tip of Spitsbergen (Quadfasel et al., 1988; Loeng, 1991; Fer et al., 2003; Skogseth et al., 2005).

The water column profiles were depicted in **Figure 3** by a selected station from each region that represents typical biogeochemical features. As is shown in the figure, the water column was well-mixed at the shallow stations in the PKF, where AW was the dominant water mass with temperature 2°C and salinity 34.9 throughout the water column (**Figure 3A**). Vertical profiles exhibited clear site-specific patterns for temperature, salinity and density (**Figure 3A**). At VR and YP, AW occupied the 300–350 m upper layer (**Figure 3A**). Underneath, the temperature decreased to 0°C with a strong thermocline and MAW extended to the depth of 500 m in YP and 600 m in VR. Underneath MAW, DW displayed a uniform salinity profile (~34.85) with 0 to −1°C temperature range. Temperature and salinity profiles were distinct in SS and SP despite their proximity (~30 km). SS was fully occupied with AW (4.3°C, ~35 salinity) from the surface down to 150 m; at greater depth, temperature

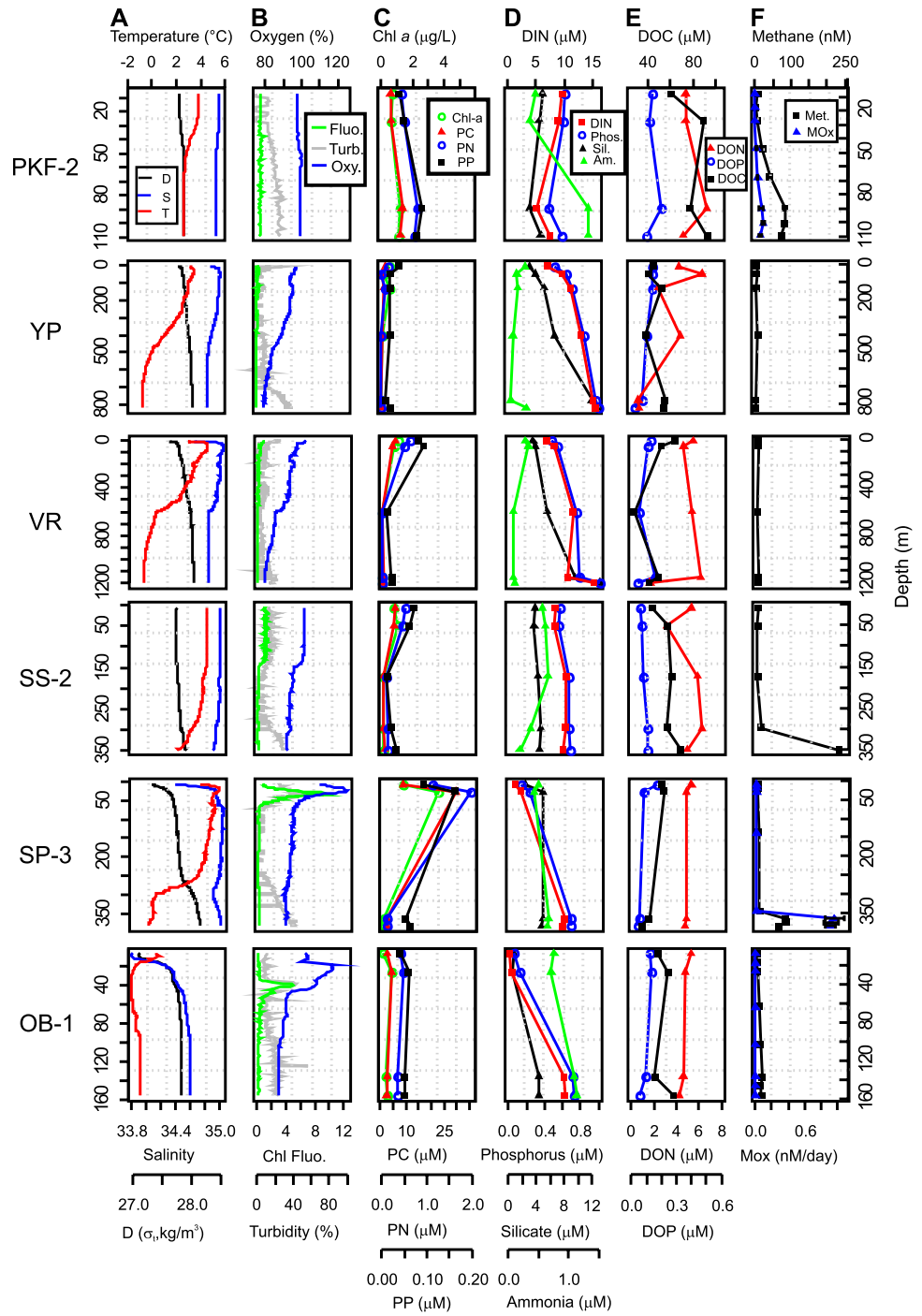

FIGURE 3 | Depth profiles of selected stations. Each row of profiles represents the typical features from regions listed in **Table 1**. Abbreviations are PC, PN, PP, particulate carbon, nitrogen and phosphorus; DOC, DON, DOP, dissolved organic carbon, nitrogen and phosphorus; DIN, dissolved inorganic nitrogen; D, density; T, temperature; S, salinity; Chl Fluo., Chlorophyll fluorescence; Mox, methane oxidation.

decreased slightly to 2°C at the bottom (**Figure 3A**). Three distinct layers were characterized at SP: a cold, fresh surface layer at the top 20–30 m, a warm and saline AW layer from 30 to 300 m, and cold and saline DW from 300 m to the bottom (**Figure 3A**). At the OB site strong Arctic influence was prominent with a two-layered structure, consisting of SW (top 20 m) above a sharp pycnocline and ArW from 30 m to the bottom at ~150 m (**Figure 3A**).

Chl fluorescence did not exhibit any clear peak and were around zero in the water column for May 2017 (CAGE-17-1

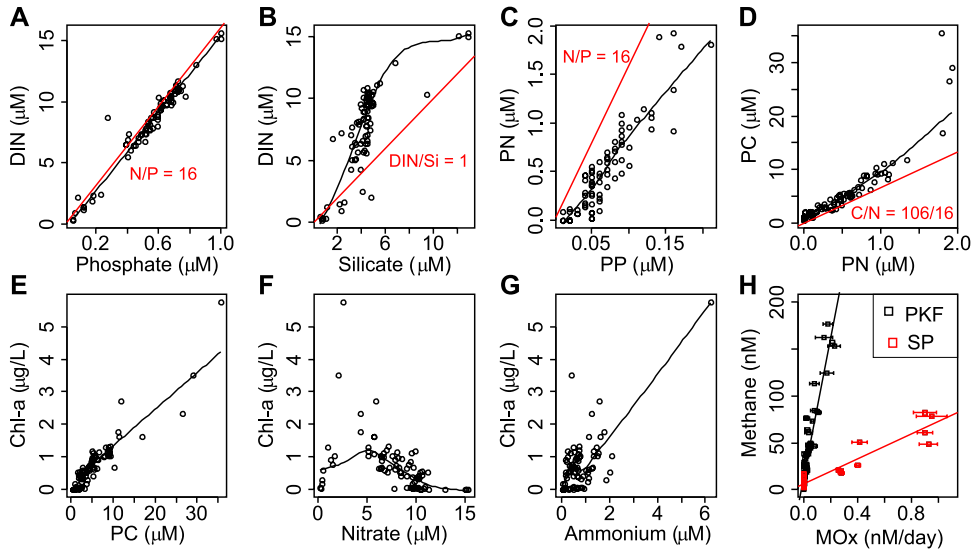

FIGURE 4 | Individual relationships between biogeochemical parameters. The black lines show local polynomial regressions between the variables. Redfield ratios are provided in red at the top panel. The relationship between methane and methane oxidation rates (MOx) and corresponding linear regression lines are provided in black and red corresponding to Prins Karl Forland (PKF) and Storfjordrenna Pingos (SP). Error bars represent standard deviation of MOx measurements. Abbreviations are PC, PN, PP, particulate carbon, nitrogen and phosphorus; DIN, dissolved inorganic nitrogen; Chl-a, Chlorophyll a.

cruise) whereas distinct maxima were detected at SP and OB at 40 m depth in late June (CAGE-17-2 cruise) (**Figure 3B**). This difference in Chl fluorescence signal between the cruises was also detected in surface Chl *a* concentration averages retrieved from satellite data (**Supplementary Figure S1**). To depict a relative distribution of oxygen more accurately, dissolved oxygen concentrations were converted into oxygen saturation assuming that 100% saturation at 1 atm and 4°C corresponds to 10.92 mg/L. Oxygen saturation varied in 92–102% range within AW that occupied PKF and upper layers of VR, YP, and SS and uniformly decreased to 80–85% at the bottom in DW. Along with the peaks in Chl fluorescence signal, oxygen saturation increased up to 110–125% at the upper layers of OB and SP and dropped back to 85–90% in ArW at the bottom layers (**Figure 3B**). Turbidity was elevated at the bottom of the water column at all stations and its profiles were analogous to the fluorescence profiles at the upper layers (**Figure 3B**).

Chl *a* concentrations ranged from 0.00 to 5.75 μg/L (average 0.75 μg/L) (**Supplementary Table S2**) with the highest concentration in SP corresponding with the CTD Chl fluorescence peak at 40 m at this site (**Figure 3C**). Particulate matter concentrations were always in line with the Chl *a* concentrations (**Figure 3C**). Maximum concentrations were measured at SP-1 (28 m) for particulate C (35.64 μM) and particulate N (1.93 μM) and in PKF for particulate P (0.21 μM). Chl *a* vs particulate C, N and P displayed positive linear correlations in all samples (r = 0.93, 0.84, and 0.76, respectively, $p < 0.001$) (**Figures 4C–E**).

Maximum dissolved nutrient concentrations were detected in the DW layer (<800 m; 15.3 μM, 1.00 μM, and 13.0 μM for nitrate, phosphate, and silicate respectively) implying a marked regeneration at depth (**Figure 3D**). We found lowest concentrations at the OB surface likely due to the dilution by sea-ice meltwaters and earlier surface bloom (**Figure 3D**). Here, concentrations dropped to 0.19 μM, 0.05 μM, and 0.54 μM for nitrate, phosphate, and silicate, respectively (**Supplementary Table S2**). Ammonium concentrations varied in a narrow range from 0.04 μM to 2.08 μM in all samples (**Supplementary Table S2**) except the maximum value (6.21 μM) measured at SP-1 (28 m). DIN and phosphate ratios were close to the Redfield ratio (1958) (ratio of carbon: nitrogen: phosphorus as 106:16:1 often found in marine phytoplankton soft tissue) in all samples (**Figure 4**). DIN to silicate ratio however, was higher than one in most of the samples.

Our measurements showed that the variation of DOC, DON, and DOP was low comparing all sites (**Figure 3E** and **Supplementary Table S2**). The DOC concentration range was from 26.9 to 104.0 μM however, 80% of the measurements were between 40 and 80 μM. The highest DOC concentration was measured at the surface layer (0–5 m) of PKF and the minimum concentration was at the surface of the OB. Similar vertical profiles were observed for DON and DOP concentrations with ranges of 0.00–7.43 μM and 0.00–0.60 μM, respectively (**Supplementary Table S2**). On average, DON and DOP contributed 39% and 20% of the total dissolved nitrogen and phosphorus pool, respectively, and highest contributions were measured for OB surface water.

Methane concentrations were often elevated in the vicinity of seeps (**Figure 3F** and **Supplementary Figure S2**). Dissolved methane resulted in high concentrations in the bottom waters and decreased rapidly to atmospheric equilibrium levels except at PKF (**Figure 3F**). Here, numerous seeps were located in shallow waters and methane concentrations were ~five times higher at the surface (14.9 nM) compared to the atmospheric equilibrium (3.2 nM at 34.8 psu and 6°C; (Wiesenburg and Guinasso, 1979)). The highest methane concentration (263 nM) was

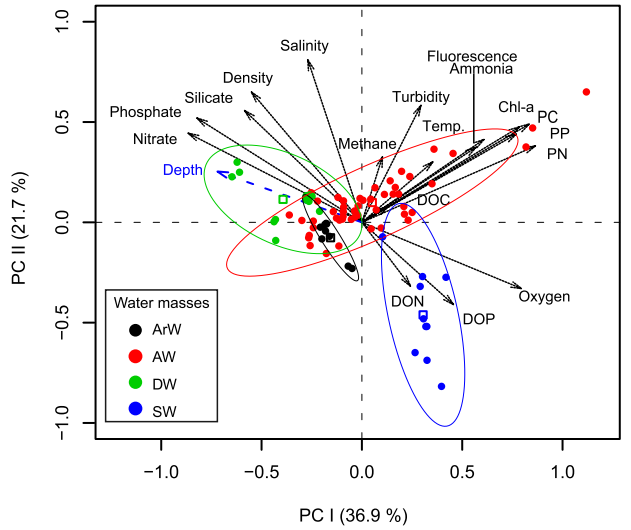

FIGURE 5 | Principle Component Analysis biplot of the biochemical parameters. The explained variances are provided on the x- and y-axis in parentheses. Coloured ellipses represent 95% confidence interval for water mass group centroids of Surface water (SW), Deep Water (DW), Atlantic Water (AW), and Arctic Water (ArW). Centroids are represented by open square symbols. Abbreviations are PC, PN, PP, particulate carbon, nitrogen and phosphorus; DIN, dissolved inorganic nitrogen; DOC, DON, DOP, dissolved organic carbon, nitrogen and phosphorus; Chl-a, Chlorophyll a.

measured at the bottom of SS-2 (**Figure 3F**). Average methane concentrations for all stations were 63 nM (bottom), 39 nM (25 m above seafloor) and 9 nM (5 m below surface).

We measured MOx rates at 96 sampling points at PKF, SP, and OB (**Supplementarys Table S2 and Figure S2A**). Average MOx rates were almost 10 times higher at SP (0.31 nM/day) compared to PKF (0.04 nM/day) and there was no detectable MOx activity at OB (**Figure 3** and **Supplementary Figure S2B**). MOx rates were positively correlated with the methane concentrations in PKF (correlation coefficient r = 0.91, $p < 0.001$, number of sub-samples $n = 64$) and SP (r = 0.94, $p < 0.001$, $n = 32$) separately and showed two different responses (**Figure 4H**).

A principal component analysis of the biochemical parameters displayed a correspondence with the water mass characteristics of the samples within the first two principal components (PC) as 36.9 and 21.7% variance explained, respectively (**Figure 5**). Primary production related parameters (Chl *a*, particulate C, N, P, Chl fluorescence, ammonium) and dissolved nutrients were the main components on the PC-1 which partially represent the separation between DW and AW, whereas SW largely represented by DON, DOP and oxygen concentrations on the PC-2 axis (**Figure 5**).

Dissolved Organic Matter Molecular Composition

From all the sampling sites, 19,641 distinct formulas were obtained after removing the duplicate formulas in positive and negative mode ESI samples with the molecular mass range of 211 to 989 Da (**Figure 6A**). From all assigned formulas, 6,947and 2,356 were unique to seep and non-seep samples respectively (**Figure 6B**), and 10,338 formulas were found in both (**Figure 6C**). All assigned elemental composition varied in the range of $C_{7\text{-}75}H_{6\text{-}74}N_{0\text{-}2}O_{1\text{-}25}S_{0\text{-}1}$ with the percentages of 41% CHO, 39% CHNO, 13% CHNOS, 7% CHOS for seep and 41% CHO, 36% CHNO, 15% CHNOS, 8% CHOS for non-seep samples. Using our modified characterization classification criteria based on H:C and O:C groupings on van Krevelen diagrams, molecular formulas averaged 74% LGN, 8% UHC, 14% LPD, 4% CAR for seep and 76% LGN, 9% UHC, 11% LPD, 4% CAR for non-seep chemical species (**Figure 6B**).

IndVal analysis for seep versus non-seep comparisons of all molecular formulas determined that 922 and 129 formulas were associated with the seep and non-seep samples respectively (**Figure 6D**). That is, the formulas that are more frequently observed in a compound class group (**Supplementary Table S1**) considered as associated. Given that, seep associated formulas (IndVal ≥ 0.7; $p \leq 0.01$) were composed of 72% LGN, 23% LPD, and 5% UHC. Non-seep associated formulas (IndVal ≥ 0.7; $p \leq 0.01$) were predominantly composed of LGN (52%), UHC (43%), and only 6 formulas were assigned CAR (5%) chemical species (**Figure 6D**).

The number of formulas in seep and non-seep samples ranged from 3,211 to 9,534 and from 3,120 to 6,815 respectively (**Figure 7A**). The lowest number of formulas were obtained in the PKF-7 (non-seep) and the highest number of formulas were obtained in PKF-3 (seep) (**Figure 7A**). Samples on the seepage sites of PKF and SS were higher in MLB_L (18 to 27%) compared to the other samples and had characteristically higher LPD chemical species (12 to 21%) (**Figures 7B,C**). CAR and UHC contents were highest in non-seep PKF-7 station (8%) and YP station (14%) comparatively and the greatest percentages of LGN (82%) were observed in OB-1 station (**Figures 7D–F**).

Percentages in CHO and CHOS based formulas were varied in a range from 34 to 49% and 3 to 12%, respectively except the YP bottom sample in which CHOS composition percent was 25% (**Figures 7G–I** and **Supplementary Figure S2**). CHON composition percentages were highest in the PKF and SS seep stations (35 to 43%). CHONS composition percentages were highest (23%) in non-seep PKF-7 station (**Figure 7J**).

NMDS analysis from Jaccard distances based on DOM composition revealed a high level of association at two dimensions (stress = 0.12). Samples from the same site/station displayed similar DOM composition (**Figure 8**). PERMANOVA test on Jaccard distances revealed that DOM compositions were most significantly ($p < 0.001$) associated with station (coefficient of determination $R^2 = 0.59$), site ($R^2 = 0.35$) and seep influence ($R^2 = 0.17$). Environmental variables that showed linear correlation to NMDS ordination scores were temperature, salinity, density, oxygen ($p < 0.001$), methane ($p < 0.019$), and DOC concentrations ($p < 0.028$). NMDS scores displayed significant correlations with chemical diversity, number of formulas, heteroatomic compositions and molecular species compositions of the samples ($p < 0.001$). The most variable DOM composition was found at the PKF seep sites explained by number of formulae and chemical diversity. NMDS biplot revealed that DOM composition of PKF seep samples displayed

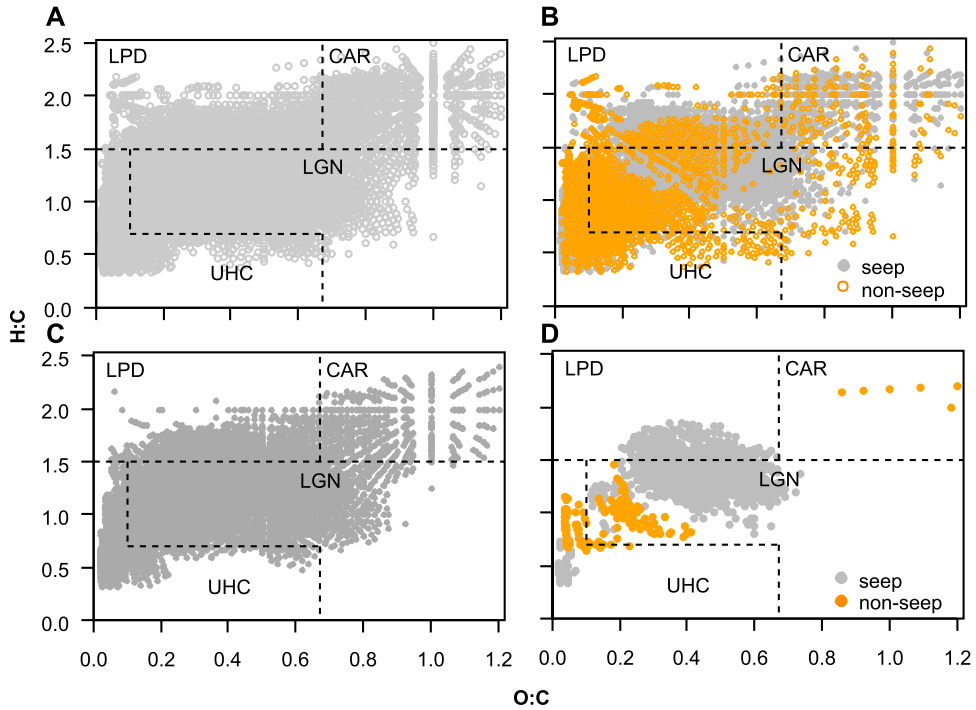

FIGURE 6 | (A) All assigned dissolved organic matter formulas in all samples **(B)** unique molecular formulas that are found in seep (grey) and non-seep (orange) samples **(C)** molecular formulas commonly found in seep and non-seep samples **(D)** Seep versus non-seep associated formulas based on comparisons by IndVal analysis (IndVal ≥ 0.7; $p \leq 0.01$). Each point in the diagrams represents a single formula assigned from one resolved mass spectral peak. Note: these van Krevelen diagrams contain molecular formulas from combined positive and negative mode ESI FT-ICR MS assignments. Abbreviations are LPD, lipid- and protein-like; CAR, carbohydrate-like; LGN, lignin- &tannin-like; UHC, unsaturated hydrocarbon- &condensed aromatic-like; O:C, oxygen to carbon ratio; H:C, hydrogen to carbon ratio.

positive correlation with the percentages of MLB_L, LPD, and CHON compositions (Student's t-test, $p < 0.01$) and OB samples were associated with higher aromaticity, LGN, and CHOS composition (Student's t-test, $p < 0.01$) (**Figure 8**).

DISCUSSION

Oceanographic Characteristics of the Study Sites

As the main driver of the hydrography, the West Spitsbergen Current (WSC) brings AW which gradually mixes with the locally formed cold fjord and shelf waters over the West Spitsbergen Shelf and the Arctic waters in Storfjordrenna and Barents Sea (Loeng, 1991; Harris et al., 1998). Therefore, the water column mainly comprises AW in PKF, VR, YP, SS, and SP sites (**Figure 2**). DW was dominant in the bottom part of YP, VR, SS, and SP (**Figure 3**). OB was the only region that was fully occupied by ArW. SW was present in all regions, except at PKF where the well-mixed water column was entirely occupied by AW.

Nutrients and Chl *a* concentrations were consistent with previous observations in the study sites (Hodal et al., 2012; Tremblay et al., 2015; Randelhoff et al., 2018). Higher nitrate/silicate ratios were apparent in AW (**Figure 4B**) implying earlier diatom uptake based on 1/1 demand on nitrate and silicate (Erga et al., 2014). Nevertheless, AW seems to be the main source of nutrients in virtue of higher average concentrations and well-developed Chl *a* sub-surface maxima in the stratified SP region. Ratio of particulate C/N/P – 83/7.6/1 **Figures 4A–D** in comparison to 106/16/1 - C/N/P Redfield ratio (Redfield, 1958) implies that the nitrogen was the limiting factor on primary production. Yet, the elevation of Chl *a* and the depletion of nitrate were associated with the increase in ammonia presumably by remineralisation and restored DIN/phosphate ratio back to the Redfield ratio of 16 (**Figure 4A**). This is also in agreement with the previous findings (Olsen et al. 2003) that defines depletion of nitrate as an indicator of blooms in AW, whereas phosphate and silicate ranges in similar pattern of variability.

Silicate demanding diatoms are the dominant producer in the upper layer of the ArW during the retraction of sea-ice and gradually sink to the deeper layers (Loeng and Drinkwater, 2007). Accordingly, minimum levels of nitrate/silicate ratios were found in ArW as average 2.57 ± 0.7 with depleted surface nutrients indicating a diatom bloom prior to sampling. As the Chl fluorescence peak at 40 m at OB indicates (**Figure 3B**), the active community of diatoms might have moved along the nitricline in late June.

Bulk concentrations of the dissolved organic matter (DOC, DON, DOP) did not indicate any distinct trend within the studied samples (**Figure 3E**). High percentages of LPD content and N-containing formulas at PKF were not directly correlated with the

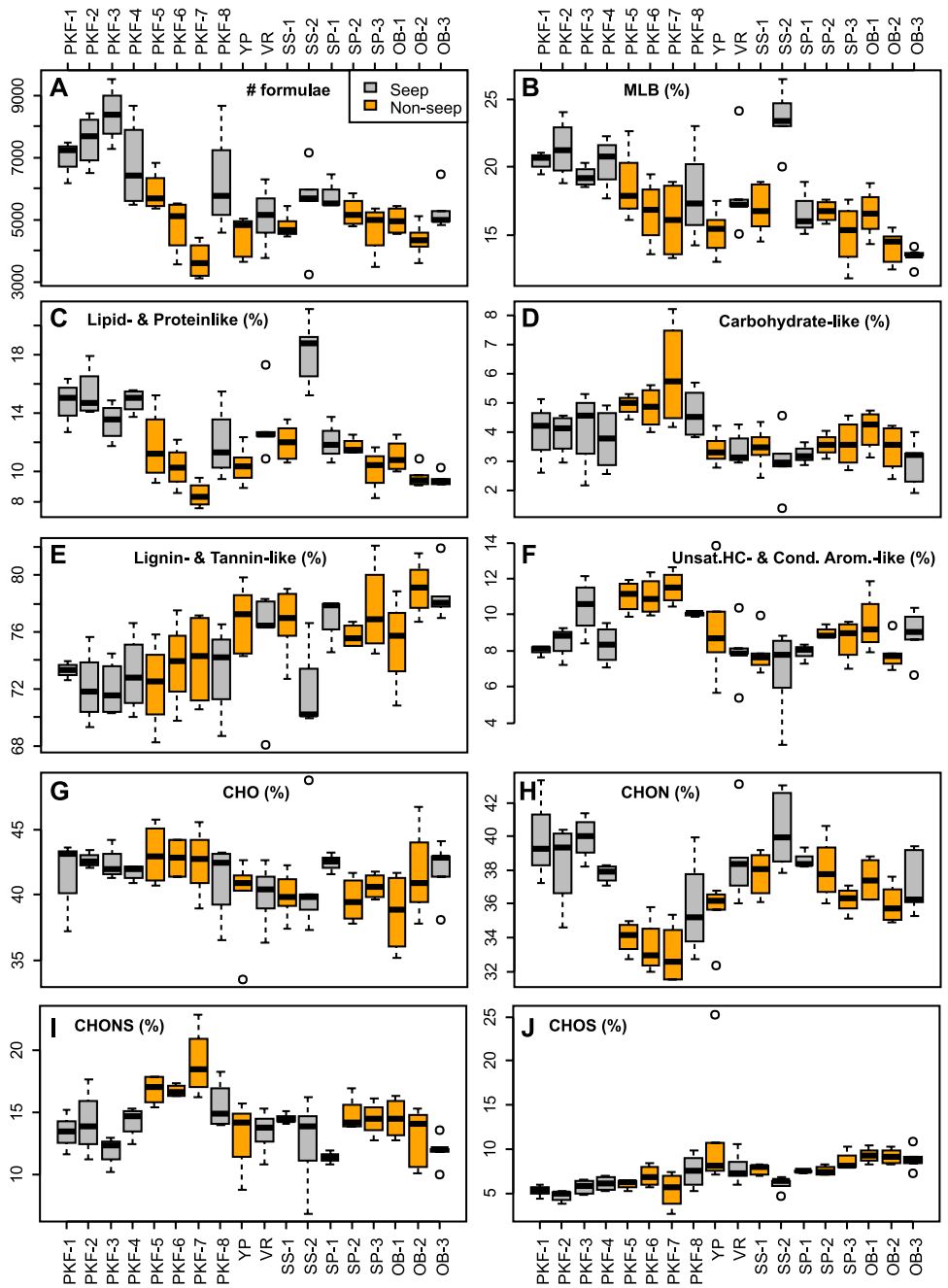

FIGURE 7 | Dissolved organic matter composition data determined by ESI FT-ICR MS organized by sampling stations shown as boxplots for **(A)** number of molecular formulas, **(B)** percentages of chemical lability (MLB_L; D'Andrilli et al., 2015) **(C–F)** chemical groups based on modified regions of characterization classes on van Krevelen diagrams (**Figure 2**), and **(G–J)** and heteroatomic content. Seep and non-seep stations are colored by grey and orange, respectively. Stations are abbreviated as given in **Table 1**.

bulk DON concentrations. As a proxy to primary production, Chl *a* concentrations did not show any detectable correlation with the DOM compositions. Chl peaks at SP and the previous diatom bloom at OB were not linked with any unique DOM composition. A similar DOM molecular composition can arise from many biotic processes and these findings may be due to the simultaneous bacterial consumption that follows bio-labile, autochthonous production of DOM. This result is consistent with the previous observation by Osterholz et al. (2014) in Arctic fjords which suggested rapid transformation of DOM by the microbial community without any detectable imprint in neither DOM compositions nor bulk concentrations.

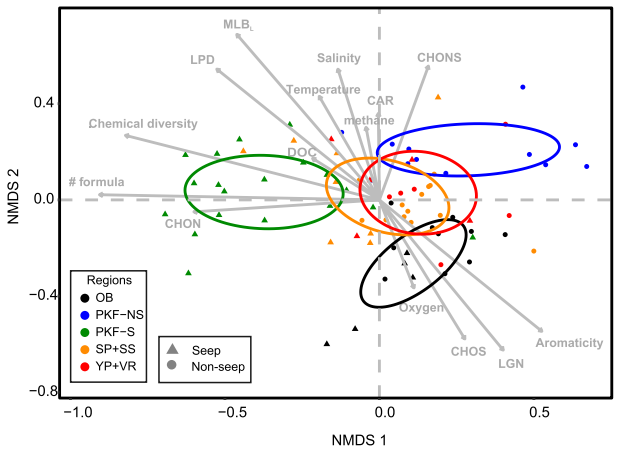

FIGURE 8 | Non-metric multidimensional scaling (NMDS) biplot of Jaccard distances from the presence/absence matrix of dissolved organic matter molecular formula compositions containing $C_cH_hN_nO_oS_s$ by ESI FT-ICR MS. Samples are coded by colour and shape for site and seepage influence, respectively. Arrow vectors represent environmental variables (oxygen, DOC, temperature, salinity, and methane concentration), numerical observations (number of formulas, chemical diversity, aromaticity (Hockaday et al., 2009)) and molecular percentages (CHOS, CHON, CHONS, LPD, LGN, CAR, MLB_L,) that show significant correlation ($p < 0.05$) with the NMDS scores. Coloured ellipses represent 95% confidence interval of the group centroids. Abbreviations are LPD, lipid- and protein-like; CAR, carbohydrate-like; LGN, lignin-&tannin-like; UHC, unsaturated hydrocarbon- &condensed aromatic-like; DOC, dissolved organic carbon; MLB_L, percentages of formulas above the molecular lability boundary (D'Andrilli et al. 2015).

Effect of Hydrography on Methane Concentrations and Methane Oxidation Distributions

Spatial and temporal variability of MOx was shown to be high on the continental margin of Svalbard and at PKF in previous studies where MOx rates were reported between 0.001 and up to 3.2 nM/day (Steinle et al., 2015; Ferré et al., 2020). Our MOx rates from the PKF site (max 0.23 nM/day) were low compared to overall ranges (**Supplementary Table S2**). Rather than elevated methane concentrations, which were not entirely related to high MOx rates, the size of a MOB community may be the more relevant factor of an active MOB community (Steinle et al., 2015). Moreover, the succession of MOB communities depends largely on circulation patterns and water column hydrography (Steinle et al., 2015; Silyakova et al., 2020). In accordance with this, we observed in our study site-specific positive correlations between methane concentrations and MOx rates at PKF and SP (**Figure 4H**). MOx was 10 times more efficient at SP (rate constant $k_{MOx} = 6 \times 10^{-3}\,day^{-1}$) than in PKF ($k_{MOx} = 6 \times 10^{-4}\,ay^{-1}$), presumably due to the difference in the hydrography or the size of methanotrophic community. At SP, a well-defined pycnocline (**Figure 4A** SP-3 panel) hindered the transport of gas bubbles to upper layers (Damm et al., 2005; Damm et al., 2008; Gentz et al., 2014; Jansson et al., 2019) whereas the vertical transport of methane was easier in uniform and shallow water column at PKF (**Figure 4A** PKF-2 panel).

Notably, water column stratification and the size of the MOB were possibly not the only parameters affecting MOB efficiency. Since MOx activity was rapidly exhausted at the bottom of SP well before reaching the pycnocline (~100 m above bottom; **Figure 3F** SP-3 panel). Water mass distribution and current regimes were different between sites. DW occupied the bottom of SP, whereas PKF was entirely composed of AW (**Figure 3A**). As previously reported, PKF is influenced by WSC with a strong monthly mean current velocity of 0.2 m/s (von Appen et al., 2016) continuously transporting MOB populations northwards out of the PKF area (Graves et al., 2015; Steinle et al., 2015). In contrast, the mean geostrophic velocity at SP is in the range of 0.02–0.07 m/s (Skogseth et al., 2005; Skogseth et al., 2007). Longer residence times possibly facilitates MOB to metabolize methane more efficiently, therefore higher MOx rates were observed at SP (**Figure 3F**). MOx was undetected in OB even above the seeps with high methane concentrations (**Figure 3F**) indicating that a substantial active population of MOB in OB was not present (note that we did not determine MOB community sizes in our survey).

Evaluation of Dissolved Organic Matter Compositions

Analysis of DOM with ESI FT-ICR MS provides a qualitative assessment of molecular-level elemental composition linked to the ionization efficiency of polar constituents of the sample and experimental settings. Using ESI FT-ICR MS, we determined chemical composition, interpreted chemical characteristics, and evaluated the presence or absence of molecular formulas to qualitatively understand DOM composition in the water column at the different sampling sites.

DOM molecular composition patterns were consistent with those of previous reports (Hertkorn et al., 2013; Osterholz et al., 2014; D'Andrilli et al., 2015; Kujawinski et al., 2016), having characteristically large percentages of LGN compounds (68–82%, **Figures 6**, **7E**). Although the FT-ICR MS instrument does not generate structural DOM data, naturally occurring chemical possibilities of CHNOS molecular formula indicate the potential for polycarboxylated substances such as lignins, tannins, terpenes, and carboxyl-rich alicyclic molecules (CRAM) that share similar structural information with a wide range of eukaryotic and prokaryotic membrane constituents and secondary metabolites (Hertkorn et al., 2006). These groups of chemical species are derived from decades of accumulated microbial degradation products which ultimately lead to similar compositional patterns in many marine environments (Koch et al., 2005).

Formulas interpreted as LPD and CAR (12 to 27%, **Figures 6**, **7B–D**) with more hydrogen saturation (H:C ≥ 1.5) are considered to comprise of bio-labile species (D'Andrilli et al., 2015) and likely indicate recent autochthonous microbial production (hours to days). Bio-labile DOM is considered to be most energetically favorable for microbial uptake or for extracellular degradation (Koch et al., 2014; Carlson and Hansell, 2015) and therefore its chemical composition provides insight about the potential biological patterns of seep versus non-seep sites. Accordingly, LPD chemical species were found with greater atomic heterogeneity in seep sites (**Figures 7G–J**) indicating higher

potential for seep-driven microbial activity (Kujawinski, 2011; D'Andrilli et al., 2019).

Three to 14% of the formulas were interpreted as UHC in all samples and similarly represented in seep and non-seep stations (**Figure 7F**). DOM of this type is most likely generated by legacy sinking of refractory materials (from a microbial perspective), undergoing no further biological degradation, e.g., the end-products of biomass combustion or petrogenic/pyrogenic origin, which were thermally fused in the deep layers of sediment and mechanically brought up into the water column by bubbles and seeping fluids.

All DOM sample molecular compositions were predominantly grouped by site and seep influence (**Figure 8**). The largest dissimilarity in molecular composition was between the PKF-S (seep stations in PKF) and PKF-NS (non-seep stations in PKF) sites across NMDS-1 axis which correlated with the number of formulas, N-containing composition (see **Figure 7H**) and chemical diversity (**Figure 8**). On the diagonal axis between NMDS-1 and NMDS-2, OB DOM composition grouped separately with explained differences positively correlating with the aromaticity, oxygen, CHOS content, and LGN composition. That diagonal axis also implies the correlation of MLB_L and LPD composition with the seep samples in PKF and SS. Therefore, we relate higher number of molecular formulas, chemical diversity, CHON composition, and LPD chemical species to unique DOM production at the seep sites. This pattern was most pronounced at PKF-S possibly due to prevalent seepage activity combined with strong ventilation at the shallow water column. We observed a similar pattern also at SS-2 where DOM composition displayed considerably high percentages of bio-labile nature (LPD) compared to the non-seep station SS-1 (**Figure 7C**). This provides evidence that seep-related microbial processes may have a significant influence on DOM composition with more bio-labile and nitrogen composition.

We suggest that the combination of positive and negative mode ESI contributed greatly to identifying distinct DOM molecular formulas at seep and non-seep sites. CHO and CHON chemical species were more efficiently ionized in positive ESI (**Supplementary Figure S5**) and provided a more comprehensive analysis of the DOM composition of all samples. Negative ESI is more frequently used in marine DOM research due to its better ionization efficiency of acidic and carboxylic compounds (Sleighter and Hatcher, 2007). However, more information about the polar fraction of marine DOM as well as other natural environments is gained by combining positive and negative ESI FT-ICR MS data sets (Hertkorn et al., 2013; Ohno et al., 2016).

In addition, positive ESI FT-ICR MS also detected unique CHOS composition near the bottom of the YP station (**Supplementary Figure S4**). These chemical species can be considered as 'black sulphur' due to compositional similarity with black carbon and black nitrogen in the condensed aromatics region of the van Krevelen diagram having large hydrogen deficiency and limited oxygenation (Hertkorn et al., 2013; Hertkorn et al., 2016). Although the origin of these chemical species is not known, high sulfur content suggests that anoxic sedimentary microbial processes may play a role in their production.

Do Cold Seeps Alter Dissolved Organic Matter Composition?

Cold seeps in the Arctic Ocean originate from a variety of sources and geochemical mechanisms (Bünz et al., 2012; Sahling et al., 2014; Serov et al., 2015; Andreassen et al., 2017; Panieri et al., 2017). Seeping fluids consist of predominantly methane (99.7–99.9%), yet other hydrocarbons and sulphurous compounds may also migrate with seeping fluids and methane, all of which provide a source for chemosynthetic organisms (Levin, 2005; Vanreusel et al., 2009; Panieri et al., 2017; Sen et al., 2018; Åström et al., 2018). Seeping gases form bubbles and rise up through the water column (Westbrook et al., 2009; Berndt et al., 2014). Along its trajectory towards the upper layers, methane exchanges with more abundant dissolved gases such as nitrogen, enriched in the surrounding water and promotes MOx (James et al., 2016; Steinle et al., 2016; Jansson et al., 2019). Hydroacoustic surveys demonstrated that seeps can stay active for weeks to decades (Gentz et al., 2014; Veloso-Alarcón et al., 2019) however, the fate of methane at active flares sites is highly dependent on bubble size, salinity, and water velocity (Jansson et al., 2019). Therefore, considering the effects of ocean currents, upwelling, or redox changes, availability of methane for MOB can be sporadic and the potential rates may not be maintained persistently (Reeburgh, 2007; Mau et al., 2013; Steinle et al., 2015; Steinle et al., 2016; Steinle et al., 2017). For this reason, seep influence on DOM composition was not always directly linked to methane concentration, and seep versus non-seep definition was solely based on echosounder data. Since MOx is the main removal mechanism of dissolved methane in the water column, low concentration of methane at seep stations (e.g., VR) may indicate efficient microbial filtering which eliminates methane simultaneous to its dispersion. Oppositely, high concentration of methane at non-seep stations (e.g., SP-3, PKF-5, and PKF-6; see **Supplementary Figure S2A**) may indicate inefficiency of MOx or advection of MOB by currents.

We found a significant correlation between seep activity and DOM composition in terms of its bio-lability, chemical diversity, number of formulas and LPD as well as CHON formula contents (**Figures 7**, **8**). Naturally, MOx is a likely mechanism driving variation in DOM compositions at seep and non-seep stations. However, correlation between seep activity and DOM composition was not observed directly by MOx rates or methane concentrations (**Supplementary Figure S2**). For instance, despite the differences in DOM compositions, non-seep stations in PKF and SP had similar ranges of MOx rates with the seep stations in the same sites (**Supplementary Figure S2B**). One possible explanation may be the dynamic hydrography and consequent elimination of MOx in the region (Steinle et al., 2015). All observed ranges of methane concentrations and MOx rates were low during our survey compared to the results reported at Berndt et al. (2014) and Steinle et al. (2015) and slightly higher than Ferré et al. (2020). However, it is possible that distinct DOM composition associated with MOx activity would persist even if MOB communities diminished, MOx rates decreased, and lower concentrations of methane were measured. In effect, this may lead to a "legacy" fingerprint of methane-influenced DOM composition in the water column, which may be considerably diverse. Therefore, we

attribute the largest variety of DOM compositions for seep vs. non-seep comparisons to a multitude of biogeochemical factors rather than one driving variable such as MOx rates or methane concentration. This effect was most noticeable at PKF where the contrast in seepage activity (number of active seeps; see **Figure 1**) and DOM composition was highly variable from seep to non-seep locations.

Although we hypothesised that MOx would be the main cause of the compositional differences of DOM in seep sites to non-seep sites, other mechanisms may contribute to DOM signatures such as seep-driven primary production. Pohlman et al. (2017) showed that the carbon dioxide uptake rate was two times higher at the seep site of PKF than at the non-seep coastal site. They suggested that stimulation of primary production and consequent decrease of the carbon dioxide level were enhanced with the contribution of methane-enriched bottom waters. The compositional differences we observed might support this hypothesis since more bio-labile and heterogeneous composition may be an indication of fresh primary production at the seep site. However, similar to the MOx rates and methane concentrations, Chl *a* concentration, Chl fluorescence, or nutrient concentrations did not display any noticeable trend from seep to non-seep sites (**Supplementary Figure S1**).

Seeping DOM is another possible mechanism for the compositional differences at seep and non-seep sites. Sedimentary methanotrophic microbes are predominantly anaerobic (Knittel and Boetius, 2009) and likely produce chemical species, different from the metabolites released from active MOB in the overlaying methane-rich water masses. Sedimentary-derived metabolites reach the upper water layers by ventilation due to the upstream of bubbles and vertical mixing, thereby potentially modifying the DOM composition at seep sites. Seeping DOM and consequent compositional differences were previously shown in hydrothermal vents by stable carbon isotope analyses, highlighting the role of crustal microbial communities in DOM synthesis, strong enough to change the compositional character of the overlying ocean (McCarthy et al., 2011). Similarly, Pohlman et al., (2011) showed the contribution of sedimentary DOC flux from methane hydrate seeps to the deep seawater. However, both studies indicated that carbon flux from the sediment was ^{14}C-depleted, considerably aged (5,000 to 15,000 years) and possibly consisting of recalcitrant nature which may be contributing to the LGN chemical species observed at the seep sites.

Lastly, DOM composition may be affected by seep-driven microbial modifications. For instance, continuous methane flow from the seafloor might disturb higher trophic level organisms which feed on DOM consumers and autochthonous DOM producers enumerate rapidly above seeps. To our knowledge, this theory has not been previously studied at seep sites. However, in glucose augmented incubation experiments, Kujawinski et al. (2016) showed that organisms larger than 1.0 μm dominantly affected the bacterial diversity and the DOM composition in seawater. They found that the DOM composition was comprised of lipid- and peptide-like chemical species in <1.0 μm filtered surface sea water during the nine days incubation. Unfortunately, despite the number of studies on MOB taxonomy (Kalyuzhnaya et al., 2019), DOM composition coupling with other microbes and higher organisms remains unknown.

Overall, the mechanisms of different DOM compositions at seep and non-seep sites are likely a combination of many factors. MOx, seep fertilization, seep-driven microbial modifications, and seeping of sedimentary DOM are identified here as possible factors. DOM reflects a number of geochemical and molecular processes on different timescales and potentially years of aggregation whereas seep-driven processes are site specific and may only persist on shorter timescales. Therefore, the modification of DOM by seep-driven processes and relative contribution on total water column biogeochemistry is difficult to capture *in situ* when the other factors are not constrained. Controlled experiments with constrained effects may target the exact products more specifically.

SUMMARY AND CONCLUSION

Cold seeps are being studied intensively due to the possible influence of escaping methane on atmospheric gas compositions and consequent effect on global climate change. Our investigation in the water column showed that the direct and indirect impacts of seeping fluids are also evident for water column biogeochemical concentrations and DOM composition. Our findings at cold seeps of the continental shelf of Svalbard and in the Barents Sea revealed that DOM composition is associated with methane influenced water column activity and spatial distribution of active seeps. DOM appeared more bio-labile and had higher chemical diversity and LPD composition at seeps compared to non-seep areas. Compositional differences of DOM between seep and non-seep sites might be related to a multitude of environmental factors such as MOx, seep fertilization, seep-driven microbial modifications, and seeping of sedimentary DOM. However, no single process was identified as the sole mechanism for unique DOM composition at these sites. DOM composition did not directly correlate to Chl *a*, nutrient concentration, or water temperature, but the hydrography and the nutrient distributions confirmed the local influences of main water masses and primary production cycles.

The underlying mechanisms of seep influence on DOM compositions are yet to be elaborated in controlled laboratory experiments. In order to link the production and consumption of DOM composition to certain seep-specialized microbial groups, incubation experiments with controlled variables (e.g., microbial cultures, temperatures, methane and nutrient concentrations) and further metabolomics analyses on microbe vs. DOM interactions are needed. Expectedly, combinations of all ongoing processes and co-occurring microbial consortia are extremely complex and possibly hinder identifiable interactions on DOM compositions, however in our study, we showed that unique seep DOM compositions and character can be identified. We recommend the analysis technique of ultrahigh resolution mass spectrometry that we used for our analyses as a

promising tool to decipher methane seep associated patterns at the molecular level. Moreover, our combination of biological and chemical techniques provided insight into methane-driven biogeochemical DOM processes in the ocean water column.

DATA AVAILABILITY STATEMENT

The data and the code for statistical analyses are available in the UiT Open Research Data repository in Sert et al. (2020).

AUTHOR CONTRIBUTIONS

MS, FG, AS, and HN designed the study. MS, FG, and HN collected samples. FG and HN measured methane oxidation rates. JD analyzed dissolved organic matter samples, generated formula lists and wrote mass spectrometry methodology. MS wrote the paper with considerable input from JD, FG, HN, MG, AP, BF, and AS.

FUNDING

This study is funded by the Research Council of Norway through CAGE (Centre for Gas Hydrate, Environment and Climate) project number 223259. The publication charges for this article have been funded by a grant from the publication fund of UiT The Arctic University of Norway. AP and MG were supported by the Norwegian Polar Institute and the Polish-Norwegian Research Programme operated by the National Centre for Research and Development under the Norwegian Financial Mechanism 2009–2014 in the frame of project contract Pol–Nor/197511/40/ 2013, CDOM-HEAT.

ACKNOWLEDGMENTS

We would like to acknowledge the crew of R/V Helmer Hanssen during the cruises CAGE-17-1 and CAGE-17-2 and chief scientists Tine Rasmussen and Giuliana Panieri. We thank Colin A. Stedmon for DOC concentration analyses and valuable discussion on DOM dynamics. Authors would like to thank Jorun Karin Egge, Sigrid Øygarden, Matteus Lindgren, and Linda Fonnes Lunde for the analyses of particulate matter, chlorophyll *a*, methane and nutrients. FT-ICR mass spectra were generated at the National High Magnetic Field Laboratory (NHMFL), Tallahassee, FL, United States, supported by funding through the National Science Foundation Division of Materials Research 1644779 and the State of Florida. We acknowledge Dr. Rebecca Ware and the Ion Cyclotron Resonance Facility Staff at the NHMFL for FT-ICR MS instrument support and data processing challenges.

SUPPLEMENTARY MATERIAL

The Supplementary Material for this article can be found online at: https://www.frontiersin.org/articles/10.3389/feart.2020.552731/full#supplementary-material.

REFERENCES

Amon, R. M. W., and Benner, R. (1994). Rapid cycling of high-molecular-weight dissolved organic matter in the ocean. *Nature* 369, 549–552. doi:10.1038/369549a0

Andreassen, K., Hubbard, A., Winsborrow, M., Patton, H., Vadakkepuliyambatta, S., Plaza-Faverola, A., et al. (2017). Massive blow-out craters formed by hydrate-controlled methane expulsion from the Arctic seafloor. *Science* 356, 948–953. doi:10.1126/science.aal4500

Åström, E. K. L., Carroll, M. L., Ambrose, W. G., Sen, A., Silyakova, A., and Carroll, J. (2018). Methane cold seeps as biological oases in the high-Arctic deep sea. *Limnol. Oceanogr.* 63, S209–S231. doi:10.1002/lno.10732

Berndt, C., Feseker, T., Treude, T., Krastel, S., Liebetrau, V., Niemann, H., et al. (2014). Temporal constraints on hydrate-controlled methane seepage off svalbard. *Science* 343, 284–287. doi:10.1126/science.1246298

Bünz, S., Polyanov, S., Vadakkepuliyambatta, S., Consolaro, C., and Mienert, J. (2012). Active gas venting through hydrate-bearing sediments on the vestnesa ridge, offshore w-svalbard. *Mar. Geol.* 332-334, 189–197. doi:10.1016/j.margeo.2012.09.012

Carlson, C. A., Ducklow, H. W., and Michaels, A. F. (1994). Annual flux of dissolved organic carbon from the euphotic zone in the northwestern Sargasso Sea. *Nature* 371, 405–408. doi:10.1038/371405a0

Carlson, C. A., Hansell, D. A., Nelson, N. B., Siegel, D. A., Smethie, W. M., Khatiwala, S., et al. (2010). Dissolved organic carbon export and subsequent remineralization in the mesopelagic and bathypelagic realms of the north atlantic basin. *Deep Sea Res. Part II Top. Stud. Oceanogr.* 57, 1433–1445. doi:10.1016/j.dsr2.2010.02.013

Carlson, C. A., and Hansell, D. A. (2015). "Chapter 3 - DOM sources, sinks, reactivity, and budgets," in *Biogeochemistry of marine dissolved organic matter*. 2nd Edn, Editors D. A. Hansell and C. A. Carlson (Boston, MA: Academic Press), 65–126.

Corilo, Y. (2014). *PetroOrg software*. Tallahassee, FL: Florida State University, Omics LLC.

Damm, E., Mackensen, A., Budéus, G., Faber, E., and Hanfland, C. (2005). Pathways of methane in seawater: plume spreading in an Arctic shelf environment (SW-Spitsbergen). *Continent. Shelf Res.* 25, 1453–1472. doi:10.1016/j.csr.2005.03.003

Damm, E., Kiene, R. P., Schwarz, J., Falck, E., and Dieckmann, G. (2008). Methane cycling in Arctic shelf water and its relationship with phytoplankton biomass and DMSP. *Mar. Chem.* 109, 45–59. doi:10.1016/j.marchem.2007.12.003

De Cáceres, M., and Legendre, P. (2009). Associations between species and groups of sites: indices and statistical inference. *Ecology* 90, 3566–3574. doi:10.1890/08-1823.1

Dittmar, T., Koch, B., Hertkorn, N., and Kattner, G. (2008). A simple and efficient method for the solid-phase extraction of dissolved organic matter (SPE-DOM) from seawater. *Limnol. Oceanogr. Methods* 6, 230–235. doi:10.4319/lom.2008.6

D'Andrilli, J., Cooper, W. T., Foreman, C. M., and Marshall, A. G. (2015). An ultrahigh-resolution mass spectrometry index to estimate natural organic matter lability: FTICRMS organic matter molecular lability index. *Rapid Commun. Mass Spectrom.* 29, 2385–2401. doi:10.1002/rcm.7400

D'Andrilli, J., Junker, J. R., Smith, H. J., Scholl, E. A., and Foreman, C. M. (2019). DOM composition alters ecosystem function during microbial processing of isolated sources. *Biogeochemistry* 142 (2), 281–298. doi:10.1007/s10533-018-00534-5

Erga, S. R., Ssebiyonga, N., Hamre, B., Frette, Ø., Rey, F., and Drinkwater, K. (2014). Nutrients and phytoplankton biomass distribution and activity at the Barents Sea polar front during summer near hopen and storbanken. *J. Mar. Syst.* 130, 181–192. doi:10.1016/j.jmarsys.2012.12.008

Fer, I., Skogseth, R., Haugan, P. M., and Jaccard, P. (2003). Observations of the storfjorden overflow. *Deep Sea Res. Oceanogr. Res. Pap.* 50, 1283–1303. doi:10.1016/S0967-0637(03)00124-9

Ferré, B., Jansson, P. G., Moser, M., Serov, P., Portnov, A., Graves, C. A., et al. (2020). Reduced methane seepage from Arctic sediments during cold bottom-water conditions. *Nat. Geosci.* 13, 144–148. doi:10.1038/s41561-019-0515-3

Ferré, B., Mienert, J., and Feseker, T. (2012). Ocean temperature variability for the past 60 years on the norwegian-svalbard margin influences gas hydrate stability on human time scales: bottom water temperature and gas hydrate. *J. Geophys. Res. Oceans* C10017. doi:10.1029/2012jc008300

Gentz, T., Damm, E., Schneider von Deimling, J., Mau, S., McGinnis, D. F., and Schlüter, M. (2014). A water column study of methane around gas flares located at the West Spitsbergen continental margin. *Continent. Shelf Res.* 72, 107–118. doi:10.1016/j.csr.2013.07.013

Grasshoff, K., Kremling, K., and Ehrhardt, M. (1999). *Methods of seawater analysis. 3rd, completely revised and enlarged edition*. New York, NY: Wiley VCH.

Graves, C. A., Steinle, L., Rehder, G., Niemann, H., Connelly, D. P., Lowry, D., et al. (2015). Fluxes and fate of dissolved methane released at the seafloor at the landward limit of the gas hydrate stability zone offshore western svalbard: dissolved methane OFF western svalbard. *J. Geophys. Res. Oceans* 120, 6185–6201. doi:10.1002/2015JC011084

Hanson, R. S., and Hanson, T. E. (1996). Methanotrophic bacteria. *Microbiol. Rev.* 60, 439–471. doi:10.1128/mmbr.60.2.439-471

Harris, C. L., Plueddemann, A. J., and Gawarkiewicz, G. G. (1998). Water mass distribution and polar front structure in the western Barents Sea. *J. Geophys. Res.* 103, 2905–2917. doi:10.1029/97JC02790

Hertkorn, N., Benner, R., Frommberger, M., Schmitt-Kopplin, P., Witt, M., Kaiser, K., et al. (2006). Characterization of a major refractory component of marine dissolved organic matter. *Geochem. Cosmochim. Acta* 70, 2990–3010. doi:10.1016/j.gca.2006.03.021

Hertkorn, N., Harir, M., Koch, B. P., Michalke, B., and Schmitt-Kopplin, P. (2013). High-field NMR spectroscopy and FTICR mass spectrometry: powerful discovery tools for the molecular level characterization of marine dissolved organic matter. *Biogeosciences* 10, 1583–1624. doi:10.5194/bg-10-1583-2013

Hertkorn, N., Harir, M., Cawley, K. M., Schmitt-Kopplin, P., and Jaffé, R. (2016). Molecular characterization of dissolved organic matter from subtropical wetlands: a comparative study through the analysis of optical properties, NMR and FTICR/MS. *Biogeosciences* 13, 2257–2277. doi:10.5194/bg-13-2257-2016

Hockaday, W. C., Purcell, J. M., Marshall, A. G., Baldock, J. A., and Hatcher, P. G. (2009). Electrospray and photoionization mass spectrometry for the characterization of organic matter in natural waters: a qualitative assessment. *Limnol. Oceanogr. Methods* 7, 81–95. doi:10.4319/lom.2009.7.81

Hodal, H., Falk-Petersen, S., Hop, H., Kristiansen, S., and Reigstad, M. (2012). Spring bloom dynamics in Kongsfjorden, Svalbard: nutrients, phytoplankton, protozoans and primary production. *Polar Biol.* 35, 191–203. doi:10.1007/s00300-011-1053-7

Hodgkins, S. B., Tfaily, M. M., Podgorski, D. C., McCalley, C. K., Saleska, S. R., Crill, P. M., et al. (2016). Elemental composition and optical properties reveal changes in dissolved organic matter along a permafrost thaw chronosequence in a subarctic peatland. *Geochem. Cosmochim. Acta* 187, 123–140. doi:10.1016/j.gca.2016.05.015

Holm-Hansen, O., Lorenzen, C. J., Holmes, R. W., and Strickland, J. D. H. (1965). Fluorometric determination of chlorophyll. *ICES J. Mar. Sci.* 30, 3–15. doi:10.1093/icesjms/30.1.3

Holm-Hansen, O. and Riemann, B. (1978). Chlorophyll a determination: improvements in methodology. *Oikos* 30, 438–447. doi:10.2307/3543338

Jaccard, P. (1912). The distribution of the flora in the alpine zone.1. *New Phytol.* 11, 37–50. doi:10.1111/j.1469-8137.1912.tb05611.x

James, R. H., Bousquet, P., Bussmann, I., Haeckel, M., Kipfer, R., Leifer, I., et al. (2016). Effects of climate change on methane emissions from seafloor sediments in the Arctic Ocean: a review. *Limnol. Oceanogr.* 61, S283–S299. doi:10.1002/lno.10307

Jansson, P., Ferré, B., Silyakova, A., Dølven, K. O., and Omstedt, A. (2019). A new numerical model for understanding free and dissolved gas progression toward the atmosphere in aquatic methane seepage systems: marine two-phase gas model in one dimension. *Limnol. Oceanogr. Methods* 17, 223. doi:10.1002/lom3.10307

Kalyuzhnaya, M. G., Gomez, O. A., and Murrell, J. C. (2019). "The methane-oxidizing bacteria (methanotrophs)," in *Taxonomy, genomics and ecophysiology of hydrocarbon-degrading microbes handbook of hydrocarbon and lipid microbiology*. Editor T. J. McGenity (Cham, Switzerland: Springer International Publishing), 1–34.

Kalyuzhnaya, M. G., Yang, S., Rozova, O. N., Smalley, N. E., Clubb, J., Lamb, A., et al. (2013). Highly efficient methane biocatalysis revealed in a methanotrophic bacterium. *Nat. Commun.* 4, 2785. doi:10.1038/ncomms3785

Kim, S., Kramer, R. W., and Hatcher, P. G. (2003). Graphical method for analysis of ultrahigh-resolution broadband mass spectra of natural organic matter, the van krevelen diagram. *Anal. Chem.* 75, 5336–5344. doi:10.1021/ac034415p

Knittel, K., and Boetius, A. (2009). Anaerobic oxidation of methane: progress with an unknown process. *Annu. Rev. Microbiol.* 63, 311–334. doi:10.1146/annurev.micro.61.080706.093130

Koch, B. P., Kattner, G., Witt, M., and Passow, U. (2014). Molecular insights into the microbial formation of marine dissolved organic matter: recalcitrant or labile?. *Biogeosciences* 11, 4173–4190. doi:10.5194/bg-11-4173-2014

Koch, B. P., Witt, M., Engbrodt, R., Dittmar, T., and Kattner, G. (2005). Molecular formulae of marine and terrigenous dissolved organic matter detected by electrospray ionization Fourier transform ion cyclotron resonance mass spectrometry. *Geochem. Cosmochim. Acta* 69, 3299–3308. doi:10.1016/j.gca.2005.02.027

Kujawinski, E. B. (2011). The impact of microbial metabolism on marine dissolved organic matter. *Annu. Rev. Mar. Sci.* 3, 567–599. doi:10.1146/annurev-marine-120308-081003

Kujawinski, E. B., Longnecker, K., Barott, K. L., Weber, R. J. M., and Kido Soule, M. C. (2016). Microbial community structure affects marine dissolved organic matter composition. *Front. Mar. Sci.* 3. doi:10.3389/fmars.2016.00045

Lê, S., Josse, J., and Husson, F. (2008). FactoMineR: a package for multivariate analysis. *J. Stat. Software* 25, 1–18. doi:10.18637/jss.v025.i01

Lechtenfeld, O. J., Kattner, G., Flerus, R., McCallister, S. L., Schmitt-Kopplin, P., and Koch, B. P. (2014). Molecular transformation and degradation of refractory dissolved organic matter in the Atlantic and Southern Ocean. *Geochem. Cosmochim. Acta* 126, 321–337. doi:10.1016/j.gca.2013.11.009

Levin, L. A. (2005). Ecology of cold seep sediments: interactions of fauna with flow, chemistry and microbes. *Oceanogr. Mar. Biol.* 43, 1–46. doi:10.1201/9781420037449-3

Loeng, H., and Drinkwater, K. (2007). An overview of the ecosystems of the Barents and Norwegian Seas and their response to climate variability. *Deep Sea Res. Part II Top. Stud. Oceanogr.* 54, 2478–2500. doi:10.1016/j.dsr2.2007.08.013

Loeng, H. (1991). Features of the physical oceanographic conditions of the Barents Sea. *Polar Res.* 10, 5–18. doi:10.3402/polar.v10i1.6723

Marshall, A. G., and Verdun, F. R. (1990). *Fourier transforms in NMR, optical, and mass spectrometry*. Amsterdam, Netherlands: Elsevier.

Mau, S., Blees, J., Helmke, E., Niemann, H., and Damm, E. (2013). Vertical distribution of methane oxidation and methanotrophic response to elevated methane concentrations in stratified waters of the arctic fjord storfjorden (Svalbard, Norway). *Biogeosciences* 10, 6267–6278. doi:10.5194/bg-10-6267-2013

McCarthy, M. D., Beaupré, S. R., Walker, B. D., Voparil, I., Guilderson, T. P., and Druffel, E. R. M. (2011). Chemosynthetic origin of 14C-depleted dissolved organic matter in a ridge-flank hydrothermal system. *Nat. Geosci.* 4, 32–36. doi:10.1038/ngeo1015

Murrell, J. C. (20101953–1966). "The aerobic methane oxidizing bacteria (methanotrophs)," in *Handbook of hydrocarbon and lipid microbiology*. Editor K. N. Timmis (Berlin, Heidelberg: Springer).

Myhre, C. L., Ferré, B., Platt, S. M., Silyakova, A., Hermansen, O., Allen, G., et al. (2016). Extensive release of methane from Arctic seabed west of Svalbard during summer 2014 does not influence the atmosphere. *Geophys. Res. Lett.* 43, 4624. doi:10.1002/2016GL068999

Niemann, H., Steinle, L., Blees, J., Bussmann, I., Treude, T., Krause, S., et al. (2015). Toxic effects of lab-grade butyl rubber stoppers on aerobic methane oxidation. *Limnol. Oceanogr. Methods* 13, 40–52. doi:10.1002/lom3.10005

Ohno, T., Sleighter, R. L., and Hatcher, P. G. (2016). Comparative study of organic matter chemical characterization using negative and positive mode electrospray ionization ultrahigh-resolution mass spectrometry. *Anal. Bioanal. Chem.* 408, 2497–2504. doi:10.1007/s00216-016-9346-x

Oksanen, J., Blanchet, F. G., Friendly, M., Kindt, R., Legendre, P., McGlinn, D., et al. (2018). Vegan: community ecology package. Available at: https://CRAN.R-project.org/package=vegan.

Olsen, A., Johannessen, T., and Rey, F. (2003). On the nature of the factors that control spring bloom development at the entrance to the Barents Sea and their interannual variability. *Sarsia* 88, 379–393. doi:10.1080/00364820310003145

Osterholz, H., Dittmar, T., and Niggemann, J. (2014). Molecular evidence for rapid dissolved organic matter turnover in Arctic fjords. *Mar. Chem.* 160, 1–10. doi:10.1016/j.marchem.2014.01.002

Panieri, G., Bünz, S., Fornari, D. J., Escartin, J., Serov, P., Jansson, P., et al. (2017). An integrated view of the methane system in the pockmarks at Vestnesa Ridge, 79°N. *Mar. Geol.* 390, 282–300. doi:10.1016/j.margeo.2017.06.006

Paulino, A. I., Heldal, M., Norland, S., and Egge, J. K. (2013). Elemental stoichiometry of marine particulate matter measured by wavelength dispersive X-ray fluorescence (WDXRF) spectroscopy. *J. Mar. Biol. Ass.* 93, 2003–2014. doi:10.1017/S0025315413000635

Peterson, M. L., Lang, S. Q., Aufdenkampe, A. K., and Hedges, J. I. (2003). Dissolved organic carbon measurement using a modified high-temperature combustion analyzer. *Mar. Chem.* 81, 89–104. doi:10.1016/S0304-4203(03)00011-2

Pohlman, J. W., Bauer, J. E., Waite, W. F., Osburn, C. L., and Chapman, N. R. (2011). Methane hydrate-bearing seeps as a source of aged dissolved organic carbon to the oceans. *Nat. Geosci.* 4, 37–41. doi:10.1038/ngeo1016

Pohlman, J. W., Greinert, J., Ruppel, C., Silyakova, A., Vielstädte, L., Casso, M., et al. (2017). Enhanced CO2 uptake at a shallow Arctic Ocean seep field overwhelms the positive warming potential of emitted methane. *Proc. Natl. Acad. Sci. U.S.A.* 114, 5355–5360. doi:10.1073/pnas.1618926114

Qian, J., and Mopper, K. (1996). Automated high-performance, high-temperature combustion total organic carbon analyzer. *Anal. Chem.* 68, 3090–3097. doi:10.1021/ac960370z

Quadfasel, D., Rudels, B., and Kurz, K. (1988). Outflow of dense water from a svalbard fjord into the fram strait. *Deep Sea Res. Part A. Oceanogr. Res. Papers* 35, 1143–1150. doi:10.1016/0198-0149(88)90006-4

R Core Team (2018). *R: a language and environment for statistical computing*. Vienna, Austria: R Foundation for Statistical Computing.

Randelhoff, A., Reigstad, M., Chierici, M., Sundfjord, A., Ivanov, V., Cape, M., et al. (2018). Seasonality of the physical and biogeochemical hydrography in the inflow to the arctic ocean through fram strait. *Front. Mar. Sci.* 5, 224. doi:10.3389/fmars.2018.00224

Redfield, A. (1958). The biological control of chemical factors in the environment. *Sci. Prog.* 11, 150–170.

Reeburgh, W. S. (2007). Oceanic methane biogeochemistry. *Chem. Rev.* 107, 486–513. doi:10.1021/cr050362v

Repeta, D. J. (2015). "Chapter 2–chemical characterization and cycling of dissolved organic matter," in *Biogeochemistry of marine dissolved organic matter*. 2nd Edn, Editors D. A. Hansell and C. A. Carlson (Boston, MA: Academic Press), 21–63.

Rudels, B., Meyer, R., Fahrbach, E., Ivanov, V. V., Østerhus, S., Quadfasel, D., et al. (2000). Water mass distribution in fram strait and over the Yermak Plateau in summer 1997. *Ann. Geophys.* 18, 687–705. doi:10.1007/s00585-000-0687-5

Sahling, H., Römer, M., Pape, T., Bergès, B., dos Santos Fereirra, C., Boelmann, J., et al. (2014). Gas emissions at the continental margin west of Svalbard: mapping, sampling, and quantification. *Biogeosciences* 11, 6029–6046. doi:10.5194/bg-11-6029-2014

Sen, A., Åström, E. K. L., Hong, W.-L., Portnov, A., Waage, M., Serov, P., et al. (2018). Geophysical and geochemical controls on the megafaunal community of a high Arctic cold seep. *Biogeosciences* 15, 4533–4559. doi:10.5194/bg-15-4533-2018

Serov, P., Portnov, A., Mienert, J., Semenov, P., and Ilatovskaya, P. (2015). Methane release from pingo-like features across the South Kara Sea shelf, an area of thawing offshore permafrost. *J. Geophys. Res. Earth Surf.* 120, 1515–1529. doi:10.1002/2015JF003467

Sert, M. F., D'Andrilli, J., Gründger, F., Niemann, H., Granskog, M. A., Pavlov, A. K., et al. (2020). Replication data for: arctic cold seeps alter dissolved organic matter composition at the svalbard continental margin and the barents Sea. doi:10.18710/JHB371

Silyakova, A., Jansson, P., Serov, P., Ferré, B., Pavlov, A. K., Hattermann, T., et al. (2020). Physical controls of dynamics of methane venting from a shallow seep area west of svalbard. *Continent. Shelf Res.* 194, 104030. doi:10.1016/j.csr.2019.104030

Skogseth, R., Haugan, P. M., and Jakobsson, M. (2005). Watermass transformations in storfjorden. *Continent. Shelf Res.* 25, 667–695. doi:10.1016/j.csr.2004.10.005

Skogseth, R., Sandvik, A. D., and Asplin, L. (2007). Wind and tidal forcing on the meso-scale circulation in Storfjorden, Svalbard. *Continent. Shelf Res.* 27, 208–227. doi:10.1016/j.csr.2006.10.001

Sleighter, R. L., and Hatcher, P. G. (2007). The application of electrospray ionization coupled to ultrahigh resolution mass spectrometry for the molecular characterization of natural organic matter. *J. Mass Spectrom.* 42, 559–574. doi:10.1002/jms.1221

Steinle, L., Graves, C. A., Treude, T., Ferré, B., Biastoch, A., Bussmann, I., et al. (2015). Water column methanotrophy controlled by a rapid oceanographic switch. *Nat. Geosci.* 8, 378–382. doi:10.1038/ngeo2420

Steinle, L., Maltby, J., Treude, T., Kock, A., Bange, H. W., Engbersen, N., et al. (2017). Effects of low oxygen concentrations on aerobic methane oxidation in seasonally hypoxic coastal waters. *Biogeosciences* 14, 1631–1645. doi:10.5194/bg-14-1631-2017

Steinle, L., Schmidt, M., Bryant, L., Haeckel, M., Linke, P., Sommer, S., et al. (2016). Linked sediment and water-column methanotrophy at a man-made gas blowout in the North Sea: implications for methane budgeting in seasonally stratified shallow seas: linked sediment and water methanotrophy. *Limnol. Oceanogr.* 61, S367–S386. doi:10.1002/lno.10388

Tremblay, J.-É., Anderson, L. G., Matrai, P., Coupel, P., Bélanger, S., Michel, C., et al. (2015). Global and regional drivers of nutrient supply, primary production and CO2 drawdown in the changing arctic ocean. *Prog. Oceanogr.* 139, 171–196. doi:10.1016/j.pocean.2015.08.009

Valentine, D. L., Blanton, D. C., Reeburgh, W. S., and Kastner, M. (2001). Water column methane oxidation adjacent to an area of active hydrate dissociation, Eel River Basin. *Geochem. Cosmochim. Acta* 65, 2633–2640. doi:10.1016/s0016-7037(01)00625-1

Vanreusel, A., Andersen, A., Boetius, A., Connelly, D., Cunha, M., Decker, C., et al. (2009). Biodiversity of cold seep ecosystems along the european margins. *Oceanography* 22, 110–127. doi:10.5670/oceanog.2009.12

Veloso-Alarcón, M. E., Jansson, P., Batist, M. D., Minshull, T. A., Westbrook, G. K., Pälike, H., et al. (2019). Variability of acoustically evidenced methane bubble emissions offshore western svalbard. *Geophys. Res. Lett.* 46, 9072–9081. doi:10.1029/2019GL082750

Venables, W. N., and Ripley, B. D. (2002). *Modern applied statistics with S. Fourth*. New York, NY: Springer.

von Appen, W.-J., Schauer, U., Hattermann, T., and Beszczynska-Möller, A. (2016). Seasonal cycle of mesoscale instability of the West spitsbergen current. *J. Phys. Oceanogr.* 46, 1231–1254. doi:10.1175/JPO-D-15-0184.1

Westbrook, G. K., Thatcher, K. E., Rohling, E. J., Piotrowski, A. M., Pälike, H., Osborne, A. H., et al. (2009). Escape of methane gas from the seabed along the West Spitsbergen continental margin. *Geophys. Res. Lett.* 36 L15608. doi:10.1029/2009gl039191

Wiesenburg, D. A., and Guinasso, N. L. (1979). Equilibrium solubilities of methane, carbon monoxide, and hydrogen in water and sea water. *J. Chem. Eng. Data* 24, 356–360. doi:10.1021/je60083a006

Williams, P. M., and Druffel, E. R. M. (1987). Radiocarbon in dissolved organic matter in the central north pacific ocean. *Nature* 330, 246–248. doi:10.1038/330246a0

Winkler, L. W. (1888). Die bestimmung des im wasser gelösten sauerstoffes. *Ber. Dtsch. Chem. Ges.* 21, 2843–2854. doi:10.1002/cber.188802102122

Conflict of Interest: The authors declare that the research was conducted in the absence of any commercial or financial relationships that could be construed as a potential conflict of interest.

frontiers in Earth Science

ORIGINAL RESEARCH
published: 21 December 2020
doi: 10.3389/feart.2020.568566

A Long-Term Geothermal Observatory Across Subseafloor Gas Hydrates, IODP Hole U1364A, Cascadia Accretionary Prism

Keir Becker[1]*, *Earl E. Davis*[2], *Martin Heesemann*[3], *John A. Collins*[4] and *Jeffrey J. McGuire*[5]

[1]Rosenstiel School of Marine and Atmospheric Science, University of Miami, Miami, FL, United States, [2]Pacific Geoscience Centre, Geological Survey of Canada, Sidney, BC, Canada, [3]Ocean Networks Canada, University of Victoria, Victoria, BC, Canada, [4]Woods Hole Oceanographic Institution, Woods Hole, MA, United States, [5]U.S. Geological Survey, Menlo Park, CA, United States

OPEN ACCESS

Edited by:
Tamara Baumberger,
Oregon State University, United States

Reviewed by:
Michael Riedel,
GEOMAR Helmholtz Center for Ocean Research Kiel, Germany
Anne M. Tréhu,
Oregon State University, United States
Man-Yin Tsang,
University of Toronto, Canada

***Correspondence:**
Keir Becker
kbecker@rsmas.miami.edu

Specialty section:
This article was submitted to Biogeoscience, a section of the journal Frontiers in Earth Science

Received: 01 June 2020
Accepted: 20 November 2020
Published: 21 December 2020

Citation:
Becker K, Davis EE, Heesemann M, Collins JA and McGuire JJ (2020) A Long-Term Geothermal Observatory Across Subseafloor Gas Hydrates, IODP Hole U1364A, Cascadia Accretionary Prism. Front. Earth Sci. 8:568566. doi: 10.3389/feart.2020.568566

We report 4 years of temperature profiles collected from May 2014 to May 2018 in Integrated Ocean Drilling Program Hole U1364A in the frontal accretionary prism of the Cascadia subduction zone. The temperature data extend to depths of nearly 300 m below seafloor (mbsf), spanning the gas hydrate stability zone at the location and a clear bottom-simulating reflector (BSR) at ~230 mbsf. When the hole was drilled in 2010, a pressure-monitoring Advanced CORK (ACORK) observatory was installed, sealed at the bottom by a bridge plug and cement below 302 mbsf. In May 2014, a temperature profile was collected by lowering a probe down the hole from the ROV ROPOS. From July 2016 through May 2018, temperature data were collected during a nearly two-year deployment of a 24-thermistor cable installed to 268 m below seafloor (mbsf). The cable and a seismic-tilt instrument package also deployed in 2016 were connected to the Ocean Networks Canada (ONC) NEPTUNE cabled observatory in June of 2017, after which the thermistor temperatures were logged by Ocean Networks Canada at one-minute intervals until failure of the main ethernet switch in the integrated seafloor control unit in May 2018. The thermistor array had been designed with concentrated vertical spacing around the bottom-simulating reflector and two pressure-monitoring screens at 203 and 244 mbsf, with wider thermistor spacing elsewhere to document the geothermal state up to seafloor. The 4 years of data show a generally linear temperature gradient of 0.055°C/m consistent with a heat flux of 61–64 mW/m^2. The data show no indications of thermal transients. A slight departure from a linear gradient provides an approximate limit of ~10^{-10} m/s for any possible slow upward advection of pore fluids. *In-situ* temperatures are ~15.8°C at the BSR position, consistent with methane hydrate stability at that depth and pressure.

Keywords: heat flux, geothermal gradient, gas hydrates, bottom-simulating reflector, pore-fluid advection, borehole observatory, Integrated Ocean Drilling Program

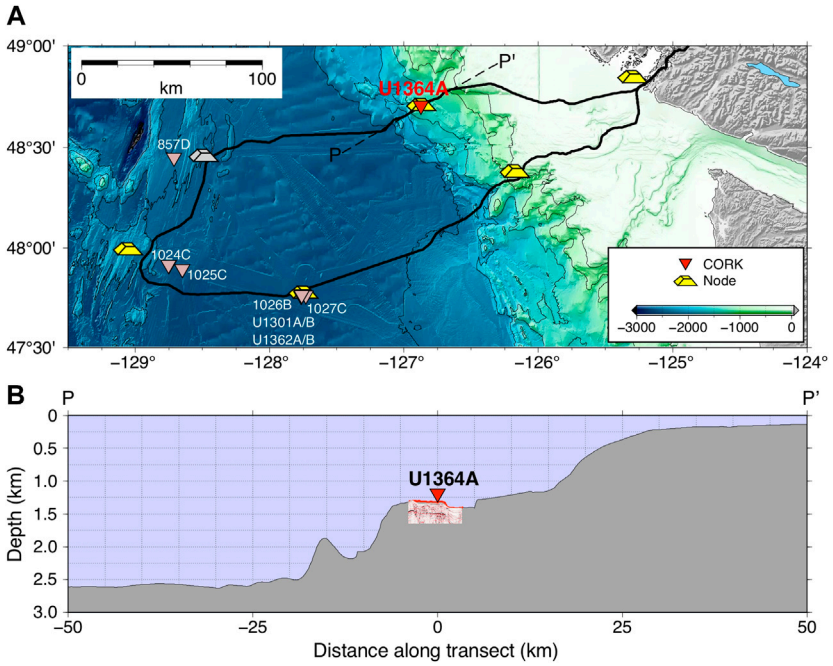

FIGURE 1 | (A) Location of Hole U1364A, Ocean Networks Canada (ONC) cabled observatory nodes, and other CORK sites in the northeast Pacific. **(B)** Location of Hole U1364A along bathymetric profile P-P′ shown in **(A)**. An expanded version of the small seismic section in the vicinity of Hole U1364A is shown in **Figure 3**.

INTRODUCTION

The stability of methane hydrates in continental margin sediments has long been known to be strongly dependent on temperature and pressure (e.g., Kvenvolden and Barnard, 1983; Hyndman et al., 1992), such that seismically determined depths to bottom-simulating reflectors (BSRs) that often mark the base of gas hydrate stability (BGHS) have been used by many authors to estimate heat flux through the sedimentary section above the BSR (e.g., Yamano et al., 1982; Davis et al., 1990; Hyndman et al., 1992). However, there have been only a few direct measurements of temperature within the gas hydrate stability zone (GHSZ) made in scientific ocean drilling, and even fewer long-term time-series measurements of temperature across the GHSZ. The best previous example of the latter was at Ocean Drilling Program (ODP) Site 892 at Hydrate Ridge in the southern Cascadia accretionary prism, where thermal results were enigmatic with respect to inferred depths of methane hydrate stability (Davis et al., 1995). This paper describes 4 years of temperature time-series data in the northern Cascadia accretionary prism, at Integrated Ocean Drilling Program (IODP) Site U1364, spanning a clear BSR and the GHSZ. These data are consistent with and resolve more clearly the previously interpreted temperature gradient and temperature at the BGHS at the site. They also improve the estimate of heat flux at depth and provide an upper limiting constraint on the rate of any vertical pore-fluid expulsion.

As shown in **Figure 1**, Site U1364 lies ~20 km landward of the toe of the Cascadia subduction zone accretionary prism, where much of the thick section of turbidite and hemipelagic sediments deposited on the eastern flank of the Juan de Fuca Ridge is scraped off the underthrusting oceanic crust (Davis and Hyndman, 1989; Hyndman et al., 1992; Westbrook et al., 1994). Convergence of the Juan de Fuca oceanic plate relative to the North American continental plate occurs in a direction roughly normal to the continental margin at a rate of about 42 mm/yr (DeMets et al., 1990). A topographic trench at this subduction zone is absent as a consequence of the extremely high rate of turbidite sediment supply from the continent during the Pleistocene (Davis and Hyndman, 1989). At the accretionary prism toe or deformation front, where the seawardmost thrust fault of the accretionary complex intersects the seafloor, the sediments that bury the eastern Juan de Fuca Ridge flank are approximately 2.7 km thick. At Site U1364 the accreted sedimentary section is nearly doubled to a thickness of approximately 5 km (Yuan et al., 1994). With such tectonic thickening and compaction, pore fluids are expelled, and gas - primarily methane - is transported upward to contribute to the formation of gas hydrates in the upper few hundred meters of the sediment section (Davis et al., 1990; Hyndman and Davis, 1992; Haacke et al., 2007; Riedel et al., 2010a).

Site U1364 lies at a position where the fluid expulsion rate, estimated on the basis of the rates of compaction and vertical growth of the prism, reaches a cross-margin maximum, and where a clearly developed BSR marks the BGHS (Davis et al., 1990; Hyndman and Davis, 1982). That rationale had previously been used in selecting the locations of adjacent ODP Site 889 and IODP Site U1327; the three sites essentially share a common location within a diameter of 700 m (**Figure 2**), with each being at least 1 km away from any mapped locations of seafloor cold vents (Scherwath et al., 2019). Cores and logs from Sites 889, 890, and U1327 (Westbrook et al., 1994; Riedel et al., 2010a) have documented the nature of the incoming

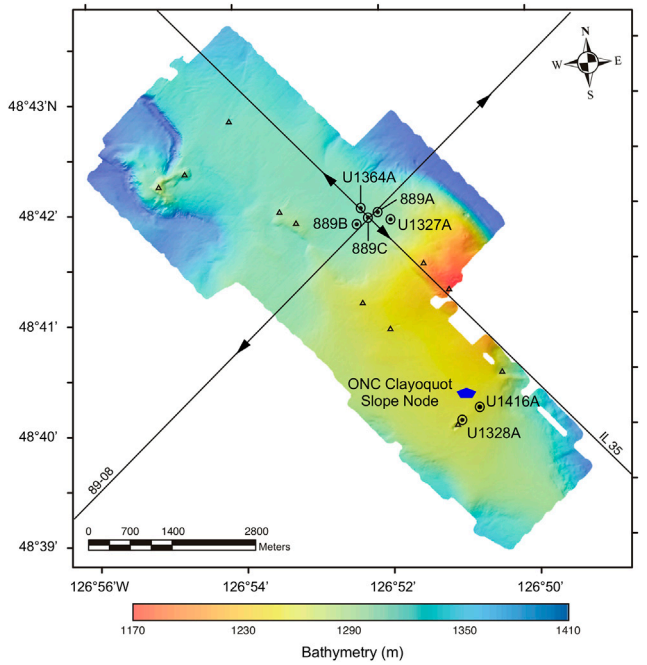

FIGURE 2 | Borehole locations from ODP Leg 146 (889A-C), Expedition 311 (U1327A, U1327B, and U1328A), Expedition 341S (U1416A), and Expedition 328 (U1364A) on multibeam bathymetric data from Paull et al. (2015). Also shown is approximate position of the ONC Clayoquot Slope node. Arrowheads on PGC 89-08 and IL35 seismic lines show approximate extents of sections shown in **Figure 3**. Triangles show locations of mapped seafloor formation fluid or gas seeps from Scherwath et al. (2019). Site U1416A is not discussed in this paper, but it is shown because it is the location of a SCIMPI (Simple Cabled Instrument to Measure Parameters *In Situ*) observatory also intended to monitor temperatures down to BSR depths (Expedition 341S Scientists and Engineers, 2013; Lado-Insua et al., 2013).

undeformed sediments, the compaction history during accretion, the details of the lithology, and the distribution and composition of gas hydrates across the area. In particular, they show that 1) pore fluids are significantly freshened below the upper unit of undeformed slope sediments, which should affect estimates of the depth limit of the GHSZ; and 2) there are geochemical and carbon isotope signatures for primarily microbial gas generation at this location, as summarized by Riedel et al. (2010a). At the three previous sites, ten subseafloor sediment temperature measurements down to ~210 mbsf constrained an average temperature gradient of 0.055°C/m, with an estimated temperature of 15–16°C at the BGHS estimated at ~230 mbsf in the area (Exp 311 Scientists et al., 2006a; Riedel et al., 2010a).

METHODS: BOREHOLE OBSERVATORY AND TEMPERATURE SENSOR CONFIGURATION

During IODP Expedition 328 in 2010, Hole U1364A was drilled without coring or any logging to a total depth of 336 mbsf through roughly 90 m of gently deformed slope-basin deposits and underlying sediments of the accretionary prism that are folded and faulted on a scale too small to be resolved in seismic reflection profiles (**Figure 3**). An "Advanced CORK" (ACORK) borehole observatory was installed immediately after drilling (Davis et al., 2012), configured as shown in **Figure 3A** projected onto trench-normal seismic line PGC 89-08. The ACORK was constructed around solid 10.75-inch casing, left open at the wellhead above seafloor but sealed at the bottom of the casing with a bridge plug backed with cement. This left the interior open to a depth of 302 mbsf for instruments requiring thermal or mechanical-but not direct-contact with the formation. Formation fluid pressures are transmitted to sensors at the wellhead via 2.03-m-long circumferential sand-packed filter screens and 3-mm-diameter (1/8-inch i.d.) stainless steel hydraulic tubing mounted on the outside of the casing. Screens (numbered S1 to S4 from bottom to top) are positioned at depths of 304 mbsf, 244 mbsf, 203 mbsf, and 156 mbsf. The middle two pressure monitoring screens were positioned 14 m below and 27 m above the base of the gas hydrate stability zone at 230 mbsf to observe the effects of free gas and gas hydrate in the sediment matrix, and diffusive signals originating at the hydrate-gas boundary. The lowermost and uppermost screens were placed 74 m below and above the boundary, a distance that was anticipated to be sufficient to avoid hydrologic complications originating at the boundary. Initial results (Davis et al., 2012) indicated that collapse of the formation around the installation provided good hydraulic isolation of the three deepest screens, but the seafloor reference pressure gauge had failed. Therefore, the input to the gauge originally assigned to the uppermost screen was switched from formation to the seafloor to provide a continuing reference pressure signal.

In July of 2016, we installed a combined seismometer/tiltmeter/thermistor array in the central bore of the ACORK, using the ROV Jason from R/V Sikuliaq. An earlier depth check conducted in May of 2014 with a Seabird conductivity-temperature-depth (CTD) profiler on an ROV-mounted winch had indicated the likely presence of fill below 300 mbsf. To minimize risk on deployment, the 2016 sensor string was designed to terminate above that section, somewhat above the deepest pressure-monitoring screen. The seismometer/tiltmeter package was mechanically clamped to the casing at 280 mbsf and cabled to a master control unit that landed in the ACORK wellhead (McGuire et al., 2018). During deployment, a 24-thermistor cable was married to the seismometer/tiltmeter string, with the deepest thermistor positioned at 268 mbsf, roughly midway between the two deepest screens. The thermistor cable was a Concerto T24 unit manufactured by Richard Brancker Research Ltd., with nominal resolution of 0.001°C in the expected range of 2–20°C. It had been designed with variable spacing between sensors of 4–18 m, with closely spaced sections around the upper three pressure monitoring screens and BSR and wider spacing elsewhere (**Figure 3B**). The temperature sensors are numbered T1 to T24 from bottom to top.

The output from the temperature data logger was fed to the master sensor string control unit, which was also designed to

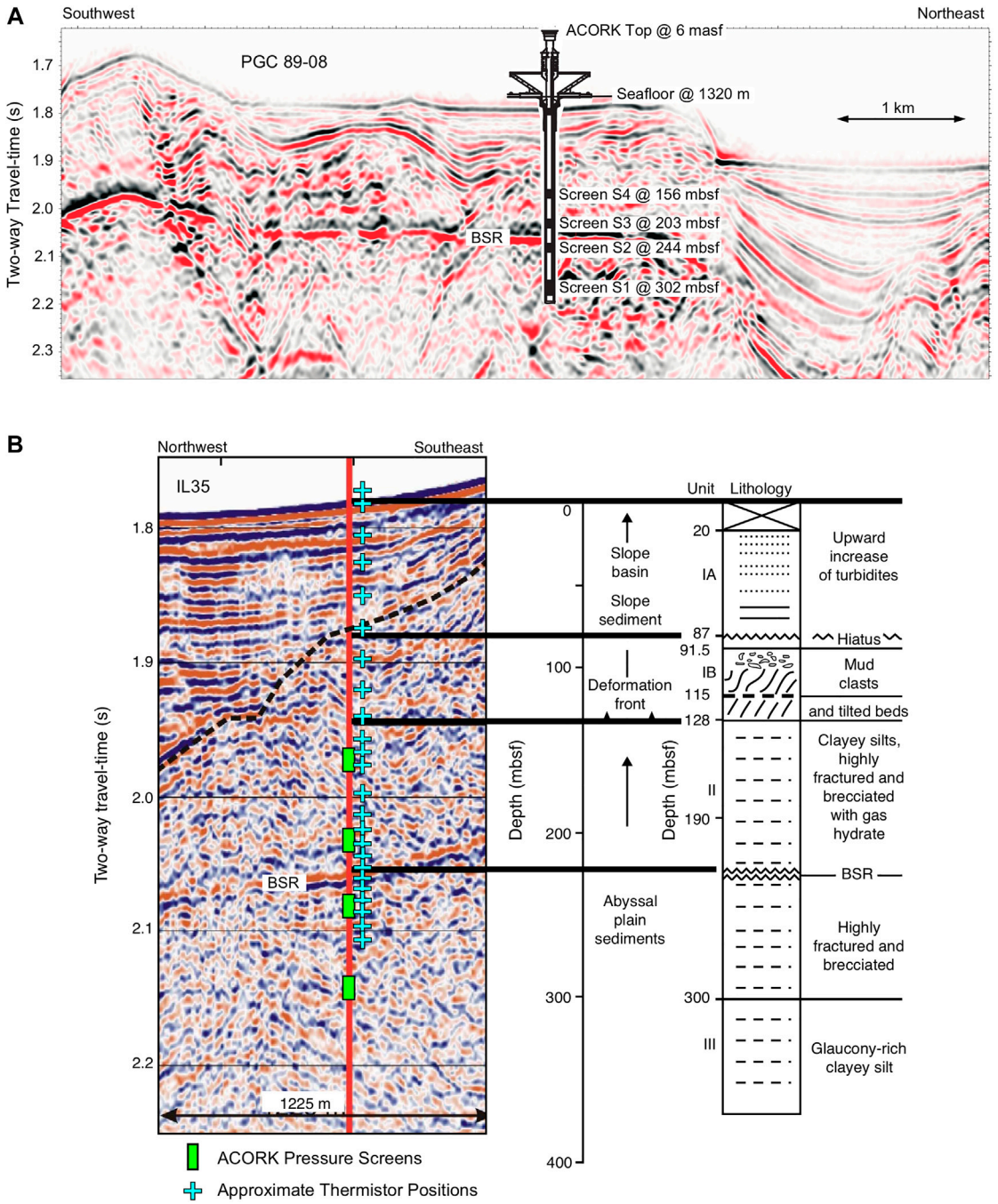

FIGURE 3 | (A) Expanded view of the PGC 89-08 seismic image highlighted in **Figure 1B**, showing BSR and configuration of the ACORK in Hole U1364A including its four downhole pressure-monitoring screens. **(B)** Position of Hole U1364A (red vertical line) on seismic cross line IL35 correlated with lithology derived from core samples at Sites 899 and U1327A. Approximate positions of ACORK pressure monitoring screens and thermistor cable sensors are shown as green rectangles and blue crosses, respectively, with exaggerated vertical scales. **(A)** and **(B)** are both modified from Expedition 311 Scientists (2006b).

allow direct connection for power and data streaming to the Ocean Networks Canada (ONC) cable at its Clayoquot Slope node. That connection could not be completed in 2016 but was successfully made in June of 2017, after which temperature data were logged continuously at one-minute intervals with the exception of a few short ONC outages. During the 2016 deployment cruise, about 1 day of initial temperature data had been logged to a shipboard computer while we remained connected to the installation via Jason. Unfortunately, in May of 2018 the main internet switch in the master control unit failed, ending the streaming of all data including temperature. The entire 2016 inside-casing instrument string was pulled from the hole in

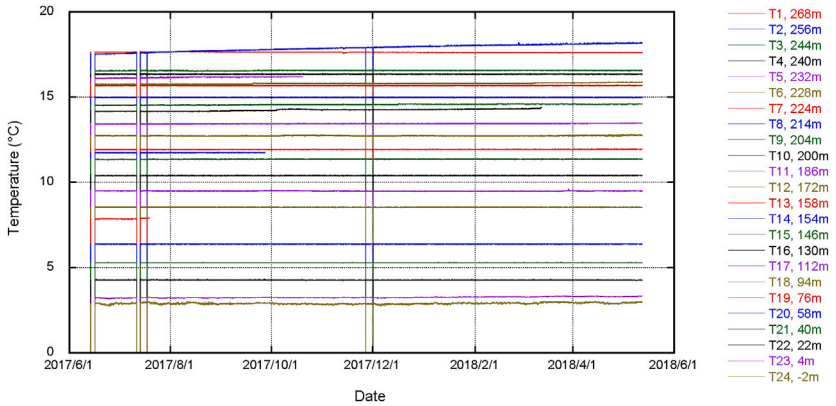

FIGURE 4 | Eleven-month time-series of temperatures recorded from June 2017 through May 2018 with the thermistor cable originally deployed in July 2016. As detailed in the text, compromised later sections of readings from five sensors have been masked from this plot.

late summer 2019, also using Jason from R/V Sikuliaq, for replacement of the internet switch, refurbishment, and redeployment hopefully in the near future. Monitoring of pressure data via an independent ONC cable connection has not been affected.

RESULTS

Hole U1364A Temperature Time-Series Data

Figure 4 shows the eleven-month time-series of thermistor cable data from the June 2017 ONC connection to the May 2018 failure of the internet switch in the main control unit for the sensor string. For most of the sensors, the long-term records are quite stable, but four or five sensors displayed indications of sudden or gradual degradation, possibly due to seawater penetration into the cable. For four of those sensors, only the more stable early sections of data are shown on **Figure 4** and used in subsequent analyses. In particular, readings from T14 (154 mbsf) and T10 (200 mbsf) showed abrupt deviations and subsequent unstable readings starting in late September 2017 and mid-March 2018, respectively. In addition, readings from T19 (76 mbsf) and T5 (232 mbsf) showed upward drifts with steadily increasing noise levels (to >1°C) beginning in August and October 2017, respectively. The record from T2 (256 mbsf) also shows a slow upward drift but without increasing noise levels, eventually reaching higher apparent temperatures than the deepest sensor T1 (268 mbsf). This is probably due to slow failure of T2, but we cannot definitively rule out some other cause such as formation warming at that depth or slow convective overturn deep in the hole. Convection of the fluids within casing is not unexpected for a hole of this diameter and temperature gradient, but it does not normally disturb the average gradient (e.g., Diment, 1967; Sammel, 1968). Therefore, the T2 readings are still shown on **Figure 4**, but they were not used in analyses of temperature gradient or heat flux in sections below. In addition, the record from T24, at a position within the ACORK but above seafloor, clearly shows tidal variations in bottom-water temperatures, and the T23 record from just below seafloor shows more attenuated tidal variations that are barely discernible on **Figure 4**.

Hole U1364A Temperature-Depth Profiles

Figure 5 compares 1) initial temperature data from the May 2014 CTD depth check, 2) the values at the end of the day of shipboard monitoring of thermistor cable readings during the July 2016 sensor string deployment, and 3) thermistor cable readings for June 2017, December 2017 and May 2018 excluding the later questionable segments of data for the five sensors described above. Previous ODP/IODP sediment probe data are also shown for reference, and they are discussed in the following paragraph. The 2014 and 2016 readings are quite consistent and nearly linear with depth, with the exception that deeper than 260 mbsf the depth check CTD readings are somewhat higher than the initial cable values, suggesting a slight convex-upward trend in the cable readings. The ACORK casing had been left open at the seafloor from 2010 to 2016, so there could have been some convective exchange of ocean bottom and in-casing fluids during that period. The wellhead control unit for the 2016 sensor string probably would have inhibited any such exchange after its deployment, although it should be noted it was not designed to perfectly seal the casing volume at the wellhead. The 2017–2018 profiles are remarkably linear and best fit with a linear temperature gradient of 0.055°C/m. The profiles constrain a temperature of ~15.8°C at the ~230 m depth of the BGHS. This is consistent with the stability field for methane hydrates at that depth/pressure and 3.0–3.5% salinity (Expedition 311 Scientists et al., 2006b, based on Sloan 1998).

The best-fit linear gradient from our data of 0.055°C/m is consistent with the value reported for the average of ODP/IODP sediment probe readings at nearby Sites 889, 890, and U1327 (Expedition 311 Scientists et al., 2006b). Despite this consistency, **Figure 5** shows that several of those ODP/IODP probe readings seem to plot below our profiles, especially data from Sites 889/890. This may be due to a combination of temporal variability of

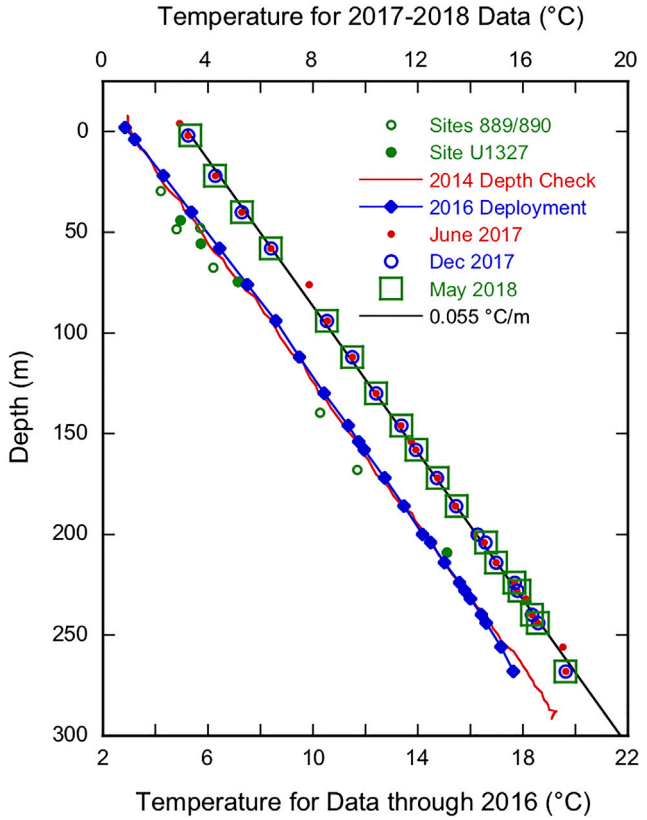

FIGURE 5 | Comparison of temperature-depth profiles in Hole U1364A obtained with: the 2014 downgoing CTD depth check, the 2016 initial deployment of the thermistor cable, and representative thermistor cable readings logged by ONC in June 2017, December 2017, and May 2018. Note that the temperature scale for the 2014 and 2016 data is shifted by −2°C for visual clarity. For reference, also shown are earlier downhole temperature probe readings obtained in Sites 889 and 890 in 1992 (Shipboard Scientific Party, 1994) and Site U1327 in 2011 (Expedition 311 Scientists, 2006b).

bottom water temperatures as discussed below in **Section 4.3** and uncertainties introduced by the normal ODP/IODP practice of correcting probe readings so that temperatures within the drillpipe measured during a stop at mudline depths match known bottom-water temperature. That correction is based on the assumption that the drillpipe acts as a perfect heat exchanger, cooling the surface seawater used to pump the probe down the pipe to the bottom-water value. The corrections for this effect applied to the two deepest readings from Site 889 shown on **Figure 5** were substantial, −1.3°C (Shipboard Scientific Party, 1994), so there may be larger uncertainties with those data compared to our 2014–2018 data.

The 2014–2018 profiles shown in **Figure 5** show no clear indications of transients at the level of the BSR or pressure-monitoring screens during the four-year period of collection of temperature data in Hole U1364A. The profiles do hint at a small degree of convex-upward curvature that might arise from diffuse upward pore-fluid migration associated with the gas hydrate stability zone as modeled by Hyndman and Davis (1982) and Riedel et al. (2010a). Estimating heat flux at depth and properly assessing an upper limit on possible fluid advection consistent with the temperature profiles first requires careful assessment of the *in-situ* thermal conductivity.

DISCUSSION

Thermal Conductivity and Heat Flux Estimates

Unfortunately, there are much greater uncertainties in the *in situ* thermal conductivity than the temperature profile. As reported by Shipboard and Scientific Party (1994), Expedition 311 Scientists et al. (2006b), and Riedel et al. (2010b), thermal conductivity measurements on ODP and IODP cores from Sites 889 and U1327 display considerable scatter with no clear depth trend. Much of the scatter might be due to variable disturbances in the coring and recovery processes, including de-gassing effects. In addition, Riedel et al. (2010b) noted that Site 889 values are about 10% higher on average than Site U1327 values. The same needle-probe method was used (Von Herzen and Maxwell, 1959), but with different instruments; this is unlikely the cause of the difference in conductivities, but an uncertainty of at least 10% cannot be eliminated (Riedel et al., 2010b). Therefore, Expedition 311 Scientists et al. (2006b) and Riedel et al. (2010b) used an average value of 1.1 W/m-K ± 10% to estimate a heat flux of 61–62 mW/m^2 at the sites. Applying that same conductivity value to our nearly linear gradient of 0.055°C/m yields a similar estimate of 60.5 mW/m^2 conductive heat flux through the section.

The Expedition 311 Scientists et al. (2006b) also noted that the conductivities for the more competent cores approached the "regional trend" of conductivity vs. depth developed by Davis et al. (1990) based on a seismic velocity to porosity to conductivity transform. Where thermal conductivity varies in a known way with depth, Bullard (1939) first suggested a transform to thermal resistance, the integral to a given depth of the inverse of the conductivity, with the slope of a plot of temperature vs thermal resistance providing a determination of conductive heat flux. The Davis et al. (1990) computation suggested a variation of conductivity that could be fit by a second order polynomial in depth with a seafloor value of 1.07 W/m-K. In an independent and potentially more reliable approach specific to the site, we also applied the relationship between thermal conductivity and porosity developed by Goto and Matsubayashi (2009) for Cascadia Basin sediments to the logging-while-drilling (LWD) porosity profile collected in Hole U1327A. The LWD data showed porosities decreasing with depth down to ~120 mbsf, a higher porosity zone at ~120–140 mbsf, and more uniform average values in the deeper section other than higher values just below the BSR (Expedition 311 Scientists et al., 2006b). This approach allowed computation of a detailed profile of the variation of *in situ* thermal conductivity with depth, and an integration to estimate thermal resistance at each thermistor depth. As shown in **Figure 6**, plots of thermistor cable temperatures vs. thermal resistance are quite linear for both models. The slopes yield conductive heat flux values of 63 mW/m^2 using the Davis et al. (1990) model and 64 mW/m^2 using the Goto and Maysubayashi (2009) model.

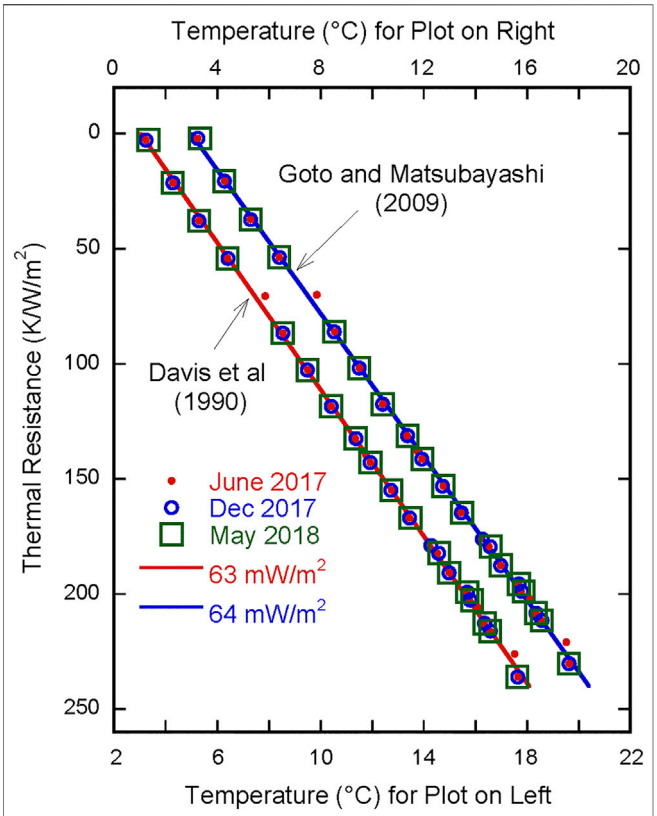

FIGURE 6 | Thermistor cable temperatures in Hole U1364A plotted against integrated thermal resistance, using the models of Davis et al. (1990) and Goto and Matsubayashi (2009) for the depth variation of thermal conductivity at the site. Note that the temperature scales for the two plots are offset by 2°C to avoid direct overlap.

Constraints on Advection Rates

The linearity of the temperature-thermal resistance plots in **Figure 6** suggests that an increase of conductivity with depth might explain at least some of the slightly convex-upward nature of the temperature-depth plots in **Figure 5**. Given the uncertainties in the depth variation of the *in-situ* conductivity profile, it is debatable whether it is valid to interpret an upward advection rate from the slight apparent curvature in the temperatures vs depth. Nevertheless, we applied the method of Bredehoeft and Papadopulos (1965) to define an upper limit to a possible advection rate consistent with the temperature data. That analysis suggests a value of 0.1 for the Bredehoeft and Papadopulos (1965) "β" parameter over the 268 m subseafloor depth range of the May 2018 thermistor cable data (**Figure 7**). β is defined as vρcL/k, where v is vertical advection rate, ρ and c are density and specific heat of the pore fluid, respectively, L is the vertical range of temperature measurements (268 m), and k is average thermal conductivity in that range. Using 1.1 W/m-K for average conductivity, 1,030 kg/m^3 for density of somewhat freshened pore fluids, and 3850 J/kg-K for specific heat of the pore fluids yields an estimate of upward vertical advection rate on the order of ~1×10^{-10} m/s. This is remarkably similar in order of magnitude to the maximum expulsion rate of nearly 3 mm/yr estimated by Hyndman and Davis (1982) at the general position of Hole U1364A on the northern Cascadia margin and background methane flux rates estimated by Riedel et al. (2006a) at Site U1328. We consider our estimate an upper limit for reasons described above and because the Bredehoeft and Papadopulos (1965) method is especially sensitive to the value of the deepest temperature reading, which in this case falls below the generally linear trends shown in **Figures 5** and **6**.

Relevance to Regional Heat Flux Measurements

Several hundred km farther south along the Cascadia Margin, Tréhu (2006) conducted an extensive program of downhole temperature probe measurements during ODP Leg 204 drilling at southern Hydrate Ridge offshore Oregon. That study produced comparable results to ours: a slightly lower average heat flux value of ~55 mW/m^2 and nearly linear temperature-depth profiles generally consistent with predicted temperatures at the base of the GHSZ as estimated from BSR depths there.

As reported in **Section 4.1**, the 61–64 mW/m^2 range of heat flux values we obtain from the thermistor cable readings in Hole U1364A is very close to the values obtained in nearby Sites 889,

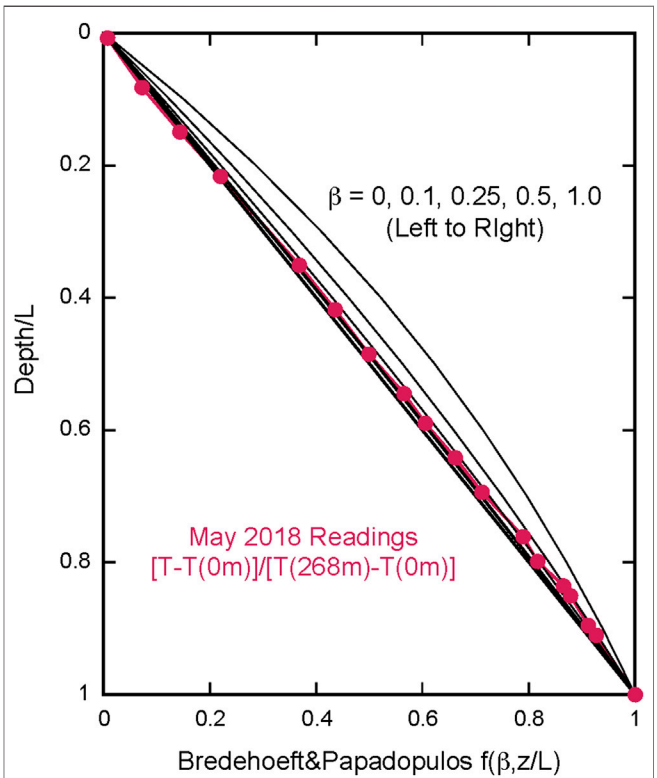

FIGURE 7 | Non-dimensionalized May 2018 thermistor cable readings plotted against the Bredehoeft and Papadopulos (1965) f(β,z/L) function along with characteristic type curves values for values of β associated with upward migration of pore-fluids. As detailed in the text, the consistency of the temperature data with the type curve for β = 0.1 suggests an upward pore-fluid migration rate no greater than ~10^{-10} m/s.

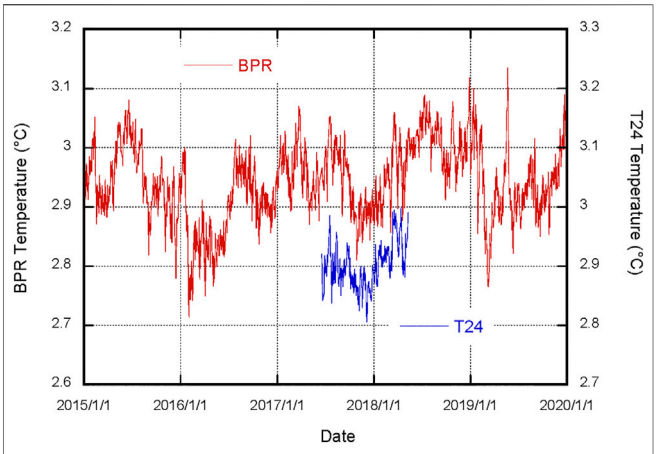

FIGURE 8 | Daily running averages of the internal temperature sensor for BPR NC89 deployed near the ONC Clayoquot Slope node, ~3 km southeast of Hole U1364A. Also shown is the 11-months record of the uppermost Hole U1364A thermistor 4 m above seafloor, with an offset in the vertical temperature scale to avoid obscuring the BPR record during that time.

890, U1327, and U1328. It is also close to the average value of 58 mW/m^2 obtained with a 4-m long probe during a regional heat flux survey in 2000 with trench-normal and trench-parallel lines crossing over Site U1328 (Riedel et al., 2006a). However, earlier trench normal heat flow surveys with a 2.5-m long probe in the same area yielded significantly higher values (Davis et al., 1990). Riedel et al. (2006b) suggested that this discrepancy might be attributed to time-varying perturbations to shallow sediment temperatures from bottom-water temperature changes at time scales of a few months to years.

This interpretation is supported by the combination of our significantly deeper heat flux determination in Hole U1364A, and a ten-year bottom-water temperature time-series obtained with a nearby bottom pressure recorder (BPR) ~3 km away near the ONC Clayoquot Slope node (**Figure 2**). Daily running averages of the BPR temperatures from 2015–2020 are plotted in **Figure 8** and clearly show variations in bottom-water temperature of up to ±0.15°C over time scales of months to nearly 2 years. The analysis of Davis et al. (2003) shows that downward propagation of bottom-water temperature variations of those magnitudes and time scales into the sediments will produce significant temporal perturbations to temperature gradients in the uppermost 2–3 m of sediments – the depth range penetrated by shallow heat flow probes. If similar variations in bottom-water temperatures were occurring at the times of the early heat flux surveys, they could indeed explain the differences between the Davis et al. (1990), Riedel et al. (2006a), and Riedel et al. 2006b) regional heat flux trends. This argues for caution in using short-probe heat flux determinations on the upper slopes of accretionary prisms as thermal constraints on models of deep-seated tectonic processes and state at subduction zones.

Deeper borehole data like the thermistor cable data from Hole U1364A - and downhole probe data like those of Tréhu (2006) - are out of range of the effects of such bottom-water temperature perturbations, and in that sense provide much more reliable measurements of seafloor heat flux and deep thermal structure. While our data and those of Tréhu (2006) represent just two well documented studies, it is notable that the downhole temperature profiles are consistent with predicted methane hydrate stability at both locations. This further validates the technique of estimating seafloor heat flux from BSR depths, as long as BSR depths are well constrained by seismic data and thermal conductivity profiles can be accurately determined.

CONCLUSION

Four years of discrete and continuous temperature logging in Hole U1364A on the Vancouver Margin accretionary prism has provided important constraints on the geothermal state and an upper limit on possible pore-fluid flow in the prism associated with the BSR and BGHS penetrated at ~230 mbsf at this location. The temperature profiles have remained quite constant over those 4 years, defining a nearly linear temperature gradient of 0.055°C/m with no indications of *in-situ* transients during the period. This gradient is consistent with a conductive heat flux of 61–64 mW/m^2 depending on the model adopted for the less constrained variation of thermal conductivity with depth at the site. The generally linear temperature profiles could also be consistent with a slight convex-upward curvature associated with upward pore-fluid migration at low rates no greater than 10^{-10} m/s, the same order as previously modeled by Hyndman and Davis (1982) to bring methane from depth to the gas hydrate stability zone. Finally, the temperature data show *in-situ* values at the BSR depth of ~15.8°C, consistent with predicted methane hydrate stability at that depth and pressure.

DATA AVAILABILITY STATEMENT

The thermistor cable temperature data used in this report are available from the Ocean Networks Canada data portal as specified in Ocean Networks Canada Society (2020). (Note that the archived thermistor cable data include periodic spikes during the first 6 months of 2017 recording that were caused by regular ground-fault checks of the WHOI borehole instruments; those spikes have been filtered out from any data used in this report.) The 2014 CTD data from Hole U1364A are available on Scholars Portal Dataverse as specified in Davis et al. (2020).

AUTHOR CONTRIBUTIONS

KB obtained NSF funding for the thermistor cable installed in Hole U1364A, participated in the design and installation of the combined sensor string installed in 2016, and led interpretation of the thermistor cable data and writing of this manuscript. ED was chief scientist of the IODP expedition that installed the ACORK in Hole U1364A in 2010, led interpretation of pressure data from the ACORK and the 2014 effort to conduct a depth check in the hole with CTD, and collaborated on the design of the thermistor cable and interpretation of the geothermal data. MH participated in the ACORK installation expedition and interpretation of

pressure data and was instrumental in organizing the ONC archiving of the thermistor cable data. JM led the Woods Hole Oceanographic Institution (WHOI) efforts for Keck Foundation funding for the seismic-strain-tilt components of the sensor string and NSF funding for the 2016 installation cruise, and he was chief scientist for that installation cruise. JC was co-investigator for the WHOI Keck Foundation and NSF funding, participated in the 2016 installation cruise, and was chief scientist on the 2019 cruise to recover the sensor string from Hole U1364A.

FUNDING

KB was supported by NSF grant OCE-1259718 for construction and deployment of the thermistor cable in the hole. Construction of the seismic-strain-tilt instrumentation was supported by a Keck Foundation grant to WHOI, and deployment and recovery of the integrated sensor string was supported by NSF grant OCE-1259243 to JM and JC. Support for the pressure-monitoring instrumentation and 2014 CTD profile was provided by the Geological Survey of Canada and Ocean Networks Canada.

ACKNOWLEDGMENTS

Drilling of Hole U1364A and installation of the ACORK infrastructure was carried out by the Integrated Ocean Drilling Program using D/V JOIDES Resolution. The CTD used in the 2014 depth check was provided by D. Fornari, WHOI. We thank the officers and crews of the JOIDES Resolution, ROPOS, Sikuliaq, and Jason for outstanding support for the at-sea deployments. We thank J. OBrien and K. von der Heydt for engineering support in designing and deploying the WHOI/RSMAS borehole instrument package, and D. Kot, J. Ryder, and I. Kulin for additional technical support during the deployment cruise. An early draft of this manuscript benefitted greatly from comments by H. Villinger. We thank reviewers C. Ruppel and S. Hickman for careful and constructive comments that prompted significant improvements to this report.

REFERENCES

Bredehoeft, J. D., and Papadopulos, I. S. (1965). Rates of vertical groundwater movement estimated from the Earth's thermal profile. *Water Resour. Res.* 1, 325–328. doi:10.1029/WR001i002p00325

Bullard, E. C. (1939). Heat flow in South Africa. *Proc. R. Soc. London Ser. A* 173, 474–502. doi:10.1098/rspa.1939.0159

Davis, E.,Heesemann, M., and the IODP Expedition 328 Scientists and Engineers. (2012). IODP expedition 328: early results of cascadia subduction zone ACORK observatory. *Sci. Rep.* 13, 12–18. doi:10.2204/iodp.sd.13.02.2011

Davis, E. E., and Hyndman, R. D. (1989). Accretion and recent deformation of sediments along the northern Cascadia subduction zone. *Geol. Soc. Am. Bull.* 101, 1465–1480. doi:10.1130/0016-7606(1989)101<1465:AARDOS>2.3.CO;2

Davis, E. E., Becker, K., Wang, K., and Carson, B. (1995). "Long-term observations of pressure and temperature in Hole 892B, Cascadia accretionary prism," in Proceedings of ODP, Science Results. Editors B. Carson, G. K. Westbrook, R. Musgrave, and E. Suess (College Station, TX: Ocean Drilling Program), Vol. 146, 299–311.

Davis, E. E., Hyndman, R. D., and Villinger, H. (1990). Rates of fluid expulsion across the northern Cascadia accretionary prism: constraints from new heat flow and multichannel seismic reflection data. *J. Geophys. Res.* 95, 8869–8889. doi:10.1029/JB095iB06p08869

Davis, E. E., McGuire, J. J., Heesemann, M., Becker, K., and Collins, J. A. (2020). CTD profile in IODP CORK U1364A borehole at ONC NEPTUNE observatory site Clayoquot Slope, Cascadia Accretionary Prism. Scholars Portal Dataverse, V1. doi:10.5683/SP2/4QZBZV

Davis, E. E., Wang, K., Becker, K., Thomson, R. E., and Yashayaev, I. (2003). Deep-ocean temperature variations and implications for errors in seafloor heat flow determinations. *J. Geophys. Res.* 108, 2034–2039. doi:10.1029/2001JB001695

DeMets, C., Gordon, R. G., Argus, D. F., and Stein, S. (1990). Current plate motions. *Geophys. J. Int.* 101, 425–478. doi:10.1111/j.1365-246X.1990.tb06579.x

Diment, W. H. (1967). Thermal regime of a large diameter borehole: instability of the water column and comparison of air- and water-filled conditions. *Geophysics* 32, 720–726. doi:10.1190/1.1439885

Expedition 341S Scientists and Engineers (2013). Simple cabled instrument for measuring parameters in situ (SCIMPI) and hole 858G CORK replacement. IODP Preliminary 341S Report. doi:10.2204/iodp.pr.341S.2013

Expedition 311 Scientists (2006a). "Expedition 311 summary," in The expedition 311 scientists, proceedings of IODP. Editors M. Riedel, T. S. Collett, and M. J. Malone (Washington, DC: IODP-MI), Vol. 311. doi:10.2204/iodp.proc.311.101.2006

Expedition 311 Scientists (2006b). "Site U1327," in The expedition 311 scientists, proceedings of IODP. Editors M. Riedel, T. S. Collett, and M. J. Malone (Washington, DC: IODP-MI), Vol. 311. doi:10.2204/iodp.proc.311.105.2006

Goto, S., and Matsubayashi, O. (2009). Relations between the thermal properties and porosity of sediments in the eastern flank of the Juan de Fuca Ridge. *Earth Planets Space* 61, 863–870. doi:10.1186/BF03353197

Haacke, R. R., Westbrook, G. K., and Hyndman, R. D. (2007). Gas hydrate fluid flow and free gas: formation of the bottom-simulating reflector. *Earth Planet. Sci. Lett.* 261, 407–420. doi:10.1016/j.epsl.2007.07.008

Hyndman, R. D., and Davis, E. E. (1982). A mechanism for the formation of methane hydrate and seafloor bottom-simulating reflectors by vertical fluid expulsion. *J. Geophys. Res.* 97, 7025–7041. doi:10.1029/91JB03061

Hyndman, R. D., Foucher, J. P., Yamano, Y., and Fisher, A. (1992). Deep sea bottom-simulating-reflectors: calibration of the base of the hydrate stability field as used for heat flow estimates. *Earth Planet. Sci. Lett.* 109, 289–301. doi:10.1016/0012-821X(92)90093-B

Kvenvolden, K. A., and Barnard, L. A. (1983). "Hydrates of natural gas in continental margins," in *Studies in continental margin geology*. Editors J. S. Watkins and C. L. Drake (American Association of Petroleum Geologists Memoir), Vol. 34, 631–640.

Lado-Insua, T., Moran, K., Kulin, I., Farrington, S., and Newman, J. B. (2013). SCIMPI: a new borehole observatory. *Sci. Drill.* 16, 57–61. doi:10.5194/sd-16-57-2013

McGuire, J. J., Collins, J. A., Davis, E., Becker, K., and Heesemann, M. (2018). A lack of dynamic triggering of slow slip and tremor indicates that the shallow Cascadia megathrust offshore Vancouver Island is likely locked. *Geophys. Res. Lett.* 28, 11,095–11,103. doi:10.1029/2018GL079519

Ocean Networks Canada Society (2020). ODP 1364A borehole temperature logger deployed 2016-07-01 (Ocean Networks Canada Society.). Available at: https://doi.org/10.34943/1ab823b8-0dcf-48e4-b9f0-67d52989b772.

Paull, C. K., Caress, D. W., Thomas, H., Lundsten, E., Anderson, K., Gwiazda, R., et al. (2015). Seafloor geomorphic manifestations of gas venting and shallow subbottom gas hydrate occurrences. *Geosphere* 2, 491–513. doi:10.1130/FES01012.1

Riedel, M., Collett, T. S., and Malone, M. (2010a). "The expedition 311 scientists, expedition 311 synthesis: scientific findings," in Proceedings of IODP. Editors M. Riedel, T. S. Collett, and M. J. Malone (Washington, DC: IODP-MI), Vol. 311. doi:10.2204/iodp.proc.311.213.2010

Riedel, M., Novosel, I., Spence, G. D., Hyndman, R. D., Chapman, R. N., Solem, R. C., et al. (2006a). Geophysical and geochemical signatures associated with gas hydrate-related venting in the northern Cascadia margin. *GSA Bulletin* 118, 23–38. doi:10.1130/B25720.1

Riedel, M., Tréhu, A., and Spence, G. D. (2010b). Characterizing the thermal regime of cold vents at the northern Cascadia margin from bottom-simulating reflector distributions, heat-probe measurements and borehole temperature data. *Mar. Geophys. Res.* 31, 1–16. doi:10.1007/s11001-010-9080-2

Riedel, M., Willoughby, E. C., Chen, M. A., He, T., Novosel, I., Schwalenberg, K., et al. (2006b). "Gas hydrate on the northern Cascadia margin: regional geophysics and structural framework," in The expedition 311 scientists, proceedings of IODP. Editors M. Riedel, T. S. Collett, and M. J. Malone (Washington, DC: IODP-MI), Vol. 311. doi:10.2204/iodp.proc.311.109.2006

Sammel, E. A. (1968). Convective flow and its effect on temperature logging in small-diameter wells. *Geophysics* 33, 1004–1012. doi:10.1190/1.1439977

Scherwath, M., Thomsen, L., Riedel, M., Römer, M., Chatzievangelou, D., Schwender, J., et al. (2019). Ocean observatories as a tool to advance gas hydrate research. *Earth Space Sci.* 6, 2644–2652. doi:10.1029/2019EA00762

Sloan, E. D. (1998). *Clathrate hydrates of natural gases*. 2nd Edn. New York: Marcel Dekker.

Tréhu, A. (2006). "Subsurface temperatures beneath southern Hydrate Ridge," in Proceedings ODP, science results. Editors A. Tréhu, G. Bohrmann, M. E. Torres, and F. S. Colwell (College Station, TX: Ocean Drilling Program), 1–26. doi:10.2973/odp.proc.sr.204.114.2006

Von Herzen, R. P., and Maxwell, A. E. (1959). The measurement of thermal conductivity of deep-sea sediments by a needle probe method. *J. Geophys. Res.* 64, 1557–1563. doi:10.1029/JZ064i010p01557

Westbrook, G. K., Carson, B., Musgrave, R. J., et al. (1994). Proceedings of ODP, initial reports (College Station, TX: Ocean Drilling Program), Vol. 146.

Shipboard Scientific Party (1994). "Site 889 and 890," in Proceedings of ODP, initial Reports. Editors G. K. Westbrook, B. Carson, R. J. Musgrave, et al. (College Station, TX: Ocean Drilling Program), Vol. 146, 127–239.

Yamano, M., Uyeda, S., Aoki, Y., and Shipley, T. H. (1982). Estimates of heat flow derived from gas hydrates. *Geology* 10, 339–343. doi:10.1130/0091-7613(1982)10<339:EOHFDF>2.0.CO;2

Yuan, T., Spence, G. D., and Hyndman, R. D. (1994). Seismic velocities and inferred porosities in the accretionary wedge sediments at the Cascadia margin. *J. Geophys. Res.* 99, 4413–4427. doi:10.1029/93JB03203

Disclaimer: Any use of trade, firm, or product names is for descriptive purposes only and does not imply endorsement by the U.S. Government.

Conflict of Interest: The authors declare that the research was conducted in the absence of any commercial or financial relationships that could be construed as a potential conflict of interest.

The reviewer MR declared a past co-authorship with one of the authors MH to the handling editor. The reviewer AMT declared a past co-authorship with one of the authors JC to the handling editor.

frontiers in Earth Science

ORIGINAL RESEARCH
published: 12 February 2021
doi: 10.3389/feart.2020.570742

Biomarker and Isotopic Composition of Seep Carbonates Record Environmental Conditions in Two Arctic Methane Seeps

Haoyi Yao[1], Giuliana Panieri[1]*, Moritz F. Lehmann[2], Tobias Himmler[1,3] and Helge Niemann[1,2,4,5]*

[1]CAGE—Centre for Arctic Gas Hydrate, Environment and Climate, Department of Geosciences, UiT the Arctic University of Norway, Tromsø, Norway, [2]Department of Environmental Sciences, University of Basel, Basel, Switzerland, [3]Geological Survey of Norway, Trondheim, Norway, [4]Department of Marine Microbiology and Biogeochemistry, NIOZ Royal Institute for Sea Research, Texel, Netherlands, [5]Department of Earth Sciences, Faculty of Geosciences, Utrecht University, Utrecht, Netherlands

Present-day activity of cold seeps in the ocean is evident from direct observations of methane emanating from the seafloor, the presence of chemosynthetic organisms, or the quantification of high gas concentrations in sediment pore waters and the water column. Verifying past cold seep activity and biogeochemical characteristics is more challenging but may be reconstructed from proxy records of authigenic seep carbonates. Here, we investigated the lipid-biomarker inventory, carbonate mineralogy, and stable carbon and oxygen isotope compositions of seep-associated carbonates from two active Arctic methane seeps, located to the northwest (Vestnesa Ridge; ~1,200 m water depth) and south (Storfjordrenna; ~380 m water depth) offshore Svalbard. The aragonite-dominated mineralogy of all but one carbonate sample indicate precipitation close to the seafloor in an environment characterized by high rates of sulfate-dependent anaerobic oxidation of methane (AOM). In contrast, Mg-calcite rich nodules sampled in sediments of Storfjordrenna appear to have formed at the sulfate-methane-transition zone deeper within the sediment at lower rates of AOM. AOM activity at the time of carbonate precipitation is indicated by the ^{13}C-depleted isotope signature of the carbonates [–20 to –30‰ Vienna Pee Dee Belemnite (VPDB)], as well as high concentrations of ^{13}C-depleted lipid biomarkers diagnostic for anaerobic methanotrophic archaea (archaeol and sn2-hydroxyarchaeol) and sulfate-reducing bacteria (iso and anteiso-C15:0 fatty acids) in the carbonates. We also found ^{13}C-depleted lipid biomarkers (diploptene and a 4α-methyl sterol) that are diagnostic for bacteria mediating aerobic oxidation of methane (MOx). This suggests that the spatial separation between AOM and MOx zones was relatively narrow at the time of carbonate formation, as is typical for high methane-flux regimes. The seep-associated carbonates also displayed relatively high δ^{18}O values (4.5–5‰ VPDB), indicating the presence of ^{18}O-enriched fluids during precipitation, possibly derived from destabilized methane gas hydrates. Based on the combined isotopic evidence, we suggest that all the seep carbonates resulted from the anaerobic oxidation of methane during intense methane seepage. The seepage likely was associated to gas hydrates destabilization, which led to the methane ebullition from the seafloor into the water column.

Keywords: gas hydrate, Arctic, seep carbonate, methane seep, lipid biomarkers

OPEN ACCESS

Edited by:
Ira Leifer, Bubbleology Research Intnl, United States

Reviewed by:
Huan Cui, Université de Paris, France
Joachim Reitner, University of Göttingen, Germany

****Correspondence:***
Haoyi Yao
haoyi.yao11@gmail.com
Giuliana Panieri
Giuliana.panieri@uit.no

Specialty section:
This article was submitted to Biogeoscience, a section of the journal Frontiers in Earth Science

Received: *08 June 2020*
Accepted: *30 December 2020*
Published: *12 February 2021*

Citation:
Yao H, Panieri G, Lehmann MF, Himmler T and Niemann H (2021) Biomarker and Isotopic Composition of Seep Carbonates Record Environmental Conditions in Two Arctic Methane Seeps. Front. Earth Sci. 8:570742. doi: 10.3389/feart.2020.570742

INTRODUCTION

Marine sediments contain large quantities of methane in the form of free- or dissolved gas, or gas hydrate. While the benthic methane reservoir is relatively stable at present, concern exists that a warmer future ocean will facilitate higher methane emission rates from the seafloor to the water column and potentially to the atmosphere (Kennet, 2000; Dickens, 2003). Gas hydrates are particularly susceptible to dissociation if bottom water heat efficiently penetrates into the seafloor (MacDonald et al., 1994; Dickens et al., 1995; Kennett, 2000; Dickens, 2003). In the Arctic Ocean, climate change causes atmospheric temperatures to increase much faster than in lower latitudes (IPCC, 2013; Bintanja, 2018). Bottom-water warming may thus be more severe in the Arctic. It may render Arctic gas hydrate deposits in sediments in shallow waters particularly vulnerable to destabilization. Knowledge of the emission history of Arctic seeps is thus crucial in order to understand how environmental parameters have affected methane emissions in the past, and in order to estimate how these will modulate methane emission in the future.

Past methane seepage can be deciphered from relicts of microbial communities that are dependent on methane, which are recorded in authigenic seep carbonates (e.g., Peckmann and Thiel, 2004). At present, most methane in ocean sediments is consumed through the microbially mediated sulfate-dependent anaerobic oxidation of methane-AOM (e.g., Reeburgh, 2007):

$$CH_4 + SO_4^{2-} \rightleftarrows HS^- + HCO_3^- + H_2O \quad (1)$$

The oxidation of methane coupled to the reduction of sulfate forms a zone in sediments, where both methane and sulfate are both consumed and this zone is known as the sulfate-methane transition zone (SMTZ). AOM is mediated by anaerobic methanotrophic archaea (ANME), typically forming syntrophic partnerships with sulfate-reducing bacteria (SRB; Knittel and Boetius, 2009). Methane bypassing the AOM filter can then be oxidized by aerobic methanotrophic bacteria (MOB) at the seafloor or in the water column (Niemann et al., 2006; Knief, 2015; James et al., 2016). At highly active gas seeps, the spatial distance between these activity horizons in the sediments, one that is dominated by AOM and the other one by MOx, can be at the centimeter or even millimeter scale (Niemann et al., 2006; Elvert and Niemann, 2008). The AOM end-products HS^- and HCO_3- result in increased alkalinity in the sediment pore waters, which facilitates precipitation of authigenic carbonates. The precipitating carbonates can then encase the methanotrophic communities that were present in the sediments at the time of their precipitation. Molecular fossils such as lipid biomarkers of aerobic and anaerobic methanotrophic microbes are typically ^{13}C-depleted because AOM, as well as MOx, strongly discriminate against methane containing the heavy isotope ^{13}C. Lipids of these communities have a high preservation potential in seep carbonates (Peckmann et al., 1999; Niemann et al., 2005; Birgel et al., 2008; Birgel et al. 2011), thus allowing to reconstruct past microbial communities at the seep site (Niemann and Elvert, 2008).

Carbonates can form nodules, slabs, crusts, chimneys and sometimes massive pavements at cold seeps (Aloisi et al., 2000; Reitner et al., 2005; Krause et al., 2017). Seep carbonates are preserved at the seafloor or within sediments even after the methane flux has diminished and thus constitute a geological record of past seepage (e.g., Peckmann and Thiel, 2004; Feng et al., 2010; Crémière et al., 2016a; Sauer et al., 2017). The mineralogy and isotopic signatures of seep carbonates, as well as its lipid biomarker inventory, can provide information on the environmental conditions and microbial communities during past seepage episodes, and potential changes of the ascending fluids over time (Argentino et al., 2019).

Because of the carbon isotope effects associated with AOM and the usually ^{13}C depleted signature of the methane substrate, seep carbonates typically display low $\delta^{13}C$ values reflecting the incorporation of predominantly methane-derived carbon (Peckmann et al., 1999; Aloisi et al., 2000; Crémière et al., 2016b; Yao et al., 2020). In contrast, the carbonate O-isotope ratios are influenced by the fluid source water; thus, the $\delta^{18}O$ values of carbonates have been used as a proxy to determine the origin of fluids with differential ^{18}O-signatures, e.g., gas hydrate derived water, water from clay dehydration, or seawater (Bohrmann et al., 1998; Aloisi et al., 2000; Han and Aizenberg, 2003; Feng et al., 2014; Dessandier et al., 2020). Finally, the mineralogy of seep carbonates (aragonite vs. calcite or dolomite) indicates whether they were formed close to the seafloor (aragonite) or rather in the deeper sediments (calcite/high-Mg and calcite/dolomite) (Bohrmann et al., 1998; Aloisi et al., 2000; Haas et al., 2010).

In this study, we investigated seep carbonates sampled from the seafloor and sediment cores obtained at two active seep sites in the Arctic Ocean with underlying gas hydrates: 1) the deepwater Vestnesa Ridge (~1,200 m water depth) and the 2) Storfjordenna gas hydrate mound in shallower waters (~380 m water depth; **Table 1**; **Figure 1**) (Bünz et al., 2012; Panieri et al., 2017; Serov et al., 2017). Macroscopic images of the studied carbonates are shown in **Figure 2**. We studied the carbonate geochemistry to elucidate the history of hydrocarbon seepage at these systems and to reveal potential factors influencing the fluid discharge for the different settings in the past. We used carbonate-C and -O isotope ratio measurements to constrain the carbon sources and to assess the possible influence of seawater and/or fluid from gas hydrates during carbonate precipitation. Seep carbonate-associated lipid biomarkers were analyzed to determine the microbial communities that were present at the time of carbonate precipitation. In this context, one of the prime objectives was to compare the isotope- and lipid biomarker-geochemical imprint of carbonates formed at the seafloor vs. those formed in deeper sediments, in order to find potential links between carbonate formation, methanotrophic communities and differential methane-seepage activity.

STUDY AREA

Vestnesa Ridge (~1,200 m water depth) is a NW-SE trending sediment drift off NW Svalbard. The eastern ridge segment is characterized by numerous pockmarks actively releasing methane

TABLE 1 | List of studied seep carbonates, sample locations, and remarks describing the samples and where they were collected.

Name	Sample ID	Location	Water depth (m)	Coordinates	Remarks
S-1	HH1029	Storfjordrenna	378	76.1069°N 15.9679°E	ROV-sampled seabed crust
S-2	HH1077	Storfjordrenna	378	76.1070°N 15.9694°E	ROV-sampled seabed crust
S-3	1520GC	Storfjordrenna	380	76.1,057°N 15.9661°E	Weakly lithified carbonate nodules, sampled with a gravity core at depth of 282 cmbsf
V-1	P1606002	Vestnesa Ridge	1,204	79.0026°N 69213°E	ROV-sampled seabed crust (P002 in **Figure 1**)
V-2	P1606011	Vestnesa Ridge	1,207	79.0076°N 6.8993°E	ROV-sampled seabed crust (P011 in **Figure 1**)
V-3	P1606012	Vestnesa Ridge	1,207	79.0077°N 68992°E	ROV-sampled seabed crust (P012 in **Figure 1**)
V-4	GeoB21616-1-2R-1E	Vestnesa Ridge	1,210	79.0069°N 69041°E	Cored crust sampled from MeBo core 127 at sediment depth of ~590–595 cmbsf (MeBo 127 in **Figure 1**)

GC, gravity core; ROV, remotely operated underwater vehicle; cmbsf, centimetres below seafloor.

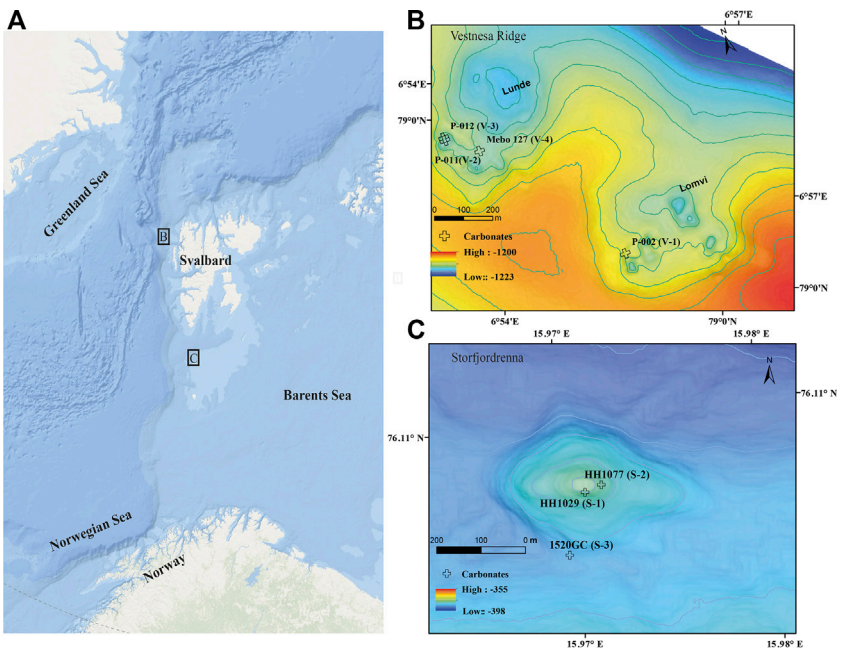

FIGURE 1 | (A) Overview of sampling locations at Vestnesa Ridge off NW Svalbard, and Storfjordrenna gas hydrate mound in the NW Barents Sea (Arctic base map from ArcGIS). **(B,C)** Detailed bathymetry maps and respective seep carbonate sample locations.

of a mixed microbial/thermogenic origin from the seafloor (e.g., Panieri et al., 2017; Pape et al., 2020). Previous investigations showed that the pockmarks cluster along sub-vertical faults (Plaza-Faverola et al., 2015). These investigations also suggest that seepage has likely been ongoing since the early Pleistocene (Knies et al., 2018).

Storfjordrenna is a trough-mouth fan south of Svalbard, NW Barents Sea, and the bathymetry (~380 m water depth) was highly influenced by the repeated growth and retreat of grounding glaciers. In contrast to Vestnesa Ridge, Storfjordenna was affected directly by the pressure release after the retreat of the grounded Scandinavian Ice Sheet during the last deglaciation, causing the destabilization of gas hydrate, which in turn led to the formation of seabed gas hydrate mounds, so-called gas hydrate pingos, that are up to 500 m in diameter and 10 m in height (Serov et al., 2017). Methane release from several seafloor mounds was observed previously, and shallow gas hydrates were recovered from several mounds, including the one studied here. The gas hydrate system of Storfjordrenna probably has existed since ~30,000 years BP (Serov et al., 2017), and comprises both active and inactive mounds, reflecting the spatio-temporal heterogeneity with regards to

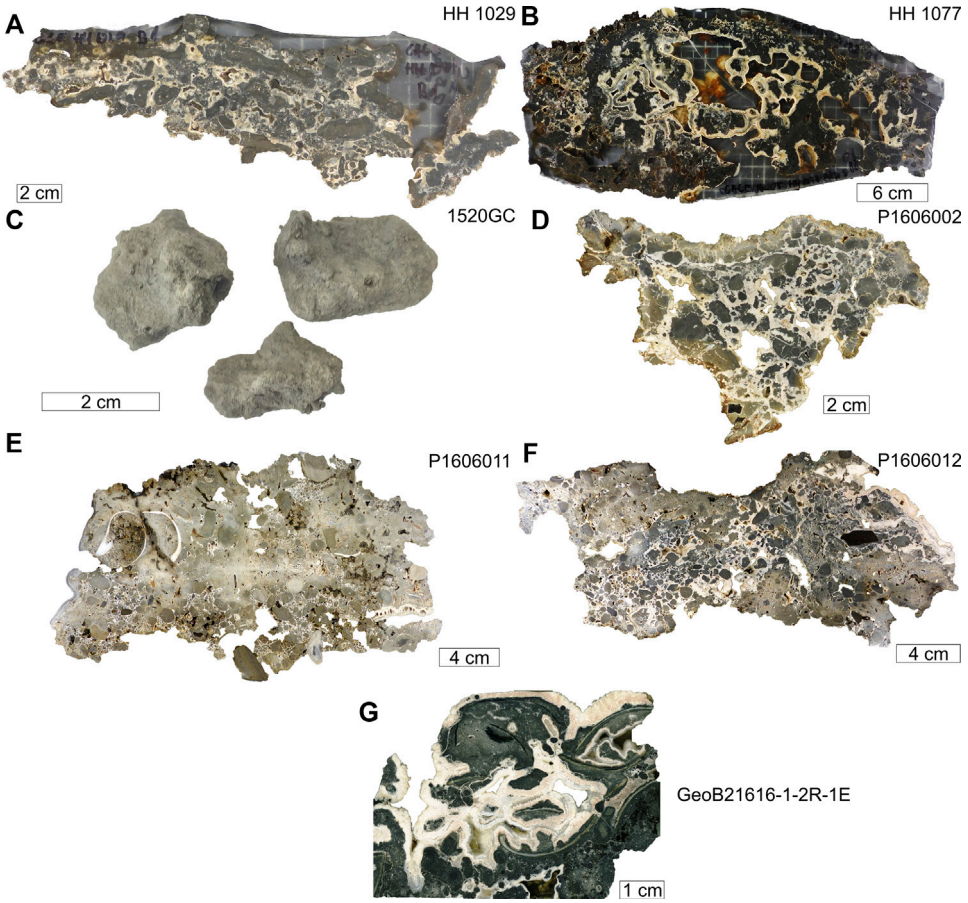

FIGURE 2 | Macroscopic photographs of the investigated seep carbonates [**(A–C)**: Storfjordrenna gas hydrate mound; **(D–G)**: Vestnesa Ridge)]; samples **(A,B,D–G)** are epoxy-impregnated cut slabs. **(A,B,D–G)** Porous intraformational breccias composed of rounded, dark gray microcrystalline aragonite cemented sediment clasts cemented by mm-to cm-thick whitish void-filling aragonite (adapted from Himmler et al., 2019). **(C)** Light gray microcrystalline Mg-calcite cemented sediment nodules. **(E–G)** with sporadic pebble-sized glaciogenic debris and bioclasts (gastropod and bivalve shell fragments).

methane transport and fluid seepage (Hong et al., 2017; 2018; Sen et al., 2018a; Yao et al., 2020).

MATERIALS AND METHODS

Sample Collection

At Vestnesa Ridge, seafloor samples (V-1, V-2, and V-3) were collected with the ROV Ægir 6000 during the R/V *G.O. Sars* cruise P1606 in 2016. The core sample (V-4) was retrieved during the cruise with R/V *Maria S. Merian*, expedition MSM 57, with the deep-sea drill rig MARUM-MeBo 70 in 2016. The carbonate specimen analyzed here was recovered from core MeBo 127 (V-4) at a sediment depth of ~ 5 m (Himmler et al., 2019). At the Strofjordrenna mound, seep carbonates were sampled from the seafloor (S-1 and S-2, **Table 1**) using the ROV by NTNU AMOS (Norwegian University of Science and Technology, Centre for Autonomous Marine Operations and Systems), and from the subsurface, using gravity coring (S-3) during expedition CAGE 15-6 on board of R/V *Helmer Hanssen* in 2016.

Carbonate Carbon and Oxygen Isotopes

Subsamples for stable carbon and oxygen isotope ratio analyses of samples S1, S2, and V1-V3 were obtained from freshly cut surfaces with a hand-held microdrill. Carbonate powders were treated at 70°C with anhydrous phosphoric acid in a GasBench II preparation line connected to a Thermo Scientific Delta V Advantage isotope ratio mass spectrometer (Thermo Fisher Scientific) at the Tallinn University of Technology (TUT), Estonia (Himmler et al., 2019). For stable carbon and oxygen isotopes of samples S-3 and V-4, subsamples were pulverized using an agate mortar, and the sample powders were placed in Thermo Scientific vials and flushed with helium gas. Afterward, five drops of anhydrous phosphoric acid were added manually. After equilibration (>3 h at 50°C), the liberated gas was analyzed on a Gasbench II and MAT253 Isotope Ratio Mass Spectrometer at UiT.

The $\delta^{13}C$ and $\delta^{18}O$ values are reported in per mill (‰) relative to the Vienna Pee Dee Belemnite (VPDB) standard. Normalization to the VPDB for carbon and oxygen isotope ratios was done using in-house standards. Analytical precision was estimated based on replicate measurements of samples and

standards (e.g., NBS-19, NBS-18), and was better than 0.1‰ for $\delta^{13}C$ and $\delta^{18}O$ analyses with the MAT253 IRMS and better than 0.2‰ for analyses of drilled samples with the Delta V Advantage.

Theoretical $\delta^{18}O$-fluid values were calculated using the fractionation factor-temperature relationship after Kim et al. (2007) (**Eq. 2**), and Grossman and Ku (1986) (**Eq. 3**), assuming O-isotope equilibrium with the ambient water during carbonate formation:

$$1000 \ln a_{aragonite-water} = 17.88 \times \frac{103}{T\,(Kelvin)} - 31.14 \quad (2)$$

$$\delta^{18}O_{water}\ (SMOW) = \delta^{18}O_{aragonite}\ (PDB) - \frac{19.7 - t\ (℃)}{4.34} \quad (3)$$

Mineralogy and Petrography

Mineralogical compositions were determined by X-ray diffraction (XRD) on homogenized bulk-rock powders. All samples were analyzed on a Bruker D8 Advance X-ray diffractometer (Cu Kα radiation in 3–75° 2θ range; Sauer et al., 2017). Quantitative data were obtained with the Rietveld algorithm-based code, Topas-5, provided by Bruker. A displacement correction of the spectrum was applied relative to the main quartz peak, and the Mg content in calcite was quantified based the single peak displacement (calcite d_{104}) in the diffraction pattern to estimate the amount of $MgCO_3$ mol% (mole percentage vs. the total carbonate content) in the analyzed samples (Goldsmith et al., 1958).

Petrographic thin sections (~30 μm thick; 6.5 cm × 5 cm) of ROV-sampled and the cored seep carbonate crust samples were prepared from epoxy-fixed cut slabs. Thin sections have been examined with transmitted polarized light microscopy using a Zeiss Axioplan2 equipped with an AxioCam ERc 5s digital camera. Single images were stitched together using the tiles tool of the Zeiss ZEN blue software.

Lipid Biomarkers

Seep carbonates were crushed into centimetre-sized chips and thoroughly washed with deionized (DI) water. Similarly, loose sediment was removed from the weakly lithified carbonate nodules by washing with DI. The cleaned chips and nodules were placed with sanitized stainless-steel tweezers into a glass beaker before slowly adding 37% HCl to dissolve the carbonate matrix (Niemann et al., 2005). The resulting solution was extracted with organic solvents, and lipids were analyzed according to previously reported protocols (Elvert et al., 2003) with modification for alcohol derivatization and instrument setup (Niemann et al., 2005; Blees et al., 2014). Briefly, a total lipid extract (TLE) was obtained by four-step solvent extraction with decreasing polarity of the carbonate solution: dichloromethane (DCM)/methanol (MeOH) 1:2; DCM/MeOH 2:1; and two times DCM. The TLE was then saponified with 12% KOH in MeOH for 3 h at 80°C. A neutral fraction was extracted with hexane before methylation with BF_3/MeOH of the fatty acids, yielding fatty acid methyl esters (FAMEs) for gas-chromatographic (GC) analysis. Concentrations of the different fractions were examined using a GC (Thermo Scientific TRACETM Ultra, Rxi-5ms column) with flame ionization detection (FID). Identification of individual compounds after GC was achieved by quadrupole mass spectrometry (GC-MS) (Thermo Scientific DSQ II). Compound-specific stable carbon isotope ratios were determined using an isotope ratio mass spectrometry (IRMS) unit (Thermo Scientific Delta V Advantage) coupled to a GC setup with the same specification as outlined above. Concentrations and stable carbon isotope ratios were calibrated/normalized using internal standards. Compounds specific stable carbon isotope compositions are reported as $\delta^{13}C$ in ‰ relative to VPDB, and have an analytical error of less than ±1.5‰.

RESULTS

Carbonate Mineralogy, Petrography and Stable Carbon and Oxygen Isotopes

Aragonite and magnesium calcite dominated the carbonate mineralogy of the seafloor samples from both Storfjordrenna (S1-S2) and Vestnesa Ridge (V1-V3). The in-core sample from Storfjordrenna (S-3) was comprised mainly of high-Mg-calcite, whereas the MeBo core sample (V-4) from 590 to 595 cmbsf was mostly aragonitic. Quartz and plagioclase were the main non-carbonate minerals in the samples (**Table 2**).

The seabed-sampled carbonate crusts comprised porous intraformational breccias of microcrystalline carbonate-cemented sediment clasts. Cement consists of mm-to cm-thick aragonite (**Figure 2**). Carbonates sampled from the shallow subsurface (S-3) comprised gray Mg-calcite-cemented, irregular shaped nodules (~2 cm in diameter; **Figure 2**). Clotted and peloidal fabrics, as well as cemented tubes of siboglinid tube worms are common in the Storfjordrenna crusts (**Figures 3A**,**B**; Sen et al., 2018b). The carbonates contained a few mollusc-shell fragments (bivalves and gastropods) (**Figure 3C-F**). The carbonate-cemented sediment clasts of the breccias contained abundant silt to fine-sand sized siliciclastic grains, mostly quartz and feldspar. Fine grained cryptocrystalline aragonite was abundant in the cored sample (V-4), enclosing microcrystalline aragonite-cemented sediment.

The carbonate $\delta^{13}C$ values ranged from −36 to −20‰, and the $\delta^{18}O$ values from 4 to 7‰ (**Figure 4**). The dashed lines in **Figure 4** represent the calculated theoretical $\delta^{18}O$ of aragonite formed in isotopic equilibrium with sea water according to **Eqs. 2** and **3** (aragonite-1 and -2), respectively, and assuming ambient seawater temperatures (−1.5 and 1.9°C) and $\delta^{18}O$ (0‰) at the two study sites. The $\delta^{18}O$ values of the investigated seep carbonates were all above the calculated values for aragonite-1 and -2.

Lipid Biomarker Inventory

Lipid contents and compound-specific $\delta^{13}C$ values are listed in **Table 3**. In the fatty-acid fraction of all samples, we found iso- and anteiso-C15:0 fatty acids with low $\delta^{13}C$-values in the range of −60 to −100‰. Similarly, the isoprenoid glycerol diethers archaeol and *sn2*-hydroxyarchaeol were detected in the alcohol fractions of all samples with $\delta^{13}C$-values of −83 to −109‰. The irregular isoprenoid hydrocarbon crocetane was not detectable in

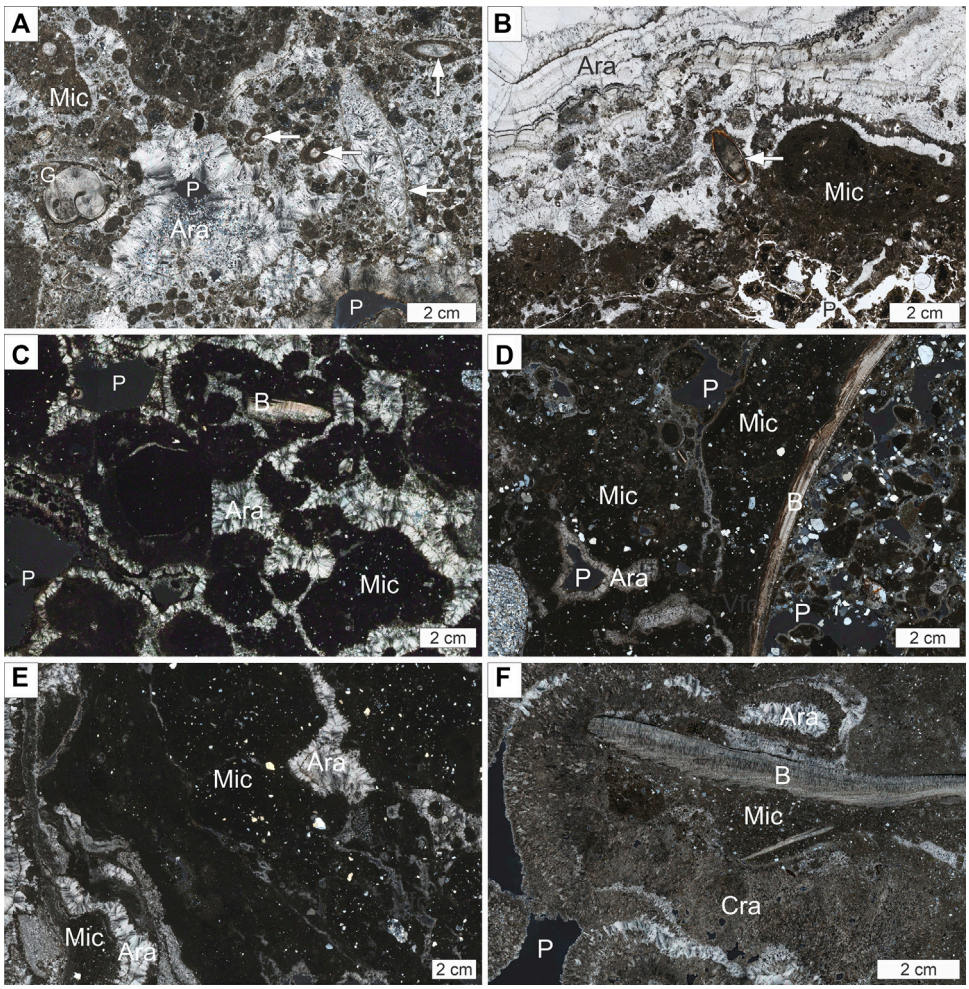

FIGURE 3 | Representative photomicrographs (stitched tiles) of the seep carbonate crusts. **(A)** Microcrystalline aragonite-cemented sediment (Mic) clasts with abundant silt-sized quartz, gastropod fragment(G), and abundant clotted micrite clasts and peloids cemented by botryoidal and fibrous aragonite (*Ara*); arrows point to cemented tube worm tubes; cross-polarized light, pore space (P) appears dark [sample HH 1029 (S-1)] **(B)** Porous (P) microcrystalline aragonite-cemented sediment (Mic) with abundant silt-sized quartz (lower image half) and cm-thick aragonite cement (*Ara*) with abundant clotted micrite inclusions and multiple thin dark bandings; arrow points to tube worm [parallel-polarized light, pore space appears bright; HH 1077(S-2)]. **(C)** Microcrystalline aragonite-cemented sediment (Mic) clasts with abundant silt-sized quartz cemented by botryoidal aragonite (*Ara*); note a bivalve shell fragment (B); cross-polarized light, pore space (P) appears dark [P1606002(V-1)]. **(D)** Microcrystalline aragonite-cemented sediment (Mic) with abundant silt to fine sand sized quartz; not quartzite pebble (lower left) and bivalve shell (B); pores and fractures are lined with botryoidal and fibrous aragonite (*Ara*); cross-polarized light, pore space (P) appears dark [P1606011(V-2)]. **(E)** Microcrystalline aragonite-cemented sediment (Mic) with abundant silt-sized quartz and fracture-filling botryoidal aragonite (*Ara*); cross-polarized light [P1606012(V-3)]. **(F)** Microcrystalline aragonite cemented sediment (Mic) with abundant silt-sized quartz and bivalve fragment (B) surrounded by cryptocrystalline aragonite (Cra) and botryoidal aragonite (*Ara*); cross-polarized light, pore space (P) appears dark [GeoB21616-1-2R-1 E (V-4)]. **(C–F)** adapted from Himmler et al. (2019).

the cored nodule carbonate from Storfjordrenna 1520GC (S-3), and we only found minor amounts in the seafloor crust from Vestnesa (V-3). The irregular isoprenoid hydrocarbon 2,6,10,15,19-pentamethyleicosane (PMI) was present in all samples, but concentrations in V-1 and V-2 were low (0.05 and 0.03 μg/g carbonate). The δ^{13}C-values of the isoprenoid hydrocarbons were always below −91‰.

Typical MOx-related lipids such as a 4α-methyl sterol and diplotene were also present in all samples, with δ^{13}C values of about −50‰. We found substantially lower isotope signatures in these compounds only in the Vestnesa core carbonate (V-4; 4α-methyl sterol: −108‰, Diploptene: −79‰).

DISCUSSION

Lipid Biomarker Constrains on Microbial Communities During Carbonate Precipitation

AOM Communities

At cold seeps, a substantial fraction of the uprising methane is consumed in sediments by anaerobic methane-oxidizing archaea (ANME-1, -2, -3), often in association with sulfate-reducing partner bacteria of the DSS and DSB clade (Knittel and Boetius, 2009; Milucka et al., 2012; Wegener et al., 2015;

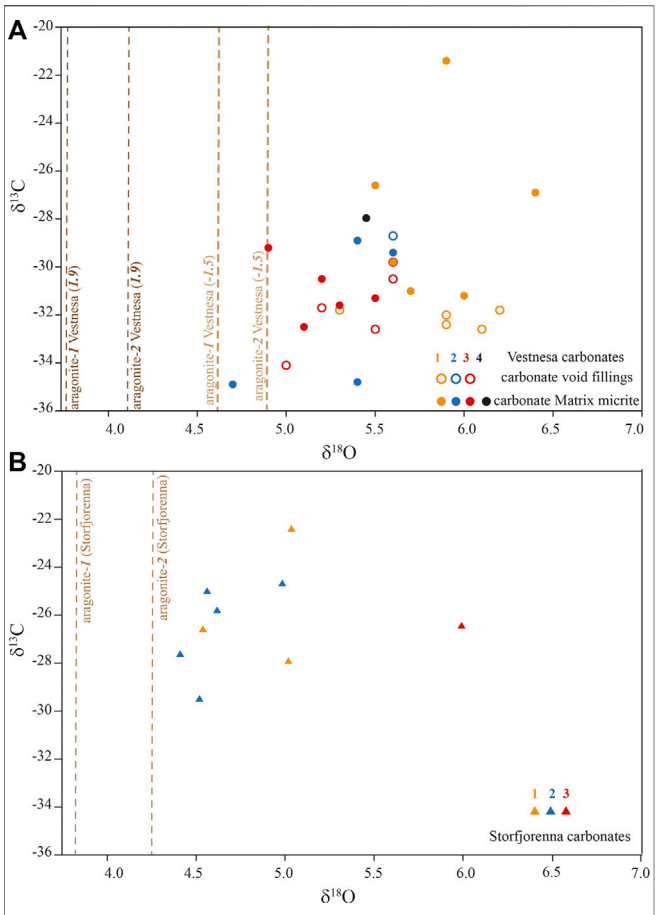

FIGURE 4 | Carbonate stable carbon and oxygen isotope compositions in **(A)**. Vestnesa Ridge and **(B)** Storfjordrenna. The dashed lines indicate the theoretical $\delta^{18}O$ values of aragonite-1 (Kim et al., 2007), aragonite-2 (Grossman and Ku, 1986) expected for precipitation in equilibrium with bottom water temperature, according to **Eqs. 2** and **3**, respectively. For Vestnesa, two different temperatures were assumed based on the reconstructed temperature from foraminifera (Dessandier et al., 2019).

Gründger et al., 2019). Methane bypassing the AOM filter and reaching oxic sediments at the seafloor or the water column then can be consumed by methanotrophic bacteria (MOB) which mediate the aerobic oxidation of methane (MOx; Niemann et al., 2006; Reeburgh, 2007; Steinle et al., 2015). Specific lipid biomarkers can be used to identify the dominant microbes involved in AOM and MOx (Elvert and Niemann, 2008; Niemann and Elvert, 2008), and to differentiate between the two main modes of methane oxidation. Lipids of (methanotrophic) microbes are encased in the carbonate matrix at the time of mineral precipitation. Lipids can hence be used to assess the biogeochemical environment. (Blumenberg et al., 2004; Niemann and Elvert, 2008; Birgel et al., 2011; Himmler et al., 2015).

Diagnostic archaeal and bacterial lipids detected here were strongly depleted in ^{13}C, providing conclusive evidence for the occurrence of microbial communities performing AOM (Niemann and Elvert, 2008), as well as MOx (Elvert and Niemann, 2008). Overall, the lipid biomarker inventory characterized by low *sn2*-hydroxyarchaeol/archaeol ratios <0.3 and an aiC15:0/iC15:0 FA ratio of 0.1–1.2 was similar to carbonates from other seep sites, including the Congo Fan (Feng et al., 2010), the Gulf of Mexico (Birgel et al., 2011; Feng et al., 2014), and the South China Sea (Guan et al., 2016). In contrast, quite different ANME- and SRB-related lipids were found at other seep sites (e.g., with a much higher *sn2*-hydroxyarchaeol/archaeol ratio $\gg 1$; Niemann et al., 2005; Niemann et al., 2006; Guan et al., 2019). This difference in lipid contents is most likely related to different types of microorganisms that become encased in the carbonate precipitates (Niemann and Elvert, 2008).

Indeed, ANME-1/DSS, ANME-2/DSS, and ANME-3/DBB consortia can be distinguished based on their lipid biomarker and isotopic fingerprints (Niemann and Elvert, 2008). For example, ANME-2/DSS consortia are characterized by the presence of crocetane, while PMIs with four and five double bonds without any higher saturated homologs were only found in ANME-3. Both ANME-2 and -3 are characterized by an elevated (typically >1.1) *sn2*-hydroxyarchaeol (OH-ar) to archaeol (OH-ar/ar) ratio, which distinguishes them from ANME-1/DSS (Niemann and Elvert, 2008). Accordingly, the low OH-ar/ar ratios of 0.1–0.3 (**Table 3**) suggest the presence of ANME-1/DSS. However, we also observed high concentrations of crocetane in all carbonates except for S-3 and V-3. Crocetane is abundant in ANME-2, but is typically only found in minor amounts, or not at all, in ANME-1 (Niemann and Elvert, 2008 and reference therein). Its absence, while not conclusively diagnostic, is consistent with an ANME-1/DSS dominated seep environments (Haas et al., 2010). ANME-1 microbes at some ancient seeps have been identified in a similar manner (Peckmann et al., 2009; Natalicchio et al., 2015). We argue that the lower stability of *sn2*-hydroxyarchaeol can explain our finding of low OH-ar/ar ratios (in the presence of elevated crocetane concentrations), i.e., *sn2*-hydroxyarchaeol loses its hydroxyl group during (early) diagenesis so that the *sn2*-hydroxyarchaeol to archaeol ratio decreases. Furthermore, the saturated hydrocarbon crocetane is probably more stable, such that its presence in our carbonate samples indicates that the AOM community at the time of precipitation was either ANME-2 dominated or comprising a mixture of ANME-2 and ANME-1. Only carbonate S-3 did not contain detectable amounts of crocetane, pointing to ANME-1 as the dominant AOM microbes in this sample. Carbonate sample S-3 also contained a higher proportion of Mg-calcite, suggesting a lower methane flux at the time of precipitation (see *Discussion* in the following section). This is also consistent with a prevalence of ANME-1, which often dominates low methane flux sites (Knittel et al., 2005; Gründger et al., 2019). It was shown previously that the dominant microbial community in relatively deep sediments (70 cmbsf) at the Storfjordrenna seeps was ANME-1/Seep-SRB1 (Gründger et al., 2019), which is consistent with the lipid biomarker signature of the Mg-calcite dominated nodular seep carbonate (S3) recovered from 282 cmbsf. However, we also found signatures typical for MOx communities in this carbonate (see section *MOx-Communities* below), which raises the question of

TABLE 2 | Mineralogical compositions (weight-%) of the carbonates.

Name	Sample ID	Aragonite	Mg-calcite	Dolomite	Quartz	Plagioclase
S-1	HH1029	55	23		10	3
S-2	HH1077	75	10		7	2
S-3	1520GC		60	1	23	4
V-1	P1606002	61	11	Trace	12	5
V-2	P1606011	40	2		23	11
V-3	P1606012	70				
V-4	MeBo 127	77	2		10	4

Mg-calcite, magnesium-calcite.

whether the carbonate was indeed precipitated in deep anoxic sediments.

^{13}C-depleted, terminally branched ai-C15:0 and i-C15:0 fatty acids are diagnostic biomarkers for SR partner bacteria (Niemann and Elvert, 2008). The ratio of ai-C15:0/i-C15:0 of ~1 in all samples points to ANME-2 associated SEEP-SRB1 or *Desulfobulbus* associated to ANME-3. However, we could not find the fatty acid cyC17:0ω5,6, which is typically indicative of the ANME-2 associated SRB, nor-C17:1ω6 which is diagnostic for the ANME-3 partner SRB (Niemann and Elvert, 2008 and reference therein). Nevertheless, with respect to the probable prevalence of ANME-2 in the studied systems (except sample S3), we suggest that the fatty acid pattern is rather indicative of the ANME-2 associated SEEP-SRB1.

MOx-Communities

The seep carbonates contained high abundances of ^{13}C-depleted diplotene and 4α-methyl sterol (compound Ib in Elvert and Niemann, 2008), respectively, which were suggested as characteristic markers for Type I MOB (Elvert and Niemann, 2008). MOx is a strictly aerobic process usually occuring at the seafloor or in the water column, where both dissolved oxygen and methane are available. To the best of our knowledge, only a few indications exists from fresh water environments that some MOB-type microbes can use alternative electron acceptors such as nitrate or sulfate (van Grinsven et al., 2020a; van Grinsven et al., 2020b). But the environmental significance of these modes of methane oxidation, in particular in marine systems, is unclear. Both, the seafloor and core samples at Vestnesa Ridge (V1–V4) contained diplotene and the 4α-methyl sterol with a substantial to moderate ^{13}C-depletion (−108 to −45‰), similar to what has been observed in some of the modern seep carbonates (Birgel et al., 2011; Himmler et al., 2015; Guan et al., 2016) and in surface sediments of active cold seeps (Elvert and Niemann, 2008). Following those findings, we propose that their presence in seep carbonates indicates less reducing, or intermittent microaerophilic, conditions during carbonate precipitation (Birgel et al., 2011). The co-encasing of both AOM and MOx-derived lipids strongly suggests that the spatial distance between AOM and MOx zones must have been very small. Such conditions are typically found in present-day systems where the methane flux rates are very high, preventing sulfate from penetrating deeper into the seafloor and thus limiting AOM to the sediment surface (Niemann et al., 2006; Lösekann et al., 2007; Lee et al., 2019). We argue that the co-occurrence of AOM- and MOB-derived lipids furthermore demonstrates that, at the time of carbonate precipitation, the system must have vented vigorously, releasing substantial amounts of methane into the water column. Sedimentary MOx communities typically occur when methane bypasses the AOM filter in deeper sediments (Niemann et al., 2006; Birgel et al., 2011; Steinle et al., 2016). MOx alone is typically less effective compared to AOM with regards to preventing methane emissions from the seafloor because MOx demands oxygen, which restricts MOx communities often to a thin layer at the sediment surface. Hence, sedimentary MOx can only retain a rather limited fraction of benthic methane, in particular when the overall methane flux is high. In contrast, in systems characterized by low methane fluxes, methane is typically consumed in deeper sediment layers, within a well-defined SMTZ (Knittel and Boetius, 2009), so that MOB communities generally do not develop at the sediment surface. Thus, we interpret our biomarker-based finding that both aerobic and anaerobic methanotrophs were encapsulated in the same carbonate matrix reflecting past periods of high methane flux. These high-flux periods could have also been related to a non-steady state of methane flux with a not fully-developed AOM community, or episodic pulses of high methane fluxes that bypass the AOM barrier and reach oxic surface sediments (Yao et al., 2019).

Our biomarker findings are also consistent with the mineralogical composition of the carbonate samples. Highest hopanoid contents were found in the aragonite-dominated core carbonate in Vestnesa (V-4), with ANME-2/DSS most likely as the dominant consortia. Together, the geochemical and mineralogical evidence suggest that carbonates retrieved from the sediment cores in Vestnesa were precipitated very close to the seafloor (Himmler et al., 2019), i.e., a favourable environment for MOx. Nevertheless, at this point, we cannot sufficiently explain the presence of MOB-diagnostic hopanoids in sample S-3 from Storfjordrenna. All evidence (other than the presence of isotopically depleted MOB lipids in the carbonate), point to the S-3 carbonate precipitation in deeper sediment layers, and a persistent anoxic environment that would not support MOB community development. Possibly, the Mg-calcite dominated carbonate nodule precipitated in reduced sediments that were still close enough to the redox-transition zone to also encase MOx-related lipids. Alternatively, it may have formed in deeper sediments, and subsequently exposed to a more oxic environment and overprinted by a second layer of MOB-derived lipids before burial in deeper sediments.

Carbonate δ^{13}C and δ^{18}O Indicate Gas Hydrate Dissociation During Precipitation

Sampled carbonates from the seabed and core samples from both Storfjordrenna and Vestnesa display very negative δ^{13}C values (**Figure 2**). The observed δ^{13}C values (−36 to −20‰) fall into the typical δ^{13}C range for methane seep carbonates (Lein, 2004; Naehr et al., 2007). Seep-carbonate δ^{13}C reflects a mixture of different carbon sources including dissolved inorganic carbon (DIC) from seawater, oxidized organic matter, and residual DIC

TABLE 3 | Lipid biomarker concentrations and compound-specific $\delta^{13}C$ values.

	HH 1029 (S-1)		HH 1077 (S-2)		1520 GC (S-3)		P1606002 (V-1)		P1606011 (V-2)		P1606012 (V-3)		MeBo 127 (V-4)	
	Concentration (µg/g carbonate)	$\delta^{13}C$ (‰)	Concentration (µg/g carbonate)	$\delta^{13}C$ (‰)	Concentration (µg/g carbonate)	$\delta^{13}C$ (‰)	Concentration (µg/g carbonate)	$\delta^{13}C$ (‰)	Concentration (µg/g carbonate)	$\delta^{13}C$ (‰)	Concentration (µg/g carbonate)	$\delta^{13}C$ (‰)	Concentration (µg/g carbonate)	$\delta^{13}C$ (‰)
I-15-FA	0.30	−62	0.31	−76	0.42	−39	0.85	−74	0.40	−83	2.79	−91	0.76	−99
Ai-15-FA	0.35	−64	0.45	−76	0.34	−33	0.85	−71	0.40	−70	0.35	−78	0.87	−90
Ar	1.00	−102	3.64	−99	0.49	−90	0.71	−99	0.67	−104	0.82	−105	11.37	−109
OH-Ar	0.16	−95	0.94	−101	0.07	−93	0.13	n.d.	0.13	−103	0.27	−105	0.49	−83
4α methyl sterol	0.04	−45	0.14	−57	0.29	−64	0.02	−52	0.03	−46	0.02	−61	0.16	−108
Diploptene	0.08	−54	0.36	−52	0.15	−46	0.17	−51	0.18	−52	0.15	n.d.	0.70	−79
crocetane	0.36	−97	1.65	−105	n.d.	n.d.	0.30	−99	0.47	−103	0.05	n.d.	1.76	−115
PMI:0	0.07	−91	0.20	−96	0.09		0.03		0.05	−100	0.03	n.d.	0.14	−113
OH-Ar/Ar	0.2		0.3		0.1		0.2		0.2		0.3		0.04	
Ai-15-FA/I-15-FA	1.2		1.4		0.8		0.9		1.0		0.1		1.1	
$\Delta\delta^{13}C$ Ar-OH-Ar	−6		3		3				−1				−27	

FA, fatty acids; PMI, pentamethyleicosane; Ar, archaeol; OH-Ar, sn2-hydroxylarchaeol; n. d, not determined, content too low for accurate analysis.

affected by methanogenesis in addition to DIC derived from AOM (e.g., Peckmann and Thiel, 2004). AOM produces very low-$\delta^{13}C$ DIC carbon isotope signatures because the organisms preferentially utilize an already ^{13}C-depleted carbon source (i.e., methane) for biomass production, and additionally discriminate against ^{13}C during methane oxidation (Whiticar, 1999; Holler et al., 2009). The methane source at both sampling locations represents a mixture of thermogenic and microbial origins, with $\delta^{13}C$ values of −48‰ at Storfjordrenna (Serov et al., 2017), and −54‰ at Vestnesa (Panieri et al., 2017), respectively. Porewater DIC $\delta^{13}C$ at Storfjordrenna is about −28‰, and −32‰ at Vestnesa Ridge. The average $\delta^{13}C$ value of organic carbon from the investigated Storfjordrenna gas hydrate mound is −26‰ (**Supplementary Table S1**), and around −25‰ (Sauer et al., 2020) at Vestnesa. Mineralization of organic carbon produces DIC with almost the same carbon isotope composition (Presley and Kaplan, 1968). Given that the observed carbonate $\delta^{13}C$ values (−36 to −20‰) best match the pore water DIC $\delta^{13}C$ values, and are generally lower than those expected for DIC produced from organic matter remineralization, we conclude that the carbonates have incorporated a higher portion of methane-derived porewater DIC, compared to carbon from sedimentary organic matter or seawater-derived carbon.

Information on the oxygen isotopic composition of the fluid (from which the carbonates precipitated) can be deduced from seep carbonate $\delta^{18}O$-values (e.g., Greinert et al., 2001; Naehr et al., 2007). In turn, the ^{18}O-signature of the ambient water can be used to constrain the environmental setting of carbonate precipitation. Assuming that aragonite formed in isotopic equilibrium with bottom water at temperatures that are similar to those today, and assuming a $\delta^{18}O$-value of 0‰ (V-SMOW) for the seawater, the theoretical $\delta^{18}O$ aragonite values would be 3.8 (**Eq. 2**) – 4.3‰ (**Eq. 3**) in Storfjordrenna, and 3.8 (**Eq. 2**)–4.9‰ (**Eq. 3**) at Vestnesa Ridge. Remarkably, the measured carbonate $\delta^{18}O$-values are substantially higher than these calculated equilibrium values (**Figure 4**). The higher $\delta^{18}O$ values of the authigenic carbonates suggest the incorporation of O-atoms from an ^{18}O-enriched fluid during carbonate precipitation. Such ^{18}O-enriched fluid might originate from gas hydrate dissociation (Hesse and Harrison, 1981; Ussler and Paull, 1995), clay mineral dehydration (Hesse, 2003), or deep-sourced fluids modified by mineral-water interactions (Giggenbach, 1992). The lipid and mineralogy data suggest that most of our samples (except S-3) were formed close to the seafloor, yet the observed carbonate $\delta^{18}O$ values clearly do not support O incorporation from average seawater and suggest that O-isotope exchange with ^{18}O-rich fluids overprinted the seawater $\delta^{18}O$-signal of about 0‰. Discerning a fluid source (e.g., gas hydrate vs. mineral dewatering) based on the carbonate $\delta^{18}O$ values alone is ambiguous. Yet, considering that gas hydrates are present in shallow sediments at both sampling sites (Panieri et al., 2017; Serov et al., 2017), it seems reasonable that at least some of the ^{18}O-enrichment of the carbonate can be attributed to O-atom incorporation from fluids derived from gas hydrate dissociation (Greinert et al.,

2001; Naehr et al., 2007), as assumed from ^{18}O-enrichment in foraminifera shells in the same region (Dessandier et al., 2019).

Seep Carbonate Mineralogy

All carbonates recovered from Vestnesa Ridge (at the seafloor and in the core; V1–V4) as well as Storfjordrenna carbonates S1 and S2 are predominantly composed of aragonite, whereas the nodular carbonate from Storfjordrenna (S-3) was mostly Mg-calcite. This difference in seep carbonate mineralogy has been observed previously (Bohrmann et al., 1998; Crémière et al., 2016b), and was attributed to the formation environment (Burton, 1993; Mazzini et al., 2004). At seeps, carbonate precipitation occurs when the fluids become oversaturated with AOM-produced bicarbonate and if the required dissolved cations (i.e., Ca^{2+}, Sr^{2+}, Mg^{2+}) are available. More precisely, formation of aragonite is favored over Mg-calcite at high-sulfate and low-sulfide concentrations (Burton, 1993; Bayon et al., 2007). Therefore, aragonite-dominated seep carbonates are expected to form closer to the seafloor because of the higher sulfate concentration in seawater, as sulfate is generally depleted in deeper sediments (Bohrmann et al., 1998; Aloisi et al., 2000; Feng et al., 2014; Crémière et al., 2016b). Precipitation of aragonite at the seafloor is consistent with our findings of co-occuring AOM and MOx-derived lipids in the carbonates, which also indicate precipitation close the sea floor. The Mg-calcite rich sample from Storfjordrenna, on the other hand, indicates a formation at a relatively low methane flux in deeper sediments.

SUMMARY AND CONCLUSION

In this study, seep-carbonate samples from two active Arctic gas hydrate sites, Vestnesa Ridge and Storfjordrenna gas hydrate mounds, were investigated. The carbonate carbon and oxygen isotope ratios, carbonate mineralogy, and lipid biomarker inventories indicate where, and under which environmental conditions, the carbonates were formed originally. The ^{13}C-depleted carbon and ^{18}O-enriched isotope signatures of all carbonates reflect methane carbon incorporation (via AOM), and a precipitation environment where carbonates are formed in isotopic equilibrium with porewater affected by gas hydrate dissociation. ^{13}C-depleted biomarkers in all samples reveal the presence of ANME-2/DSS microbial consortia at the time of carbonate precipitation and their entombment in the authigenic carbonate matrix. Furthermore, the recovery of lipids in the mostly aragonitic carbonates, which typically originate from aerobic methanotrophs, indicates the close proximity of anoxic and oxic methane oxidation zones in the shallow sediments, implying high methane fluxes and probably methane ebullition to the water column at the time when the carbonates were precipitated. We suggest that the combined analysis of carbonate mineralogy and lipid biomarker contents in a geochronological context (e.g., through U/Th-dating of carbonates) has the potential to reconstruct the magnitude of seepage activity in the past.

DATA AVAILABILITY STATEMENT

The original contributions presented in the study are included in the article/**Supplementary Material**, further inquiries can be directed to the corresponding author.

AUTHOR CONTRIBUTIONS

HY collected the samples and performed the biomarker analysis under supervision with GP and HN. TH provided support for mineralogy and ML provided support for biomarker experiments. All authors contributed to the writing of the manuscript at all stages.

FUNDING

This work was supported by the Research Council of Norway through its Centre of Excellence funding scheme for CAGE, project number 223259, and partially by the NORCRUST project, grant number 255150.

ACKNOWLEDGMENTS

We thank Tõnu Martma from the Tallinn University of Technology for the stable isotope analyses, Jasmin Schoenenberger from NGU for the XRD analysis of carbonate samples, as well as the captain, crew members, and scientific team of R/V Helmer Hanssen, R/V G.O. Sars, R/V Maria S. Merian for their contribution during the research cruises CAGE 15-6, P1606 and MSM57.

SUPPLEMENTARY MATERIAL

The Supplementary Material for this article can be found online at: https://www.frontiersin.org/articles/10.3389/feart.2020.570742/full#supplementary-material.

REFERENCES

Aloisi, G., Pierre, C., Rouchy, J.-M., Foucher, J.-P., and Woodside, J. (2000). Methane-related authigenic carbonates of Eastern Mediterranean Sea mud volcanoes and their possible relation to gas hydrate destabilisation. *Earth Planet Sci. Lett.* 184, 321–338. doi:10.1016/S0012-821X(00)00322-8

Argentino, C., Lugli, F., Cipriani, A., Conti, S., and Fontana, D. (2019). A deep fluid source of radiogenic Sr and highly dynamic seepage conditions recorded in Miocene seep carbonates of the northern Apennines (Italy). *Chem. Geol.* 522, 135–147. doi:10.1016/j.chemgeo.2019.05.029

Bayon, G., Pierre, C., Etoubleau, J., Voisset, M., Cauquil, E., Marsset, T., et al. (2007). Sr/Ca and Mg/Ca ratios in Niger Delta sediments: implications for authigenic carbonate genesis in cold seep environments. *Mar. Geol.* 241, 93–109. doi:10.1016/j.margeo.2007.03.007

Bintanja, R. (2018). The impact of Arctic warming on increased rainfall. *Sci. Rep.* 8, 16001. doi:10.1038/s41598-018-34450-3

Birgel, D., Feng, D., Roberts, H. H., and Peckmann, J. (2011). Changing redox conditions at cold seeps as revealed by authigenic carbonates from Alaminos Canyon, northern Gulf of Mexico. *Chem. Geol.* 285, 82–96. doi:10.1016/j.chemgeo.2011.03.004

Birgel, D., Himmler, T., Freiwald, A., and Peckmann, J. (2008). A new constraint on the antiquity of anaerobic oxidation of methane: late Pennsylvanian seep limestones from southern Namibia. *Geology* 36, 543. doi:10.1130/g24690a.1

Blees, J., Niemann, H., Wenk, C. B., Zopfi, J., Schubert, C. J., Jenzer, J. S., et al. (2014). Bacterial methanotrophs drive the formation of a seasonal anoxic benthic nepheloid layer in an alpine lake. *Limnol. Oceanogr.* 59, 1410–1420. doi:10.4319/lo.2014.59.4.141E

Blumenberg, M., Seifert, R., Reitner, J., Pape, T., and Michaelis, W. (2004). Membrane lipid patterns typify distinct anaerobic methanotrophic consortia. *Proc. Natl. Acad. Sci. U.S.A.* 101, 11111–11116. doi:10.1073/pnas.0401188101

Bohrmann, G., Greinert, J., Suess, E., and Torres, M. (1998). Authigenic carbonates from the Cascadia subduction zone and their relation to gas hydrate stability. *Geology*. Editor C. K. Paull and W. P. Dillon, 26, 647–650. doi:10.1130/0091-7613(1998)026<0647:acftcs>2.3.co;2

Bünz, S., Polyanov, S., Vadakkepuliyambatta, S., Consolaro, C., and Mienert, J. (2012). Active gas venting through hydrate-bearing sediments on the Vestnesa Ridge, offshore W-Svalbard. *Mar. Geol.* 332-334, 189–197. doi:10.1016/j.margeo.2012.09.012

Burton, E. A. (1993). Controls on marine carbonate cement mineralogy: review and reassessment. *Chem. Geol.* 105, 163–179. doi:10.1016/0009-2541(93)90124-2

IPCC, et al. (2013). "Climate change 2013: the physical science basis," in *Contribution of working group I to the fifth assessment report of the intergovernmental panel on climate change*. Editors T. F. Stocker, D. Qin, G.-K. Plattner, M. M. B. Tignor, S.K. Allen, J. Boschung, et al. (Cambridge, United Kingdom and New York, NY, USA:Cambridge University Press), 1535.

Crémière, A., Lepland, A., Chand, S., Sahy, D., Condon, D. J., Noble, S. R., et al. (2016a). Timescales of methane seepage on the Norwegian margin following collapse of the Scandinavian Ice Sheet. *Nat. Commun.* 7, 11509. doi:10.1038/ncomms11509

Crémière, A., Lepland, A., Chand, S., Sahy, D., Kirsimäe, K., Bau, M., et al. (2016b). Fluid source and methane-related diagenetic processes recorded in cold seep carbonates from the Alvheim channel, central North Sea. *Chem. Geol.* 432, 16–33. doi:10.1016/j.chemgeo.2016.03.019

Dessandier, P.-A., Borrelli, C., Yao, H., Sauer, S., Hong, W.-L., and Panieri, G. (2020). Foraminiferal δ18O reveals gas hydrate dissociation in Arctic and North Atlantic ocean sediments. *Geo Mar. Lett.* 40, 507–523. doi:10.1007/s00367-019-00635-6

Dickens, G. R. (2003). Rethinking the global carbon cycle with a large, dynamic and microbially mediated gas hydrate capacitor. *Earth Planet Sci. Lett.* 213, 169–183. doi:10.1016/s0012-821x(03)00325-x

Dickens, G. R., O'Neil, J. R., Rea, D. K., and Owen, R. M. (1995). Dissociation of oceanic methane hydrate as a cause of the carbon isotope excursion at the end of the Paleocene. *Paleoceanography* 10, 965–971. doi:10.1029/95pa02087

Elvert, M., Boetius, A., Knittel, K., and Jørgensen, B. B. (2003). Characterization of specific membrane fatty acids as chemotaxonomic markers for sulfate-reducing bacteria involved in anaerobic oxidation of methane. *Geomicrobiol J.* 20, 403–419. doi:10.1080/01490450303894

Elvert, M., and Niemann, H. (2008). Occurrence of unusual steroids and hopanoids derived from aerobic methanotrophs at an active marine mud volcano. *Org. Geochem.* 39, 167–177. doi:10.1016/j.orggeochem.2007.11.006

Feng, D., Birgel, D., Peckmann, J., Roberts, H. H., Joye, S. B., Sassen, R., et al. (2014). Time integrated variation of sources of fluids and seepage dynamics archived in authigenic carbonates from Gulf of Mexico Gas Hydrate Seafloor Observatory. *Chem. Geol.* 385, 129–139. doi:10.1016/j.chemgeo.2014.07.020

Feng, D., Chen, D., Peckmann, J., and Bohrmann, G. (2010). Authigenic carbonates from methane seeps of the northern Congo fan: microbial formation mechanism. *Mar. Petrol. Geol.* 27, 748–756. doi:10.1016/j.marpetgeo.2009.08.006

Giggenbach, W. F. (1992). Isotopic shifts in waters from geothermal and volcanic systems along convergent plate boundaries and their origin. *Earth Planet Sci. Lett.* 113, 495–510. doi:10.1016/0012-821X(92)90127-H

Goldsmith, J. R., Graf, D. L., Chodos, A. A., Joensuu, O. I., and Mcvicker, L. D. (1958). Relation between lattice constants and composition of Ca-Mg carbonates. *Am. Mineral.* 43, 84–101.

Greinert, J., Bohrmann, G., and Suess, E. (2001). "Gas hydrate-associated carbonates and methane-venting at hydrate ridge: classification, distribution, and origin of authigenic lithologies," in *Natural gas hydrates: occurrence, distribution, and detection* (Washington, DC: American Geophy-sical Union, 99–113.

Grossman, E. L., and Ku, T.-L. (1986). Oxygen and carbon isotope fractionation in biogenic aragonite: Temperature effects. *Chem. Geol. Isot. Geosci.* 59, 59–74. doi:10.1016/0168-9622(86)90057-6

Gründger, F., Carrier, V., Svenning, M. M., Panieri, G., Vonnahme, T. R., Klasek, S., et al. (2019). Methane-fuelled biofilms predominantly composed of methanotrophic ANME-1 in Arctic gas hydrate-related sediments. *Sci. Rep.* 9, 9725. doi:10.1038/s41598-019-46209-5

Guan, H., Feng, D., Wu, N., and Chen, D. (2016). Methane seepage intensities traced by biomarker patterns in authigenic carbonates from the South China Sea. *Org. Geochem.* 91, 109–119. doi:10.1016/j.orggeochem.2015.11.007

Guan, H., Sun, Z., Mao, S., Xu, L., Cao, H., and Geng, W. (2019). Authigenic carbonate formation revealed by lipid biomarker inventory at hydrocarbon seeps: A case study from the Okinawa Trough. *Mar. Petrol. Geol.* 101, 502–511.

Haas, A., Peckmann, J., Elvert, M., Sahling, H., and Bohrmann, G. (2010). Patterns of carbonate authigenesis at the Kouilou pockmarks on the Congo deep-sea fan. *Mar. Geol.* 268, 129–136. doi:10.1016/j.margeo.2009.10.027,2010

Han, Y. J., and Aizenberg, J. (2003). Effect of magnesium ions on oriented growth of calcite on carboxylic acid functionalized self-assembled monolayer. *J. Am. Chem. Soc.* 125, 4032–4033. doi:10.1021/ja034094z

Hesse, R. (2003). Pore water anomalies of submarine gas-hydrate zones as tool to assess hydrate abundance and distribution in the subsurface what have we learned in the past decade? *Earth Sci. Rev.* 61, 149–179. doi:10.1016/S0012-8252(02)00117-4

Hesse, R., and Harrison, W. E. (1981). Gas hydrates (clathrates) causing pore-water freshening and oxygen isotope fractionation in deep-water sedimentary sections of terrigenous continental margins. *Earth Planet Sci. Lett.* 55, 453–462. doi:10.1016/0012-821X(81)90172-2

Himmler, T., Birgel, D., Bayon, G., Pape, T., Ge, L., Bohrmann, G., et al. (2015). Formation of seep carbonates along the Makran convergent margin, northern Arabian Sea and a molecular and isotopic approach to constrain the carbon isotopic composition of parent methane. *Chem. Geol.* 415, 102–117. doi:10.1016/j.chemgeo.2015.09.016

Himmler, T., Sahy, D., Martma, T., Bohrmann, G., Plaza-Faverola, A., Bünz, S., et al. (2019). A 160,000-year-old history of tectonically controlled methane seepage in the Arctic. *Sci. Adv.* 5, eaaw1450. doi:10.1126/sciadv.aaw1450

Holler, T., Wegener, G., Knittel, K., Boetius, A., Brunner, B., Kuypers, M. M., et al. (2009). Substantial (13) C/(12) C and D/H fractionation during anaerobic oxidation of methane by marine consortia enriched *in vitro*. *Environ. Microbiol. Rep.* 1, 370–376. doi:10.1111/j.1758-2229.2009.00074.x

Hong, W. L., Torres, M. E., Carroll, J., Crémière, A., Panieri, G., Yao, H., et al. (2017). Seepage from an arctic shallow marine gas hydrate reservoir is insensitive to momentary ocean warming. *Nat. Commun.* 8, 15745. doi:10.1038/ncomms15745

Hong, W.-L., Torres, M. E., Portnov, A., Waage, M., Haley, B., and Lepland, A. (2018). Variations in gas and water pulses at an arctic seep: fluid sources and methane transport. *Geophys. Res. Lett.* 45, 4153. doi:10.1029/2018gl077309

James, R. H., Bousquet, P., Bussmann, I., Haeckel, M., Kipfer, R., Leifer, I., et al. (2016). Effects of climate change on methane emissions from seafloor sediments in the Arctic Ocean: A review. *Limnol. Oceanogr.* 61 (S1), S283–S299.

Kennett, J. P., Cannariato, K. G., Hendy, I. L., and Behl, R. J. (2000). Carbon isotopic evidence for methane hydrate instability during quaternary interstadials. *Science* 288, 128–133. doi:10.1126/science.288.5463.128

Kim, S.-T., O'Neil, J. R., Hillaire-Marcel, C., and Mucci, A. (2007). Oxygen isotope fractionation between synthetic aragonite and water: influence of temperature and Mg2+ concentration. *Geochem. Cosmochim. Acta* 71, 4704–4715. doi:10.1016/j.gca.2007.04.019

Knief, C. (2015). Diversity and habitat preferences of cultivated and uncultivated aerobic methanotrophic bacteria evaluated based on pmoA as molecular marker. *Front. Microbiol.* 6 (487), 1346. doi:10.3389/fmicb.2015.01346

Knies, J., Daszinnies, M., Plaza-Faverola, A., Chand, S., Sylta, Ø., Bünz, S., et al. (2018). Modelling persistent methane seepage offshore western Svalbard since

early Pleistocene. *Mar. Petrol. Geol.* 91, 800–811. doi:10.1016/j.marpetgeo.2018.01.020

Knittel, K., and Boetius, A. (2009). Anaerobic oxidation of methane: progress with an unknown process. *Annu. Rev. Microbiol.* 63, 311–334. doi:10.1146/annurev.micro.61.080706.093130

Knittel, K., Lösekann, T., Boetius, A., Kort, R., and Amann, R. (2005). Diversity and distribution of methanotrophic archaea at cold seeps. *Appl. Environ. Microbiol.* 71 (1), 467–479. doi:10.1128/AEM.71.1.467-479.2005

Krause, S., Niemann, H., and Treude, T. (2017). "Methane seeps in a changing climate." in *Life at vents and seeps*. Editor J. Kallmeyer (Berlin, Boston: De Gruyter), 1–32.

Lein, A. Y. (2004). Authigenic carbonate formation in the ocean. *Lithol. Miner. Resour.* 39 (1), 1–30. doi:10.1023/B:LIMI.0000010767.52720.8f

Lösekann, T., Knittel, K., Nadalig, T., Fuchs, B., Niemann, H., Boetius, A., et al. (2007). Diversity and abundance of aerobic and anaerobic methane oxidizers at the Haakon Mosby Mud Volcano, Barents Sea. *Appl. Environ. Microbiol.* 73 (10), 3348–3362.

Kim, S. -T., O'Neil„ J. R., Hillaire-Marcel, C., and Mucci, A. (2007). Oxygen isotope fractionation between synthetic aragonite and water: influence of temperature and Mg2+ concentration. Geochimica et Cosmochimica Acta. 71 (19), 4704–4715.

MacDonald, I. R., Guinasso, N. L., Jr., Sassen, R., Brooks, J. M., Lee, L., and Scott, K. T. (1994). Gas hydrate that breaches the sea floor on the continental slope of the Gulf of Mexico. *Geology* 22, 699–702. doi:10.1130/0091-7613

Mazzini, A., Ivanov, M. K., Parnell, J., Stadnitskaia, A., Cronin, B. T., Poludetkina, E., et al. (2004). Methane-related authigenic carbonates from the Black Sea: geochemical characterisation and relation to seeping fluids. *Mar. Geol.* 212, 153–181. doi:10.1016/j.margeo.2004.08.001

Milucka, J., Ferdelman, T. G., Polerecky, L., Franzke, D., Wegener, G., Schmid, M., et al. (2012). Zero-valent sulphur is a key intermediate in marine methane oxidation. *Nature* 491, 541–546. doi:10.1038/nature11656

Naehr, T. H., Eichhubl, P., Orphan, V. J., Hovland, M., Paull, C. K., Ussler, W., et al. (2007). Authigenic carbonate formation at hydrocarbon seeps in continental margin sediments: a comparative study. *Deep Sea Res. Part II Top. Stud. Oceanogr.* 54, 1268–1291. doi:10.1016/j.dsr2.2007.04.010

Natalicchio, M., Peckmann, J., Birgel, D., and Kiel, S. (2015). Seep deposits from northern Istria, Croatia: a first glimpse into the Eocene seep fauna of the Tethys region. *Geol. Mag.* 152, 444–459. doi:10.1017/S0016756814000466

Niemann, H., Duarte, J., Hensen, C., Omoregie, E., Magalhães, V. H., Elvert, M., et al. (2006). Microbial methane turnover at mud volcanoes of the gulf of Cadiz. *Geochem. Cosmochim. Acta* 70 (21), 5336–5355. doi:10.1016/j.gca.2006.08.010

Niemann, H., and Elvert, M. (2008). Diagnostic lipid biomarker and stable carbon isotope signatures of microbial communities mediating the anaerobic oxidation of methane with sulphate. *Org. Geochem.* 39, 1668–1677. doi:10.1016/j.orggeochem.2007.11.003

Niemann, H., Elvert, M., Hovland, M., Orcutt, B., Judd, A., Suck, I., et al. (2005). Methane emission and consumption at a North Sea gas seep (Tommeliten area). *Biogeosciences* 2, 335–351. doi:10.5194/bg-2-335-2005

Panieri, G., Bünz, S., Fornari, D. J., Escartin, J., Serov, P., Jansson, P., et al. (2017). An integrated view of the methane system in the pockmarks at Vestnesa Ridge, 79°N. *Mar. Geol.* 390, 282–300. doi:10.1016/j.margeo.2017.06.006

Pape, T., Bünz, S., Hong, W.-L., Torres, M. E., Riedel, M., Panieri, G., et al. (2020). Origin and transformation of light hydrocarbons ascending at an active pockmark on Vestnesa Ridge, Arctic Ocean. *J. Geophys. Res.: Solid Earth* 125, e2018JB016679. doi:10.1029/2018jb016679

Peckmann, J., Birgel, D., and Kiel, S. (2009). Molecular fossils reveal fluid composition and flow intensity at a Cretaceous seep. *Geology* 37, 847–850. doi:10.1130/G25658A.1

Peckmann, J., and Thiel, V. (2004). Carbon cycling at ancient methane-seeps. *Chem. Geol.* 205, 443–467. doi:10.1016/j.chemgeo.2003.12.025

Plaza-Faverola, A., Bünz, S., Johnson, J. E., Chand, S., Knies, J., Mienert, J., et al. (2015). Role of tectonic stress in seepage evolution along the gas hydrate-charged Vestnesa Ridge, Fram Strait. *Geophys. Res. Lett.* 42, 733–742. doi:10.1002/2014gl062474

Presley, B. J., and Kaplan, I. R. (1968). Changes in dissolved sulfate, calcium and carbonate from interstitial water of near-shore sediments. *Geochem. Cosmochim. Acta* 32, 1037–1048. doi:10.1016/0016-7037(68)90106-3

Reitner, J., Peckmann, J., Blumenberg, M., Michaelis, W., Reimer, A., and Thiel, V. (2005). Concretionary methane-seep carbonates and associated microbial communities in Black Sea sediments. *Palaeogeogr. Palaeoclimatol. Palaeoecol* 227, 18–30. doi:10.1016/j.palaeo.2005.04.033

Reeburgh, W. S. (2007). Oceanic methane biogeochemistry. *Chem. Rev*, 107, 486–513.

Sauer, S., Crémière, A., Knies, J., Lepland, A., Sahy, D., Martma, T., et al. (2017). U-Th chronology and formation controls of methane-derived authigenic carbonates from the Hola trough seep area, northern Norway. *Chem. Geol.* 470, 164–179. doi:10.1016/j.chemgeo.2017.09.004

Sauer, S., Hong, W. L., Yao, H., Knies, J., Lepalnd, A., Klug, M., et al. (2020). Methane transport and sources in an Arctic deep-water cold seep offshore NW Svalbard (Vestnesa Ridge, 79°N). *Deep Sea Res. Part I: Oceanogr. Res. Papers* 167, 103430. doi:10.1016/j.dsr.2020.103430

Sen, A., Åström, E. K. L., Hong, W.-L., Portnov, A., Waage, M., Serov, P., et al. (2018a). Geophysical and geochemical controls on the megafaunal community of a high Arctic cold seep. *Biogeosci. Discuss.* 15, 4533–4559. doi:10.5194/bg-15-4533-2018

Sen, A., Duperron, S., Hourdez, S., Piquet, B., Léger, N., Gebruk, A., et al. (2018b). Cryptic frenulates are the dominant chemosymbiotrophic fauna at Arctic and high latitude Atlantic cold seeps. *PloS One* 13 (12), e0209273. doi:10.1371/journal.pone.0209273

Serov, P., Vadakkepuliyambatta, S., Mienert, J., Patton, H., Portnov, A., Silyakova, A., et al. (2017). Postglacial response of Arctic Ocean gas hydrates to climatic amelioration. *Proc. Natl. Acad. Sci. U. S. A.* 114 (24), 6215–6220. doi:10.1073/pnas.1619288114

Steinle, L., Graves, C. A., Treude, T., Ferré, B., Biastoch, A., Bussmann, I., et al. (2015). Water column methanotrophy controlled by a rapid oceanographic switch. *Nat. Geosci.* 8 (5), 378–382.

Steinle, L., Schmidt, M., Bryant, L., Haeckel, M., Linke, P., Sommer, S., et al. (2016). Linked sediment and water-column methanotrophy at a man-made gas blowout in the North Sea: implications for methane budgeting in seasonally stratified shallow seas. *Limnol. Oceanogr.* 61 (S1), S367–S386.

Ussler, W., and Paull, C. K. (1995). Effects of ion exclusion and isotopic fractionation on pore water geochemistry during gas hydrate formation and decomposition. *Geo Mar. Lett.* 15, 37–44. doi:10.1007/BF01204496

van Grinsven, S., Damsté, J. S. S., Asbun, A. A., Engelmann, J. C., Harrison, J., and Villanueva, L. (2020a). Methane oxidation in anoxic lake water stimulated by nitrate and sulfate addition. *Environ. Microbiol.* 22 (2), 766–782. doi:10.1111/1462-2920.14886

van Grinsven, S., Damsté, J. S. S., Harrison, J., and Villanueva, L. (2020b). Impact of electron acceptor availability on methane-influenced microorganisms in an enrichment culture obtained from a stratified lake. *Front. Microbiol.* 11, 403. doi:10.3389/fmicb.2020.00715

Wegener, G., Krukenberg, V., Riedel, D., Tegetmeyer, H. E., and Boetius, A. (2015). Intercellular wiring enables electron transfer between methanotrophic archaea and bacteria. *Nature* 526, 587–590. doi:10.1038/nature15733

Whiticar, M. J. (1999). Carbon and hydrogen isotope systematics of bacterial formation and oxidation of methane. *Chem. Geol.* 161 (1-3), 291–314. doi:10.1016/S0009-2541(99)00092-3

Yao, H., Hong, W. L., Panieri, G., Sauer, S., Torres, M. E., Lehmann, M. F., et al. (2019). Fracture-controlled fluid transport supports microbial methane-oxidizing communities at Vestnesa Ridge. *Biogeosciences* 16, 2221–2232. doi:10.5194/bg-16-2221-2019

Yao, H., Niemann, H., and Panieri, G. (2020). Multi-proxy aproach to unravel methane emission history of an Arctic cold seep. *Quat. Sci. Rev.* 244, 106490.

Conflict of Interest: The authors declare that the research was conducted in the absence of any commercial or financial relationships that could be construed as a potential conflict of interest.

frontiers in Earth Science

ORIGINAL RESEARCH
published: 18 February 2021
doi: 10.3389/feart.2020.600733

A Monte Carlo Model of Gas-Liquid-Hydrate Three-phase Coexistence Constrained by Pore Geometry in Marine Sediments

Jiangzhi Chen[1]*, *Alan W. Rempel*[2] *and Shenghua Mei*[1]

[1]*Institute of Deep-Sea Science and Engineering, Chinese Academy of Sciences, Sanya, China,* [2]*Department of Earth Sciences, University of Oregon, Eugene, OR, United States*

Gas hydrates form at relatively high pressures in near-surface, organic-rich marine sediments, with the base of the hydrate stability field and the onset of partial gas saturation determined by temperature increases with depth. Because of pore-scale curvature and wetting effects, the transition between gas hydrate and free gas occurrence need not take place at a distinct depth or temperature boundary, but instead can be characterized by a zone of finite thickness in which methane gas bubbles and hydrate crystals coexist with the same aqueous solution. Previous treatments have idealized pores as spheres or cylinders, but real pores between sediment grains have irregular, largely convex walls that enable the highly curved surfaces of gas bubbles and/or hydrate crystals within a given pore to change with varying conditions. In partially hydrate-saturated sediments, for example, the gas–liquid surface energy perturbs the onset of gas–liquid equilibrium by an amount proportional to bubble-surface curvature, causing a commensurate change to the equilibrium methane solubility in the liquid phase. This solubility is also constrained by the curvature of coexisting hydrate crystals and hence the volume occupied by the hydrate phase. As a result, the thickness of the three-phase zone depends not only on the pore space geometry, but also on the saturation levels of the hydrate and gaseous phases. We evaluate local geometrical constraints in a synthetic 3D packing of spherical particles resembling real granular sediments, relate the changes in the relative proportions of the phases to the three-phase equilibrium conditions, and demonstrate how the boundaries of the three-phase zone at the base of the hydrate stability field are displaced as a function of pore size, while varying with saturation level. The predicted thickness of the three-phase zone varies from tens to hundreds of meters, is inversely dependent on host sediment grain size, and increases dramatically when pores near complete saturation with hydrate and gas, requiring that interfacial curvatures become large.

Keywords: gas hydrates, wetting, irregular pores, capillary effects, clathrates

OPEN ACCESS

Edited by:
Martin Scherwath,
University of Victoria, Canada

Reviewed by:
Hugh Daigle,
University of Texas at Austin, United States
Jean-Marc Simon,
Université de Bourgogne, France

***Correspondence:**
Jiangzhi Chen
chenjz@idsse.ac.cn

Specialty section:
This article was submitted to Biogeoscience, a section of the journal Frontiers in Earth Science

Received: *31 August 2020*
Accepted: *18 December 2020*
Published: *18 February 2021*

Citation:
Chen J, Rempel AW and Mei S (2021) A Monte Carlo Model of Gas-Liquid-Hydrate Three-phase Coexistence Constrained by Pore Geometry in Marine Sediments. Front. Earth Sci. 8:600733. doi: 10.3389/feart.2020.600733

1 INTRODUCTION

Natural gas hydrates are ice-like compounds that commonly form in permafrost and marine sediments from mixtures of methane and water (Sloan and Koh, 2007). As a promising source for future energy, methane hydrate has attracted much attention from the oil and gas industry, with further motivation for their study coming from the need to quantify methane migration in sediments (e.g., Nole et al., 2016), assess submarine landslide risk (e.g., Sultan et al., 2004; Handwerger et al., 2017), and understand the material cycle in benthic ecology (e.g., Suess et al., 1999). Seismic data and drilling logs from natural hydrate reservoirs have identified anomalies of high saturation level (i.e., hydrate pore volume fraction) within layers of comparatively coarse sediments, suggesting heterogeneous hydrate accumulation rates that depend not only on temperature and pressure but also on sediment properties (e.g., Borowski, 2004; Malinverno, 2010; Wang et al., 2011; Bahk et al., 2013). Experimental studies also demonstrate that pore sizes play an important role in controlling the spatial and temporal distribution of hydrate deposits (e.g., Yousif et al., 1991; Yousif and Sloan, 1991; Chong et al., 2015; Liu et al., 2015).

The formation of gas hydrate in permafrost and marine sediments is often approximated using the constraint of local bulk equilibrium between a combination of up to three methane-bearing phases: free methane gas (G), methane hydrate (H), and dissolved methane in aqueous solutions (L), in which the methane solubility is a unique function of temperature, pressure and salinity (e.g., Sloan and Koh, 2007). A more precise understanding of these systems must account for perturbations to this bulk phase behavior imposed by the surface properties and geometry of sediment particles, with the gas and hydrate acting most commonly as non-wetting phases, whereas the aqueous solution wets particle surfaces. As hydrate forms or dissociates, hydrate crystals or gas bubbles approach the pore walls, and the phase behavior is affected by the surface energy of the curved L-H or L-G interface, with high curvature causing elevated local dissolved methane concentrations. By constraining allowable interface curvatures, heterogeneously distributed sediment pores introduce deviations in the equilibrium methane concentration at *in situ* temperature and pressure conditions (Clennell et al., 1999; Henry et al., 1999; Daigle and Dugan, 2011; Rempel, 2011; Dai et al., 2012; Cook and Malinverno, 2013; VanderBeek and Rempel, 2018), thereby affecting both the growth of hydrate deposits and their decomposition. Existing works that approximate the role of pore geometry mostly focus on the average pore size, often simplifying the pores as circular cylinders (e.g., Millington and Quirk, 1961; Wilder et al., 2001; Denoyel and Pellenq, 2002) or spheres connected by cylindrical throats (e.g., Jang and Santamarina, 2011; Liu and Flemings, 2011). These simple pore models provide useful insight into how hydrate forms and dissociates in sediments, but they fail to capture variations in curvature as phase boundaries evolve. Rempel (2011) avoided this limitation by considering triangular pores, and a subsequent two-dimensional treatment (e.g., Rempel, 2012) examined the crevice spaces between random close-packed spheres. By treating granular porous media as packed three-dimensional spherical grains, Chen et al., (2020) used Monte Carlo sampling to effectively approximate the constraints of pore geometry on phase boundary curvatures in a two-component system within randomly packed, poly-dispersed sediments. In this work, focused on three-phase coexistence, we first outline the basic phase behavior expected within 2D triangular pores, and then extend the treatment using an averaging method to approximate the behavior in pores between spherical grains, before examining the fully 3D problem with a Monte Carlo method.

2 EQUILIBRIUM METHANE CONCENTRATION GRADIENT IN SEDIMENTS

In marine sediments that are sufficiently coarse-grained for pore-scale curvature effects to be negligible, bulk three-phase equilibrium at the base of the hydrate stability zone (BHSZ) occurs at a distinct depth that is uniquely determined by the pressure, temperature and salinity. Above the bulk BHSZ, the equilibrium methane solubility of the binary L-H system increases with depth, whereas below the BHSZ, the equilibrium is between liquid and free gas, and the methane solubility decreases with depth, driven by increases in the ambient temperature. In typical circumstances with heterogeneously distributed micron-scale pores, however, the hydrate phase, gas phase and aqueous methane solution may coexist in a zone of finite thickness where the upper and lower boundaries are shifted according to the solubility perturbations associated with confining the hydrate and gas phases in tight, and variable effective pore sizes.

The shift in methane solubility from bulk conditions in L-H and L-G two-phase equilibrium can be approximated as follows. For the L-G equilibrium,

$$\mathrm{CH_4\,(g)} \rightleftharpoons \mathrm{CH_4\,(aq)}, \tag{1}$$

the thermodynamic relations for the methane solubility in molar fraction require

$$\left.\frac{\partial \ln x_{gl}}{\partial T}\right|_P = \frac{\Delta^{gl}_{\mathrm{sol}} H_m}{RT^2} < 0, \quad \left.\frac{\partial \ln x_{gl}}{\partial P}\right|_T = \frac{V_m - \overline{V}_m}{RT} \approx \frac{1}{P} > 0, \tag{2}$$

where $\Delta^{gl}_{\mathrm{sol}} H_m$ is the molar heat of solution of methane gas (negative for this exothermic reaction), V_m is molar volume of methane gas, and $\overline{V}_m$ is the partial molar volume of methane in water, which is negligible compared with V_m. Partial pressure from water vapor is also negligible because in the temperature range of interest, the saturation vapor pressure is less than 1 kPa, which is much smaller than the hydrostatic pressure. Similarly for the L-H equilibrium,

$$\mathrm{CH_4\,(aq)} + \mathrm{nH_2O} \rightleftharpoons \mathrm{CH_4\,.\,nH_2O\,(s)}, \tag{3}$$

the methane solubility follows

$$\left.\frac{\partial \ln x_{hl}}{\partial T}\right|_P = \frac{\Delta^{hl}_{\mathrm{sol}} H_m}{RT^2} > 0, \quad \left.\frac{\partial \ln x_{hl}}{\partial P}\right|_T = \frac{V_h - \overline{V}_m - nV_w}{RT} < 0, \tag{4}$$

where $\Delta_{\mathrm{sol}} H^{hl}_m$ is the solution heat, and V_h is the molar volume of the hydrate.

TABLE 1 | Nominal parameter values for methane gas, methane hydrate, and water based on homogeneous three-phase equilibrium conditions T_3 = 295 K and P_3 = 30 MPa at Blake Ridge. Note that the molar dissociation heat of hydrate is $\Delta_{dis}H_m = \Delta^{hl}_{sol}H_m - \Delta^{gl}_{sol}H_m \approx 54$ kJ/mol, consistent with existing measurements (Anderson, 2004; Gupta et al., 2008).

Model parameters			Value
Methane molar dissolution heat (Duan and Mao, 2006)	$\Delta^{gl}_{sol}H_m$	[kJ mol^{-1}]	−12.59
Hydrate molar dissolution heat (Lu et al., 2008)	$\Delta^{hl}_{sol}H_m$	[kJ mol^{-1}]	41.96
Molar volume of water (Wagner and Pruss, 1993)	V_w	[cm^{3}mol^{-1}]	17.93
Partial molar volume of methane in water (Duan and Mao, 2006)	$\overline{V}_m$	[cm^{3}mol^{-1}]	38.87
Molar volume of hydrate (Sun and Duan, 2005)	V_h	[cm^{3}mol^{-1}]	135.4
Hydration number	n		~ 6
Geothermal gradient (Ruppel, 1997)	G_T	[K m^{-1}]	3.69×10^{-2}
Hydrostatic pressure gradient (Ruppel, 1997)	G_P	[Pa m^{-1}]	1×10^4
G-L surface tension	γ_{gl}	[J m^{-2}]	0.07
H-L surface tension (Hardy, 1977)	γ_{hl}	[J m^{-2}]	0.029

Adopting a coordinate axis with the z-direction pointing vertically downwards, the bulk BHSZ is at depth z_3 below the seafloor, corresponding to a three-phase equilibrium condition

$$T_3 = T_0 + G_T z_3, \quad P_3 = P_0 + G_P z_3, \quad x_{gl}(z_3) = x_{hl}(z_3) = x_3, \quad (5)$$

where T_0 and P_0 are the temperature and pressure at the seafloor, and G_T and G_P are the temperature gradient and pressure gradient, respectively, in the sediment. The respective solubilities vary with depth near z_3 according to

$$g_{gl} = \left.\frac{\mathrm{d}\ln x_{gl}}{\mathrm{d}z}\right|_{z_3} = \frac{\Delta^{gl}_{sol}H_m}{RT_3^2}G_T + \frac{1}{P_3}G_P, \quad (6)$$

$$g_{hl} = \left.\frac{\mathrm{d}\ln x_{hl}}{\mathrm{d}z}\right|_{z_3} = \frac{\Delta^{hl}_{sol}H_m}{RT_3^2}G_T + \frac{V_h - \overline{V}_m - nV_w}{RT_3}G_p, \quad (7)$$

where the pressure dependence of L-H solubility is in fact negligible because the volume change is relatively small without the presence of a free gas phase. For illustration, we consider perturbations around the three-phase equilibrium $T_3 \approx 295$ K and $P_3 \approx 30$ MPa, and use nominal values for G_T and G_P at Blake Ridge (**Table 1**) so that

$$g_{gl} = -0.309\,\mathrm{km}^{-1}, \quad g_{hl} = 2.09\,\mathrm{km}^{-1}. \quad (8)$$

Because $|g_{hl}| > |g_{sl}|$ (i.e., $|d\ln x_{hl}z| > |d\ln x_{gl}z|$), the gradient of the gas solubility is much gentler than that of the hydrate solubility, as depicted in **Figure 1**. The bulk solubilities at $z = z_3 + \Delta z$ are approximately

$$x_{gl}(z) = x_3 \exp\left(g_{gl}\Delta z\right), \quad x_{hl}(z) = x_3 \exp\left(g_{hl}\Delta z\right). \quad (9)$$

Curved surfaces of gas bubbles and methane hydrates within the confined pore space elevate the chemical potential of the non-wetting gas and hydrate phases. At a depth z where three phases coexist, setting the radius of the methane bubble to r_g, and the radius of the hydrate crystal to r_h, the shifted solubilities are

$$x'_{gl}\left(r_g\right) = x_{gl}\left(1 + \frac{\gamma_{gl}}{P_3 + G_P\Delta z}\frac{2}{r_g}\right),$$
$$x'_{hl}(r_h) = x_{hl}\exp\left[\frac{2V_h\gamma_{hl}}{Rr_h(T_3 + G_T\Delta z)}\right]. \quad (10)$$

Equilibrium between the phases requires

$$x'_{gl}\left(r_g\right) = x'_{hl}(r_h), \quad (11)$$

which is expanded to

$$\frac{2V_h\gamma_{hl}}{r_h R(T_3 + G_T\Delta z)} = \left(g_{gl} - g_{hl}\right)\Delta z + \ln\left(1 + \frac{2\gamma_{gl}}{r_g}\frac{1}{P_3 + G_P\Delta z}\right). \quad (12)$$

Equation 12 describes the chemical equilibrium when three phases coexist. With r_h and r_g constrained from the pore distribution, the offset Δz gives the thickness of the three-phase zone. In simple porous sediment model with a single pore size so that $r_h = r_g$, the three-phase zone shrinks to one unique depth. With heterogeneously distributed effective pore sizes, however, we expect the BHSZ to be characterized by a zone of three-phase coexistence bounded by depths corresponding to equilibrium conditions for which the hydrate crystals and gas bubbles each have different interfacial curvatures (**Figure 1**) that are nevertheless related by the constraint that each of these non-wetting phases must also be in equilibrium with a wetting aqueous solution containing the same concentration of dissolved methane. Combined with the geometric constraints derived below, **Eq. 12** enables us to determine the thickness of the three-phase zone.

3 GEOMETRIC CONSTRAINTS WITHIN PORES

Models consisting of regular pores with concave interior walls, such as spheres or cylinders, permit very little variation to phase boundary curvature, as non-wetting phases fill pore centers and the wetting phase occupies thin films that coat pore walls. In natural irregular pores with predominantly convex interior walls, as the non-wetting phase grows, the phase boundary intrudes further into crevices between solid grains where the wetting phase persists in ever-shrinking convexly bounded pockets. One simplified pore model with features resembling such diminishing crevices is a 2D triangular pore; a more realistic 3D model can be constructed using a conglomerate of packed

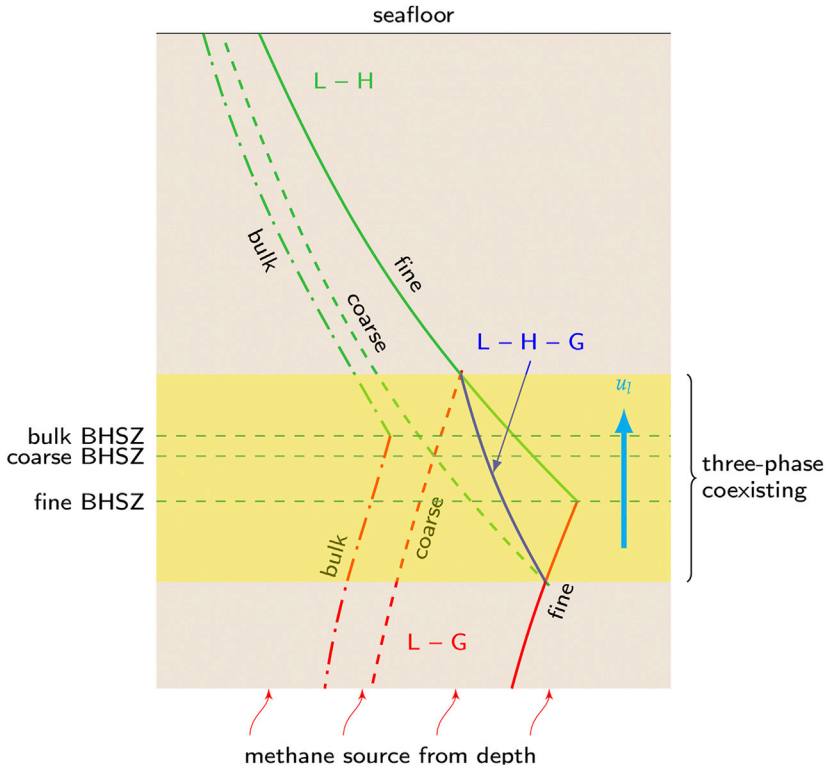

FIGURE 1 | The three-phase coexisting zone near the bulk BHSZ. Above the BHSZ, no methane gas is present, and the methane solubility is determined by L-H equilibrium, increasing with depth (green curves). Below the BHSZ, hydrate dissociates so that dissolved methane is instead constrained by equilibrium with free methane gas, and the solubility decreases with depth due to increasing temperature (red curves). Bulk solubility curves correspond to the scenario where pore-scale effects can be neglected. In smaller pores, however, two-phase solubility curves shift toward higher values. The hydrate and methane gas phases can first coexist with the same aqueous solution when the emergent free gas phase at the upper boundary of the zone of three phase coexistence has the smallest possible curvature (i.e., largest radius), while the curvature that characterizes crystals of the residual hydrate phase must remain continuous with the value set by the hydrate saturation level in the two-phase L-H zone above; a parallel set of restrictions pertains at the lower boundary with the roles of gas and hydrate reversed. The dark L-H-G line labels the methane solubility such that even the smallest pores are filled with one non-wetting phase.

particles, idealized here as spherical grains. With changing temperatures and/or pressures, for example with increased depth below the seafloor, the hydrate phase (H) is expected to dissociate and a new non-wetting phase (G) will emerge from the wetting phase (L) so that a two-phase equilibrium (L-H) configuration gives way to a new three-phase equilibrium (G-L-H).

The zone of three-phase coexistence may have a finite thickness with varying saturation levels for the non-wetting phases, before reverting to a different two-phase equilibrium (L-G) at still greater depths. Importantly, at the onset of three-phase coexistence, surface energy considerations imply that the emergent phase (in this scenario, G at the top, H at the bottom) is bounded by the largest surface of constant curvature that can fit within the pore space (i.e., a sphere). This simplifies the geometry of the emergent phase considerably and facilitates determination of the three-phase zone thickness while avoiding the need to consider the regions of variable curvature adjacent to the extended wetting films that coat both non-wetting phases elsewhere. A second useful constraint is that the curvature of the residual phase (in this scenario, H at the top, G at the bottom) must remain continuous across the three-phase boundary.

With the two constraints, we can describe the evolution of saturation levels of the non-wetting phases when crossing the boundary from regions of two-phase equilibrium into the zone of three-phase equilibrium. For example, in the L-H region immediately above the three-phase zone, hydrate is the only non-wetting phase in pores, separated from pore walls by films of liquid phase. The hydrate crystals have a radius r_h controlled by the surface energy. At low hydrate saturations, the crystals may take a spherical form, whereas at high saturation levels (with abundant methane), small spheres may coalesce, and occupy the largest pore with bumps growing into nearby crevices with the radius r_h. Across the three-phase boundary, a portion of hydrate dissociates, and spherical methane gas bubbles emerge with radius $r_g > r_h$ tangent to the walls of the largest pores and hydrate crystals, whereas remaining hydrate resides in smaller pores and extends into crevices with the same interfacial radius r_h as the crystals in the L-H region right above. At the base of the three-phase zone, where hydrate is the emergent phase and free gas the residual phase, a parallel set of constraints applies with continuous gas radius r_g and spherical hydrate crystals characterized by $r_h > r_g$. For the 2D triangular pore model, an analytical description of these geometrical constraints is available; for the 3D model, we developed an averaging method to

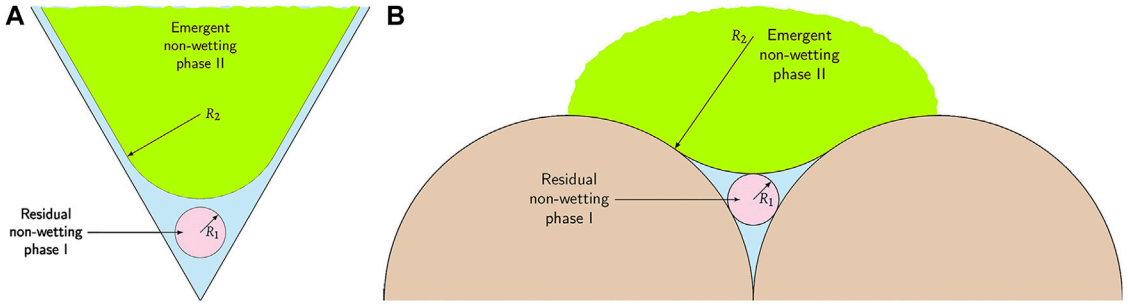

FIGURE 2 | Schematic of three-phase coexistence in **(A)** one 2D equilateral triangular pore and **(B)** residual liquid reservoir inside one crevice in 3D spherical grains. As the non-wetting phase II emerges, the area or volume occupied by non-wetting phase I shrinks.

represent a mono-dispersed scenario. We describe the geometrical constraints for these two idealized cases next, before outlining our Monte Carlo approach to addressing a more realistic synthetic sediment consisting of randomly packed spherical particles in **Section 3.2**.

3.1 Geometric Constraints

3.1.1 Simplified 2D Triangular Pores

In a 2D equilateral triangular pore with sides of length W, the radius of the residual non-wetting phase I near the vertices is R_1 (**Figure 2A**). The total pore area is

$$A_0 = \frac{\sqrt{3}}{4}W^2. \tag{13}$$

In the case where its boundaries are idealized as spherical, the total area of non-wetting phase I in three vertices is

$$\pi R_1^2 \le A_1 \le 3\pi R_1^2 \tag{14}$$

where the inequality means not all vertices are necessarily hosting phase I. When a new non-wetting phase II emerges, it must have lower surface energy (i.e., larger radius) so it locates near the center of the pore, with $R_2 \approx 3R_1$, and

$$A_2 = \frac{(h-d)^2}{h^2}A_0 - (3\sqrt{3} - \pi)R_2^2. \tag{15}$$

where $h = W/2\sqrt{3}$, and d is the film thickness far from vertices along pore walls. The saturations of each phase are

$$S_1 = \frac{A_1}{A_0}, \quad S_2 = \frac{A_2}{A_0}, \quad S_w = 1 - S_1 - S_2. \tag{16}$$

In the limit that $R_2 \gg d$, the saturation of the emergent phase is

$$S_2 \approx 1 - \frac{R_2^2}{W^2}\left(12 - \frac{4\pi}{\sqrt{3}}\right). \tag{17}$$

Here, the pore geometry requires $R_2 \le h = W/(2\sqrt{3})$ so phase II has minimum saturation $S_2 \approx 0.6$, and at the onset of three-phase coexistence S_1 may have a range of values below 0.2. However, it remains possible for the two non-wetting phases to occupy separate nearby pores as long as $R_2 \approx 3R_1$, and S_2 remains a valid description of the saturation level of the emergent phase in equilibrium with L alone at the onset of three-phase coexistence. These geometric constraints apply only at the boundaries of the three-phase zone, and not further within the zone itself. Instead, the gas and hydrate interfacial curvatures within the interior of the three-phase zone depend on the amount of methane present, since it must be partitioned between L, H, and G. It is possible that inside the zone, pores are under-filled, i.e., neither residual phase I and emergent phase II are above a saturation level of 0.6, which we will discuss later.

3.1.2 Mono-Dispersed 3D Pores

A similar approach combined with an averaging method can be used to obtain saturation estimates in 3D pores. In a mono-dispersed 3D sediment with particle radii R, the entire volume of each pore in a virtual triclinic cell bounded by eight grains with internal angles α, β, and γ is

$$V_0 = 8R^3\sqrt{1 + 2\cos\alpha\cos\beta\cos\gamma - \cos^2\alpha - \cos^2\beta - \cos^2\gamma} - \frac{4\pi}{3}R^3. \tag{18}$$

Using the hyper-volume formula (Mackay, 1974), the radius of the largest inscribed sphere is

$$r(\alpha,\beta,\gamma) = R\left[\left(\begin{array}{c}\dfrac{3 - 2\cos\alpha - 2\cos\beta - 2\cos\gamma}{1 - \cos^2\alpha - \cos^2\beta - \cos^2\gamma + 2\cos\alpha\cos\beta\cos\gamma} \\ + \dfrac{2\cos\alpha\cos\beta + 2\cos\beta\cos\gamma + 2\cos\gamma\cos\alpha}{1 - \cos^2\alpha - \cos^2\beta - \cos^2\gamma + 2\cos\alpha\cos\beta\cos\gamma} \\ - \dfrac{\cos^2\alpha + \cos^2\beta + \cos^2\gamma}{1 - \cos^2\alpha - \cos^2\beta - \cos^2\gamma + 2\cos\alpha\cos\beta\cos\gamma}\end{array}\right)^{\frac{1}{2}} - 1\right] \tag{19}$$

Phase II attains equilibrium as the new non-wetting phase with radius $R_2 \le r(\alpha,\beta,\gamma)$ given by **Eq. 19**. Similar to the 2D case, the emergent phase II may appear as spheres with radius $R_2 \le r(\alpha,\beta,\gamma)$ adjacent to phase I, or as a contorted body intruding into all possible interstitial sites, with a surface characterized by small bumps of R_2 tangent to the bounding sediment particles to form crevices. The residual non-wetting phase I may stay inside one or more crevices, as shown in **Figure 2B**. Neglecting the small volumes contributed by liquid films, as before, we have

$$R_1 = \frac{(R\cot\delta - R_2)^2}{2(R + R\cot\delta - R_2)} \tag{20}$$

where $\delta = \arcsin[R/(R+R_2)]$. The wetting phase volume is well-approximated as filling a trio of minor crevices (two of which are bounded on one side by phase II while the other sides approach particle surfaces), so that the wetting volume is

$$V_w = 6\pi R_2^2\left(R - \delta\sqrt{R_2(R_2+2R)}\right) - V_1. \tag{21}$$

Here, the total volume V_1 occupied by phase I is bounded between the volume of balls of radius R_1 and that of three tori

$$\pi R_1^3 \le V_1 \le 6\pi R_1^3\sqrt{1 + 2R/R_1}, \tag{22}$$

while the volume occupied by phase II is

$$V_2 = V_0 - 6\pi R_2^2\left[R - \delta\sqrt{R_2(R_2+2R)}\right]. \tag{23}$$

Finally, the saturation levels can be written as

$$S_1 = \frac{V_1}{V_0}, \quad S_2 = \frac{V_2}{V_0}, \quad S_w = \frac{V_w}{V_0}. \tag{24}$$

For the collective values of R_1, R_2, and S_2 over numerous pores, these values are averaged over angles α, β, and γ (see **Appendix 1** for details).

At the top and bottom of the three-phase coexisting zone, we recognize the emergent phase II as the gas and hydrate phases, respectively. The analyses for the 2D and 3D scenarios suggest that the saturation of the residual phase S_1 can vary within a range, while the saturation of the emergent phase S_2 is better constrained.

3.2 Monte Carlo Simulation of 3D Pores

In natural, randomly packed sediments, clearly the virtual cell of **Section 3.1.2** may be heavily distorted, and the distributions of angles are affected by grain radii, so the averaging method may not work properly. We develop a Monte Carlo scheme to simulate the growth of the emergent phase as constrained by the pore geometry, as well as the requirement imposed by continuity of solubility. We test the method here using the mono-dispersed random close pack of Finney (1970), and sample the cross-section of the pack with N = 2000 random test points. For each test point located in the pore space, we find the largest inscribed sphere containing the test point, which is recognized as emergent phase II with a radius R_2, and in the crevices formed between the sphere and two tangent particles, we calculate a tangent coplanar sphere as residual phase I. There may be more than one possible crevice in each pore because the phase II sphere may touch as many as four particles, and we choose the largest residual phase I sphere, with radius R_1. We record all pairs of phase I and II sphere radii (R_1, R_2), and sort them according to the values of R_2. This sorting procedure enables us to approximate the saturation level of phase II with radius R_2 as the proportion of sampled points that are encompassed by phase II (see Chen et al., 2020, for a more detailed discussion). After scaling with particle radius, we solve for the corresponding Δz using **Eq. (12)**. The Monte Carlo sampling procedure results in different estimates of Δz for estimates of the emergent-phase saturation S_2, and we recognize the envelope of extremal values as approximating the depth range of three-phase coexistence.

4 MODEL RESULTS

We seek the upper and lower depth limits that define the zone where three-phase equilibrium may occur. At the top of this zone, free gas is the emergent phase II and hydrate is the residual phase I, whereas at the bottom these roles are reversed, with the gas constituting the residual phase I and hydrate the emergent phase II. By applying the geometric constraints derived in the 2D and 3D scenarios just described to **Eq. 12**, we can determine the dependence of Δz on S_2. For uniform 2D triangular pores (**Figure 3A**), the pore geometry requires $R_2 \le W/(2\sqrt{3})$, so that the minimum $S_2 \approx 0.6$. For 3D pores in mono-dispersed grains (**Figure 3B**), the thickness of the three-phase zone is the average over all pores, and the minimum S_2 is around 0.75. Because the z-direction points downwards, the figures are plotted with flipped Δz so that shallower locations (negative Δz) are above deeper locations (positive Δz).

The two scenarios behave similarly. With larger pores, the zone of three-phase coexistence is thin, but as pore size decreases (represented by the different lines in **Figure 3**, with sizes noted in the legends), the upper and lower boundaries of the three-phase zone deviate further from zero, corresponding to a thicker zone of three-phase coexistence. In the smaller pores of finer sediments, the hydrate phase begins to dissociate and the gas phase emerges at a depth much shallower than the bulk BHSZ, but the hydrate phase may also persist to a depth far below the bulk BHSZ. The thickness of the zone of three-phase coexistence is constrained as well by the requirement that solubility remain continuous across the boundaries with adjacent two-phase zones, leading to the dependence on S_2 — the saturation of emergent phase.

Figure 4 compares the 3D average result from **Section 3.1.2** with the Monte Carlo simulation result from **Section 3.2**. The upper and lower bounds of the Monte Carlo results match well with the average curves at the beginning, but deviate further at high saturation levels. In finer sediments, boundaries marked by the Monte Carlo results begin to deviate further from the averaging result. We attribute this discrepancy to errors in the averaging procedure produced by distortions to the virtual cell.

We emphasize that it is not necessarily the case that any particular pore in the zone of three-phase coexistence can hold all three phases, and in fact such a configuration is only possible at very high methane input. Nevertheless, since the volume occupied by phase I determines its interfacial curvature and hence the methane solubility in the adjacent two-phase zone, together with the pore size constraint on the geometry available for phase II, this implies that the three-phase thickness (i.e., bounded by the first appearance of a secondary non-wetting phase) must depend on both the saturation of the primary (residual) non-wetting phase and the pore size distribution.

5 DISCUSSION

5.1 Growth of the New Phase

The geometric constraints applied in the 2D and 3D scenarios treat the emergent phase as volumetrically dominant, limited in

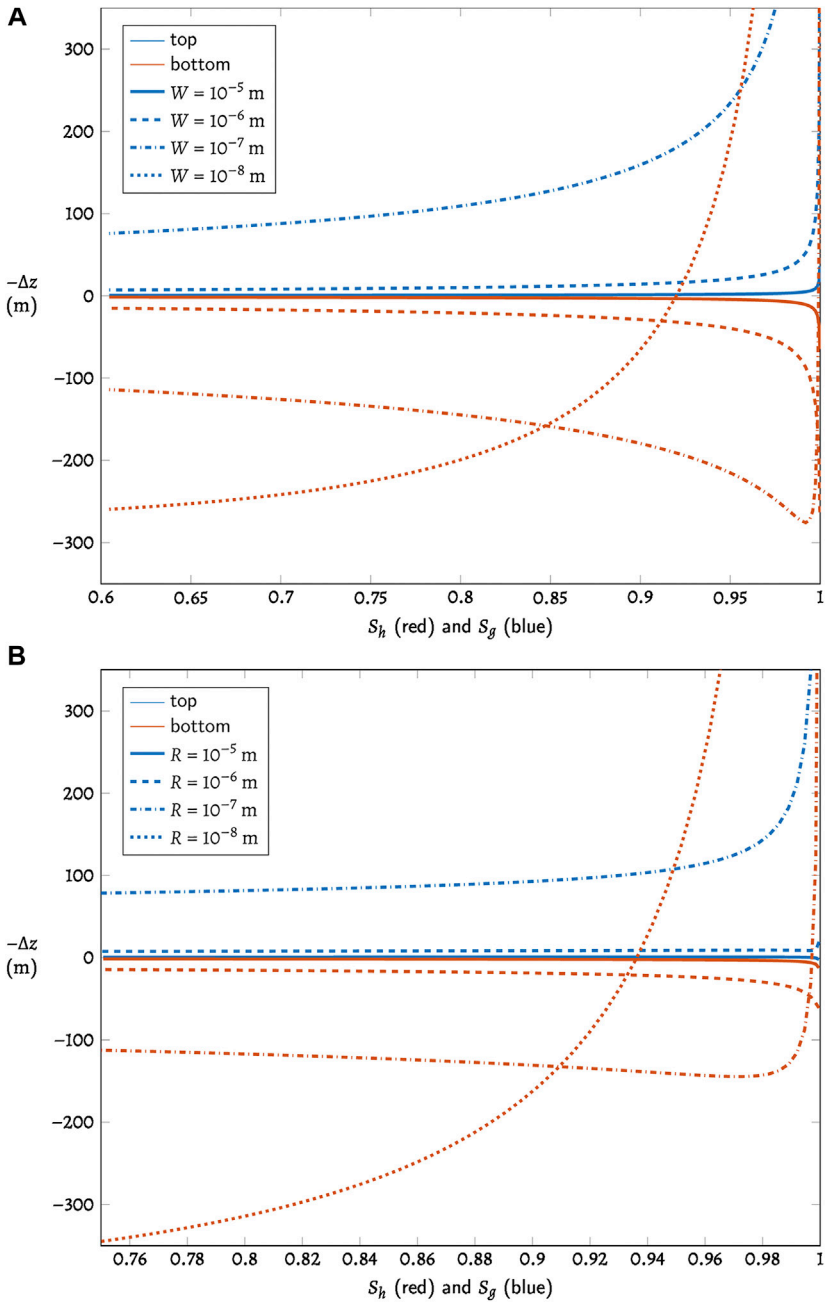

FIGURE 3 | The shifted three-phase boundary Δz_b and Δz_t at the first appearance of the emergent phase II as a function of the saturation level S_2, shown for the different values of **(A)** pore size W and **(B)** grain size R noted in the legend. Note that since z is pointing downwards, we have the z-axis flipped so that shallower location stays above deeper locations.

extent by the pore walls and residual phase. It must be noted that the radius of the emergent phase may be restricted by the presence of the residual phase; when the new phase nucleates, it is assumed to form near an interface with the residual phase, essentially replacing much of the pre-existing phase I to reach the minimum free-energy configuration while maintaining the same phase I curvature as that which pertains outside the three-phase coexisting zone.

Alternatively, the new phase could grow in the largest pores, either without being adjacent to the residual phase, or by completely replacing the residual phase that would have occupied those pores under the slightly perturbed conditions in the adjacent two-phase zone. In this situation, to satisfy the continuity of phase I curvature with that outside the three-phase zone, phase I can persist either in the form of small residual inclusions within pore crevices, or as a body filling almost all of

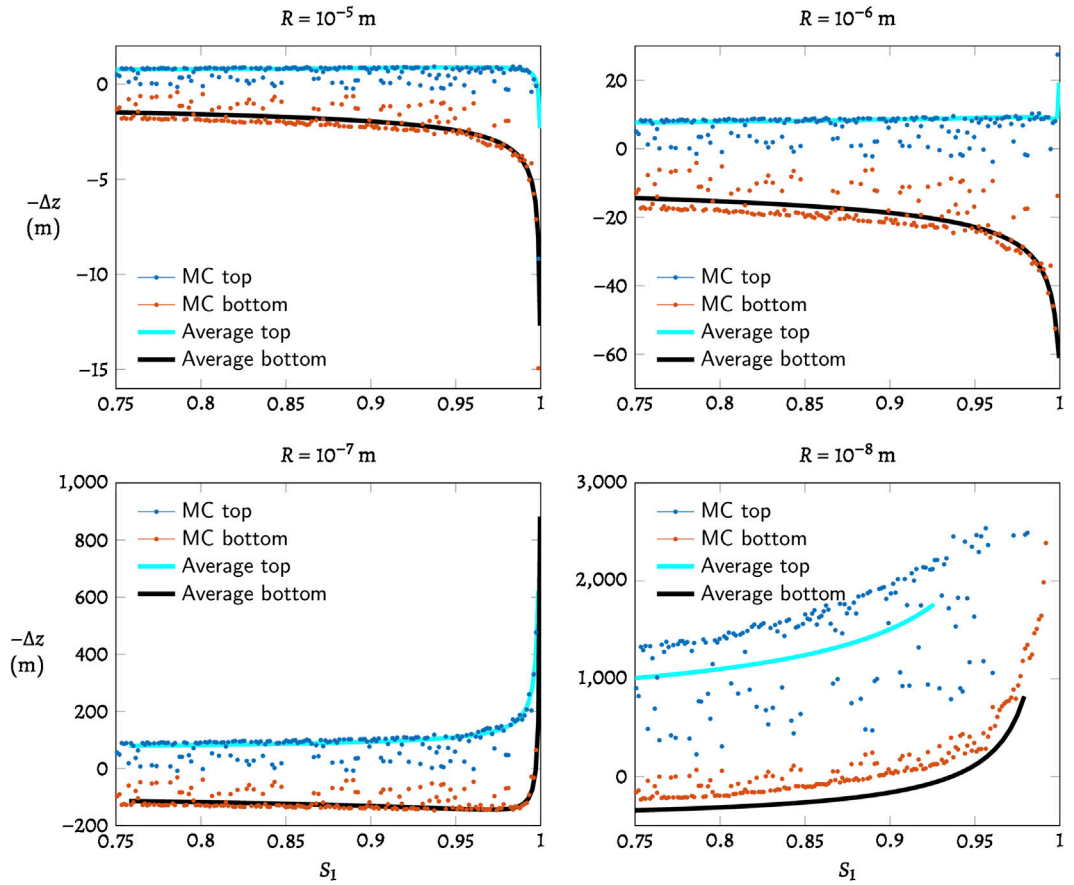

FIGURE 4 | Monte Carlo simulation of shifted three-phase boundary Δz_b and Δz_t for residual phase I before the appearance of emergent phase II as a function of grain size R, and comparison with 3D averaging results (black and cyan solid lines). The upper and lower bounds begin to deviate when the saturation is high and R is significantly reduced.

smaller pores with bumps of small radii R_1. In the first case, the small radius characterizing the residual phase in the two-phase region suggests high methane solubility, which is unstable because the chemical potential can be further minimized by increasing R_1 and reducing methane solubility. The second case leads to unrealistically high saturation levels for the hydrate crystals or methane bubbles.

5.2 Under-Filled Region Within the Zone

In our models, both non-wetting phases are mobile in the pores as long as not limited by the pore walls and the other non-wetting phase. At the boundaries, the emergent phase spans the pore center while the residual phase stays in the crevices. If the residual phase occupies a significant fraction of the pore, emergent phase may not be able to touch the pore walls, resulting in a lower saturation (< 0.6 for the 2D pores and < 0.75 for 3D pores). This under-filling scenario can be intuitively investigated for the 2D model, where the residual phase has a radius $R_1 > W/(6\sqrt{3})$, or $S_1 > 0.2$ (**Figure 5**). The value of R_2 is smaller accordingly, and so is the value of S_2. Ignore d and let $R_1 = \alpha W$, and we can find the corresponding R_2

$$\frac{R_2}{W} = \frac{1}{\sqrt{3}} - \frac{2}{3}\sqrt{\sqrt{3}\alpha - 2\alpha^2} - \frac{\alpha}{3} \tag{25}$$

where $2\sqrt{3} \le \alpha^{-1} \le 6\sqrt{3}$. In this configuration, R_1 and R_2 are symmetric, and it is easy to calculate that the offsets is smaller than the configuration in **Figure 2A**. We postulate that for the 3D pores, the under-filled configuration also gives smaller offsets. The three-phase zone is bounded by the maximum offset possible with given pore structure, pressure, and temperature, and under-filling cases are located in between the maxima. In pores located near the middle of the three-phase zone, both non-wetting phases may be under-filling, allowing the transition from L-H above the three-phase zone to L-G beneath the three-phase zone. Therefore, when seeking the boundaries of the three-phase zone, we need only consider configurations in which the emergent phase fills pore centers.

5.3 Shifted BHSZ and BSR

The bottom simulating reflector (BSR) is commonly interpreted as marking the BHSZ, which is the boundary separating the hydrate phase above from the free gas phase below. However, due to perturbations in salinity and the pore scale effects described here, hydrates can still be present at equilibrium below the bulk

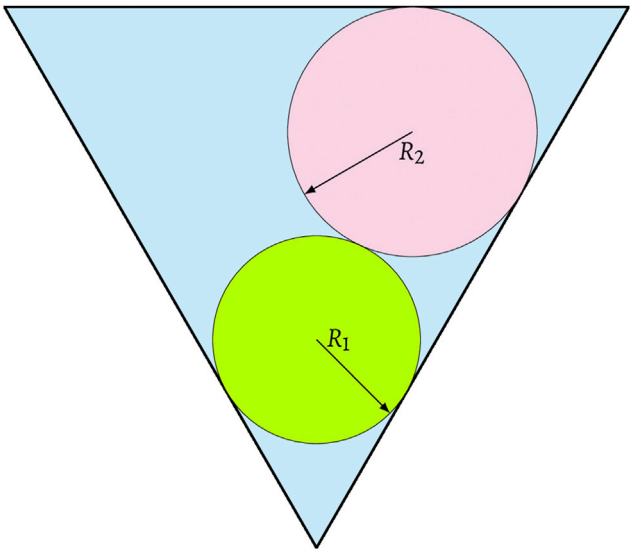

FIGURE 5 | A schematic of an under-filled configuration where phase I prevents phase II to span the pore center in a triangular pore.

BHSZ while free gas bubbles can persist above the bulk BHSZ. Our calculations show that the resulting zone of three-phase coexistence can vary in thickness from only a few meters to many tens of meters. This may cause the temperature and pressure at the BSR to deviate from three-phase equilibrium conditions, and the observed depth of BSR may differ from the bulk BHSZ. For example, the Ocean Drilling Project Leg 164 at Blake Ridge found that the temperatures at the BSR are 0.5°–2.9 °C lower than the theoretical equilibrium temperature; this corresponds to an upwards shift of 30–100 m above the bulk BHSZ, assuming a geothermal gradient of ~ 30 °C/km (Ruppel, 1997). Liu and Flemings (2011) showed that it is also possible to have the top of the three-phase zone below the bulk equilibrium depth, resulting in a deeper BHSZ. Such discrepancies have been attributed to shifted hydrate equilibria in porous media. In **Figure 4** the simulated top positions in some cases are lower than the bulk BHSZ. Our model predicts that a zone of three-phase coexistence can be expected to span the bulk BHSZ, with its upper boundary shifted toward colder temperatures by an amount controlled both by the hydrate saturation in the L-H region above, and the largest pore sizes available to emergent gas bubbles, giving a quantitative explanation for the observed discrepancy.

5.4 Implications for Poly-Dispersed and Non-Spherical Granular Sediments

Our model deals with simplified pores in mono-dispersed spherical grains, and our averaging method is strictly valid only for pores bounded by grains in direct contact. Theoretically, crevices can occur between separated grains, but as the distance between the two grains increases, it is much more difficult for liquid connecting the grains to form a concave meniscus with positive mean curvature. Hence, at low liquid saturations, most liquid stays in crevices between contacting grains. In real sediments, grains are poly-dispersed and irregular. If the grains are silt-sized and assumed spherical and contacting, we can model a random packing using the drop-and-roll method (Chen et al., 2020) with the particle sizes following a specified distribution, and apply the Monte Carlo method similarly. When the particle sizes follow a log-normal distribution $\ln \mathcal{N}(\mu, \sigma^2)$, our simulation results suggest that the shifted three-phase zone will remain mostly the same as in the mono-dispersed situation, except that the relevant grain size R should be comparable to the median radius $R_m = \exp(\mu)$ (defined by particle count rather than weight).

Constructing realistic synthetic packings that incorporate highly non-spherical grains, as expected of sediments with significant clay contents, is a more challenging numerical problem. Chen et al., (2020) pursued a simplified strategy in which two-phase saturation predictions were performed on a mono-dispersed packing with particle radii chosen so that the specific surface area matched the measured value for a silt loam (73 m^2/g: 33% sand, 49% silt, 18% clay by weight; Or and Tuller, 1999). Comparisons with partial saturation measurements showed excellent agreement when the non-wetting phase occupied more than 90% of the pore space, and the agreement remained acceptable down to about 60% non-wetting phase saturation. Further exploration of these results suggests that most of the residual wetting phase under these conditions is found in the increased numbers of small crevice-like regions in the vicinity of particle contacts. In sediment with significant amounts of non-spherical grains such as clay minerals, the crevice-like regions may be smaller, which limits the size of residual phase, and possibly will cause a thicker three-phase zone.

5.5 Sensitivity of Emergent Phase Stability to Residual Phase Saturation

Because residual phase saturation has a strong influence on the thickness of the zone of three-phase coexistence, it is possible to estimate the saturation of the hydrate or gas phase from BSR observations if the median particle size is known or can be estimated. However, since both the saturation level of the residual phase and the particle size of the host sediment can vary over short distances, we may expect that in some patches there may be interleaving of two-phase and three-phase zones. This further complicates the interpretation of BSR observations, and may be responsible for discontinuities in BSR location.

6 CONCLUSION

By approximating porous sediments as consisting of pores with diminishing crevices, we have demonstrated that near the base of the gas hydrate stability field, the upper (cold) boundary of a three-phase region is set by the gas—liquid surface energy of the first spherical bubbles that can form in the partially hydrate-saturated sediments, while the lower (warm) boundary is controlled by the surface energy of the first hydrate crystals that can form in the partially gas-saturated sediments. Of more fundamental importance, our analysis shows that the thickness of the three-phase zone depends not only on the

grain-size distribution, increasing dramatically from tens of meters in porous sediments with a median grain size of 1 μm to hundreds of meters when the median grain size is 0.1 μm, but that in a given sediment the thickness is also sensitive to the saturation levels of hydrate and gas at the boundaries with the two-phase zones above and below.

DATA AVAILABILITY STATEMENT

The original contributions presented in the study are included in the article/Supplementary Material, further inquiries can be directed to the corresponding author.

AUTHOR CONTRIBUTIONS

JC and AR conceived the original idea of how the residual phase must affect the thickness three-phase coexisting zone, and how it might be calculated. SM helped JC with the numerical implementation of these ideas in the Monte Carlo calculations. All authors contributed toward the writing, interpretations, and editing.

FUNDING

JC was supported by funding from the National Natural Science Foundation of China (Grant No. 41804085). SM was supported by Chinese Academy of Sciences (No. QYZDY-SSW-DQC029) and the National Natural Science Foundation of China (No. 41674097).

ACKNOWLEDGMENTS

AR appreciates the motivation and context gained during many stimulating discussions at the 2020 GRC on Natural Gas Hydrate Systems, chaired by Timothy Collett.

REFERENCES

Anderson, G. K. (2004). Enthalpy of dissociation and hydration number of methane hydrate from the Clapeyron equation. *J. Chem. Therm.* 36, 1119–1127. doi:10.1016/j.jct.2004.07.005

Bahk, J.-J., Kim, D.-H., Chun, J.-H., Son, B.-K., Kim, J.-H., Ryu, B.-J., et al. (2013). Gas hydrate occurrences and their relation to host sediment properties: results from second Ulleung basin gas hydrate drilling expedition, East Sea. *Mar. Petrol. Geol.* 47, 21–29. doi:10.1016/j.marpetgeo.2013.05.006

Bordia, R. K. (1984). A theoretical analysis of random packing densities of monosized spheres in two and three dimensions. *Scripta Metall.* 18, 725–730. doi:10.1016/0036-9748(84)90328-4

Borowski, W. S. (2004). A review of methane and gas hydrates in the dynamic, stratified system of the Blake ridge region, offshore South Eastern North America. *Chem. Geol.* 205, 311–346. doi:10.1016/j.chemgeo.2003.12.022

Chen, J., Mei, S., Irizarry, J. T., and Rempel, A. W. (2020). A Monte Carlo approach to approximating the effects of pore geometry on the phase behavior of soil freezing. *J. Adv. Model. Earth Syst.* 12, e2020MS002117. doi:10.1029/2020ms002117

Chong, Z. R., Yang, M., Khoo, B. C., and Linga, P. (2015). Size effect of porous media on methane hydrate formation and dissociation in an excess gas environment. *Ind. Eng. Chem. Res.* 55, 7981–7991. doi:10.1021/acs.iecr.5b03908

Clennell, M. B., Hovland, M., Booth, J. S., Henry, P., and Winters, W. J. (1999). Formation of natural gas hydrates in marine sediments: 1. conceptual model of gas hydrate growth conditioned by host sediment properties. *J. Geophys. Res.* 104, 22985–23003. doi:10.1029/1999jb900175

Cook, A. E., and Malinverno, A. (2013). Short migration of methane into a gas hydrate-bearing sand layer at Walker Ridge, Gulf of Mexico. *Geochem. Geophys. Geosyst.* 14, 283–291. doi:10.1002/ggge.20040

Dai, S., Santamarina, J. C., Waite, W. F., and Kneafsey, T. J. (2012). Hydrate morphology: physical properties of sands with patchy hydrate saturation. *J. Geophys. Res.* 117, B11205. doi:10.1029/2012jb009667

Daigle, H., and Dugan, B. (2011). Capillary controls on methane hydrate distribution and fracturing in advective systems. *Geochem. Geophys. Geosyst.* 12, Q01003. doi:10.1029/2010gc003392

Denoyel, R., and Pellenq, R. J. M. (2002). Simple phenomenological models for phase transitions in a confined geometry. 1: melting and solidification in a cylindrical pore. *Langmuir* 18, 2710–2716. doi:10.1021/la015607n

Duan, Z., and Mao, S. (2006). A thermodynamic model for calculating methane solubility, density and gas phase composition of methane-bearing aqueous fluids from 273 to 523K and from 1 to 2000bar. *Geochem. Cosmochim. Acta* 70, 3369–3386. doi:10.1016/j.gca.2006.03.018

Dullien, F. (2012). *Porous media fluid transport and pore structure*. San Diego, CA: Elsevier Science.

Finney, J. L. (1970). Random packings and the structure of simple liquids. i. the geometry of random close packing. *Proc. R. Soc. A* 319, 479–493. doi:10.1098/rspa.1970.0189

Gupta, A., Lachance, J., Sloan, E. D., and Koh, C. A. (2008). Measurements of methane hydrate heat of dissociation using high pressure differential scanning calorimetry. *Chem. Eng. Sci.* 63, 5848–5853. doi:10.1016/j.ces.2008.09.002

Handwerger, A. L., Rempel, A. W., and Skarbek, R. M. (2017). Submarine landslides triggered by destabilization of high-saturation hydrate anomalies. *Geochem. Geophys. Geosyst.* 18, 2429–2445. doi:10.1002/2016gc006706

Hardy, S. C. (1977). A grain boundary groove measurement of the surface tension between ice and water. *Phil. Mag.* 35, 471–484. doi:10.1080/14786437708237066

Henry, P., Thomas, M., and Clennell, M. B. (1999). Formation of natural gas hydrates in marine sediments: 2. thermodynamic calculations of stability conditions in porous sediments. *J. Geophys. Res.* 104, 23005–23022. doi:10.1029/1999jb900167

Jang, J., and Santamarina, J. C. (2011). Recoverable gas from hydrate-bearing sediments: pore network model simulation and macroscale analyses. *J. Geophys. Res.* 116. doi:10.1029/2010jb007841

Liu, W., Wang, S., Yang, M., Song, Y., Wang, S., and Zhao, J. (2015). Investigation of the induction time for THF hydrate formation in porous media. *J. Nat. Gas Sci. Eng.* 24, 357–364. doi:10.1016/j.jngse.2015.03.030

Liu, X., and Flemings, P. B. (2011). Capillary effects on hydrate stability in marine sediments. *J. Geophys. Res.* 116. doi:10.1029/2010jb008143

Lu, W., Chou, I. M., and Burruss, R. C. (2008). Determination of methane concentrations in water in equilibrium with Si methane hydrate in the absence of a vapor phase by *in situ* Raman spectroscopy. *Geochem. Cosmochim. Acta* 72, 412–422. doi:10.1016/j.gca.2007.11.006

Mackay, A. L. (1974). Generalized structural geometry. *Acta Crystallogr. A* 30, 440–447. doi:10.1107/s0567739474000945

Malinverno, A. (2010). Marine gas hydrates in thin sand layers that soak up microbial methane. *Earth Planet Sci. Lett.* 292, 399–408. doi:10.1016/j.epsl.2010.02.008

Millington, R. J., and Quirk, J. P. (1961). Permeability of porous solids. *Trans. Faraday Soc.* 57, 1200. doi:10.1039/tf9615701200

Nole, M., Daigle, H., Cook, A. E., and Malinverno, A. (2016). Short-range, overpressure-driven methane migration in coarse-grained gas hydrate reservoirs. *Geophys. Res. Lett.* 43, 9500–9508. doi:10.1002/2016gl070096

Or, D., and Tuller, M. (1999). Liquid retention and interfacial area in variably saturated porous media: upscaling from single-pore to sample-scale model. *Water Resour. Res.* 35, 3591–3605. doi:10.1029/1999wr900262

Rempel, A. W. (2011). A model for the diffusive growth of hydrate saturation anomalies in layered sediments. *J. Geophys. Res.* 116, B10105. doi:10.1029/2011jb008484

Rempel, A. W. (2012). Hydromechanical processes in freezing soils. *Vadose Zone J.* 11, vzj2012.0045. doi:10.2136/vzj2012.0045

Ruppel, C. (1997). Anomalously cold temperatures observed at the base of the gas hydrate stability zone on the U.S. Atlantic passive margin. *Geology* 25, 699–702. doi:10.1130/0091-7613(1997)025<0699:actoat>2.3.co;2

Sloan, E. D., and Koh, C. (2007). *Clathrate hydrates of natural gases*. Boca Raton, FL: CRC Press.

Suess, E., Torres, M. E., Bohrmann, G., Collier, R. W., Greinert, J., Linke, P., et al. (1999). Gas hydrate destabilization: enhanced dewatering, benthic material turnover and large methane plumes at the cascadia convergent margin. *Earth Planet Sci. Lett.* 170, 1–15. doi:10.1016/s0012-821x(99)00092-8

Sultan, N., Cochonat, P., Foucher, J.-P., and Mienert, J. (2004). Effect of gas hydrates melting on seafloor slope instability. *Mar. Geol.* 213, 379–401. doi:10.1016/j.margeo.2004.10.015

Sun, R., and Duan, Z. (2005). Prediction of CH_4 and CO_2 hydrate phase equilibrium and cage occupancy from ab initio intermolecular potentials. *Geochem. Cosmochim. Acta* 69, 4411–4424. doi:10.1016/j.gca.2005.05.012

VanderBeek, B. P., and Rempel, A. W. (2018). On the importance of advective versus diffusive transport in controlling the distribution of methane hydrate in heterogeneous marine sediments. *J. Geophys. Res. Solid Earth* 123, 5394–5411. doi:10.1029/2017jb015298

Wagner, W., and Pruss, A. (1993). International equations for the saturation properties of ordinary water substance. Revised according to the international temperature scale of 1990. Addendum to J. Phys. Chem. Ref. Data 16, 893 (1987). *J. Phys. Chem. Ref. Data* 22, 783–787. doi:10.1063/1.555926

Wang, X., Hutchinson, D. R., Wu, S., Yang, S., and Guo, Y. (2011). Elevated gas hydrate saturation within silt and silty clay sediments in the Shenhu area, South China Sea. *J. Geophys. Res.* 116. doi:10.1029/2010jb007944

Wilder, J. W., Seshadri, K., and Smith, D. H. (2001). Modeling hydrate formation in media with broad pore size distributions. *Langmuir* 17, 6729–6735. doi:10.1021/la010377y

Yousif, M. H., Abass, H. H., Selim, M. S., and Sloan, E. D. (1991). Experimental and theoretical investigation of methane-gas-hydrate dissociation in porous media. *SPE Reservoir Eng.* 6, 69–76. doi:10.2118/18320-pa

Yousif, M. H., and Sloan, E. D. (1991). Experimental investigation of hydrate formation and dissociation in consolidated porous media. *SPE Reservoir Eng.* 6, 452–458. doi:10.2118/20172-pa

Conflict of Interest: The authors declare that the research was conducted in the absence of any commercial or financial relationships that could be construed as a potential conflict of interest.

APPENDIX

1 Averaging Method in Random Packing of Mono-Dispersed Spherical Grains

Bordia (1984) provided a theoretical method to average properties in mono-dispersed random packings. The packing can be viewed as consisting of numerous virtual triclinic cells formed by eight grains (**Figure A1**), where P_1, P_2, P_3, and P_4 are actual grains, and the other four are virtual, with each side $2R$ and three random angles α, β, and γ.

The triclinic cells have two limits. One is the loose limit which is a simple cubic, where

$$\alpha = \beta = \gamma = \frac{\pi}{2} \tag{A1}$$

while the tight limit is the face-centered cubic packing

$$\alpha = \beta = \gamma = \frac{\pi}{3}. \tag{A2}$$

For an arbitrary property Y, in one arbitrary cell, its value is $Y(\alpha, \beta, \gamma)$, and the three independent varying angles α, β, and γ are assumed uniformly distributed in $[\pi/3, \pi/2]$, so they have the same probability density function

$$\psi(\alpha) = \psi(\beta) = \psi(\gamma) = \frac{6}{\pi} \tag{A3}$$

and the bulk property Y can be calculated by

$$\begin{aligned} \langle Y \rangle &= \int_{\frac{\pi}{3}}^{\frac{\pi}{2}} \int_{\frac{\pi}{3}}^{\frac{\pi}{2}} \int_{\frac{\pi}{3}}^{\frac{\pi}{2}} Y(\alpha, \beta, \gamma) \psi(\alpha) \psi(\beta) \psi(\gamma) \, d\alpha \; d\beta \; d\gamma \\ &= \left(\frac{6}{\pi}\right)^3 \int_{\frac{\pi}{3}}^{\frac{\pi}{2}} \int_{\frac{\pi}{3}}^{\frac{\pi}{2}} \int_{\frac{\pi}{3}}^{\frac{\pi}{2}} Y(\alpha, \beta, \gamma) \, d\alpha \; d\beta \; d\gamma. \end{aligned} \tag{A4}$$

For example, if Y is the packing factor F, in one cell the packing factor is

$$F(\alpha, \beta, \gamma) = \frac{4\pi R^3}{3V(\alpha, \beta, \gamma)} \tag{A5}$$

where the volume of the cell is

$$V(\alpha, \beta, \gamma) = 8R^3 \sqrt{1 + 2\cos\alpha\cos\beta\cos\gamma - \cos^2\alpha - \cos^2\beta - \cos^2\gamma}. \tag{A6}$$

And the mean bulk packing factor is

$$\langle F \rangle = \left(\frac{6}{\pi}\right)^3 \int_{\frac{\pi}{3}}^{\frac{\pi}{2}} \int_{\frac{\pi}{3}}^{\frac{\pi}{2}} \int_{\frac{\pi}{3}}^{\frac{\pi}{2}} F(\alpha, \beta, \gamma) \, d\alpha \, d\beta \, d\gamma \approx 0.599 \tag{A7}$$

close to 0.6 for random loose packing (Dullien, 2012).

For poly-dispersed grains, the virtual cell may be heavily distorted, and the distributions of angles are affected by grain radii, so the averaging method may not work properly.

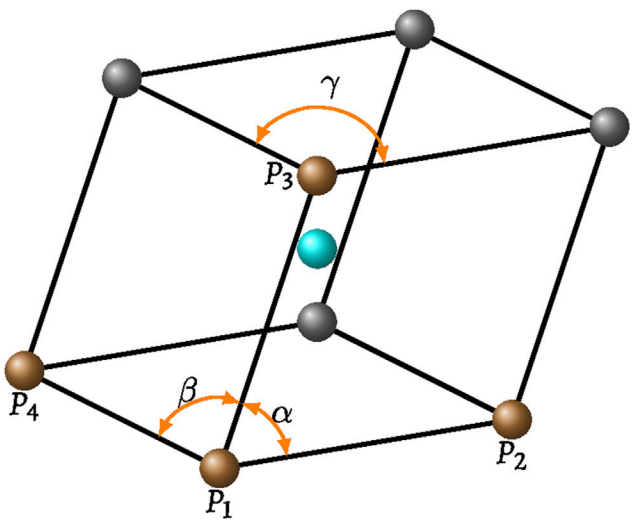

FIGURE A1 | A virtual triclinic cell formed by eight grains with each side $2R$ and three random angles α, β, and γ. Bonds mean the two grains are in contact. The brown dots represent centers of actual grains, the gray dots are for virtual grains, and the cyan dot is the interstitial site.

frontiers in Earth Science

ORIGINAL RESEARCH
published: 23 February 2021
doi: 10.3389/feart.2020.601254

Controls on Gas Emission Distribution on the Continental Slope of the Western Black Sea

Michael Riedel[1], Line Hähnel[1,2], Jörg Bialas[1], Anna Katharina Bachmann[3,4], Stefanie Gaide[3], Paul Wintersteller[3], Ingo Klaucke[1] and Gerhard Bohrmann[3]*

[1]GEOMAR Helmholtz Centre for Ocean Research Kiel, Kiel, Germany, [2]GeoZentrum Nordbayern, Friedrich-Alexander University Erlangen-Nürnberg, Erlangen, Germany, [3]University Bremen, MARUM–Center for Marine Environmental Sciences and Faculty of Geoscience, Bremen, Germany, [4]Wageningen University and Research, Wageningen, Netherlands

The continental slopes of the Black Sea show abundant manifestations of gas seepage in water depth of <720 m, but underlying controls are still not fully understood. Here, we investigate gas seepage along the Bulgarian and Romanian Black Sea margin using acoustic multibeam water column, bathymetry, backscatter, and sub-bottom profiler data to determine linkages between sub-seafloor structures, seafloor gas seeps, and gas discharge into the water column. More than 10,000 seepage sites over an area of ~3,000 km^2 were identified. The maximum water depth of gas seepage is controlled by the onset of the structure I gas hydrate stability zone in ~720 m depth. However, gas seepage is not randomly distributed elsewhere. We classify three factors controlling on gas seepage locations into depositional, erosional, and tectonic factors. Depositional factors are associated with regionally occurring sediment waves forming focusing effects and mass-transport deposits (MTDs) with limited sediment drape. Elongated seafloor depressions linked to faulting and gas seepage develop at the base between adjacent sediment waves. The elongated depressions become progressively wider and deeper toward shallow water depths and culminate in some locations into clusters of pockmarks. MTDs cover larger regions and level out paleo-topography. Their surface morphology results in fault-like deformation patterns of the sediment drape on top of the MTDs that is locally utilized for gas migration. Erosional factors are seen along channels and canyons as well as slope failures, where gas discharge occurs along head-scarps and ridges. Sediment that was removed by slope failures cover larger regions down-slope. Those regions are devoid of gas seepage either by forming impermeable barriers to gas migration or by removal of the formerly gas-rich sediments. Deep-rooted tectonic control on gas migration is seen in the eastern study region with wide-spread normal faulting promoting gas migration. Overall, gas seepage is widespread along the margin. Gas migration appears more vigorous in shallow waters below ~160 m water depth, but the number of flare sites is not necessarily an indicator of the total volume of gas released.

Keywords: black sea, gas venting, structural control, faulting, gas hydrates, Danube deep-sea fan

OPEN ACCESS

Edited by:
Martin Scherwath, University of Victoria, Canada

Reviewed by:
Jeffrey Beeson, Oregon State University, United States
Marc De Batist, Ghent University, Belgium

****Correspondence:***
Michael Riedel
mriedel@geoamr.de

Specialty section:
This article was submitted to Biogeoscience, a section of the journal Frontiers in Earth Science

Received: *31 August 2020*
Accepted: *15 December 2020*
Published: *23 February 2021*

Citation:
Riedel M, Hähnel L, Bialas J, Bachmann AK, Gaide S, Wintersteller P, Klaucke I and Bohrmann G (2021) Controls on Gas Emission Distribution on the Continental Slope of the Western Black Sea. Front. Earth Sci. 8:601254. doi: 10.3389/feart.2020.601254

INTRODUCTION

Studies on Gas Hydrates and Gas Venting in the Black Sea

In 1974, sampling of natural gas hydrates has been described for the first time in the Black Sea (Yefremova and Zhizchenko, 1974). Since then, many research expeditions and projects were undertaken to study the occurrence and distribution of methane gas and gas hydrates along the continental margins of the Black Sea (see e.g., Ginsburg, 1998; Vassilev and Dimitrov, 2002; Bohrmann et al., 2003; Starostenko et al., 2010; Haeckel et al., 2017).

Over the course of the past 20 years of research on gas hydrates conducted in the Black Sea, numerous active gas expulsion sites, mud volcanoes, and indicators for gas and hydrate distribution have been found (e.g., Ergün et al., 2002; Vassilev and Dimitrov 2002; Greinert et al., 2006; Klaucke et al., 2006; Naudts et al., 2006; Popescu et al., 2007; Sahling et al., 2009; Greinert et al., 2010; Pape et al., 2010; Starostenko et al., 2010; Römer et al., 2012; Römer et al., 2019; Körber et al., 2014; Hillman et al., 2018a; Wu et al., 2019; Zander et al., 2019).

According to current temperature and salinity conditions in the Black Sea gas hydrate of structure I is stable in water depth greater than 720 m (e.g., Pape et al., 2011; Riboulot et al., 2017). Depending on the depth of the seafloor and the temperature gradient in the sediments, gas hydrates are expected to be stable within 200 m–300 mbsf (Bialas et al., 2014; Zander et al., 2017; Riboulot et al., 2018), defining upper and lower limits of the bottom-simulating reflector (BSR) distribution as initially shown by Popescu et al. (2006). As part of these investigations, several authors identified that gas seepage sites are not necessarily randomly distributed, but show some association to structural and seafloor morphological features, such as slump scars, canyon flanks, or ridges (Naudts et al., 2006; Naudts et al., 2009; Riboulot et al., 2017; Römer et al., 2019). In a study along the Bulgarian slope in the south-western Black Sea, Xu et al. (2018) reported on active gas expulsion above the gas hydrate stability field that appears in unique elongated, slope-parallel depressions. Similar observations were made at other margins where elongated depressions are either interpreted as merging of pockmark-chains (e.g., Pilcher and Argent, 2007; Çifçi et al., 2003; Reiche et al., 2011) or as a result of extensional cracking and linked to slope failures (e.g., Driscoll et al., 2000; Mienert et al., 2010; Laberg et al., 2013). All these studies highlighted the need of multibeam bathymetry and water column data for the identification of gas seepages.

In our new study, we refer specifically to gas hydrate-related studies based on the expeditions from the French-Romanian BlaSON project (e.g., Popescu et al., 2006; Popescu et al., 2007), the French GHASS expedition (Ker and Riboulot, 2015), the German MSM34 expedition (Bialas et al., 2014) and the most recent expeditions M142 (Bohrmann, 2018) and M143 (Riedel et al., 2018) with the latter three conducted as part of the German SUGAR-III program. Using the MARUM MeBo200 seafloor drilling system (Freudenthal and Wefer, 2013), two deep drill sites up to 146 m below seafloor (mbsf) and to the depth of the base of gas hydrate stability were accomplished (Bohrmann, 2018; Freudenthal et al., 2020) into the Danube deep sea fan (Site GeoB22603–1, MeBo-16; GeoB22605–1, MeBo-17, **Figure 1**). A summary of many of these activities and findings in the Black Sea was recently provided by Minshull et al. (2020) as part of the European Union-funded project "Marine gas hydrate–an indigenous resource of natural gas for Europe" (MIGRATE). Bialas et al. (2020) jointly summarized seismic and electromagnetic results achieved for the north-western margin within the SUGAR III project.

As part of R/V *Meteor* expeditions M142 and M143 seafloor mapping along the Romanian shelf and slope was expanded from the initial coverage achieved during R/V *Maria S. Merian* expedition MSM34 (Bialas et al., 2014) and the GHASS expedition onboard R/V *Pourquoi pas?* (Ker and Riboulot, 2015). Discoveries of clustered gas seepage as reported by Riboulot et al. (2017) were confirmed and observations were expanded further West and East along the slope in water depths of 200–800 m up to the Ukrainian border (**Figure 1**). As a result of these new surveys, a total region of ~3,400 km^2 was additionally mapped with multibeam echosounder systems and combined with ~4 kHz sub-bottom profiler data acquisition.

Understanding the regional distribution and amount of gas venting is an important element in estimating the geological methane budget at continental margins and implications on the global climate (e.g., Judd et al., 2002; Ruppel and Kessler, 2017 and references therein). How much of the methane that is emitted at the seafloor actually reaches the atmosphere is still poorly constrained (e.g., McGinnis et al., 2006) and depends on many factors (other than water depth) including bubble size and rise rates (e.g., Greinert et al., 2010). The shallower the water depth of a given gas seep, the higher the percentage of methane transfer to the atmosphere (e.g., Schmale et al., 2010; Ruppel and Kessler, 2017). In our study we first show a comprehensive, regional inventory of gas accumulation and seepage manifestations including the outer continental shelf. From this we determine three levels of control of venting distribution: physical-chemical controls, sedimentological controls, and structural controls. While the presence of gas vents was previously mapped in sub-regions of our study area and mostly explained by canyon and slope failure head-scarps exposing gas-bearing sediment layers or providing structural focusing for gas migration (e.g., Naudts et al., 2006; Riboulot et al., 2017), our new data show 1) large regions of the study area in water depths shallower than the upper limit of GHSZ that are devoid of gas vents, 2) widespread mass transport deposits without clear correlation to gas venting, and 3) the continental shelf to be the region with the highest gas flare density. Possible explanations for these observations are discussed in the light of morpho-sedimentological interpretations of the newly acquired geo-acoustical data. In particular, we show that paleo-topography and older structures have a strong deterministic influence on the distribution of gas seepage irrespective of more recent sediment deposition (drape).

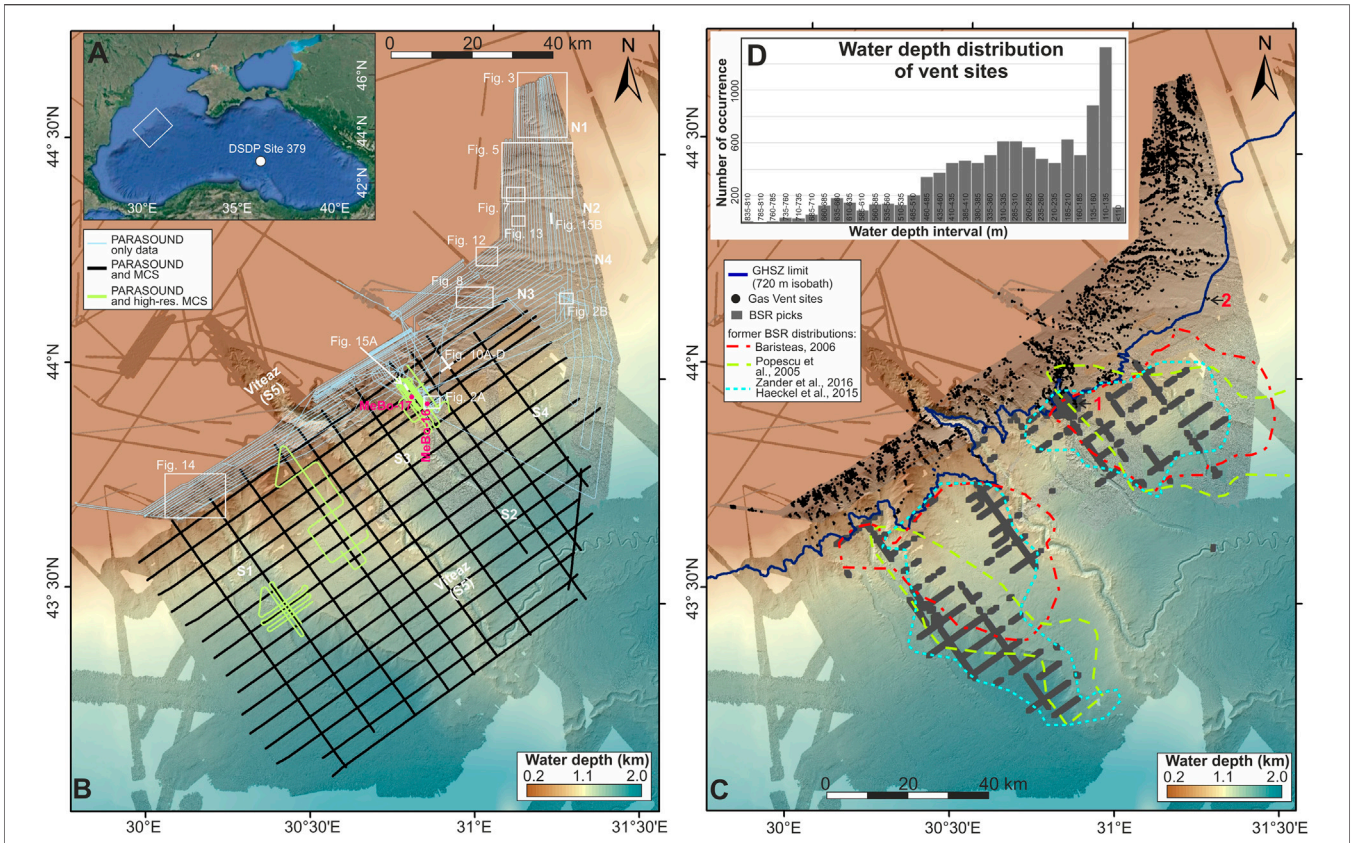

FIGURE 1 | (A) Study region of expeditions MSM34, M142, and M143 (white rectangle) in the western Black Sea. **(B)** Seafloor bathymetry of the study region and outline of data utilized in this study with naming of channel systems. Following Winguth et al. (2000) the S1–S4 channels are linked to the Danube fan and the N1–N4 channels are linked to the Dnepr fan. Location of areas studied in detail in this study are indicated by white rectangles. **(C)** Seafloor bathymetry overlain with location of gas seeps. The seismically determined bottom-simulating reflector (BSR) occurs exclusively deeper than 720 m which is the inferred limit of the gas hydrate stability zone (GHSZ). In comparison, earlier outlines of BSR-distributions are shown. Two sites of gas venting deeper than the 720 m isobath (labeled in red) are linked to vent sites with gas hydrate occurrences. **(D)** Histogram of the water depth distribution of all vent sites mapped in the region. Water depth at the vent site locations was taken from the newly acquired bathymetry of expeditions M142 and M143.

Geological Background

The Black Sea Basin is a back-arc basin that formed due to the closure of the Thetys Ocean and has undergone several phases of extension and closure since the Neogene (Robinson et al., 1996). Our study region in the North-Western Black Sea (**Figure 1**) is a typical passive margin setting with wide continental shelves (Ryan et al., 1997), and dominated by several large-scale submarine channel systems, with the Viteaz or Danube channel being the largest system seen (Winguth et al., 2000). Nine channel systems have been identified in our study region (**Figure 1**). The S1 to S5 channels are linked to the Danube river, whereas the N1 to N4 channels have been linked to the Dnepr river (Wong et al., 1994; Wong et al., 1997; Winguth et al., 2000). The sediments found in the two associated deep-sea fans consist of mainly fine-grained turbidites and form stacks of alternating channel and levees deposits interspersed with mass-transport deposits (Popescu et al., 2001; Popescu et al., 2004; Hillman et al., 2018a). The deep-sea fans began to develop ~900 ka BP (Winguth et al., 2000) and the Viteaz Channel is the most recently active channel. It began to develop around 25 ka BP during the last glacial maximum (LGM) when sea-level in the Black Sea was 100–150 m lower than today (e.g., Lericolais et al., 2009; Lericolais et al., 2013). During the LGM, sea water in the Black Sea was also fresher with a salinity of 3–4 PSU (practical salinity unit) compared to today's value of ~22 PSU (Özsoy and Ünlüata, 1997). Bottom-water temperatures during the LGM were ~4°C (e.g., Soulet et al., 2010) compared to today's temperature of ~9°C (Degens and Ross, 1974; Vassilev and Dimitrov, 2002). Implications of this drastic change in temperature and pressure conditions on the gas hydrate regime of the Black Sea have been described by Poort et al. (2005), Riboulot et al. (2018), and Ker et al. (2019) and the equilibration process in the sub-surface is still ongoing (e.g., Hillman et al., 2018b). The temperature increase at the sea floor has resulted in an up-dip migration of the upper limit (feather edge) of the base of gas hydrate stability zone, which is one of the primary controls on the limits of gas venting occurrences in the region (e.g., Riboulot et al., 2017).

DATA AND METHODS

Multibeam and Water-Column Data

During expeditions M142 and M143 onboard the R/V *Meteor* the hull-mounted Kongsberg EM710 (1°/1° beam angle and 70–100 kHz operating frequency) multibeam echosounder (MBES) system was the primary acquisition system in water depths <600 m. The ping rate (dependent on water depth) was up to 40 Hz. In water depth of >600 m, a hull-mounted Kongsberg EM122 12 kHz MBES system was used during cruises MSM34 (2°/2° beam angle), M142, and M143 (1°/2° beam angle). The EM122 ping rate was also adjusted dependent on water depth with a maximum rate of 5 Hz. In both systems, the maximum swath angle was set to 130° (Bohrmann, 2018), running in equidistance mode for spacing the beams across track. Survey speed during acquisition was varying between 3 and 8 kn. Motion data and static offsets were recorded by the ship's internal sensors and directly applied to the two MBES data sets. Weather conditions during multibeam data acquisition were often severe with significant wave heights, deteriorating data quality. Manual editing of the data was therefore performed to clean the data using the open-source software MB-System (Caress et al., 2017). The multibeam data from both surveys were corrected post-expedition to include the measured sound velocity profiles (Bohrmann, 2018) prior to merging the data sets into one bathymetric depth map. A tide correction by utilizing the Oregon State University (OSU) Tidal Prediction Software OTPS (http://volkov.oce.orst.edu/tides/otps.html) was also performed. The various multibeam data sets were ultimately gridded with a 10 m by 10 m regular spacing. Additional details on the physical settings of the two multibeam systems installed on the R/V *Meteor* can be found in the M142 cruise report available online (Bohrmann, 2018).

Water column data from the two MBES of all expeditions were displayed post-acquisition using the QPS Fledermaus™ FM-Midwater-Tool to detect gas flares. Individual gas flares are seen as semi-vertical high-amplitude anomalies in the water-column data and are traced from swath to swath until the gas flare can be traced to the actual outlet at the seafloor. If this was not possible, the best projection of seafloor position is made according to the survey conditions (direction and speed of travel). Gas flares may be detected during multiple passes over the same region but the manual pick of the exact seafloor location may be somewhat different between overlapping lines, also due to the nature of gas venting changing over time. In order to avoid false counting of gas flares, picks within a critical distance from each other from overlapping lines were treated as one gas vent location and presented as such in the maps. This distance is water-depth dependent linked to the range in the beam-angle and swath width. In water depths of <200 m, the critical distance is 25 m, and this increases to 50 m for larger water depths.

Backscatter

Seafloor backscattering strength was determined from both shipborne multibeam systems EM122 and EM710 operated during expeditions M142 and M143. We processed the data using MB-system routine "mbbackangle" (Caress et al., 2017) to generate average seafloor backscatter values by binning them according to their grazing angle and averaging the amplitudes within each bin. The number of grazing angle bins was set to 81 and the maximum angle considered was set to 80. The grazing angle has been corrected for varying across-track bottom slopes, and amplitude correction tables within MB-system have been applied using a reference angle of 60°. The resulting backscatter mosaic grids have a resolution of 10 m by 10 m regular spacing. Mainly due to the different frequencies utilized for the EM710 and EM122 MBES, the resulting seafloor backscatter maps cannot be merged. In fact, the products highlight different aspects of the seafloor. While EM710 backscatter illuminates the seafloor morphology but less sediment specific characteristics, EM122 backscatter emphasizes the sediment differences by penetrating into the sub-surface on a meter scale. Partial severe weather conditions during data acquisition effected the data quality due to a significantly lower signal to noise ratio, especially the EM710 data. Therefore, we only use seafloor backscatter derived from the EM122 system, as it was overall less affected by the severe weather conditions.

PARASOUND Sub-Bottom Profiler Data

The PARASOUND echosounder installed on board the R/V *Meteor* and R/V *Maria S. Merian* utilizes the parametric effect which results from the nonlinear relation of pressure and density during sonar propagation. Two high-intensity acoustic waves with frequencies of 18–20 kHz (primary high frequency, PHF) and 22–24 kHz were used to create a secondary high (40–42 kHz, SHF) and a secondary low-frequency (~4 kHz, SLF) pulse. The opening angle of the transducer is 4° by 5°, which corresponds to a footprint size of about 7% of the water depth. While the SLF is used for the sub-bottom profiling, the PHF can be used to image gas bubbles in the water column. The PHF data have been used occasionally to verify gas flare detection in the EM122 data, mainly for data from expedition MSM34. For the purpose of this study, we mostly focus on the SLF data for sub-seafloor imaging, as water column imaging for gas flare detection was made primarily with the EM710 and EM122 multibeam systems. The SLF during the M142 was set to 3.6 kHz to limit the interference with the EM122 signal. The pulse shape was set to continuous wave mode with one period per pulse and a pulse length of 0.25 ms. The sub-bottom profiler data show penetration depths varying from only 20 m across the shelf region to >100 m in deeper water settings. For display purposes we always use the instantaneous amplitude (envelope) attribute, and where required to highlight deeper occurrences, we used a time-varying gain function with 50 ms window length. The PARASOUND data are used to describe the sedimentary environment. The acoustic data are further used to identify the presence of free gas in the subsurface. The presence of free gas was identified either from high-amplitude reflections (bright-spots) and/or from acoustic masking of sediment reflections underneath the bright spot.

Multichannel Seismic Data

During expedition MSM34 (Bialas et al., 2014) a grid of 27 regional 2-D multichannel seismic (MCS) data was acquired covering the area of the Danube deep-sea fan with the S1–S5 channel systems (**Figure 1B**). The regional 2-D MCS data were acquired using a single GI gun (volume ~4 L, 250 in^3) as acoustic source and a single streamer with a total active length of 1050 m (168 channels). A high-resolution subset of 2-D MCS lines was acquired but with a smaller-sized GI gun (1.5 L, 90 in^3) and shorter streamer (237.5 m active length, 76 channels). Additional high-resolution 3-D seismic data were acquired with the P-cable system in two regions linked to the SUGAR program activities (details see e.g., Zander et al., 2017; Hillman et al., 2018a; Hillman et al., 2018b; Bialas et al., 2020). Processing of the 2-D regional and high-res MCS data included geometry definition and sorting to common-mid-point locations, band-pass filtering (10–180 Hz), followed by velocity analysis with normal move-out (NMO) correction, and stacking. Post-stack time migration was performed subsequently using the MCS-derived NMO-velocities.

Gas Hydrate Stability Zone and Methane Solubility Calculations

Methane is the dominant gas in the sedimentary system of the Danube deep-sea fan as shown by previous work (Riboulot et al., 2018; Ker et al., 2019) and new drilling with the MARUM MeBo200 system during the M142 expedition (Pape et al., 2020). No significant amounts of other hydrocarbons were detected so that we assume a pure methane system in the modeling of the gas hydrate stability in our study region following the theory described by Tishchenko et al. (2015). Temperature data in the water column are used from multiple water-column measurements during the M142 expedition (Bohrmann, 2018). The sub-seafloor temperature gradient is assumed to follow an average of 24°C/km for the regional extrapolation of the base of gas hydrate stability. Local variations in the temperature gradient may occur and topographic effects could add complexity to the sub-surface temperature regime (as noted by Hillman et al., 2018b), but can be neglected here as we do not derive site-specific properties.

Gas venting and free gas within sediments were observed mostly above the feather edge of the GHSZ (~720 m water depth). In order to investigate the nature of free gas occurrences in the sediments and their acoustic character in sub-bottom profiler data, we model methane gas solubilities for methane in seawater following the equation provided by Duan and Mao (2006) and implemented in the SUGAR toolbox (KosselBigalke et al., 2013). Two generic diagrams of solubility as function of pressure (at constant temperature and salinity) as well as solubility as function of temperature (at constant pressure and salinity) are shown in **Supplementary Figure S1**.

RESULTS

General Locations of Bottom-Simulating Reflectors Relative to the Limit of GHSZ

Figure 1 shows an overview of observations of the BSR in the MCS data set available and previous outlines of BSR occurrences from Baristeas (2006), Popescu et al. (2006), Haeckel et al. (2015), and Zander et al. (2016). The BSR is identified from the data as a prominent reflection that is sub-parallel to the seafloor but crossing deeper stratigraphy and has a reflection polarity opposite to the seafloor. In some areas, up-dip truncations of high-amplitude reflections align in a BSR-like pattern. The up-dip extent of the BSR coincides with the 720 m isobath (**Figure 1C**) which is the shallow-water limit of the methane hydrate stability zone for the current bottom-water conditions (9°C, 22 PSU). The BSR is distributed across the Danube deep-sea fan in a non-uniform pattern. Three main patches of BSR occurrences are seen closely tied to the channel-levee deposits.

Controls on Gas Seepage Distribution

Gas venting is not randomly distributed in water depths <720 m across the study region (**Figure 1C**). On first inspection, the gas vent locations are closely aligned to the ridges of the sub-marine canyons and channels. They also occur at head-scarps of slope-failures. Additionally, the densest occurrence of venting is seen on the outer continental shelf in the western-most region upslope of the S1 channel/canyon system and the eastern-most region linked to the N1 channel system. With few exceptions, there are no gas vents seen deeper than the 720 m isobath limit (**Figure 1C**). A histogram of the depth-distribution of all mapped vents is given in **Figure 1D**. The highest abundance of mapped flares is in 110–135 m of water depth on the outer continental shelf. Two prominent exceptions (**Figure 2**) are sites of active gas discharge with known near-seafloor gas hydrate occurrences recovered in gravity cores. The first example is near the MeBo200 drilling Site MeBo-16 and gas hydrate was seen in the cored sediment (**Figure 2A**, Bohrmann, 2018), which was also previously reported from the GHASS expedition (Ker and Riboulot, 2015). A second example is linked to a site of mud volcanoes observed in ~760 m water depth, just SE of the feather-edge of gas hydrate stability (**Figure 2B**). Here, recovery of gas hydrates in sediment cores was reported by Akhmetzhanov and Falkenstein (2017) as part of reconnaissance surveys conducted in the region by industry.

In the following, we present several examples of gas venting patterns typical for the region offshore Bulgaria and Romania (see **Figure 1** for an overview of these areas). We include venting-occurrences at canyons (*Canyons–Sediment Erosion, Head-Scarps and Mass Flows*), faults (*Gas Venting and Fault Occurrences*), sediment waves and elongated depressions (*Sediment Wave Patterns and Elongated Depressions*), mass-transport deposits (MTDs, *Mass-Transport Deposits*), isolated occurrences or chains of pockmarks (*Pockmarks*), and at the western-most shelf region (*Shelf Region With Highest Gas Flare Occurrence*). Occurrences of chimney-like structures are described in *Seismic Chimney Structures*. The nature of the acoustic reflectivity from the top of free gas occurrence is described in *Step-Wise Top of Gas Reflection*. In all these settings, multibeam seafloor mapping is combined with water-column acoustic imaging of the gas flares, backscatter imagery, and sub-bottom profiler imaging.

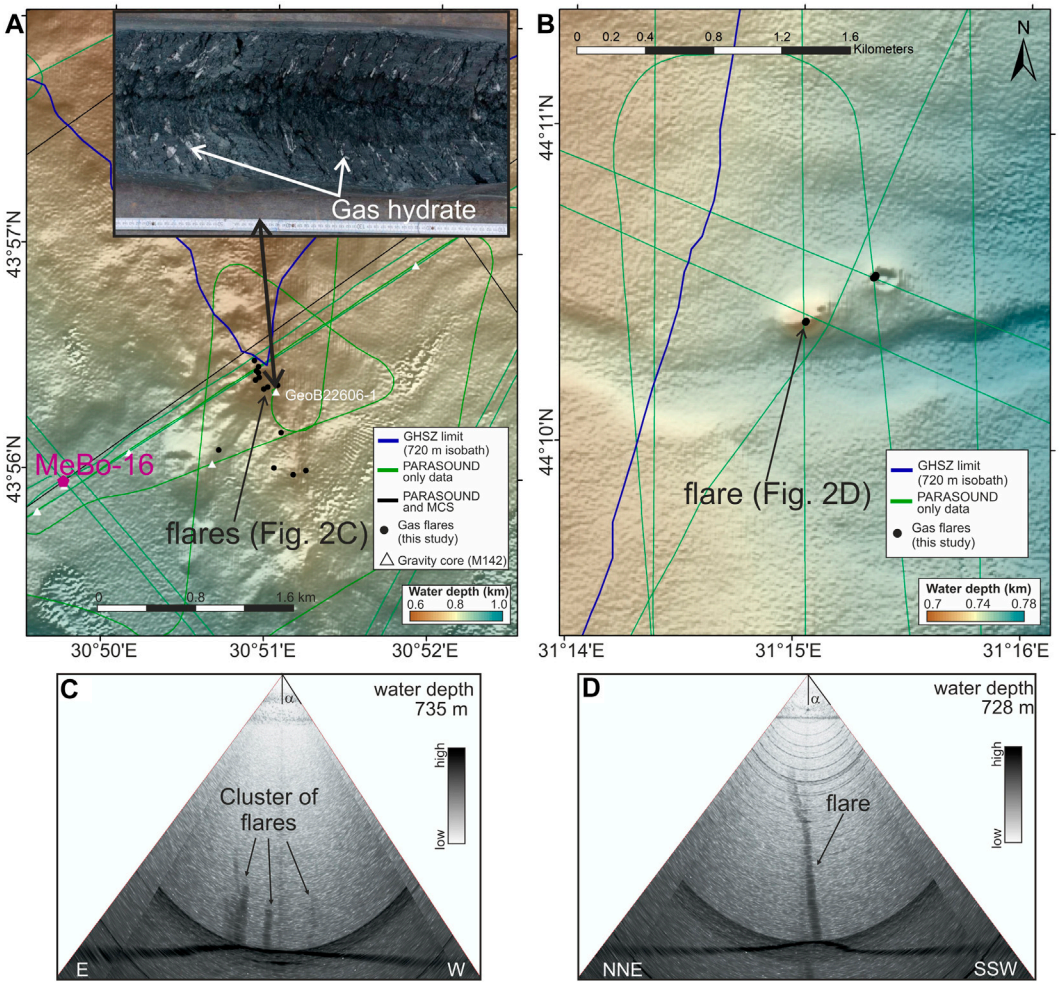

FIGURE 2 | Example of two sites with gas hydrate recovery investigated during M142: **(A)** Site close to drill site MeBo-16 with gas hydrate recovered in gravity core (station GeoB22606–1, inset image) and **(B)** site of two mud volcanoes, 500–800 m west of the hydrate feather edge (720 m isobath). **(C,D)** are examples of gas flares seen in the EM710 water column data. Beam-opening angle α is 60°.

Canyons–Sediment Erosion, Head-Scarps and Mass Flows

The northern-most region of our study area is dominated by the large N1 channel and canyon system (**Figure 3**). Although only partially imaged, the canyon starts as a NS-oriented incision, which turns eastwards at a latitude of approximately 44° 35′N. Due to its location, the canyon was defined to belong to the Dnepr river-fan system (Winguth et al., 2000) rather than the Danube deep-sea fan which is located further to the west. The canyon is ~2,500 m wide at its flat base, but spans a total width of nearly 10 km between the eastern and western canyon head-scarps (**Figure 3A**). The inner base of the canyon shows an overall smooth seafloor that deepens eastwards. The western and eastern flanks are dominated by numerous head-scarps and tributary canyons feeding into the main drainage system (**Figure 3B**). Backscatter intensity increases from the head-scarps into the main channel floor and subsequently decreases down-slope along the channel floor. Gas venting across this canyon system is almost exclusively associated with scarps, with the gas vent sites outlining the canyon walls.

The canyon floor is covered with a homogenous sediment drape of ~3–5 m thickness above an acoustically turbid unit, interpreted as a small MTD (**Figure 4A**) that also shows high backscatter intensity on the EM122 backscatter data. Furthermore, the entire region around the canyon is characterized by a thick package of relatively uniform sedimentary layers. The sub-bottom profiler data image up to 100 m of sediment (~120 ms two-way time) of seafloor-parallel layers that at the canyon walls are heavily faulted in response to slope instability and mass-failure (**Figure 4B**). Gas venting occurs almost exclusively where the faults crop out at the seafloor.

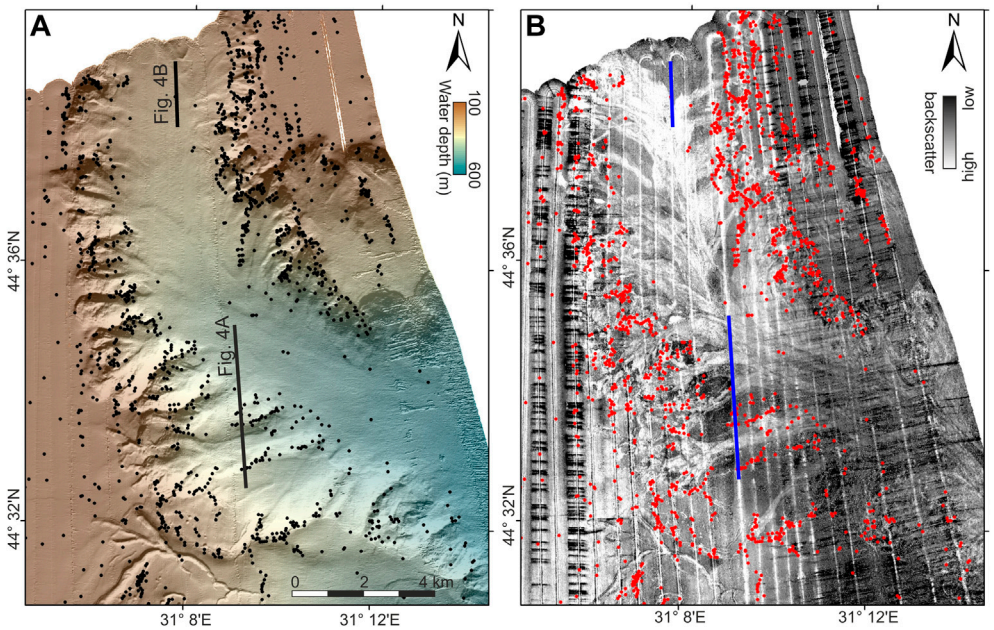

FIGURE 3 | Northern-most N1 canyon system, associated with the Dnepr river system. **(A)** Multibeam data with overlay of gas vent sites (black dots). **(B)** Seafloor backscatter with overlay of gas vents (red dots) highlighting individual chutes of mass-transport material removed from the canyon walls. These deposits overlap and merge in the talweg of the canyon. Gas seeps are tightly linked to the head-scarps and remaining ridges in the canyon walls. Two examples of sub-bottom profiler data are given in **Figure 4**. Poor weather conditions created the black-and-white striping pattern on some of the lines.

Gas Venting and Fault Occurrences

South of the N1 northern canyon system, a smaller, E-W oriented canyon system (N2, Winguth et al., 2000) is observed between 44° 30.4′N and 44° 22.5′N (**Figure 5**). Here, the canyon is only ~1 km wide at its base and is covered with a homogenous drape of 3–5 m thick sediments (**Figure 5C**). The most significant feature across this canyon system is the occurrence of E-W oriented normal faults with a seafloor offset of up to 20 m (**Figure 6A**). Individual fault traces can be followed for nearly 20 km in E-W extent. The region of normal faulting stretches N-S for almost 16 km. At the western edge of the data coverage, the talweg of this canyon has been cut by one of the normal faults after the canyon has ceased being active (**Figure 5C**). Gas venting is abundant along the canyon walls and is strikingly linked to the fault outcrops (**Figures 5E,F**, **Figures 6D,F**). High backscatter zones indicate several smaller mass-failures at the head-scarps of the outer canyon walls (**Figure 6B**). As seen at the N1 canyon, the high backscatter intensity stems from buried mass-transport deposits that are covered by a homogenous sediment drape of 3–5 m thickness (**Figure 6B**). On top of the northern plateau of this N2 canyon, a series of pockmarks and smaller fault-scarps are seen, many of which show gas venting. Wider depressions can be identified from the sub-bottom profiler data as erosional gullies (**Figure 6C**).

Prominent normal faults in this region frequently split laterally into smaller sub-faults (**Figure 7A**) often only few 10 s of meters apart. They appear in multibeam bathymetry data as lineaments with a small depression. The backscatter return is higher than background along the entire fault traces. Gas vents are seen along these fault traces that are as narrow as 15 m (**Figure 7B**) but cut the entire sediment package imaged by the sub-bottom profiler (**Figure 7C**). At some locations along these faults, gas venting forms semi-circular pockmarks, mostly on elevated topographic features (**Figure 7A**).

Sediment Wave Patterns and Elongated Depressions

The multibeam data reveal a smooth but regularly undulating topography in many regions of the study area (**Figure 8**), that may be described as "hummocky terrain" and was previously interpreted as sediment wave crests (Riboulot et al., 2017). Elongated depressions that develop between crests are narrow with steep edges and the depressions are linked to sub-seafloor faulting penetrating at least 100 m (**Figure 9**). These features are associated with gas discharge and occur in a predominant direction (10°–25° clockwise from North) following the overall orientation of crests (**Figure 8**). We observe a progressive evolution in these features. In deep water depth (~500 m) the depressions start as thin sinusoidal lineaments on the seafloor (**Figure 8A**) linked to individual small-offset faults (**Figure 9A**). The fault offset itself is often below the resolution of the acoustic data but reflectivity is characteristically reduced (or blurred) at the fault location itself in a cone-shaped pattern. In shallower water (300–400 m) the depressions widen and deepen with each depression including several of these small-offset faults. Gas accumulation in the subsurface is generally identified by increased seismic or acoustic reflection amplitudes. Focusing of the gas is controlled by the topography, where gas accumulates underneath the crest (**Figures 9C,D**), but upward

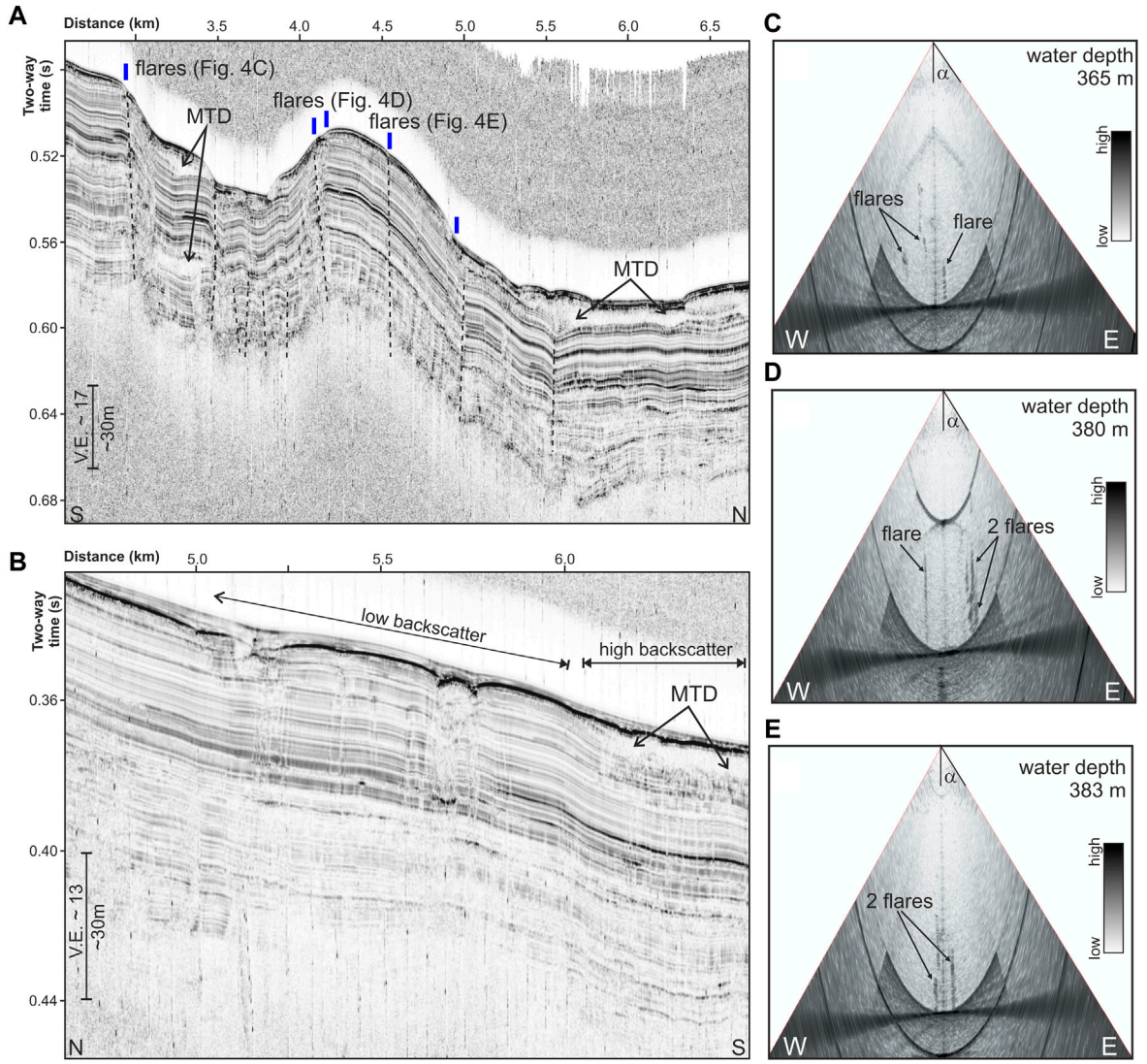

FIGURE 4 | Acoustic sub-bottom profiler data of features of the northern-most N1 canyon. **(A)** Section across the canyon wall showing in the southern half a faulted sedimentary package with gas seeps (location indicated by blue lines). Faults are indicated by dashed black lines. The northern half of the section is within the talweg of the canyon with a shallow mass-transport deposit (MTD) near the seafloor. Although the MTD is covered by 3–5 m thick layered (recent) sediment, seafloor backscatter is high only where the MTD occurs. This is seen especially in the section shown in **(B)**. **(C–E)** Examples of gas flares from the EM710 water column data along section shown in **(A)**. Beam-opening angle α is 60°.

migration is facilitated by faults at the knick-point between neighboring crests. Seafloor backscatter is high along the small fault patterns and in the depressions, not only where gas is seen escaping at the seafloor (**Figure 8B**). Gas venting along the elongated depression continues across head-scarps into the region of mass wasting.

Low-frequency airgun seismic data with coincident high-resolution sub-bottom profiler data are available for only a sub-region of the zones with elongated depressions and crests. The seismic data show a deeper set of sediment waves now covered in parts by an MTD that levels out the paleo (initial) sediment wave topography (**Figure 10**). The old sediment wave structure and MTDs are both subsequently draped by a relatively homogenous sediment package of ~30 m thickness. Gas has migrated upward and accumulates in the crests creating local bright spots and velocity-reduction related sags underneath. In some instances, this gas has been able to migrate through the MTD and accumulates at the top of the MTD layer. Gas seeps out at the seafloor only where gas has accumulated at greater depth and migration to the seafloor is facilitated by a set of small-offset faults that are imposed by the rough topography of the MTD into the veneer of layered sediments.

Mass-Transport Deposits

Large-scale MTDs occur at several locations (**Figure 11**). The MTDs are characterized by a chaotic to transparent seismic

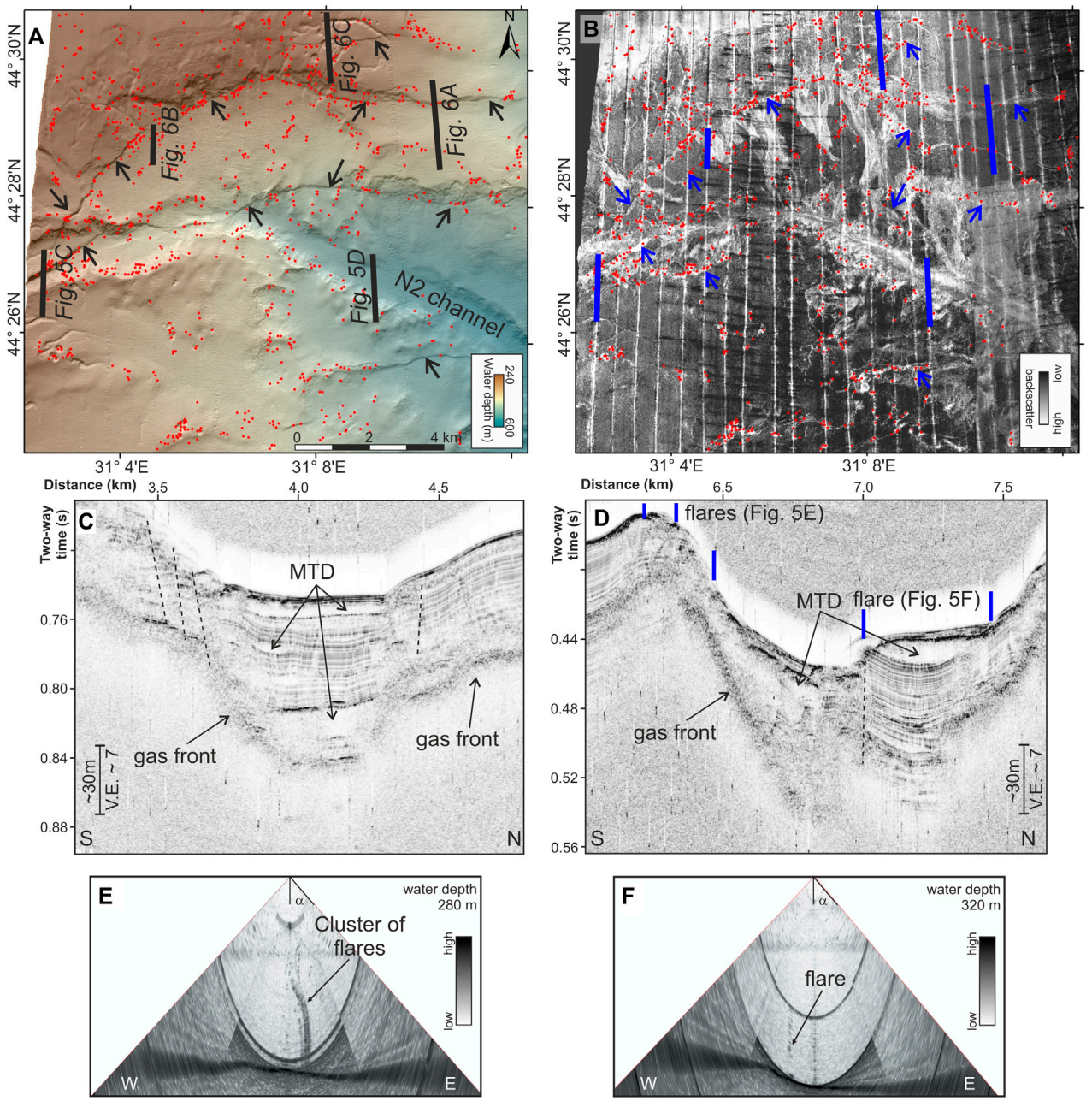

FIGURE 5 | Examples from the N2 channel systems: **(A)** multibeam bathymetry and **(B)** seafloor backscatter. Location of gas seeps are shown as red dots. Dominant E-W trending normal faults are indicated by arrows. Buried, small-scale mass-transport deposits show high seafloor backscatter. Sub-bottom profiler data (black/blue thick lines in **(A,B)**) across the talweg of the EW-canyon system showing **(C)** 3–5 m thick drape on top of the youngest mass-transport deposit from the time when the canyon was last active, **(D)** fault cutting the talweg. Faults are indicated by dashed black lines. **(E,F)** are examples of gas flares from the EM710 water column data along section shown in **(D)**. Beam-opening angle α is 60°.

reflection pattern and the absence of any clear layering. The lower boundary can be either conformable to the underlying strata, or irregular and incised into them. The upper boundary is often irregular and lacks a coherent reflection. MTDs show a positive impedance contrast at the top, but a negative impedance contrast at the base (Riedel et al., 2020), which indicates that they are of denser material than the surrounding sediment layers. One could infer that the MTDs are therefore less permeable than hemipelagic sediments (as e.g. described by Hillman et al., 2018a). These MTDs almost all originate at erosional head-scarps at the slope edge in water depths ~120–200 m. The MTDs cover deeper sediment-wave topography but their own rough surface still impacts gas migration. The rough topography from small-scale heterogeneities results in a fault-like pattern in

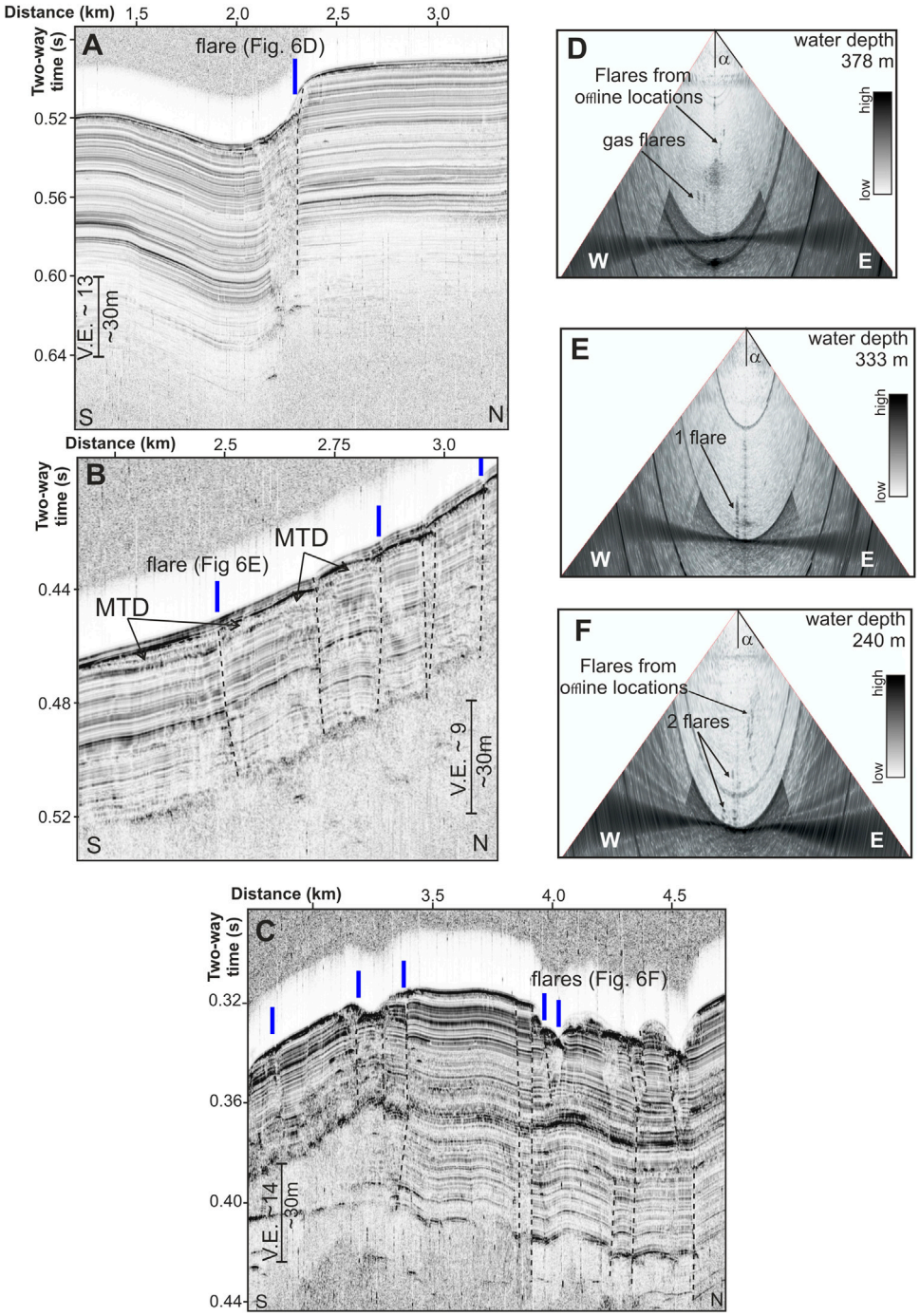

FIGURE 6 | Sub-bottom profiler showing **(A)** ~20 m vertical offset at E-W trending normal fault, **(B)** mass-transport deposit (MTD) sluffed off the canyon wall creating high seafloor backscatter although it is covered by 3–5 m thick sediment drape, and **(C)** fault-related erosional gullies (elongated depressions) on top of the N2 canyon plateau. Location of gas venting sites are shown as vertical blue lines. Selected faults are indicated by dashed black lines. **(D–F)** Examples of gas flares from the EM710 water column data. Beam-opening angle α is 60°.

the sediment drape which can be locally exploited for gas migration (**Figure 10B**). Where the MTDs are only covered by recent post-glacial Holocene sediments and are buried by 3–5 m of sediment at most, we observe no gas venting at all (marked as Regions 1 – 3 in **Figure 11**).

Pockmarks

More than 340 individual pockmarks, typically 40–50 m wide, occur unevenly distributed in the study area. Pockmarks are only seen east of the S2 channel (30° 46′E) and are most abundant around the upper canyon-segments of the S4, N3, and

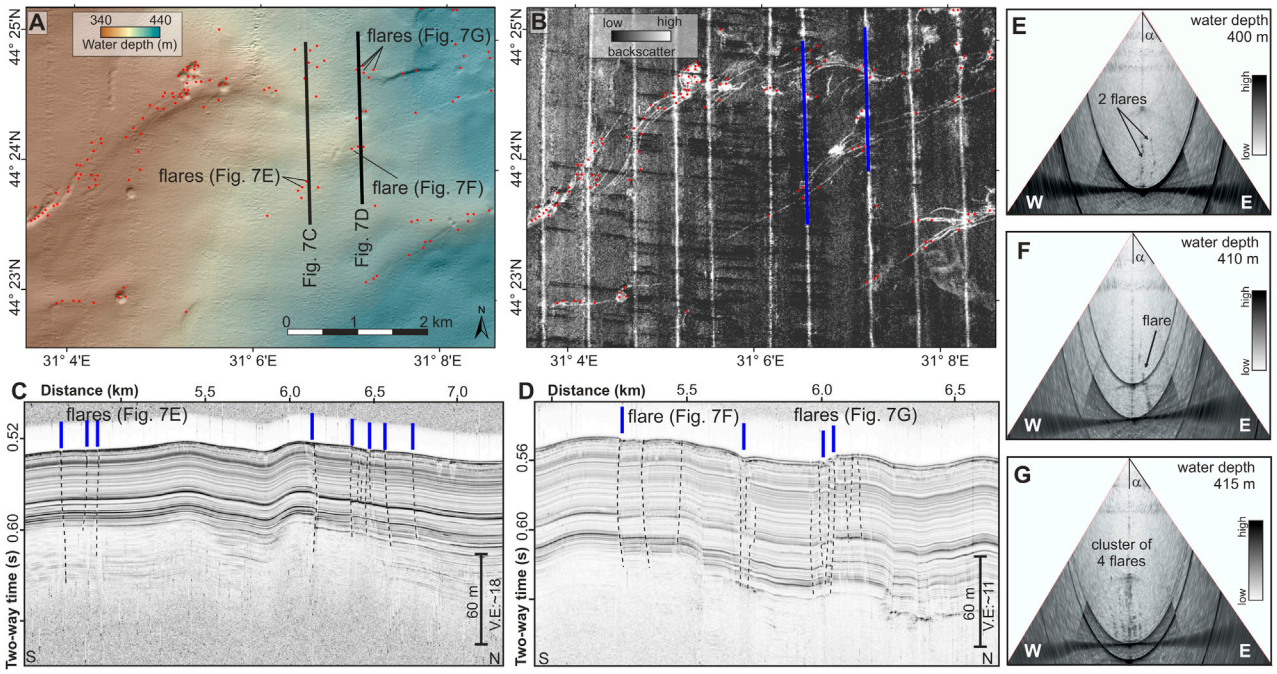

FIGURE 7 | Normal faults in the region of the N2-channel system show branching into several smaller sub-faults as seen in **(A)** the multibeam bathymetry and **(B)** as high seafloor backscatter return. **(C)** Sub bottom profiler data (black/blue line in **(A,B)**) show small-offset faults (black dashed lines) cutting the entire sediment sequence. Gas seepage shown as red dots in **(A,B)** correlate to the fault location as shown by blue lines in **(C,D)**. **(E–G)** Examples of gas flares from the EM710 water column data. Beam-opening angle α is 60°.

N4 channels in water depth <480 m. Most of these pockmarks are semi-circular depressions and several of these features merged into larger elongated depressions. The pockmarks often cluster and occur in chains along structural highs or morphological features such as canyon walls (**Figure 12A**). Within this type of pockmark occurrence, the largest pockmarks are up to 350 m in diameter (measuring the width of the depressions). Gas venting is constrained to the outer rims of the pockmark, but given the uncertainty in the location of an individual vent (25–50 m), no clear correlation in vent outlet to pockmark morphology can be defined. Not all pockmarks have shown active gas discharge at the time of data acquisition but our backscatter data show that these structures usually are associated with high backscatter indicative of gas-rich sediments (**Figure 12B**). The typical structure of these pockmarks shows doming at the rim and a central depression (10–20 m deep) from where material has been eroded (**Figure 12C**). The pockmark and surrounding topographic ridges also show normal faulting, all promoting upward gas migration.

Some pockmarks occur isolated and are not associated to underlying topographic highs (**Figure 13A**). These are also the largest pockmarks seen and their diameter can be up to 1000 m. A characteristic feature of these pockmarks is the occurrence of ring-faults that also show high backscatter (**Figure 13B**). Gas venting is strictly associated to the ring faults although gas is seen trapped in sedimentary layers everywhere underneath the pockmark. Although free gas occurs within these sediment layers, concentration may not be high as acoustic wipe-outs masking deeper sediment stratigraphy are not created. The inner depression of these pockmarks is only ~5 m deeper than the surrounding topography and no erosion has removed any of the sediments (**Figure 13C**). The isolated pockmarks are, however, linked to larger fault-segments (**Figures 3D, 13B**) that often can be traced over several kilometers.

Shelf Region With Highest Gas Flare Occurrence

Dense clusters of gas vents on the shelf in water depths <150 m were observed in the western-most portion of the study region (**Figure 14**). Here, gas flares are associated with a characteristic speckled backscatter signal of the seafloor. Gas detection from the water column multibeam data is often limited to a small region long the track line but the backscatter data reveal a wide-spread occurrence of the speckled high-amplitude seafloor backscatter intensity. Sub-bottom profiler imaging reveals a veneer of layered sediment draping an erosional unconformity (**Figure 14C**) of a former anticlinal structure. Free gas is seen in the sub-surface sediments from numerous small pockets of high amplitude reflections that sometimes merge into continuous gas-fronts acoustically masking underlying structures. The clusters of gas venting and high backscatter speckles at the seafloor are associated with topographic variations on that unconformity, in particular where dipping strata crop out at the unconformity.

Seismic Chimney Structures

Some of the gas accumulations are forming structures called seismic chimneys (e.g., described previously for our research region by Hillman et al., 2018a), with a high-reflectivity top

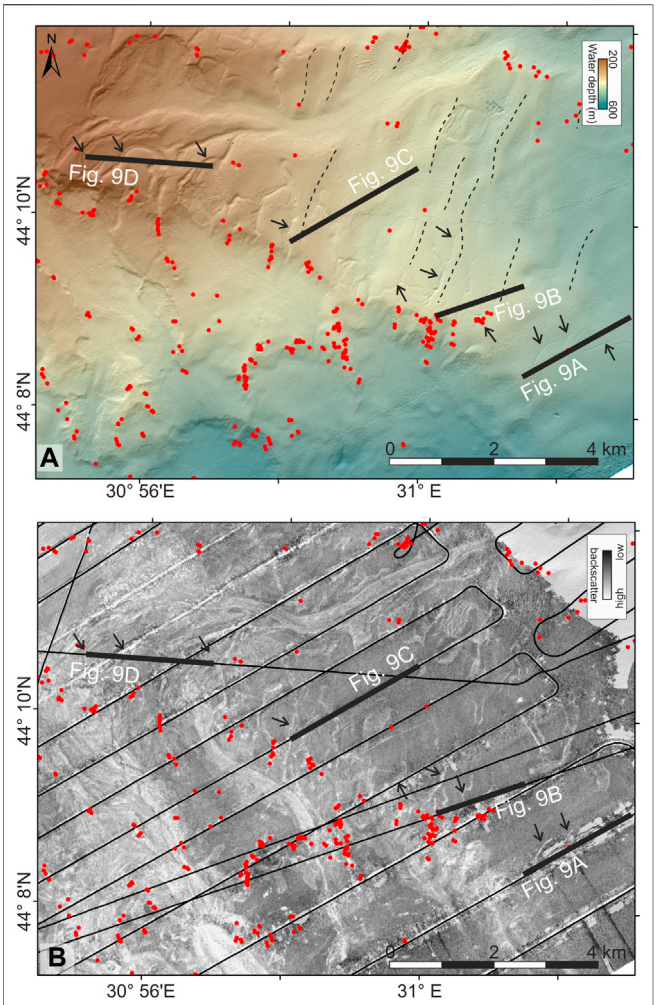

FIGURE 8 | Example of the seafloor morphology in a region with old sediment-wave crests (now draped) creating sub-seafloor pathways for upward migrating gas (red dots are seep sites). **(A)** multibeam bathymetry and **(B)** seafloor backscatter. Dotted lines in **(A)** are some examples of the old wave-crest outline. Solid black lines are sections of sub-bottom profiler data shown in **Figure 10**.

and semi-vertical acoustic wipe-out underneath (**Figure 10**). More than 50 of these chimneys have been detected in the seismic and sub-bottom profiler data to date. They occur along the slope only in the region up to the S4 channel system (**Figure 11**). No such vertical chimneys are seen further to the east linked to channels N1–N4. Examples of chimney structures seen in the region are included in **Figure 10**.

Step-wize Top of Gas Reflection

In many cases the occurrence of free gas is creating a diffuse front in the acoustic sub-bottom profiler data (see e.g., **Figures 6A,B** or 9 days). Acoustic imaging beneath such a gas front may be limited (reduced reflectivity) or completely masked. Free gas within the sediment can also create isolated bright spots or enhance the reflectivity of individual reflectors for some distance without diminishing acoustic penetration (e.g., **Figures 3D**, **13C**). A different observation of free gas occurrence in layered sediments can be made across topographic changes. Here, the top of free gas is mimicking seafloor topography, but still appears to be discretely bound to individual sedimentary layers creating a step-wize pattern (**Figure 15**). This bottom-simulating nature is best observed across larger topographic changes and when the acoustic data is acquired up/down slope. The free gas enhances the acoustic reflectivity of a given sediment layer at a critical depth (**Figure 15**). The layer remains acoustically bright for some distance before returning to a normal reflectivity as seen elsewhere along the profile. Several bright reflections can be stacked on top of each other (**Figure 15B**).

DISCUSSION

Combining data from several research expeditions, we identified >10,100 individual vent sites within the Romanian and Bulgarian margin linked to the Danube deep-sea fan and eastern extension to the Dnepr fan (up to the Ukrainian exclusive economic zone). Gravity coring and gas sampling indicate that the gas may originate from *in situ* microbial production or from deeper (upward migrating) biogenic sources. Deep drilling in 2017 (Bohrmann, 2018) also showed little amounts of thermogenic gases and methane was the dominant gas sampled in sediments of the upper ~150 mbsf (Pape et al., 2020). Thus, all references made to gas hydrate stability are for a methane-only structure I gas hydrate system.

Separation of Bottom-Simulating Reflector and Gas Venting

The limitation of gas vents to water depths above the depth-limit of the GHSZ at ~720 m water depth (**Figure 1**) was previously discussed as primary controlling factor in the occurrence of gas vents (e.g., Riboulot et al., 2017; Hillman et al., 2018a). Two prominent exceptions of gas vents in water depths >720 m were identified. These two locations are associated with shallow sub-surface gas hydrate occurrences (**Figure 2**). Gas venting may here be linked to deeper-rooted gas-migration pathways that can circumvent the GHSZ-limit by advection of warm-fluid, thus locally creating a warped GHSZ as e.g., described at vent systems in the Gulf of Mexico (Macelloni et al., 2015) or Lake Baikal (De Batist et al., 2002). Alternatively, larger fluid-pressure may lead to sediment fracturing and release of gas to the seafloor (e.g., Daigle et al., 2011; PaullCaress et al., 2015).

The 720 m isobath is also strongly correlated to the onset of the BSR in seismic data. Several previous BSR-distributions were proposed (Popescu et al., 2006; Baristeas, 2006; Haeckel et al., 2015; Zander et al., 2016) as summarized in **Figure 1C**. All these previous analyses are in general agreement with each other but differ slightly from our new interpretation. All previous maps seemingly interpolated occurrences across regions of clear BSR absences, especially between the eastern levee of the S1-channel and western levee of the Viteaz channel. The absence of a BSR reflection or amplitude truncations at the BGHSZ is an important indication for the general absence of free gas in the system, either due to a lack of *in situ* microbial production or advection of gas

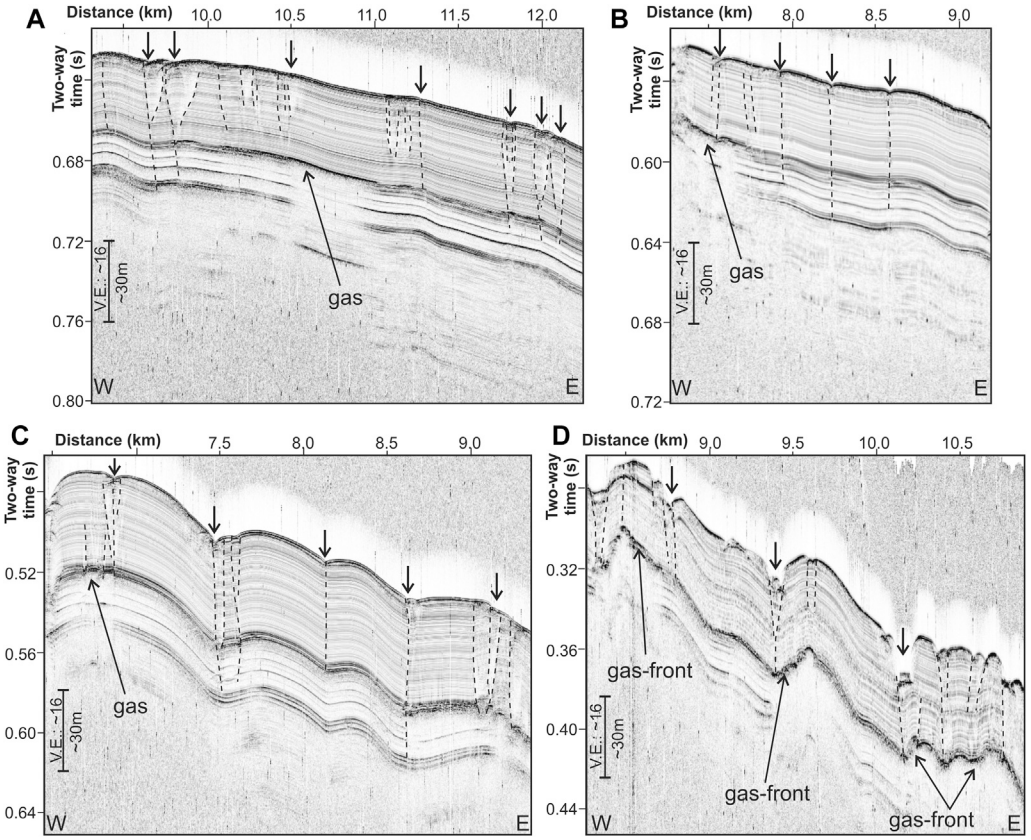

FIGURE 9 | Examples of sub-bottom profiler data showing evolution of elongated depressions (marked with arrows) and faults (black dashed lines). **(A)** In deeper water the fault-offsets between adjacent sediment layers are below resolution limit of acoustic data and acoustic reflectivity is only blurred or generally decreased, **(B)** upward migrating gas creates slightly larger seafloor depressions, **(C)** several faults merge and, **(D)** create wider elongated depressions.

from below. The BSR correlates with the 720 m isobath and no discrepancies exist between a theoretical GHSZ and seismic observations. Previously, apparent discrepancies were discussed by Riboulot et al. (2017) and explained by a possible evolution of the degassing zone between individual expeditions (spanning >10 years) or differences in the data analyses (acoustic gas flare detection vs. seismic data acquisition). Yet, the discrepancies most likely resulted from optimistic interpolation of sparse data.

The BSR is generally interpreted to be the seismic expression of the BGHSZ and mark the onset of free gas below hydrate-bearing sediments (e.g., Spence et al., 2010). Thus, the nearly complete regional separation of BSR and gas vent occurrences indicates that gas hydrate may form a seal for upward migration of gas. In regions with gas hydrate occurrences, gas migration may be deflected and occur more horizontally along the BGHSZ up to the upper depth limit of gas hydrate stability in ~720 m water depth. From this location onwards into shallower water, gas can then also migrate upwards along structural pathways and form vents at the seafloor. Alternatively, the separation of the BSRs and vent sites may indicate that any free gas that migrates upwards from greater depth is not deflected horizontally at a hydrate-permeability boundary but is instead incorporated into the sediment pore space either by forming additional gas hydrate or being dissolved in the pore water if the system is undersaturated relative to methane.

Structural and Sedimentological Controls on Gas Vent Distribution

Additional controls on venting by canyon erosion and slope failure head-scarps exposing gas-bearing sediment layers or providing structural focusing for gas migration were previously discussed by Riboulot et al. (2017) for the Danube deep-sea fan region or by Naudts et al. (2006) for the Dnepr fan system. However, several intriguing observations in our new data warrant some additional explanations.

Buried Sediment Waves

The depositional history of the study region has a much larger impact on the occurrence of gas venting than previously thought. Sediment waves associated with channel-levee systems are seen along all major channels where not removed by mass wasting events. We can observe the sediment wave pattern in MCS data up to a depth of ~250 mbsf (**Figure 10A**) although MCS data coverage is not uniform across all regions

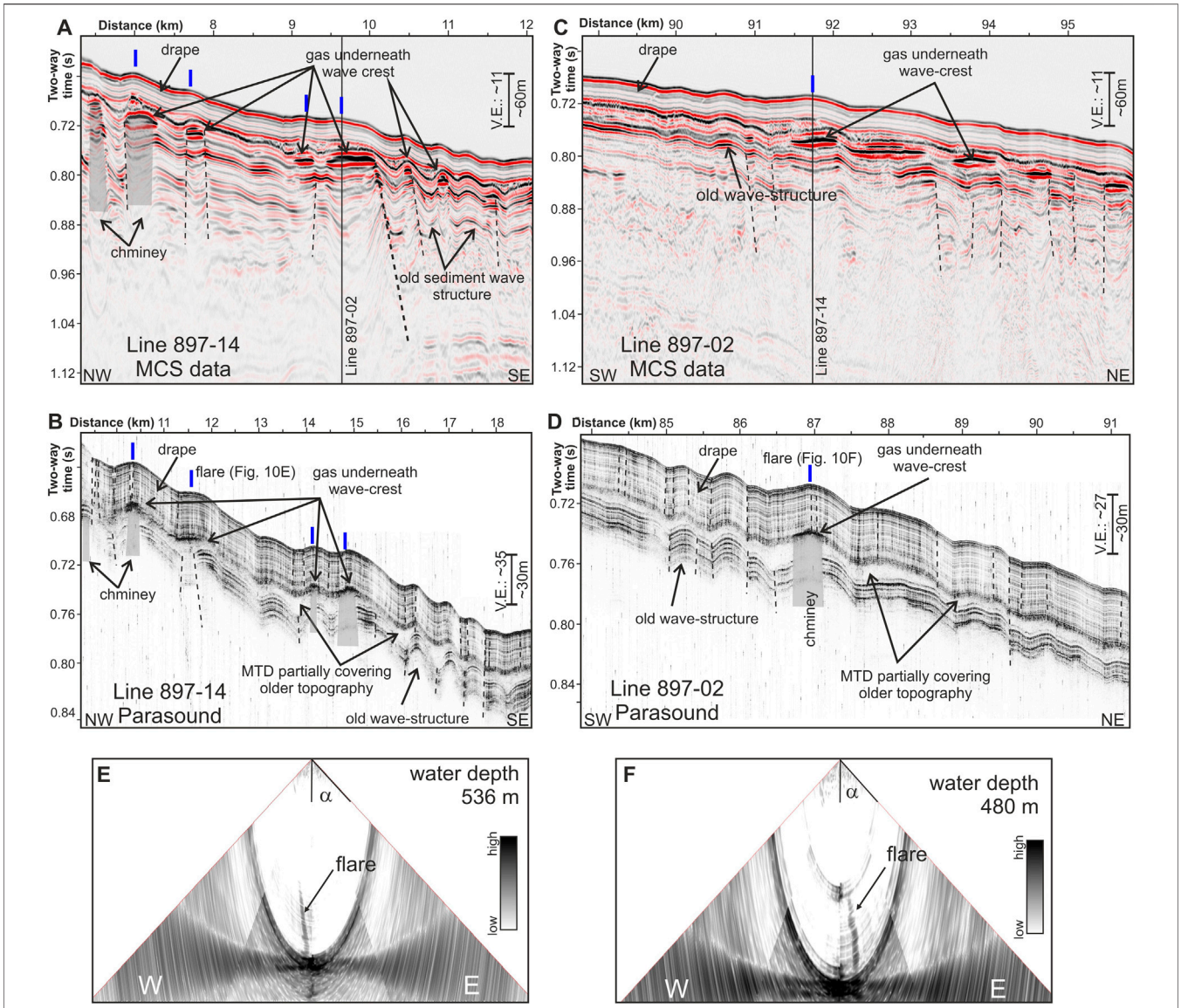

FIGURE 10 | Examples of airgun multichannel seismic data showing deeper (older) sediment-waves structure, that are draped by the veneer of sediment imaged in sub-bottom profiler data. **(A,B)** are coincident along line 897–14, **(C,D)** are coincident on line 897–02. Gas accumulates underneath the wave crests and in part penetrates the mass-transport deposit (MTD). Gas venting (vertical blue lines) occurs at the seafloor where upward gas migration from the lower accumulation is facilitated by small-offset discontinuities (faults) in the overlying veneer (drape) of layered sediments. These faults (black dashed lines) are created from the rough topography of the MTD. **(E,F)** Examples of gas flares from the EM122 water column data (expedition MSM34). Beam-opening angle α is 60°.

mapped and some gaps in observations exist. The observations shown in **Figure 10** act as type-example for the other occurrences and linkages of sediment waves and patterns of gas migration and gas venting at the seafloor. The paleo sediment wave topography defines a structural control (trap) for gas accumulations at depths of typically 60–80 mbsf (**Figure 10A**). The old topography has only partially been leveled out by MTDs and was subsequently draped by a veneer of layered sediments leaving a remaining morphology on the current seafloor. That residual wave-like pattern influences the development of faulting (ultimately, they merge and develop into larger elongated depressions) and thus the location of gas discharge at the seafloor.

Mass Transport Deposits

Large scale MTDs occur in the study area (**Figure 12**) and were proposed to act as an impermeable barrier (Hillman et al., 2018a). However, the rough topography of an MTD and associated small-scale heterogeneities create a fault-like pattern in the sediment drape which can be locally exploited for gas migration (**Figures 1D**, **11B**). There are incidences, where gas has clearly pierced through the entire MTD (see

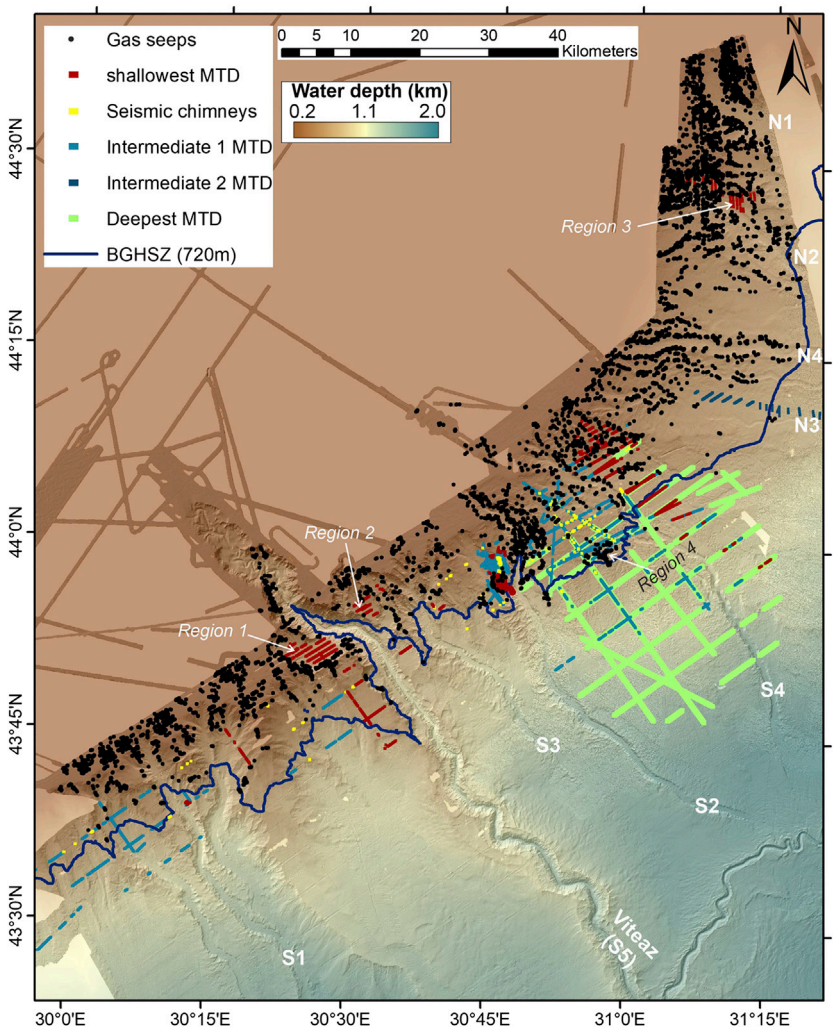

FIGURE 11 | Overview of mass-transport deposits (MTDs) within the uppermost ~100 m below seafloor correlating to occurrences of gas vent sites. Three regions devoid of vents are linked to recent mass-transport deposits and seafloor failure (Regions 1–3). In the central region between the S2 and S4 channel, up to three MTDs are stacked. Here, the highest density of seismic chimneys (vertical columns of gas accumulation, Hillman et al., 2018a) are observed (Region 4).

e.g., **Figure 13**; Region 4 marked in **Figure 12**). Since the piercements of MTDs by gas all occur within much older (deeply buried) MTDs, the gas may have had more time to accumulate and thus create sufficient pressure to overcome an impermeable barrier imposed by the MTD. This may explain the notable cluster of seismic chimney structures in a region of wide-spread MTD occurrence (Region 4 in **Figure 12**).

Where the MTDs are only covered by recent (post-glacial) Holocene sediments and are buried by 3–5 m of sediment at most (**Figures 4**, **6**), we observe no gas venting at all (e.g., Region 1–3 marked in **Figure 12**). This may be the result of the MTD acting as a permeability barrier. Another reason for the absence of gas vents at locations of the youngest MTDs may be that gas-rich sediments were simply removed. Thus, gas may have escaped during the failure and there was not enough time since the failure and new deposition to accumulate new gas that could then overcome the permeability barrier of the MTD.

Faulting

Around the N1 and N2 channel systems we identified abundant mostly E-W oriented normal faults, all strongly associated with gas seepage. This region lies within the tectonic realm of the Histria Depression (e.g., Dinu et al., 2005). The latest sequence of sediment deposited in the region of these two channels are of Miocene age (referred to as Pontian deposits by Dinu et al., 2005) and are described as being highly affected by normal faults that are either controlled by extension or differential compaction within the thick sediment wedge. Thus, the normal faulting we observe may be linked to those large-scale tectonic fault patterns in the Western Black Sea.

The faulting imaged around the N1 and N2 channels is characteristically associated with high backscatter intensity on the seafloor along the often only 15 m wide individual fault traces (e.g., **Figures 5**, **7B**). Gas vents are seen tied to the fault traces at some locations. We therefore interpret the high

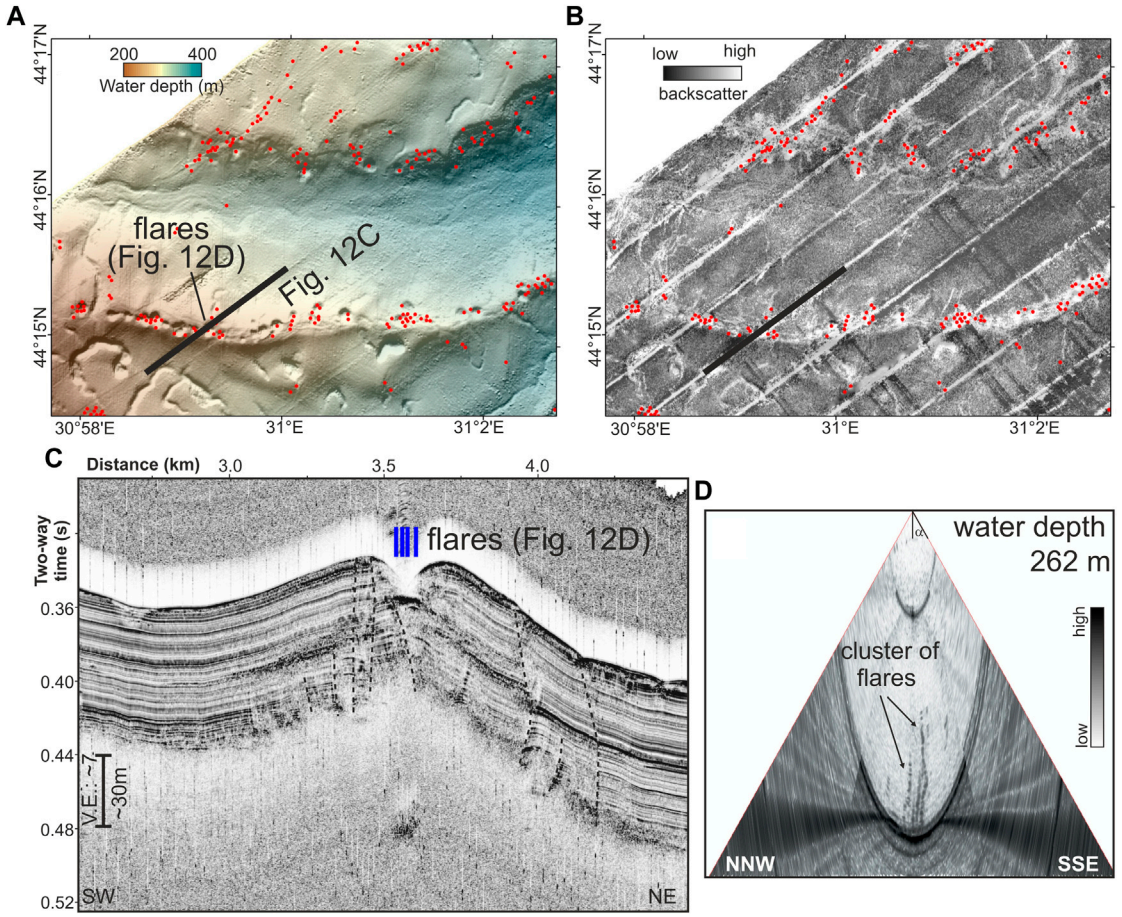

FIGURE 12 | Examples of pockmark-chains along ridges and canyon wall at the upper-slope portion of the N4 channel: **(A)** multibeam bathymetry and **(B)** seafloor backscatter. Structural focusing of gas migration toward the highest elevation creates gas outlets on top of the ridges. Additional gas venting comes from faulting associated with seafloor instabilities and slumping at the canyon walls. The sub-bottom profiler data **(C)** show small offset faults (black dashed lines) around a pockmark and that sediments are removed from the central portion of the (circular) depression. **(D)** Inside the pockmark several gas vents are seen in the EM710 water column data. Beam-opening angle α is 60°.

backscatter signal to reflect generally abundant gas within the sediment. Gas venting may be episodic in time and therefore venting is not always seen when faults were crossed. This close association of faults with high seafloor backscatter intensity and venting is highlighted at the ring-faults around pockmarks (**Figure 13**).

A similar association of gas in sediments and high backscatter intensity along small faults is seen at the region of elongated depressions (**Figure 8**). However, here, the faults are not primarily a result of a large-scale tectonic stress regime, but linked to patterns within a sediment drape deposited above paleo-sediment wave crests.

The Shelf Region

Along the shelf portion of the study area imaged, the highest density of gas flares is seen (depth-bin from 110–135 m, **Figure 1D**) but here, seafloor is mostly flat with no obvious erosional cuts from channels or canyons or faulting (**Figure 14**). However, the sub-bottom profiler imaging revealed that the flat seafloor with apparently no structural features visible is a result of a homogenous drape of post-glacial sediment above an erosional unconformity. The thickness of the drape and layering within it varies along the region but it is not controlling the gas occurrences. The gas venting activity across the shelf is best visualized by the speckled nature of the seafloor in the backscatter data. Although we could not image gas flares in the water column across all of the individual patches (in part due to the beam-angle limits of the EM systems or weather state), whenever we saw a gas flare in the water column, it corresponds to a patch of high backscatter with a 1:1 correlation. Therefore, we interpreted all these features to be gas vent outlets. The sub-region shown in **Figure 14D** alone with an area of ~3.5 km^2 hosts a total of 250 gas flares from the water column data analysis and about half of the seafloor is marked by high-amplitude speckles in the backscatter image. The area most affected by gas venting matches regions where the sub-bottom profiler data show dipping strata

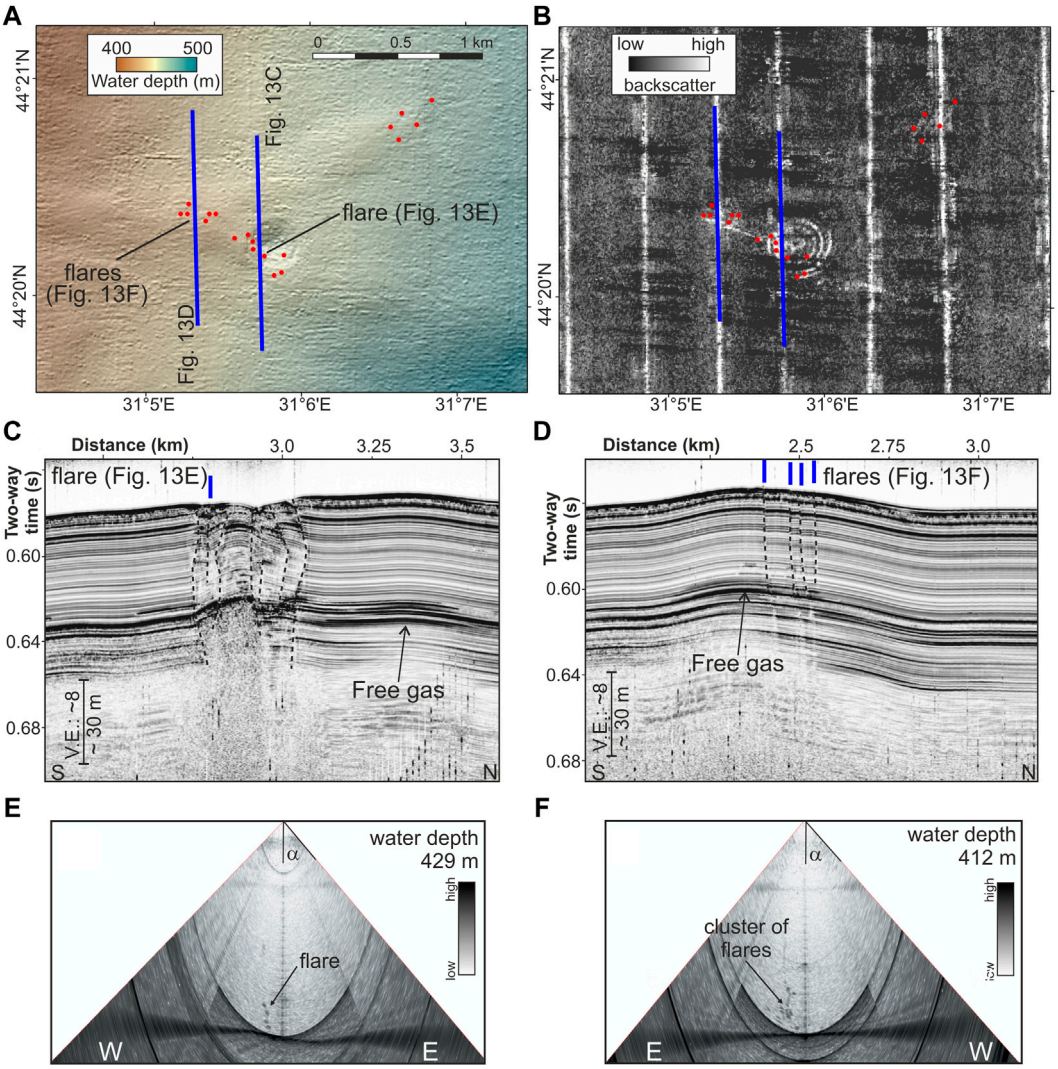

FIGURE 13 | Example of ring-faults around isolated pockmarks. **(A)** Multibeam bathymetry, **(B)** seafloor backscatter, with gas seepage shown as red dots. Blue lines indicate location of sub-bottom data shown in **(C,D)**. A nearly E-W trending fault cuts the pockmark and is identified by high backscatter signal along which gas escape is seen NW of the pockmark, tightly linked to small-offset fault-branches. Black dashed lines on sub-bottom profiler data show faults. **(E,F)** Examples of gas flares from the EM710 water column data (expedition MSM34). Beam-opening angle α is 60°.

eroded at the unconformity. From those crop-out locations gas migrates through the drape (mostly vertical) to the seafloor. As no faulting was identified on the shelf associated with the speckled seafloor, gas may be able to migrate through the drape of sediments simply by its own buoyancy as the supposedly high-porosity sediments (no cores available) are not forming a permeability barrier. Although we lack direct age control, it is likely that the drape of sediments is younger than the LGM and represents the depositional history since sea-level started to rise after the last glaciation. Thus, gas venting is controlled by the paleo-seafloor structure and not recent processes.

From these observations, we propose that most gas venting seen at the seafloor may be from a deeper source that has seen some distance of upward migration (though it still is of microbial origin) and not from *in situ* production.

The general shelf to deep-water trend of reduction in the number of gas flares (**Figure 1D**, also noted by Naudts et al. (2006) in the Dnepr fan region) may be linked to the distance to source of organic material (river input). Additionally, it may be associated with an overall change in sediment grain size, with finer material in deeper water creating a less permeable layer (veneer) that requires hydro-fracturing where simple gas buoyancy is insufficient.

The fact that apparently most gas venting is seen on the shelf adds to other studies world-wide (e.g., Schmale et al., 2005; Shakhova et al., 2010; Borges et al., 2016; Ruppel and Kessler, 2017; Johnson et al., 2019) proposing that gas emission on continental shelf regions are a significant contributor of methane to the atmosphere as gas is not fully consumed or dissolved into the ocean on its path through the water column.

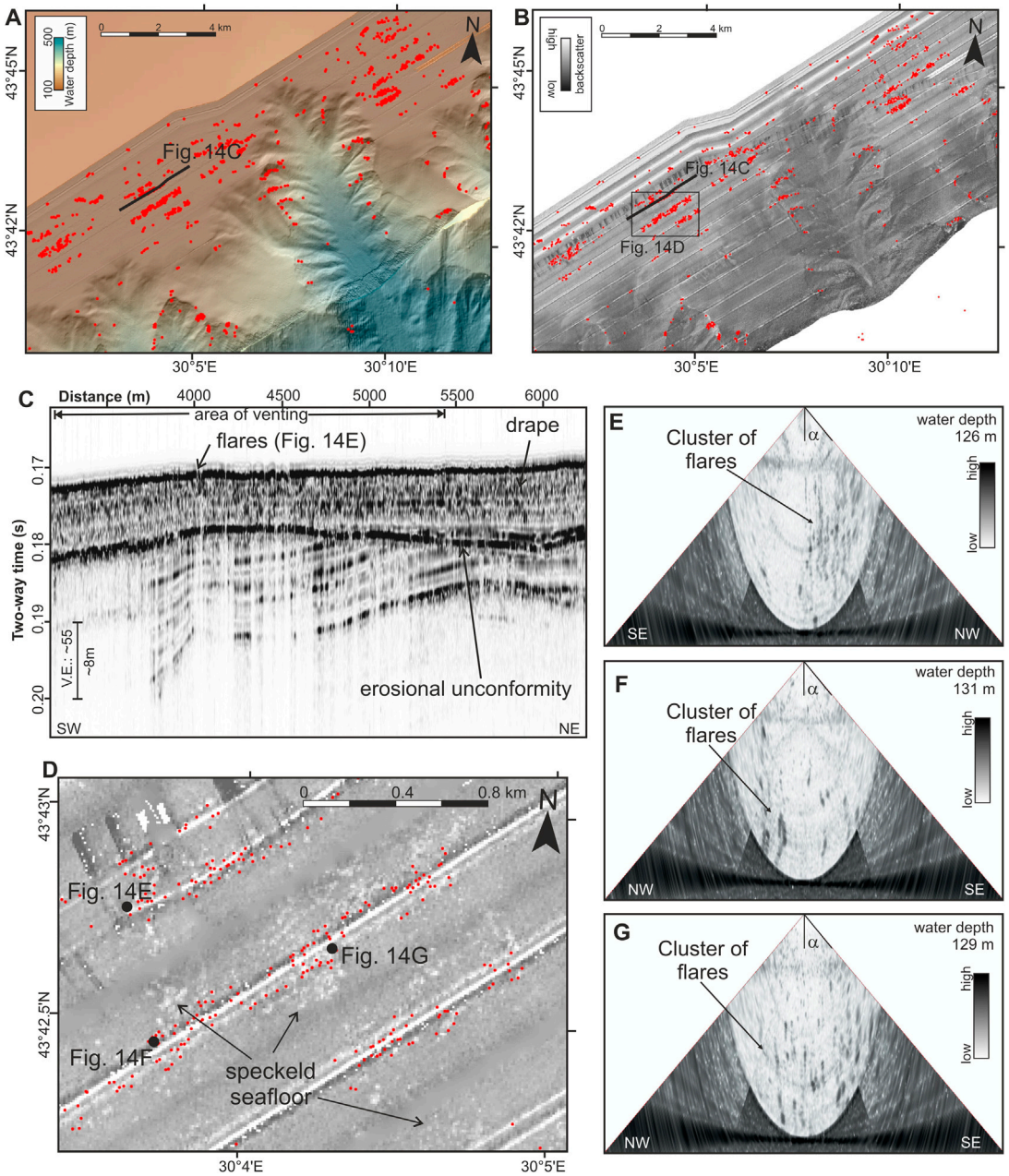

FIGURE 14 | Examples of gas vent occurrences (red dots) along the western portion of the shelf region in our study area. Shown are **(A)** water depth, and **(B)** seafloor backscatter near the S1 channel head. **(C)** The sub-profiler data reveal a drape of post-glacial sediments (~10 m thick) above an erosional unconformity. Here, the gas flares are occurring in dense clusters that also can be seen in the backscatter data as high-amplitude patches, described as speckled seafloor **(D)**. **(E–G)** are examples of EM710 multibeam data showing abundant gas flares in the water column above the speckled seafloor.

Temperature and Pressure Control on Solubility

The gas occurrence within the sediments is further controlled by gas solubility (general dependencies of solubility with pressure and temperature are shown in **Supplementary Figure S1**). Where no advection from below adds methane to overcome the solubility threshold, free gas can only form when temperature and pressure conditions are allowing free gas bubbles to form. In this depth interval above the GHSZ, we deal with a two-phase system (salt-water and gas) only (Riboulot et al., 2018; Ker et al., 2019). Below a depth of ca. 20 mbsf, we observe low pore-fluid salinities near 3-4 with little variation with greater depth (Bohrmann, 2018; Riedel et al., 2020). Salinity increases toward the seafloor to the average value of ~22 of the Black Sea water body (Özsoy and Ünlüata, 1997). If temperature increases with sub-seafloor depth, solubility is reduced (at constant hydrostatic pressure) and free gas bubbles

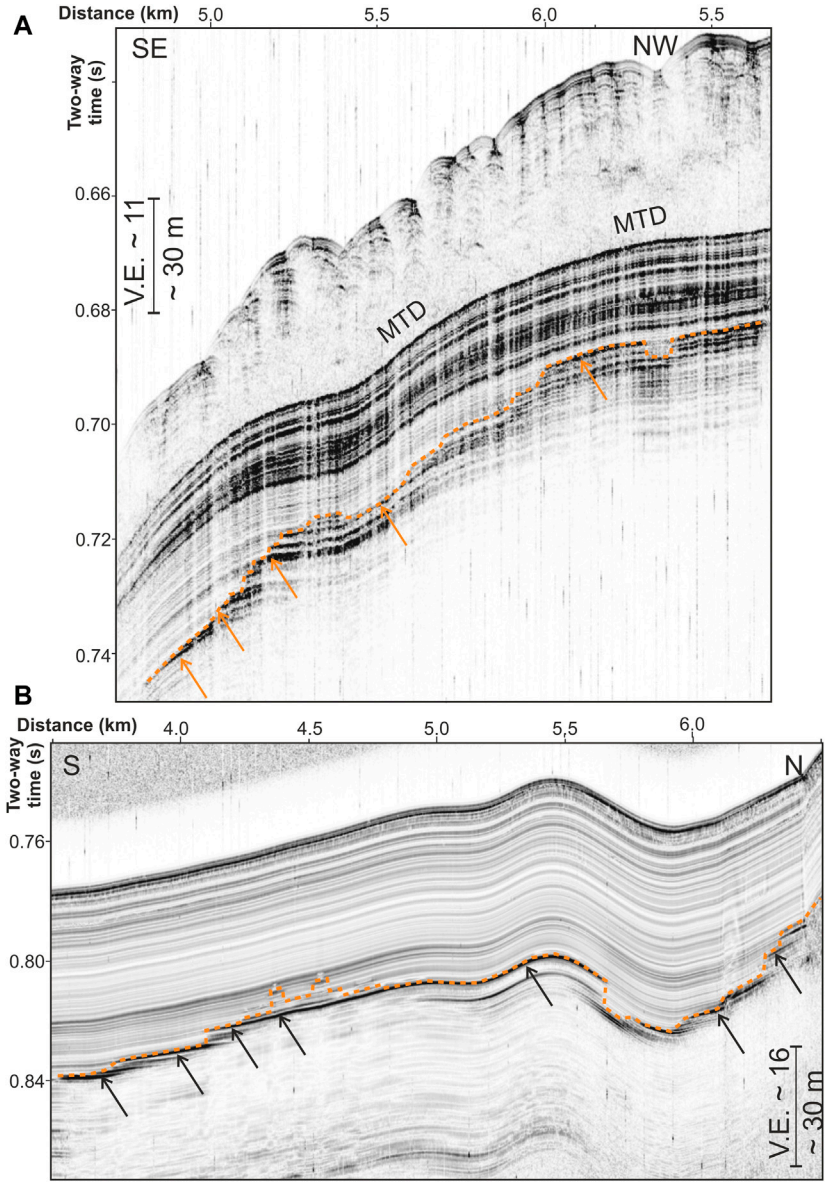

FIGURE 15 | Two examples of free gas in sediments enhancing the layer's reflectivity without creating gas-masking. **(A)** Example near the S2 channel, **(B)** example from the eastern study region around the N2 channel. The free gas occurrences are marked by an increase in reflectivity (orange arrows and dotted line) of individual layers. As seafloor depth decreases, the top of free gas jumps to the next shallower sedimentary layer without forming a continuous (diffuse) gas front as observed in other locations (compare to **Figure 14D**). This bottom-simulating nature is explained by the pressure and temperature dependence of methane gas solubility (see **Supplementary Figure S1** for schematic functions). The mass-transport deposit (MTD) seen in **(A)** is also mapped across the region (compare to **Figure 11**, referred to as intermediate MTD 1).

can form assuming the same *in situ* methane concentrations. If pressure increases, more methane can be dissolved in the pore water, thus free gas bubble formation is prohibited.

The bottom-simulating nature of the depth of the top of free gas in sediment layers and its lateral change is likely the result of this dependency of gas solubility on temperature and pressure. Following e.g., a specific layer from greater water depth (at constant burial below seafloor, thus same sub-seafloor temperature and salinity), hydrostatic pressure slowly decreases along this layer until free gas bubbles can form. Similarly, when following a layer to deeper water, gas solubility decreases until free gas content becomes too low to be imaged at this sub-seafloor depth and the apparent top of free gas jumps to the next layer at greater depth where temperatures are higher (**Figure 15**). Gas solubility can be further limited by pore-shape and capillary effects, which are grain-size and pore-shape dependent. Those effects would ride on top of the main pressure/temperature (P/T) controls and could locally modify the top of free gas. However, without additional sediment grain size information, no further explanations to this effect can be given and the step-wize and semi-bottom-simulating

nature of the top of free gas is well explained with the main P/T effects on solubility. We observe this behavior mostly in sub-seafloor depths of 30–50 m. At these depths, *in situ* salinity is around 3–4, sub-seafloor temperature may only be ~1 °C warmer than at the seafloor given regional thermal gradients measured (Hillman et al., 2018a). With drastically changing salinity toward the seafloor, no clear bottom-simulating effect may be created at shallower sub-seafloor depths in shallower water.

CONCLUDING SUMMARY

Gas venting has been observed along several portions of the continental margin of the Black Sea region from offshore western Bulgaria (e.g,. Xu et al., 2018) to the Romanian sector (Riboulot et al., 2017) of the Danube deep-sea fan, as well as offshore Crimea (Naudts et al., 2006) and the Kerch peninsula (e.g,. Römer et al., 2019). Our new study using newly collected data off Bulgaria and Romania closes a gap between previously mapped regions and complements previous work and augments the knowledge of the structural and sediment depositional control on gas migration. While confirming the observations and conclusions made by previous researchers especially on the general limitation of gas venting to shallower water depths above the GHSZ outcrop at ~720 m water depths, we show additional controls on gas migration and gas vent formation at the seafloor. Three levels of additional control were identified:

(1) A first-order control is governed from sediment depositional styles and character that has imposed a specific topography of sediment waves linked to channel and levee systems. Gas accumulates beneath sediment wave crests (forming a structural trap) after migration from the deeper subsurface. Further migration to the seafloor and venting is facilitated through small-scale sediment heterogeneities. Mass-transport deposits level out some of the deeper (initial) sediment-wave topography but seem not to impose a strict permeability barrier for upward gas migration. In regions of shallow MTDs with <5 m burial depths gas venting is absent. Large-scale tectonic normal faulting with offsets visible at the seafloor also sets a general pattern for upward gas migration as seen in particular in the north-eastern portion of the study region that is associated to the Dnepr fan system.
(2) A second-order control is from seafloor-shaping processes such as canyon formation and slope failures cutting through the drape of the uppermost 100 m of sediment. Here, gas migration is promoted from local removal of sediment and exposure of permeable strata at outcrops.
(3) A third level of control is given by small-scale faulting (meter to sub-meter scale) that provides pathways for further upward gas migration from deeper accumulations. In all instances, we observe normal faulting either from the large-scale tectonic regime or from gravitational collapse and instability of the formations.

A chemical control on free gas (bubble) formation and occurrence within sediment layers that then may get further funnelled to the seafloor through structural controls is determined by the general temperature and pressure effect on methane solubility. Here, we observe a characteristic bottom-simulating gas charging (and associated enhanced acoustic reflectivity without an acoustic wipe-out) in sediment layers at depth of ~30–50 mbsf.

DATA AVAILABILITY STATEMENT

The multibeam seafloor and water-column acoustic data analyzed for this study can be found in the PANGAEA data base (https://www.pangaea.de/). EM122 bathymetry data for expedition MSM34 (https://doi.org/10.1594/PANGAEA.860486); EM122 raw data for expedition MSM34 (https://doi.org/10.1594/PANGAEA.894399); EM710 raw data for expedition M142 (https://doi.org/10.1594/PANGAEA.895530); EM122 raw data for expedition M142 (https://doi.org/10.1594/PANGAEA.895506); EM710 raw data for expedition M143 (https://doi.org/10.1594/PANGAEA.895497); EM122 raw data for expedition M143 (https://doi.org/10.1594/PANGAEA.895437).

AUTHOR CONTRIBUTIONS

Detection of gas flare locations was done by MR, LH, and AB. SG and PW provided gridded multibeam bathymetry and backscatter data for expeditions M142 and M143. MR and LH conducted main analysis and interpretation of multibeam and PARASOUND data. Funding for expeditions from which data were used was obtained by JB and IK (MSM34), GB (M142), as well as JB and MR (M143). IK, JB, GB, and MR were chief scientists of expeditions MSM34/1, MSM34/2, M142, and M143, respectively.

FUNDING

Expeditions MSM34 and M142 were fully integrated into the German collaborative gas hydrate program SUGAR, which also provided the funding for scientific work of the cruise (BMWi 03SX20A, BMBF 03SX381F, BMBF 03G0819A, and 03G0856). Cruise MSM34 was further supported by project MIDAS (EU grant 603418). Additional funds came from the Bremen DFG-Research Center/Excellence Cluster "The Ocean in the Earth System".

ACKNOWLEDGMENTS

The authors would like to thank all ship-crews, support staff, and scientific personnel involved in conducting ship-based work and analyses during expeditions onboard R/V *Maria S. Merian* (MSM34) and R/V *Meteor* (M142, M143).

SUPPLEMENTARY MATERIAL

The Supplementary Material for this article can be found online at: https://www.frontiersin.org/articles/10.3389/feart.2020.601254/full#supplementary-material.

REFERENCES

Akhmetzhanov, A., and Falkenstein, B. (2017). The power of high-tech: unlocking the black sea's potential, 336. Available at: https://oiljournal.info/en/content/nv/336/the-power-of-high-tech-unlocking-the-black-sea-s-potential/ (Accessed July 10, 2020).

Baristeas, N. (2006). Seismische fazies, tektonik und gashydratvorkommen im nordwestlichen schwarzen meer. Diploma Thesis. Hamburg: University Hamburg, 110.

Bialas, J., Klaucke, I., and Haeckel, M. (2014). GEOMAR Report No. 15. Fs maria s. merian fahrtbericht/cruise report MSM-34/1 & 2–sugar site. Kiel: GEOMAR Helmholtz Centre for Ocean Research Kiel, 109 (Accessed January 5, 2021).

Bialas, J., Bohlen, T., Dannowski, A., Eisenberg-Klein, G., Gassner, L., Gehrmann, R., et al. (2020). Joint interpretation of geophysical field experiments in the danube deep-sea fan, black sea. *J. Mar. Pet. Geol.* 121, 15. doi:10.1016/j.marpetgeo.2020.104551

Bohrmann, G. (2018). R/V METEOR cruise report M142, drilling gas hydrates in the danube deep-sea fan, black sea, varna–varna–varna, 04 november–22 november–09 december 2017. berichte, MARUM–zentrum für marine umweltwissenschaften, fachbereich geowissenschaften, universität bremen. Available at: http://publications.marum.de/id/eprint/3698 (Accessed January 5, 2021), Vol. 320, 121.

Bohrmann, G., Ivanov, M., Foucher, J. P., Spieß, V., Bialas, J., Weinrebe, W. R., et al. (2003). Mud volcanoes and gas hydrates in the black sea–new data from dvurechenskii and odessa mud volcanoes. *Geo Mar. Lett.* 23 (3-4), 239–249. doi:10.1007/s00367-003-0157-7

Borges, A. V., Champenois, W., Gypens, N., Delille, B., and Harlay, J. (2016). Massive marine methane emissions from near-shore shallow coastal areas. *Sci. Rep.* 6, 27908. doi:10.1038/srep27908

Caress, D. W., Chayes, D. N., and dos Santos Ferreira, C. (2017). MB-system: mapping the seafloor. Available at: http://www.mbari.org/products/research-software/mb-system/ (Accessed January 5, 2021).

Çifçi, G., Dondurur, D., and Ergün, M. (2003). Deep and shallow structures of large pockmarks in the turkish shelf, eastern black sea. *Geo Mar. Lett.* 23, 311–322. doi:10.1007/s00367-003-0138-x

Daigle, H., Bangs, N. L. B., and Dugan, B. (2011). Transient hydraulic fracturing and gas release in methane hydrate settings: a case study from southern hydrate ridge. *G-cubed* 12 (12), 12022. doi:10.1029/2011GC003841

De Batist, M., Klerkx, J., Van Rensbergen, P., Vanneste, M., Poort, J., Golmshtok, A., et al. (2002). Active hydrate destabilization in lake baikal, siberia ?. *Terra. Nova* 14 (6), 436–442. doi:10.1046/j.1365-3121.2002.00449.x

Degens, E. T., and Ross, D. A. (1974). *The black sea–geology, chemistry, and biology.* Tulsa, USA: The American Association of Petroleum Geologists.

Dinu, C., Wong, H. K., Tambrea, D., and Matenco, L. (2005). Stratigraphic and structural characteristics of the romanian black sea shelf. *Tectonophysics* 410, 417–435. doi:10.1016/j.tecto.2005.04.012

Driscoll, N. W., Weissel, J. K., and Goff, J. A. (2000). Potential for large-scale submarine slope failure and tsunami generation along the U.S. mid-Atlantic coast. *Geology* 28, 407–410. doi:10.1130/0091-7613(2000)28<407: PFLSSF>2.0.CO;2

Duan, Z., and Mao, S. (2006). A thermodynamic model for calculating methane solubility, density and gas phase composition of methane-bearing aqueous fluids from 273-523 K and from 1 to 2000 bar. *Geochem. Cosmochim. Acta* 70, 3369–3386. doi:10.1016/j.gca.2006.03.018

Ergün, M., Dondurur, D., and Çifçi, G. (2002). Acoustic evidence for shallow gas accumulations in the sediments of the eastern black sea. *Terra. Nova* 14 (5), 313–320. doi:10.1046/j.1365-3121.2002.00434.x

Freudenthal, T., Bohrmann, G., Gohl, C., Klages, J. P., Riedel, M., Wallmann, K., et al. (2020). More than ten years of successful operation of the MARUM-MeBo sea bed drilling technology: highlights of recent drilling campaigns. *EGU General Assembly* [Epub ahead of print]. doi:10.5194/egusphere-egu2020-5089

Freudenthal, T., and Wefer, G. (2013). Drilling cores on the sea floor with the remote-controlled sea floor drilling rig MeBo. *Geosci. Instrum. Methods Data Syst.* 2 (2), 329–337. doi:10.5194/gi-2-329-2013

Ginsburg, G. D. (1998). "Gas hydrate accumulation in deep-water marine sediments," in *Gas hydrates: relevance to world margin stability and climate change.* Editors J.-P. Henriet and J. Mienert (London, United Kingdom: Geological Society, London, Special Publications), Vol. 137, 51–62. Available at: https://sp.lyellcollection.org/content/specpubgsl/137/1/51.full.pdf (Accessed June 25, 2020).

Greinert, J., Artemov, Y., Egorov, V., De Batist, M., and McGinnis, D. (2006). 1300-m-high rising bubbles from mud volcanoes at 2080 m in the black sea: hydroacoustic characteristics and temporal variability. *Earth Planet Sci. Lett.* 244 (1–2), 1–15. doi:10.1016/j.epsl.2006.02.011

Greinert, J., McGinnis, D. F., Naudts, L., Linke, P., and De Batist, M. (2010). Atmospheric methane flux from bubbling seeps: spatially extrapolated quantification from a black sea shelf area. *J. Geophys. Res. Oceans* 115, C01002. doi:10.1029/2009JC00538

Haeckel, M., Bialas, J., Klaucke, I., Wallmann, K., Bohrmann, G., Schwalenberg, K., et al. (2015). Gas hydrate occurrences in the black sea–new observations from the german sugar project Fire in the ice US department of energy (UD DoE) methane hydrate newsletter, (Morgantown, WV: . NETL.). Available at: http://oceanrep.geomar.de/30761/1/Haeckel%20et.al.pdf (Accessed July 10, 2020), Vol. 15, 6–9.

Haeckel, M., Zander, T., Burwicz, E., Bialas, J., Berndt, C., Dannowski, A., et al. (2017). "The gas hydrate system of the danube deep-sea fan in the black sea", in 9th international conference on gas hydrates, Denver, CO, June 15–30, 2017 (Colorado School of Mines).

Hillman, J. I. T., Klaucke, I., Bialas, J., Feldman, H., Drexler, T., Awwiller, D., et al. (2018a). Gas migration pathways and slope failures in the danube fan, black sea. *Mar. Petrol. Geol.* 92, 1069–1084. doi:10.1016/j.marpetgeo.2018.03.025

Hillman, J. I. T., Burwicz, E., Zander, T., Bialas, J., Klaucke, I., Feldman, H., et al. (2018b). Investigating a gas hydrate system in apparent disequilibrium in the danube fan, black sea. *Earth Planet Sci. Lett.* 502, 1–11. doi:10.1016/j.epsl.2018.08.051

Johnson, H. P., Merle, S., Salmi, M., Embley, R., Sampaga, E., and Lee, M. (2019). Anomalous concentration of methane emissions at the continental shelf edge of the northern Cacadia margin. *J. Geophys. Res. Solid Earth* 124 (3), 2829–2843. doi:10.1029/2018JB016453

Judd, A. G., Hovland, M., Dimitrov, L. I., Gil, S. G., and Jukes, V. (2002). The geological methane budget at continentla margins and its influence on climate change. *Geofluids* 2, 109–126. doi:10.1046/j.1468-8123.2002.00027.x

Ker, S., and Riboulot, V.GHASS Cruise Team (2015). GHASS cruise report. Available at: https://archimer.ifremer.fr/doc/00300/41141/last (Accessed June 25, 2020), 53.

Ker, S., Thomas, Y., Riboulot, V., Sultan, N., Bernard, C., Scalabrin, C., et al. (2019). Anomalously deep BSR related to a transient state of the gas hydrate system in the western black sea. *G-cubed* 20, 442–459. doi:10.1029/2018GC007861

Klaucke, I., Sahling, H., WeinrebeBlinova, W. V., Bürka, D., Lursmanashvili, N., and Bohrmann, G. (2006). Acoustic investigation of cold seeps offshore georgia, eastern black sea. *Mar. Geol.* 231 (1–4), 51–67. doi:10.1016/j.margeo.2006.05.011

Körber, J. H., Sahling, H., Pape, T., dos Santos Ferreira, C., MacDonald, I. R., and Bohrmann, G. (2014). Natural oil seepage at kobuleti ridge, eastern black sea. *Mar. Petrol. Geol.* 50, 68–82. doi:10.1016/j.marpetgeo.2013.11.007

KosselBigalke, E. N., Piñero, E., and Haeckel, M. (2013). The SUGAR Toolbox–a library of numerical algorithms and data for modelling of gas hydrate systems and marine environments. *Geomar Rep.* 8, 160. doi:10.3289/geomar_rep_ns_8_2013

Laberg, J. S., Baeten, N. J., Lågstad, P., Forwick, M., and Vorren, T. O. (2013). Formation of a large submarine crack during the final stage of retrogressive mass wasting on the continental slope offshore northern norway. *Mar. Geol.* 346, 73–78. doi:10.1016/j.margeo.2013.08.008

Lericolais, G., Bulois, C., Gillet, H., and Guichard, F. (2009). High frequency sea level fluctuations recorded in the black sea since the LGM. *Global Planet. Change* 66 (1–2), 65–75. doi:10.1016/j.gloplacha.2008.03.010

Lericolais, G., Bourget, J., Popescu, I., Jermannaud, P., Mulder, T., Jorry, S., et al. (2013). Late Quaternary deep-sea sedimentation in the western Black Sea: new insights from recent coring and seismic data in the deep basin. *Global Planet. Change* 103, 232–247. doi:10.1016/j.gloplacha.2012.05.002

Macelloni, L., Lutken, C. B., D'Emidio, M., Sleeper, K., McGee, T. M., GargSimonetti, S. A., et al. (2015). Heat-flow regimes and the hydrate stability zone of a transient, thermogenic, fault-controlled hydrate system (Woolsey Mound northern Gulf of Mexico). *J. Mar. Pet. Geol.* 59, 491–504. doi:10.1016/j.marpetgeo.2014.09.010

McGinnis, D. F., Greinert, J., Artemov, Y., Beaubien, S. E., and Wuest, A. (2006). Fate of rising methane bubbles in stratified waters: how much methane reaches the atmosphere?. *J. Geophys. Res.* 111, C09007. doi:10.1029/2005JC003183

Mienert, J., Vanneste, M., Haflidason, H., and Bünz, S. (2010). Norwegian margin outer shelf cracking: a consequence of climate-induced gas hydrate dissociation?. *Int. J. Earth Sci.* 99, 207–225. doi:10.1007/s00531-010-0536-z

Minshull, T. A., Marín-Moreno, H., Betlem, P., Bialas, J., Buenz, S., Burwicz, E., et al. (2020). Hydrate occurrence in Europe: a review of available evidence. *J. Mar. Pet. Geol.* 111, 735–764. doi:10.1016/j.marpetgeo.2019.08.014

Naudts, L., Greinert, J., Artemov, Y., Staelens, P., Poort, J., Van Rensbergen, P., et al. (2006). Geological and morphological setting of 2778 methane seeps in the Dnepr paleo-delta, northwestern black sea. *Mar. Geol.* 227, 177–199. doi:10.1016/j.margeo.2005.10.005

Naudts, L., Greinert, J., Artemov, Y., and De Batist, M. (2009). Geo- and hydroacoustic manifestations of shallow gas and gas seeps in the Dnepr paleodelta, northwestern black sea. *Lead. Edge* 28 (9), 51–63. doi:10.1190/1.3236372

Özsoy, E., and Ünlüata, Ü. (1997). Oceanography of the black sea: a review of some recent results. *Earth Sci. Rev.* 42 (4), 231–272. doi:10.1016/S0012-8252(97)81859-4

Pape, T., Bahr, A., Rethemeyer, J., Kessler, J. D., Sahling, H., Hinrichs, K-U., et al. (2010). Molecular and isotopic partitioning of low-molecular-weight hydrocarbons during migration and gas hydrate precipitation in deposits of a high-flux seepage site. *Chem. Geol.* 269 (3-4), 350–363. doi:10.1016/j.chemgeo.2009.10.009

Pape, T., Bahr, A., Klapp, S. A., Abegg, F., and Bohrmann, G. (2011). High-intensity gas seepage causes rafting of shallow gas hydrates in the southeastern black sea. *Earth Planet Sci. Lett.* 307 (1-2), 35–46. doi:10.1016/j.epsl.2011.04.030

Pape, T., Haeckel, M., Riedel, M., Kölling, M., Schmidt, M., Wallmann, K., et al. (2020). Formation pathways of light hydrocarbons in deep sediments of the danube deep-sea fan, western black sea. *Mar. Petrol. Geol.* 122, 104627. doi:10.1016/j.marpetgeo.2020.104627

PaullCaress, C. K. D. W., Thomas, H., Lundsten, E., Anderson, K., Gwiazda, R., Riedel, M., et al. (2015). Seafloor geomorphic manifestations of gas venting and shallow subbottom gas hydrate occurrences. *Geosphere* 11 (2), 491–513. doi:10.1130/GES01012.1

Pilcher, R., and Argent, J. (2007). Mega-pockmarks and linear pockmark trains on the west african continental margin. *Mar. Geol.* 244, 15–32. doi:10.1016/j.margeo.2007.05.002

Poort, J., Vassilev, A., and Dimitrov, L. (2005). Did postglacial catastrophic flooding trigger massive changes in the black sea gas hydrate reservoir?. *Terra. Nova* 17 (2), 135–140. doi:10.1111/j.1365-3121.2005.00599.x

Popescu, I., De Batist, M., Lericolais, G., Nouzé, H., Poort, J., Panin, N., et al. (2006). Multiple bottom-simulating reflections in the black sea: potential proxies of past climate conditions. *Mar. Geol.* 227, 163–176. doi:10.1016/j.margeo.2005.12.006

Popescu, I., Lericolais, G., Panin, N., Wong, H.., and Droz, L. (2001). Late quaternary channel avulsions on the danube deep-sea fan, black sea. *Mar. Geol.* 179, 25–37. doi:10.1016/S0025-3227(01)00197-9

Popescu, I., Lericolais, G., Panin, N., Normand, A., Dinu, C., and Le Drezen, E. (2004). The danube submarine canyon (Black Sea): morphology and sedimentary processes. *Mar. Geol.* 206, 249–265. doi:10.1016/j.margeo.2004.03.003

Popescu, I., Lericolais, G., Panin, N., De Batist, M., and Gillet, H. (2007). Seismic expression of gas and gas hydrates across the western black sea. *Geo Mar. Lett.* 27, 173–183. doi:10.1007/s00367-007-0068-0

Reiche, S., Hjelstuen, B. O., and Haflidason, H. (2011). High-resolution seismic stratigraphy, sedimentary processes and the origin of seabed cracks and pockmarks at nyegga, mid-norwegian margin. *Mar. Geol.* 284, 28–39. doi:10.1016/j.margeo.2011.03.006

Riboulot, V., Cattaneo, A., Scalabrin, C., Gaillot, A., Jouet, G., Ballas, G., et al. (2017). Control of the geomorphology and gas hydrate extent on widespread gas emissions offshore romania. *Bull. Soc. Géol. Fr.* 188 (4), 26. doi:10.1051/bsgf/2017182

Riboulot, V., Ker, S., Sultan, N., Thomas, Y., Marsset, B., Scalabrin, C., et al. (2018). Freshwater lake to salt-water sea causing widespread hydrate dissociation in the black sea. *Nat. Commun.* 9 (1). doi:10.1038/s41467-017-02271-z

Riedel, M., Gausepohl, F., Gazis, I., Hähnel, L., Kampmeier, M., Urban, P., et al. (2018). Report of Cruise M143 SLOGARO–slope failures and active gas expulsion along the Romanian margin–investigating relations to gas hydrate distribution, Varna (Romania) – heraklion (Greece) 12.02.-22.12.2017, Berichte aus dem GEOMAR Helmholtz-Zentrum für Ozeanforschung Kiel Nr. 42. Available at: https://www.geomar.de/en/research/publications-oceanrep/geomar-report (Accessed January 5, 2021), 43–8113.

Riedel, M., Freudenthal, T., Bergenthal, M., Haeckel, M., Wallmann, K., Spangenberg, E., et al. (2020). Physical properties and core-log seismic integration from drilling at the danube deep sea fan, black sea. *Mar. Petrol. Geol.* 114, 104192. doi:10.1016/j.marpetgeo.2019.104192

Robinson, A. G., Rudat, J. H., Banks, C. J., and Wiles, R. L. F. (1996). Petroleum geology of the black sea. *Mar. Petrol. Geol.* 13, 195–223. doi:10.1016/0264-8172(95)00042-9

Römer, M., Sahling, H., Pape, T., Bahr, A., Feseker, T., Wintersteller, P., et al. (2012). Geological control and magnitude of methane ebullition from a high-flux seep area in the black sea–the kerch seep area. *Mar. Geol.* 319, 57–74. doi:10.1016/j.margeo.2012.07.005

Römer, M., Sahling, H., dos Santos Ferreira, C., and Bohrmann, G. (2019). Methane gas emissions of the black sea—mapping from the crimean continental margin to the kerch peninsula slope. *Geo Mar. Lett.* 40, 467–480. doi:10.1007/s00367-019-00611-0

Ruppel, C. D., and Kessler, J. D. (2017). The interaction of climate change and methane hydrates. *Rev. Geophys.* 55 (1), 126–168. doi:10.1002/2016RG000534

Ryan, W. B., Pitman, W. C., III, Major, C. O., Shimkus, K., Moskalenko, V., Jones, G. A., et al. (1997). An abrupt drowning of the black sea shelf. *Mar. Geol.* 138, 119–126. doi:10.1016/S0025-3227(97)00007-8

Sahling, H., Bohrmann, G., Artemov, Y. G., Bahr, A., Brüning, M., Klapp, S. A., et al. (2009). Vodyanitskii mud volcano, sorokin trough, black sea: geological characterization and quantification of gas bubble streams. *J. Mar. Pet. Geol.* 26 (9), 1799–1811. doi:10.1016/j.marpetgeo.2009.01.010

Schmale, O., Greinert, J., and Rehder, G. (2005). Methane emission from high-intensity marine gas seeps in the black sea into the atmosphere. *Geophys. Res. Lett.* 32, L07609. doi:10.1029/2004GL021138

Schmale, O., Beaubian, S., Rehder, G., Greinert, J., and Lombardi, S. (2010). Gas seepage in the Dnepr paleo-delta area (NW-Black Sea) and its regional impact on the water column methane cycle. *J. Mar. Syst.* 80 (1-2), 90–100. doi:10.1016/j.jmarsys.2009.10.003

Shakhova, N. E., and AlekseevSemiletov, V. A. I. P. (2010). Predicted methane emission on the east siberian shelf. *Dokl. Earth Sci.* 430, 190–193. doi:10.1134/S1028334X10020091

Soulet, G., Delaygue, G., and Vallet-Coulomb, C. (2010). Glacial hydrologic conditions in the Black Sea reconstructed using geochemical pore water profiles. *Earth Planet Sci. Lett.* 296 (1-2), 57–66. doi:10.1016/j.epsl.2010.04.045

Spence, G. D., Haacke, R. R., and Hyndman, R. D. (2010). "Seismic indicators of natural gas hydrate and underlying free gas," in *Geophysical characterization of gas hydrates.*. Editors M. Riedel, E. C. Willoughby, and S. Chopra (Tulsa, OK: SEG Geophysical Developments), Vol. 14, 39–71.

Starostenko, V., Rusakov, O., Shnyukov, E., Kobolev, V., and Kutas, R. (2010). Methane in the northern black sea: characterization of its geomorphological and geological environments. *J. Geol. Soc. London Spec. Publ.* 340, 57–75. doi:10.1144/SP340.5

Tishchenko, P., Hensen, C., Wallmann, K., and Wong, C. S. (2005). Calculation of the stability and solubility of methane hydrate in seawater. *Chem. Geol.* 219 (1-4), 35–52. doi:10.1016/j.chemgeo.2005.02.008

Vassilev, A., and Dimitrov, L. I. (2002). Spatial and quantity evaluation of the black sea gas hydrates. *Russ. Geol. Geophys.* 43, 672–684.

Winguth, C., Wong, H. K., PaninDinu, N. C., Georgescu, P., Ungureanu, G., Kruglikov, V. V., et al. (2000). Upper quaternary water level history and sedimentation in the northwestern black sea. *Mar. Geol.* 167 (1), 127–146. doi:10.1016/S0025-3227(00)00024-4

Wong, H. K., Panin, N., Dinu, C., Georgescu, P., and Rahn, C. (1994). Morphology and post-chaudian (Late Pleistocene) evolution of the submarine danube fan complex. *Terra. Nova* 6, 502–511. doi:10.1111/j.1365-3121.1994.tb00894.x

Wong, H. K., Winguth, C., Panin, N., Dinu, C., Wollschlager, M., Georgescu, P., et al. (1997). The Danube and Dniepr fans, morphostructure and evolution. *GeoEcoMarina* 2, 77–102.

Wu, T., Sahling, H., Feseker, T., Rendle-Bühring, R., Wei, J., Wintersteller, P., et al. (2019). Morphology and activity of the helgoland mud volcano in the sorokin trough, northern black sea. *Mar. Petrol. Geol.* 99, 227–236. doi:10.1016/j.marpetgeo.2018.10.017

Xu, C., Greinert, J., Haeckel, M., Bialas, J., Dimitrov, L., and Zhao, G. (2018). The character and formation of elongated depressions on the upper bulgarian slope. *J. Ocean Univ. China* 17 (3), 555–562. doi:10.1007/s11802-018-3460-7

Yefremova, A. G., and Zhizchenko, B. P. (1974). Occurrence of crystal hydrates of gases in the sediments of modern marine basins. *Akademii Nauk SSSR* 214, 1179–1181.

Zander, T., Deusner, C., Garziglia, S., Kossel, E., Haeckel, M., Gupta, S., et al. (2016). Seismic and geotechnical characterization of hydrated sediments in a sand-rich setting: field work and lab experiment results report for MIDAS, managing impacts of deep-sea resource exploitation, 53. Available at: https://www.eu-midas.net/sites/default/files/deliverables/MIDAS_D1.5_FINAL_lowres.pdf (Accessed August 25, 2020).

Zander, T., Haeckel, M., Berndt, C., Chi, W-C., Klaucke, I., Bialas, J., et al. (2017). On the origin of multiple BSRs in the danube deep-sea fan, black sea. *Earth Planet Sci. Lett.* 462, 15–25. doi:10.1016/j.epsl.2017.01.006

Zander, T., Haeckel, M., Klaucke, I., Bialas, J., Klaeschen, D., Papenberg, C., et al. (2019). New insights into geology and geochemistry of the kerch seep area in the black sea. *J. Mar. Pet. Geol.* 113, 104162. doi:10.1016/j.marpetgeo.2019.104162

Conflict of Interest: The authors declare that the research was conducted in the absence of any commercial or financial relationships that could be construed as a potential conflict of interest.

frontiers in Earth Science

ORIGINAL RESEARCH
published: 05 March 2021
doi: 10.3389/feart.2021.557634

Gas Emissions in a Transtensile Regime Along the Western Slope of the Mid-Okinawa Trough

Ang Li[1,2], Feng Cai[1,2], Nengyou Wu[1,2], Qing Li[1,2], Guijing Yan[1,2], Yunbao Sun[1,2], Gang Dong[1,2], Di Luo[1,2] and Xingxing Wang[1,2]*

[1]Key Laboratory of Gas Hydrate, Ministry of Natural Resources, Qingdao Institute of Marine Geology, Qingdao, China, [2]Laboratory for Marine Mineral Resources, Qingdao National Laboratory for Marine Science and Technology, Qingdao, China

Gas emissions from the seabed are favored by tectonically active settings and their distribution is often linked to the nearby faults. Here we use the multi-beam echo-sounder (MBES) and the multi-channel seismic (MCS) data and a sediment core to show multiple gas emissions near the fault complex out of the shelf of the Mid-Okinawa Trough. The features indicating the gas emissions include 1) a set of the conical positive reliefs at the seabed, 2) the bundle-shaped clusters of the high-backscattering intensities in the water column, and 3) the sub-circular medium-to high-backscattering patches at the level of the seabed. These features together show that the free gases can escape from the marine sediments then rise in the water column at present, while some other gases trapped in the sub-seafloor sediment might contribute to the precipitation of the authigenic carbonates in the past. The spatial relationship between the gas emissions and the faults suggests that the faulting driven by the back-arc extension should provide the permeable migration pathways for the gas emissions to operate, and thus determines where most of them could potentially occur. The area surrounding the restraining bend concentrates part of the gas emissions rather than along the fault lines, due to the lateral compression and the structural complexity. This is demonstrated by the results of the numerical model of finite element method (FEM), which shows two gas emissions are within the compressed zone of the modeled restraining step-over. This study provides new evidence of the role of the tectonic stresses in determining the sites of degassing of marine sediments.

Keywords: gas emission, gas plume, multi-beam echo-sounder, Okinawa trough, transtension

OPEN ACCESS

Edited by:
Tamara Baumberger, Oregon State University, United States

Reviewed by:
Moab Praxedes Gomes, Federal University of Rio Grande do Norte, Brazil
Jiliang Wang, Institute of Deep-Sea Science and Engineering (CAS), China
Wei Zhang, Guangzhou Marine Geological Survey, China

****Correspondence:***
Ang Li
ang.li_cn@outlook.com

Specialty section:
This article was submitted to Biogeoscience, a section of the journal Frontiers in Earth Science

Received: *01 May 2020*
Accepted: *14 January 2021*
Published: *05 March 2021*

Citation:
Li A, Cai F, Wu N, Li Q, Yan G, Sun Y, Dong G, Luo D and Wang X (2021) Gas Emissions in a Transtensile Regime Along the Western Slope of the Mid-Okinawa Trough. Front. Earth Sci. 9:557634. doi: 10.3389/feart.2021.557634

INTRODUCTION

Gas emission in the marine environment has attracted significan research attention over the past few decades. The abundance of gas emissions could indicate the potential accumulation of hydrocarbons and, if ambient conditions were proper, the gas hydrates (Riedel et al., 2018). Gases leaked from the seabed constitute an important part of methane transported into the ocean (Judd et al., 2002; Feng et al., 2018). As a member of the potent greenhouse gases, methane can sometimes reach the shallow seawater by forming ascending streams of gas bubbles and possibly enter the atmosphere (McGinnis et al., 2006; Westbrook et al., 2009). This fate of methane has been questioned by the study in the Arctic Ocean, in which enhanced methane concentration was detected close to the gas emissions near the seabed but not in the seawater near the sea level (Myhre et al., 2016). Therefore, whether methane escaping from marine sediments can contribute to climatic warming is controversial. If dissolving

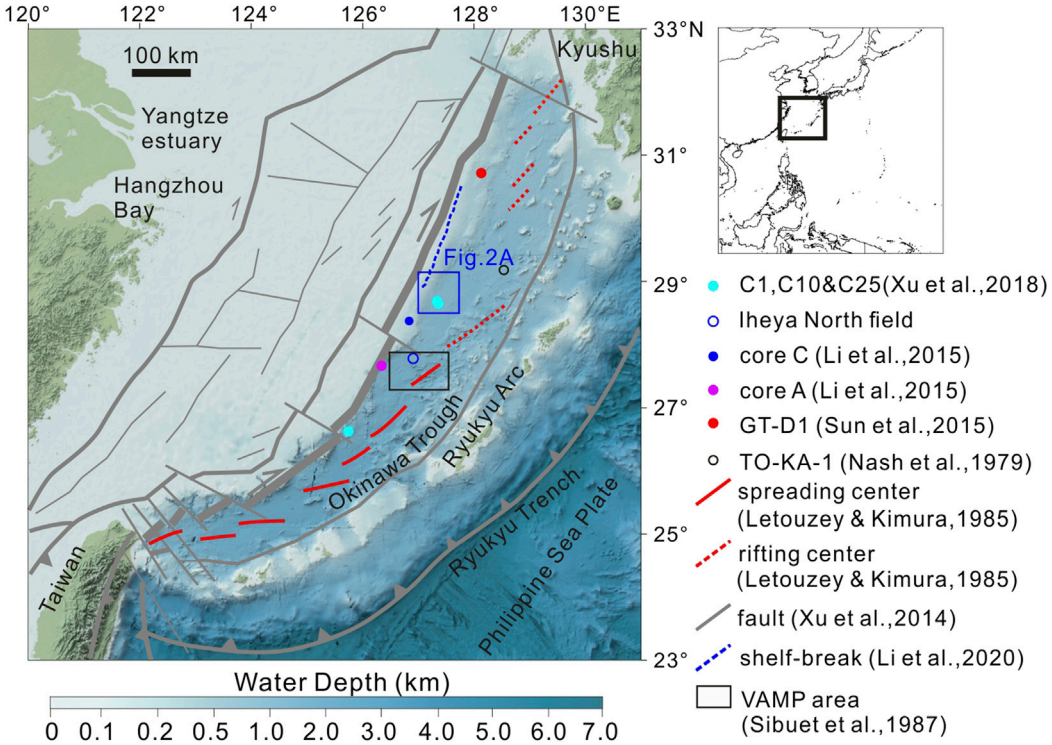

FIGURE 1 | Bathymetric map showing the study area in the Okinawa Trough. The bathymetric data are downloaded from https://maps.ngdc.noaa.gov/viewers/bathymetry (color bar—GEBCO2014 Bathymetry Color Scale). The methane seepages have been recorded at the sites of Cores A and C, C01, C10 and GT-D1 (Li et al., 2015; Sun et al., 2015; Xu et al., 2018).

into the seawater is the fate for most of this methane, the oceans would likely experience deoxygenation and acidification (Biastoch et al., 2011; Yamamoto et al., 2014).

Gas emissions emerge intermittently surrounding the continental shelves and slopes, and are sometimes coated by hydrates in the deep-water settings (Somoza et al., 2003; Sauter et al., 2006; Römer et al., 2012; Smith et al., 2014; Rümer et al., 2017). Free gases can bypass the less permeable sediments alone or be expulsed together with pore fluids and mud-rich sediments (Gennari et al., 2013; Cartwright and Santamarina, 2015). The geological records of such processes include a spectrum of surface expressions such as pockmark (Hustoft et al., 2009; Wang et al., 2018), mud cone (Roberts, 2001), mud volcano (Huguen et al., 2004) and carbonate mound (Schmidt et al., 2005). Gas emissions through these morphological features sometimes have the geophysical signature of the acoustic flares in the water column (i.e., gas plume, Heeschen et al., 2003; Dupre et al., 2015), which can be detected by multi-beam echo-sounder, and gas chimneys imaged by seismic data in the subsurface (Cartwright and Santamarina, 2015; Li et al., 2017).

Ongoing research probes into how geological processes control gas emissions and the one that has been studied most on global scale is the tectono-structural process (Ciotoli et al., 2020). Gas emissions have been detected in the extensional (Plaza-Faverola and Keiding, 2019), the compressive (Reed et al., 1990; Watson et al., 2019), the sheared (Huguen et al., 2004; Geli et al., 2008) and the mixed deformation regimes (Plaza-Faverola et al., 2014). The faults formed in these settings can indicate the stress regime surrounding gas emissions, and sometimes served as the escaping conduits for them (Ciotoli et al., 2020). The gas emissions in the Mid-Okinawa Trough have been inferred only by geochemical analysis (Xu et al., 2018) and what geological process controlled their distribution is not fully understood.

In this study, we use multi-beam echo-sounder (MBES) and multi-channel seismic (MCS) data to show multiple gas emissions out of the shelf of the Mid-Okinawa Trough and consider how faulting determines their potential locations. Here the nearby fault complex is formed in the transtensile regime, accompanied by local compressions surrounding the restraining bend. The finite element method (FEM) is used to simulate the stress regime surrounding two of these emissions in a restraining step-over. The consistency of the modeling result with the geophysical observation supports the role of local lateral compression in promoting gas emissions.

GEOLOGICAL SETTING

The Okinawa Trough is an incipient back-arc basin in the East China Sea and displays as an arcuate geometry in plan view (**Figure 1**). It formed after the middle Miocene due to the crustal stretching (Lee et al., 1980), driven by the subduction of the Philippine Sea Plate under the Eurasian Plate (Kimura, 1985;

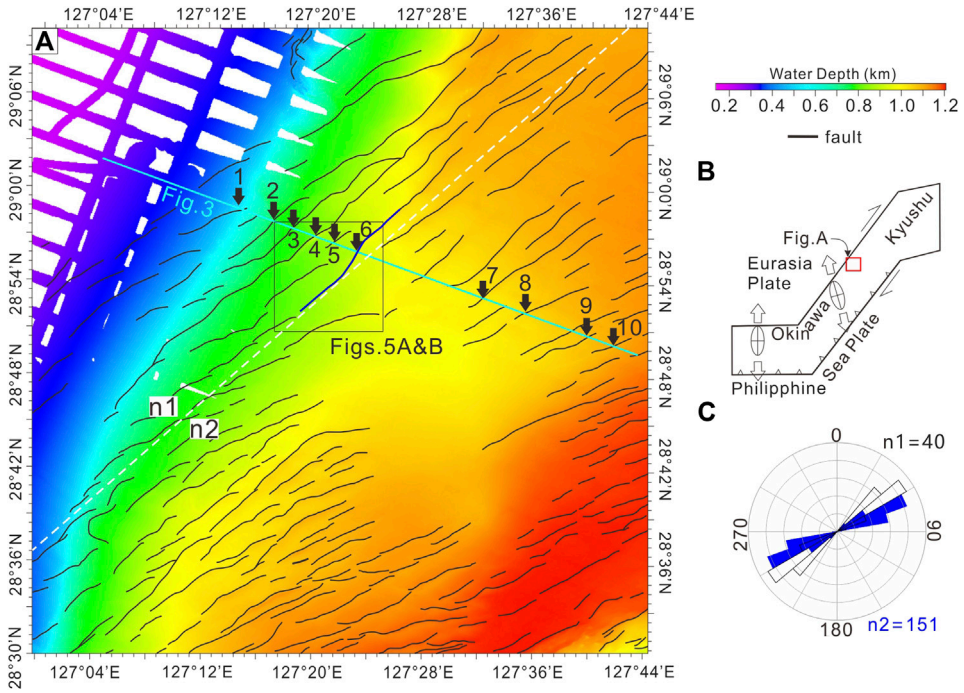

FIGURE 2 | (A) The bathymetric map showing the distribution of the fault scarps. It is mapped based on the MBES data. The blue line is the fault incorporated into the model. **(B)** The schematic figure showing the regional tectonic setting and the direction of extension (hollow arrows) in the Okinawa Trough (from Fabbri et al., 2004). **(C)** Rose diagram showing the orientations of the fault groups (n1 and n2, bounded by the white dashed line in Fig. **A**).

Gungor et al., 2012). This tectonic activity accounts for the multiple periods of rifting and the latest one is still active at present (Kimura, 1985; Letouzey and Kimura, 1985; Yamaji, 2003). The en-echelon grabens bounded by the faults and the stepped, sometimes unclear rifting centers in the Mid-Okinawa Trough have been revealed before by some sparse seismic profiles (Kimura, 1985; Letouzey and Kimura, 1985; Sibuet et al., 1987). Such shallow structures and basaltic ridges have also been seen in the area of volcanic arc-rift migration phenomenon (VAMP, shown in **Figure 1**) (Sibuet et al., 1987). To the north, the faults formed by transtension have been mapped in detail by combining the multi-beam echo-sounder and the multi-channel seismic data in an area of ~5300 km^2 (**Figures 2A**, **3**). Their strikes change from ~N60°E in the shelf-slope setting (marked by n1) to ~ N70°E in the deep-water basin (marked by n2, **Figure 2**). The faults in the deep-water basin are mostly normal, while those in the slope often have scarps that are subparallel with each other (**Figures 2**, **3**). There are some small-scale faults affected by strike-slip in the fault blocks, leaving minor positive relief at the seabed (**Figures 3F,G**). The observations of the fault pattern are consistent with the previous interpretation of the basin-scale tectonic regime that is characterized by extension near the rifting center and strike slip in outer shelf-slope setting (**Figure 2B**) (Xu et al., 2014; Liu et al., 2016).

The sedimentary study in the Mid-Okinawa Trough focuses on the sediment provenance and its variation during late Quaternary (Dou et al., 2010a, Dou et al., 2010b; Li et al., 2019). The largest contribution to the sediment deposits there is from the Yellow River since the last deglaciation, while other limited sources include Yangtze River-derived and Taiwan-derived sediments (Dou et al., 2010b; Li et al., 2019). In the Middle to Late Holocene, the sediments delivered into the basin was hindered by the barrier effect of the strengthened Kuroshio Current (Dou et al., 2010b; Li et al., 2019). The geophysical observation associated with sedimentary features in the Mid-Okinawa Trough is the shelf-margin delta clinoforms straddling around the shelf edge formed during sea-level lowstands in the shelf-slope setting (Berné et al., 2002; Li et al., 2014; Li et al., 2020). No considerable canyons and basin-floor fan have been detected yet in the area between 28°30′N and 29°10′N (Li et al., 2020). The near-seafloor sediments are mostly mud and the clay mineral is dominated by illite and smectite (core Oki02, Zheng et al., 2014; core M063–05, Li et al., 2019). An area of ~1.2 × ~0.3 km crust of the authigenic carbonate at the water depth of ~600 m has been found near seabed methane seepage by the visual data recorded by a remotely operated vehicle (ROV) ~200 km to the north of the study area. These outcropping carbonates consist of aragonite, pyrite and gypsum, and the isotopic measurements show that the methane feeding their growth is mostly biogenic (Cao et al., 2020).

The Okinawa Tough is known for the seafloor methane seepages and multiple ones along its western slope have been revealed by the record of the geochemical data from the pore water of the gravity cores (C01, C10, cores A and C, and GT-D1, marked in **Figure 1**) (Li et al., 2015; Sun et al., 2015; Xu et al., 2018). The relatively thin Sulfate-Methane Transition Zone at

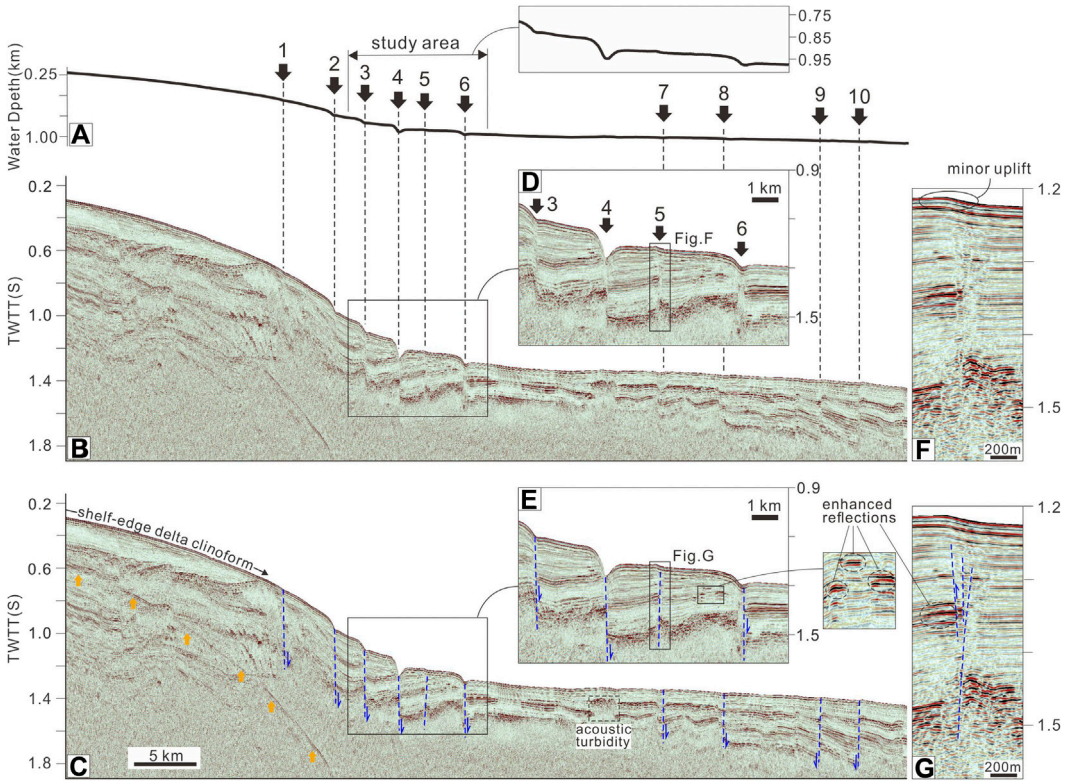

FIGURE 3 | (A,B) A representative seismic cross section and its bathymetric profile. Its location is marked in **Figure 2A**. The presence of the faults marked by numbers 1–10 can be identified both on the bathymetric profile and the seismic cross section **(B,C)**. **(D–G)** Zoomed-in figures showing the faults and their interpretations. Orange arrows mark the seabed multiples.

some sites (e.g., C25 in **Figure 1**) suggests rapid transport of dissolved methane toward the surface (Xu et al., 2018). Escaping of free methane gas has been inferred before to occur near the suspected mud volcano, while the geophysical evidence is recorded in the seismic cross section (**Figure 3**). The features associated with free gases include the ~2.2 km-wide acoustic turbidity out of the study area and some local enhanced reflections at different horizons within it (**Figure 3**).

MATERIALS AND METHODS

Acoustic Data and Sediment Core

We installed a Kongsberg EM122 multi-beam echo-sounder (MBES) system for the acquisition of the acoustic data of the seawater and the seabed. The system mounted by *R/V Haidahao* has a swath angle of 130° and can transmit and receive up to 288 simultaneous beams with a beamwidth of 1°. It has a sounding frequency of 12 kHz and up to 864 soundings per ping in the dual-swath mode. The positioning and the monitoring systems are NAVCOMSF-3050 and Kongsberg SIS, respectively. The parameters of roll, pitch and heading have been corrected during a Sea Acceptance Test before data acquisition. The distances between the dip-oriented and the strike-oriented track lines are 4 and 8 km, respectively. The recorded data, vessel information, and sound velocity profile (SVP) have been integrated and processed by using the QPS Qimera software (including sound velocity correction, creating dynamic surface, etc.). The velocity of the seawater was measured by using the system of the Sea-Bird 911 plus CTD and the X-CTD. QPS Qimera and Fledermaus softwares were used for visualization of the gas plumes in fan view and space, respectively. The swath width increases from 0.94 km on the shelf (water depth of 200 m) to 5.9 km in the deep-water basin (water depth of 1090 m). The recorded backscatter values of the seafloor mosaic images were normalized in Fledermaus software. The cell size of the backscattering images is 11.83 m.

A SIG pulse L5 sparker (20–1000 Hz) was employed at the 1–2 m below the sea level for acquiring the two-dimensional (2-D) high-resolution seismic data. The ship towed the 48-channel streamer (294 m long). The data were sampled at an interval of 0.5 ms and then processed on board by using the ProMAX system (including pre-filtering, NMO, de-noising, etc.). The 2-D multichannel seismic (MCS) data can show the clear image of ~550 ms in TWTT below the seabed with a vertical resolution of ~2 m. Positive polarity is defined by a peak on the seismic trace and displayed as a black-red loop on the cross section.

The acquisition of the *in-situ* sediment cores at D5 was carried out by the seabed drilling rig *Seabull*. It was deployed from *R/V Haidahao* to recover sediments as deep as 55.1 m below the seafloor. The lithology of the sediment cores is not fully recorded.

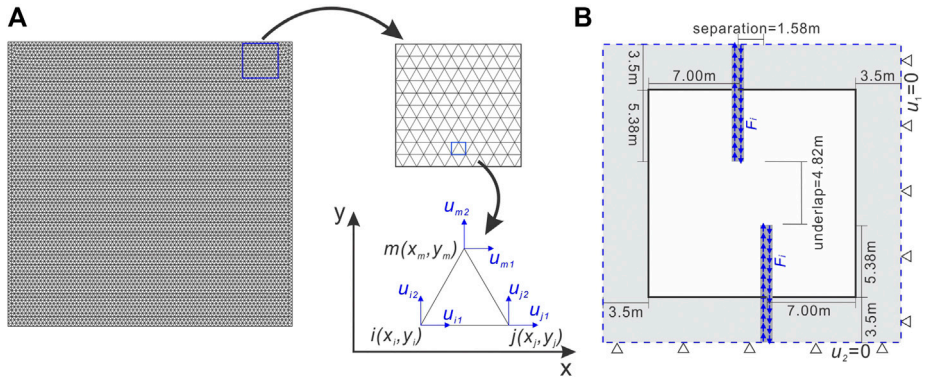

FIGURE 4 | (A) The discretization results of the numerical model. The finite elements are the equilateral triangles except those near the boundaries. Each node has two dimensions of displacements (u_1 and u_2). **(B)** The model is set up with two fault segments. The results bounded by the black box are shown in **Figure 9**. The area marked in grey color is set to eliminate the boundary effect.

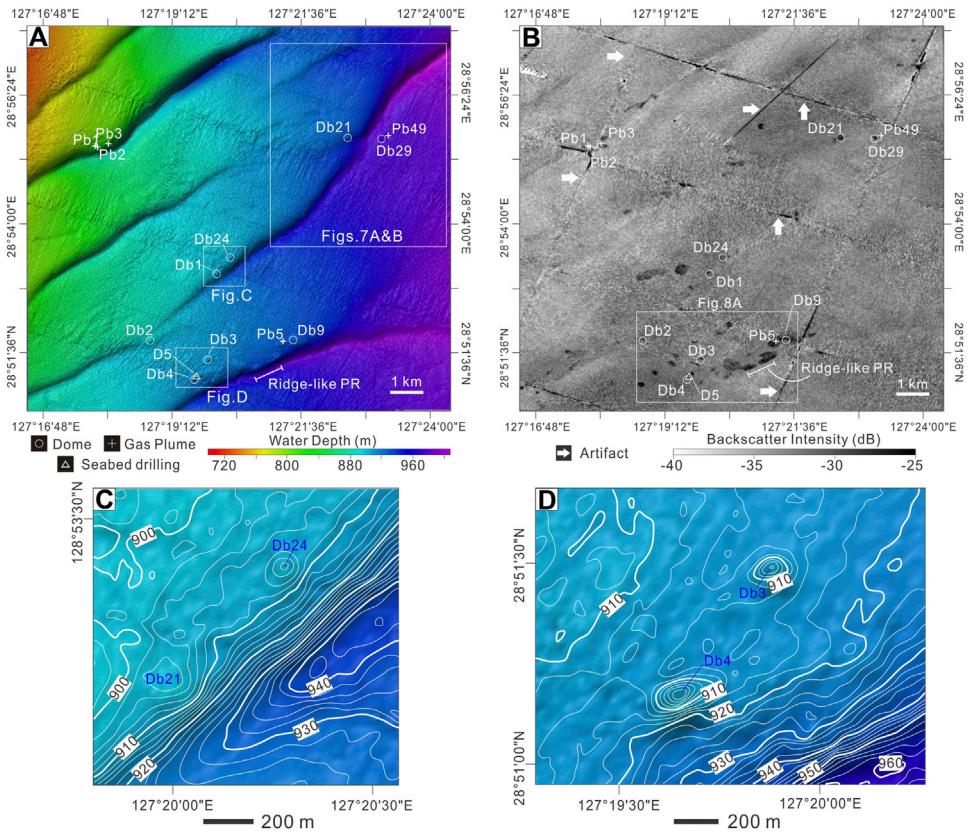

FIGURE 5 | (A) Bathymetric map showing the locations of the features associated with gas emission. All of the curvilinear features at the seabed have been confirmed to be the fault scarps (Li et al., 2021). PR–positive relief in this and the subsequent figures. **(B)** The map of the backscattering intensity at the level of the seabed. Please note the anomalous backscattering intensities occur not only surrounding the domed seabed but also at the relatively flat places. The white arrows mark the artifacts along the nadir lines. **(C,D)** The bathymetric maps near some examples of the positive reliefs (Db24, 21, 3 and 4). The contour interval is 2 m.

Finite Element Method

The FEM has been widely used in the tectonic analysis by considering stress transferring across the interface of the neighboring elements and solving the matrix equation. In this study, we use the FEM to show the role of the shear stress in causing the local compression surrounding the restraining bend between two faults. The 2-D square plane is used to model the marine sediments in plan view, through which the

TABLE 1 | Parameters used in this model (after Nabavi et al., 2017).

Parameters	
Young's modulus (E)	22 GPa
Poisson's ratio (υ)	0.24
Initial force (F_i)	8×10^7 N
Width of fault zone	0.2 m
Length of fault	8.88 m

gas-rich focused fluid flow passed. The dimension of the model is 0.1% of the real one observed in the geophysical data (shown in **Figure 4**; **Table 1**) and the side length is 22.58 m. The peripheral 3.5 m-wide area is modeled to eliminate the effect of the boundary conditions (**Figure 4**). The sediments are assumed to be isotropic. The square plane was discretized into 18620 triangular elements (9508 nodes), most of which are equilateral ones (the discretization of the code distmesh2d can be downloaded from http://persson.berkeley.edu/distmesh/) and the side length is 0.25 m (**Figure 4**). The stiffness matrix of each triangular element $[k]$, for unit thickness, is:

$$[k] = \int\int_A [B]^T [D][B]dxdy \tag{1}$$

where $[B]$ is the strain matrix and $[D]$ is the elastic matrix (Timoshenko and Goodier, 1982). They are expressed as:

$$[B] = \frac{1}{2A}\begin{bmatrix} b_i & 0 & b_j & 0 & b_m & 0 \\ 0 & c_i & 0 & c_j & 0 & c_m \\ c_i & b_i & c_j & b_j & c_m & b_m \end{bmatrix} \tag{2}$$

$$[D] = \frac{E(1-\upsilon)}{(1+\upsilon)(1-2\upsilon)}\begin{bmatrix} 1 & \frac{\upsilon}{1-\upsilon} & 0 \\ \frac{\upsilon}{1-\upsilon} & 1 & 0 \\ 0 & 0 & \frac{1-2\upsilon}{2(1-\upsilon)} \end{bmatrix} \tag{3}$$

where E and υ are Young's modulus and Poisson's ratio, respectively. A is the area of each triangular element and expressed as:

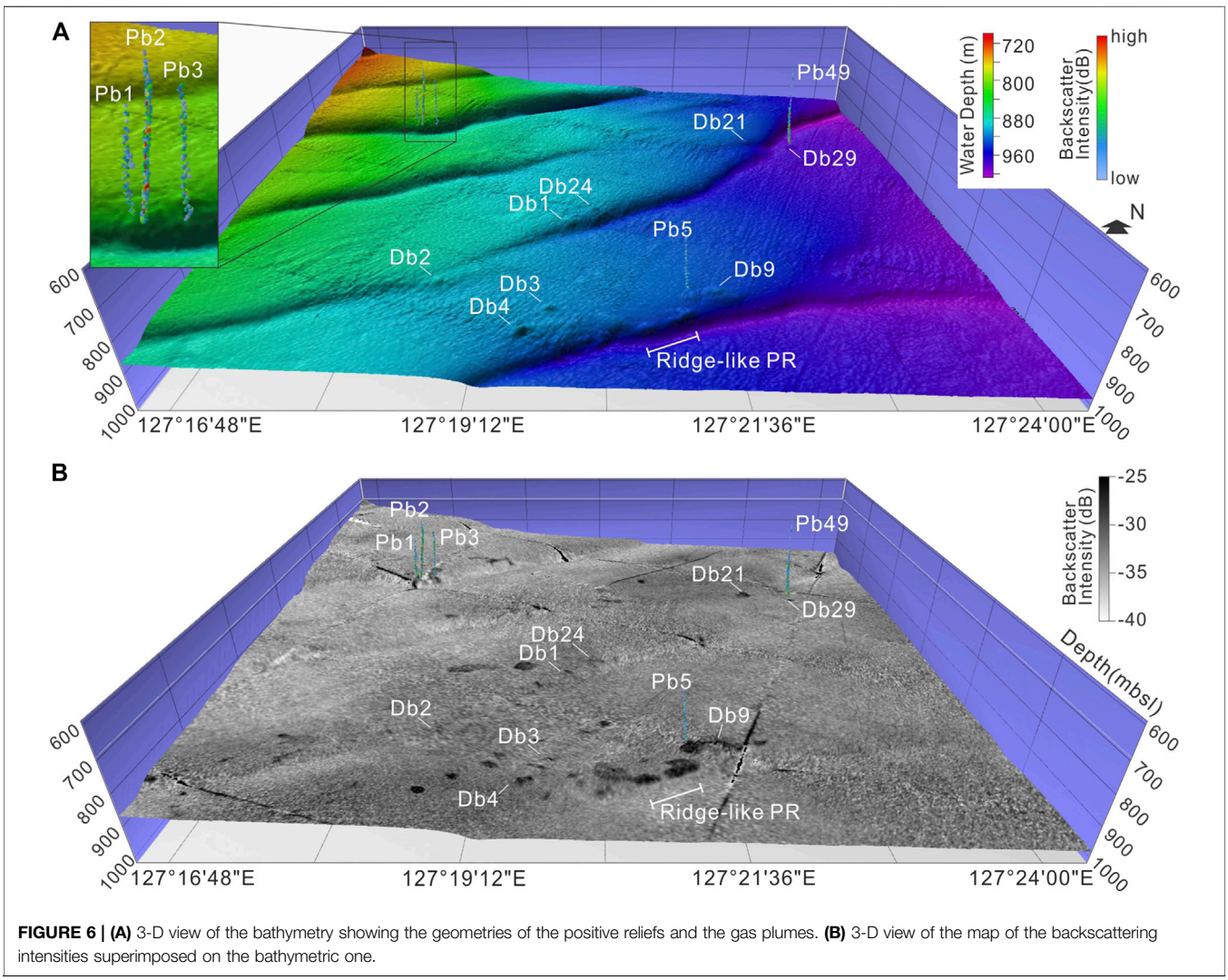

FIGURE 6 | (A) 3-D view of the bathymetry showing the geometries of the positive reliefs and the gas plumes. **(B)** 3-D view of the map of the backscattering intensities superimposed on the bathymetric one.

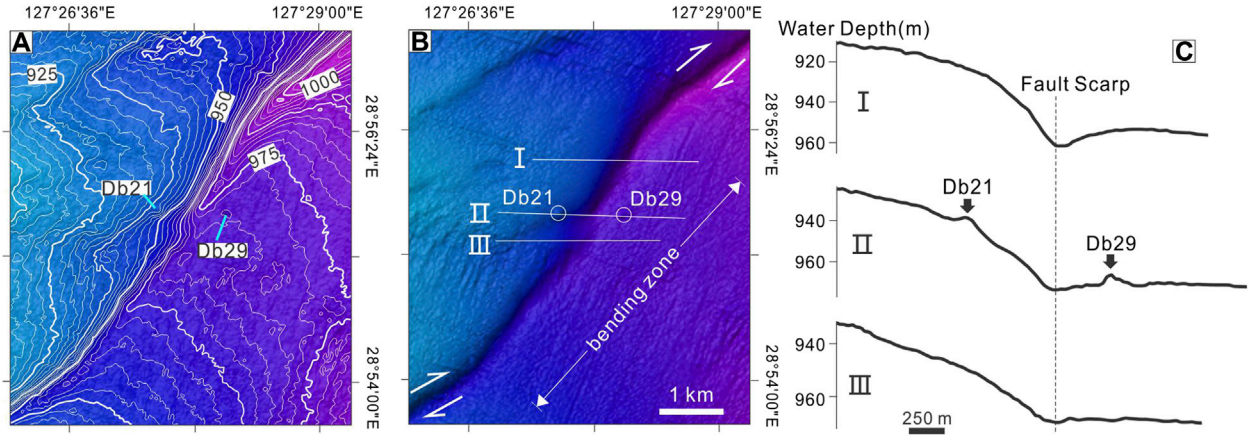

FIGURE 7 | Zoomed-in figure showing the bathymetry **(A)** and the spatial relationship between the fault, the restraining bend and two emission sites **(B)**. The contour interval is 2.5 m. **(C)** Three bathymetric profiles transecting the fault scarp and the positive reliefs of Db21 and 29.

$$A = \frac{1}{2}\left(x_j \times y_m - x_m \times y_j + x_m \times y_i - x_i \times y_m + x_i \times y_j - x_j \times y_i\right) \tag{4}$$

and,

$$\begin{aligned} b_i &= y_j - y_m,\ b_j = y_m - y_i, b_m = y_i - y_j \\ c_i &= x_m - x_j,\ c_j = x_i - x_m, c_m = x_j - x_i \end{aligned} \tag{5}$$

Based on the principle of minimum potential energy, the global balance equation for the entire planar sediments is:

$$[K]\{u\} = \{P\} \tag{6}$$

where $[K]$ is the global stiffness matrix and can be assembled from the stiffness matrix of each triangular element. u is the nodal displacement vector and in this study has two dimensions u_1 and u_2 (x- and y-direction, respectively). P is the nodal force vector. The displacements u_1 at left and right boundaries and u_2 at upper and lower ones are set to zero (**Figure 4**). This boundary condition makes the solutions of $\{u\}$ are unique. Either of the fault zones is 8.88 m long and the horizontal separation is 1.58 m. The geometry of part of the fault is not input into the model so that the dense elements can reveal the features within the bend. Two groups of initial forces (F_i) are set to act on the nodes of two faulted zones and either group has opposite directions (**Figure 4**). **Equation 6** is solved using MATLAB's MLDIVIDE function. The nodal stresses are the weighted average of the neighboring triangular elements. The maximum and minimum principal stresses (σ_1, σ_3) and the Von Mises stresses (σ_{VM}) are expressed as:

$$\left.\begin{matrix}\sigma_1 \\ \sigma_3\end{matrix}\right\} = \frac{\sigma_x + \sigma_y}{2} \pm \sqrt{\left(\frac{\sigma_x - \sigma_y}{2}\right)^2 + \tau_{xy}^2} \tag{7}$$

$$\sigma_{VM} = \sqrt{\sigma_y^2 + \sigma_y^2 - \sigma_x\sigma_y + 3\tau_{xy}^2} \tag{8}$$

where σ_x, σ_y and τ_{xy} are the normal stresses along the x- and y-directions and the shear stresses, respectively. Similar to previous study (e.g., Liu et al., 2010), this model has been tested in a simple case of stepover (90° neutral). In this study, the modeling results are rotated counterclockwise by 39° for comparison with the geophysical observation. The modeling results of the absolute values of stress and displacements are uncertain but instead show a relative pattern. The physical properties of the rocks in the study area have not been tested before, and their values used here are from the previous study using FEM to model stresses in a general case (**Table 1**; Nabavi et al., 2017).

TABLE 2 | Geometries of positive reliefs.

	Length of long axis (m)	Water depth (m)	Elevation (m)	If gas plume exists nearby
Db1	149.7	907.1	6.1	No
Db3	249.2	914.1	10.1	No
Db4	323.5	916.2	16.3	No
Db5	291.8	889.0	4.9	No
Db9	435.3	937.6	8.6	Yes
Db21	264.4	944.2	4.8	No
Db24	175.9	903.1	3.1	No
Db29	251.5	971.6	5.5	Yes

RESULTS

Morphological Features

The seabed in the study area dips southeastwards and the dipping angle decreases seawards, ranging from ~1.5° at the water depth of ~700 m to ~0.5° at >950 m. It is marked by a set of the aligned breaks in the relief along the fault scarps (**Figure 5**). The linear-curvilinear scarps have a NE-SW trend and their separation distance in plan view is ~2.5 km. The vertical displacements of the scarps are 15–90 m and the offsets along each fault plane can be clearly observed on the seismic profiles (**Figure 3**). Some positive reliefs (named with Db) are located close to two of these faults (**Figures 5**, **6**, **7**).

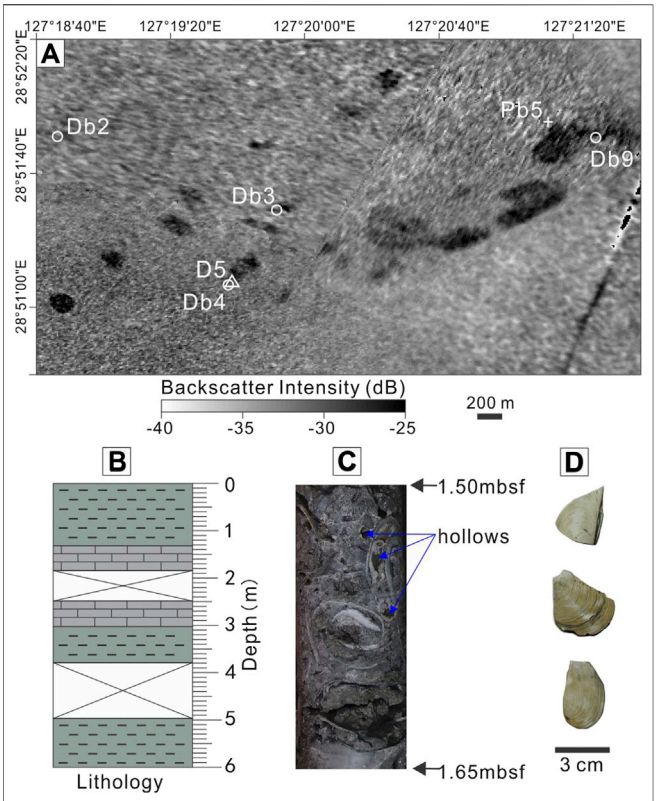

FIGURE 8 | (A) Zoom-in map of the backscattering intensity. Please note that D5 is located within the medium-to high-backscatter areas. **(B)** The recorded lithology of the sediment cores in the upper 6 m. The photos of the carbonate core **(C)** and the angular shells **(D)** are shown here.

Only one positive relief (Db29) is observed to the east of the nearby fault scarp (**Figures 5**, **6**). The water depth, the length of the long axis and the elevation of the positive reliefs are shown in **Table 2**. Most of them have conical geometries (**Figures 5C,D**). There is a ~1 km long ridge-like positive relief elongated along the fault (**Figures 5**, **6**). In the northeastern part of the study area (white box in **Figure 5A**), part of the NE-SW oriented fault scarp bends landwards. Db21 and Db29 are located at either side of the bending zone and have a similar distance away from it, forming a sub-symmetric feature in plan view (**Figure 7**).

Hydroacoustic Features

Five bundle-like clusters of the acoustic anomalies have been identified in the study area (**Figure 6**). The gas plumes (named with Pb and numbers) have a higher backscattering intensity than the seawater of the background (**Figure 6**). The relatively high-backscatter intensities occur in the lower and the middle parts of each gas plume (**Figure 6**). The gas plumes have a height of 163–355 m. Two of the gas plumes (Pb5 and Pb49) emanated from the surrounding areas of the positive reliefs, while the other three ones (Pb1-3) cluster around the arcuate part of one fault (**Figures 5**, **6**).

Backscattering Features at the Seabed

There are some medium-to high-backscatter areas at the level of the seabed (shown as the bright black patches in **Figures 5B**, **6B**). Their intensities are 5–10 dB higher than the mean of those of the background marine sediments. The bright patches are sub-circular, sub-elliptical or irregular in plan view (**Figure 5B**). Most of them cover an area of <0.1 km^2 and the largest one occurs near the ridge-like positive relief (~0.3 km^2, **Figure 5B**). Part of the bright areas are located close to the fault scarps, while the rest occur at the places where there is no topographic anomaly (**Figures 5B**, **6B**). Not all of the positive reliefs are superimposed by the areas of the enhanced backscattering intensities.

Sediment Cores

D5 is located within a medium-to high-backscatter area of the seabed (**Figure 8**). The upper 6 m-long sediment cores at D5 mainly consist of greyish clay and a strong H_2S odor was smelt during processing the samples prior to the on-board test. Angular shells occur at the depth of ~0.45 m (**Figure 8**). Neither gas hydrates nor soupy structures were found. Carbonates occur at the depth ranges of 1.33–1.85 m and 2.50–3.05 m deep and hollows and shells are common within them (**Figure 8**).

Numerical Model

The variations of the displacements along x- and y-directions (u_1, u_2) display different symmetric patterns (**Figure 9**). The u_1 values are near zero in the middle zone, increasing and decreasing along the positive and the negative y-directions toward the upper and the lower boundaries. There are some anomalous values near the fault tips (**Figure 9**). The variations of the u_2 values are symmetric about the faults and their linkage zone. Positive and negative values occur to the left and the right side of the symmetric line (**Figure 9**). The normal stresses along x- and y-direction (σ_x, σ_y) show the opposite variation pattern (**Figure 9**). The lobe-like zones of the positive and negative σ_x values are located inside and outside the linkage zone, respectively. This pattern is converse for the σ_y values (**Figure 9**). The zones of high values of maximum principal stresses (high-σ_1 zone) and low values of minimum principal stresses (low-σ_3 zone) are both near the fault tips. For σ_1 and σ_3, two zones extending from the fault tips coalesce within the linkage zone to form a sigmoidal geometry (**Figure 9**). The extending directions are slightly different between σ_1 and σ_3. The σ_1 directions between the faults are almost perpendicular to that of the segment between them (red dashed line in **Figure 9**). The arrays sharing such direction together form a lozenge-like zone (blue dashed line in **Figure 9**). The zone of similar geometry also occurred in the modeling results of a transpression zone in the strike-slip setting by Nabavi et al., 2017. The directions of the maximal principal stresses within it will rotate more parallel with the trend of the fault as the underlap distance decreases (Nabavi et al., 2017). The lobes of enhanced Von Mises stresses (σ_{VM}) do not deflect near the fault tips and the coalesced zone shows a symmetric pattern about the segment linking the fault tips.

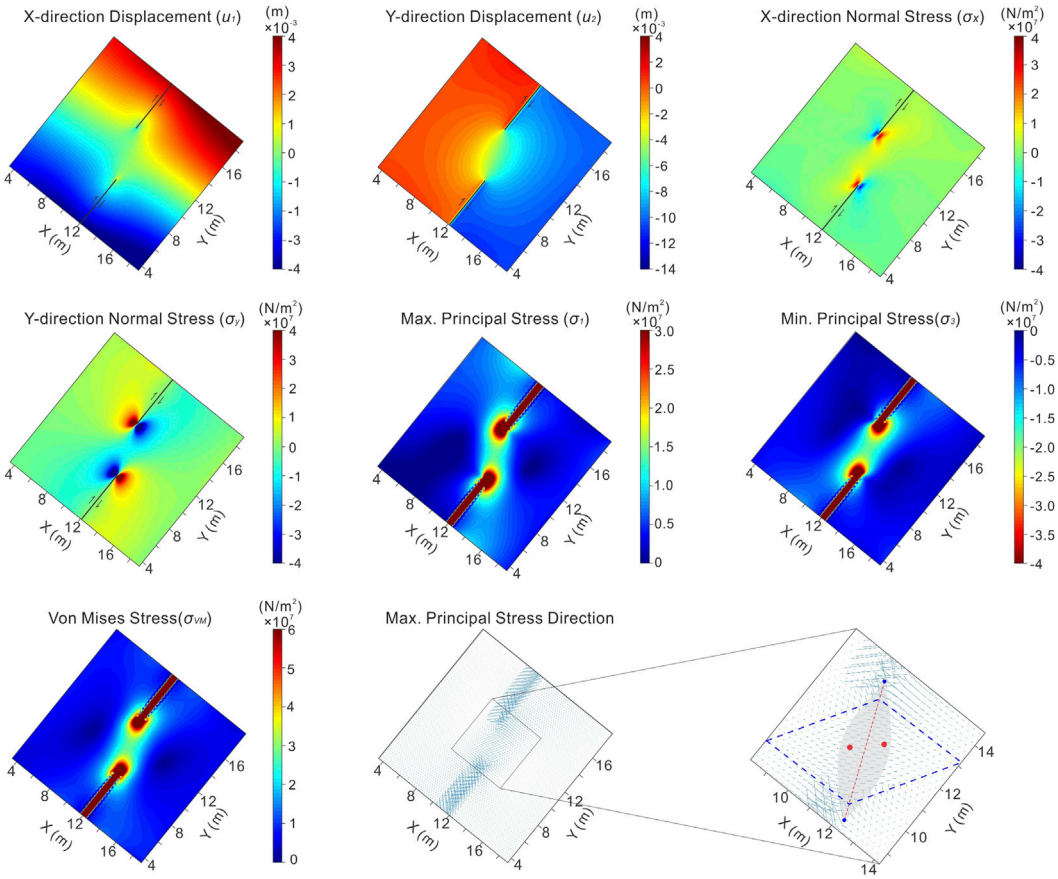

FIGURE 9 | Numerical modeling results of the distribution of displacements, normal stresses, maximal and minimal principal stresses and Von Mises stress in the hypothetical strike-slip setting. Red and blue dots mark the locations of the gas emissions (Db21 and 29) and the fault tips, respectively. Their locations in plan view are plotted based on the MBES data shown in **Figures 5** and **7**. The red dashed line represents the segment between the fault tips and the gray zone suggests the conceptual area of the restraining bend. The area bounded by the dashed blue line marks the lozenge-like zone sharing the same direction of the maximal principal stress and has been seen in the modeling result by Nabavi et al., 2017.

DISCUSSION

Acoustic Features Associated with Gas Emission

The gas plumes are compelling evidence of the present-day emission of the gas bubbles from the seabed. Their presence indicates that the free gas bubbles can rise through the water column by hundreds of meters before breaking up. It has to be stated that the frequency of 12 kHz used in this study for data acquisition is not high enough to reveal all of the emissions of gas bubbles, particularly for those consisting of dispersed gas bubbles (i.e., no considerable bubble stream). The gas plumes observed here should represent high gas flux and the rapid discharge of free gases.

The maps of the backscattering intensity show that some bright patches scatter around the seabed (**Figures 5**, **6**). The enhancement of the intensity should be attributed to the presence of authigenic carbonates accompanied by the free methane gases in the sub-seafloor sediments (Fonseca, 2001; Naudts et al., 2008). The cores of the authigenic carbonates associated with methane seepage have been got near Db4 (D5 in **Figure 5**), and anomalous backscattering intensity has also been observed there. The bicarbonate required for the formation of these carbonates is from the anaerobic oxidation of methane (AOM, Dale et al., 2008), which suggests high-flux methane had passed through the areas of these carbonates for years. Therefore, the bright patches of the backscattering intensity indicate the places of gas escaping that were active in the recent past.

The locations of the positive reliefs have a good match with those of the patches of the medium-to high-backscattering intensity (**Figures 5**, **6**). Some hypotheses have been proposed how the sub-conical cones formed. They could result from the vertical displacement of sediments during the expulsion of pore fluids, the buoyancy of vertically continuous gas accumulation (Koch et al., 2015), or volume expansion during the formation of gas hydrate pingoes (Serié et al., 2012). These mechanisms point toward the occurrence of free gases bypassing the shallow underconsolidated sediments, though which one works here is not clear. The

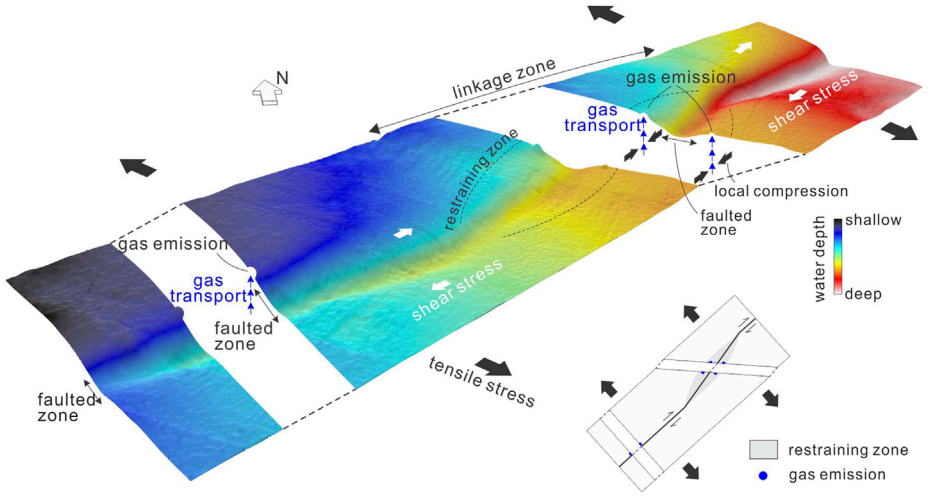

FIGURE 10 | Conceptual model showing the gas emissions in the transtensile regime. Inset shows the locations of the restraining zone and the gas emissions in plan view.

positive reliefs and the authigenic carbonates can both be taken as the geological expressions of the intermittent methane-rich gas emissions. These expressions can sometimes coalesce at the level of the seabed to form a larger one (e.g., ridge-like positive relief, **Figures 5**, **6**).

Gas Emission in Transtensile Regime

The close spatial relationship between the faults and the acoustic features suggests the role of the faulting in determining the potential locations of gas emission. Consistent with the interpretations in the previous studies (e.g., Kimura, 1985; Gungor et al., 2012), the NE-SW oriented faults here are interpreted to form during the episodic back-arc rifting of the Okinawa Trough. It has to be stated that their trends are slightly different from those observed at the seabed in the deep-water setting ~45 km to the east of the study area (**Figure 2**). The difference of the fault trend between the deep-water setting and the slope here could be explained by the oblique rifting in the northern and the middle part of the Okinawa Trough (Fabbri et al., 2004). Its physical modeling results confirm this difference between the rift axis zone and the slope (Autin et al., 2013). It is very likely that part of the free gases in the subsurface escaped along the vertically permeable sediments of the damage zone of the faults that formed by back-arc rifting. The resultant extension would affect gas emissions more in the area closer to the rifting center (**Figure 1**; Li et al., 2021), in which the strike-slip component is few. Therefore, the faulting driven by back-arc extension provided the migration pathways and the preferential exits for the free gases, and thus determines the potential locations of gas emissions at the seabed.

Apart from the tensile stress, the shear one also has a contribution to the gas emissions (**Figure 10**). The start of the gas emission requires lasting building up of the pore pressure and this can be primed by the local compression in the transtensive settings. The excess pore pressures are expected to occur in the restraining bend (**Figure 10**). This is supported by the numerical modeling results showing that the relatively high σ_1 within the bend (**Figure 9**). These modeled stresses are almost perpendicular to that of the segment between the fault tips (red dashed line in **Figure 9**) and cause local compression toward it. This compression has also been evidenced by sediment thickening close to the restraining bend in a sand-box model (McClay and Bonora, 2001). Overall, the shallow sediments near these reliefs are most likely to be compressed as the tectonic activity continued and the resultant increasing pore pressure primed the formation of the gas emissions (**Figure 10**). How these gas emissions formed is different from that in the Lusi mud volcano in Indonesia. The gas emissions there are located very close to a planar strike-slip fault and its activity is interpreted to significantly reduce the critical fluid pressure required to induce sediment fluidization (Mazzini et al., 2009). It is concluded that the restraining bend, other than the strike-slip fault planes, could be the potential place for the gas emissions bypassing the shallow marine sediments.

CONCLUSION

Multiple gas emissions are distributed unevenly along the faults at the seabed in the western slope of the Mid-Okinawa Trough. Part of the gas bubbles formed the gas plumes after escaping from the seabed, but did not reach the shallow seawater. Some other gases were trapped immediately below the domed seabed and at the places where there are no local morphological features. As a result of the ongoing back-arc rifting, the faulting allowed the free gases in the subsurface to pass through the shallow sediments. The components of the shear stresses caused local compression within the bending zone of the fault and the resultant increased pore pressure primed the formation of the gas emissions.

DATA AVAILABILITY STATEMENT

The original contributions presented in the study are included in the article/Supplementary Material, further inquiries can be directed to the corresponding author.

AUTHOR CONTRIBUTIONS

AL offered the key idea, designed and ran the FEM modelling, and drafted the manuscript. FC, NW and QL managed the project of the geophysical survey, provided the available data and the context of the methane seeps, vents and emissions in the Okinawa Trough. GY, GD and DL did the work of data processing and visualization. YS and XW checked the validity of the FEM model and made comments about the manuscript text.

FUNDING

This research is supported by the projects of the National Key R&D Program of China (2018YFC0310001), the National Natural Science Foundation of China (91858208 and 42006066) and Shandong Provincial Natural Science Foundation, China (ZR201807100270).

ACKNOWLEDGMENTS

We are grateful for the efforts made by the crew members in acquiring the geophysical data. We thank Tingting Wu from Guangzhou Marine Geological Survey for making suggestions concerning improving the imaging quality of the gas plumes. We thank three anonymous reviewers for their constructive comments.

REFERENCES

Autin, J., Bellahsen, S., Husson, L., Beslier, M. O., and d'Acremont, E. (2013). The role of structural inheritance in oblique rifting: Insights from analogue models and application to the Gulf of Aden. *Tectonophysics,* 607, 51–54.

Berné, S., Vagner, P., Guichard, F., Lericolais, G., Liu, Z., Trentesaux, A., et al. (2002). Pleistocene forced regressions and tidal sand ridges in the East China Sea. *Mar. Geol.* 188 (3-4), 293–315. doi:10.1016/s0025-3227(02)00446-2

Biastoch, A., Treude, T., Rüpke, L. H., Riebesell, U., Roth, C., Burwicz, E. B., et al. (2011). Rising Arctic Ocean temperatures cause gas hydrate destabilization and ocean acidification. *Geophys. Res. Lett.* 38 (8), 1–5. doi:10.1029/2011GL047222

Cao, H., Sun, Z., Wu, N., Liu, W., Liu, C., Jiang, Z., et al. (2020). Mineralogical and geochemical records of seafloor cold seepage history in the northern Okinawa Trough, East China Sea. *Deep Sea Res. Oceanogr. Res. Pap.* 155, 103165. doi:10.1016/j.dsr.2019.103165

Cartwright, J., and Santamarina, C. (2015). Seismic characteristics of fluid escape pipes in sedimentary basins: implications for pipe genesis. *Mar. Petrol. Geol.* 65, 126–140. doi:10.1016/j.marpetgeo.2015.03.023

Ciotoli, G., Procesi, M., Etiope, G., Fracassi, U., and Ventura, G. (2020). Influence of tectonics on global scale distribution of geological methane emissions. *Nat. Commun.* 11 (1), 2305–2308. doi:10.1038/s41467-020-16229-1

Dale, A. W., Regnier, P., Knab, N. J., Jørgensen, B. B., and Van Cappellen, P. (2008). Anaerobic oxidation of methane (AOM) in marine sediments from the Skagerrak (Denmark): II. Reaction-transport modeling. *Geochem. Cosmochim. Acta* 72 (12), 2880–2894. doi:10.1016/j.gca.2007.11.039

Dou, Y., Yang, S., Liu, Z., Clift, P. D., Shi, X., Yu, H., et al. (2010a). Provenance discrimination of siliciclastic sediments in the middle Okinawa Trough since 30 ka: constraints from rare earth element compositions. *Mar. Geol.* 275 (1–4), 212–220. doi:10.1016/j.margeo.2010.06.002

Dou, Y., Yang, S., Liu, Z., Clift, P. D., Yu, H., Berne, S., et al. (2010b). Clay mineral evolution in the central Okinawa Trough since 28 ka: implications for sediment provenance and paleoenvironmental change. *Palaeogeogr. Palaeoclimatol. Palaeoecol.* 288 (1–4), 108–117. doi:10.1016/j.palaeo.2010.01.040

Dupre, S., Scalabrin, C., Grall, C., Augustin, J., Henry, P., Şengor, A. M. C., et al. (2015). Tectonic and sedimentary controls on widespread gas emissions in the sea of Marmara: results from systematic, shipborne multibeam echo sounder water column imaging. *J. Geophys. Res. Solid Earth* 120 (5), 2891–2912. doi:10.1002/2014jb011617

Fabbri, O., Monie, P., and Fournier, M. (2004). Transtensional deformation at the junction between the Okinawa trough back-arc basin and the SW Japan Island arc. *Geol. Soc. London Spec. Publ.* 227 (1), 297–312. doi:10.1144/gsl.sp.2004.227.01.15

Feng, D., Qiu, J., Hu, Y., Peckmann, J., Guan, H., Tong, H., et al. (2018). Cold seep systems in the South China Sea: an overview. *J. Asian Earth Sci.* 168, 3–16. doi:10.1016/j.jseaes.2018.09.021

Fonseca, L. (2001). A model for backscattering angular response of gassy sediments: applications to petroleum exploration and development programs. Ph.D. thesis. Durham, NH: University of New Hampshire. 36, 56–103.

Geli, L., Henry, P., Zitter, T., Dupre, S., Tryon, M., Cagatay, M. N., et al. (2008). Gas emissions and active tectonics within the submerged section of the North Anatolian Fault zone in the Sea of Marmara. *Earth Planet Sci. Lett.* 274 (1–2), 34–39. doi:10.1016/j.epsl.2008.06.047

Gennari, G., Spezzaferri, S., Comas, M. C., Ruggeberg, A., Lopezrodriguez, C., and Pinheiro, L. M. (2013). Sedimentary sources of the mud-breccia and mud volcanic activity in the Western Alboran Basin. *Mar. Geol.* 339, 83–95. doi:10.1016/j.margeo.2013.04.002

Gungor, A., Lee, G. H., Kim, H. J., Han, H. C., Kang, M. H., Kim, J., et al. (2012). Structural characteristics of the northern Okinawa Trough and adjacent areas from regional seismic reflection data: geologic and tectonic implications. *Tectonophysics* 522–523, 198–207. doi:10.1016/j.tecto.2011.11.027

Heeschen, K. U., Tréhu, A. M., Collier, R. W., Suess, E., and Rehder, G. (2003). Distribution and height of methane bubble plumes on the Cascadia Margin characterized by acoustic imaging. *Geophys. Res. Lett.* 30 (12). doi:10.1029/2003gl016974

Huguen, C., Mascle, J., Chaumillon, E., Kopf, A., Woodside, J., and Zitter, T. (2004). Structural setting and tectonic control of mud volcanoes from the central mediterranean ridge (eastern mediterranean). *Mar. Geol.* 209 (1-4), 245–263. doi:10.1016/j.margeo.2004.05.002

Hustoft, S., Dugan, B., and Mienert, J. (2009). Effects of rapid sedimentation on developing the Nyegga pockmark field: constraints from hydrological modeling and 3-D seismic data, offshore mid-Norway. *Geochem. Geophys. Geosyst.* 10 (6). doi:10.1029/2009gc002409

Judd, A. G., Hovland, M., Dimitrov, L. I., Gil, S. G., and Jukes, V. (2002). The geological methane budget at Continental Margins and its influence on climate change. *Geofluids* 2 (2), 109–126. doi:10.1046/j.1468-8123.2002.00027.x

Kimura, M. (1985). back-arc rifting in the Okinawa trough. *Mar. Petrol. Geol.* 2 (3), 222–240. doi:10.1016/0264-8172(85)90012-1

Koch, S., Berndt, C., Bialas, J., Haeckel, M., Crutchley, G., Papenberg, C., Haeckel, M., and Greinert, J. (2015). Gas-controlled seafloor doming. *Geology,* 43 (7), 571–574. doi:10.1016/0025-3227(80)90032-8

Lee, C., Shor, G. G., Bibee, L. D., Lu, R. S., and Hilde, T. W. (1980). Okinawa Trough: origin of a back-arc basin. *Mar. Geol.* 35 (1–3), 219–241. doi:10.1016/0025-3227(80)90032-8

Letouzey, J., and Kimura, M. (1985). Okinawa Trough genesis: structure and evolution of a backarc basin developed in a continent. *Mar. Petrol. Geol.* 2 (2), 111–130. doi:10.1016/0264-8172(85)90002-9

Li, A., Cai, F., Wu, N., Li, Q., Yan, G., Sun, Y., et al. (2020). Late Pleistocene shelf-edge delta clinoforms along the rift margin of the northern Okinawa Trough. *Geol. J.* 55, 6450–6461.

Li, A., Cai, F., Wu, N., Li, Q., Yan, G., Sun, Y., et al. (2021). Structural controls on widespread methane seeps in the back-arc basin of the Mid-Okinawa trough. *Ore Geol. Rev.* 129, 103950, 1–12. doi:10.1016/j.oregeorev.2020.103950

Li, A., Davies, R. J., and Mathias, S. (2017). Methane hydrate recycling offshore of Mauritania probably after the last glacial maximum. *Mar. Petrol. Geol.* 84, 323–331. doi:10.1016/j.marpetgeo.2017.04.007

Li, G., Li, P., Liu, Y., Qiao, L., Ma, Y., Xu, J., et al. (2014). Sedimentary system response to the global sea level change in the East China Seas since the last glacial maximum. *Earth Sci. Rev.* 139, 390–405. doi:10.1016/j.earscirev.2014.09.007

Li, Q., Cai, F., Liang, J., Shao, H., Dong, G., Wang, F., et al. (2015). Geochemical constraints on the methane seep activity in western slope of the middle Okinawa Trough, the East China Sea. *Sci. China Earth Sci.* 58 (6), 986–995. doi:10.1007/s11430-014-5034-x

Li, Q., Zhang, Q., Li, G., Liu, Q., Chen, M. T., Xu, J., et al. (2019). A new perspective for the sediment provenance evolution of the middle Okinawa Trough since the last deglaciation based on integrated methods. *Earth Planet Sci. Lett.* 528, 115839. doi:10.1016/j.epsl.2019.115839

Liu, B., Li, S. Z., Suo, Y. H., Li, G. X., Dai, L. M., Somerville, I. D., et al. (2016). The geological nature and geodynamics of the Okinawa Trough, western pacific. *Geol. J.* 51, 416–428. doi:10.1002/gj.2774

Liu, M., Wang, H., and Li, Q. (2010). Inception of the eastern California shear zone and evolution of the Pacific-North American plate boundary: from kinematics to geodynamics. *J. Geophys. Res. Solid Earth* 115 (B7), 1–12. doi:10.1029/2009JB007055

Mazzini, A., Nermoen, A., Krotkiewski, M., Podladchikov, Y. Y., Planke, S., and Svensen, H. (2009). Strike-slip faulting as a trigger mechanism for overpressure release through piercement structures. Implications for the Lusi mud volcano, Indonesia. *Mar. Petrol. Geol.* 26 (9), 1751–1765. doi:10.1016/j.marpetgeo.2009.03.001

McClay, K., and Bonora, M. (2001). Analog models of restraining stepovers in strike-slip fault systems. *Am. Assoc. Pet. Geol. Bull.* 85 (2), 233–260. doi:10.1306/8626c7ad-173b-11d7-8645000102c1865d

McGinnis, D. F., Greinert, J., Artemov, Y., Beaubien, S. E., and Wuest, A. (2006). Fate of rising methane bubbles in stratified waters: how much methane reaches the atmosphere? *J. Geophys. Res.: Oceans* 111 (C9). doi:10.1029/2005jc003183

Myhre, C. L., Ferré, B., Platt, S., Silyakova, A., Hermansen, O., Allen, G., et al. (2016). Extensive release of methane from Arctic seabed west of Svalbard during summer 2014 does not influence the atmosphere. *Geophys. Res. Lett.* 43 (9), 4624–4631. doi:10.1002/2016gl068999

Nabavi, S. T., Alavi, S. A., Mohammadi, S., Ghassemi, M. R., and Frehner, M. (2017). Analysis of transpression within contractional fault steps using finite-element method. *J. Struct. Geol.* 96, 1–20. doi:10.1016/j.jsg.2017.01.004

Naudts, L., Greinert, J., Artemov, Y. G., Beaubien, S. E., Borowski, C., and De Batist, M. (2008). Anomalous sea-floor backscatter patterns in methane venting areas, Dnepr paleo-delta, NW Black Sea. *Mar. Geol.* 251 (3-4), 253–267. doi:10.1016/j.margeo.2008.03.002

Plaza-Faverola, A., and Keiding, M. (2019). Correlation between tectonic stress regimes and methane seepage on the western Svalbard margin. *Solid Earth* 10 (1), 79–94. doi:10.5194/se-10-79-2019

Plaza-Faverola, A., Pecher, I., Crutchley, G., Barnes, P. M., Bünz, S., Golding, T., et al. (2014). Submarine gas seepage in a mixed contractional and shear deformation regime: cases from the Hikurangi oblique-subduction margin. *Geochem., Geophys., Geosyst.* 15 (2), 416–433. doi:10.1002/2013gc005082

Reed, D. L., Silver, E. A., Tagudin, J. E., Shipley, T. H., and Vrolijk, P. (1990). Relations between mud volcanoes, thrust deformation, slope sedimentation, and gas hydrate, offshore North Panama. *Mar. Petrol. Geol.* 7 (1), 44–54. doi:10.1016/0264-8172(90)90055-l

Riedel, M., Scherwath, M., Römer, M., Veloso, M., Heesemann, M., and Spence, G. D. (2018). Distributed natural gas venting offshore along the Cascadia margin. *Nat. Commun.* 9, 3264. doi:10.1038/s41467-018-05736-x

Roberts, H. H. (2001). Fluid and gas expulsion on the northern gulf of Mexico continental slope: mud-prone to mineral-prone responses. *Nat. Gas Hydrates Geophys. Monogr. ser* 124, 145–161. doi:10.1029/gm124p0145

Römer, M., Sahling, H., Pape, T., Bahr, A., Feseker, T., Wintersteller, P., et al. (2012). Geological control and magnitude of methane ebullition from a high-flux seep area in the Black Sea—the Kerch seep area. *Mar. Geol.* 319-322, 57–74. doi:10.1016/j.margeo.2012.07.005

Römer, M., Wenau, S., Mau, S., Veloso, M., and Bohrmann, G. (2017). Assessing marine gas emission activity and contribution to the atmospheric methane inventory: a multidisciplinary approach from the Dutch Dogger bank seep area (North Sea). *Geochem., Geophys., Geosyst.* 18 (7), 2617–2633. doi:10.1002/2017gc006995

Sauter, E. J., Muyakshin, S. I., Charlou, J. L., Schlüter, M., Boetius, A., Jerosch, K., et al. (2006). Methane discharge from a deep-sea submarine mud volcano into the upper water column by gas hydrate-coated methane bubbles. *Earth Planet Sci. Lett.* 243 (3–4), 354–365. doi:10.1016/j.epsl.2006.01.041

Schmidt, M., Hensen, C., Mörz, T., Müller, C., Grevemeyer, I., Wallmann, K., et al. (2005). Methane hydrate accumulation in "Mound 11" mud volcano, Costa Rica forearc. *Mar. Geol.* 216 (1–2), 83–100. doi:10.1016/j.margeo.2005.01.001

Serié, C., Huuse, M., and Schødt, N. H. (2012). Gas hydrate pingoes: deep seafloor evidence of focused fluid flow on continental margins. *Geology* 40 (3), 207–210. doi:10.1130/g32690.1

Sibuet, J. C., Letouzey, J., Barbier, F., Charvet, J., Foucher, J. P., Hilde, T. W., et al. (1987). Back arc extension in the Okinawa trough. *J. Geophys. Res.: Solid Earth* 92 (B13), 14041–14063. doi:10.1029/JB092iB13p14041

Smith, A. J., Mienert, J., Bünz, S., and Greinert, J. (2014). Thermogenic methane injection via bubble transport into the upper Arctic Ocean from the hydrate-charged Vestnesa ridge, Svalbard. *Geochem. Geophys. Geosyst.* 15 (5), 1945–1959. doi:10.1002/2013gc005179

Somoza, L., Leon, R., Ivanov, M., Fernández-Puga, M., Gardner, J., Hernández-Molina, F., et al. (2003). Seabed morphology and hydrocarbon seepage in the Gulf of Cadiz mud volcano area: acoustic imagery, multibeam and ultra-high resolution seismic data. *Mar. Geol.* 195 (1–4), 153–176. doi:10.1016/s0025-3227(02)00686-2

Sun, Z., Wei, H., Zhang, X., Shang, L., Yin, X., Sun, Y., et al. (2015). A unique Fe-rich carbonate chimney associated with cold seeps in the Northern Okinawa Trough, East China Sea. *Deep-Sea Res. Part I. Oceanogr. Res. Pap.* 95, 37–53. doi:10.1016/j.dsr.2014.10.005

Timoshenko, S. P., and Goodier, J. N. (1982). *Theory of elasticity*. 3rd Edn. Singapore: McGraw-Hill International Editions.

Wang, J., Wu, S., Kong, X., Ma, B., Li, W., Wang, D., et al. (2018). Subsurface fluid flow at an active cold seep area in the Qiongdongnan Basin, northern South China Sea. *J. Asian Earth Sci.* 168, 17–26. doi:10.1016/j.jseaes.2018.06.001

Watson, S. J., Mountjoy, J. J., Barnes, P. M., Crutchley, G. J., Lamarche, G., Higgs, B., et al. (2019). Focused fluid seepage related to variations in accretionary wedge structure, Hikurangi margin, New Zealand. *Geology* 48 (1), 56–61. doi:10.1130/g46666.1

Westbrook, G. K., Thatcher, K. E., Rohling, E. J., Piotrowski, A. M., Pälike, H., Osborne, A. H., et al. (2009). Escape of methane gas from the seabed along the West Spitsbergen continental margin. *Geophys. Res. Lett.* 36 (15). doi:10.1029/2009gl039191

Xu, C., Wu, N., Sun, Z., Zhang, X., Geng, W., Cao, H., et al. (2018). Methane seepage inferred from pore water geochemistry in shallow sediments in the western slope of the Mid-Okinawa trough. *Mar. Petrol. Geol.* 98, 306–315. doi:10.1016/j.marpetgeo.2018.08.021

Xu, J., Ben-Avraham, Z., Kelty, T., and Yu, H. S. (2014). Origin of marginal basins of the NW Pacific and their plate tectonic reconstructions. *Earth Sci. Rev.* 130, 154–196. doi:10.1016/j.earscirev.2013.10.002

Yamaji, A. (2003). Slab rollback suggested by latest Miocene to Pliocene forearc stress and migration of volcanic front in southern Kyushu, northern Ryukyu Arc. *Tectonophysics,* 364 (1-2), 9–24. doi:10.1002/2014gl060483

Yamamoto, A., Yamanaka, Y., Oka, A., and Abe-Ouchi, A. (2014). Ocean oxygen depletion due to decomposition of submarine methane hydrate. *Geophys. Res. Lett.* 41 (14), 5075–5083. doi:10.1002/2014gl060483

Zheng, X., Li, A., Wan, S., Jiang, F., Kao, S. J., and Johnson, C. (2014). ITCZ and ENSO pacing on east asian winter monsoon variation during the Holocene: sedimentological evidence from the Okinawa trough. *J. Geophys. Res.: Oceans* 119 (7), 4410–4429. doi:10.1002/2013jc009603

Conflict of Interest: The authors declare that the research was conducted in the absence of any commercial or financial relationships that could be construed as a potential conflict of interest.

frontiers in Earth Science

ORIGINAL RESEARCH
published: 24 March 2021
doi: 10.3389/feart.2021.531714

Distribution of Methane Plumes on Cascadia Margin and Implications for the Landward Limit of Methane Hydrate Stability

Susan G. Merle[1], Robert W. Embley[1], H. Paul Johnson[2], T.-K. Lau[1], Benjamin J. Phrampus[3], Nicole A. Raineault[4] and Lindsay J. Gee[4]*

[1]The Cooperative Institute for Marine Resources Studies - Oregon State University, and NOAA PMEL Earth Ocean Interactions Program, Newport, OR, United States, [2]School of Oceanography, University of Washington, Seattle, WA, United States, [3]US Naval Research Laboratory, Code 7432, Stennis Space Center, Hancock County, MS, United States, [4]Ocean Exploration Trust Inc., Narragansett, RI, United States

Nearly 3,500 methane bubble streams, clustered into more than 1,300 methane emission sites, have been identified along the US Cascadia margin, derived both from archived published data and 2011, 2016–2018 dedicated multibeam surveys using co-registered seafloor and water column data. In this study, new multibeam sonar surveys systematically mapped nearly 40% of the US Cascadia margin, extending from the Strait of Juan de Fuca in the north to the Mendocino fracture zone in the south, and bounded East–West by the coast and the base of the accretionary prism. The frequency-depth histogram of the bubble emission sites has a dominant peak at the 500 m isobar, which extends laterally along much of the Cascadia margin off Oregon and Washington. Comparisons with published seismic data on the distribution of bottom simulating reflectors (BSR), which is the acoustic impedance boundary between methane hydrate (solid phase) and free gas phase below, correlates the bottom simulating reflectors upward termination of the feather edge of methane hydrate stability (FEMHS) zone and the newly identified bubble emission sites off Oregon and Washington. The Cascadia margin off northern California, where the BSR ends seaward of the FEMHS, has fewer sites centered on the 500 m isobaths, although data are more limited there. We propose that the peak in bubble emission sites observed near the 500 m isobath results from migration of free gas from beneath the solid phase of the BSR upslope to the FEMHS termination zone, and suggest that this boundary will be useful to monitor for a change in methane release rate potentially related to a warming ocean.

Keywords: methane, bubble emission sites, seeps, Cascadia, multibeam, seismic reflection, bubble streams

OPEN ACCESS

Edited by:
Martin Scherwath, University of Victoria, Canada

Reviewed by:
Pablo Garcia Del Real, TE SubCom, United States
Benedicte Ferre, Arctic University of Norway, Norway

****Correspondence:***
Susan G. Merle
susan.merle@noaa.gov
susan.merle@oregonstate.edu

Specialty section:
This article was submitted to Biogeoscience, a section of the journal Frontiers in Earth Science

Received: *31 January 2020*
Accepted: *08 February 2021*
Published: *24 March 2021*

Citation:
Merle SG, Embley RW, Johnson HP, Lau T-K, Phrampus BJ, Raineault NA and Gee LJ (2021) Distribution of Methane Plumes on Cascadia Margin and Implications for the Landward Limit of Methane Hydrate Stability. Front. Earth Sci. 9:531714. doi: 10.3389/feart.2021.531714

INTRODUCTION

Methane is a strong greenhouse gas that significantly contributes to the ongoing anthropogenic warming of the earth (Kvenvolden 1988b; Bangs et al., 2005; Kretschmer et al., 2015; Saunois et al., 2016; Ruppel and Kessler, 2017). Methane is generated naturally in many terrestrial environments such as wetlands, and peat bogs. Human-induced sources include landfills, livestock, industrial resource extraction and melting permafrost (Ciais et al., 2014; Hope and Schaefer, 2016). Methane

gas is also being continually produced by microbial and thermogenic processes in marine sediments and exits the seafloor in thousands of bubble streams distributed over most continental margins (Von Rad et al., 2000; Muller-Karger et al., 2005; Skarke et al., 2014; Geersen et al., 2016; Egger et al., 2018; Hong et al., 2018). Under certain pressure–temperature (P–T) conditions with high concentrations of methane in the pore water, methane hydrate, an ice-like substance, is formed in large quantities within the upper few hundred meters of the sedimentary section on many continental margins (Ewing and Hollister, 1972; Kvenvolden, 1993; Ruppel and Kessler, 2017). Factors such as the geothermal gradient, pore water methane concentrations, tidal pressures, near-bottom water velocities and local tectonics can modulate the release of free gas from below the sediment layers that contain solid methane hydrate (Thomsen et al., 2012; Johnson et al., 2015; Phrampus et al., 2017; Salmi et al., 2017; Egger et al., 2018; Johnson et al., 2019). Bottom simulating reflectors (BSRs), seen in seismic profiles on the margin, are the acoustic impedance boundary between methane hydrate (solid phase) and the free gas phase below. The distribution of methane emission sites and their relationship to the underlying hydrate zone are important to understand as ocean warming, long and short-term tectonic strain, eustatic sea level change, and geothermal heat flow affect the stability zone of methane hydrate. On active continental margins, regional tectonics likely control a large portion of the methane throughput to the ocean. It is important to identify the present distribution of seafloor methane bubble emission sites in light of a continued ocean warming that could potentially dissociate the upper edge of the hydrate layer in the future.

Methane contained within the sediment pore fluids is utilized by erobic methane oxidizing archea and sulphate-reducing bacteria that form the basis of a unique chemosynthetic food web (Levin, 2005; Graves et al., 2017). Oxidation of methane by methanotrophs precipitates large amounts of solid carbonate deposits at the sediment/seawater boundary (Johnson et al., 2003). Because many of the seafloor methane exit sites are biological hotspots (Salmi et al., 2011), knowledge of the distribution of methane emission sites, also referred to as seep ecosystems in historical literature (Field and Jennings, 1987; Collier and Lilley, 2005; Levin, 2005; Torres et al., 2009; Hautala et al., 2014; Johnson et al., 2015), is necessary to assess the importance of seeps on continental margins, providing a valuable data source for research on the interplay between these biological hotspots and fisheries.

CASCADIA MARGIN GEOLOGY

The USCM is a 1,000 km-long convergent accretionary margin that evolved during a long period of under-thrusting of the Juan de Fuca plate beneath the North American plate (**Figures 1**–**5**). Tectonic strain over the past tens of millions of years has resulted in a large volume of terrigenous, organic-rich, sedimentary and volcanic terranes that have been accreted to the continent (Snavely, 1987). This process continues at present with the strain occurring primarily during periodic megathrust earthquakes along the Cascadia subduction zone (Goldfinger et al., 2012). The present accretionary prism is the result of a long history of convergence where sediments are deposited, compressed, and gradually uplifted (Kulm and Fowler, 1974; Carson, 1977). Brittle fracturing of the accretionary prism nucleates faults, while folding, diapirism, and mud volcanism steepen slopes, precipitating mass failures at various scales on the continental slope. Tectonic strain expels methane-rich sediment pore fluids produced by both microbial and thermogenic processes (Suess et al., 1999; Tréhu et al., 1999). These organic-rich fluids migrate upward, diffusing through the sediment column, and flowing along permeable strata and fractures. In water depths below 500 m, methane migrates toward the seafloor and enters the methane hydrate stability zone and forms a solid hydrate-rich layer within the uppermost sedimentary column. In areas of high concentrations of hydrate, the previously permeable sediments can form an impermeable layer that traps the gas phase below. Methane gas can escape where this hydrate layer is breached by upward migrating diapirs, faults, rapid downcutting by canyons, or sediment slope failures (Orange and Breen, 1992; Johnson et al., 2019). For normal seawater salinities, methane hydrate forms in the P–T conditions existing from abyssal depths to an upper limit of 500 m on the USCM, which is defined as the feather edge of methane hydrate stability (FEMHS) (Hautala et al., 2014; Davies et al., 2015; Johnson et al., 2015; Phrampus et al., 2017; Ruppel and Kessler, 2017).

BACKGROUND OF SUBMARINE COLD SEEP DISCOVERIES

Submarine cold seeps are characterized by particular fauna that rely on methane for chemosynthetic reactions. Initial discoveries of submarine cold seeps were serendipitous. Some of the first cold seep sites were found by the deep submergence vehicle (DSV) Alvin at the base of the Florida escarpment (Paull et al., 1984) and near the toe of the accretionary prism off the Oregon coast (Suess et al., 1985; Kulm et al., 1986). Cold seeps with hydrate exposure and bubble streams at the seafloor were later found at Hydrate Ridge off Oregon (Suess et al., 1999), Barkley Canyon off Vancouver Island (Chapman et al., 2004), and Eel Canyon off northern California (Paull et al., 2014). Later, bubble streams rising through the water column (also called flares) were detected by acoustic single beam sonars (Judd and Hovland, 2008). Johnson et al. (2015) identified 195 known locations of bubble streams and seeps on the Cascadia margin, compiling an inventory based on historic methane emission sites (Carson et al., 1990; Collier and Lilley, 2005; Torres et al., 2009; Salmi et al., 2011), locations of fishermen-reported sonar flares, and University of Washington R/V *Thompson* EM302 multibeam water column data. The more recent study by Riedel et al. (2018) identified an additional 929 bubble stream locations, with the majority of sites on the British Columbia and northern Washington margins. A large portion of the latter were located with EK60 single-beam sonar during the U.S. National Marine Fishery Service fishery stock assessment surveys on the west coast.

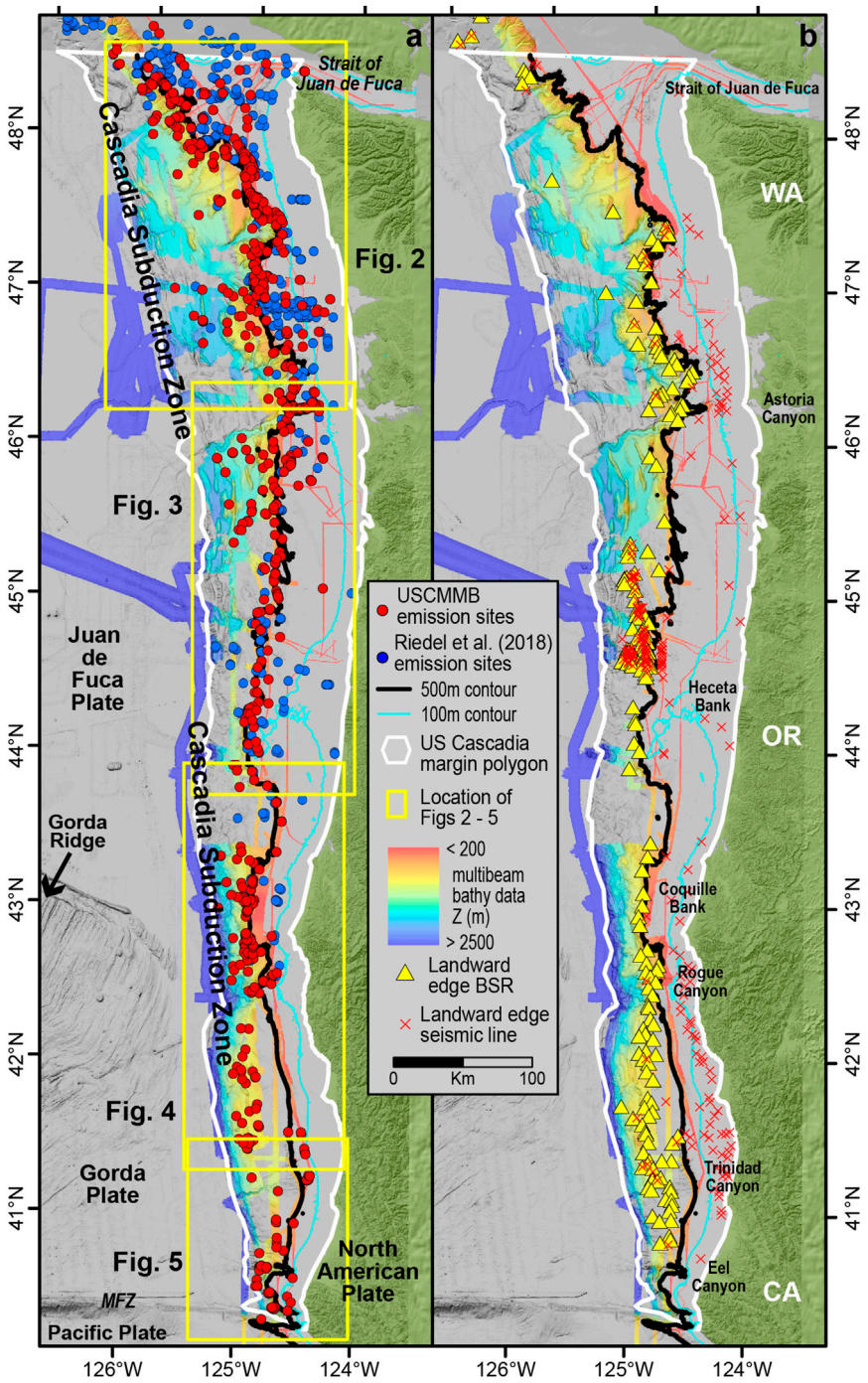

FIGURE 1 | (A, B) Bathymetric map depicting the U.S. Cascadia margin area (white polygon) stretching from the Strait of Juan de Fuca in the north to the Mendocino fracture zone (MFZ) in the south. Colored bathymetry is a compilation of the eight multibeam surveys (USCMMB) with co-registered seafloor and water column data presented in this paper. Gray background grid from Goldfinger et al. (2017). **(A)** Yellow boxes indicate the location of four detailed maps to follow (**Figures 2**–**5**). Red circles are the U.S. Cascadia margin multibeam (USCMMB) methane bubble emission sites. Blue circles are Riedel et al. (2018) emission sites. **(B)** Map revised from Phrampus et al. (2017). Red X's indicate the landward end of seismic lines. Black line is 500-m depth contour. Yellow triangles depict the FEMHS or the landward-most observed BSRs. BSRs are observed at the end of the seismic line if the red X's overlay the yellow triangles. Abbreviations: WA (Washington), OR (Oregon) and CA (California).

It is important to note that seepages of methane-rich fluids are more abundant than indicated by the inventory of bubble emission sites. Although the advent of multibeam water column mapping enables many emission sites to be discovered based on the location of bubble streams (Westbrook et al., 2009; Skarke et al., 2014), bubble streams form only when gas-saturated

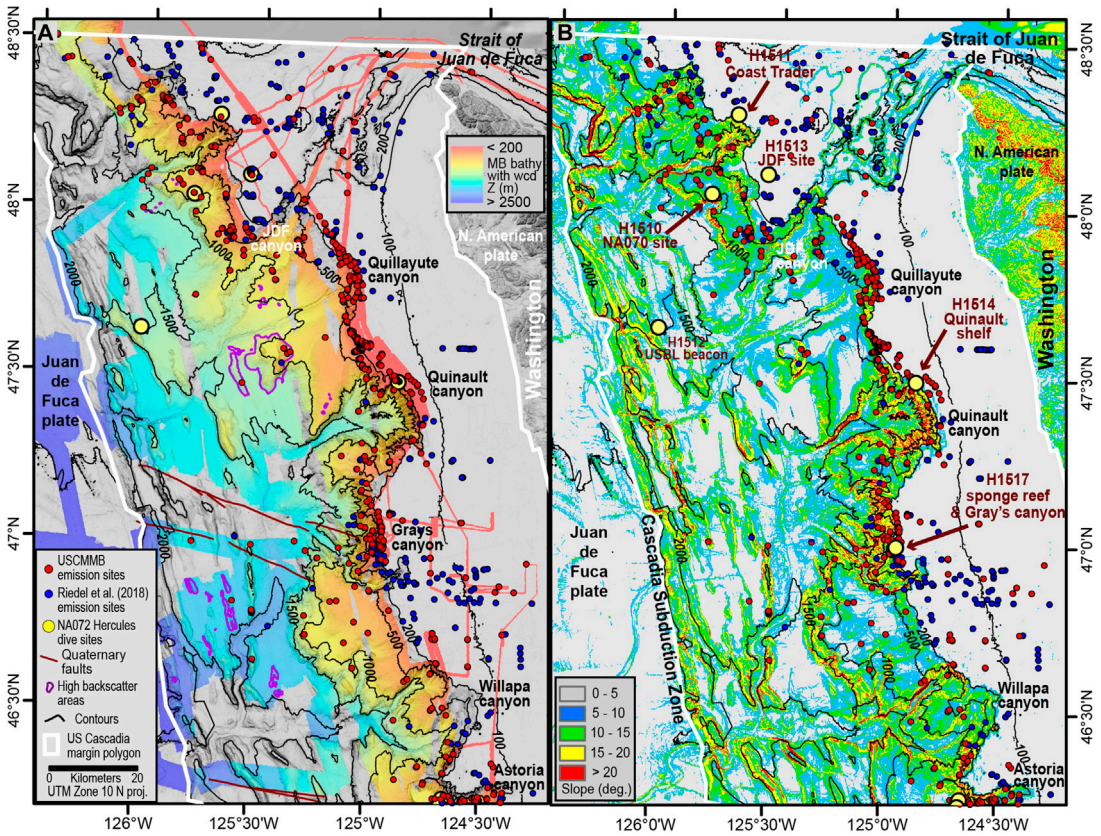

FIGURE 2 | Bathymetry and slope maps of Washington Cascadia margin–Strait of Juan de Fuca to Astoria Canyon. Black seafloor contours and slope map derived from grey-scale background grid, Goldfinger et al. (2017). **(A)** Bathymetric map with major seafloor features labeled. Colored bathymetry data are from the USCMMB database. Red circles are the USCMMB emission sites. Blue circles are Riedel et al. (2018) emission sites. High seafloor backscatter areas outlined by purple polygons. Quaternary faults from Goldfinger and Kulm (1997). USCMMB bathymetry and emission site data north of Astoria Canyon to the Strait of Juan de Fuca published in Johnson et al. (2019). **(B)** Slope map of the same area shown in **(A)**. NA072 *Hercules* remotely operated vehicle (ROV) dive sites represented by yellow circles, as well as dive number and name (e.g., H1677).

fluids are delivered rapidly to the seafloor for emission into the water column. For example, bubble streams were not reported at some historic seep areas that were studied during submersible dives on the Oregon margin (Kulm et al., 1986; Orange et al., 1997). Similarly, small seep areas were found on a 2016 dive on the wall of the deep section of Trinidad Canyon (1,950–2,150 m) off northern California, although a multibeam water column survey failed to identify bubble streams over the same site (**Figures 5A,B**), (Embley et al., 2017).

Conversely, carbonate hardgrounds, which result from methane oxidation and form over long periods (10^2–10^3 years), represent past fluid discharge sites and do not identify currently active fluid emission areas (Kulm et al., 1986; Bohrmann et al., 1998). Also, bubble streams can be non-uniform in flux rate and can be modulated by tidal pressures and near-bottom currents over short intervals (Archer, 2007; Thomsen et al., 2012; Philip et al., 2016a; Sun et al., 2020) and geological processes over longer periods. In any case, due to the ephemeral nature of individual bubble streams and/or the lack of a gas phase at some seeps, there are limits to how well we can interpret the distribution of active bubble emission sites with even modern remote sensing methods.

Large-scale systematic surveys required the development of advanced multibeam sonars with a water column imaging capability (Gardner et al., 2009; Skarke et al., 2014; Urban et al., 2017). Where ground-truth data of the sonar images exist, most of these water column bubble streams are co-located with cold fluid seeps on the seafloor (Judd and Hovland, 2008; Greinert et al., 2010). The converse is not true, as not all cold fluid seeps have associated bubble plumes. In this study, new multibeam sonar surveys systematically mapped nearly 40% of the US Cascadia margin, extending from the Strait of Juan de Fuca in the north to the Mendocino fracture zone in the south, and bounded East-West by the coast and the base of the accretionary prism (**Table 1**; **Figures 1A**, **Supplementary Figure S1**). The eight new shipboard multibeam surveys with corresponding water column data reported here will henceforth be referred to as the US Cascadia Margin MultiBeam (USCMMB) dataset.

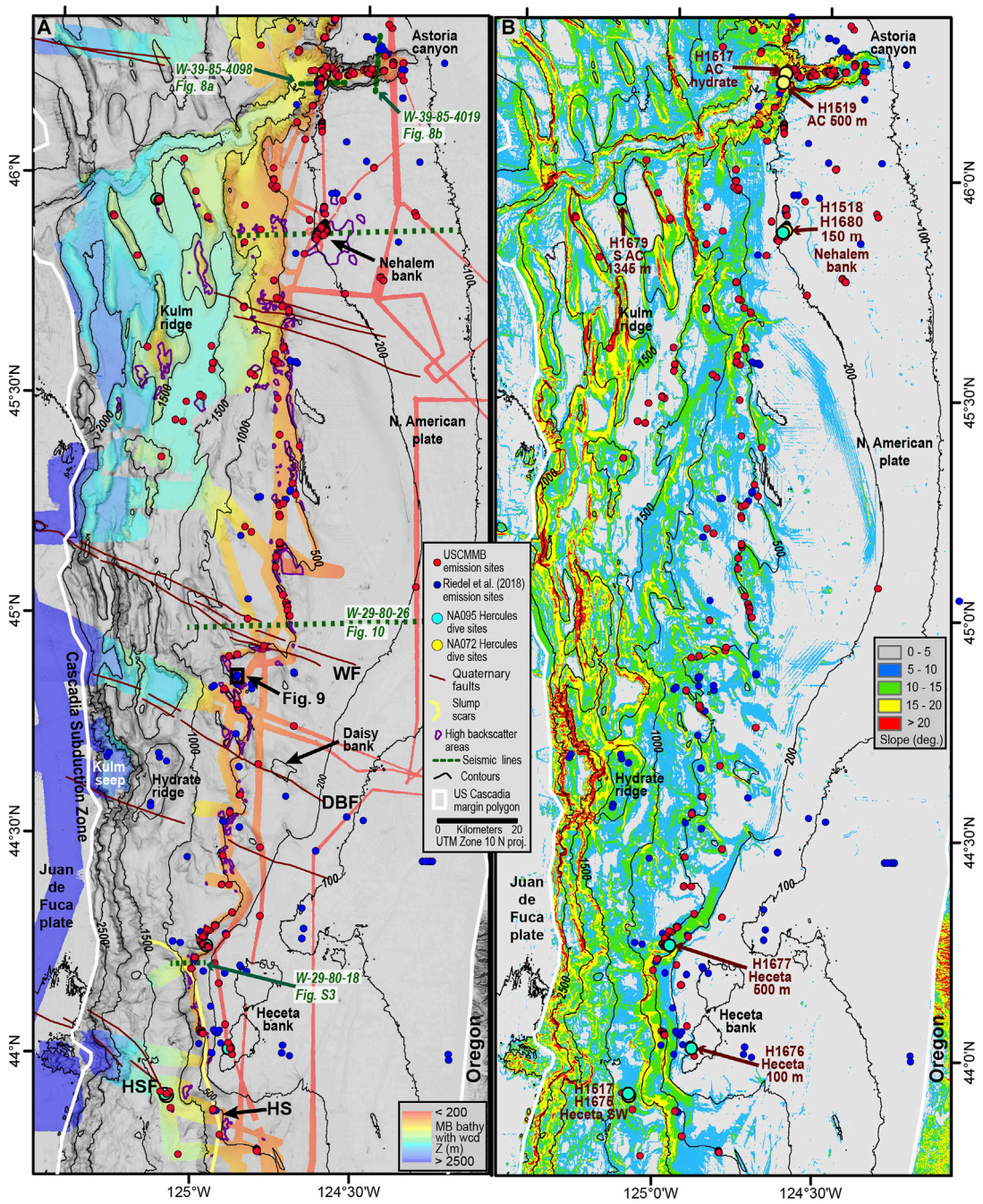

FIGURE 3 | Bathymetry and slope maps of Cascadia margin—Astoria Canyon to Heceta Bank. Annotations and data sets same as in **Figure 2**. **(A)** Bathymetric map with major seafloor features labeled. Green dashed lines are the location of multi-channel seismic profiles. WF—Wecoma Fault, DBF - Daisy Bank Fault, HSF - Heceta South Fault (all in Goldfinger and Kulm, 1997); HS–Heceta Slump (Goldfinger et al., 2000). Slump scars from Goldfinger et al. (2000). **(B)** Slope map of the same area shown in **(A)**.

A major result of our data analyses is that a significant concentration of bubble emission sites is located within a narrow depth range centered on the FEMHS, which is located at ~500 m depth along Cascadia. Johnson et al. (2015) previously documented a robust concentration of sites at the FEMHS along the Washington and northern Oregon Cascadia margin. Here we present the new data inventory from the eight USCMMB cruises, combined with the historical data published by Johnson et al. (2015) and Riedel et al. (2018) (**Table 1**). Importantly, we extend the survey region southward along the full Cascadia active

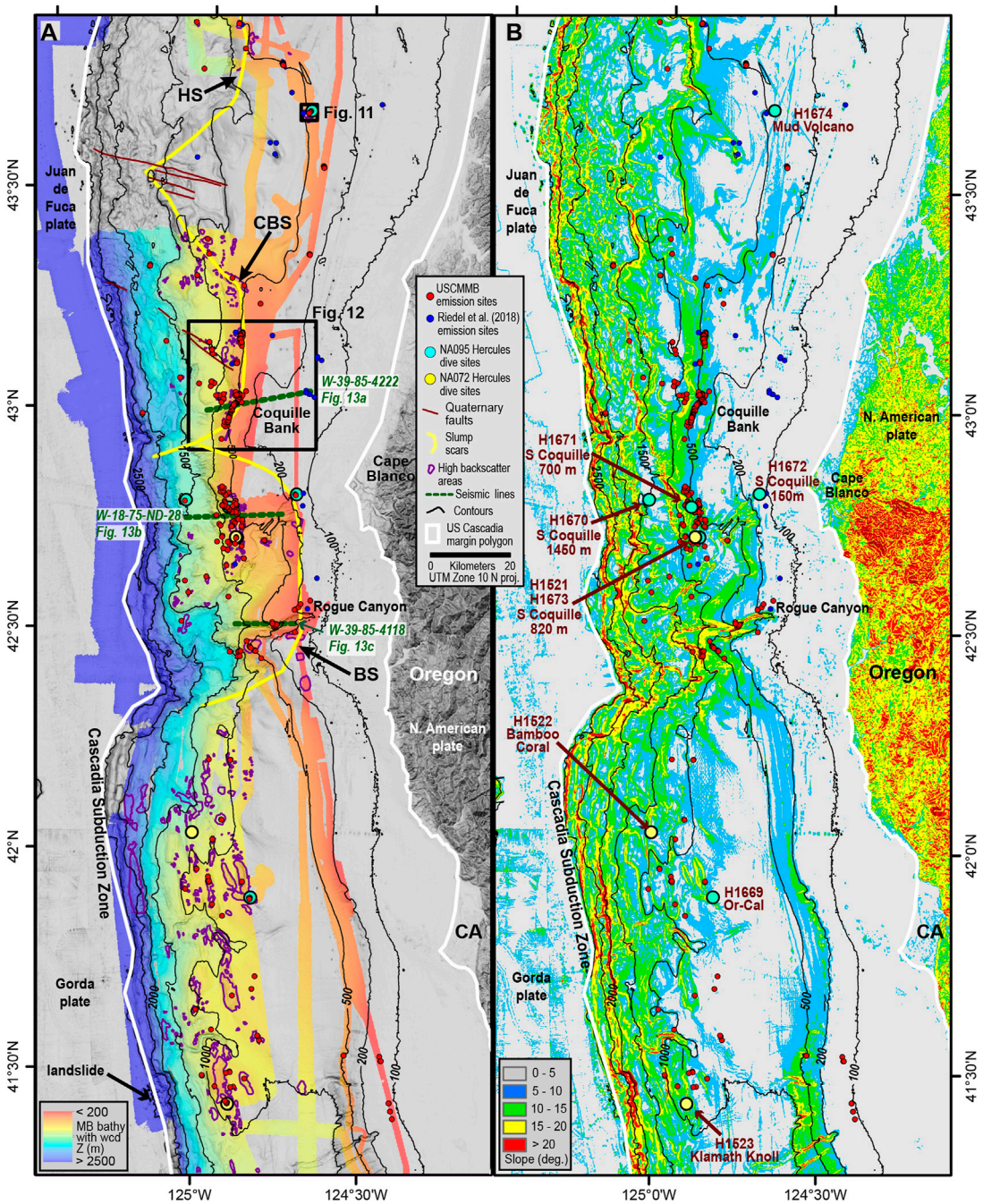

FIGURE 4 | Bathymetry and slope maps of Cascadia margin - Heceta Bank to Trinidad Canyon. Annotations and data sets same as in **Figure 2**. **(A)** Bathymetric map of with major seafloor features labeled. HS–Heceta slide, CBF–Coos Basin slide, BS–Blanco slide (Goldfinger et al., 2000). **(B)** Slope map of the same area shown in **(A)**.

margin, and now include the Oregon and Northern California margins. In this analysis, the depth distribution of bubble streams is compared to seafloor morphology and overlain on a previously published dataset on the extent of the BSRs from multi-channel seismic reflections, which are available over much of the Cascadia accretionary prism (**Figures 1B**, **3A**, **4A**, **Supplementary Figure S3**), (Phrampus et al., 2017).

DATA AND ANALYSIS

The new USCMMB acoustic dataset presented here consists of eight co-registered multibeam seafloor and water column surveys (**Table 2**), which identified 2,510 individual bubble streams on the US Cascadia margin from the Strait of Juan de Fuca (JDF) in the north to the Mendocino fracture zone (MFZ) in the south

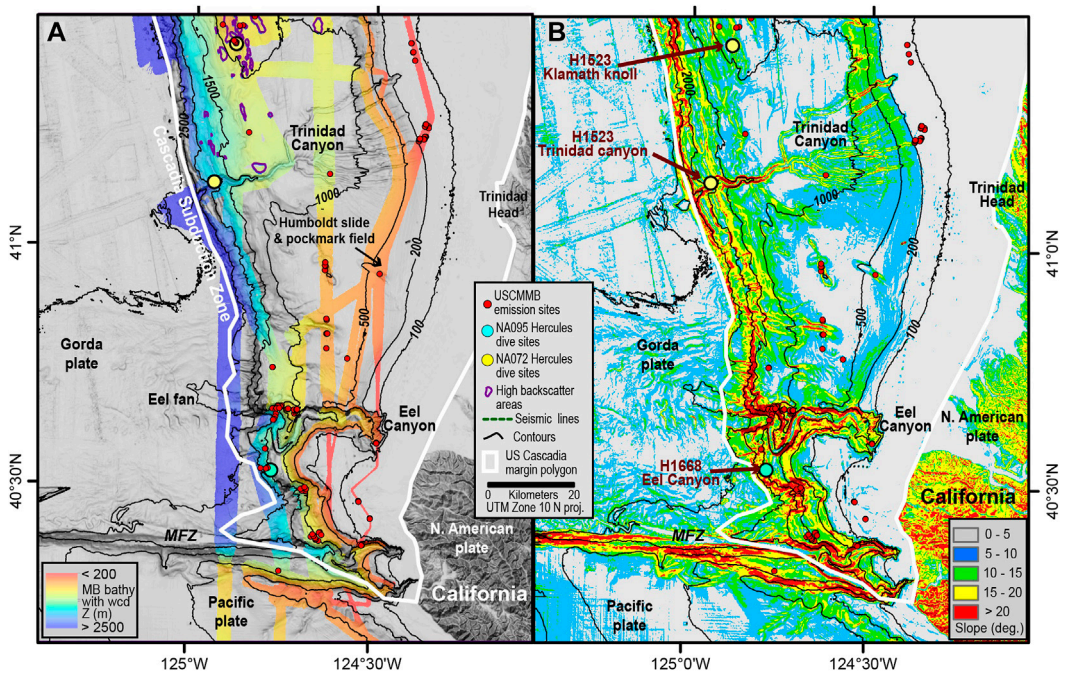

FIGURE 5 | Bathymetry and slope maps of Cascadia margin - Trinidad Canyon to Cape Mendocino. Annotations and data sets same as in **Figure 2**. **(A)** Bathymetric map with major seafloor features labeled. **(B)** Slope map of the same area shown in **(A)**.

(**Supplementary Table S1**). When those data are combined with the Johnson et al. (2015) and Riedel et al. (2018) bubble plume inventories along the USCM, they total 3,481 individual bubble streams (**Supplementary Table S2**). To prevent over-counting of duplicate bubble streams that were identified on different expeditions, individual bubble streams were clustered into emission sites using a 300-m radius spatial filter, based on the Johnson et al. (2015) methodology. That methodology was derived when Johnson et al., 2015 realized the plumes appeared as clusters, which argues that they have a single sub-surface source and that a deep pathway breaks up into an abundance of smaller vents nearer the surface. They rigorously took the center of a number of these clusters and drew circles of increasing radius around them and counted the number of bubble streams in each circle. When the number of streams counted in the circles of increasing radius stopped increasing, the interpretation was that it was one sub-surface site, similar to hydrothermal vent fields. The 2510 USCMMB individual bubble streams clustered into 848 bubble emission sites (**Supplementary Table S3**). When all 3,481 bubble streams were re-clustered in this study, a total of 1,300 bubble emission sites were identified (**Figures 1A–5A**, **Supplementary Table S4**). The clustered bubble emission sites, rather than the individual bubble streams, were utilized for all statistical analyses in this manuscript (**Table 1**). USCMMB emission site depths were derived from high resolution multibeam data collected on the eight expeditions highlighted in this study, and gridded at 25-m resolution. The emission site depth information for the "ALL" sites data, which combines the USCMMB and Riedel et al. (2018) datasets, was derived from the Goldfinger et al. (2017) grid at 100 m resolution. Therefore, the emission site depth information is more accurate for the USCMMB dataset than for the "ALL" sites compilation.

The USCMMB surveys (**Figures 1A–5A**, **Supplementary Figure S1**; **Table 2**) mapped a total of 36,336 km^2 of seafloor, which represents 39% of the US Cascadia continental margin (**Figure 1A**, **Supplementary Figure S2**; **Table 1**). The numbers for each survey in **Table 2** are specific to each multibeam expedition. Due to overlapping surveys, the total seafloor mapped is larger in **Table 2** than **Table 1**, which reduces the total seafloor mapped because of those coinciding survey areas. Five of the eight datasets were collected on the E/V *Nautilus* during 2016 and 2017. The 30 kHz acoustic frequency of the EM302 multibeam system on the E/V *Nautilus* and the R/V *Thompson* is optimal for surveying the continental slope in water depths ranging from 200–3,200 m. Those two vessels located a combined 1949 bubble streams. A 12 kHz EM122 system on the R/V *Revelle* only detected three bubble streams on a transit swath, most likely due to high survey speed and the lower frequency sonar. An EM710 system (70 kHz) on the NOAA Ship *Rainier* surveyed just landward of the heads of Quinault and Quillayute submarine canyons on the Washington margin in depths that range from 100 to 300 m and located more than 500 bubble streams from this limited area (Johnson et al., 2019). Information regarding specific multibeam data availability are in the **Supplementary Material** document.

All eight of the multibeam water column datasets in this study were processed using the QPS FMMidwater© computer program, which provides location and extraction of features from within the water column. Identification of bubble streams was based on identifying acoustic reflection features that were required to: 1)

TABLE 1 | Bubble emission site statistics–US cascadia margin.

Depth range (m)	Area of margin (km2)	% Of margin	Area mapped—USCMMB data (km2)	% Of margin mapped—USCMMB data	# Of USCMMB sites	% Of total USCMMB sites (849)	Normalized USCMMB: % Of sites/% mapped	Normalized USCMMB sites: % Sites/% margin [zmb]	# Of all sites: USCMMB and Riedel et al. (2018) [zgold]	% Of all sites: USCMMB and Riedel et al. (2018) [zgold]	Normalized all sites: % Sites/% margin [zgold]
000–100	17,711	19.07	346.3	2.0	10	1.18	0.602	0.062	69	5.3	0.3
100–200	16,436	17.69	2032.4	12.4	226	26.62	2.153	1.504	464	35.7	2.0
200–300	3,795	4.09	929.8	24.5	59	6.95	0.284	1.701	97	7.5	2.0
300–400	3,054	3.29	1,052.9	34.5	26	3.06	0.089	0.931	46	3.5	1.0
400–500	3,139	3.38	1,648.4	52.5	115	13.55	0.258	4.008	144	11.1	3.1
500–600	2,864	3.08	1939.7	67.7	141	16.61	0.245	5.386	163	12.5	4.3
600–700	2,848	3.07	1,654.1	58.1	47	5.54	0.095	1.806	58	4.5	1.5
700–800	2,584	2.78	1,590.8	61.6	46	5.42	0.088	1.948	57	4.4	1.5
800–900	2,676	2.88	1,672.9	62.5	39	4.59	0.073	1.595	43	3.3	1.3
900–1,000	2,840	3.06	1993.9	70.2	22	2.59	0.037	0.848	31	2.4	0.7
1,000–1,100	2,817	3.03	1915.7	68.0	27	3.18	0.047	1.049	30	2.3	0.8
1,100–1,200	2,531	2.72	1,601.7	63.3	22	2.59	0.041	0.951	20	1.5	0.6
1,200–1,300	2,218	2.39	1,446.9	65.2	15	1.77	0.027	0.740	19	1.5	0.5
1,300–1,400	2,308	2.48	1,512.9	65.5	10	1.18	0.018	0.474	10	0.8	0.4
1,400–1,500	2,848	3.07	1947.5	68.4	5	0.59	0.009	0.192	7	0.5	0.2
1,500–1,600	3,164	3.41	2047.6	64.7	10	1.18	0.018	0.346	11	0.8	0.2
1,600–1700	3,253	3.50	2,145.9	66.0	15	1.77	0.027	0.504	13	1.0	0.3
1700–1800	3,096	3.33	2019.7	65.2	6	0.71	0.011	0.212	7	0.5	0.1
1800–1900	2,625	2.83	1,611.6	61.4	4	0.47	0.008	0.167	4	0.3	0.1
1900–2000	2,419	2.60	1,543.2	63.8	3	0.35	0.006	0.136	4	0.3	0.1
2000–2,100	1748	1.88	849.2	48.6	1	0.12	0.002	0.063	3	0.2	0.1
2,100–2,200	1,431	1.54	561.5	39.2	0	0.00	0.000	0.000	0	0.0	0.0
2,200–2,300	1,123	1.21	485.1	43.2	0	0.00	0.000	0.000	0	0.0	0.0
2,300–2,400	894	0.96	426.4	47.7	0	0.00	0.000	0.000	0	0.0	0.0
2,400–2,500	700	0.75	333.4	47.6	0	0.00	0.000	0.000	0	0.0	0.0
2,500–2,600	445	0.48	256.2	57.6	0	0.00	0.000	0.000	0	0.0	0.0
2,600–2,700	298	0.32	165.5	55.6	0	0.00	0.000	0.000	0	0.0	0.0
2,700–2,800	235	0.25	119.9	51.0	0	0.00	0.000	0.000	0	0.0	0.0
2,800–2,900	270	0.29	136.1	50.4	0	0.00	0.000	0.000	0	0.0	0.0
2,900–3,000	296	0.32	174.4	58.9	0	0.00	0.000	0.000	0	0.0	0.0
>3,000	220	0.24	145.3	66.1	0	0.00	0.000	0.000	0	0.0	0.0
Totals	92,886	100	36,307		849	100			1,300	100.0	

U.S. Cascadia margin multibeam (USCMMB): 8 multibeam surveys with co-registered seafloor and water column data. Only data on the U.S. margin. Portions of these surveys on the Washington margin were published in Johnson et al. (2019)

Riedel et al. (2018) data set includes data published in Johnson et al. (2015). A majority of those data are from fisheries sonar systems, specifically EK60 single beam data, and have no corresponding seafloor data

Bubble emission site statistical information, on the USCM. These statistics were utilized to create the histograms on ***Figure 7****. Zmb indicates that the depths were derived from the USCMMB bathymetry grid at 25 m resolution. Zgold indicates that the emission site depths were derived from the Goldfinger et al. (2017) compilation at 100 m resolution.*

TABLE 2 | USCMMB Co-registered seafloor and water column data surveys.

Survey	Ship	MB system	Freq (kHz)	Dates	# Bubble streams	Area mapped (km^2)	Depth range (m)
RR1712	R/V *Revelle*	EM122	12	7/23 2017	3	520	50–2,695
NA088	E/V *Nautilus*	EM302	30	9/13 to 9/18 2017	40	4,675	85–2,800
NA080	E/V *Nautilus*	EM302	30	5/26 to 6/4 2017	199	5,700	80–3,070
NA078	E/V *Nautilus*	EM302	30	8/20 to 9/4 2016	56	5,480	140–3,100
NA072	E/V *Nautilus*	EM302	30	6/1 to 6/20 2016	854	8,010	100–2,965
NA070	E/V *Nautilus*	EM302	30	6/1 to 6/20 2016	1	515	95–1760
1605 R A	NOAA ship *Rainier*	EM710	70	5/9 to 5/12 2016	558	740	115–1,375
TN265	R/V *Thompson*	EM302	30	4/29 to 6/24 2011	799	16,705	20–3,110

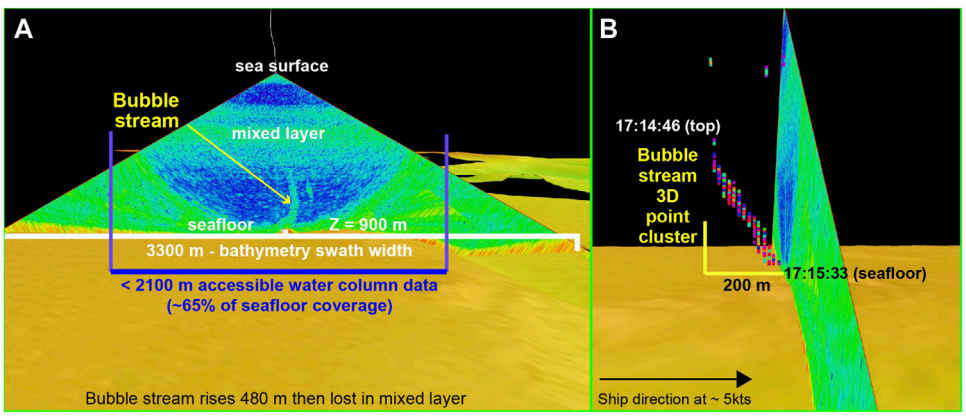

FIGURE 6 | Fledermaus© depictions of co-registered seafloor and water column data. **(A)** Midwater data beam fan view overlaid on concurrently collected seafloor bathymetry data. The horizontal width of effective water column data coverage, in this instance, is <65% of the width of bathymetric seafloor coverage. In this example, a bubble stream rises 480 m and is lost when it intersects the mixed layer. **(B)** 3-D view of a point cluster object representing a bubble stream wafting in the water column during the NA072 expedition. Hotter colors in the point clusters represent higher amplitude values in the water column data. In this instance, the individual bubble stream seen in **(A)** was visible in ~15 dual swath pings covering a 200 m along-track distance over the seafloor, during the course of 47 s at five knots.

originate at the seafloor, 2) appear as a flare-shaped echo pattern within the water column data (Urban et al., 2017; Riedel et al., 2018), and 3) could be traced across several pings as they rise toward the sea surface. Several views of the data are available with the processing software, but the beam fan panel was exclusively employed to locate the bubble streams for consistency. When a bubble stream was detected, the seafloor location was "geo-picked" from a single ping within the beam fan view (**Figure 6**). Rise heights of the bubble streams within the water column were recorded for the majority of the multibeam surveys (**Supplementary Table S1**).

The beam fan view is indicative of the geometry of multibeam sonar systems and illustrates the limitations of the multibeam water column data (**Figure 6A**). The fan-shaped ping only allows visualization of the entire water column at nadir, with decreasing vertical extent of water column data available toward the edge of the swath. Bubble streams on the outer beams of a swath can be clipped and true rise heights not always identified. Due to the beam fan geometry, the percentage of horizontal area available within the water column data is less than the percentage of seafloor data, and that factor can be exacerbated by insufficient swath overlap, rapid ship speeds, noisy surface ocean conditions, and biota obscuring the bubble streams. Constructing 3D views (**Figure 6B**) allows visualization of the bubble stream in the along-track direction.

To examine sub-seafloor structures located beneath the plume emission sites, seismic profiles were processed using archival Multi Channel Seismic (MCS) data, which are publicly available at the U.S. Geological Survey (USGS) website: https://walrus.wr.usgs.gov/namss/. Plotting, viewing, and enhancing contrast values of the MCS data were executed with MATLAB® software.

DISTRIBUTION OF COLD SEEPS ALONG CASCADIA MARGIN

Overall Distribution

Figure 1A shows the distribution of the USCMMB bubble emission sites (red circles) and historical seep sites (blue circles) along the entire USCM. **Figure 1B** depicts the landward edge of the BSR from historical seismic data on the margin. **Figure 2**–five zoom in on those data latitudinally from north to south. The left side of **Figure 2**–five show the bubble emission sites overlaid on the USCMMB bathymetry data. The right side of **Figures 2**–**5** show a slope map of the margin with

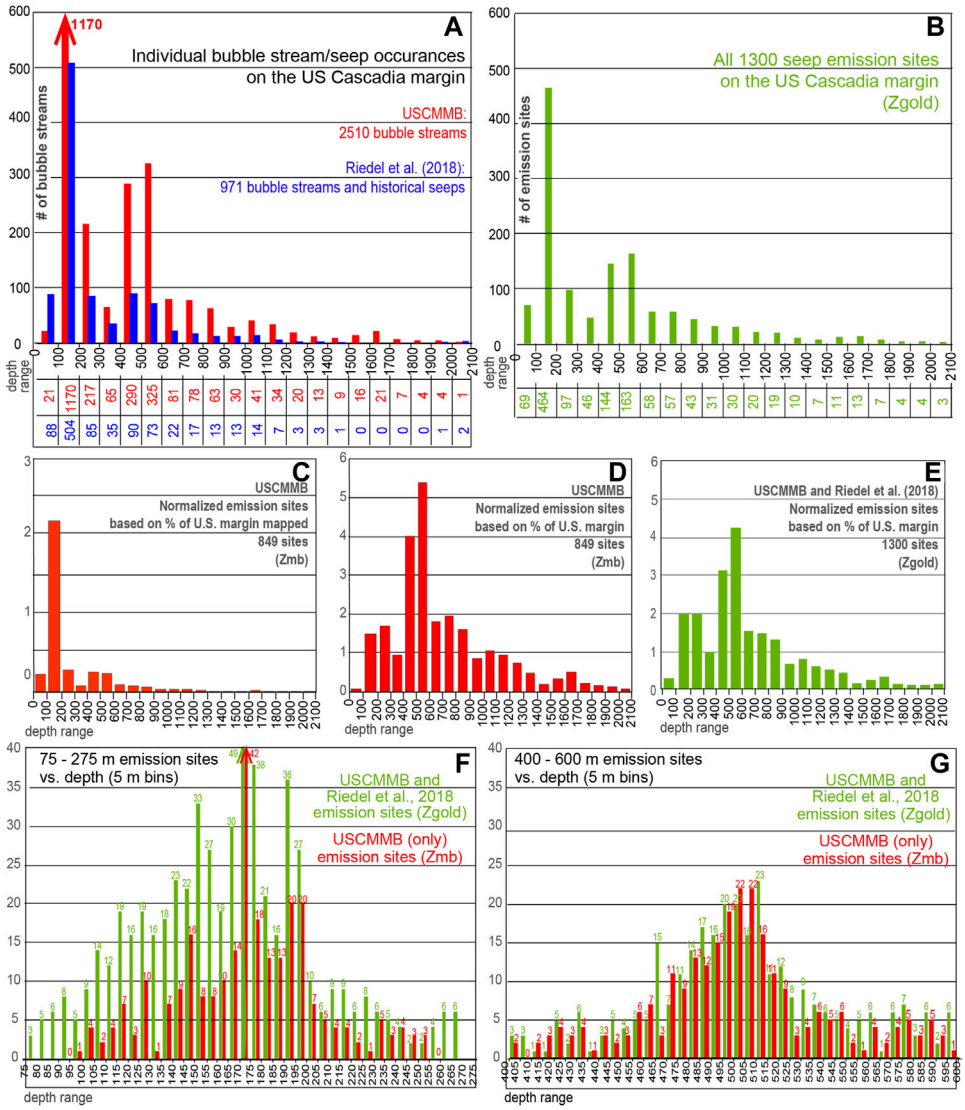

FIGURE 7 | Histograms of USCM bubble stream/emission site data. USCMMB emission site depth values were derived from 25 m multibeam grid (Zmb). Riedel et al. 2018 site depth information from Goldfinger et al. (2017) compilation at 100 m resolution (Zgold). Therefore depth values are more accurate when using the Zmb grid numbers. **(A)** Histogram comparing individual bubble streams from the USCMMB database to the Riedel et al. (2018) data set, which includes the Johnson et al. (2015) compilation. Beneath the depth range intervals are bubble stream numbers from each data set. **(B)** All the data sets on the USCM combined and clustered into 300 m radii emission sites. Noted beneath the depth range intervals are the number of emission sites within that depth range. **(C)** Normalized histogram of the UCMMB emission sites on the USCM based on the % of the seafloor mapped. The normalization involves the % of emission sites per 100 m depth interval divided by the % of the depth interval that has been mapped. **(D)** Normalized histogram of the USCMMB emission sites on the USCM. The normalization involves the % of total sites per 100 m interval divided by the % of the margin within that 100 m interval. **(E)** Normalized histogram of all 1,300 emission sites on the margin, combining the USCMMB and Riedel et al. (2018) data. The same normalization method as in **(D)**. **(F)** 5-m binned histograms of the shallow peak in emission site data. The numbers above the histogram bars are the number of sites per 5 m bin (in **F** and **G**). **(G)** 5-m binned histograms of the FEMHS peak.

added ROV dive site locations from R/V *Nautilus* expeditions on the margin. Geological interpretations of quaternary faults, slump scars, high backscatter areas and seismic lines utilized in this study are also presented.

Histograms of USCM bubble stream emission site data are presented in **Figure 7**. The frequency histogram of individual bubble stream depths for all inventoried data on the USCM (USCMMB, plus Johnson et al., 2015, and Riedel et al., 2018) is shown in **Figure 7A**. The Riedel et al. (2018) data coverage only extends south to 42°30′N, on the southern Oregon margin. Most of the upper slope and shelf coverage is from EK60 sonar, and differs from the USCMMB data in that the footprint of the EK60 is more than 4 times narrower than that of multibeam sonar at 200 m water depth. On the other hand, the EK60 surveys, which consist of E-W lines extending from the shallow continental shelf to ~800 m mid-water depth, in groups of repeat lines spaced approximately 35 km apart on a N-S grid, provide a relatively evenly parsed sampling of the continental shelf and slope for all of

Washington and northern and central Oregon. These historical fisheries survey data supplement the USCMMB acoustic water column data set, which has limited coverage in water depths less than 200 m (~14% mapped), but accounts for 37% of the area of the USCM (**Figures 1–5**, **Supplementary Figure S2**; **Table 1**).

Johnson et al. (2015) determined the 300 m standard radius filter by testing clustered radii of 0.150, 300, and 500 m, to identify a characteristic length scale for emission sites where the number of total sites counted would become almost constant with increasing radii. Applying the 300-m radius spatial filter used for the data to the combined USCMMB and historical data sets (Johnson et al., 2015; Riedel et al., 2018) yields a total of 1,300 emission sites (**Figure 7B**) on the margin. Histograms of emission site data exhibit prominent peaks on the outer edge of the continental shelf at 100–200 m and on the upper slope at 400–600 m (**Figures 7F,G**), and then significantly decrease when extended downward to 2,100 m on the accretionary prism. The highest density of emission sites occurs in shallow water, less than 200 m, off the Washington and northern Oregon coasts.

In order to evaluate the statistical significance of the combined datasets shown in **Figures 7A,B,D–G**, we first consider only the USCMMB data since actual seafloor areal coverage can be quantified using those surveys (**Figures 7C,D**, **Supplementary Figure S1A**). Analysis of the USCMMB data yield a total of 2,510 bubble streams (**Supplementary Table S1**) that were then grouped into 849 bubble emission sites (**Supplementary Table S3**). 28% of the total emission sites located in the USCMMB surveys lie within the 0–200 m depth range, a total of 238 sites, which accounts for the large peak in the histogram at the 100–200 m depth interval. A smaller peak brackets the FEMHS between 400–600 m, where 29% (253 emission sites) of the total sites identified lie. Moreover, most of the sites shallower than 200 m are concentrated on the Washington and northern Oregon margins (north of 4,5°45″N). The importance of that will not be truly provable until more data are collected south of that boundary from systematic surveys similar to Riedel et al. (2018) in this sparsely surveyed area, using appropriate multibeam bathymetry tools to determine if the gap in seepage may be real. For comparision, about 37% of the U.S. margin is less than 200 m deep, but only 2% of the 0–100 m depth range, and only 12% of the 100–200 m range has been mapped by multibeam sonar with water column coverage (**Table 1**, **Supplementary Figures S1B and S2**).

To avoid duplicate counts of bubble streams discovered in multiple datasets, the bubble streams were clustered into bubble emission sites and normalized in two different ways (See Supplemental Material). First, because all the water column data in the USCMMB inventory have co-registered multibeam seafloor data, only those sites could be normalized based on the percentage of the USCM mapped (**Figure 7C**; **Table 1**). Even though only a small percentage of the shallow water portion of Cascadia (<200 m) has co-registered seafloor-water column data, there is a large peak in the histogram in the 100–200 m range. Second, the emission site counts were normalized based on the area of the USCM per 100 m depth interval, after Johnson et al. (2015). In just the USCMMB data, two distinct peaks found in the un-clustered data (individual bubble streams) are still present in the clustered (emission sites) normalized histogram (**Figure 7D**). One of those peaks is in the 100–300 m depth range and the other peak is between 400 and 600 m. **Figure 7E** shows a normalized histogram produced similarly that includes the USCMMB data, the Riedel et al. (2018), and Johnson et al. (2015) data on the US margin. Similar peaks in the histogram are evident in the 100–300 m, and 400–600 m depth ranges.

Approximately 75% of the bubble emission sites in this inventory of the USCM occur within the shelf and upper slope (0–600 m) and only a residual of 25% have been identified in the range from 600 m water depth to the abyssal base of the accretionary prism (**Table 1**). However, a much greater percentage of the deeper zone below 500 m has been surveyed, so it seems likely that future shallow water depth surveys would increase the ratio of shallow vs. deep sites. In any case, the overarching observation of this study is that the majority of bubble plume sites are near or shallower than the FEMHS, which has also been reported for other continental margins, including the Gulf of Oman (Von Rad et al., 2000), US Atlantic (Skarke et al., 2014), and Svalbard, north of Norway (Sahling et al., 2014). Sites on Cascadia deeper than 525 m all lie below the upper water depth of the regional hydrate stability zone (Hautala et al., 2014; Phrampus et al., 2017) and if sufficient methane is present in the sediment pore fluid, hydrate should exist in the upper layers of the seafloor. However, the emission peak centered at the FEMHS depth of 500 m includes many sites along Washington, northern Oregon and in the vicinity of Rogue Canyon and Coquille Bank (**Figures 1A–4A**). A higher-resolution depth histogram of the USCMMB emission site data shows well defined distributions of sites centered on, respectively, 150–200 m (**Figure 7F**), and 465–535 m (**Figure 7G**). The high percentage of sites located near 500 m raises the question of a possible correlation with the emission depths and the FEMHS (see section "**The FEMHS**").

The Continental Shelf

USCMMB, Riedel et al. (2018) and Johnson et al. (2019) data show that the Washington and northern Oregon continental shelfs are "hotspots" for methane seeps (**Figures 2**, **3**). The peak in bubble emission sites at the continental shelf break at 165–200 m (**Figure 7F**) is heavily weighted toward surveys conducted on the Washington and northernmost Oregon continental shelf, and 19% of the sites in this study for the entire USCM occur within that depth range. The USCMMB coverage in shallow water is limited south of Nehalem Bank so the current data coverage is not adequate for major conclusions regarding the overall distribution of seeps in shallow water along the entire USCM.

The high density of methane emission sites in shallow water depths on northern Cascadia, north of Nehalem Bank (**Figures 2**, **3**), has been ascribed to sources beneath the wide continental shelf underlain by kilometers-thick organic rich sediments deposited during Pleistocene low sea level stands (Riedel et al., 2018; Johnson et al., 2019) have demonstrated that many of the sites on the outer continental shelf along the Washington margin are correlated with listric faults just east of the heads of some of the major submarine canyons (Juan de Fuca, Quillayute and Quinault). In addition, mud/shale diapirs generated within the Melange and Broken Formation of Eocene to Middle Miocene age (Snavely, 1987;

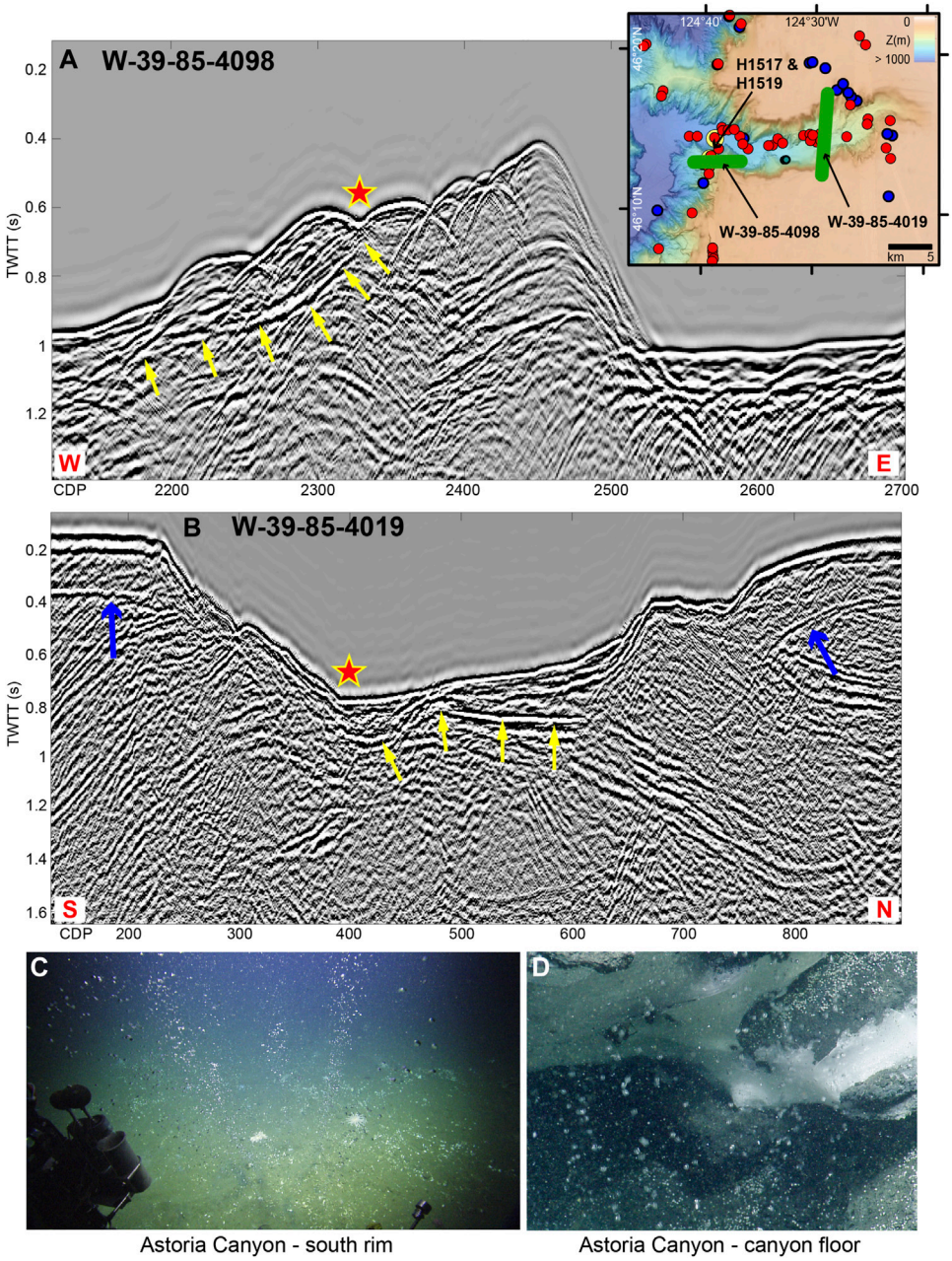

FIGURE 8 | MCS profiles across Astoria Canyon (Upper right inset) Green lines show the profiles extent. Red and blue circles indicate bubble emission sites. 2016 ROV *Hercules* dive sites are noted. Red stars represent methane emission sites. Yellow arrows point to BSR reflectors. **(A)** W–E MCS profile W-39–85-4,098 (location on inset and **Figure 3**) at Astoria Canyon over emission sites at ~500 m, the FEMHS. The BSR reflector intersects the seafloor at the depth of ~500 m. **(B)** N–S MCS profile W-39–85-4,019 (location on inset map and **Figure 3**). Red star marks where the seismic line intersects a cluster of methane emission sites exposed at a depth of ~575 m water on the canyon floor. Yellow arrows point to probable BSRs. Blue arrows point to acoustic multiples. **(C)** Vigorous methane bubble streams at site on south rim of Astoria Canyon at ~500 m: taken with high definition camera on dive H1519. **(D)** Close-up of methane bubbles stream from beneath layer of methane hydrate (white layer on right side) on the floor of Astoria Canyon at ~850 m. Taken with high definition camera on dive H1517.

McNeill et al., 2000; Johnson et al., 2019) are associated with many of the sites and may provide vertical pathways from the underlying methane source. Johnson et al. (2019) hypothesized that the shallow peak on the outer shelf of Washington, in particular the emission fields parallel to the shelf edge near the submarine canyon heads off Washington (**Figure 2**), is due to listric faulting and diapirism within a period of intra-seismic extension. There is also evidence for extensive diapirism and listric faulting at shelf and slope depths for portions of the northern Oregon (this study and Snavely, 1987) and southern Oregon margin (Clarke et al., 1985), although existing data are too sparse to generalize to the entire USCM (**Figures 1–5**).

The FEMHS

The FEMHS on the Washington and northern Oregon portion of Cascadia has been estimated to be between 500 ± 4 m and only slightly deeper on southern Cascadia (Hautala et al., 2014; Johnson et al., 2015), so a statistical peak of seeps at 470–525 m closely brackets that water depth range, with 13% of the sites within that range (**Figure 7G**). Sites within the 470–525 m peak on the landward edge of the upper continental slope occur along the Washington and large sections of the Oregon margins (**Figures 2–4**). Our surveys combined with the historic sites only show a few sites within the 470–525 m depth range (**Figures 4**, **5**) on the southern Cascadia segment adjacent to the northern California coastline. We propose that this peak in bubble plume emission site depths arises from gas migrating through the upper sediment column below the impermeable cap formed by the presence of solid hydrate within the sediment pores. This migration continues both vertically and landward until the point where seawater P–T conditions do not facilitate the formation of any solid hydrate, and the disappearance of the impermeable cap allows egress of the methane into the ocean. This is a model previously proposed for other temperate latitude margins including the US East coast (Sharke et al., 2014) and Makran margins (Von Rad et al., 2000). Similar emission site distributions near the regional FEMHS are also found on Arctic margins and could produce a positive correlation between melting permafrost due to a warming environment and an increased methane gas flux as seawater bubble streams. (Kvenvolden et al., 1993; Nimblett and Ruppel 2003; Westbrook et al., 2009; Biastoch et al., 2011; Berndt, et al., 2014; Frederick, and Buffett 2014; Graves et al., 2015; and; Ruppel et al., 2016). Upward migration of buoyant gas beneath an impermeable sediment cap with solid hydrate-filled pore spaces is enhanced by the steep gradients of the seafloor that occur on the continental slope. (**Figures 2B–5B**).

The emission depth peak that correlates with the FEMHS at 500–510 m in the USCMMB data has a nearly bell-shaped normal distribution curve in the depth-frequency histogram (**Figure 7G**, red bars). A range of variations and uncertainties in relevant physical variables along the margin can affect the exact FEMHS location producing the stochastic depth distribution of the bubble emission sites near the 500 m isobath. Steep seafloor slopes would amplify this effect and would narrow the concentration of sites located near the FEMHS zone depth. The slope maps of the Washington and Oregon margins (**Figures 2B–4B**) do appear to show steep topography within this depth range at the slope break. However, our coverage is not uniformly complete, e.g., in some places there are only one or two multibeam survey lines covering the upper slope.

BSRS AND BUBBLE EMISSION SITES NEAR THE FEMHS

Entire Margin

Along the Cascadia margin, oblique subduction drives compressional folding and thrust faulting normal to the margin as well as NW-SE oriented strike-slip faults between rotational blocks within the forearc (**Figures 2A–4A**), (Goldfinger and Kulm, 1997; Han et al., 2017; Han et al., 2018). Methane and other hydrocarbons are generated by biogenic and thermogenic processes within the sedimented accretionary wedge. Sediment compression begins on the incoming abyssal plain, seaward of the deformation front, and high pore pressures have been observed west of the accretionary front, which along the USCM ranges in depth from 3,100 m in the south to 2,450 m in the north, with the exception of a shallower value of 2,500 m just north of the Mendocino FZ in northern California. In the lower margin, methane concentrations may not have reached saturation values in the pore fluid, and methane-enriched fluid flow is diffuse without producing gas phase emissions (Kulm et al., 1986; Salmi et al., 2017). The majority of deep water bubble streams on the Cascadia accretionary prism occur on the northern Oregon margin, in the vicinity of Hydrate Ridge off central Oregon, and on the southern Oregon and northernmost California margin (**Figures 3A–5A**). These sites are typically located on the summits and/or flanks of the first few anticlinal ridges landward of the deformation front. The area where free gas is present at depth below the methane hydrate layer can be determined by mapping the presence of the BSR on seismic reflection records such as seen in **Figures 8A,B**, as well as subsequent figures.

The compilation of archival MCS data in Phrampus et al. (2017) plots the landward limit of the BSRs relative to the FEMHS (**Figure 1B**). This compilation shows that BSRs present on the upper slope (shallower than 750 m water depth) often correlates with the presence of gas bubble streams at 500 m at the eastern end of the profile. Although the seismic data coverage in the Phrampus et al. (2017) study is incomplete, BSRs reach the upper slope in latitude bands defined by 46.0–47.5°N, 44.0–45.0°N, and 42.5–43.4°N. BSRs can be traced to near the FEMHS on some seismic profiles off northern Oregon, central Oregon in the vicinity of Heceta Bank (**Supplementary Figure S4**), (Torres et al., 2009), and southern Oregon on the western edge of Coquille Bank (Phrampus et al., 2017). Also, BSRs terminate 15–25 km seaward of the FEMHS in the relatively dense MCS profile coverage between 40.3°N at Cape Mendocino and 42.0°N (**Figure 1B**).

Within the present inventory, bubble emission sites occurring near the FEMHS are common along much of the Washington and northern/central Oregon margin, generally corresponding to the areas of upper slope BSRs (Phrampus et al., 2017; Salmi et al., 2017). Conversely, they are not present on the upper slope of the northern California margin, where the BSR images appear limited to the lower slope (**Supplementary Figure S3**). Analyses of some seismic reflection profiles (next section) indicate that the BSR can sometimes be traced up to very near the FEMHS, although the resolution of those data is not precise enough to measure the exact depth of disappearance of the reflector. Our observations are consistent with the concentration of gas plumes at sites near the 500 m isobaths, where there is coincidence of the landward limits of both the FEMHZ and the BSR. We suggest that this is caused by gas migration along the base of the hydrate layer and exiting at the FEMHS.

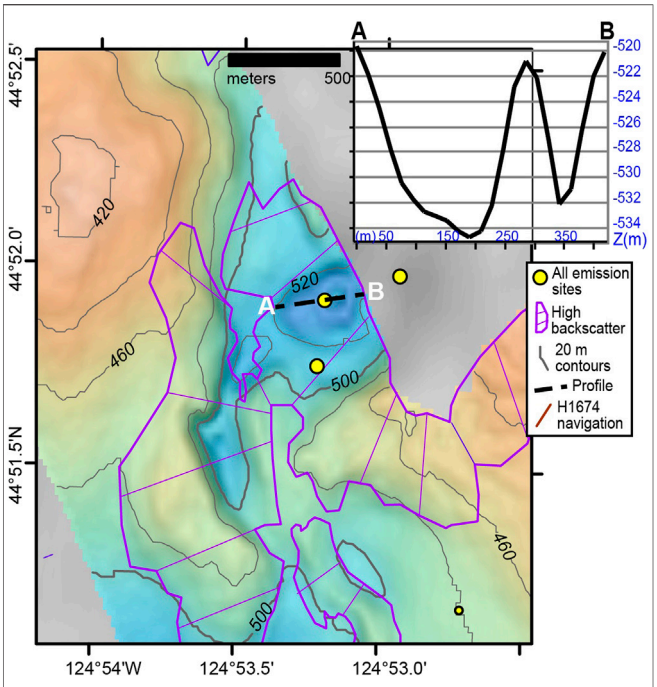

FIGURE 9 | Possible pockmark on the Oregon margin with several bubble emission sites within and on the rim of the depression. Emission sites (yellow dots) at/near the 500 m FEMHS zone. Areas of high backscatter delimited by purple outline and hatch lines. Upper right inset is a profile over the collapse. EM302 bathymetry overlaid on background grid depicts the 14 m dip on the western edge of the depression, a mound in the center and another 12 m dip on the eastern edge.

Washington Margin

Archival MCS coverage on the Washington margin is relatively abundant and the BSR has been mapped onto the mid and upper slope off southern Washington (**Figure 1B**, **Supplementary Figure S3**). Johnson et al. (2015), Phrampus et al. (2017), Salmi et al., 2017, and Johnson et al. (2019) previously examined Washington margin bubble stream distribution with respect to the underlying BSR and thus will not be covered in this manuscript. It should be noted that Phrampus et al. (2017) indicate a gap in the BSR distribution between 47.5 and 48.25°N on the Washington margin. Coincidentally, the shelf break bubble emission sites are particularly abundant within that same latitudinal range (**Figure 2**). Holbrook et al. (2002) and Johnson et al. (2019) suggest that a correlation between the presence of subseafloor BSRs and subsurface methane emission sites are independent factors and that a hydrate/gas interface can occur even when the BSR is not imaged in the seismic profile.

Astoria Canyon

Astoria Canyon is a dynamic environment where several simultaneous geological processes could produce enhanced gas emissions. First, the topography of a canyon concentrates geothermal gradient isotherms directly below the valley (Poort et al., 2007) resulting in higher heat flow through the floor, which distorts the BSR reflectors and causes 'feather-edge' methane emissions to occur deeper than the normal FEMHS (Hautala et al., 2014; Salmi et al., 2017). Second, gas accumulating within an over-pressured gas-rich high porosity zone beneath the BSR

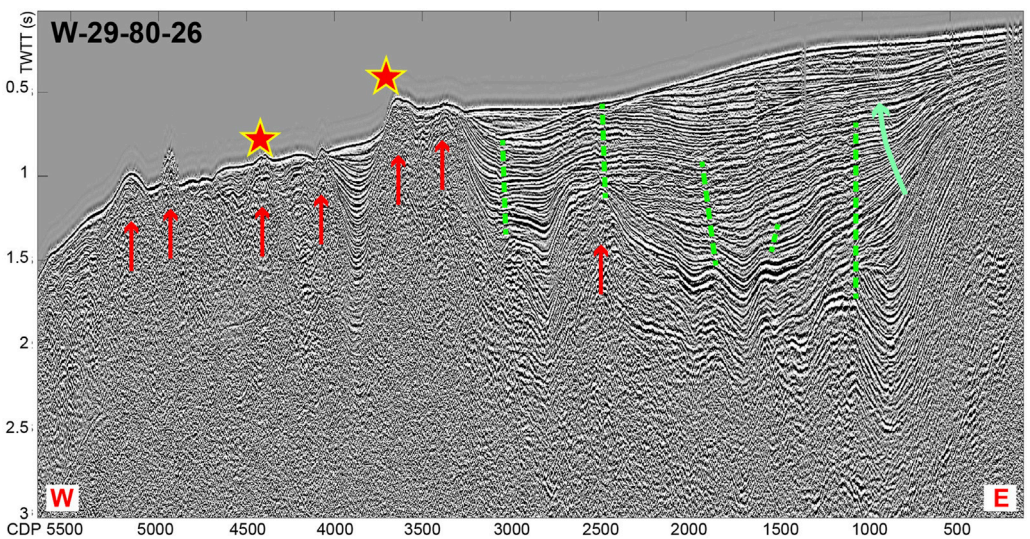

FIGURE 10 | West-to-east MCS profile W-29–80–26 north of Newport on the central Oregon margin (see **Figure 3A**). Red stars represent methane emission sites. Red arrows are diapirs with gas blanking apparent. Green dashed lines are offsets of sediment layers due to faulting. There is clear evidence of upward migration of diapirs that result in nearby venting at 500 m (~CDP 3700) and 730 m (~CDP 4400) water depth. Listric faulting is evident in the fanning of sediment layers near the landward **(right)** side of profile where the green arrow shows rotation and seaward thickening of sediment layers. The faults adjacent to the diapirs illustrate that the diapirs are being thrust upward. The listric faults shown as green dashed lines at the landward edge of the profile suggest long-term post-seismic extension of the upper margin–similar to the WA margin (Johnson et al., 2019).

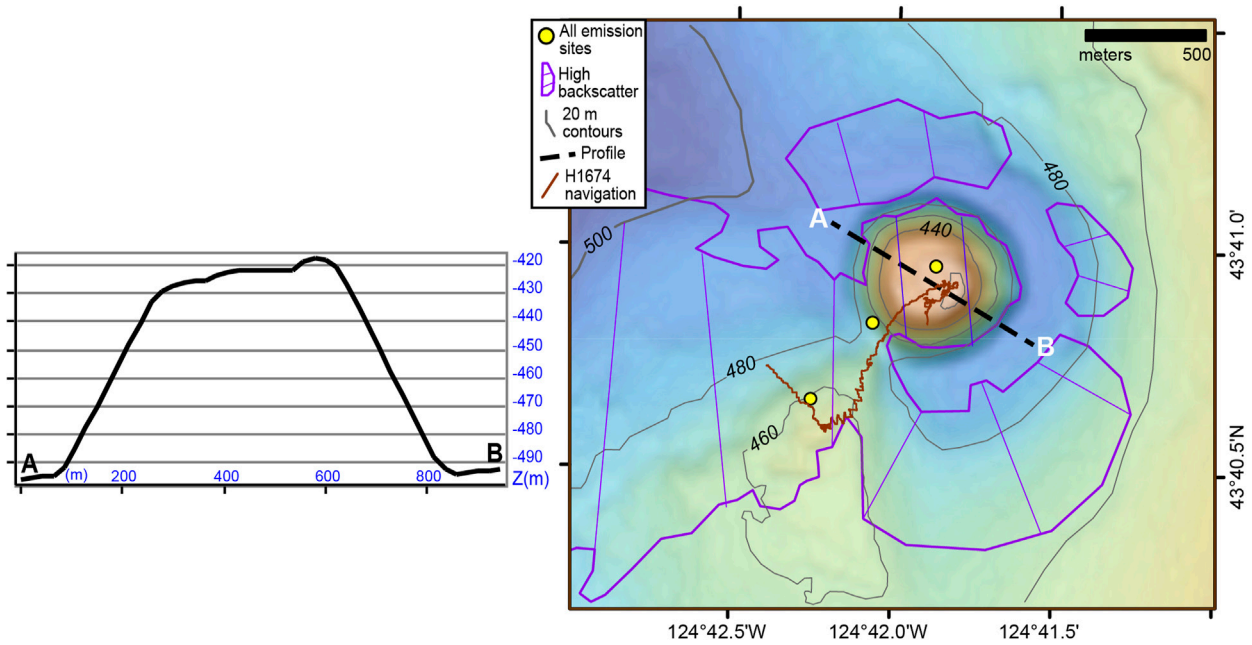

FIGURE 11 | Mud volcano on the Oregon Cascadia margin. The profile to the left indicates that the feature rises ~80 m from a moat-like surrounding circular depression. The mud volcano and surrounding seafloor exhibit high backscatter values, with the exception of the depression that flanks the feature. Emission sites (yellow dots) at/near the 500 m FEMHS zone. Areas of high backscatter delimited by purple outline and hatch lines.

(Crutchley et al., 2015) would migrate toward the canyon axis (Orange and Breen, 1992) and has been proposed to create hydrofractured pathways for gas egress (Tréhu et al., 2004). An ROV dive within the canyon thalweg at 850 m depth discovered gas bubble streams likely released from the free-gas zone beneath the overlying solid hydrate layer (Baumberger et al., 2018). We think it's likely that this and other gas plumes in the down-cut section of Astoria canyon are locally controlled by the opening of pathways to permeable sediment horizons by faults beneath the canyon and erosional turbidity currents and slumping of the canyon walls (**Figure 3**).

Acoustically bright bubble streams were identified on the south rim of Astoria Canyon near the 500 m isobath where an E-W MCS profile (W-39_4,098; **Figure 8A**) shows a shoaling BSR. This and other BSRs discussed below were identified by the acoustic wave polarity reversal relative to the seafloor reflection, which is characteristic of BSRs. The BSR is detectable up to/near the FEMHS at 500 m (0.68 s two-way travel time). A Hercules remotely operated vehicle (ROV) dive there in 2016 found a number of steady-state, high-flux bubble streams (**Figure 8C**), (Embley et al., 2017; Baumberger et al., 2018; Seabrook et al., 2018).

Almost all the canyon-parallel clusters of bubble emission sites occur within the portion of the canyon that is incised into the continental shelf, down to a water depth of 700 m. Within the shelf, gas emissions occur along the canyon thalweg and near the base of the canyon walls. The complex topography of the canyon produces East–West oriented MCS images that are difficult to interpret due to 3D topographic effects. However, several archival North–South MCS lines oriented orthogonal to the canyon thalweg provide a vertical cross-section through margin sediments that contain BSR images associated with known active methane emission sites. **Figure 8B** shows one of these North–South profiles (W-39–85–4,019) that intersects a cluster of methane emission sites exposed at 577 m water depth on the canyon floor.

Astoria Canyon is a dynamic environment where several simultaneous geological processes could produce enhanced gas emissions. First, the topography of a canyon concentrates geothermal gradient isotherms directly below the valley (Poort et al., 2007) resulting in higher heat flow through the floor, which distorts the BSR reflectors and causes 'feather-edge' methane emissions to occur deeper than the normal FEMHS (Hautala et al., 2014; Salmi et al., 2017). Second, gas accumulating within an over-pressured gas-rich high porosity zone beneath the BSR (Crutchley et al., 2015) would migrate toward the canyon axis (Orange and Breen, 1992) and has been proposed to create hydrofractured pathways for gas egress (Tréhu et al., 2004). The concentration of gas plumes in this down-cut section of the canyon could be controlled by the outcropping of permeable sediment horizons and/or faults within the canyon. Finally, erosional turbidity currents and slumping of the canyon walls can also create new pathways. An ROV dive within the canyon thalweg at 850 m discovered gas bubble streams venting from beneath a layer of methane hydrate that probably exposed one of the permeable horizons (**Figure 8D**). The gas bubble emissions at a depth of 850, 350 m below the FEMHS, could be coming from the free-gas zone beneath the overlying solid hydrate layer (Baumberger et al., 2018), or from canyon-enhanced currents such as have been

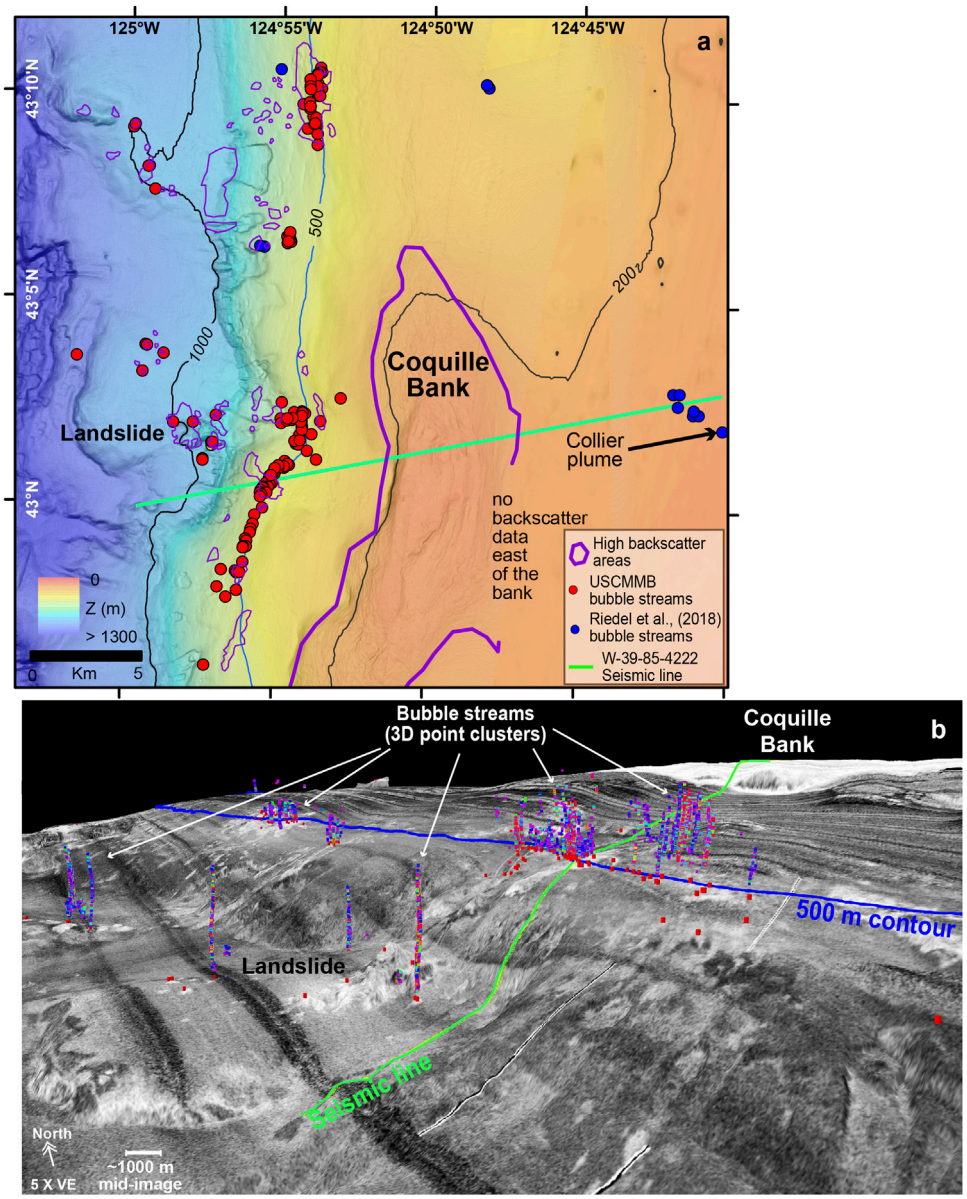

FIGURE 12 | 2D and 3D images of Coquille Bank in an area of an unusual number of bubble streams along the 500vm contour. **(A)** 2D north-up map of central-northern Coquille Bank and shelf. Red and blue circles are individual bubble streams, which range in depth from <200 to >1,000 m. Landslide features are evident along the slope. The green line represents MCS profile W-39–85-4,222 across the seeps (**Figure 13A**). Purple polygons define areas of high acoustic backscatter. **(B)** 3D view of EM302 bathymetry of Coquille Bank overlaid with seafloor backscatter, as viewed from the southwest looking onto area of **(A)**. Red cylinders on the seafloor are individual bubble stream locations. High amplitude bubble streams are characterized as 3D point clusters rising from the seafloor into the water column. The 500 m contour (blue line) and seismic line (light green line) are shown. White patches in the backscatter data are indicative of harder substrate and may represent areas of carbonates. 5 times vertical exaggeration.

documented for erosion of seafloor hydrate in Barkley Canyon (Thomsen et al., 2012).

Northern Oregon Margin–Astoria Canyon to Heceta Bank

On the N–S multibeam transits between Astoria Canyon and southern Heceta Bank, more than 60 gas emission sites were detected at or near the 500 m isobath (**Figure 3**). Although USCMMB selectively surveyed along the 500 m depth contour, the Riedel et al. (2018) east-west fisheries sonar lines also include about a third of the total number of detected seep sites along this section within the same depth range. In comparison with other areas of the Cascadia margin where we purposely surveyed along the 500 m isobath, this area appears to be a "hotspot" for 500 m emission sites, continuing the trend from the Washington

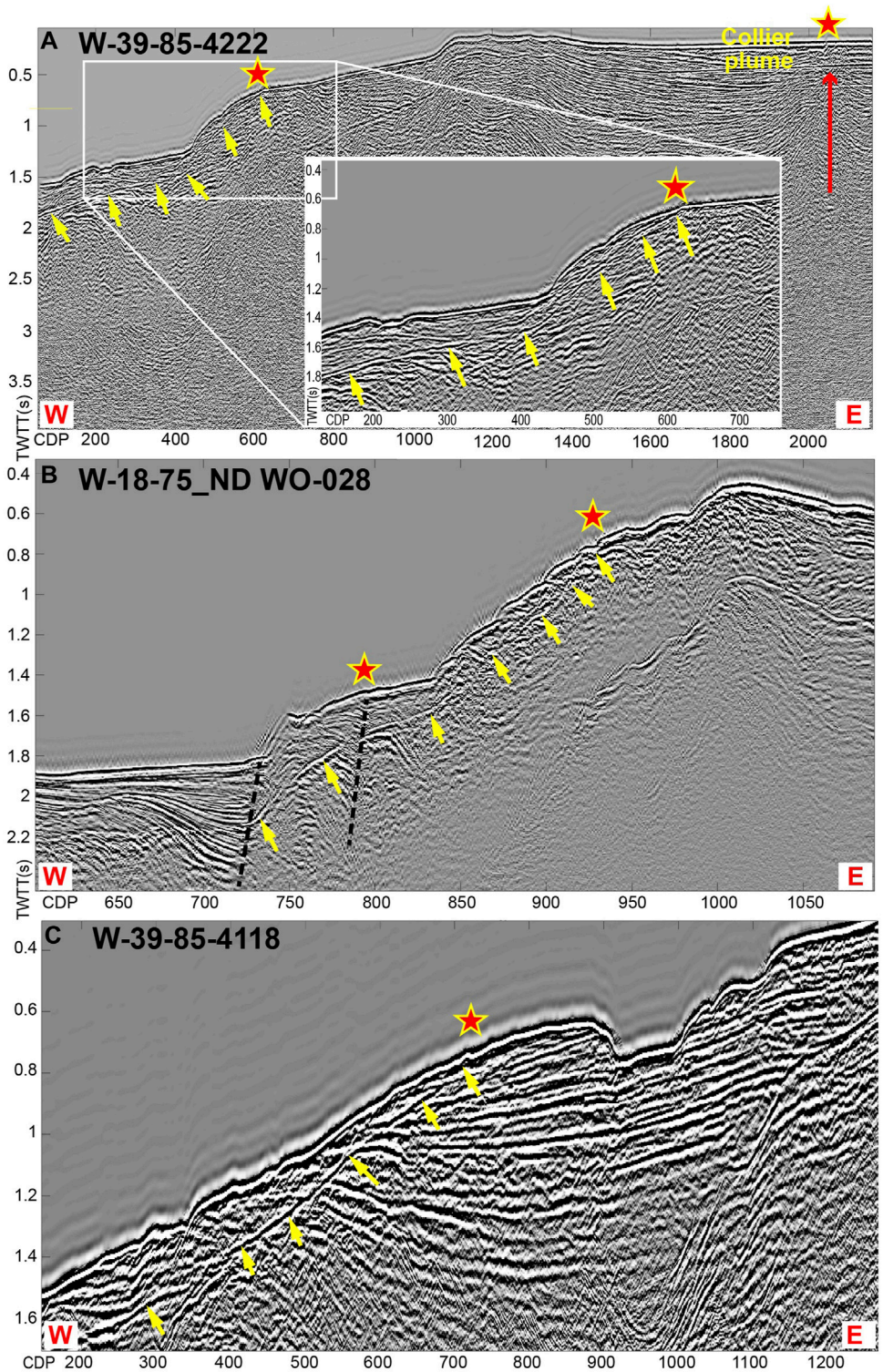

FIGURE 13 | MCS profiles across Coquille Bank and Rogue Canyon, southern Oregon margin. Red stars represent methane emission sites. Yellow arrows point to BSR reflectors. **(A)** W–E MCS profile W-39–85–4,222 across Coquille Bank (**Figures 4A**, **12**). Emission at east **(right)** end of profile (156 m water depth) is site of a submersible study by Collier and Lilley (2005). Location on **Figure 11A**. Note large diapir rising beneath this site (red arrow) with interior gas wipe-outs. Seaward site is at the FEMHS. Right lower center image is a blow up of BSR shoaling to the feather edge at 483 m. **(B)** MCS profile W-18–75_ND-28 across southern Coquille Bank (**Figure 4A**). This profile has a BSR that ends at 500 m water depth (~CDP 925), with a bubble emission site nearby. The deeper bubble emission site is at 1,067 m water depth (~CDP 780) and appears co-located with a fault (black dashed line at CDP 780)—and the fault intersects and disrupts the BSR. There is another fault at the base of the slope where the sediment layers fan out, suggesting rotation on a listric fault (black dashed line at CDP 725).

margin. Most of these sites are located within areas of high amplitude backscatter associated with seafloor carbonate deposits, which also are associated with methane emissions (Kulm and Suess, 1990; Carson et al., 1994; Johnson et al., 2003). Many of the bubble emission sites in this region overlie diapirs apparent in the MCS data on steep local slopes. In one location (~44°52′N), bubble emission sites are concentrated within a large (1.5 km diameter) depression (**Figure 9**) in an area of high acoustic backscatter that covers an extensive area of the upper slope. The concentration of methane bubble emission sites associated with the depression near the FEMHS appears to implicate dissociating methane hydrate, similar to those described by Paull et al. (2014). A well-defined BSR approaches the emission site on an MCS profile shown in Tréhu et al. (1995). Active diapirs in this area (Profile W-29–80–26; **Figure 10**) could cause uplift, triggering dissociation of hydrate, breaching of the impermeable cap overlying the free gas zone, with the resulting expulsion of gas creating the carbonate-rimmed pockmarks similar to those described elsewhere (Hovland et al., 1987; Salmi et al., 2011; Skarke et al., 2014). The steep local seafloor slopes in this region (**Figure 3B**) would enhance lateral landward migration of gas beneath the BSR and emissions near the FEMHS.

Heceta Bank

Bubble emission sites in the vicinity of Heceta Bank occur along the 500 m isobath and on the summit of the topographic high bank in water depths as shallow as 80 m (**Figure 3**). Heceta Bank is a remnant of the outer high formed by underthusting of sediments (Kulm and Fowler, 1974; Fleming and Trehu, 1999). Pockmarks are common on the seaward slope between 150 and 400 m. Analysis of carbon isotopes from ROV-recovered authigenic carbonate samples show a mixed biogenic and thermogenic signature (Torres et al., 2009). Visual exposures of methane hydrate deposits were found in small depressions in association with bubble streams and concentrations of tubeworms, clams, microbial mats and other chemosynthetic life (Embley et al., 2017; Baumberger et al., 2018). Vigorous bubble streams were found during ROV dive H1677 (**Figure 3B**) at 500 m water depth at the head of the small canyon at the northwest corner of the bank (44°50′N). A MCS profile (W-29–80–18; **Supplementary Figure S4**) just to the south of this site shows a shallowing of the BSR to 600 m, and sediment slope failures that suggest long term instability in this area (Trehu et al., 1995; Torres et al., 2009), which is within the headwall region of the Heceta megaslide (HS; **Figure 3**) which were described in previous studies (Goldfinger et al., 2000).

Another bubble emission site just south of Heceta Bank (43°52.5′N:124°55.6′W) at ~500 m was visited in 2001 by the ROPOS ROV (Torres et al., 2009), and bubble streams were observed within a large seep and carbonate area. Analysis of the carbonates revealed that one carbonate sample from that site is likely sourced from dissociated methane hydrate. Our observations of additional dense gas bubble streams and high flux seafloor vents along the 500 m isobath bounding Heceta Bank supports the Torres et al. (2009) hypothesis of a relationship between long-term seafloor uplift and dissociation of hydrate as a possible cause of slope instability in the Heceta Bank region.

Southern Oregon—Heceta Bank to Rogue Canyon

South of Heceta Bank, bubble stream emission sites are sparsely distributed along the NA072 traverses that bracket the 500 m isobath. However, one of these sites appears to be a mud volcano (at 43°41′N) (**Figures 4A**, **11**). The bubble streams are sited near/on a truncated 1 km diameter cone rising 80 m from a base at 500 m water depth. There is a diapir-like structure beneath this feature (westernmost side of Figure 10 of Clarke et al., 1985), and this morphology is interpreted as a constructional feature built by fluidized, gas-rich, over-pressured sediment flowing from a central vent (Brown, 1990; Dimitrov, 2002). An ROV dive (H1674) in 2018 (**Figure 4B**) identified extensive carbonate deposits and seeps on the flank and summit (Baumberger et al., 2019). A cluster of bubble emission sites is also located on a previously active diapir located 12 km SW of the mud volcano site at 480–750 m depth (Clarke et al., 1985).

To the south, on the western edge of Coquille Bank, there are two linear N–S arrays of 13 (northern) and 21 (southern) emission sites that closely follow the 500 m FEMHS isobath (**Figures 4A**, **12A**), which is the approximate location of the landward edge of the BSR over much of the margin. Several well-defined slide scars and slump masses occur west and downslope of these sites, and the high backscatter patches (**Figure 12B**) of presumptive carbonate deposits overlap much of the slope encompassing the bubble emission sites, suggesting long-term methane venting. Profile W-39–85-4,222 (**Figure 13A** and inset) crosses the southern cluster of 500 m sites and indicates that the BSR continues up to near the 500 m water depth, where the emission sites are concentrated, suggesting that a substantial sub-surface gas reservoir is being tapped.

Placed within a regional context, sites on the western edge of Coquille Bank are along the proposed headwall area of a large mega-slide, the Coos basin slide (CBS) (**Figure 4A**), that was dated at 450 Ka. by Goldfinger et al. (2000). This is one of several mega-slides mapped by the extent on their slump deposits buried in the Cascadia basin. Goldfinger et al. 2000 also propose that the mega-slides account for the disrupted topography in this area, specifically the absence of accretionary anticlinal ridges that are found north of Heceta Bank and between the Rouge and Trinidad Canyons. The numerous recent slide scars and slump masses, and the wave-cut strata of Coquille Bank on the shelf, are manifestations of both long- and short-term uplift in this region (Kulm and Fowler, 1974; Burgette et al., 2009).

Bubble emission sites on the upper slope southwest of Coquille Bank (42°45′N) lie within the area of the Blanco mega-slide (BS), which is dated at 1,209 ± 112 Ka by Goldfinger et al. (2000) (**Figure 4A**). This area is geologically complex, with seep sites occurring from 400 to 1,100 m depth. The slope is disrupted by numerous slide scars and erosional channels at scales from <1 to 10 km. The E–W MCS profile through the emission site clusters (W-18–75-ND-28; **Figure 13B**) shows a BSR shoaling to the FEMHS that coincides with an active bubble emission site. Slump

topography is also present on the upper slope in this area with faults present on the lower slope, one of which is coincident with a bubble emission site. Helium-3 anomalies in the bubble stream fluid samples taken from this site are consistent with deep faulting on the upper slope (H1521; **Figure 4B**), (Baumberger et al., 2018). Future 3D seismic studies will assist in determining the depth of the faulting, which is most likely connected to mantle rock because of the Helium-3 signal.

Southern Cascadia Margin–Coquille Bank to Cape Mendocino

South of Coquille Bank, the Rogue Canyon area lies within the southern half of the Blanco mega-slide (BS; **Figure 4A**) and contains scattered bubble emission sites associated with sediment slope failures and sediment channels. Several emission sites occur on the west wall of the largest of the Rogue Canyon channels where a prominent BSR shoals near the FEMHS at 500 m (profile W-39–85-4,118; **Figure 13C**); a pattern similar to other profiles discussed previously from the Oregon margin. The Rogue Canyon area is approximately at the latitude where the landward extension of the BSR moves seaward (**Figure 1B**), (Phrampus et al., 2017).

Our multibeam coverage between Rogue Canyon and Trinidad Canyon is dense on the middle and lower continental slope at depths greater than 600 m, but is sparse on the upper slope and continental shelf (**Figures 4A**, **5A**). Our USCMMB survey bracketed the 500 m isobath, but did not detect any sites except on the wall of the Rogue Canyon. In this area, a significant extent of mid-lower continental slope (>600 m) is associated with large N-S tectonic thrust ridges, many of which are covered with high acoustic backscatter seafloor reflections and bubble emission sites on their crest or sides. Several dives with the Hercules ROV in this area in 2016 and 2018 (H1522, H1523, and H1669; **Figure 4B**) reveal that these zones are covered by extensive carbonate pavements.

Although the USCMMB between Trinidad Canyon and Cape Mendocino has sparse overall multibeam coverage, we again surveyed along the 500 m isobath through this region (**Figure 5A**). Even with these new data, only a small number of sites on/near the FEMHS have been identified, in contrast with the rest of Cascadia margin. This is consistent with the seaward shift of the landward limit of the BSR in this region (**Figure 1B**), (Phrampus et al., 2017).

This southernmost area of Cascadia margin is impacted by the tectonic influence of the Mendocino triple junction, which is the intersection of the San Andreas transform fault, the Mendocino transform fault linking to the Gorda ridge, and the Cascadia subduction zone (**Figures 1A**, **5A**). Because of the proximity of the triple junction, this is the only area of the Cascadia margin with high levels of historical seismicity (Furlong and Schwartz, 2004; Dziak et al., 2011). High erosion rates from rapid uplift in the adjacent California coast range drain sediment through several large submarine canyons that are incised into the continental shelf and slope, producing substantial forearc basin deposits (Eel river basin) and a deep-water sediment fan (Eel fan) seaward of the accretionary front (Puig et al., 2003). The combination of high sedimentation and high seismicity results in chronic sediment slope failures. As an example, the Humbolt slide was a well-studied sediment failure triggered on the upper margin slope by a large earthquake in 1980, after which excess rates of gas were released into the overlying water column (Field and Jennings, 1987). Numerous bubble streams have been mapped on the continental shelf by Yun et al. (1999) between Trinidad head and Eel Canyon. Bubble streams occur at known seep sites near the 500 m isobath (Orphan et al., 2004; Levin, 2005) and near and within adjacent areas where hydrate has been cored near the seabed (Kennicutt et al., 1989; Brooks et al., 1991). In deeper water, clusters of bubble emission sites and seeps are located in several large sediment failures on the walls of Eel Canyon and on the adjacent accretionary front to the south between 1750 and 2073 m (**Figure 5A**), (Gardner et al., 2009; Paull et al., 2014). Hydrate was also found on the seafloor in the headwall region of one of these slides (Paull et al., 2014) and was sampled on Hercules dive H1668 in the same area (Baumberger et al., 2019), (**Figure 5B**).

DISCUSSION

The new dataset shows a clear clustering of methane emission sites centered on the FEMHS along the majority of the along-strike length of the Cascadia margin. The depth of the FEMHS is the limit above which there is no impermeable hydrate barrier to prevent the egress of gas into the ocean, and gas seep sites appear to be concentrated at this boundary. The association of methane seeps and carbonate pavements with most of the 500 m sites indicates that fluid emissions through the sediment-water interface have been occurring for 100–1,000s of years at these locations and within this narrow 500 m depth range (Teichert et al., 2003), and are unlikely to be the result of a recent environmental change (Hautala et al., 2014).

One possible explanation for this observation is the common occurrence of the regional BSR shoaling very close to the FEMHS at the location of the MCS profile (**Figures 1B**, **Supplementary Figure S3**). The presence of the BSR is an observation of the presence of free gas below the solid hydrate in the sediment pore spaces, rather than the P–T conditions that allow for the theoretical presence of significant free gas. The existence of this sub-seafloor barrier suggests that free gas collects and migrates beneath the lower surface of the hydrate layer. This upward and landward migration of free gas into shallower depths is then emitted into seawater at the first available exit point permitted by the P–T conditions. This pattern has been observed at other temperate continental margins such as the US East coast (Skarke et al., 2014) and Makran (von Rad, 2000) and on the Arctic margin of Svalbard (Westbrook et al.,2009), although the latter also has significant seasonal temperature variations. One other prediction from this hypothesis is that sites at the FEMHS will be more vigorous and less time variable, because of a steady-state supply of gas generated over a wide area of the margin surface and then concentrated along the pressure gradient. The presence of bubble streams along the 500 m isobaths means the methane is sufficiently concentrated for gas ebullition rather than diffuse flow. The presence of diapirs and

faults underlay and steepen the continental slope along Cascadia, and this topography would serve to enhance gas migration landward along the Washington and Oregon margin (Johnson et al., 2019 and this study).

The FEMHS 500 m isobath zone is a key boundary in assessing the potential for increased mass flux of methane to the seafloor and water column due to ocean warming that might cause increased hydrate dissociation along the FEMHS (Westbrook et al., 2009; Hautala et al., 2014; Darnell and Flemings, 2015; Johnson et al., 2015; Ruppel and Kessler, 2017). There are some well-constrained examples of previous long-term warming moving the BSR upward in the sedimentary column (e.g., Bangs et al., 2010), therefore as the current ocean warming trends continue, some movement of this thermal stability limit is likely. For example, Phrampus and Hornbach (2012) modeled significant changes in the course of the Gulf Stream in the western Atlantic due to warming. Our data show what appears to be a normal distribution of sites centered on the 500 m isobath, which constitutes the FEMHS for the Cascadia margin. Although additional data are necessary to support this interpretation, long-term monitoring of this boundary, especially where the BSR approaches the FEMHS, could benefit from resurvey(s) of the 500 m isobath to identify deviations from the normal distribution curve. We estimate that a shipborne survey with two multibeam lines along the 500 m isobath on Cascadia margin (about 1 week of ship time plus transits) on a decadal schedule could effectively monitor this boundary. Where well-defined BSRs are present up to or near the FEMHS, high resolution seismic resurveys could be used to monitor shifts in the landward edge of the BSR.

SUMMARY/CONCLUSION

We have compiled an inventory of methane gas emission sites from dedicated multibeam surveys (USCMMB) and recently published archival data across the full along-strike length of the US portion of the Cascadia margin. For the USCMMB data inventory, the distribution of bubble emission sites on the US Cascadia margin, when normalized to the survey coverage and area of depth intervals, reveals two primary populations of methane seep peaks, one at continental shelf depth centered at 175 m, and the other closely bracketing the upper limit of the FEMHS at 500 m.

Cascadia methane plumes are extraordinarily abundant and appear to have clearly identifiable origins; 1) on the continental shelf, upward migration from sediment loading is enhanced and localized by specific fault zones. 2) at the continental shelf edge, the abundance of plume sites follows the deep westward reaction faulting that follows and is associated with megathrust faulting of the Cascadia Subduction Zone (Wang and Hu, 2006; Wang et al., 2012; Johnson et al., 2019). 3) At the FEMHS, roughly 500 m water depth, the concentration of methane plumes appears associated with the disappearance of the solid hydrate cap, which allows the migration of methane gas through the sediments at the P–T equilibrium point for Cascadia.

The remaining plumes are sparsely distributed on the lower margin between the 500 m isobath and the deformation front do not have a clearly understood source region, although studies on the Oregon margin have correlated the active plume sites and tectonic faults on the lowermost margin tip. It is significant, but not yet understood why there are no methane plumes deeper or westward of the deformation front, although multiple surveys have been conducted in this area. Clearly, sediment loading, methane gas buoyancy and the faulting associated with the formation of an active margin from previously undisturbed sediments combine to produce a very complex system that produces an abundance of methane vents on the Cascadia margin.

Overall, 75% of bubble emission sites occur on the upper slope and shelf at less than 600 m water depth, with 25% in deeper water. Many of the deeper sites on the middle and lower slope (>525 m) are coincident with major compressional anticlinal and diapiric ridges within the accretionary prism. With more surveys, the ratio of shallow to deep sites is predicted to increase, since only 14% of the shallow areas less than 200 m depth has been surveyed. These results are similar to recent summaries of historical data along other parts of the Cascadia by Johnson et al. (2015, 2019) and Riedel et al. (2018). The distribution of bubble emission sites along the Cascadia margin as a whole is consistent with free gas emissions occurring predominantly at or immediately shallower than the upper limit of the FEMHS, which has also been observed at other continental margins.

The statistical peak of emission site depths centered on the FEMHS is striking. Looking at the USCMMB and fisheries sonar data (Riedel et al., 2018) where they overlap from 48.0° to 43.5°N, sites within the narrow depth range of 475–525 m are common on the Washington and Oregon margin but are sparse within the Northern California segment. Even if recent anthropogenic warming at the depth of the FEHMS is presently dissociating hydrate to some degree (Johnson et al., 2015), the association of methane-mediated carbonate deposits with many of the 500 m sites indicates that gas emissions through the sediment-water interface have been occurring for 100s–1000s of years within this depth range.

Gas outflow occurring at the depth of the FEMHS is likely because the thermal dissolution of solid hydrate in sediment pore spaces would allow free gas egress to the ocean. The Cascadia margin is an example of where methane in the gas phase can migrate beneath the impermeable cap of hydrate-filled sediment pores within the free gas zone below the BSR. This capped upward flow is also concentrated along structures such as rising diapirs and faults, with amplification along steep topographic slopes and moving landward until the P–T conditions do not facilitate the formation of solid hydrate, allowing egress of methane through the sediments into the ocean. An anthropogenic warming ocean would induce seaward migration of the FEMHS in the future, a process that could be monitored by geophysical techniques now in hand.

DATA AVAILABILITY STATEMENT

Information on data availability for each of the multibeam surveys is provided in the Supplemental Material document,

section II: Metadata–Multibeam Water Column Data Expeditions, Data Availability, Data Analysis and Credits. Raw multibeam data can be downloaded at Rolling Deck to Repository (R2R) as well as at NOAA National Centers for Environmental Information (NCEI) for all surveys except those on the R/V Nautilus. The positions of individual bubble streams and clustered emission sites for all the water column data will be available for download on the NOAA EOI website at the time of publication. https://www.pmel.noaa.gov/eoi/Cascadia-margin.html. Multi Channel Seismic (MCS) data, which are publicly available at the U.S. Geological Survey (USGS) website: https://walrus.wr.usgs.gov/namss/.

AUTHOR CONTRIBUTIONS

SM co-wrote the manuscript with RE and HPJ. SM post-processed multibeam seafloor and water column data for expeditions TN265, NA070, NA072, NA078 and RR1712. SM performed statistical analysis on all the multibeam datasets and combined the Riedel et al. (2018) bubble stream data with the USCMMB data for additional analysis. SM created the figures and tables in the manuscript, and participated in NA072 and NA078 expeditions at sea. RE was lead scientist on the NA072 expedition wrote portions of sections describing and interpreting the pattern of methane seeps on within the context of the regional and local geology. HPJ analyzed the seismic profiles utilized in several figures. BP enhanced the manuscript with his previous work on the BSR seismic database and contributed data for figures in the manuscript, modified from Phrampus et al. (2017). T-KL clustered the individual bubble streams into 300 m seep emission sites. NR was expedition leader on NA072 and NA078. NR contributed to the processing of seafloor and water column data on both expeditions. LG was expedition leader on NA080 and NA088. LG contributed to the processing of seafloor and water column data on both expeditions.

FUNDING

We thank the NOAA Office of Exploration and Research (OER) for funding scientific personnel and post-expedition data analysis for E/V *Nautilus* expeditions NA072, NA078, NA080 and NA088. Ship time for those *Nautilus* expeditions was funded by Ocean Exploration Trust (OET) and OER. Additional funding for RWE, SGM, Tamara Baumberger and Camilla Wilkinson work on Cascadia margin provided by NOAA Pacific Marine Environmental Laboratory (PMEL). Support for this study was also supplied by the NOAA Earth-Ocean Interactions (EOI) Program and the Cooperative Institute for Marine Resources Studies (CIMRS) under NOAA Cooperative Agreement No. NA110AR4320091.

ACKNOWLEDGMENTS

We are grateful to the team on the E/V *Nautilus* for their assistance during the NA072 ROV expedition, and at-sea data processing and analysis performed by the OET mapping team on all E/V *Nautilus* expeditions. Special thanks for the assistance and support provided by Tamara Baumberger (OSU/NOAA EOI) both during NA072 and as chief scientist on NA095, and for providing guidance on this manuscript. HPJ and Erica Sampaga (Univ. of Washington) processed water column multibeam data from the NOAA ship *Rainier* expedition 1605RA, with ship time supported by the NOAA Olympic Coast Marine National Sanctuary. Thanks as well to the crews and scientific party, Chris Romsos (OSU) chief scientist, on the R/V *Thompson* for collecting seafloor and water column data during the TN265 expedition. Also thanks to chief scientist Bill Chadwick (NOAA EOI) and the crew of the R/V *Revelle* for collecting seafloor and water column data on the margin during the RR1712 expedition. Informative discussions with Anne Trehu and Marta Torres on Cascadia margin seeps were important in the cruise planning for NA072. William W. Chadwick, and Jeff Beeson provided valuable edits to the manuscript. The USGS MCS data were downloaded from this website: https://walrus.wr.usgs.gov/namss/survey. PMEL Contribution Number: 5060.

SUPPLEMENTARY MATERIAL

The Supplementary Material for this article can be found online at: https://www.frontiersin.org/articles/10.3389/feart.2021.531714/full#supplementary-material.

REFERENCES

Archer, D. (2007). Methane hydrate stability and anthropogenic climate change. *Biogeosciences.* 4 (4), 521–544. doi:10.5194/bg-4-521-2007

Bangs, N. L. B., Musgrave, R. J., and Tréhu, A. M. (2005). Upward shifts in the southern Hydrate Ridge gas hydrate stability zone following postglacial warming, offshore Oregon. *J. Geophys. Res.* 110, 39. doi:10.1029/2004JB003293

Bangs, N. L., Hornbach, M. J., Moore, G. F., and Park, J.-O. (2010). Massive methane release triggered by seafloor erosion offshore southwestern Japan. *Geology* 38, 1019–1022. doi:10.1130/G31491.1

Baumberger, T., Embley, R. W., Merle, S. G., Lilley, M. D., Raineault, N. A., and Lupton, J. E. (2018). Mantle-derived Helium and multiple methane sources in gas bubbles of cold seeps along the Cascadia continental margin. *Geochem. Geophys. Geosyst.* 19, 4476–4486. doi:10.1029/2018GC007859

Baumberger, T., Merle, S. G., Wilkinson, C., Roe, K., Buck, N., Embley, R. W., et al. (2019). further exploration of methane seeps on the Cascadia margin. *Oceanography* 32.(Suppl. 40-41). 1. doi:10.5670/oceanog.2019.supplement.01

Berndt, C., Feseker, T., Treude, T., Krastel, S., Liebetrau, V., Niemann, H., et al. (2014). Temporal constraints on hydrate-controlled methane seepage off svalbard. *Science* 343 (6168), 284–287. doi:10.1126/10.1126/science.1246298

Biastoch, A., Treude, T., Rüpke, L. H., Riebesell, U., Roth, C., Burwicz, E. B., et al. (2011). Rising Arctic Ocean temperatures cause gas hydrate destabilization and ocean acidification. *Geophys. Res. Lett.* 38, L08602. doi:10.1029/2011GL047222

Bohrmann, G., Greinert, J., Suess, E., and Torres, M. (1998). Authigenic carbonates from the Cascadia subduction zone and their relation to gas hydrate stability.

Geology 26 (7), 1654–1656. doi:10.1130/0091-7613(1998)026<0647:acftcs>2.3.co;2

Brooks, J. M., Field, M. E., and Kennicutt, M. C., II (1991). Observations of gas hydrates in marine sediments, offshore northern California. *Mar. Geology.* 96, 103–109. doi:10.1016/0025-3227(91)90204-h

Brown, K. M. (1990). The nature and hydrogeologic significance of mud diapirs and diatremes for accretionary systems. *J. Geophys. Res.* 95 (B6), 8969–8982. doi:10.1029/jb095ib06p08969

Burgette, R. J., Weldon, R. J., and Schmidt, D. A. (2009). Interseismic uplift rates for western Oregon and along-strike variation in locking on the Cascadia subduction zone. *J. Geophys. Res.* 114 (B1), 112. doi:10.1029/2008JB005679

Carson, B., Seke, E., Paskevich, V., and Holmes, M. L. (1994). Fluid expulsion sites on the Cascadia accretionary prism: mapping diagenetic deposits with processed GLORIA imagery. *J. Geophys. Res.* 99 (B6), 11959–11969. doi:10.1029/94jb00120

Carson, B., Suess, E., and Strasser, J. C. (1990). Fluid flow and mass flux determinations at vent sites on the Cascadia margin accretionary prism. *J. Geophys. Res.* 95 (B6), 8891–8897. doi:10.1029/jb095ib06p08891

Carson, B. (1977). Tectonically induced deformation of deep-sea sediments off Washington and northern Oregon: mechanical consolidation. *Mar. Geol.* 24, 289–307. doi:10.1016/0025-3227(77)90073-1

Chapman, R., Pohlman, J., Coffin, R., Chanton, J., and Lapham, L. (2004). Thermogenic gas hydrates in the northern Cascadia margin. *Eos Trans. AGU.* 85, 361–365. doi:10.1029/2004eo380001

Ciais, P., Dolman, A. J., Bombelli, A., Duren, R., Peregon, A., Rayner, P. J., et al. (2014). Current systematic carbon-cycle observations and the need for implementing a policy-relevant carbon observing system. *Biogeosciences.* 11, 3547–3602. doi:10.5194/bg-11-3547-2014

Clarke, S. H., Field, M. E., and Hirozawa, C. A. (1985). Reconnaissance geology and geologic hazards of the offshore Coos Bay basin, Oregon. *U.S. Geol. Surv. Bull.* 1645, 114. doi:10.3133/b1645

Collier, R. W., and Lilley, M. D. (2005). Composition of shelf methane seeps on the cascadia continental margin. *Geophys. Res. Lett.* 32, L06609. doi:10.1029/2004GL022050

Crutchley, G. J., Fraser, D. R. A., Pecher, I. A., Gorman, A. R., Maslen, G., and Henrys, S. A. (2015). Gas migration into gas hydrate-bearing sediments on the southern hikurangi margin of New Zealand. *J. Geophys. Res. Solid Earth.* 120 (2), 725–743. doi:10.1002/2014jb011503

Darnell, K. N., and Flemings, P. B. (2015). Transient seafloor venting on continental slopes from warming-induced methane hydrate dissociation. *Geophys. Res. Lett.* 42, 10765–10772. doi:10.1002/2015gl067012

Davies, R. J., Yang, J., Li, A., Mathias, S., and Hobbs, R. (2015). An irregular feather-edge and potential outcrop of marine gas hydrate along the mauritanian margin. *Earth Planet. Sci. Lett.* 423, 202–209. doi:10.1016/j.epsl.2015.04.013

Dimitrov, L. I. (2002). Mud volcanoes—the most important pathway for degassing deeply buried sediments. *Earth-sci. Rev.* 59 (1–4), 49–76. doi:10.1016/S0012-8252(02)00069-7

Dziak, R. P., Hammond, S. R., and Fox, C. G. (2011). A 20-year hydroacoustic time series of seismic and volcanic events in the Northeast Pacific Ocean. *Oceanography* 24 (3), 280–293. doi:10.5670/oceanog.2011.79

Egger, M., Riedinger, N., Mogollón, J. M., and Jørgensen, B. B. (2018). Global diffusive fluxes of methane in marine sediments. *Nat. Geosci.* 11, 421–425. doi:10.1038/s41561-018-0122-8

Embley, R., Raineault, N., Merle, S., Baumberger, T., Seabrook, S., and Hammond, S. (2017). Water column and cold seep exploration of the Cascadia Margin.*Oceanogr. Front. Ocean Explor Suppl.* 30, 28–30. doi:10.1130/ges00648.1

Ewing, J. I., and Hollister, C. D. (1972). *Regional aspects of deep sea drilling in the western north Atlantic. Initial reports of the deep sea drilling project*, Vol. 85. Washington: U.S. Government Printing Office, 951–973. doi:10.2973/dsdp.proc.11.132.1972

Field, M. E., and Jennings, A. E. (1987). Seafloor gas seeps triggered by a northern California earthquake. *Mar. Geol.* 77, 39–51. doi:10.1016/0025-3227(87)90082-x

Fleming, S. W., and Tréhu, A. M. (1999). Crustal structure beneath the central Oregon convergent margin from potential-field modeling: evidence for a buried basement ridge in local contact with a seaward dipping backstop. *J. Geophys. Res.* 104.(B9), 20431–20447. doi:10.1029/1999jb900159

Frederick, J. M., and Buffett, B. A. (2014). Taliks in relict submarine permafrost and methane hydrate deposits: pathways for gas escape under present and future conditions. *J. Geophys. Res. Earth Surf.* 119, 106–122. doi:10.1002/2013JF002987

Furlong, K. P., and Schwartz, S. Y. (2004). Influence of the mendocino triple junction on the tectonics of coastal California. *Annu. Rev. Earth Planet. Sci.* 32, 403–433. doi:10.1146/annurev.earth.32.101802.120252

Gardner, J. V., Malik, M., and Walker, S. (2009). Plume 1400 meters high discovered at the seafloor off the northern California margin. *Eos Trans. AGU.* 90, 275. doi:10.1029/2009eo320003

Geersen, J., Scholz, F., Linke, P., Schmidt, M., Lange, D., Behrmann, J. H., et al. (2016). Fault zone controlled seafloor methane seepage in the rupture area of the 2010 Maule earthquake, Central Chile. *Geochem. Geophys. Geosyst.* 17.(11), 4802–4813. doi:10.1002/2016GC006498

Goldfinger, C., Galer, S., Beeson, J., Hamilton, T., Black, B., Romsos, C., et al. (2017). The importance of site selection, sediment supply, and hydrodynamics: a case study of submarine paleoseismology on the Northern Cascadia margin, Washington USA. *Mar. Geol.* 384, 4–46. doi:10.1016/j.margeo.2016.06.008

Goldfinger, C., Kulm, L. D., McNeil, L. C., and Watts, P. (2000). Super-scale failure of the southern Oregon cascadia margin. *Pure Appl. Geophys.* 157, 1189–1226. doi:10.1007/s000240050023

Goldfinger, C., Kulm, L. D., Yeats, R. S., McNeill, L., and Hummon, C. (1997). Oblique strike-slip faulting of the central cascadia submarine forearc. *J. Geophys. Res.* 102, 8217–8243. doi:10.1029/96jb02655

Goldfinger, C., Nelson, C. H., Morey, A. E., Johnson, J. E., Patton, J. R., Karabanov, E., et al. (2012). Turbidite event history—methods and implications for holocene paleoseismicity of the cascadia subduction zone. Corvallis, OR, United States: Oregon State University. Paper 1661–F, 170 p. Available at https://pubs.usgs.gov/pp/pp1661f/. doi:10.3133/pp1661f

Graves, C. A., James, R. H., Sapart, C. J., Stott, A. W., Wright, I. C., Berndt, C., et al. (2017). methane in shallow subsurface sediments at the landward limit of the gas hydrate stability zone offshore western Svalbard. *Geochimica et Cosmochimica Acta.* 198, 419–438. doi:10.1016/j.gca.2016.11.015

Graves, C. A., Steinle, L., Rehder, G., Niemann, H., Connelly, D. P., Lowry, D., et al. (2015). Fluxes and fate of dissolved methane released at the seafloor at the landward limit of the gas hydrate stability zone offshore western svalbard. *J. Geophys. Res. Oceans.* 120, 6185–6201. doi:10.1002/2015jc011084

Greinert, J., Lewis, K. B., Bialas, J., Pecher, I. A., Rowden, A., Bowden, D. A., et al. (2010). methane seepage along the hikurangi margin, New Zealand: overview of studies in 2006 and 2007 and new evidence from visual, bathymetric and hydroacoustic investigations. *Mar. Geology.* 272, 6–25. doi:10.1016/j.margeo.2010.01.017

Han, S., Bangs, N. L., Carbotte, S. M., Saffer, D. M., and Gibson, J. C. (2017). Links between sediment consolidation and Cascadia megathrust slip behaviour. *Nat. Geosci.* 10, 954. doi:10.1038/s41561-017-0007-2

Han, S., Carbotte, S. M., Canales, J. P., Nedimović, M. R., and Carton, H. (2018). Along-trench structural variations of the subducting juan de fuca plate from multichannel seismic reflection imaging. *J. Geophys. Res. Solid Earth.* 123 (4), 3122–3146. doi:10.1002/2017jb015059

Hautala, S. L., Solomon, E. A., Johnson, H. P., Harris, R. N., and Miller, U. K. (2014). Dissociation of cascadia margin gas hydrates in response to contemporary ocean warming. *Geophys. Res. Lett.* 41 (23), 8486–8494. doi:10.1002/2014GL061606

Holbrook, W. S., Gorman, A. R., Hornbach, M., Hackwith, K. L., Nealon, J., Lizarralde, D., et al. (2002). Seismic detection of marine methane hydrate. *Lead. Edge* 21 (7), 686–689. doi:10.1190/1.1497325

Hong, W.-L., Torres, M. E., Portnov, A., Waage, M., Haley, B., and Lepland, A. (2018). Variations in gas and water pulses at an arctic seep: fluid sources and methane transport. *Geophys. Res. Lett.* 45, 4153–4162. doi:10.1029/2018gl077309

Hope, C., and Schaefer, K. (2016). Economic impacts of carbon dioxide and methane released from thawing permafrost. *Nat. Clim. Change* 6 (1), 56–59. doi:10.1038/nclimate2807

Hovland, M., Talbot, M. R., Qvale, H., Olaussen, S., and Aasberg, L. (1987). Methane-related carbonate cements in pockmarks of the North Sea. *J. Sediment. Res.* 57 (5), 881–892. 10.1306/212F8C92-2B24-11D7-8648000102C1865D

Johnson, H. P., Merle, S., Salmi, M., Embley, R., Sampaga, E., and Lee, M. (2019). Anomalous concentration of methane emissions at the continental shelf edge of

the northern cascadia margin. *J. Geophys. Res. Solid Earth* 124, 2829. doi:10.1029/2018JB016453

Johnson, H. P., Miller, U. K., Salmi, M. S., and Solomon, E. A. (2015). Analysis of bubble plume distributions to evaluate methane hydrate decomposition on the continental slope. *Geochem. Geophys. Geosyst.* 16 (11), 3825–3839. doi:10.1002/2015GC005955

Johnson, J. E., Goldfinger, C., and Suess, E. (2003). Geophysical constraints on the surface distribution of authigenic carbonates across the hydrate ridge region, Cascadia margin. *Mar. Geol.* 202 (1-2), 79–120. doi:10.1016/S0025-3227(03)00268-8

Judd, A., and Hovland, M. (2008). *The impact on geology, biology and the marine environment*. Statoil, Norway, Cambridge University Press. doi:10.1017/CBO9780511535918

Kennicutt, M. C., Brooks, J. M., Bidigare, R. R., McDonald, S. J., Adkison, D. L., and Macko, S. A. (1989). An upper slope "cold" seep community: northern California. *Limnol. Oceanogr.* 34, 635–640. doi:10.4319/lo.1989.34.3.0635

Kretschmer, K., Biastoch, A., Rüpke, L., and Burwicz, E. (2015). Modeling the fate of methane hydrates under global warming. *Glob. Biogeochem. Cycles* 29, 610–625. doi:10.1002/2014GB005011

Kulm, L. D., Suess, E., Moore, J. C., Carson, B., Lewis, B. T., Ritger, S. D., et al. (1986). Oregon subduction zone: venting, fauna, and carbonates. *Science* 231 (4738), 561–566. doi:10.1126/science.231.4738.561

Kulm, L. D., and Fowler, G. A. (1974). "A test of the imbricate thrust model," in *The geology of continental margins. Oregon continental margin structure and stratigraphy*. Editors C. A. Burke and C. L. Drake (Berlin, Heidelberg: Springer), 261–283.

Kulm, L. D., and Suess, E. (1990). Relationship between carbonate deposits and fluid venting: Oregon accretionary prism. *J. Geophys. Res.* 95 (B6), 8899–8915. doi:10.1029/jb095ib06p08899

Kvenvolden, K. A., Collett, T. S., and Lorenson, T. D. (1993). Studies of permafrost and gas hydrates as possible sources of atmospheric methane at high latitudes. in *Biogeochemistry of global change*. Editor R. S. Oremland (New York: Springer), 487–501. doi:10.1007/978-1-4615-2812-8

Kvenvolden, K. A. (1993). Gas hydrates-geological perspective and global change. *Rev. Geophys.* 31.(2), 173–187. doi:10.1029/93rg00268

Kvenvolden, K. A. (1988b). Methane hydrate—a major reservoir of carbon in the shallow geosphere? *Chem. Geol.* 71, 41–51. doi:10.1016/0009-2541(88)90104-0

Levin, L. A. (2005). *Ecology of cold seep sedimentsinteractions of fauna with flow, chemistry and microbes. Oceanography and marine biology: an annual review*. Boca Raton: CRC Press, 11–56. doi:10.1201/9781420037449

McNeill, L. C., Goldfinger, C., Kulm, L. D., and Yeats, R. S. (2000). Tectonics of the neogene cascadia forearc basin: investigations of a deformed late miocene unconformity. *Geol. Soc. Am. Bull.* 112 (8), 1209–1224. doi:10.1130/0016-7606(2000)112<1209:totncf>2.0.co;2

Nimblett, J., and Ruppel, C. (2003). Permeability evolution during the formation of gas hydrates in marine sediments. *J. Geophys. Res.* 108 (B9), 2420. doi:10.1029/2001JB001650

Orange, D. L., and Breen, N. A. (1992). The effects of fluid escape on accretionary wedges 2. seepage force, slope failure, headless submarine canyons, and vents. *J. Geophys. Res.* 97, 9277–9295. doi:10.1029/92jb00460

Orange, D. L., McAdoo, B. G., Casey Moore, J., Tobin, H., Screaton, E., Chezar, H., et al. (1997). headless submarine canyons and fluid flow on the toe of the cascadia accretionary complex. *Basin Res.* 9, 303–312. doi:10.1046/j.1365-2117.1997.00045.x

Orphan, V. J., Ussler, W., III, Naehr, T. H., House, C. H., Hinrichs, K.-U., and Paull, C. K. (2004). Geological, geochemical, and microbiological heterogeneity of the seafloor around methane vents in the Eel River Basin, offshore California. *Chem. Geol.* 205, 265–289. doi:10.1016/j.chemgeo.2003.12.035

Paull, C. K., Hecker, B., Commeau, R., Freeman-Lynde, R. P., Neumann, C., Corso, W. P., et al. (1984). Biological communities at the Florida escarpment resemble hydrothermal vent taxa. *Science* 226, 965–967. doi:10.1126/science.226.4677.965

Paull, C. K., Caress, D. W., Thomas, H., Lundsten, E., Anderson, K., Gwiazda, R., et al. (2014). seafloor geomorphic manifestation of gas venting and shallow subbottom gas hydrate occurrences. *Geophere* 11 (2), 491–513. doi:10.1130/GEOS01012.1

Philip, B. T., Denny, A. R., Solomon, E. A., and Kelley, D. S. (2016a). Time-series measurements of bubble plume variability and water column methane distribution above Southern hydrate ridge, Oregon. *Geochem. Geophys. Geosyst.* 17, 1182–1196. doi:10.1002/2016gc006250

Phrampus, B. J., and Hornbach, M. J. (2012). Recent changes to the Gulf Stream causing widespread gas hydrate destabilization. *Nature* 490 (7421), 527. doi:10.1038/nature11528

Phrampus, B. J., Harris, R. N., and Tréhu, A. M. (2017). Heat flow bounds over the cascadia margin derived from bottom simulating reflectors and implications for thermal models of subduction. *Geochem. Geophys. Geosyst.* 18, 3309. doi:10.1002/2017GC007077

Poort, J., Kutas, R. I., Klerkx, J., Beaubien, S. E., Lombardi, S., Dimitrov, L., et al. (2007). Strong heat flow variability in an active shallow gas environment, Dnepr palaeo-delta, Black Sea. *Geo-Mar Lett.* 27, 185–195. doi:10.1007/s00367-007-0072-4

Puig, P., Ogston, A. S., Mullenbach, B. L., Nittrouer, C. A., and Sternberg, R. W. (2003). Shelf-to-canyon sediment-transport processes on the Eel continental margin (northern California). *Mar. Geol.* 193 (1–2), 129–149. doi:10.1016/s0025-3227(02)00641-2

Riedel, M., Scherwath, M., Römer, M., Veloso, M., Heesemann, M., and Spence, G. D. (2018). distributed natural gas venting offshore along the cascadia margin. *Nat. Commun.* 9, 3264. doi:10.1038/s41467-018-05736-x

Ruppel, C. D., Herman, B. M., Brothers, L. L., and Hart, P. E. (2016). Subsea ice-bearing permafrost on the U.S. Beaufort margin: 2. borehole constraints. *Geochem. Geophys. Geosyst.* 17, 4333–4353. doi:10.1002/2016GC006582

Ruppel, C. D., and Kessler, J. D. (2017). The interaction of climate change and methane hydrates. *Rev. Geophys.* 55 (1), 126–168. doi:10.1002/2016RG000534

Sahling, H., Römer, M., Pape, T., Bergès, B., dos Santos Fereirra., C., Boelmann, J., et al. (2014). gas emissions at the continental margin west of Svalbard: mapping, sampling, and quantification. *Biogeosciences* 11, 6029–6046. doi:10.5194/bg-11-6029-2014

Salmi, M. S., Johnson, H. P., and Harris, R. N. (2017). Thermal environment of the Southern Washington region of the cascadia subduction zone. *J. Geophys. Res. Solid Earth* 122 (8), 5852–5870. doi:10.1002/2016jb013839

Salmi, M. S., Johnson, H. P., Leifer, I., and Keister, J. E. (2011). Behavior of methane seep bubbles over a pockmark on the cascadia continental margin. *Geosphere* 7 (6), 1273–1283. doi:10.1130/GES00648.1

Saunois, M., Bousquet, P., Poulter, B., Peregon, A., Ciais, P., Canadell, J. G., et al. (2016). The global methane budget 2000–2012. *Earth Syst. Sci. Data* 8 (2), 697–751. doi:10.5194/essd-8-697-2016

Seabrook, S., C. De Leo, F.F. C., Raineault, N., Thurber, A. R., and Thurber, A. R. (2018). heterogeneity of methane seep biomes in the Northeast Pacific. *Deep Sea Res. Part Topical Stud. Oceanogr.* 150, 195–209. doi:10.1016/j.dsr2.2017.10.016

Skarke, A., Ruppel, C., Kodis, M., Brothers, D., and Lobecker, E. (2014). Widespread methane leakage from the sea floor on the northern US Atlantic margin. *Nat. Geosci* 7, 657–661. doi:10.1038/NGEO2232

Snavely, P. D., Jr (1987). "Tertiary geologic framework, neotectonics, and petroleum potential of the Oregon-Washington continental margin," in *Geology and resource potential of the continental margn of western north America and adjacent ocean basins-beaufort sea to baja California. Circum-pacific council for energy and mineral resources*. Editors D. W. Scholl, A. Grantz, and J. C. Vedder (Houston, TX), 305–335.

Suess, E., Carson, B., Ritger, S. D., Moore, J. C., Jones, M. L., Kulm, L. D., et al. (1985). Biological communities at vent sites along the subduction zone off Oregon. *Bull. Biol. Soc. Wash.* 6, 475–484.

Suess, E., Torres, M. E., Bohrmann, G., Collier, R. W., Greinert, J., Linke, P., et al. (1999). Gas hydrate destabilization: enhanced dewatering, benthic material turnover and large methane plumes at the Cascadia convergent margin. *Earth Planet. Sci. Lett.* 170, 1–15. doi:10.1016/s0012-821x(99)00092-8

Sun, T., Ellis, S., and Saffer, D. (2020). Coupled evolution of deformation, pore fluid pressure, and fluid flow in shallow subduction forearcs. *J. Geophys. Res. Solid Earth* 125, e2019JB019101. doi:10.1029/2019jb019101

Teichert, B. M. A., Eisenhauer, A., Bohrmann, G., Haase-Schramm, A., Bock, B., and Linke, P. (2003). U/Th systematics and ages of authigenic carbonates from Hydrate Ridge, cascadia margin: recorders of fluid flow variations. *Geochimica et Cosmochimica Acta* 67.(20), 3845–3857. doi:10.1016/s0016-7037(03)00128-5

Thomsen, L., Barnes, C., Best, M., Chapman, R., Pirenne, B., Thomson, R., et al. (2012). Ocean circulation promotes methane release from gas hydrate outcrops

at the NEPTUNE canada barkley canyon node. *Geophys. Res. Lett.* 39 (16), 113. doi:10.1029/2012GL052462

Torres, M. E., Embley, R. W., Merle, S. G., Trehu, A. M., Collier, R. W., Suess, E., et al. (2009). methane sources feeding cold seeps on the shelf and upper continental slope off central Oregon, USA. *Geochem. Geophys. Geosystems*.10 (11), 67. doi:10.29/2009/GC002518

Tréhu, A. M., Flemings, P. B., Bangs, N. L., Chevallier, J., Gràcia, E., Johnson, J. E., et al. (2004). feeding methane vents and gas hydrate deposits at south hydrate ridge. *Geophys. Res. Lett.* 31. doi:10.1016/s0012-821x(04)00219-5

Tréhu, A. M., Lin, G., Maxwell, E., and Goldfinger, C. (1995). A seismic reflection profile across the cascadia subduction zone offshore central Oregon: new constraints on methane distribution and crustal structure. *J. Geophys. Res.* 100 (B8), 15101–15116. doi:10.1029/95jb00240

Tréhu, A. M., Torres, M. E., Moore, G. F., Suess, E., and Bohrmann, G. (1999). Temporal and spatial evolution of a gas hydrate-bearing accretionary ridge on the Oregon continental margin. *Geol* 27, 939–942. doi:10.1130/0091-7613(1999)027<0939:taseoa>2.3.co;2

Urban, P., Köser, K., and Greinert, J. (2017). Processing of multibeam water column image data for automated bubble/seep detection and repeated mapping. *Limnol. Oceanogr. Methods* 15, 1–21. doi:10.1002/lom3.10138

von Rad, U., Berner, U., Delisle, G., Doose-Rolinski, H., Fechner, N., Linke, P., et al. (2000). Gas and fluid venting at the makran accretionary wedge off Pakistan. *Geo-Marine Lett.* 20, 10–19. doi:10.1007/s003670000033

Wang, K., Hu, Y., and He, J. (2012). Deformation cycles of subduction earthquakes in a viscoelastic Earth. *Nature* 484 (7394), 327–332. doi:10.1038/nature11032

Wang, K., and Hu, Y. (2006). Accretionary prisms in subduction earthquake cycles: the theory of dynamic coulomb wedge. *J. Geophys. Res.* 111, B06410. doi:10.1029/2005JB004094

Westbrook, G. K., Thatcher, K. E., Rohling, E. J., Piotrowski, A. M., Pälike, H., Osborne, A. H., et al. (2009). Escape of methane gas from the seabed along the west spitsbergen continental margin. *Geophys. Res. Lett.* 36 (15), 54. doi:10.1029/2009GL039191

Yeats, F. E., Varela, R., Thunell, R., Luerssen, R., Hu, C., and Walsh, J. J. (2005). The importance of continental margins in the global carbon cycle. *Geophys. Res. Lett.*, 32, L01602. doi:10.1029/2004GL021346

Yun, J. W., Orange, D. L., and Field, M. E. (1999). Subsurface gas offshore of northern California and its link to submarine geomorphology. *Mar. Geol.* 154, 357–368. doi:10.1016/s0025-3227(98)00123-6

Conflict of Interest: The authors declare that the research was conducted in the absence of any commercial or financial relationships that could be construed as a potential conflict of interest.

frontiers in Earth Science

ORIGINAL RESEARCH
published: 29 April 2021
doi: 10.3389/feart.2021.613234

Observations of Shallow Methane Bubble Emissions From Cascadia Margin

Anna P. M. Michel[1], Victoria L. Preston[1,2,3], Kristen E. Fauria[4,5] and David P. Nicholson[6]*

[1] Department of Applied Ocean Physics and Engineering, Woods Hole Oceanographic Institution, Woods Hole, MA, United States, [2] Department of Aeronautics and Astronautics, Massachusetts Institute of Technology, Cambridge, MA United States, [3] MIT-WHOI Joint Program in Oceanography/Applied Ocean Science & Engineering, Cambridge and Woods Hole, MA, United States, [4] Department of Marine Geology and Geophysics, Woods Hole Oceanographic Institution, Woods Hole, MA, United States, [5] Department of Earth and Environmental Sciences, Vanderbilt University, Nashville, TN, United States, [6] Department of Marine Chemistry and Geochemistry, Woods Hole Oceanographic Institution, Woods Hole, MA, United States

Open questions exist about whether methane emitted from active seafloor seeps reaches the surface ocean to be subsequently ventilated to the atmosphere. Water depth variability, coupled with the transient nature of methane bubble plumes, adds complexity to examining these questions. Little data exist which trace methane transport from release at a seep into the water column. Here, we demonstrate a coupled technological approach for examining methane transport, combining multibeam sonar, a field-portable laser-based spectrometer, and the ChemYak, a robotic surface kayak, at two shallow (<75 m depth) seep sites on the Cascadia Margin. We demonstrate the presence of elevated methane (above the methane equilibration concentration with the atmosphere) throughout the water column. We observe areas of elevated dissolved methane at the surface, suggesting that at these shallow seep sites, methane is reaching the air-sea interface and is being emitted to the atmosphere.

Keywords: methane, bubbles, Cascadia Margin, laser spectrometer, ocean sensing, surface vehicle, multibeam sonar, seeps

OPEN ACCESS

Edited by:
Tamara Baumberger, Oregon State University, United States

Reviewed by:
Marvin D. Lilley, University of Washington, United States
Pengfei Di, South China Sea Institute of Oceanology, Chinese Academy of Sciences, China

****Correspondence:***
Anna P. M. Michel
amichel@whoi.edu

Specialty section:
This article was submitted to Biogeoscience, a section of the journal Frontiers in Earth Science

Received: *01 October 2020*
Accepted: *06 April 2021*
Published: *29 April 2021*

Citation:
Michel APM, Preston VL, Fauria KE and Nicholson DP (2021) Observations of Shallow Methane Bubble Emissions From Cascadia Margin. Front. Earth Sci. 9:613234. doi: 10.3389/feart.2021.613234

INTRODUCTION

Methane (CH_4) seeps are found throughout the ocean at continental margins, geologically active sites (e.g., mud volcanoes), and in hydrate fields (McGinnis et al., 2006; Reeburgh, 2007). A vast number of seep sites with CH_4 bubble plumes have been identified. A central question has been whether CH_4 from these seeps reaches the sea surface and impacts the global atmospheric carbon budget (e.g., James et al., 2016; Ruppel and Kessler, 2017). Recent work suggests that CH_4 gas emitted in the deep ocean does not regularly reach the atmosphere because of gas exchange during bubble ascent, methane dissolution, and aerobic microbial oxidation of gas (e.g., Ruppel and Kessler, 2017). Yet, methane emitted from shallow sites has the potential to reach the ocean surface (McGinnis et al., 2006) and therefore has a disproportionate impact on gas flux across the air-sea interface. Several studies have documented the fate of methane gas from shallow (<100 m) seeps (Shakhova et al., 2010, 2014; Thornton et al., 2016; Pohlman et al., 2017). However, thorough assessments of shallow seep sites have not been completed in part because of the difficulty associated with studying bubble plumes due to their transient nature, stochastic release, and variable vigor. In this study, we contribute new observations from two shallow seep sites offshore Oregon that

show elevated levels of dissolved methane are present close to the ocean surface and above bubble plumes. Bubble streams have been shown to be numerous on the Cascadia Margin; for example, during a single cruise on the E/V Nautilus (NA072), over 800 bubble streams were located with multibeam sonar at depths between 104 and 2,073 m (Baumberger et al., 2018). Bubble plumes found along Hydrate Ridge, at depths greater than 500 m, have been observed using acoustic imaging to remain coherent to approximately 460 m before dissolution, and further studies have observed elevated concentrations of CH_4 in water samples around 200 m at these sites (Heeschen et al., 2003, 2005). The majority of closely studied seep sites have been found at the boundary of the hydrate stability zone, at depths between 400 and 600 m (Johnson et al., 2015), where negligible amounts of methane have been estimated to enter the atmosphere (Grant and Whiticar, 2002; Heeschen et al., 2005). Methane from shallow seep sites, just as in lakes, and reservoirs, may be greater contributors to atmospheric CH_4, as bubbles can reach the surface coherently (McGinnis et al., 2006). Therefore, shallow plume sites may significantly influence the overall contribution of CH_4 from the Cascadia Margin.

Methane within bubbles diffuses into seawater such that the concentration of dissolved CH_4 may become elevated in the water surrounding bubble plumes (e.g., McGinnis et al., 2006). Areas of elevated dissolved CH_4 have been observed at the surface of waters along Hydrate Ridge in addition to elevated surface concentrations near the coast due to upwelling (Rehder et al., 2002; Heeschen et al., 2005). Yet, few studies have demonstrated the existence of methane bubble plumes below areas of elevated CH_4 recorded at the surface ocean (Reeburgh, 2007). In addition, the spatial distribution of dissolved CH_4 in near surface waters has not been well resolved. Typically, to measure dissolved CH_4 in the water column at sea, CTD rosettes are used to collect water samples for *ex situ* analysis. The number of CTD casts that can be conducted is small compared to the size of the entire region, and the sparsity makes resolving the distribution of CH_4 in surface layers difficult.

Gas bubbles are strong acoustic reflectors such that bubble plumes can be identified by their "flare" shapes and high backscatter signal using acoustic instruments (Heeschen et al., 2003; Leifer et al., 2006; Westbrook et al., 2009). Shipboard multibeam acoustic surveys have been used to identify bubble plumes in the water column (Greinert et al., 2010; Colbo et al., 2014; Wilson et al., 2015; Loher et al., 2018). Acoustic surveys can then be used to identify plumes to ultimately inform target locations for dissolved methane measurements (e.g., via CTD casts).

In order to investigate and spatially resolve surface concentrations of dissolved methane, which would otherwise be difficult or impossible to do with CTD casts and acoustic studies alone, we apply a coupled technological approach. Specifically, we combined multibeam sonar with a field-portable laser-based spectrometer which was mounted on the ChemYak (Nicholson et al., 2018), a robotic surface kayak equipped with a suite of chemical sensors, to examine the concentration of dissolved methane near active bubble plumes. We demonstrate our technique at two shallow (<75 m depth) seep sites on the Cascadia Margin. Elevated dissolved methane (above the methane equilibration concentration with the atmosphere) was present from the seafloor throughout the water column including at the surface, suggesting that at these shallow sites, methane is reaching the air-sea interface and being emitted to the atmosphere.

MATERIALS AND METHODS

Overview

Ship-based multibeam acoustic sonar on the R/V Falkor was used to locate areas of methane seepage on the Cascadia Margin in September 2018 (Schmidt Ocean Institute Hunting Bubbles Cruise – FK180824). This multibeam sonar was utilized to find bubble plumes during bathymetric mapping surveys by searching for mid-water plume signatures in the sonar signal. At the areas of active seepage, a Niskin rosette along with a CTD were deployed for water column analysis. Dissolved methane concentrations within the Niskin bottle water samples were analyzed shipboard, immediately after collection, using a field-portable dissolved gas extractor and a laser-based spectrometer. After confirming elevated methane was present in the water column, an unmanned surface vehicle, the ChemYak, equipped with the same gas extractor and laser-based spectrometer was launched to take dense spatial measurements of dissolved methane in the near-surface waters. A surface vehicle has great benefit to shallow seep sites as they are too shallow for diving utilizing a large, deep submergence remotely operated vehicle (ROV).

Multibeam Acoustics for Seep Site Identification

The R/V Falkor has a hull-mounted Kongsberg EM710 multibeam system with an operational range of 70–100 kHz, well suited for observing shallow (<2000 m) sites. The swath width of the system is 175–250 m when working at depths of 35–75 m. Bubble plumes were initially visually identified in real time during bathymetric mapping of the areas. The latitude and longitude of the bubble plume sources were determined using the ship's location. Following the cruise, FM Midwater (QPS, Fledermaus) was used to fully process the EM710 data and for confirming bubble plume locations. The plume sites reported in this article represent all observations conducted by repeated multibeam surveys. Due to the challenges of defining unique plumes from multiple observations (Johnson et al., 2015, 2019) and the spatially and temporally discontinuous nature of bubble emissions (Westbrook et al., 2009; Römer et al., 2016), not all reported sites may be unique. Multiple bubble streams were classified as one plume when they were within close proximity (<50 m of each other).

Seep Sites

Bubble plumes were located in two shallow areas, Yachats seep site and Stonewall Bank seep site, based on the sonar surveys, utilizing a water column view approach (**Figure 1**). The Yachats seep site (44°21′N, 124°10′ W) has an average depth of 46 m, whereas the Stonewall Bank seep site (44°27′N,

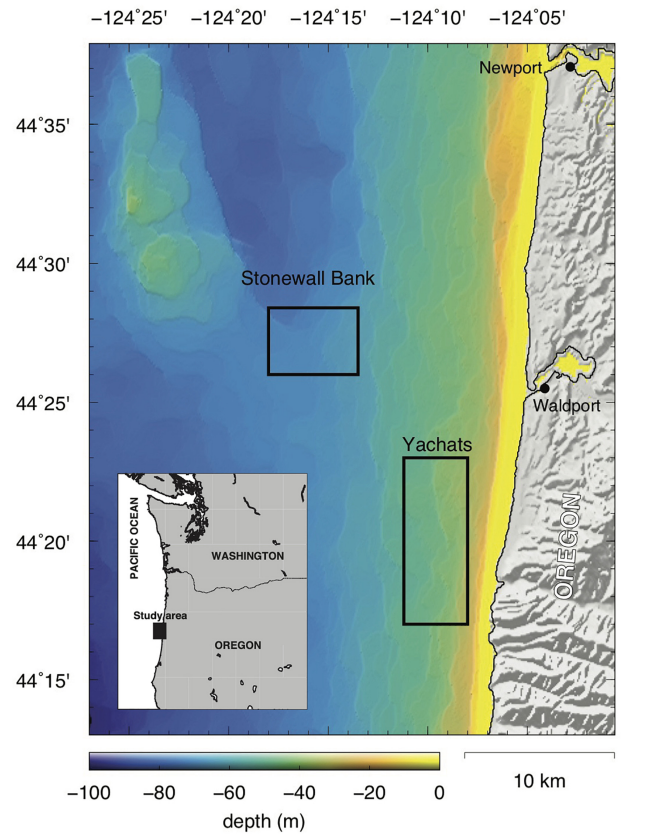

FIGURE 1 | Locations of Yachats and Stonewall Bank seep sites on the Cascadia Margin, offshore Oregon, United States. Background bathymetry sourced from GeoMapApp (http://www.geomapapp.org/).

124°16′ W), located further from shore, is slightly deeper with an average depth of 68 m. The seafloor at both sites is located above the gas hydrate stability zone. Bubble plumes in the vicinity of the Stonewall Bank site have been previously reported (NOAA Northwest Fisheries Science Center and Southwest Fisheries Science Center, 2015; Riedel et al., 2018) using an EK60 sonar. To the best of our knowledge, the Yachats seep site has not been previously identified, possibly due to its close proximity to the shore.

Dissolved Methane Analysis by Laser Based-Spectroscopy

A Los Gatos Research (LGR) Dissolved Gas Extraction Unit (DGEU), which utilizes a membrane contactor for dissolved gas extraction, was coupled to an LGR Greenhouse Gas Analyzer (GGA) to measure dissolved methane in seawater (Nicholson et al., 2018). The GGA utilizes off-axis integrated cavity output spectroscopy (OA-ICOS), for making fast (1 Hz), precise [<2 parts per billion (ppb)] measurements of methane. The GGA has a measurement range of 0 - 100 ppm and a precision of < 2 ppb (1 s). Calibration of the methane concentration was completed using gas standards (Mesa Gas) (**Supplementary Figure 1**). Methane concentration is measured by the GGA in parts per million (ppm), which is then converted to nM (nanomolar) using the salinity and temperature of the target water mass measured with a coupled CTD. The gas extraction technique does not completely separate gas from a water sample, so we apply a compensating extraction efficiency correction. For the DGEU used in this study, an extraction efficiency of 5.09% was determined by a series of validation tests previously performed in the Arctic (Manning et al., 2020) and applied to all data. When this extraction efficiency was applied to the data reported here, it resulted in consistent values for the baseline dissolved methane concentrations that are in equilibrium with atmospheric values.

Water Column Analysis

To investigate the vertical distribution of dissolved methane in the water column, water samples were collected for analysis shipboard using a Niskin rosette (SBE32 Carousel Water Sampler) at both Stonewall Bank and Yachats seep sites. Mounted to the rosette was a CTD (SBE 9 Plus) for measuring water column salinity and temperature along with a dissolved oxygen sensor (SBE 43). Three casts were made at the Yachats seep site and one cast was made at the Stonewall Bank seep site for water collection (**Table 1**). At the conclusion of each cast, water samples collected by the rosette were immediately analyzed shipboard by plumbing the DGEU inlet directly to a Niskin bottle and using the GGA to measure the methane concentration of the extracted gas. The coupling of the GGA to the DGEU for seawater analysis enables a high-precision, high sensitivity atmospheric methane sensor to be used for the rapid analysis of dissolved gases in ocean waters shipboard. It should be noted that there was a time delay between when each water sample was collected and when each Niskin bottle was analyzed with the GGA. However, any degassing that occurs from a Niskin bottle will result in an underreporting of dissolved methane concentration and not an overreporting.

In order to identify areas of elevated dissolved methane in the water column, a baseline atmospheric methane fraction of 1.86 ppm was utilized for both the Yachats and Stonewall Bank seep sites to calculate an expected equilibrium value. To convert this measurement to nM, spatially averaged, depth-dependent salinity and temperature measurements were computed from aggregated transects completed by the ChemYak for surface waters at both Yachats and Stonewall Banks sites. A dissolved methane concentration of 2.7 nM was found for the surface by using an average salinity of 32.47 PSU and a temperature of 13.18°C. For all three casts at the Yachats seep site, the equilibrium value of dissolved methane at different depths was estimated based on the salinity and temperature values measured at each of those depths during the CTD024 cast. At the Stonewall Bank seep site, the salinity and temperature values were obtained from cast CTD025.

ChemYak Robotic Kayak

The ChemYak (**Figure 2**) is a remotely controlled robotic kayak, or JetYak surface vehicle, developed at the Woods Hole Oceanographic Institution outfitted with a suite of chemical sensors for *in situ* greenhouse gas measurements in coastal and polar environments (Kimball et al., 2014; Nicholson et al., 2018;

TABLE 1 | Niskin rosette / CTD casts.

Seep site	Cast number	Location	Date/time of cast (GMT)	Depths of water collection (m)
Yachats	CTD022	44° 20.82′ N, 124° 10.25′ W	September 11, 2018 at 00:53	2, 5, 8, 12, 20, 25, 30, 45
	CTD023	44° 21.76′ N, 124° 9.77′ W	September 11, 2018 at 15:46	3, 5, 8, 12, 20, 25, 30, 37
	CTD024	44° 22.21′ N, 124° 11.08′ W	September 11, 2018 at 18:33	3, 5, 8, 13, 20, 25, 30, 35, 40, 44
Stonewall Bank	CTD025	44° 27.38′ N, 124° 15.96′ W	September 16, 2018 at 19:53	2, 6, 8, 18, 30, 40, 50, 60, 65

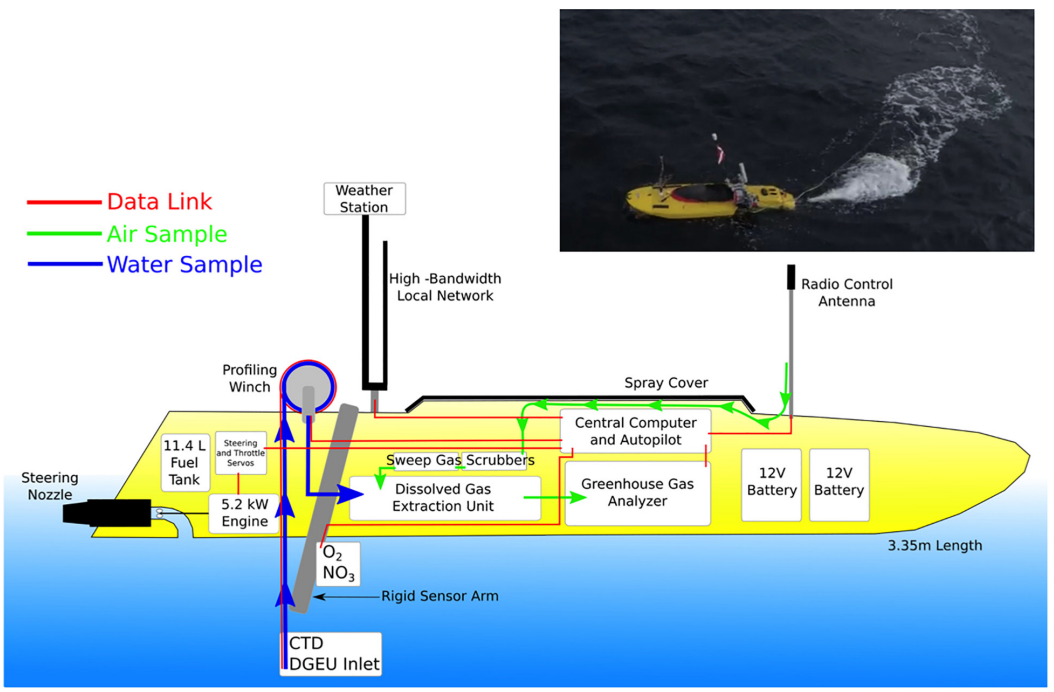

FIGURE 2 | The ChemYak, an unmanned surface vehicle, utilizes a suite of chemical sensors for surface water analysis (Kimball et al., 2014; Nicholson et al., 2018; Manning et al., 2020). Inset shows an image of the ChemYak deployed at Cascadia Margin.

Manning et al., 2020). The ChemYak chassis is a Mokai gas-powered air-jet propulsion kayak with servo-driven controls. A PixHawk autopilot and wireless radio network (2.4 GHz) is used to remotely operate the vehicle, and an onboard computer is used for data logging. The ChemYak has a draft of less than 20 cm and above water height of less than 2 m and is driven at an average speed of 1 m/s.

The ChemYak was deployed at the Cascadia Margin with a payload suite consisting of the DGEU, GGA, a CTD (RBR Concerto), and an air-marine weather station. All instruments were set to log at 1 Hz. The weather station was mounted to the mast of the vehicle (∼1.5 m above sea level), and used to log the GPS location of the vehicle, with standard 3 m accuracy for GPS navigation. A winch, with a 10 m cable, mounted at the back of the ChemYak was used to lower the CTD and the inlet tube for the DGEU into the surface waters, allowing measurements of methane to be made throughout the top 10 m of the water column. A small lag time (14–20 s) exists between the water entering the sampling tubing and the actual measurement in the GGA. The ChemYak enables fine resolution observations of surface waters due to the sampling rate of its instruments coupled to its speed, helping to reveal spatial features and resolve methane measurements in a target region of the water column that is classically difficult to capture with a Niskin rosette or with a ship flow-through system.

The ChemYak was deployed over the side of the R/V Falkor in sea state 2 conditions (smooth wavelets 0.1–0.5 m average wave height; **Table 2**) and remotely operated by a human pilot, in a secondary watercraft, who was equipped with a set of preliminary bubble plume coordinates determined from the shipboard multibeam. The secondary watercraft was deployed to enable driving and monitoring of the ChemYak in the open ocean, and to allow the human pilot to better observe sea-state conditions while operating the vehicle. The time between plume location using multibeam sonar and the deployment of the ChemYak was on the order of hours.

TABLE 2 | ChemYak deployment conditions.

Site	Date/time of deployment (GMT)	Sea state[§]	Wind force
Yachats	September 13, 2018 at 23:54 to September 14, 2018 at 01:48	2	2/3
Stonewall Bank	September 16, 2018 at 23:25 to September 17, 2018 at 02:07	2, then reducing to 1	3, then reducing to 2

[§]*Sea state 2: smooth wavelets 0.1–0.5 m average wave height; sea state 1: calm rippled 0–0.1 m average wave height.*

Following a mission and upon return to the ship, the data logged on the ChemYak computer were saved to external drives for post-processing and analysis. Quality control of the data collected by each instrument was performed by human inspection, largely to remove launch and recovery segments of the mission which tended to be noisy due to pulling air through the DGEU, to check for data dropout, and to correct for instrument time-response. Measurements from all instruments were linearly interpolated onto a common time frame in order to directly associate methane measurements with salinity, temperature, depth, and geolocation recorded by other instruments. Additionally, observations from the GGA were converted from ppm to nM following the procedure previously outlined (from Nicholson et al., 2018), using the salinity and temperature measurements from the CTD which was co-located with the DGEU inlet.

A single survey of the surface waters of each of the two seep sites, Yachats and Stonewall Bank, was completed using the ChemYak. In aggregate across the two sites, over 16,500 measurements (>4.5 recorded hours at 1 Hz logging frequency) of dissolved methane were recorded using the combined DGEU and GGA set-up on the ChemYak, representing over 20 km traveled by the ChemYak.

RESULTS

Yachats Seep Site

Multibeam sonar acoustic surveys of the Yachats area resulted in the identification of 92 seep sites with bubble plumes (**Figure 3**, **Supplementary Figure 2** and **Supplementary Table 1**). Many of these plumes were composed of multiple bubble streams (**Figure 4**). We resurveyed portions of the Yachats area 2–3 times such that a single seep site may be represented multiple times in our dataset. We do not attempt to quantify duplicate observations because: (1) the tracklines of the ship varied between surveys making direct comparisons difficult (**Supplementary Figure 2**); and (2) the intensity of bubble plumes can vary in time which also adds uncertainty to comparisons of repeat surveys.

Of the 92 bubble plumes identified, 68 were located within 50 m of the edge of a seafloor depression (i.e., potential pockmarks or trawl marks), 9 were located farther than 50 m from

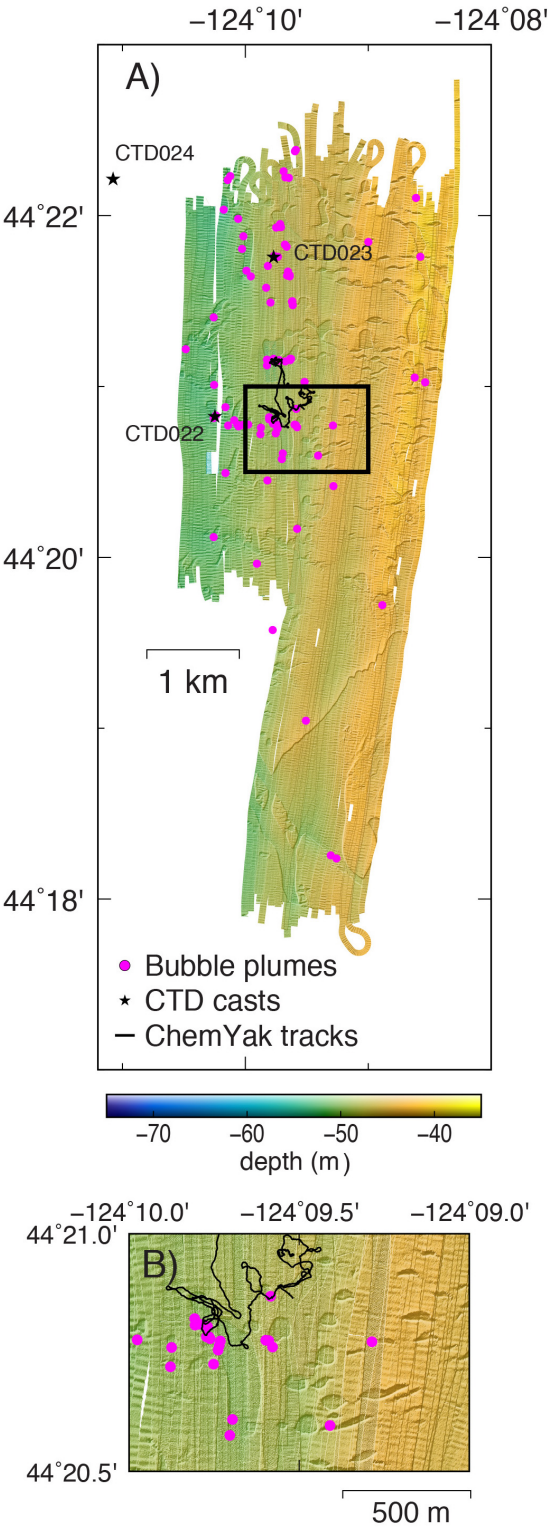

FIGURE 3 | Yachats seep site. **(A)** Locations of bubble plumes, CTD casts, and ChemYak tracks are plotted with the bottom bathymetry derived from the EM710 multibeam data and gridded at 1 m resolution. **(B)** The zoomed in area shows the pockmark features on the seafloor located close to bubble plume sites.

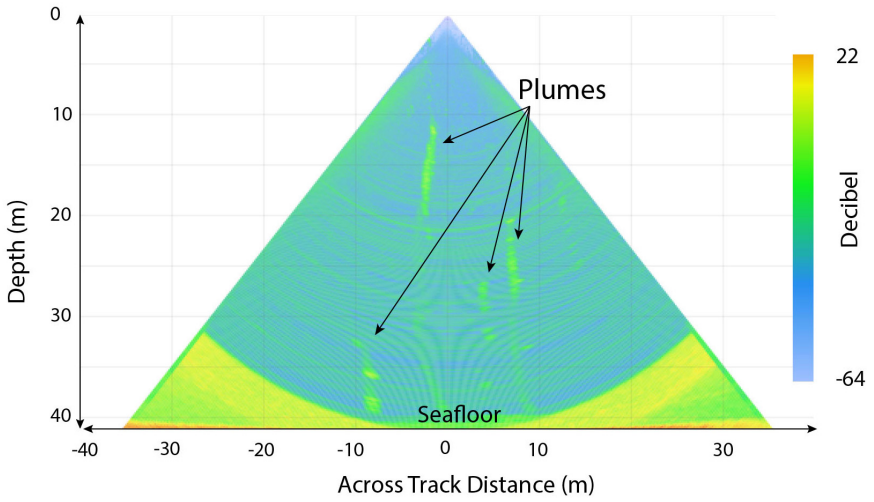

FIGURE 4 | Representative bubble plumes detected with the Kongsberg EM710 multibeam system within the Yachats study area. This image shows how multiple bubble plumes were sometimes present in close proximity on the seafloor. The plumes rise vertically and to variable distances in the water column. This 2D fan view image was created by selecting the highest hydroacoustic sounding from a 14 m thick swath and using Qimera software. These plumes were detected on September 11, 2018 at 1:39:27 UTC and at 44° 20.78′ N, 124° 9.78′ W.

a seafloor depression, and 15 were located above bathymetric features that were not resolvable (**Figure 3**).

The three CTD profiles collected at the Yachats site all showed elevated methane at depths throughout the water column (**Figure 5** and **Supplementary Table 2**). CTD022 and CTD023 were made at sites with reported bubble plumes. CTD024 was made at a location where no multibeam sonar data were collected; thus, we do not have information about its proximity to a plume. However, methane concentrations measured from CTD024 are lower than concentrations measured during casts near verified plumes (CTD022 and CTD023). During all three casts, significantly elevated methane of 9–22 nM was observed at depths between 12 and 45 m. Low oxygen levels, including hypoxic conditions at the deepest 3–7 m of each cast, were correlated with higher methane measurements.

Within the region mapped by the ChemYak, at least one coherent region of elevated methane reaching 6.5 nM was observed at the surface centered at 44° 20.93′ N, 124° 9.67′ W (**Figure 6** and **Supplementary Figure 3**).

Stonewall Bank Seep Site

Four bubble plumes were observed in the acoustic surveys of the Stonewall Bank seep site (**Figure 7**, **Supplementary Figure 4** and **Supplementary Table 3**). In the one CTD cast made at the Stonewall Bank seep site (**Figure 8** and **Supplementary Table 4**), close in proximity to an identified bubble plume, elevated methane (above expected 2.7 nM based on equilibrium) was present at depths greater than ∼ 5 m. Only above this depth, were values at or below the equilibrium value. Low oxygen levels were present along with higher methane concentrations at depth; reaching hypoxic levels at 51 m depth, and remaining hypoxic below that depth.

At Stonewall Bank, a single ChemYak survey was completed of the surface waters (**Figure 9** and **Supplementary Figure 5**). These data show several areas of elevated methane [centered at locations: (1) 44°27.7′ N, 124°16.1′ W, (2) 44°27.7′ N, 124°25.9′ W, and (3) 44°27.6′ N, 124°16.1′ W], with a high excursion (up to 40 nM) above equilibrium levels of methane at an area to the north-east of the study region at 44°27.7′ N, 124°12.1′ W, 8 m depth. Several other regions of elevated methane are observed between 0.5 and 7 m. The elevated readings at 0.5 m may be indicative of methane that can be discharged to the atmosphere.

DISCUSSION

Elevated Methane

From our examination of these two shallow (<75 m) seep sites on the Cascadia Margin, Yachats seep site and Stonewall Bank seep site, elevated dissolved methane was observed throughout the entire water column to the surface waters through the analysis of both Niskin rosette casts and the ChemYak *in situ* measurements (**Supplementary Figure 6**). Acoustic surveys demonstrated the presence of bubble plumes. ChemYak surface chemistry plots revealed that at both Yachats and Stonewall Bank, regions of elevated methane above atmospheric equilibrium values existed within the top 10 m of the water column, including elevated measurements as close as 0.5 m beneath the surface, which was our observational upper-bound in depth. The presence of elevated dissolved methane concentrations near the ocean surface suggests that outgassing of methane to the atmosphere occurs at these sites.

The concentration of dissolved methane near the ocean surface, and as measured by the ChemYak, demonstrates high spatial variability (**Figures 6**, **9**). Dissolved methane values in the top 0.5–5 m of the Yachats site range from 2.28 to 6.62 nM with

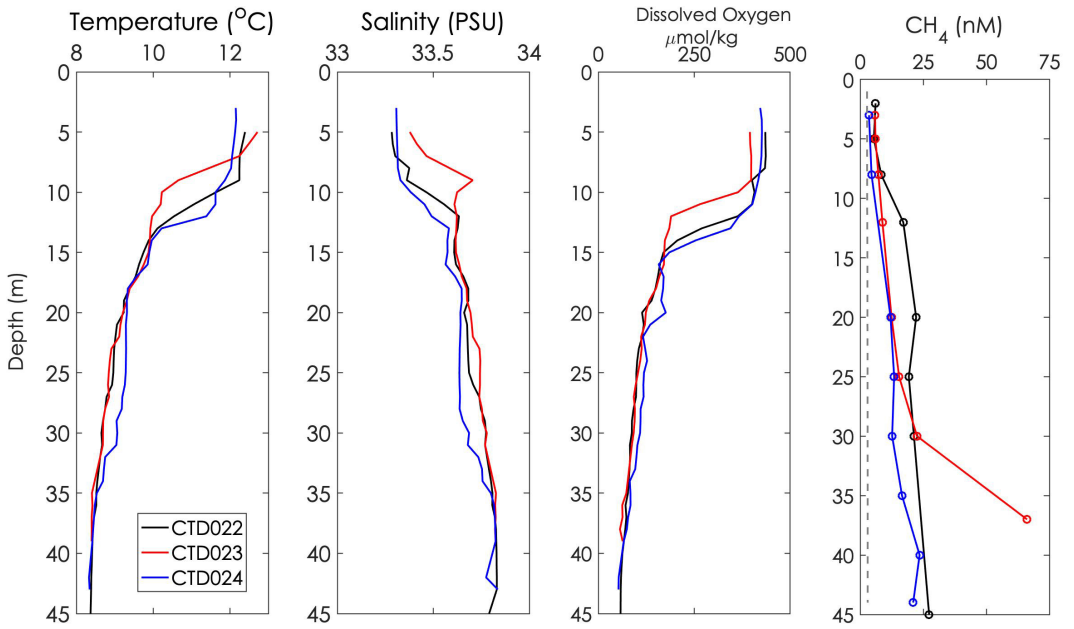

FIGURE 5 | Three CTD casts were made at the Yachats seep site. Colors shown represent: CTD022, black; CTD023, red; CTD024, blue. Analysis of the water samples collected with the Niskin bottles show the presence of elevated methane in the water column. The dashed gray line shows the methane equilibration concentration with the atmosphere calculated using temperature and salinity conditions from CTD024.

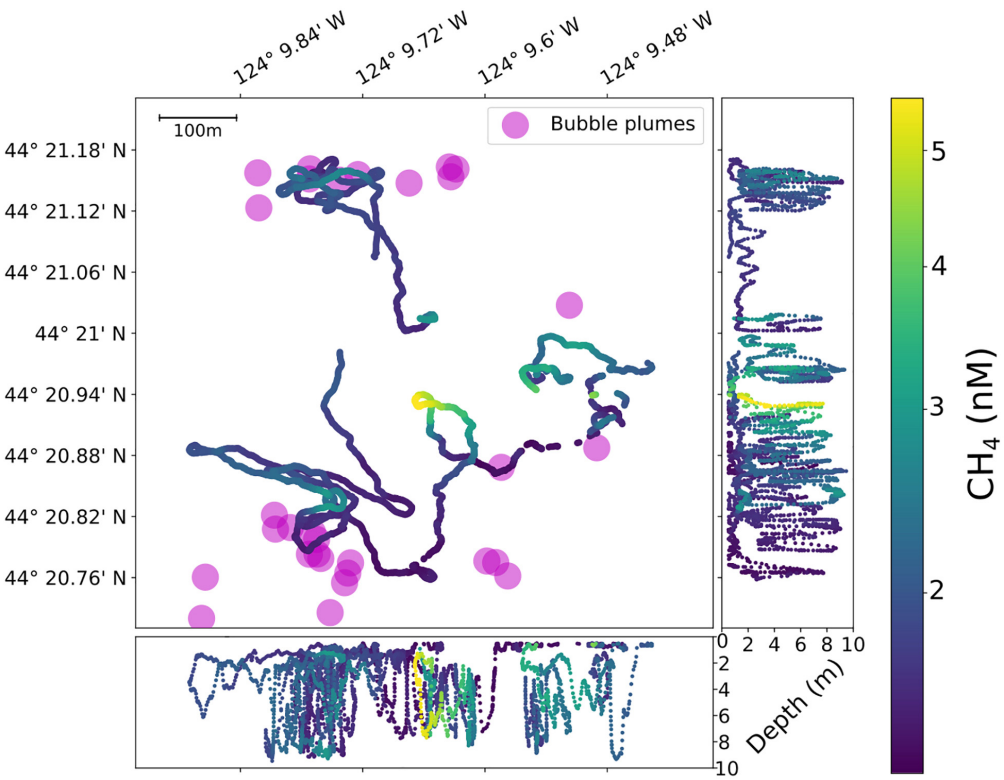

FIGURE 6 | ChemYak tracks at Yachats (September 14, 2018). The ChemYak was piloted by a human user given GPS coordinates of the bubble plumes (marked with magenta circles). The map, center, shows an overhead view of the path the ChemYak took, and the two side panels at the bottom and right show the depth of the CTD probe and gas analyzer inlet for each sample. Relatively little CH_4 elevation was observed at this site as a whole; however, several concentrated expressions of 3–7 nM were observed at depths below the top 1–2 m.

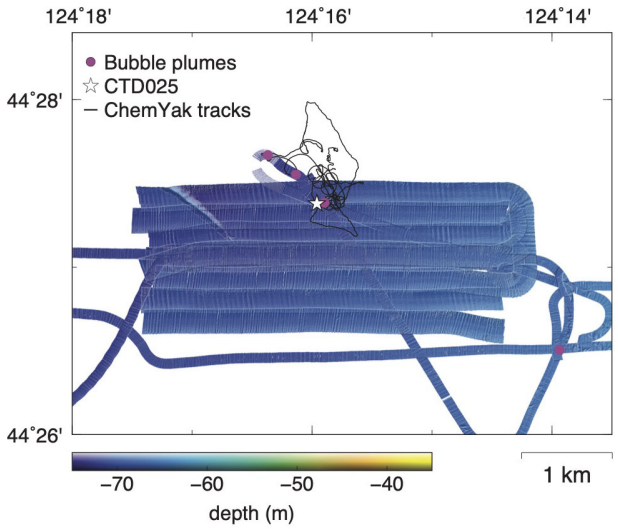

FIGURE 7 | The locations of the four bubble plumes located at Stonewall Bank seep site and CTD cast along with the ChemYak tracks. The bottom bathymetry is shown and was derived from the EM710 multibeam data and gridded at 1 m.

a mean of 2.96 ± 0.65 nM. At the Stonewall Bank site, dissolved methane in the top 0.5–5 m ranges from 0.98 to 11.63 nM with a mean of 2.31 ± 0.93 nM. Dissolved methane values in the top 0.5–1.5 m of the Yachats site range from 2.28 to 6.37 nM with a mean of 2.76 ± 0.49 nM. At the Stonewall Bank site, dissolved methane in the top 0.5–5 m ranges from 0.99 to 7.64 nM with a mean of 2.55 ± 0.76 nM. The spatial variability in surface dissolved methane that we observe suggests that point measurements (e.g., with CTD rosettes) may not be representative of even a small (<1 km^2) area.

The source of the elevated near-surface methane is important because this methane can ventilate to the atmosphere (James et al., 2016; Ruppel and Kessler, 2017). There are several possible sources for the elevated dissolved methane: the bubble plumes identified in acoustic surveys, coastal upwelling of deep and methane rich waters, and bacterial methane production. Tides can also influence the methane concentration distribution. The methane levels observed may be impacted by *in situ* aerobic methanogenesis in the water column and anaerobic methanogenesis in the sediment. In Sparrow et al. (2018), methane in surface waters of the U.S. Beaufort Sea shelf was found to be mostly derived from modern-aged carbon, both atmospheric-sourced and *in situ* produced. Offshore Oregon is also known to be a highly productive upwelling region (e.g., Mooers et al., 1976). Although we cannot rule out coastal upwelling and the importance of other sources, we suggest that bubble plumes contribute to the elevated near-surface dissolved methane concentrations we observed. The spatial variability of dissolved methane (e.g., **Figures 6**, **9**) supports arguments for local sources of methane (e.g., plumes). Local bubble plumes may also supply dissolved methane even in the event of background upwelling and other influences such as methane produced *in situ*.

Our observations reveal that the areas of highest dissolved surface methane are spatially offset from the seep sites (e.g., **Figures 6**, **9**). As a result, we conclude that the locations of methane seeps do not directly map onto areas of elevated dissolved methane at the meter scale. Instead, we speculate that dynamics in the water column (e.g., waves, inertial effects of tides, eddies, and mixing) impact dissolved methane concentrations near plumes, even when the plumes are not highly bent (e.g., **Figure 4**). One could probe water column mixing processes by examining velocity data from moorings from the nearby Coastal Endurance Array, part of the Ocean Observatories Initiative. Such analysis is outside the scope of this study and specifically is not done because our study area is ∼30 km from the closest shallow mooring. An additional source of potential offset between plume sites and elevated surface methane is the temporal offset between the ChemYak and acoustic surveys. The ChemYak and the acoustic surveys were offset by hours such that the nature of venting may have changed between surveys.

To examine the error of these measurements due to environmental variability (temperature and salinity) and any instrument error within the greenhouse gas analyzer and the dissolved gas extractor, an error analysis was completed using 50,000 Monte Carlo samples drawn from empirical distributions of salinity and temperature, and a Gaussian distribution of efficiency centered at 0.05 with 0.01 standard deviation (**Supplementary Figure 7**). At low concentration measurements, the error bound is very small, but increases with larger concentrations. Considering the interquartile range of the posterior samples of methane, converted values that represent the 1st quartile measure still imply that significant elevation of methane is present.

Calculating Emissions in Study Areas

At Stonewall Bank seep site, dissolved CH_4 was spatially variable and elevated concentrations were highly localized. At Yachats seep site, local high concentration spots were also observed, and measurements taken throughout the water column were found to be slightly above the expected equilibrium value. We estimate the potential methane flux rate per year (due primarily to diffusive transport) at these two sites based on our study measurements. The diffusive gas flux across the air-sea interface is calculated as:

$$F = kK_0\left(pC_w - pC_a\right) \tag{1}$$

where F is the air-sea flux (mass area^{-1} time^{-1}), k is the gas transfer velocity (length time^{-1}), K_0 is the solubility of the gas (mass volume^{-1} pressure^{-1}), and pC_w and pC_a are the partial pressures of methane in the water and air, respectively (Wanninkhof, 2014). The term k is calculated according to Wanninkhof (2014) and requires an estimate of the 10-m wind speed, w, and Schmidt number S_C (a function of salinity and temperature):

$$k = 0.251w^2\left(\frac{S_c}{600}\right)^{-0.5} \tag{2}$$

The equilibrium pressure of CH_4 with the atmosphere is set to 1.86 μatm for these calculations. Wind speed measurements reported from the ship were observed to be approximately

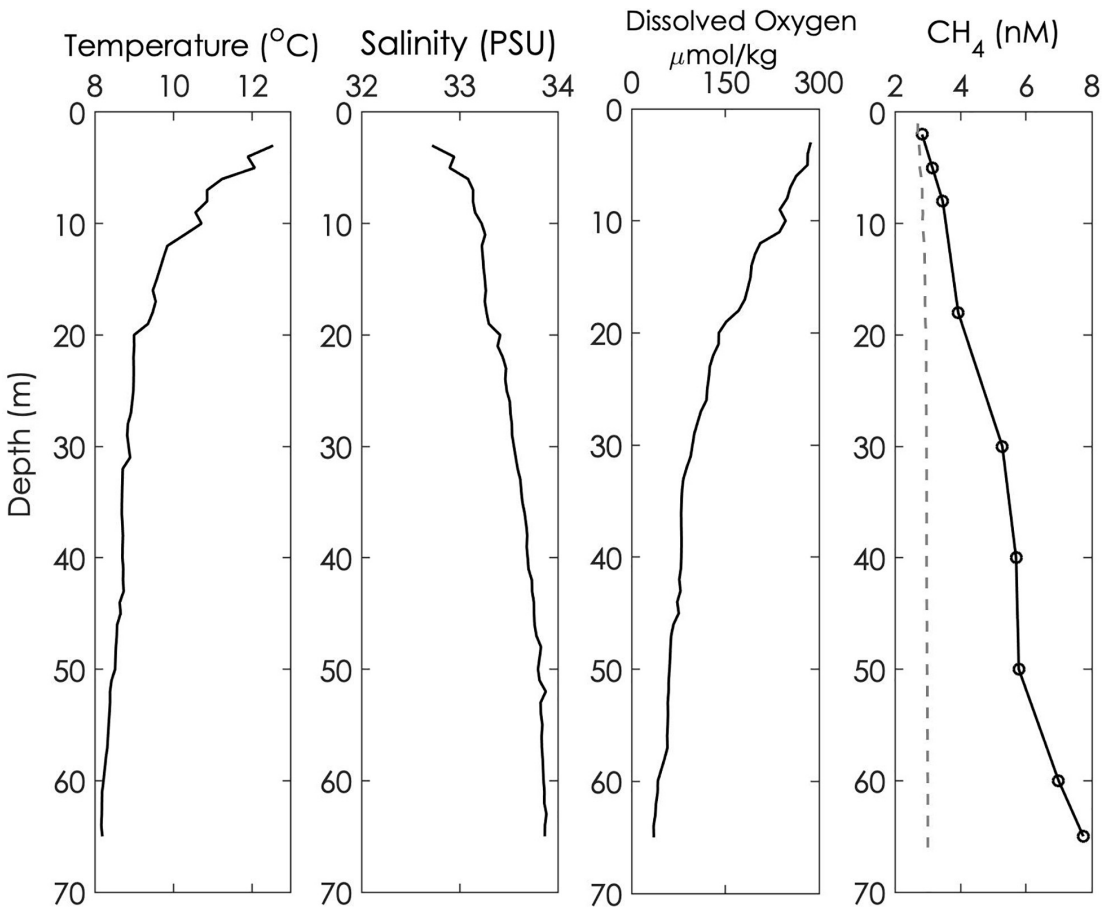

FIGURE 8 | One CTD cast (CTD025) was made at the Stonewall Bank seep site. The water samples collected with the Niskin bottles show the presence of elevated methane in the water column. The dashed gray line shows the methane equilibration concentration with the atmosphere calculated using temperature and salinity conditions from CTD025.

10 m s^{-1} sustained. By virtue of the square factor in the gas transfer velocity, wind speed is a generally dominating factor for estimating emissions. To show this, **Supplementary Figure 8** provides the relationship between wind speed and estimated flux for varying partial pressure estimates of CH_4 in water.

To constrain an estimate of flux in the study regions and demonstrate the impact of the highly localized but potent methane "hotspots," we first identify the range of observations that represent elevated methane values at the sites. This is done by empirically setting a threshold based on the distribution of methane observations (**Supplementary Figure 9**) such that the dominating background signal is separated from a long-tail, representing observations from hotspots. To estimate how hotspots change the effective annual flux at the study sites, we compute the average methane surface value with and without hotspots at each site to serve as a representative methane concentration. We then draw 50,000 samples from the empirical distributions of salinity, temperature, and wind (**Supplementary Figure 10**). Using this method, we find that the background annual flux for the Yachats site is -129 ± 50 μmol $\times$ m^{-2} $\times$ y^{-1}; including the impact of hotspots increases this estimate to 62 ± 24 μmol $\times$ m^{-2} $\times$ y^{-1}. For the Stonewall Banks site, background flux is estimated to be -455 ± 177 μmol $\times$ m^{-2} $\times$ y^{-1}; including hotspots also increases this estimate to -305 ± 119 μmol $\times$ m^{-2} $\times$ y^{-1}. Using a Welch's t-test, the difference in these distributions is statistically significant to the $p = 0.01$ level. At both sites, background saturation of methane indicates that these sites would likely serve as methane sinks, however, the influence of hotspots can reduce the efficacy of these sinks, or even create weak sources of outgassing methane. Given the relatively small area of these expressions, their potentially outsized effect on the methane budget of the region is of considerable interest, and highlights the utility of dense spatial sampling enabled by the ChemYak platform.

The flux of methane to the atmosphere could be higher than calculated if the gaseous bubbles that reach the ocean surface are considered. The acoustic water column data suggest that gas rich plumes within 10 m of the surface (e.g., **Figure 4**) are present. However, we cannot resolve features in the upper meters of the ocean surface because the Kongsberg EM710 echosounder has a minimum acquisition depth 3 m below its transducers.

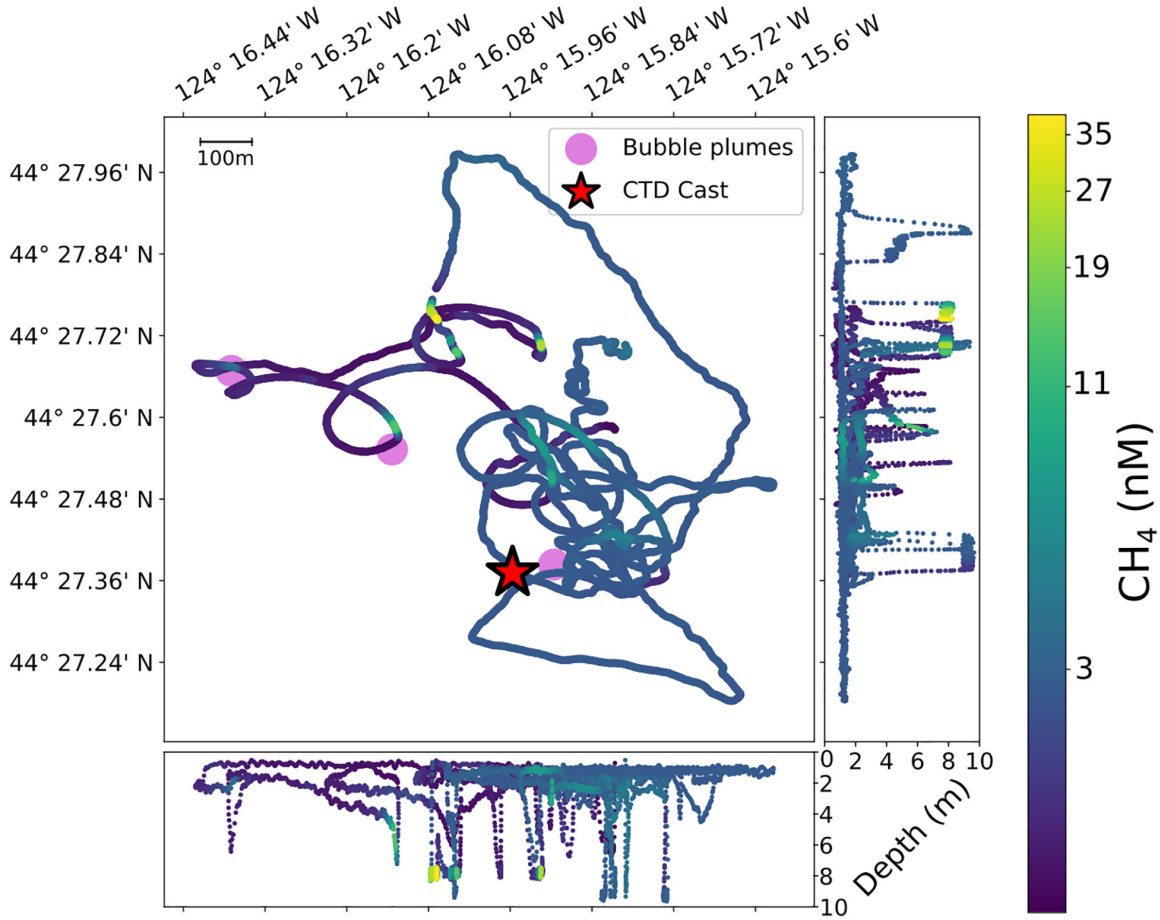

FIGURE 9 | ChemYak tracks at Stonewall Bank (September 17, 2018). The ChemYak was piloted by a human user given rough GPS coordinates of the bubble plumes (marked with magenta circles) and the CTD cast (marked with a red star). The map, center, shows an overhead view of the path the ChemYak took, and the two side panels at the bottom and right show the depth of the CTD probe and gas analyzer inlet for each sample. Significantly elevated CH_4 is found at several sites, with a peak at 38 nM detected at 8 m. CH_4 concentration levels above 2.7 nM were largely observed to the north and southeast of the field site, at depths of 0.5–7 m.

Pockmarks

Pockmarks are concave crater-like depressions that can form on the seafloor as a result of fluid expulsion including methane gas venting (e.g., Cathles et al., 2010; Davy et al., 2010). At the Yachats seep site we observe dozens of depressions that are <3 m deep and 50–1000 m wide, consistent with the morphology of pockmarks. A fraction of the seafloor depressions have lens or almond shapes and are elongated in the southwest-northeast direction; these depressions may be trawl marks. Most (68 out of 92) of the bubble plumes at the Yachats site were found within 50 m of seafloor depressions that resemble pockmarks. However, we do not resolve the specific mechanisms that relate the pockmarks to the presence of methane venting at this site.

Coupled Approach for Resolving Emissions

The coupled methodology presented here: identifying plume sources with shipboard multibeam sonar, water column analysis with a Niskin rosette, and near-surface chemistry mapping with a surface vehicle, leverages the strengths of multi-resolution approaches for understanding methane emissions and fate at shallow-water seep sites. The ChemYak, a novel surface vehicle, enabled the direct observation of near-surface dissolved methane and at a spatial resolution that cannot be assessed with CTD casts. Similar vehicles may prove useful for quantifying the chemical variability of near-surface waters at higher spatial resolutions than are currently reported. Furthermore, by combining technologies we move closer to being able to connect the discharge of methane bubbles along the seafloor to their transport and fate in the water column.

Using multibeam sonar we identified 92 and 4 bubble plumes with the Yachats and Stonewall Bank sites, respectively. The discovery of the Yachats seep site during this cruise suggests other shallow bubble sites may remain undiscovered along the Cascadia Margin. We found hot spots of dissolved methane concentrations above the atmospheric equilibrium value both at depth, as measured by the CTD casts, and near the surface as measured by the ChemYak. In addition, measurements of dissolved methane

within the surface waters demonstrated that dissolved methane is highly spatially variable and included concentrations up to 11.63 nM. The CTD values measured were at similar levels to those reported at depths up to 74 m below the surface by Heeschen et al. (2005). Bubbles were observed by Di et al. (2019); however, the seeps studied were much shallower (<20 m) than those in our study. The levels of dissolved methane measured by our study may be different than those measured by Di et al. (2019) due to proximity to a plume, currents, depth, and plume intensity.

Due to the presence of significantly elevated methane hotspots on the surface ocean, we found that methane ventilation was significantly increased as compared to presumptive background levels; at Yachats our model estimated an increase of approximately 191 $\mu mol \times m^{-2} \times y^{-1}$ and at Stonewall Bank an increase of approximately 150 $\mu mol \times m^{-2} \times y^{-1}$. Although we found that methane plumes are not decisively co-located with surface anomalies in methane concentration, the mismatch identified through high-resolution sampling invites questions about mixing processes in the water column and the temporal variability of plume discharge. We do not rule out coastal upwelling in contributing to the elevated levels of dissolved methane near the ocean surface or the transport of methane from other plumes. However, the existence of methane bubble plumes seen by the multibeam data along with areas of elevated near-surface dissolved methane suggests that shallow seeps contribute methane to the sea-air methane flux. Future work is needed to resolve the factors that contribute to the variability in methane concentrations, including examining tidal influences and bacterial methane production. In addition, further information could be gleaned about sources through the measurement of the carbon and hydrogen isotopic ratios of the methane.

DATA AVAILABILITY STATEMENT

The datasets generated for this study can be found in the **Supplementary Material**, at the R2R rolling deck to repository (10.7284/907968), and at the WHOAS data repository (https://hdl.handle.net/1912/25040).

AUTHOR CONTRIBUTIONS

AM served as Chief Scientist on the R/V Falkor cruise, co-led all ChemYak deployments, supervised all data processing efforts, and processed CTD data. DN co-led all ChemYak deployments and supervised all data processing efforts. VP processed and analyzed all ChemYak data. KF processed and analyzed all multibeam data. All authors contributed to the article and approved the submitted version.

FUNDING

Funding for VP was provided by an NDSEG Fellowship. Funding for KF was provided by a WHOI Postdoctoral Scholar Fellowship. Ship time on the R/V Falkor was provided by the Schmidt Ocean Institute (FK180824).

ACKNOWLEDGMENTS

The authors thank the Schmidt Ocean Institute and the Captain and entire crew and staff of the R/V Falkor and ROV Subastian team during the 2018 Hunting Bubbles cruise (FK180824) to Cascadia Margin. The authors thank S. D. Wankel for his contributions to the entire cruise and its planning and to B. Colson for his assistance with the ChemYak deployments. The authors greatly acknowledge K. Manganini for his work in developing the ChemYak. The authors thank K. McHugh for taking the ChemYak image shown in **Figure 2** with his drone. The authors also thank S. Soule and M. Jones for their assistance with multibeam processing, and A. Morrison for her assistance in extraction efficiency laboratory experiments for the DGEU.

SUPPLEMENTARY MATERIAL

The Supplementary Material for this article can be found online at: https://www.frontiersin.org/articles/10.3389/feart.2021.613234/full#supplementary-material

REFERENCES

Baumberger, T., Embley, R. W., Merle, S. G., Lilley, M. D., Raineault, N. A., and Lupton, J. E. (2018). Mantle–derived helium and multiple methane sources in gas bubbles of cold seeps along the Cascadia continental margin. *Geochem. Geophys. Geosyst.* 19, 4476–4486. doi: 10.1029/2018GC007859

Cathles, L. M., Su, Z., and Chen, D. (2010). The physics of gas chimney and pockmark formation, with implications for assessment of seafloor hazards and gas sequestration. *Mar. Pet. Geol.* 27, 82–91. doi: 10.1016/j.marpetgeo.2009.09.010

Colbo, K., Ross, T., Brown, C., and Weber, T. (2014). A review of oceanographic applications of water column data from multibeam echosounders. *Estuar. Coast. Shelf Sci.* 145, 41–56. doi: 10.1016/j.ecss.2014.04.002

Davy, B., Pecher, I., Wood, R., Carter, L., and Gohl, K. (2010). Gas escape features off New Zealand: evidence of massive release of methane from hydrates: massive NZ gas escape features. *Geophys. Res. Lett.* 37:L21309. doi: 10.1029/2010GL045184

Di, P., Feng, D., and Chen, D. (2019). The distribution of dissolved methane and its air-sea flux in the plume of a seep field, Lingtou Promontory, South China Sea. *Geofluids* 2019:3240697. doi: 10.1155/2019/3240697

Grant, N. J., and Whiticar, M. J. (2002). Stable carbon isotopic evidence for methane oxidation in plumes above Hydrate Ridge, Cascadia Oregon Margin: isotope evidence for methane oxidation at Hydrate Ridge. *Glob. Biogeochem. Cycles* 16, 71–71. doi: 10.1029/2001GB001851

Greinert, J., Lewis, K. B., Bialas, J. I., Pecher, A., Rowden, A., Bowden, D. A., et al. (2010). Methane seepage along the Hikurangi Margin. New Zealand: Overview of studies in 2006 and 2007 and new evidence from visual, bathymetric and hydroacoustic investigations. *Mar. Geol.* 272, 6–25. doi: 10.1016/j.margeo.2010.01.017

Heeschen, K. U., Collier, R. W., de Angelis, M. A., Suess, E., Rehder, G., Linke, P., et al. (2005). Methane sources, distributions, and fluxes from cold vent sites at Hydrate Ridge, Cascadia Margin: methane fluxes at Hydrate Ridge. *Glob. Biogeochem. Cycles* 19, n/a–n/a. doi: 10.1029/2004GB002266

Heeschen, K. U., Tréhu, A. M., Collier, R. W., Suess, E., and Rehder, G. (2003). Distribution and height of methane bubble plumes on the Cascadia Margin characterized by acoustic imaging: acoustic image of methane bubble plumes. *Geophys. Res. Lett.* 30:1643. doi: 10.1029/2003GL016974

James, R. H., Bousquet, P., Bussmann, I., Haeckel, M., Kipfer, R., Leifer, I., et al. (2016). Effects of climate change on methane emissions from seafloor sediments in the Arctic Ocean: a review: methane emissions from arctic sediments. *Limnol. Oceanogr.* 61, S283–S299. doi: 10.1002/lno.10307

Johnson, H. P., Merle, S., Salmi, M., Embley, R., Sampaga, E., and Lee, M. (2019). Anomalous concentration of methane emissions at the continental shelf edge of the Northern Cascadia Margin. *J. Geophys. Res. Solid Earth* 124, 2829–2843. doi: 10.1029/2018JB016453

Johnson, H. P., Miller, U. K., Salmi, M. S., and Solomon, E. A. (2015). Analysis of bubble plume distributions to evaluate methane hydrate decomposition on the continental slope: Plumes on Cascadia. *Geochem. Geophys. Geosyst.* 16, 3825–3839. doi: 10.1002/2015GC005955

Kimball, P., Bailey, J., Das, S., Geyer, R., Harrison, T., Kunz, C., et al. (2014). "The WHOI Jetyak: an autonomous surface vehicle for oceanographic research in shallow or dangerous waters," in *Proceedings of the 2014 IEEE/OES Autonomous Underwater Vehicles (AUV)*, (Oxford, MS: IEEE), 1–7.

Leifer, I., Luyendyk, B. P., Boles, J., and Clark, J. F. (2006). Natural marine seepage blowout: contribution to atmospheric methane: marine Seep Blowout. *Glob. Biogeochem. Cycles* 20, doi: 10.1029/2005GB002668

Loher, M., Pape, T., Marcon, Y., Römer, M., Wintersteller, P., Praeg, D., et al. (2018). Mud extrusion and ring-fault gas seepage–upward branching fluid discharge at a deep-sea mud volcano. *Sci. Rep.* 8:6275. doi: 10.1038/s41598-018-24689-1

Manning, C. C., Preston, V. L., Jones, S. F., Michel, A. P. M., Nicholson, D. P., Duke, P. J., et al. (2020). River inflow dominates methane emissions in an Arctic coastal system. *Geophys. Res. Lett.* 47:e2020GL087669. doi: 10.1029/2020GL087669

McGinnis, D. F., Greinert, J., Artemov, Y., Beaubien, S. E., and Wüest, A. (2006). Fate of rising methane bubbles in stratified waters: how much methane reaches the atmosphere? *J. Geophys. Res.* 111:C09007. doi: 10.1029/2005JC003183

Mooers, C., Collins, C., and Smith, R. (1976). The dynamic structure of the frontal zone in the coastal upwelling region off Oregon. *J. Phys. Oceanogr.* 6, 3–21.

Nicholson, D. P., Michel, A. P. M., Wankel, S. D., Manganini, K., Sugrue, R. A., Sandwith, Z. O., et al. (2018). Rapid mapping of dissolved methane and carbon dioxide in coastal ecosystems using the ChemYak autonomous surface vehicle. *Environ. Sci. Technol.* 52, 13314–13324. doi: 10.1021/acs.est.8b04190

NOAA Northwest Fisheries Science Center and Southwest Fisheries Science Center (2015). EK60 Water Column Sonar Data Collected During SH1507. NOAA National Centers for Environmental Information. doi: 10.7289/V5D50JZQ

Pohlman, J. W., Greinert, J., Ruppel, C., Silyakova, A., Vielstädte, L., Casso, M., et al. (2017). Enhanced CO_2 uptake at a shallow Arctic Ocean seep field overwhelms the positive warming potential of emitted methane. *Proc. Natl. Acad. Sci. U.S.A.* 114, 5355–5360. doi: 10.1073/pnas.1618926114

Reeburgh, W. S. (2007). Oceanic methane biogeochemistry. *Chem. Rev.* 107, 486–513. doi: 10.1021/cr050362v

Rehder, G., Brewer, P. W., Peltzer, E. T., and Friederich, G. (2002). Enhanced lifetime of methane bubble streams within the deep ocean: enhanced lifetime of methane bubbles. *Geophys. Res. Lett.* 29, 21–21. doi: 10.1029/2001GL013966

Riedel, M., Scherwath, M., Römer, M., Veloso, M., Heesemann, M., and Spence, G. D. (2018). Distributed natural gas venting offshore along the Cascadia margin. *Nat. Commun.* 9:3264. doi: 10.1038/s41467-018-05736-x

Römer, M., Riedel, M., Scherwath, M., Heesemann, M., and Spence, G. D. (2016). Tidally controlled gas bubble emissions: a comprehensive study using long-term monitoring data from the NEPTUNE cabled observatory offshore Vancouver Island: tidally controlled gas bubble emissions. *Geochem. Geophys. Geosyst.* 17, 3797–3814. doi: 10.1002/2016GC006528

Ruppel, C. D., and Kessler, J. D. (2017). The interaction of climate change and methane hydrates: climate-hydrates interactions. *Rev. Geophys.* 55, 126–168. doi: 10.1002/2016RG000534

Shakhova, N., Semiletov, I., Leifer, I., Salyuk, A., Rekant, P., and Kosmach, D. (2010). Geochemical and geophysical evidence of methane release over the East Siberian Arctic Shelf. *J. Geophys. Res.* 115:C08007. doi: 10.1029/2009JC005602

Shakhova, N., Semiletov, I., Leifer, I., Sergienko, V., Salyuk, A., Kosmach, D., et al. (2014). Ebullition and storm-induced methane release from the East Siberian Arctic Shelf. *Nat. Geosci.* 7, 64–70. doi: 10.1038/ngeo2007

Sparrow, K. J., Kessler, J. D., Southon, J. R., Garcia-Tigreros, F., Schreiner, K. M., Ruppel, C. D., et al. (2018). Limited contribution of ancient methane to surface waters of the US Beaufort Sea shelf. *Sci. Adv.* 4:eaao4842. doi: 10.1126/sciadv.aao4842

Thornton, B. F., Geibel, M. C., Crill, P. M., Humborg, C., and Mörth, C.-M. (2016). Methane fluxes from the sea to the atmosphere across the Siberian shelf seas: CH_4 fluxes from Siberian shelf seas. *Geophys. Res. Lett.* 43, 5869–5877. doi: 10.1002/2016GL068977

Wanninkhof, R. (2014). Relationship between wind speed and gas exchange over the ocean revisited: gas exchange and wind speed over the ocean. *Limnol. Oceanogr. Methods* 12, 351–362. doi: 10.4319/lom.2014.12.351

Westbrook, G. K., Thatcher, K. E., Rohling, E. J., Piotrowski, A. M., Pälike, H., Osborne, A. H., et al. (2009). Escape of methane gas from the seabed along the West Spitsbergen continental margin: Arctic methane gas plumes. *Geophys. Res. Lett.* 36, n/a–n/a. doi: 10.1029/2009GL039191

Wilson, D. S., Leifer, I., and Maillard, E. (2015). Megaplume bubble process visualization by 3D multibeam sonar mapping. *Mar. Pet. Geol.* 68, 753–765. doi: 10.1016/j.marpetgeo.2015.07.007

Conflict of Interest: The authors declare that the research was conducted in the absence of any commercial or financial relationships that could be construed as a potential conflict of interest.

frontiers in Earth Science

ORIGINAL RESEARCH
published: 07 May 2021
doi: 10.3389/feart.2021.556329

Seafloor Methane Seepage Related to Salt Diapirism in the Northwestern Part of the German North Sea

Miriam Römer[1], Martin Blumenberg[2], Katja Heeschen[3], Stefan Schloemer[2], Hendrik Müller[2], Simon Müller[2], Christian Hilgenfeldt[1], Udo Barckhausen[2] and Katrin Schwalenberg[2]*

[1] MARUM – Center for Marine Environmental Sciences and Department of Geosciences, University of Bremen, Bremen, Germany, [2] BGR – Federal Institute for Geosciences and Natural Resources, Hannover, Germany, [3] Helmholtz Centre Potsdam, German Research Centre for Geosciences (GFZ), Potsdam, Germany

OPEN ACCESS

Edited by:
Tamara Baumberger, Oregon State University, United States

Reviewed by:
Kai Mangelsdorf, Helmholtz Centre Potsdam, German Research Centre for Geosciences (GFZ), Germany
James Conrad, United States Geological Survey (USGS), United States
Martin Scherwath, University of Victoria, Canada

***Correspondence:**
Miriam Römer
mroemer@marum.de

Specialty section:
This article was submitted to Biogeoscience, a section of the journal Frontiers in Earth Science

Received: *27 April 2020*
Accepted: *12 April 2021*
Published: *07 May 2021*

Citation:
Römer M, Blumenberg M, Heeschen K, Schloemer S, Müller H, Müller S, Hilgenfeldt C, Barckhausen U and Schwalenberg K (2021) Seafloor Methane Seepage Related to Salt Diapirism in the Northwestern Part of the German North Sea. Front. Earth Sci. 9:556329. doi: 10.3389/feart.2021.556329

This study focuses on seafloor methane seep sites and their distribution in the northwestern part of the German North Sea. Methane seepage is a common phenomenon along marine shelves and known to occur in the North Sea, but proof of their existence was lacking in the study area. Using a ship-based multibeam echosounder we detected a minimum of 166 flares that are indicative for free gas releases from the seafloor in the German "Entenschnabel" area, which are not related to morphologic expressions at the seafloor. However, a group of small depressions was detected lacking water column anomalies but with indications of dissolved fluid release. Spatial analysis revealed that flares were not randomly distributed but show a relation to locations of subsurface salt diapirs. More than 60% of all flares were found in the vicinity of the salt diapir "Berta". Dissolved methane concentrations of ∼100 nM in bottom waters were ten times the background value in the "Entenschnabel" area (CH_4 < 10 nM), supporting the finding of enhanced seepage activity in this part of our study area. Furthermore, locations of flares were often related to acoustic blanking and high amplitude reflections in sediment profiler echograms, most prominently observed at location Berta. These hydroacoustic signatures are interpreted to result from increased free gas concentrations in the sediments. Electromagnetic seabed mapping depicts local sediment conductivity anomalies below a flare cluster at Berta, which can be explained by small amounts of free gas in the sediment. In our area of interest, ten abandoned well sites were included in our mapping campaign, but flare observations were spatially not related to these wells. Naturally seeping methane is presumably transported to the seafloor along sub-vertical faults, which have formed concurrently to the updoming salt. Due to the shallow water depths of 30 to 50 m in the study area, flares were observed to reach close to the sea surface and a slight oversaturation of surface waters with methane in the flare-rich northeastern part of the working area indicates that part of the released methane through seepage may contribute to the atmospheric inventory.

Keywords: gas emissions, flares, hydroacoustic mapping, subsurface gas indications, North Sea, salt diapirism

INTRODUCTION

Seafloor methane (CH_4) seepage is widely known to occur along almost all continental margins. This includes the diffusion or advection of dissolved methane from the sediment into the bottom water or the expulsion of free methane gas bubbles. Known natural seep areas in the North Sea, a shelf sea with an average water depth of 95 m, include: (1) Tommeliten seep area in the Norwegian Exclusive Economic Zone (EEZ; Hovland, 1993; Niemann et al., 2005), (2) Dutch Dogger Bank seep area in Netherlands EEZ (Schroot et al., 2005; Römer et al., 2017), (3) pockmarks in the Witch Ground Basin in the EEZ of United Kingdom (Judd et al., 1994; Böttner et al., 2019), and (4) the German Helgoland Reef pockmark field (Krämer et al., 2017; locations see **Figure 1A**). The North Sea comprises large areas where shallow gas is being trapped in Cenozoic deltaic and marine sediments and has been detected as "bright spots" in seismic data (Müller et al., 2018). The observed bright spots are characterized by high amplitude seismic reflections, which can indicate a change in pore space filling (White, 1975). Hydrocarbon migration and accumulation are often related to salt diapirism, associated faulting and gas-charged sand-filled ice-scours and channels (Woodbury et al., 1980; Schroot and Schüttenhelm, 2003). Since the Pleistocene, the area has been effected by climate and sea level variations, leading to deposits of glacial-interglacial sediments that are characterized by abundant subglacial tunnel valleys related to melt water flows (Lutz et al., 2009). In our study area, several clusters of bright spots were identified above known salt diapirs, suggesting that salt diapirism lead to fracturing of the overburden strata and formation of migration pathways as well as anticlinal structures for hydrocarbon accumulation (Müller et al., 2018).

Indications of elevated methane concentrations in the North Sea have been deduced from continuous surface water measurements (Rehder et al., 1998) and atmospheric measurements (Judd, 2015), both conducted while crossing our study area in the "Entenschnabel" (local term of that area, meaning "Duck's Bill," because of the shape of its outline, **Figure 1A**). Methane sources were thought to be related to natural seafloor seepage or alternatively to an anthropogenic well (Judd, 2015). Abandoned wells have been suggested to act as focused migration pathways for hydrocarbons after decommissioning and several recent studies on onshore boreholes have proven the release of hydrocarbons from former gas and oil wells (Kang et al., 2014; Boothroyd et al., 2016; Townsend-Small et al., 2016; Schout et al., 2019). The relative importance of this phenomenon is a matter of discussion [e.g., Schout et al. (2019) found 1 of 29 onshore wells to leak methane]. In a marine setting Vielstädte et al. (2015) studied three well sites in the North Sea and found gas bubbles emitting methane in varying amounts (1–19 tons of CH_4 per year per well). The authors demonstrated by stable carbon isotope analyses that the methane originates from shallow, microbial sources rather than the gas reservoirs. They concluded that mechanic disruption by drilling operations is responsible for methane leakages from shallow, methane-loaded sediments, and that such processes may hold for one third of wells in the North Sea. By extrapolating their observations to the roughly 11,000 abandoned well sites in the North Sea, Vielstädte et al. (2017) estimated that 3–17 kt $year^{-1}$ methane potentially escape from the seafloor, which highly exceeds naturally released methane in this area. A recent study by Böttner et al. (2020) suggests that gas release from 1792 investigated decommissioned hydrocarbon wells in the United Kingdom sector of the North Sea is with 0.9–3.7 kt $year^{-1}$ a major source of methane in the North Sea. Even larger amounts of methane are emitted through well site 22/4b that experienced a man-made blowout in 1990 (Leifer and Judd, 2015 and references therein; Rehder et al., 1998). Leifer (2015) calculated an emission of 25 kt $year^{-1}$ of methane through gas bubbles even 22 years after the blowout.

Shallow seas such as the German sector of the North Sea may potentially be prone to natural and anthropogenic methane leakages into the sea-air boundary layer, because bubbles may reach shallow water layers and the sea surface. Gas exchange leads to fast dissolution of methane out of the bubbles during their ascent in the water column but shallow seep sites are expected to transport some fraction of the methane up to the sea surface and contribute to the atmospheric methane inventory (Leifer and Patro, 2002). It has been shown for the nearby Dutch Dogger Bank seep area, located in ∼40 m water depth, that released bubbles reached the sea surface and elevated methane concentration could be detected in the air above the most intense flare areas (Römer et al., 2017). The vertical transport of dissolved methane is highly restricted by the density stratification in the water column and strong summer thermoclines can also limit the vertical gaseous transport (Schmale et al., 2010; Mau et al., 2015). For example, at the 70 m deep Tommeliten area in the Norwegian sector of the North Sea, a summer thermocline constrained methane transport to the atmosphere, and numerical modeling showed that during the summer season less than 4% of the gas initially released as bubbles at the seafloor reaches the mixed layer (Schneider Von Deimling et al., 2011). An even smaller fraction of only 3% of the total water column inventory of dissolved methane was located in the mixed surface layer above the crater of the blowout well 22/4b, revealing that methane transfer across the thermocline was strongly impeded (Sommer et al., 2015).

The area of our investigation is located in the northwestern part of the German North Sea Sector. The geology there is characterized by a prominent Mesozoic rift-structure, the so-called Central Graben. The Central Graben is genetically a half-graben, whose eastern flank is formed by a major fault array, the Schillgrund Fault, and whose western flank is dominated by a series of horst and graben structures (Arfai et al., 2014). During several Mesozoic rifting phases, organic-rich marine mudstones were deposited that are important source rocks of the southern North Sea area and pose a possible source for thermogenic gas (Wong, 2007). The Central Graben is therefore a major hydrocarbon province in the North Sea (Littke et al., 2008; Pletsch et al., 2010) and was the target area of extended oil and gas exploration and drilling activities, which resulted in more than 49 exploration drill sites in the "Entenschnabel" since 1976 (see Lower Saxony's borehole database: www.lbeg.niedersachsen.de).

This study reports on the first detection of methane seepage in the "Entenschnabel" located in the North Sea with water

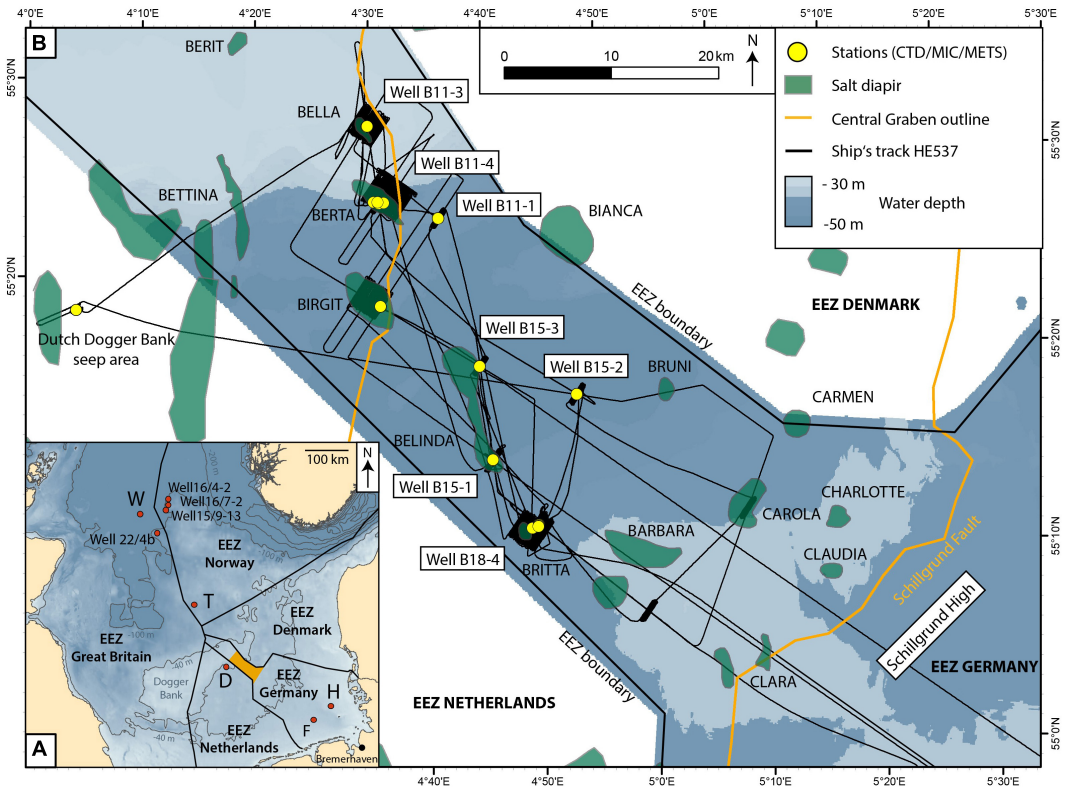

FIGURE 1 | (A) Overview of the study area in the German Exclusive Economic Zone [EEZ, Flanders Marine and Institute (2019)] of the North Sea (orange area). Known seep sites are marked as red dots. D: Dutch Dogger Bank seep area (Schroot et al., 2005), F: Figge-Maar (Thatje et al., 1999), H: Helgoland Reef pockmark field (Krämer et al., 2017), T: Tommeliten seep area (Hovland, 1993), and W: Witch Ground Basin (Judd et al., 1994). Bathymetry downloaded from www.gebco.net. **(B)** Overview of the study area in the "Entenschnabel," the northwestern part of the German EEZ. Major structural features depicted from Arfai et al. (2014) are the Central Graben (outlined in orange) and salt diapirs in the subsurface (green areas). Yellow dots point to sampling and measurement stations during R/V Heincke cruise HE537 conducted at seven abandoned well sites, a reference site at salt diapir Birgit, and the Dutch Dogger Bank seep area for comparison. Bathymetry downloaded from www.gpdn.de.

depths between 30 and 50 m. An extensive hydroacoustic mapping campaign including water column recording and sediment profiling has been conducted to determine the presence and distribution of flares indicative for gas bubble releases, as knowledge on the integrity of respective deep wells and the occurrence of natural seep sites is so far limited. Continuous and discrete measurements of dissolved methane concentrations in the water column were retrieved to support identification of seepage from the seafloor. A major focus was the investigation of gas emission in relation to subsurface salt diapir locations, seismically identified gas accumulations and abandoned well sites. Our interdisciplinary approach enabled a first characterization of the seepage detected in the work area in the North Sea.

MATERIALS AND METHODS

The data for this study were acquired during R/V Heincke cruise HE537 in July 2019. The track line shown in **Figure 1B** shows the hydroacoustic mapping strategy in the study area and illustrates the surveys focusing at six dedicated salt diapirs and seven abandoned well sites. Sediment and water samples were taken at five different salt diapir structures and two further abandoned well sites (yellow dots in **Figure 1B**). A detailed electromagnetic (EM) survey of the shallow seafloor has been analyzed at salt diapir Berta. Finally, methane sensor (METS) deployments were conducted at salt diapirs Bella, Berta, Belinda and Britta as well as the two other abandoned well sites. An example of the survey and sampling strategy is shown in the **Supplementary Figure 1**.

Hydroacoustic Data

The Kongsberg EM710 is a shallow to mid-water specific multibeam echosounder (MBES) operating between 70 and 100 kHz and an optimal depth range from 10 to 1,200 m. With a transducer configuration of 1 by 2 degrees, this system has 200 beams, with 400 soundings in high density mode, measuring both bathymetry and backscatter. The system was operated with a swath angle of 130° (65° to both sides). Vessel speed was at maximum (during transit times) 8–10 knots, however, was reduced for hydroacoustic mapping in the work area to 3–5 knots. Between the surveys, CTD profiles were carried out and used to calculate sound velocity profiles that were inserted in

the acquisition software Seafloor Information System. The open source software package MB-System (Caress and Chayes, 2017) has been utilized to post-process the bathymetric and backscatter data. The investigation of active gas emission sites on the seafloor where gas bubbles can be detected hydroacoustically in the water column (flares) was enabled by analyzing the water column data generated by the EM710. Post-cruise analyses with the FM Midwater module of QPS Fledermaus allowed for manual flare identification and geo-picking of flare sources.

Geographical visualization and statistical analysis were performed using ESRI ArcMap 10.4. The spatial analyst tool "near" was used to obtain distances of all flare positions to outlines of salt diapirs, bright spots and abandoned well sites. All results were further normalized using the ships track (distances of 10-m points to the same features) to account for the different coverages and survey focus during cruise HE537. Maps included in this study were spatially projected in UTM zone 32N (WGS84).

During the second half of cruise HE537, the hull-mounted SES-2000 medium (Innomar Technologies) sediment echosounder system was used to image shallow sedimentary structures and gas indications. The SES-2000 employs the parametric effect to achieve a small signal opening angle of about 2° at relatively low frequencies between 4 and 15 kHz. The data used in this study were recorded at 6 kHz and penetration depths down to ∼25 m below seafloor were achieved. The raw data were converted to SEGY-format using the custom PS32SGY software (Hanno Keil, University of Bremen). The data were loaded into the commercial software package Kingdom Software (IHS) for display and interpretation (i.e., mean amplitude grid calculation and horizon mapping of gas indications). Conversions from two-way-traveltime to depth have been calculated using a sound velocity of 1,500 m/s.

Electromagnetic Data

Sediment-physical properties of the seabed were mapped with MARUM's benthic EM profiler NERIDIS III, dedicated for EM seafloor classification. The bottom-towed sled has dimensions of 5.2 × 1.2 × 0.8 m, and a weight of approx. 250 kg in water. It is equipped with a horizontal EM induction-loop sensor (1 m diameter), an Attitude-Heading-Reference-System (AHRS), and conductivity-temperature-depth probe (CTD) with turbidity sensor (Müller et al., 2011). The profiler was towed in contact with the seabed at speeds of 2–4 kn (1–2 m/s). The position of the EM-sensor was determined from triangulation using the ship's differential GPS coordinates, tow cable length and water depths. EM data were measured at salt diapir Berta along 11 parallel profile lines with 50 m line spacing, covering an area of 2,300 × 600 m. Comparison of the CTD depth-profile of the bottom-towed sled with echosounder bathymetry allows to assess the position accuracy of EM soundings. Error propagation of DGPS-, layback-, and AHRS-uncertainty results in sensor positioning with about 5 m accuracy.

The central loop EM method coevally quantifies electric and magnetic properties in the topmost 1–2 m of the sediment by measuring the EM response at seven frequencies (range: 75–10 kHz) with stable sensor elevation of 25 cm (pitch varies between −0.5° and 1°). A half-space inversion method (Müller et al., 2012) was used to convert calibrated raw-data into appropriate SI units of apparent electric conductivity and magnetic susceptibility (the term apparent is used to specify that this value is derived from EM data modeling and no vertical layering is considered). The apparent conductivity of the highest (10 kHz) frequency was despiked to remove local high-amplitude anomalies of metallic objects in the subsurface and median filtered (25 samples per second raw data, 2 s median). Data were interpolated on a regular grid of 10 m cell size using inverse distance gridding (100 m search radius). A directional cosine and a 100 m low pass filter was applied to remove small line-to-line errors and noise.

Gas saturation is often calculated from EM conductivities using Archie's empirical porosity-resistivity relation (Archie, 1942) for a three-phase porous system of sediment grains, pore-fluid and resistive hydrocarbons such as gas or gas-hydrate (e.g., Schwalenberg et al., 2020):

$$\sigma_g = a\,\sigma_w\,\phi^m\,\left(1 - S_g\right)^n, \tag{1}$$

where σ_g is the electric bulk conductivity of the sediment section derived by inversion from EM data, σ_w the conductivity of the pore fluid (usually close to bottom water conductivity measured by the CTD probe), ϕ the sediment porosity and S_g the gas saturation of the pore space. Equation (1) contains empirical constants that are usually determined from physical properties measured in boreholes and on sediment samples, where a describes the tortuosity, m the cementation factor and n the saturation exponent. The latter varies from 1.8 to 4.0 but is often found close to 2.0 (e.g., Schwalenberg et al., 2017). Assuming that the lithology does not change between gas-charged and gas-free sediment sections, Eq. (1) simplifies to:

$$S_g = 1 - \left[\sigma_g / \sigma_0\right]^{\frac{1}{n}}, \tag{2}$$

where σ_0 is the background conductivity of the pore water saturated sediment and σ_g the bulk conductivity of the gas-charged sediment section (both derived by inversion from EM data). Assuming the widely used gas saturation parameter n = 2.0 one can estimate the gas-saturation from electric conductivity anomalies without actual porosity determination, although local sediment compaction or dilution is omitted.

Water Sampling

The hydro-geochemistry (e.g., temperature, oxygen saturation, fluorescence, and transmission) was analyzed and samples were taken using a CTD SBE911plus and carousel water sampler SBE32 equipped with additional sensors including oxygen sensors (SBE43), fluorometer (Wetlabs, EcoFLR), transmissiometer (Webtabs CStar, 25 cm). Bottom waters were sampled with a Mini-Multicorer (MIC). Samples from the water sampler were taken immediately and bubble free after retrieval using a silicon tube. Samples were directly transferred into 118 ml glass bottles and were acidified with 2 ml 37% HCl. The bottles

were sealed with a Teflon coated butyl rubber seal and were closed with aluminum crimp caps. Dissolved gas concentrations were determined applying a headspace equilibration technique described in detail by Schloemer et al. (2018). 25 ml of the water samples were replaced by laboratory grade Helium (5.9) and the samples equilibrated to ambient temperature varying from 23° to 28°C (since the laboratory was not air-conditioned) for at least 2 h on a laboratory shaker. After equilibration, the total headspace pressure was measured using a pressure transducer (range 0 to 160, 0.8 kPa accuracy). For gas chromatography analysis of methane and higher hydrocarbons up to i-/n-butane in the headspace a Shimadzu 14B gas chromatograph with splitless injection was used and 1 ml of the equilibrated gas was injected with a gas-tight syringe. Compounds were separated on a 3 m packed column (1/8" Porapak Q) using nitrogen as carrier gas and detected on a flame ionization detector. Methane was calibrated with a 10 ppm standard air (Linde Minican) and laboratory air diluted with helium down to 0.09 ppm CH_4. The concentrations of the dissolved methane, and if present of higher hydrocarbons, were calculated using the partial pressure, derived from fractional concentration and total headspace pressure, temperature of the sample, volume of headspace gas (25 ml) and remaining water (93 ml) applying the Henry's Law constant of methane. A correction for the salting-out effect was applied using a total salinity of 0.59 mol/L and the Setchenow constant for the analyzed components. The relative error of the GC analysis is around ± 3% and for the total analyses ~ ± 10%.

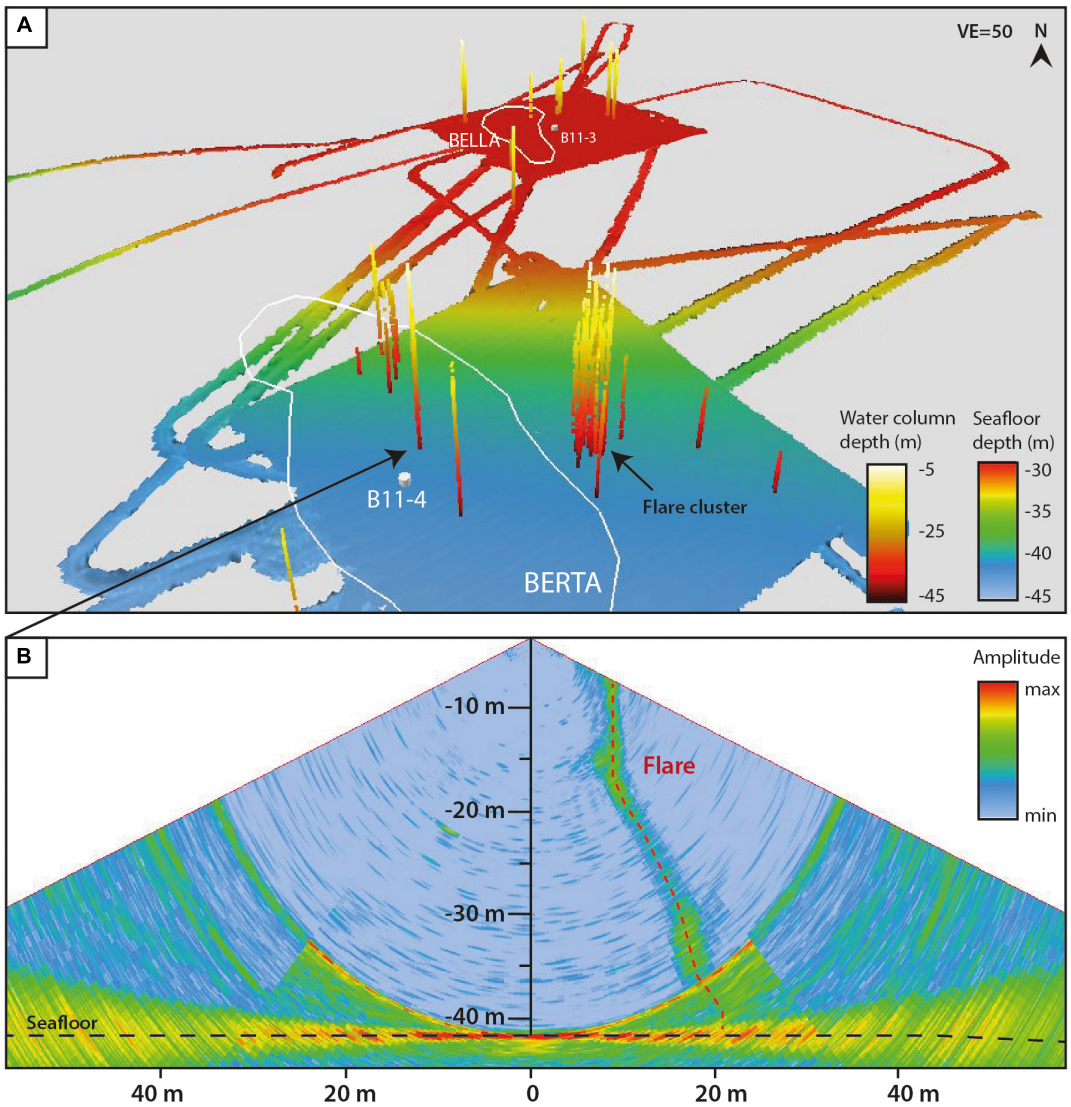

FIGURE 2 | (A) Flares extracted from the water column data imaged with the bathymetric data, recorded by ship-based multibeam echosounder Kongsberg EM710 during R/V Heincke cruise HE537. White outline: subsurface salt diapirs (Arfai et al. (2014), white dots: abandoned well sites (from Lower Saxony's borehole database: www.lbeg.niedersachsen.de). **(B)** Swath image of the water column data illustrating a flare detected above salt diapir Berta. The flare represents the pathway of gas bubbles released in 42 m water depth through almost the entire water column.

Methane Sensor Deployment

The METS from the company Franatech was mounted at a frame (together with CTD, video cameras, forward looking sonar, altimeter, and USBL transponder), which was towed 0.5–2 m above the sea floor at tow speeds of only 0.5–1 knots. The detector is a semiconductor, which is in contact with a gas-filled chamber that is separated from the surrounding water by a sintered disk supporting a gas-permeable membrane. This allows for the separation of dissolved gases from the water where the gas flow is driven by diffusion following Fick's Law. To support a constant flow of water at the outside of the membrane, a Seabird 5 M pump is used. The listed measuring range of the METS is 1–500 nM, which covers methane maxima as well as open ocean background values. The reaction time of the sensor is limited by the diffusion through the membrane. Accuracy and precision of calculated concentrations are further dependent on the response time of the temperature sensor (Pt100), listed with T90 = 1–30 min as the response of a semiconductor exposed to a target gas is highly temperature sensitive. Since the frame was towed in a nearly horizontal direction, temperatures were comparably stable and an equilibrium reached shortly after descending the frame. The sensor was calibrated by Franatech just before the HE537 cruise. Excluding the temperature dependency, the measured conductivity has a linear relationship with gas concentration. The precision of a Pt100 sensor is commonly ± 0.05°C, which induces an error of 5 nM at temperatures between 9.0 and 9.8°C as measured in the bottom water of the working area in bottom depths of 40–44 m.

RESULTS AND DISCUSSION

Gas Flare Occurrence in the "Entenschnabel"-Area

Gas emissions were detected and identified as flares in water column echograms of the MBES. Due to the limited coverage of the swath for water column observations, the total area covered for flare imaging was roughly 65 km^2. In total, 315 water column anomalies were recorded in the "Entenschnabel," in the northwestern part of the German North Sea (**Supplementary Table 1**). Flare observations were classified according to their appearance being certainly caused by gas bubble emissions or having an uncertainty of being misinterpreted and caused by schools of fish, which may have a similar appearance in the echogram as a flare. Relatively weak appearing anomalies or anomalies with anomalous shapes (deviant from a continuous

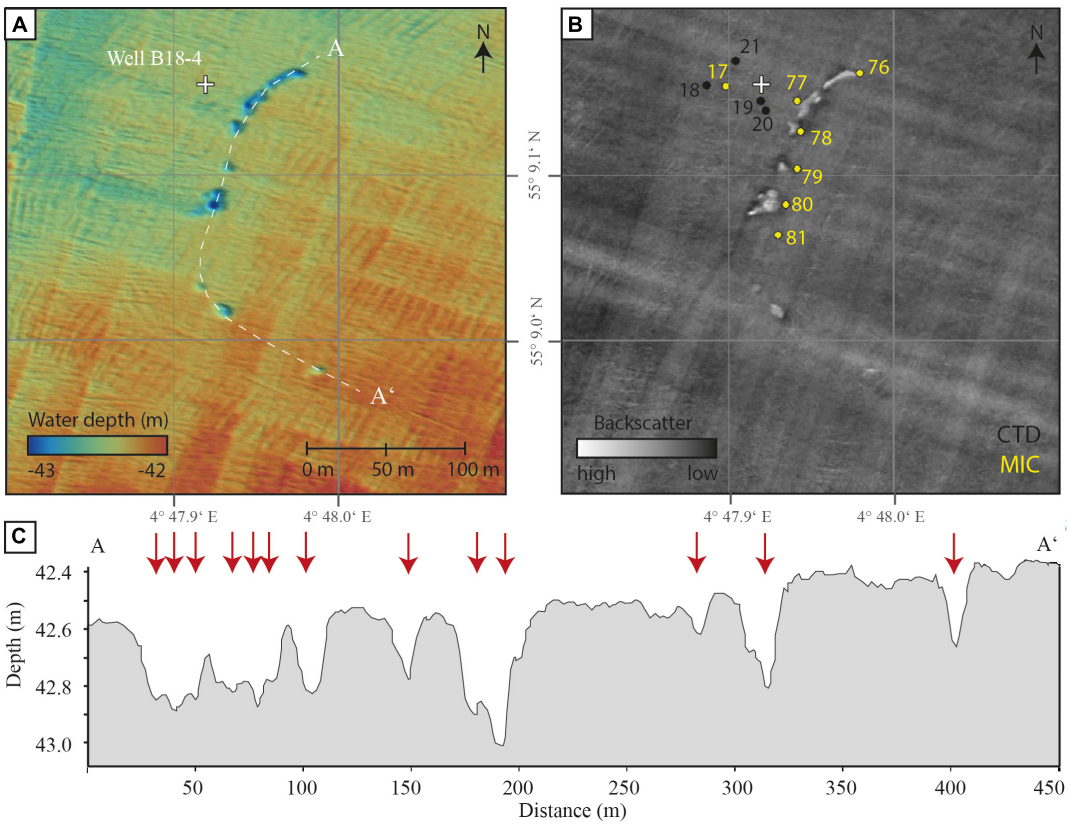

FIGURE 3 | (A) Bathymetric map of the area at salt diapir Britta, where several depressions were detected. Grid cell size is 2 m. Note: linear features in cm-scale vertically are artifacts. **(B)** The backscatter map shows that depressions are characterized by high backscatter signals (white patches). The area around well B18–4 and the depressions have been sampled for water (CTD casts) and bottom water (MIC stations) with station numbers (**Supplementary Table 2**). **(C)** Bathymetric profile crossing the depressions (marked by red arrows) from **A** to **A' (A)**, indicating their sizes, depths, and shapes.

linear feature) were therefore classified as uncertain. This uncertainty increases during bad weather conditions causing enhanced noise in the echogram or when gas emissions occur in pulses of bubble release that show up as single anomalies within the water column instead of continuous linear flares that are connected to the seafloor. Consequently, 210 flares were classified as certain flare observations, whereas 105 anomalies appeared too weak or unclear for being undoubtedly interpreted to be caused by gas bubbles. As some areas were studied multiple times, flare observations were partly repeated and flare numbers have been corrected for probable double counting. The numbers reduce to 269 detected water column anomalies of which 166 were classified as certain flare observations and 103 uncertain anomalies. Although double detection during different survey times suggests that most flares may be spatially and temporally stable, about 50 certain flares (30%) that were passed more than once were non-recurring. Natural gas emissions have often been observed to be highly transient in a variety of time scales in both the marine and freshwater settings (e.g., Tryon et al., 1999; Boles et al., 2001; Torres et al., 2002; Varadharajan and Hemond, 2012; Kannberg et al., 2013; Römer et al., 2016). It was argued that the variability of methane fluxes might be controlled by fluid flow rates mediated by microbial processes or physical changes in bottom pressure by, e.g., tides, bottom water currents, storms, swell, or earthquakes (Fechner-Levy and Hemond, 1996; Leifer and Boles, 2005; Scandella et al., 2011). Long-term monitoring or repeated observations would allow for evaluation of the variability of gas emissions and provide evidence for the controlling mechanisms in our study area.

Flare height determination is generally limited by the swath geometry, and the upper parts of most flares detected in this study are cut off in about 5–15 m below surface. Flares were detected in heights from less than 10 m and ending within the water column (as seen in **Figure 2A**) to more than 30 m to shallow water depths (e.g., the flare shown in **Figure 2B** would have probably reached the surface, if a full view would allow imaging the upper parts). Flares were detected at seafloor depths of 31 to 48 m. Bubbles released in such shallow depths are expected to reach the surface and contain some fraction of their initial methane content when reaching the sea surface, where the bubbles burst and directly contribute to the atmospheric methane inventory (Leifer and Patro, 2002). This has been measured and visually observed, e.g., at the nearby Dutch Dogger Bank seep area with a water depth of ∼40 m. In this seep area, flares were observed to reach the surface, and air measurements above some of the seep sites confirmed a transport of methane into the atmosphere (Römer et al., 2017). During the HE537 cruise, measurements of dissolved methane confirmed an oversaturation of methane in surface waters at the Dutch Dogger Bank seep area (see below). Surface water and atmospheric underway measurements reported in earlier studies from Rehder et al. (1998) and Judd (2015) passing through our "Entenschnabel" study area as well as our own measurements also detected elevated methane concentrations in surface waters (as described in section "Dissolved methane in the water column and bottom waters"), which would support the suggestion that the detected flares transport methane from the seafloor to the atmosphere.

Bathymetric mapping of the study area revealed that flare locations are not related to morphological seafloor indications (e.g., mounds, pockmarks, and linear cracks) or seafloor backscatter anomalies (due to, e.g., authigenic carbonate precipitation or colonization) that might be indicative for gas seepage. The seafloor is generally flat, between 30 and 50 m deep and smoothly slopes down from the Schillgrund High

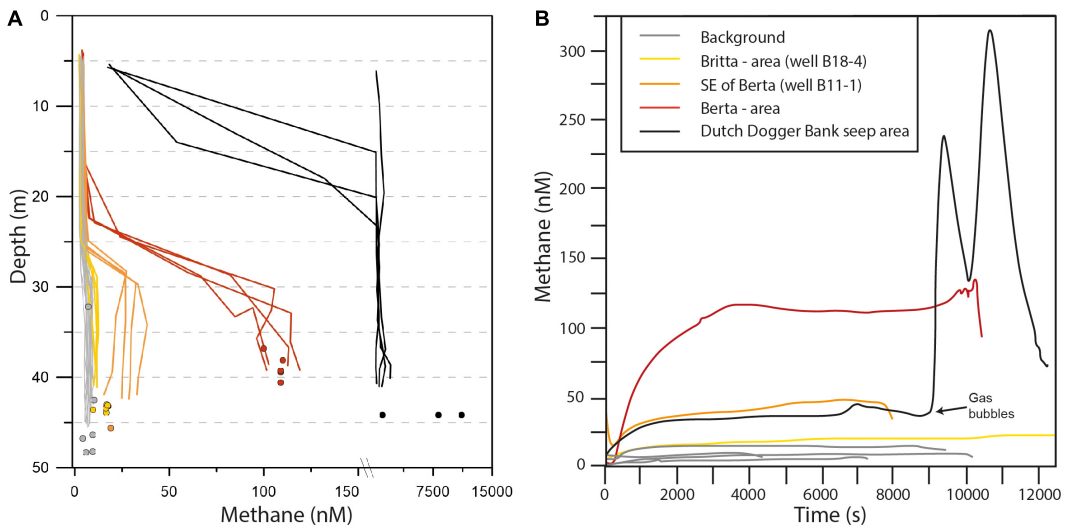

FIGURE 4 | (A) Profiles of methane in the water column of the "Entenschnabel" study area and for comparison of the Dutch Dogger Bank seep area (Please note break in the *x*-axis to address the different ranges of methane concentrations) as well as of concentrations in bottom waters (dots, MIC water samples) close to water column stations. Light gray samples represent background values at the reference site at salt diapir Birgit and four abandoned wells (wells B15–1, B15–2, B15–3, and B11–3). **(B)** Methane concentrations measured with the METS during towed deployments in seven areas in the "Entenschnabel" and the Dutch Dogger Bank seep area while passing a known flare cluster for comparison.

in the SE toward the Central Graben and further up at the northern part of the study area NW of the Central Graben. In the area of salt diapir Britta, however, we found several depressions that could have been formed by fluid release. No flares were detected in the Britta area despite several site surveys and station work. Nevertheless, the current lack or inactivity of gas release may not restrict its presence in the past forming such depressions. More than 17 depressions have been detected of which 13 appear in a semi-circular arrangement southeast of well B18–4 (**Figure 3A**). Some are partly intercalated, forming linear or composite depressions. Four other depressions were detected in distances between 460 and 980 m southwest and east of the well site (not shown). The depressions are circular to subcircular in shape with dimension of a few meters to maximal 25 m cross sections. Their shape is funnel-like with slopes of 1–5° and depths of up to ∼50 cm (**Figure 3C**). Backscatter mapping additionally revealed elevated backscatter patches related to the depressions (**Figure 3B**). Although most prominent hydrocarbon seeps have surface relief manifestations such as pockmarks (Judd and Hovland, 2007), other examples of seep areas lacking morphological features were described from the North Sea, including the Dutch Dogger Bank seep area (Schroot et al., 2005; Römer et al., 2017) and the "Heincke" seep area [Gullfaks in the Norwegian North Sea, Hovland (2007)]. It has been speculated that coarse-grained material of gravel/sand beach deposits might prevent pockmark formation (Hovland, 2007). Known natural seep sites in the North Sea correlated with pockmark formation include the large pockmarks in the Witch Ground Basin (Judd et al., 1994; Böttner et al., 2019), complex pockmarks in the Nyegga area (Hovland et al., 2005), the temporally dynamic Helgoland Reef pockmark field (Krämer et al., 2017), and small depressions at the Tommeliten seep area (Schneider Von Deimling et al., 2011). In addition, artificially created blowout events formed large depressions in the North Sea. Examples are the well site 22/4b, which displays a 50 m wide and 20 m deep depression formed in 1990 (Schneider Von Deimling et al., 2007; Leifer and Judd, 2015), and the so-called "Figge-Maar" with a depression of 400 m width and an initial depth of ∼30 m depth after a carbon dioxide eruption in 1964 (Thatje et al., 1999; see location in **Figure 1A**). The depressions detected in this study at salt diapir Britta are located in distances of 30 to 750 m of the abandoned well site B18–4, which does not exclude nor prove a generic relationship.

Dissolved Methane in the Water Column and Bottom Waters

Dissolved methane concentrations measured in bottom waters (sampled with MIC) and waters below the pycnocline (sampled with CTD) at the salt diapir Berta (close to well B11–4) were 10 to 13 times higher (max. 120 nM) than background values of about 9 nM detected in the "Entenschnabel" (**Figure 4A** and **Supplementary Table 2**). These elevated methane concentrations extended approximately 500 m to the east and west of the well site and did not increase toward the well. Slightly increased methane values of 20–30 nM also existed southeast of Berta close to abandoned well site B11–1. Well B11–1 is unlikely the origin of methane seepage, since no flares were detected near the site by hydroacoustics (coverage: 1,000 × 300 m), and we consider that diffuse seafloor venting would have led to a different methane profile with the highest amounts in the bottom water layer. However, the measured methane profiles showed slightly decreasing values with increasing depth and lower concentrations in the bottom water (**Figure 4A** and **Supplementary Table 2**). Since the most distant CTD cast from B11–1 exhibited highest methane concentrations in the deep water layer, and area B11–1 is ∼3 km apart from salt diapir Berta, a horizontal input from, e.g., the Berta seep area is feasible. Data extracted from the Operational Circulation Model of the BSH (Dick et al., 2001) show that a transport of water masses originating from the Berta area is feasible due the strong tidal currents. At the time of sampling, the current had only just switched directions after a period (5 h) of steady easterly currents (up to 24 cm/s). Compared to the Berta area the methane concentrations at the nearby Dutch Dogger Bank seep area were much higher and more variable. Here, values in the deepest water samples reached up to 2,085 nM (**Figure 4A**), which is 200 times the background value and compares well with the published concentrations of up to

TABLE 1 | Mean values of dissolved methane in the studied areas and in the water column zones.

Area	Above pycnocline			Surface waters			Bottom waters		
Name (well site)	**Ø CH_4 (nM)**	**1 σ (nM)**	***n***	**Ø CH_4 (nM)**	**1 σ (nM)**	***n***	**Ø CH_4 (nM)**	**1 σ (nM)**	***n***
Bella (B11–3)	4.2	0.5	12	4.1	0.5	4	7.0	na	2
Berta (B11–4)	5.0	1.1	18	4.5	0.5	5	106.4	4.9	10
SE of Berta (B11–1)	5.1	0.9	16	4.4	0.6	4	17.8	na	2
Belinda (B15–1)	2.6	0.2	19	2.7	0.3	4	4.2	na	2
Belinda (B15–3)	3.3	0.5	16	3.7	0.3	4	6.1	na	2
Britta	2.6	0.1	8	2.7	0.1	2	10.2	na	2
Britta (B18–4)	2.8	0.2	10	2.6	0.1	2	15.2	3.4	8
Birgit	4.0	0.5	16	3.8	0.4	4	9.5	na	3
E of Belinda (B15–2)	3.5	0.3	12	3.6	0.1	4	8.5	na	2
Dutch Dogger Bank seep area	349.7	362.7	16	79.8	106.5	4	3491.9	4149.2	7

"Above pycnocline" combines all concentrations above the thermocline, "surface" between 3 and 6 m and "bottom" the bottom water samples from MIC deployments and the deepest sample from CTD casts (for data see ***Supplementary Table 2****).*

1,628 nM by Mau et al. (2015). Bottom water samples, taken from MIC sampling, reached values of up to 11.14 μM. This compares to 113 nM measured at the Berta seep area (**Figure 4A**).

The water column methane profiles generally decrease quickly in the CTD casts toward the surface but methane concentrations vary between areas. **Table 1** shows mean values for each studied area and zones of the water column (above pycnocline, surface and bottom waters). By far the highest surface water concentrations of methane are restricted to the Dutch Dogger Bank. Here, methane concentrations at 3–6 m water depth were about 18 nM in three CTD casts (**Figure 4A**) but reached up to 263 nM at one station, clearly indicating gas emissions reaching surface waters. No shallower samples were taken due to rough weather conditions. Based on water temperature, salinity and the

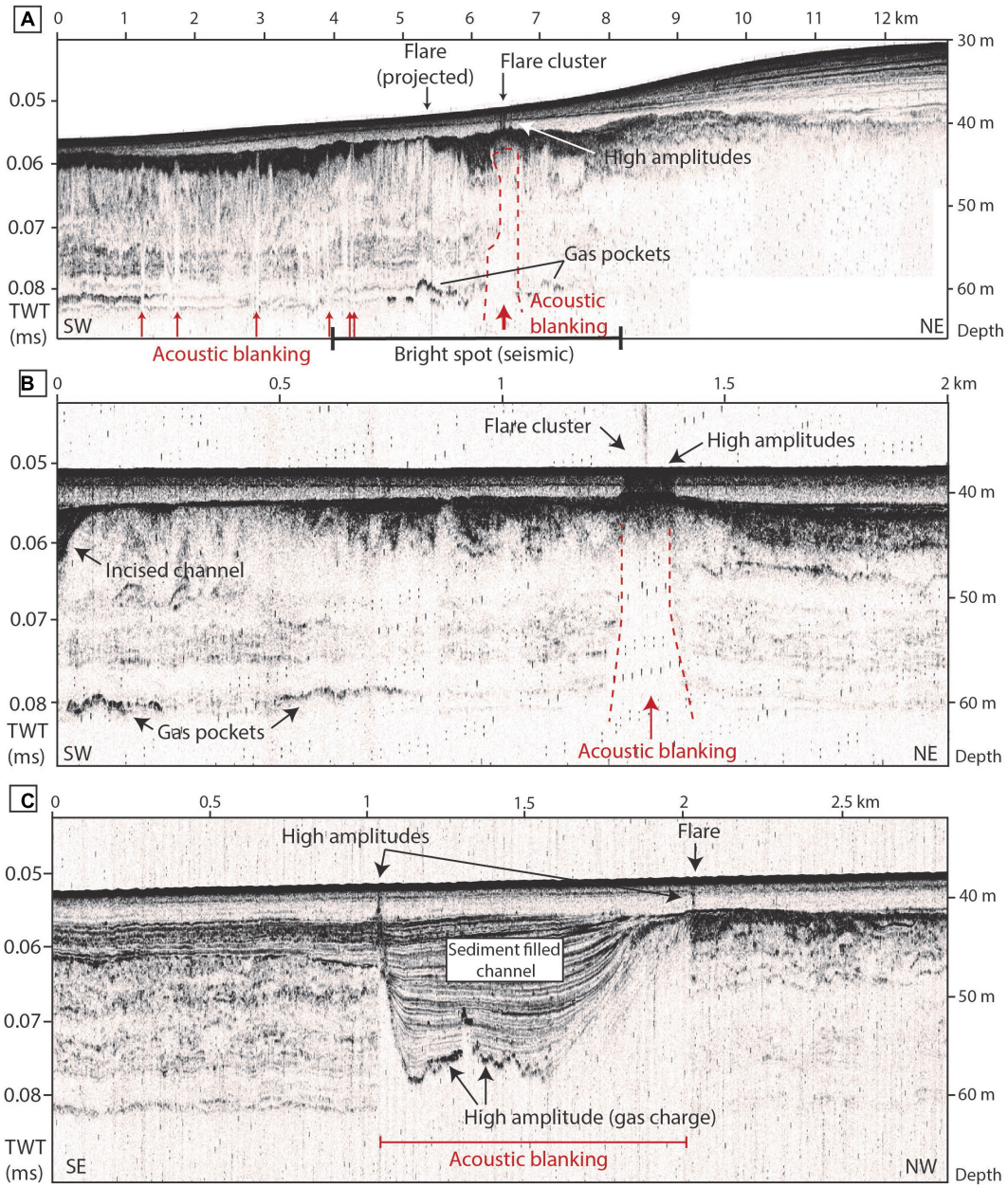

FIGURE 5 | Subbottom profiles recorded with the sediment echosounder Innomar SES-2000 during R/V Heincke cruise HE537 in the area close to salt diapir Berta. See **Figure 6B** for locations. Depth conversion has been estimated using a sound velocity of 1,500 m/s. **(A)** Profile covering the bright spot mapped in the deeper subsurface above salt diapir Berta. Acoustic blanking forming chimneys are indicated with red arrows, with the widest chimney below the flare cluster detected in the water column (red dashed line marks the outline). **(B)** Detailed profile focusing on the chimney (red dashed line), in which the high amplitudes between acoustic blanking and water column flare cluster becomes visible. **(C)** Detailed profile showing a sediment-filled channel with columnar acoustic blanking and high amplitude reflectors below, indicating increased gas concentrations migrating along the flanks of the channel up to the seafloor.

current atmospheric methane concentration of 1,877 ppb (Nov 2019; https://esrl.noaa.gov/gmd/ccgg/trends_ch4/; last visited 27.03.2020), methane concentrations in equilibrium with the overlaying air (air saturated sea water; ASSW) are in the range of 2.6 nM calculated after Wiesenberg and Guinasso (1979). In the southern "Entenschnabel" area with water sampling above salt diapirs Britta and Belinda, methane surface values were only very slightly oversaturated (**Supplementary Table 1**). The observed oversaturation increased slightly toward this northwestern part of the working area, reaching up to 5 nM at locations Berta and Bella (**Supplementary Figure 2**), representing a small source of methane to the atmosphere. This is in agreement with the increased numbers of gas flares found here compared to the southern working area and measurements by Rehder et al. (1999) of slightly elevated surface concentrations in the region.

Ethane, the only higher hydrocarbon detected, was found in trace amounts at two sites, one of them the Dutch Dogger Bank site. The second site is located above the Britta salt diapir in the southern part of the "Entenschnabel." Here, bottom water samples collected from all six MIC cores contained traces of ethane. The MIC sample taken close to well site B18–4 was devoid of ethane and showed methane concentrations close to the background (9.8 nM). The MICs with ethane originated from a series of depressions occurring in a linear array near the well site B18–4, extending further to the south (as described above, see **Figure 3B**). In addition, methane values of bottom and deep water samples were slightly elevated with concentrations of 18 nM and 12 nM, respectively. Flares were absent in the region of these depressions, and considering the very low absolute concentrations, we assume the depressions to be pockmarks characterized by diffuse fluid transport or episodically occurring gas emissions. Trace amounts of ethane are common in biogenic gases in different environments and usually methane/ethane ratios in such samples are high (>>100). We assume that the low observed methane/ethane ratios found in the depressions at Britta (∼40) are the result of the preferential oxidation of methane compared to ethane occurring during a slow diffusive ascend of the fluid. Equally low methane/ethane ratios were assigned to partly oxidized biogenic gases in ground waters based on enrichments in ^{13}C isotopes of methane (Schloemer et al., 2018). Propane, which would be an indicator for a migrated deeper sourced thermal (natural) gas, was not found, neither in the samples from the depressions in the Britta area nor in bottom waters at the Dogger Bank seep site.

The METS data are in good agreement with discrete water sampling from vertical CTD casts. Like the CTD casts, the METS profiles do not indicate any seepage of methane at salt diapir Belinda (well sites B15–3 and B15–2) and salt diapir Bella (well site B11–3; light gray lines in **Figure 4B**). At salt diapir Britta the deployments crossing the line of pockmarks detected slightly elevated methane concentrations of up to 20 nM in relatively flat time-series (**Figure 4B**) confirming a small methane flux into the water column. The pattern is similar close to well B11–1 with elevated concentrations of up to 40 nM. At Berta, where numerous gas flares were observed, the METS detected methane concentrations of ∼120 nM throughout most of the deployment (**Figure 4B**), indicating a strong oversaturation with methane over a wider area despite no active seepage having been crossed. The METS time series at Berta is relatively flat with no spikes. This is unlike a profile measured at the Dutch Dogger Bank seep area, where two clear peaks occurred during the crossing of a prominent flare cluster (**Figure 4B**).The METS data not only confirm the results from the discrete water sampling but

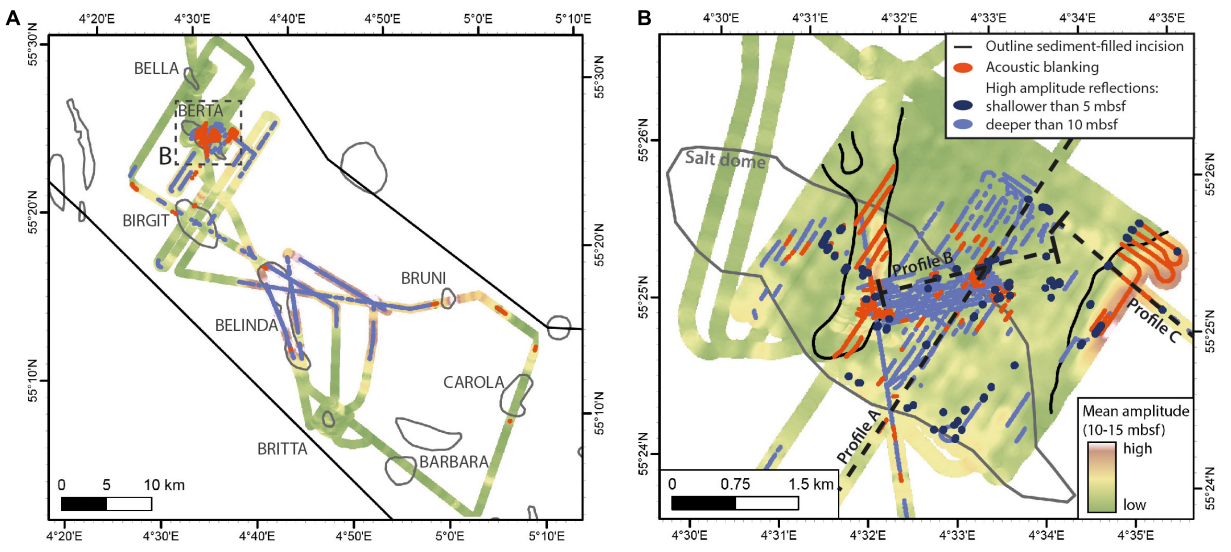

FIGURE 6 | Subbottom analysis maps showing mean amplitude values between 10 and 15 mbsf throughout the entire dataset acquired, the locations of high-amplitude reflections (blue) and acoustic blanking (red). **(A)** Overview map (interpolated raster surface from track points using kriging, grid cell size is 50 m and maximum point distance is 500 m), **(B)** detailed map of the area mapped at salt diapir Berta (interpolated raster surface from track points using kriging, grid cell size is 10 m and maximum point distance is 100 m).

show, that methane oversaturation extend beyond the small grid covered by the CTD stations.

Subsurface Gas Indications

Sediment Echosounder Profiling

Due to increased impedance contrasts resulting from enriched free gas content in the pore-space, gas in the subsurface becomes visible in sediment echosounder profiles as enhanced reflectors with high amplitudes and acoustic signal blanking appearing as vertical zones lacking any reflectors underneath these high amplitude reflections. Subsurface gas indications such as acoustic blanking and high amplitude reflections interpreted as gas pockets have been widely found and described in the Dutch North Sea sector including the nearby Dutch Dogger Bank seep area (Schroot et al., 2005; Römer et al., 2017). Subsurface acoustic blanking in our study area has been observed as (1) narrow vertical chimneys (examples shown with red arrows in **Figures 5A,B**), and (2) below subsurface seafloor incisions filled by sediments (**Figure 5C**). Chimneys were documented to reach within ∼3 m of the seafloor and are commonly few tens of meters wide. The most prominent chimney has been detected below the flare cluster at salt diapir Berta with a width of about 200 to 300 m (**Figures 5A,B**). Acoustic blanking below sediment-filled channels or basins becomes visible below the incised structure and follows the flanks up to the shallow subsurface (**Figure 5C**). This type of acoustic blanking is generally more extensive than the narrow chimneys. Acoustic blanking interpreted to result from increased free gas content were described also in relation to Pleistocene glacial valley-fills in the Netherlands EEZ (Schroot and Schüttenhelm, 2003; Schroot et al., 2005). In several sediment-filled incisions, blanking also pierces through the bottom of the channel or basin and is accompanied by high amplitude reflections at their upper limit (**Figure 5C**), where the gas appears to be hindered from further upward migration and accumulated. High amplitude reflections also occur in areas close to acoustic blanking in about 20 m depth below seafloor and were interpreted to represent gas pockets (**Figures 5A,B**). Another type of high amplitude reflections was frequently observed close to the seafloor connecting gas chimneys with flare observations in the water column (**Figures 5A–C**), appearing as narrow vertical lineations.

Gas indications in shallow sediments are most concentrated at but not restricted to the area at salt diapir Berta. The mean amplitude calculated in a sediment depth interval between 10 and 15 meters below seafloor (mbsf) illustrates differences in the "Entenschnabel" (**Figure 6A**). Whereas the northernmost part of the study area (around salt diapirs Bella and Berta) as well as the southern part (around salt diapirs Britta, Barbara and Carola) shows lowest mean amplitudes, the central part shows overall higher values indicating better sound penetration. Besides being influenced by higher gas concentrations, such differences could be also related to sedimentological differences of the deposits. However, in the central part, areas of highest mean amplitudes are related to the presence of high amplitude reflections in sediments deeper than 10 mbsf, possibly illustrating the occurrence of free gas, which rather accumulated in the subsurface and not percolated throughout the shallowest deposits. Mapping of high amplitude reflections further indicates that their occurrence is restricted to the northern and central parts (blue lines in **Figure 6A**), suggesting that these areas are influenced by higher gas concentrations. Furthermore, focused acoustic blanking zones were mapped revealing several occurrences apart from salt diapir Berta (red areas in **Figure 6A**). With few exceptions, acoustic blanking was observed close to the outlines of salt diapirs, e.g., of Birgit, Belinda, Bruni, and Carola. However, the highest abundance of acoustic blanking was detected in the area of salt diapir Berta (**Figure 6B**). In part, these were related to two sediment-filled incisions (black outlines in **Figure 6B**), which also show up as elevated mean amplitudes when deeper incised than 10 mbsf. High amplitude reflections and acoustic blanking not

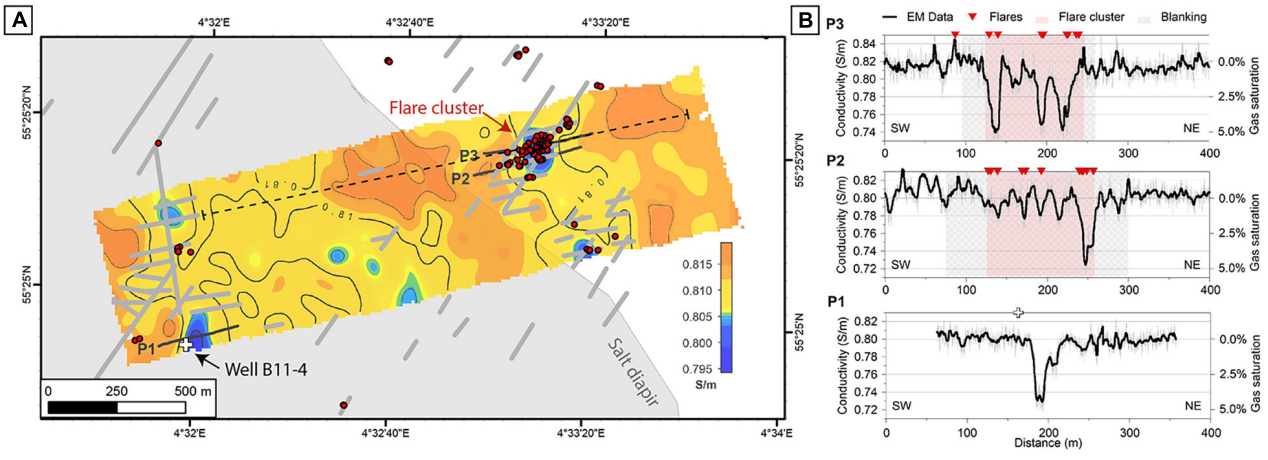

FIGURE 7 | Sediment electric conductivity data of the benthic EM Profiler. **(A)** Gridded 10 kHz EM conductivity data with flare locations (red dots), acoustic blanking from subbottom data (gray lines), and transect of subbottom profile B (**Figure 5B**; dashed line). **(B)** Selected profiles crossing conductivity minima (indicated by black lines in a; gray: raw data, black: median filtered) with projected flare locations. Background colors indicate areas of high flare density and acoustic blanking. Gas saturation estimates are based on the conductivity contrast (Eq. 1). A white cross marks the location of borehole B11–4 in both figures.

related to the sediment-filled incisions were concentrated in the northeastern part of the salt diapir.

Electromagnetic Seabed Mapping

Free gas is considered to reduce the electric conductivity of the subsurface by replacing conductive pore-fluid with resistive gas and blocking of conduction paths through the sediment (Evans et al., 1999). EM methods are therefore used to derive volume estimates of free gas in the sediment (Cheesman et al., 1993; Schwalenberg et al., 2017). However, the sediment electric conductivity is controlled by other factors as well, such as pore-water salinity and temperature, lithology, clay content, grain-size, and sorting (e.g., Winsauer et al., 1952; Jackson et al., 1978).

The survey area at salt diapir Berta including borehole B11–4 (**Figure 7A**) is dominated by fine sands, with higher (11–20%) clay and silt content in the west, and medium to coarse sands in the northeastern section (Laurer et al., 2012). Apparent electric conductivities of the sediments are in the range of 0.711–0.953 S/m and follow the general sedimentary units with slightly lower values in fine sands in the western part and highest values in coarser sands in the eastern half of the survey area. This trend is interpreted to result from sediment sorting, where porosity is reduced with increasing content of fine particles. The large-scale sedimentary units are interrupted by several distinct electric conductivity lows. A prominent low is associated with acoustic blanking visible in subbottom data (see above) below the flare cluster (**Figure 7A** and profiles P2 and P3 in **Figure 7B**). The profile view (**Figure 7B**) depicts several focused conductivity minima, less than 50 m in diameter, which are smoothed by the gridding interpolation. In profile P3, three local minima are observed, where conductivity drops from background values of 0.82 to 0.74 S/m. Neglecting the saturation term in Eq. 1 we can derive a mean porosity for the study area of approx. 40% from the background conductivity outside the anomaly using Archie coefficients $a = 1$ and $m = 1.6$ for medium-fine to coarse sands (e.g., Evans et al., 1999), and a CTD-derived pore water conductivity of 3.7 S/m. According to Eq. 2, the drop in conductivity at the flare cluster relates to a free-gas saturation up to 5% of the pore-space. Similar patterns are observed in profile P2 although less developed and frequent. Another minimum has been mapped further south that appears to follow a SSE trending structure, which roughly mimics the boundary of the salt diapir. Profile P1 identifies a bimodal conductivity anomaly with a similar drop in amplitude, about 30 m to the east of the location of borehole B11–4. Video transects did not reveal changes (e.g., small-scale morphologies or sediment characteristics) of the seafloor sediments in this region. Due to the absence of acoustic blanking in the sediment echosounder profiles, we do not expect free gas to cause this conductivity low and assume over consolidated or contaminated sediments as a result of the drilling operation that took place in 2001. Note that we made the assumption that the sediment matrix (hence porosity) does not change for gas-charged sediments, thereby the gas saturation is a pure function of the conductivity difference and the empirical saturation exponent n, and hence independent from porosity, pore-water conductivity and grain-size. However, Szpak et al. (2012) and Garcia et al. (2014) even observed higher conductivities with highest volumes of gas within pockmarks which they explain by an increase in porosity and fining of the sediment in consequence of gas migration (and potentially by gas-driven microbial activity). Consequently, even higher free-gas concentrations are required to explain the drop in conductivity below the flare clusters. The impact of gas migration on the sediment fabric may be resolved combining electric conductivity mapping with, e.g., high-resolution sediment sampling, magnetic susceptibility mapping, or joint inversion with seismic data (e.g., Müller et al., 2011; Baasch et al., 2017; Attias et al., 2020), which is out of scope in this publication.

Gas Distribution and the Shallow Gas System in the "Entenschnabel"-Area

Flare Distribution in the Study Area

The flares detected during R/V Heincke cruise HE537 were not randomly distributed in the study area. Most flares (149 out of 166 certain flares) were found in the vicinity of subsurface salt diapir structures (**Figure 8** and **Table 2**). Highest abundance of flares were located at or around salt diapir Berta (104 flares) and Bella (19 flares). Five other salt diapirs revealed the presence of 1 to 13 flares. Salt diapirs Clara, Bruni and Bettina did not show any sign of gas bubble seepage. However, they were not mapped with a larger coverage, but passed during transits with partly increased vessel speeds of 5–10 knots, limiting the data quality. In order to account for the different coverage in the study area, the fraction of each defined area that has been mapped for the presence of flares was calculated and related to the number of flare findings (**Table 2**). The results show that the flare abundance at those salt diapirs with only 1 to 13 flares are similar or only very slightly elevated in relation to transits (areas between salt diapirs). However, even when accounting for the coverage, Bella and especially Berta exhibit elevated flare abundances. The relation of gas seepage to salt diapirs is also known from closely located seep areas: the Tommeliten seep area (Hovland and Judd, 1988) and the Dutch Dogger Bank seep area (Schroot et al., 2005). Seismic studies revealed that shallow gas accumulations seem to be concentrated above salt structures, which act as focal structures for migration (Schroot et al., 2005; Müller et al., 2018). Distances of flare findings related to the outlines of subsurface salt diapirs show a clear peak in flare abundance in a distance of 1 to 500 m (**Figures 9A,B**). Most flares are actually not located directly above salt diapirs, but just around them. This observation might be interpreted to result from a certain lateral migration of gas along weakening zones or gas migration that is focused along the flanks of the diapir, probably depending on the deformation pattern above the salt diapir. Buoyant gas migrates upward to the seafloor, either along diapir-induced faults or at locations where the gas columns are tall enough that the pressure of the accumulated gas is higher than the capillary entry pressure of the unconsolidated sediments above (Müller et al., 2018). Faults are common structures at the crest of salt diapirs. They form during the growth of salt structures as a result of the deformation of the

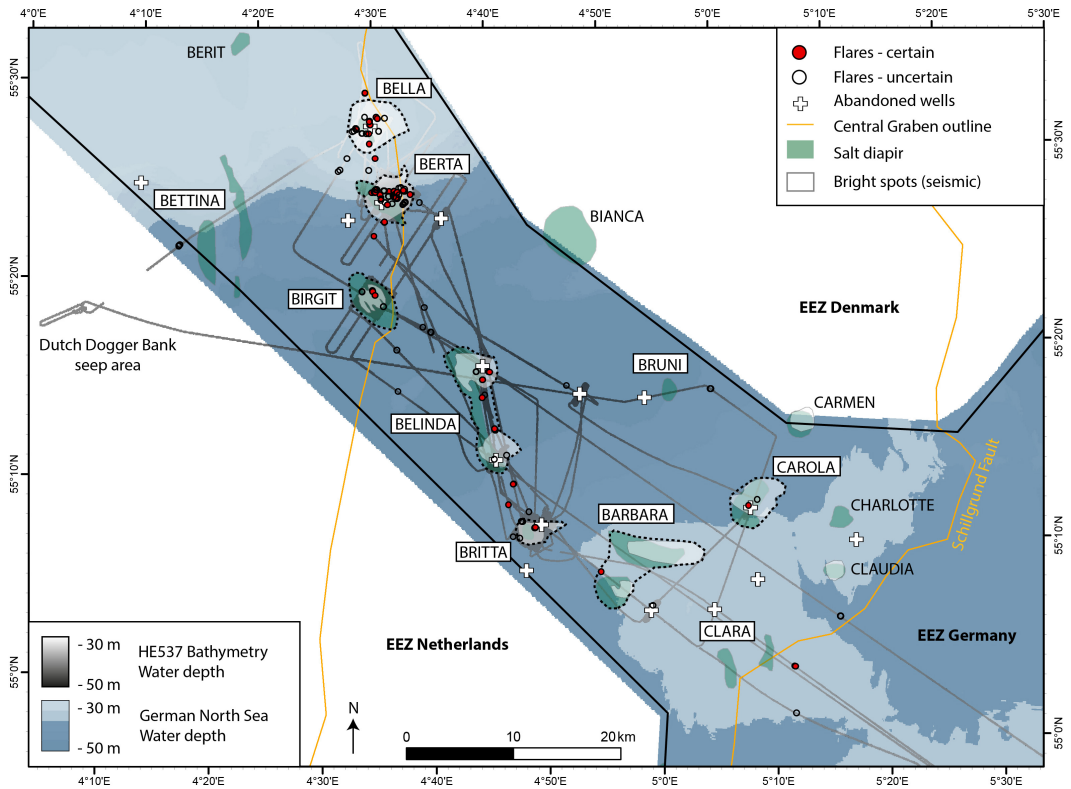

FIGURE 8 | Map compiling flare detections in relation to subsurface salt diapirs and bright spots as well as abandoned wells. Almost 90% of all detected flares were found in the vicinity of subsurface salt diapir structures [depicted from Arfai et al. (2014)]. Note that salt diapir and bright spot areas are slightly transparent to illustrate their extents where overlapping each other. Bathymetry downloaded from www.gpdn.de.

overburden (Jackson and Hudec, 2017). Shallow gas reservoirs have been detected and imaged as bright spots in about 300 to 800 mbsf (Müller et al., 2018). Distances of flare positions detected during this study were also plotted in relation to bright spot detections revealing a clear relation, with the majority of flares located directly above a bright spot (**Figures 9A,B**). Only 21% of all detected flares and 13% of flares classified as certain were found without a bright spot in the subsurface, whereas the maximum distance of a certain flare to the closest bright spot was 1.8 km.

It was examined if faults play a role as migration pathways for fluids in the "Entenschnabel" area by passing the Schillgrund fault four times during transits. This fault is the southeastern boundary of the Central Graben to the Schillgrund High (**Figure 8**). Faults and fractures were reported to relate in different ways to fluid flow patterns: acting as seals [i.e., Ligtenberg and Connolly (2003)] or providing temporally efficient migration pathways, as observed, e.g., in the Sea of Marmara (Dupré et al., 2015), the Sea of Okhotsk (Jin et al., 2011), and the Black Sea (Riboulot et al., 2017). The Schillgrund Fault has been shown to provide a pathway for salt diapirism, as salt intrusions south of salt diapirs Clara and Claudia rise up along this fault zone (Arfai et al., 2014). Salt diapirism in the Central Graben area is connected to pre-Zechstein faults (Davison et al., 2000; Ten Veen et al., 2012; Duffy et al., 2013; Arfai et al., 2014). Our water column mapping detected flares during three of the four crossings of the Schillgrund Fault zone, however, only two of the four detected flares were classified as certain. Since the two flares were closely located to salt diapir Clara, a relation of the Schillgrund Fault as active fluid migration pathway might be indicated but not proven.

TABLE 2 | Spatial analysis of flare findings at different areas including coverage for water column mapping.

Area (name)	Area (km^2)	Coverage (km^2)	Area covered (%)	Number of certain flares	Number of flares – normalized	Flares per coverage
Bella	20.3	5.4	27	19	0.71	3.52
Berta	17.7	8.4	47	104	2.19	12.38
Birgit	15.5	4.7	30	3	0.10	0.64
Britta	7.3	4.6	63	8	0.13	1.74
Belinda	35.5	5.9	17	13	0.78	2.20
Barbara	36.5	0.9	2	1	0.41	1.11
Carola	16.4	1.4	9	1	0.12	0.71
Transit	1750.8	33.7	2	17	8.83	0.50
Entire study area	1900	65	3	166	48.52	2.55

Flare numbers were normalized accounting for the area covered during HE537. The calculated values for flares per coverage illustrate that areas Bella and Berta are above the average of other areas and the entire study area.

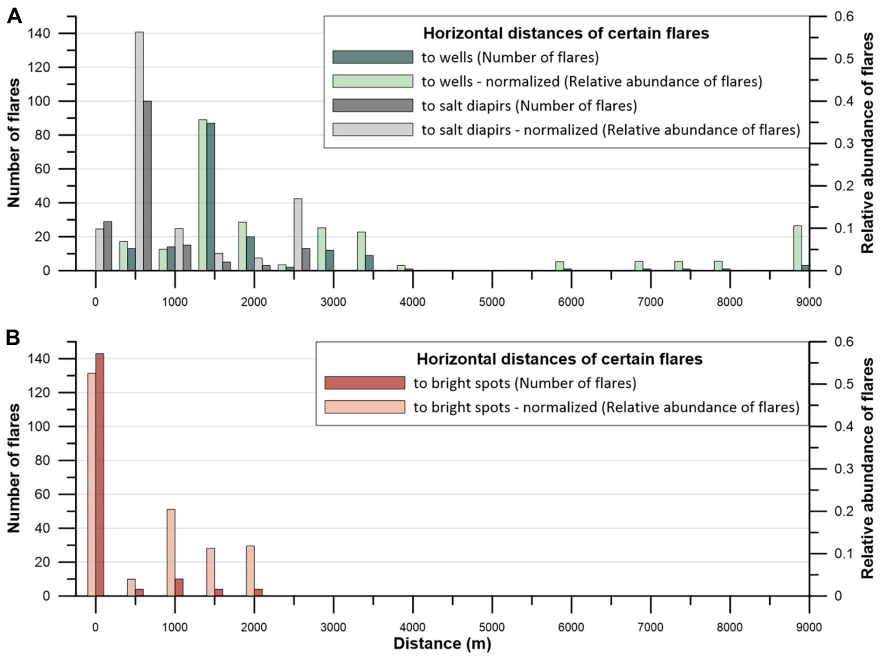

FIGURE 9 | Histogram plots showing the distances of flares to **(A)** salt diapirs, abandoned wells sites, and **(B)** bright spots (seismically identified). Only flares classified as certain were included. The histograms were binned at 500 m intervals, with the first bin = 0 m (flares plot above a salt diapir or bright spot area), second bin >0–500 m, third bin >500–1,000 m, ect. Darker colored bars illustrate the total numbers of flares, whereas the lighter colored bars indicate the relative abundance of flares including a normalization by the ship track coverage. The normalization corrects for the non-uniform mapping strategy in the study area.

Potential Gas Release Related to Abandoned Wells

Near distance analysis of flares to abandoned well sites showed a widespread distribution between 125 and 9,500 m (**Figure 9A**). Most flares were found in a distance of 1 to 1.5 km to a well site. When normalizing the distribution with the coverage during cruise HE537, individual flare findings in larger distances get amplified and the resulting distribution did not suggest a positive correlation with distance to abandoned well sites. No flare has been detected while exactly crossing one of the ten well sites surveyed during R/V Heincke cruise HE537 in the German North Sea. The closest distance of a flare to a well site is 125 m and only 13 certain flares were found in a distance of less than 500 m. However, seismic data acquired at a blowout in a Norwegian North Sea hydrocarbon exploration well indicated that gas entered into a shallow tunnel valley complex and migrated horizontally (Landrø et al., 2019), illustrating the complexity of shallow gas migration. Hence, the lack of correlation of flares with abandoned wells does not exclude any relationship particularly in complex geological settings, but we consider this to argue against a direct or indirect well-origin of gas emissions.

Six of ten wells were located in areas underlain by a bright spot, thus could be potential sites for release of shallow gas from the seafloor. Water column mapping revealed that flares were found in the vicinity of these six wells, but no flares were observed close to the four wells that are not related to a bright spot. Water column methane concentrations measured from samples at seven wells only showed clearly elevated concentrations at well B11–4 (located at salt diapir Berta). However, methane concentrations measured 500 m east and west of the well had similar values, pointing to a rather widespread gas release system above the salt diapir that is not focused at the well site. Methane concentrations were slightly above background (9 nM) in the bottom waters in the areas of wells B11–1 and B18–4 (**Table 1** and **Figure 4**), but leakage at the well sites appears unlikely due to the lack of flares and dissolved methane concentrations in the water column did not increase toward the well positions (see above).

Abandoned wells can act as migration pathways for gas through the sediment column as shown in several studies at onshore wells (Kang et al., 2014; Boothroyd et al., 2016; Townsend-Small et al., 2016; Schout et al., 2019). However, much less is known about their importance as leakage sites of methane release into the water column and subsequently into the atmosphere. In contrast to a study by Vielstädte et al. (2015), who focused on gas release at abandoned wells in the central North Sea, our study suggests that surveyed abandoned wells did not provide clear evidence for fluid release along the wells. The flares found near abandoned well sites in this study were rather interpreted to relate to a system of natural migration pathways. Vielstädte et al. (2017) discuss that one-third of all wells may potentially leak and bring the awareness of a probably unrecognized methane emission pathway contributing to the greenhouse gas inventory. Supporting this estimate, Böttner et al. (2020) could show that 28 out of 43 investigated wells in the United Kingdom sector of the North Sea release gas from the seafloor into the water column. Although our data including abandoned wells in the German EEZ do not replicate these

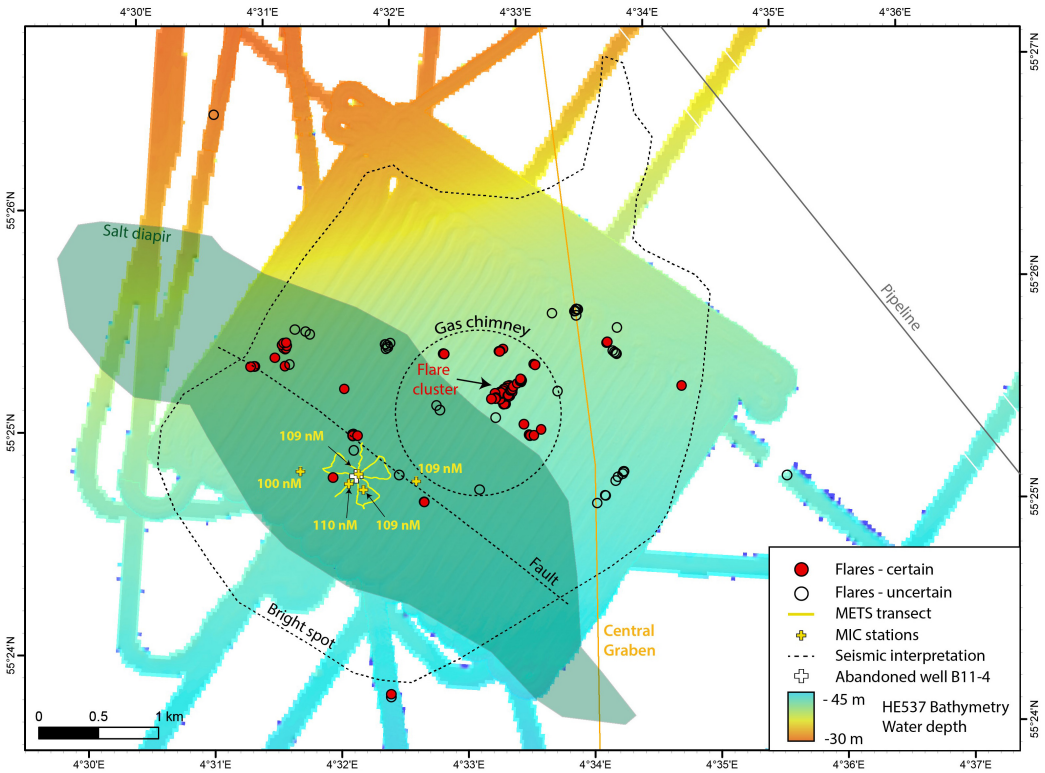

FIGURE 10 | Map compiling data acquired at salt diapir Berta, where most of the flare findings were concentrated. Seismic interpretation (bright spot extent, subsurface fault indication, and gas chimney) was depicted from Figure 7 in Müller et al. (2018). Bottom water methane concentrations (yellow numbers) do not increase toward the well site.

findings, our observations were limited to ten wells and base on infrequent crossing of the wells decades after drilling. Hence, we cannot entirely exclude methane seepage from the well sites nor can we confirm it.

Specific Gas System at Salt Diapir Berta

Flare abundance analysis has shown that the main seepage area in the "Entenschnabel" is located close to salt diapir Berta. In total, 104 flares (out of 166 flares classified as certain) were detected in this area covering about 8.4 km^2. The flare distribution shows that gas seepage is not homogeneous across the area, but is concentrated in specific areas. Most prominent is a flare cluster comprising more than half of all detected flares (66 flares) in a small area of about 300 × 100 m (**Figure 10**). All flares are located above or in the vicinity (with a maximum distance of 1.3 km) of the subsurface salt diapir. The top of the salt diapir is located in approximately 2,000 mbsf (Müller et al., 2018). Whereas 20 flares are located directly above the salt diapir, the flare cluster is about 150 to 450 m northeast of the diapir outline.

Seismic interpretation including bright spots, faults and gas chimneys [depicted from Figure 7 in Müller et al. (2018)] reveal good correlation to flare locations mapped in this study (**Figure 10**). Except for one flare, all flares are located in the area underlain by seismically detected stacked bright spots. Eight flares align along the fault plane intersection with the seafloor. Müller et al. (2018) described that the horizons above the salt diapir intersect with a NW-SE striking normal fault. In addition, increased amplitudes at the flank of the fault and at the uppermost reflections above the fault indicated gas migration from the fault toward the seafloor. The flare cluster and 15 other flares (80% of all flares at Berta) plot in the area interpreted by Müller et al. (2018) as a gas chimney, which is indicated by discontinuous low amplitude reflections from the top of the salt diapir to the center of the bright spots. Hence, seepage found at Berta appears mainly focused through naturally evolved pathways related to salt diapirism.

CONCLUSION AND OUTLOOK

Our results show that methane seepage is not uncommon in the German "Entenschnabel" region in the North Sea. An extensive mapping campaign has proven the presence of at least 166 flares. As flares were not observed closer than 125 m to a well site, we conclude that the seepage is focused on naturally evolved pathways related to salt diapirism rather than drill holes and related mechanical sediment disruption. The majority of flares were located at salt diapir Berta, which is characterized by subsurface gas indications such as acoustic blanking, high amplitude reflectors, and sediment electric conductivity anomalies. Geochemical analyses of water samples suggest a shallow, microbial origin of the gas. However, additional

deep subsurface imaging is needed to interpret the relation between salt diapirism and seepage into the water column. Our hydroacoustic flare observations imaged gas bubbles rising close to the sea surface and methane concentrations in surface waters were slightly elevated, both suggesting that gas bubbles might be a pathway to transport fractions of methane from the seafloor to the atmosphere.

Based on this study, we suggest to further characterize the nature of the active gas system in the German North Sea including the quantity of emitted methane, the gas source and address the following questions:

1. How much methane is released in form of gas bubbles and dissolved in pore water from the seafloor? Although our study did not systematically investigate the temporal variability, first results do indicate that flares are not stable over times of hours and days. Better understanding this variability and the controlling factors would be crucial to evaluate the gas quantities released.
2. Are the depressions detected at salt diapir Britta formed by fluid release? Are they related to the drilling activities at this site?
3 What is the origin of the methane emissions detected? If related to subsurface gas accumulations above salt diapirs, why is seepage mainly focused on salt diapir Berta?
4. Does methane released from the seafloor in the "Entenschnabel" reach the sea-air interface and contribute to the atmospheric inventory?
5. Is the Schillgrund Fault providing efficient fluid migration pathways

A better knowledge about shallow seep systems along continental shelf margins would be needed to evaluate the importance for gas exchange and fluid fluxes from the seafloor into the water column and eventually into the atmosphere.

DATA AVAILABILITY STATEMENT

The datasets analyzed for this study can be found in the Open Access library PANGAEA (https://www.pangaea.de/). Data associated with the article: Ship's track HE537: https://doi.pangaea.de/10.1594/PANGAEA.905303. Station list HE537: https://doi.pangaea.de/10.1594/PANGAEA.905303. Sediment echosounder data: https://doi.pangaea.de/10.1594/PANGAEA.910739. Multibeam echosounder data: https://doi.pangaea.de/10.1594/PANGAEA.912849. CTD hydrocast data: https://doi.pangaea.de/10.1594/PANGAEA.907544. METS data: https://doi.pangaea.de/10.1594/PANGAEA.915769, https://doi.pangaea.de/10.1594/PANGAEA.915770, https://doi.pangaea.de/10.1594/PANGAEA.915771, https://doi.pangaea.de/10.1594/PANGAEA.915772, https://doi.pangaea.de/10.1594/PANGAEA.915773, https://doi.pangaea.de/10.1594/PANGAEA.915774, https://doi.pangaea.de/10.1594/PANGAEA.915775, https://doi.pangaea.de/10.1594/PANGAEA.915776, https://doi.pangaea.de/10.1594/PANGAEA.915777, https://doi.pangaea.de/10.1594/PANGAEA.915778, and https://doi.pangaea.de/10.1594/PANGAEA.915779. Electromagnetic data: https://doi.pangaea.de/10.1594/PANGAEA.915602, https://doi.pangaea.de/10.1594/PANGAEA.915605, and https://doi.pangaea.de/10.1594/PANGAEA.915610.

AUTHOR CONTRIBUTIONS

KS provided funding acquisition as well as cruise preparation and management for R/V Heincke cruise HE537. MR, SM, and UB carried out on board hydroacoustic data collection. MR took care about the hydroacoustic data processing, curation, and archiving. MB, SS, and KH acquired sediment and water sampling. MB and SS conducted gas analysis. KH collected, processed, and archived the hydrological data. KH, MB, HM, and MR interpreted the METS data. HM, CH, and KS conducted, processed, and interpreted electromagnetic measurements. MR, MB, HM, KH, SS, and KS contributed to the interpretation of the results. MR took the lead in writing the manuscript. All authors helped shape the research, analysis and manuscript.

FUNDING

This study was funded through the Cluster of Excellence "The Ocean Floor – Earth's Uncharted Interface." Open access publication fees are funded by the University of Bremen. Grant GPF 18-2_18 MESSAGER ship time R/V Heincke.

ACKNOWLEDGMENTS

We greatly appreciate the shipboard support from the masters and crew of R/V Heincke cruise HE537 and the Leitstelle Deutsche Forschungsschiffe as well as the Gutachterpanel Forschungsschiffe for support to realize the cruise. We kindly acknowledge help onboard by Christian Seeger, Dennis Hagedorn, and Konstantin Reeck, and laboratory support by Daniela Graskamp and Dietmar Laszinski. We would also like to thank four reviewers for their constructive suggestions that helped to improve and strengthen our manuscript.

SUPPLEMENTARY MATERIAL

The Supplementary Material for this article can be found online at: https://www.frontiersin.org/articles/10.3389/feart.2021.556329/full#supplementary-material

Supplementary Figure 1 | Survey and sampling strategy conducted during RV HEINCKE cruise HE537 exemplified at well B15–2. The area at and around the well was covered with eleven parallel transect lines and a line spacing of about 50 m for hydroacoustic mapping including water column recording. A MIC station for bottom water sampling was taken close to the well site, whereas CTD stations have been conducted around the well site with distances between 10 and 30 m. The METS sensor was towed close to the seafloor in a star-like pattern crossing the well site four times.

Supplementary Figure 2 | Map of the study area illustrating measured methane concentrations above the pycnocline. Methane concentrations increase from the SE to the NW.

Supplementary Table 1 | List of all flare detections during R/V Heincke cruise HE537 in the "Entenschnabel" area. Date, time, geographical position, and

seafloor depth of findings are provided as well as a classification (in certain or uncertain) and the near distance calculation to salt diapirs, seismic bright spots, and abandoned wells.

Supplementary Table 2 | List of CTD and MIC stations taken during R/V Heincke cruise HE537, including geographic position, area name and measured methane and ethane concentrations in the water samples taken. bdl: below detection limit.

REFERENCES

Archie, G. E. (1942). The electrical resistivity log as an aid in determining some reservoir characteristics. *J. Pet. Technol.* 146, 54–62. doi: 10.2118/942054-g

Arfai, J., Jahne, F., Lutz, R., Franke, D., Gaedicke, C., and Kley, J. (2014). Late palaeozoic to early cenozoic geological evolution of the northwestern German North Sea (Entenschnabel): new results and insights. *Netherlands J. Geosci.* 93, 147–174. doi: 10.1017/njg.2014.22

Attias, E., Amalokwu, K., Watts, M., Falcon-Suarez, I. H., North, L., Hu, G. W., et al. (2020). Gas hydrate quantification at a pockmark offshore Norway from joint effective medium modelling of resistivity and seismic velocity. *Mar. Pet. Geol.* 113:104151. doi: 10.1016/j.marpetgeo.2019.104151

Baasch, B., Müller, H., Dobeneck, T. V., and Oberl, F. K. J. (2017). Determination of grain-size characteristics from electromagnetic seabed mapping data: a NW Iberian shelf study. *Cont. Shelf Res.* 140, 75–83. doi: 10.1016/j.csr.2017.04.005

Boles, J. R., Clark, J. F., Leifer, I., and Washburn, L. (2001). Temporal variation in natural methane seep rate due to tides, Coal Oil Point area, California. *J. Geophys. Res.* 106, 27077–27086. doi: 10.1029/2000jc000774

Boothroyd, I. M., Almond, S., Qassim, S. M., Worrall, F., and Davies, R. J. (2016). Fugitive emissions of methane from abandoned, decommissioned oil and gas wells. *Sci. Total Environ.* 547, 461–469. doi: 10.1016/j.scitotenv.2015.12.096

Böttner, C., Berndt, C., Reinardy, B. T. I., Geersen, J., Karstens, J., Bull, J. M., et al. (2019). Pockmarks in the witch ground basin, central North Sea. *Geochem. Geophys. Geosyst.* 20, 1698–1719. doi: 10.1029/2018gc008068

Böttner, C., Haeckel, M., Schmidt, M., Berndt, C., Vielstädte, L., Kutsch, J. A., et al. (2020). Greenhouse gas emissions from marine decommissioned hydrocarbon wells: leakage detection, monitoring and mitigation strategies. *Int. J. Greenh. Gas Control* 100:103119. doi: 10.1016/j.ijggc.2020.103119

Caress, D. W., and Chayes, D. N. (2017). *MB-System: Mapping the Seafloor*. Available online at: https://www.mbari.org/products/research-software/mb-system (accessed July 1, 2019).

Cheesman, S. J., Law, L. K., and Louis, B. S. (1993). A porosity mapping survey in hecate strait using a seafloor electro-magnetic profiling system. *Mar. Geol.* 110, 245–256. doi: 10.1016/0025-3227(93)90087-c

Davison, I., Alsop, I., Birch, P., Elders, C., Evans, N., Nicholson, H., et al. (2000). Geometry and late-stage structural evolution of central Graben salt diapirs, North Sea. *Mar. Pet. Geol.* 17, 499–522. doi: 10.1016/s0264-8172(99)00068-9

Dick, S., Kleine, E., and Müller-Navarra, S. H. (2001). "The operational circulation model of BSH (BSH cmod). model description and validation," in *Berichte des Bundesamtes für Seeschifffahrt und Hydrographie. 29/2001, 48* (Hamburg, Germany: Bundesamtes für Seeschifffahrt und Hydrographie).

Duffy, O. B., Gawthorpe, R. L., Docherty, M., and Brocklehurst, S. H. (2013). Mobile evaporite controls on the structural style and evolution of rift basins: danish central Graben, North Sea. *Basin Res.* 25, 310–330. doi: 10.1111/bre.12000

Dupré, S., Scalabrin, C., Grall, C., Augustin, J.-M., Henry, P., Şengör, A. M. C., et al. (2015). Tectonic and sedimentary controls on widespread gas emissions in the Sea of Marmara: results from systematic, shipborne multibeam echo sounder water column imaging. *J. Geophys. Res. Solid Earth Res.* 120, 2891–2912. doi: 10.1002/2014jb011617

Evans, R. L., Law, L. K., St. Louis, B., Cheesman, S., and Sananikone, K. (1999). The shallow porosity structure of the Eel shelf, northern California: results of a towed electromagnetic survey. *Mar. Geol.* 154, 211–226. doi: 10.1016/s0025-3227(98)00114-5

Fechner-Levy, E. J., and Hemond, H. F. (1996). Trapped methane volume and potential effects on methane ebullition in a northern peatland. *Limnol. Oceanogr.* 41, 1375–1383. doi: 10.4319/lo.1996.41.7.1375

Flanders Marine and Institute (2019). *Maritime Boundaries Geodatabase: Maritime Boundaries and Exclusive Economic Zones (200NM), version 11*.

Garcia, X., Monteys, X., Evans, R. L., and Szpak, M. (2014). Constraints on a shallow offshore gas environment determined by a multidisciplinary geophysical approach: the Malin Sea, NW Ireland. *Geochem. Geophys. Geosyst.* 15, 867–885. doi: 10.1002/2013gc005108

Hovland, M. (1993). Submarine gas seepage in the North Sea and adjacent areas. *Pet. Geol. Conf. Proc.* 4, 1333–1338. doi: 10.1144/0041333

Hovland, M. (2007). Discovery of prolific natural methane seeps at Gullfaks, northern North Sea. *Geo Mar. Lett.* 27, 197–201. doi: 10.1007/s00367-007-0070-6

Hovland, M., and Judd, A. G. (1988). *Seabed Pockmarks and Seepages*. London: Graham and Trotman.

Hovland, M., Svensen, H., Forsberg, C. F., Johansen, H., Fichler, C., Fosså, J. H., et al. (2005). Complex pockmarks with carbonate-ridges off mid-Norway: products of sediment degassing. *Mar. Geol.* 218, 191–206. doi: 10.1016/j.margeo.2005.04.005

Jackson, M. P. A., and Hudec, M. R. (2017). *Salt Tectonics: Principles and Practice*. Cambridge: Cambridge University Press.

Jackson, P. D., Taylor Smith, D., and Stanford, P. N. (1978). Resistivity-porosity-particle shape relationships for marine sands. *Geophysics* 43, 1250–1268. doi: 10.1190/1.1440891

Jin, Y. K., Kim, Y., Baranov, B., Shoji, H., and Obzhirov, A. (2011). Distribution and expression of gas seeps in a gas hydrate province of the northeastern Sakhalin continental slope, sea of Okhotsk. *Mar. Pet. Geol.* 28, 1844–1855. doi: 10.1016/j.marpetgeo.2011.03.007

Judd, A. (2015). The significance of the 22/4b blow-out site methane emissions in the context of the North Sea. *Mar. Pet. Geol.* 68, 836–847. doi: 10.1016/j.marpetgeo.2015.07.031

Judd, A., and Hovland, M. (2007). *Seabed Fluid Flow. The Impact on Geology, Biology and the Marine Environment*. Cambridge: Cambridge University Press, 475.

Judd, A., Long, D., and Sankey, M. (1994). Pockmark formation and activity, UK block 15/25, North Sea. *Bull. Geol. Soc. Denmark* 41, 34–49.

Kang, M., Kanno, C. M., Reid, M. C., Zhang, X., Mauzerall, D. L., Celia, M. A., et al. (2014). Direct measurements of methane emissions from abandoned oil and gas wells in Pennsylvania. *Proc. Natl. Acad. Sci. U. S. A.* 111, 18173–18177. doi: 10.1073/pnas.1408315111

Kannberg, P. K., Tréhu, A. M., Pierce, S. D., Paull, C. K., and Caress, D. W. (2013). Temporal variation of methane flares in the ocean above Hydrate Ridge, Oregon. *Earth Planet. Sci. Lett.* 368, 33–42. doi: 10.1016/j.epsl.2013.02.030

Krämer, K., Holler, P., Herbst, G., Bratek, A., Ahmerkamp, S., Neumann, A., et al. (2017). Abrupt emergence of a large pockmark field in the German bight, southeastern North Sea. *Sci. Rep.* 7:5150.

Landrø, M., Wehner, D., Vedvik, N., Ringrose, P., Løhre, N. L., and Berteussen, K. (2019). Gas flow through shallow sediments—a case study using passive and active seismic field data. *Int. J. Greenh. Gas Control* 87, 121–133. doi: 10.1016/j.ijggc.2019.05.001

Laurer, W. U., Naumann, M., and Zeiler, M. (2012). *Erstellung der Karte zur Sedimentverteilung auf dem Meeresboden in der deutschen Nordsee nach der Klassifikation von Figge (1981). Geopotenzial Deutsche Nordsee, Hannover/Hamburg, 19 S.* Available online at: https://www.gpdn.de/gpdn/wilma.aspx?pgId=337&WilmaLogonActionBehavior=Default (accessed April 14, 2020).

Leifer, I. (2015). Seabed bubble flux estimation by calibrated video survey for a large blowout seep in the North Sea. *Mar. Pet. Geol.* 68, 743–752. doi: 10.1016/j.marpetgeo.2015.08.032

Leifer, I., and Boles, J. (2005). Turbine tent measurements of marine hydrocarbon seeps on subhourly timescales. *J. Geophys. Res. Oceans* 110, 1–12. doi: 10.1007/978-3-030-34827-4_1

Leifer, I., and Judd, A. (2015). The UK22/4b blowout 20 years on: investigations of continuing methane emissions from sub-seabed to the atmosphere in a North Sea context. *Mar. Pet. Geol.* 68, 706–717. doi: 10.1016/j.marpetgeo.2015.11.012

Leifer, I., and Patro, R. K. (2002). The bubble mechanism for methane transport from the shallow sea bed to the surface: a review and sensitivity study. *Cont. Shelf Res.* 22, 2409–2428. doi: 10.1016/s0278-4343(02)00065-1

Ligtenberg, H., and Connolly, D. (2003). Chimney detection and interpretation, revealing sealing quality of faults, geohazards, charge of and leakage from reservoirs. *J. Geochem. Explor.* 78–79, 385–387. doi: 10.1016/s0375-6742(03)00095-5

Littke, R., Bayer, U., Gajewski, D., and Nelskamp, S. (2008). *Dynamics of Complex Intracontinental Basins: The Central European Basin System*. Berlin: Springer.

Lutz, R., Kalka, S., Gaedicke, C., Reinhardt, L., and Winsemann, J. (2009). Pleistocene tunnel valleys in the German North Sea: spatial distribution and morphology. *Zeitschrift der Deutschen Gesellschaft für Geowissenschaften* 160, 225–235. doi: 10.1127/1860-1804/2009/0160-0225

Mau, S., Gentz, T., Körber, J. H., Torres, M. E., Römer, M., Sahling, H., et al. (2015). Seasonal methane accumulation and release from a gas emission site in the central North Sea. *Biogeosciences* 12, 5261–5276. doi: 10.5194/bg-12-5261-2015

Müller, H., Von Dobeneck, T., Hilgenfeldt, C., SanFilipo, B., Rey, D., and Rubio, B. (2012). Mapping the magnetic susceptibility and electric conductivity of marine surficial sediments by benthic EM profiling. *Geophysics* 77, 1JF–Z19.

Müller, H., von Dobeneck, T., Nehmiz, W., and Hamer, K. (2011). Near-surface electromagnetic, rock magnetic, and geochemical fingerprinting of submarine freshwater seepage at Eckernförde Bay (SW Baltic Sea). *Geo Mar. Lett.* 31, 123–140. doi: 10.1007/s00367-010-0220-0

Müller, S., Reinhardt, L., Franke, D., Gaedicke, C., and Winsemann, J. (2018). Shallow gas accumulations in the German North Sea. *Mar. Pet. Geol.* 91, 139–151. doi: 10.1016/j.marpetgeo.2017.12.016

Niemann, H., Elvert, M., Hovland, M., Orcutt, B., Judd, A., Suck, I., et al. (2005). Methane emission and consumption at a North Sea gas seep (Tommeliten area). *Biogeosciences* 2, 335–351. doi: 10.5194/bg-2-335-2005

Pletsch, T., Appel, J., Botor, D., Clayton, C. J., Duin, E. J. T., Faber, E., et al. (2010). *Petroleum Geological Atlas of the Southern Permian Basin Area*. Houten: EAGE Publications.

Rehder, G., Keir, R. S., Suess, E., and Pohlmann, T. (1998). The multiple sources and patterns of methane in North Sea waters. *Aquat. Geochem.* 4, 403–427.

Rehder, G., Keir, R. S., Suess, E., and Rhein, M. (1999). Methane in the northern Atlantic controlled by microbial oxidation and atmospheric history. *Geophys. Res. Lett.* 26, 587–590. doi: 10.1029/1999gl900049

Riboulot, V., Cattaneo, A., Scalabrin, C., Gaillot, A., Jouet, G., Ballas, G., et al. (2017). Control of the geomorphology and gas hydrate extent on widespread gas emissions offshore Romania. *Bull. Soc. Geol. Fr.* 188, 12–26.

Römer, M., Riedel, M., Scherwath, M., Heesemann, M., and Spence, G. D. (2016). Tidally controlled gas bubble emissions: a comprehensive study using long-termmonitoring data from the NEPTUNE cabled observatory offshore Vancouver Island. *Geochem. Geophys. Geosyst.* 17, 1312–1338.

Römer, M., Wenau, S., Bohrmann, G., Mau, S., Veloso, M., Greinert, J., et al. (2017). Assessing marine gas emission activity and contribution to the atmospheric methane inventory: a multidisciplinary approach from the Dutch Dogger Bank seep area (North Sea). *Geochem. Geophys. Geosyst.* 18, 2617–2633. doi: 10.1002/2017gc006995

Scandella, B. P., Varadharajan, C., Hemond, H. F., Ruppel, C., and Juanes, R. (2011). A conduit dilation model of methane venting from lake sediments. *Geophys. Res. Lett.* 38, 1–6.

Schloemer, S., Oest, J., Illing, C. J., Elbracht, J., and Blumenberg, M. (2018). Spatial distribution and temporal variation of methane, ethane and propane background levels in shallow aquifers – a case study from Lower Saxony (Germany). *J. Hydrol. Reg. Stud.* 19, 57–79. doi: 10.1016/j.ejrh.2018.07.002

Schmale, O., Schneider, von Deimling, J., Gülzow, W., Nausch, G., Waniek, J. J., et al. (2010). Distribution of methane in the water column of the Baltic Sea. *Geophys. Res. Lett.* 37:L12604.

Schneider Von, Deimling, J., Brockhoff, J., and Greinert, J. (2007). Flare imaging with multibeam systems: data processing for bubble detection at seeps. *Geochem. Geophys. Geosyst.* 8, 1–7. doi: 10.1109/joe.2021.3056910

Schneider Von, Deimling, J., Rehder, G., Greinert, J., Mcginnnis, D. F., Boetius, A., et al. (2011). Quantification of seep-related methane gas emissions at Tommeliten. North Sea. *Cont. Shelf Res.* 31, 867–878. doi: 10.1016/j.csr.2011.02.012

Schout, G., Griffioen, J., Hassanizadeh, S. M., Cardon, de Lichtbuer, G., and Hartog, N. (2019). Occurrence and fate of methane leakage from cut and buried abandoned gas wells in the Netherlands. *Sci. Total Environ.* 659, 773–782. doi: 10.1016/j.scitotenv.2018.12.339

Schroot, B. M., Klaver, G. T., and Schüttenhelm, R. T. E. (2005). Surface and subsurface expressions of gas seepage to the seabed - examples from the Southern North Sea. *Mar. Pet. Geol.* 22, 499–515. doi: 10.1016/j.marpetgeo.2004.08.007

Schroot, B. M., and Schüttenhelm, R. T. E. (2003). Expressions of shallow gas in the Netherlands North Sea. *Netherlands J. Geosci.* 82, 91–105. doi: 10.1017/s0016774600022812

Schwalenberg, K., Gehrmann, R. A. S., Bialas, J., and Rippe, D. (2020). Analysis of marine controlled source electromagnetic data for the assessment of gas hydrates in the Danube deep-sea fan, Black Sea. *Mar. Pet. Geol.* 120. doi: 10.1016/j.marpetgeo.2020.104650

Schwalenberg, K., Rippe, D., Koch, S., and Scholl, C. (2017). Marine-controlled source electromagnetic study of methane seeps and gas hydrates at opouawe bank, hikurangi margin, New Zealand. *J. Geophys. Res. Solid Earth* 122, 3334–3350. doi: 10.1002/2016jb013702

Sommer, S., Schmidt, M., and Linke, P. (2015). Continuous inline mapping of a dissolved methane plume at a blowout site in the central North Sea UK using a membrane inlet mass spectrometer – water column stratification impedes immediate methane release into the atmosphere. *Mar. Pet. Geol.* 68, 766–775. doi: 10.1016/j.marpetgeo.2015.08.020

Szpak, M. T., Monteys, X., O'Reilly, S., Simpson, A. J., Garcia, X., Evans, R. L., et al. (2012). Geophysical and geochemical survey of a large marine pockmark on the Malin Shelf, Ireland. *Geochem. Geophys. Geosyst.* 13:Q01011.

Ten Veen, J. H., Van Gessel, S. F., and Den Dulk, M. (2012). Thin- and thick-skinned salt tectonics in the Netherlands; a quantitative approach. *Netherlands J. Geosci.* 91, 447–464. doi: 10.1017/s0016774600000330

Thatje, S., Gerdes, D., and Rachor, E. (1999). A seafloor crater in the German bight and its effects on the benthos. *Helgol. Mar. Res.* 53, 36–44. doi: 10.1007/pl00012136

Torres, M. E., Mcmanus, J., Hammond, D. E., Angelis, M. A., De, Heeschen, K. U., et al. (2002). Fluid and chemical fuxes in and out of sediments hosting methane hydrate deposits on Hydrate Ridge, or, i?: hydrological provinces. *Earth Planet. Sci. Lett.* 201, 525–540. doi: 10.1016/s0012-821x(02)00733-1

Townsend-Small, A., Ferrara, T. W., Lyon, D. R., Fries, A. E., and Lamb, B. K. (2016). Emissions of coalbed and natural gas methane from abandoned oil and gas wells in the United States. *Geophys. Res. Lett.* 43, 2283–2290. doi: 10.1002/2015gl067623

Tryon, M. D., Brown, K. M., Torres, M. E., Tréhu, A. M., McManus, J., and Collier, R. W. (1999). Measurements of transience and downward fluid flow near episodic methane gas vents, hydrate ridge, cascadia. *Geology* 27, 1075–1078. doi: 10.1130/0091-7613(1999)027<1075:motadf>2.3.co;2

Varadharajan, C., and Hemond, H. F. (2012). Time-series analysis of high-resolution ebullition fluxes from a stratified, freshwater lake. *J. Geophys. Res. Biogeosci.* 117, 1–15. doi: 10.15504/fmj.2016.18

Vielstädte, L., Haeckel, M., Karstens, J., Linke, P., Schmidt, M., Steinle, L., et al. (2017). Shallow gas migration along hydrocarbon wells-an unconsidered, anthropogenic source of biogenic methane in the North Sea. *Environ. Sci. Technol.* 51, 10262–10268. doi: 10.1021/acs.est.7b02732

Vielstädte, L., Karstens, J., Haeckel, M., Schmidt, M., Linke, P., Reimann, S., et al. (2015). Quantification of methane emissions at abandoned gas wells in the central North Sea. *Mar. Pet. Geol.* 68, 848–860. doi: 10.1016/j.marpetgeo.2015.07.030

White, J. E. (1975). Computed seismic speeds and attenuation in rocks with partial gas saturation. *Geophysics* 40, 224–232. doi: 10.1190/1.1440520

Wiesenberg, D. A., and Guinasso, N. L. (1979). Equilibrium solubilities of methane, carbonmonoxide and hydrogen in water and seawater. *J. Chem. Eng. Data* 24, 356–360. doi: 10.1021/je60083a006

Winsauer, W. O., Shearin, H. M., Masson, P. H., and Williams, M. (1952). Resistivity of brine saturated sands in relation to pore geometry. *Am. Assoc. Pet. Geol. Bull.* 36, 253–277.

Woodbury, H. O., Murray, I. B., and Osborne, R. E. (1980). "Diapirs and their relation to hydrocarbon accumulation," in: *Facts and Principles of World Petroleum Occurrence*, ed. A.D. Miall. Calgary: Canadian Society of Petroleum Geologists

Wong, D. A. (2007). "Jurassic," in *Geology of the Netherlands. Royal Netherlands Academy of Arts and Sciences*, eds T. E. Wong, D. A. J. Batjes, and J. De Jager (Amsterdam: Elsevier), 107–125.

Conflict of Interest: The authors declare that the research was conducted in the absence of any commercial or financial relationships that could be construed as a potential conflict of interest.

The reviewer, KM, declared a shared affiliation, with one author, KH, to the handling editor at time of review.

The reviewer, MS, declared a past co-authorship with one of the authors, MR, to the handling editor.

frontiers in Earth Science

ORIGINAL RESEARCH
published: 11 May 2021
doi: 10.3389/feart.2021.601019

Using a Ladder of Seeps With Computer Decision Processes to Explore for and Evaluate Cold Seeps on the Costa Rica Active Margin

Peter Vrolijk[1,2], Lori Summa[1,3], Benjamin Ayton[1,4], Paraskevi Nomikou[5], Andre Hüpers[6], Frank Kinnaman[7], Sean Sylva[1], David Valentine[7] and Richard Camilli[1]*

[1]Applied Ocean Science and Engineering, Woods Hole Oceanographic Institution, Woods Hole, MA, United States, [2]Earth and Environmental Science Department, New Mexico Institute of Mining and Technology, Socorro, NM, United States, [3]Department of Earth, Environmental, and Planetary Sciences, Rice University, Houston, TX, United States, [4]Computer Science and Artificial Intelligence Laboratory, Massachusetts Institute of Technology, Cambridge, MA, United States, [5]Department of Geology and Geoenvironment, National and Kapodistrian University of Athens, Athens, Greece, [6]MARUM - Center for Marine Environmental Sciences, University Bremen, Bremen, Germany, [7]Department of Earth Science, University of California Santa Barbara, Santa Barbara, CA, United States

OPEN ACCESS

Edited by:
Martin Scherwath,
University of Victoria, Canada

Reviewed by:
Mario Veloso,
GEOMAR Helmholtz Center for Ocean Research Kiel, Germany
Pengfei Di,
Chinese Academy of Sciences, China

***Correspondence:**
Peter Vrolijk
dimeguru@gmail.com

Specialty section:
This article was submitted to Environmental Informatics and Remote Sensing, a section of the journal Frontiers in Earth Science

Received: *31 August 2020*
Accepted: *18 February 2021*
Published: *11 May 2021*

Citation:
Vrolijk P, Summa L, Ayton B, Nomikou P, Hüpers A, Kinnaman F, Sylva S, Valentine D and Camilli R (2021) Using a Ladder of Seeps With Computer Decision Processes to Explore for and Evaluate Cold Seeps on the Costa Rica Active Margin. Front. Earth Sci. 9:601019. doi: 10.3389/feart.2021.601019

Natural seeps occur at the seafloor as loci of fluid flow where the flux of chemical compounds into the ocean supports unique biologic communities and provides access to proxy samples of deep subsurface processes. Cold seeps accomplish this with minimal heat flux. While individual expertize is applied to locate seeps, such knowledge is nowhere consolidated in the literature, nor are there explicit approaches for identifying specific seep types to address discrete scientific questions. Moreover, autonomous exploration for seeps lacks any clear framework for efficient seep identification and classification. To address these shortcomings, we developed a Ladder of Seeps applied within new decision-assistance algorithms (Spock) to assist in seep exploration on the Costa Rica margin during the *R/V* Falkor 181210 cruise in December, 2018. This Ladder of Seeps [derived from analogous astrobiology criteria proposed by Neveu et al. (2018)] was used to help guide human and computer decision processes for ROV mission planning. The Ladder of Seeps provides a methodical query structure to identify what information is required to confirm a seep either: 1) supports seafloor life under extreme conditions, 2) supports that community with active seepage (possible fluid sample), or 3) taps fluids that reflect deep, subsurface geologic processes, but the top rung may be modified to address other scientific questions. Moreover, this framework allows us to identify higher likelihood seep targets based on existing incomplete or easily acquired data, including MBES (Multi-beam echo sounder) water column data. The Ladder of Seeps framework is based on information about the instruments used to collect seep information (e.g., are seeps detectable by the instrument with little chance of false positives?) and contextual criteria about the environment in which the data are collected (e.g., temporal variability of seep flux). Finally, the assembled data are considered in light of a Last-Resort interpretation, which is only satisfied once all other plausible data interpretations are excluded by observation. When coupled with decision-making algorithms that incorporate expert opinion with data acquired during the Costa Rica experiment, the

Ladder of Seeps proved useful for identifying seeps with deep-sourced fluids, as evidenced by results of geochemistry analyses performed following the expedition.

Keywords: seep, autonomous exploration, Costa Rica, geochemistry, water column data, temporal variability, decision-making algorithm

INTRODUCTION

Seeps occur throughout the world along active and passive continental margins (e.g., Campbell et al., 2002), but their occurrence is rare and their distribution uneven. Comprehensive surveys do exist (e.g., Judd and Hovland, 2009; Skarke et al., 2014; Weber et al., 2014) but even they cover only a small fraction of the world's oceans. A complete description of Earth's cold seeps and their variability has yet to be attempted.

Seeps have been studied for decades as an important window into subsurface fluid processes. They occur in a range of geologic settings and exhibit a variety of fluid expulsion mechanisms that emanate from fluid sources 10 s to 1000 s of meters below the seafloor (e.g. Suess, 2018). They display a broad range of morphological characteristics at the seafloor, including convex, mound-shaped features associated with seep-related carbonates, concave pockmarks or collapse features, and mud volcanoes, ranging from less than a meter to several kilometers in diameter (e.g. Judd and Hovland, 2009). Different types of seeps support unique ecological niches (e.g., Sibuet and Olu, 1998; Sahling et al., 2003; Levin, 2005), allow scientists to track the release of greenhouse gases (e.g., methane and to a lesser extent carbon dioxide) from the Earth into the ocean/atmosphere (Judd, 2004; Leifer et al., 2006), and provide locations where deep-sourced fluids are sampled and analyzed (Kastner et al., 1991; Barnes et al., 2010). In this paper we emphasize the search for seeps that reflect a fluid migration pathway for fluids that may be affected by fluid-rock interactions at the subduction zone plate interface. Information about mineral reactions and corresponding fluid-rock interactions at the plate interface is useful for understanding earthquake and seismogenic processes (Peacock, 1990; Moore and Vrolijk, 1992), but the proposed methods apply to problems as far-reaching as ocean exploration on outer solar system worlds (e.g., Hand and German, 2018).

The search for seeps with deep-sourced fluids is challenging. Large areas of the seafloor must be surveyed at significant expense, yielding incomplete information (e.g. Judd and Hovland, 2009; Skarke et al., 2014; Weber et al., 2014). Geophysical tools used for the surveys are evolving rapidly, and as such, may have variable acquisition and processing approaches (e.g. Mitchell et al., 2018). Once seeps are found, sample collection and return programs for seep analysis are technologically difficult, expensive, and time-consuming (e.g., IODP scientific ocean drilling), similar to space exploration analogs (e.g. Perserverence and OSIRIS REx). To help address these issues, a flexible method is required that allows for the use of tools available on any particular day and the specific scientific objectives of the research. The optimal tools and datasets for one expedition may differ from those used on another.

To develop this methodology, we posed the problem of identifying seeps with deep-sourced fluids on the Costa Rica accretionary prism using limited, preliminary data collected above the seafloor. The methodology applied serves as a tool to assist scientists in the decision-making process for finding seeps in an objective and reproducible manner. Our approach is intended to improve the success of drilling programs, for example, and can be extended to alternative scientific objectives, like the discovery and characterization of subsea chemolithoautotrophic oases, oases with specific organisms (e.g., microbial mats), or comprehensive seep flux syntheses. Moreover, this methodology can be used in concert with autonomous vehicles that require a cognitive basis to recognize and identify potential targets and make autonomous decisions to deviate from a programmed path, linger at a site, and collect additional information to evaluate more fully.

Our approach comprises two crucial elements: a Ladder of Seeps and a Spock decision-assistance algorithm. The Ladder of Seeps is a rigorous framework of measurements and observations that make ship-based investigations more efficient and successful and guide autonomous vehicle exploration. In this study, the Ladder of Seeps guides a survey from the lower rung of a ladder with uncertain information about the presence of seeps, to the top rung of a ladder that identifies seeps with deep-sourced fluids derived from the subduction plate interface. Our approach is adapted from the astrobiology community (Neveu et al., 2018) and a Ladder of Life where autonomous space exploration vehicles search for evidence of life on extraterrestrial bodies. The Ladder of Life is an explicit application of the Scientific Method in that it addresses the extent to which any particular analysis addresses the goal (i.e. presence of life), evaluates information about the instruments used to make measurements (e.g., sensitivity and detectability of the sought-for signal and the chance for a false positive), and considers contextual criteria that places any measurement in the context of the feature being analyzed (how difficult is the feature to analyze, and what is the chance of a false negative?). The top ladder rung (presence of life) is only achieved as the interpretation of last resort, or when the collection of analyses has successfully ruled out any plausible competing hypotheses.

The second crucial element uses decision-making algorithms that incorporate expert opinion with knowledge gained from data collected during a cruise (e.g., machine learning) and produce an objective and reproducible record of every site-selection decision. Modern decision-making algorithms build on early Expert Systems developed to guide complex decision-making in the

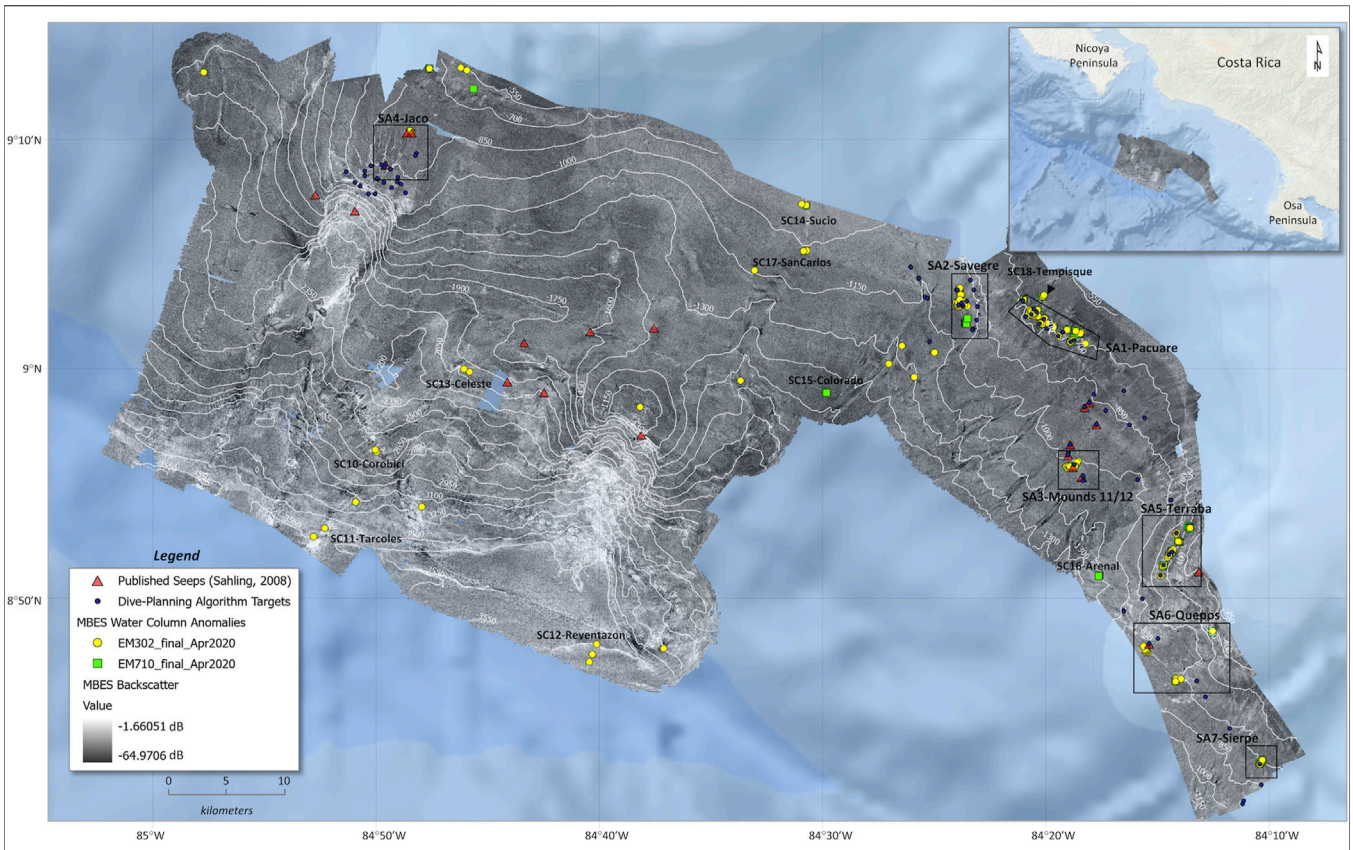

FIGURE 1 | Multibeam backscatter and bathymetry contours (meters) of full study area. Map records MBES water column anomalies identified in this study, previously published seep locations (Sahling et al., 2008), and targets identified by Spock for investigation during the expedition. Map shows uneven distribution of water-column anomalies with depth as well as tendency to occur in clusters. Many anomalies found in areas of previously identified seeps, but new locations of seepage are also observed. Seep Clusters (SC) and Arrays (SA), defined to reflect hierarchy in organization of seep features, are labeled with Costa Rican river names for purposes of communication.

geosciences (Nikolopoulos, 1997), including identifying organic molecules (Lindsay et al., 1993) and assessing whether a prospect site is likely to contain a specified ore type (Gaschnig, 1982). Unlike modern machine learning techniques, Expert Systems hard-coded geophysical or chemical knowledge through the application of a complex system of rigid rules. As a result, they tended to be difficult to extend and are brittle, with poor performance when observations failed to match their assumptions. In contrast, model-based approaches developed and applied here encode expert knowledge as "priors" with any degree of certainty, and adapt their parameters dynamically in response to data specific to the domain of interest. Experts may encode some strong priors to enforce certain relationships between observations and seepage, while allowing the algorithm to learn others. The model is chosen to allow for rapid learning and inference but remains expressive, is flexible, and seeks observations to improve its parameterization so that it becomes specialized to a local problem as new data are collected. Furthermore, the model allows previously excluded features to be added with few structural changes, so that it can be used with data outside of its original design (e.g., emerging new technologies).

The Ladder of Seeps framework implemented in decision-making algorithms seeks to improve scientific success at a lower cost. Cost arises in many forms on a research vessel: financial costs (day rate), time costs (e.g., planning missions and searching for individual seeps), risk of failure to achieve scientific objectives (e.g., missed opportunities), risk of device failure (e.g., loss of an autonomous vehicle), and energy budgets (autonomous devices). Our approach is intended to apply scarce resources efficiently to achieve the maximum scientific gain.

We tested the ladder framework implemented in decision-making algorithms as part of *R/V* Falkor (Schmidt Ocean Institute) expedition FK181210, which sailed in the Pacific Ocean off the southern coast of Costa Rica from 10 to 23 December, 2018 (**Figure 1**). The purpose of the cruise was to demonstrate the advancement of technology in autonomous exploration; conventional scientific objectives were secondary and pursued in order to test the technology systems employed. Nevertheless, we strove to emulate a conventional scientific expedition even though we had only 10 days (including transits) of ship time and compressed data collection, interpretation, and ROV mission planning into those same 10 days rather than the months available to most expeditions.

The expedition used the ship's Kongsberg EM302 and EM710 MBES instruments for mapping and the *SuBastian*[1] remotely operated vehicle (ROV) for seafloor observations and sampling. In addition, two autonomous underwater gliders (AUGs) were deployed during the cruise: AUG *Nemesis* was deployed for most of the cruise with a magnetometer and conductivity, temperature and depth (CTD) sensor payload to test vehicle endurance improvements, and AUG *Sentinel* (Duguid and Camilli, 2021) was equipped with a Doppler sonar and CTD to test and maintain an adaptive sea bottom-conforming flight path. Automated interpretation and planning processes were deployed and tested to identify potential seep targets, to arrange those targets into ROV and AUG transects that optimized scientific rewards under operational constraints, and to manage and optimize multiple, sometimes simultaneous operations in the most efficient manner possible. Lastly, an automated motion planner relying on machine vision was implemented for ROV robotic arm manipulation. Initial ROV missions used considerable information from previous studies and the geoscience staff, while later transects were planned by the automated planning processes using the ladder framework combined with preliminary real-time data collected during the expedition.

The southern coast of Costa Rica has been the focus of nearly 2 decades of seep-related research, including multiple geophysical cruises, multiple ROV and HOV expeditions, and three ODP/IODP drilling expeditions. Those studies greatly advanced understanding of deep fluid sources at subduction zone plate interfaces (e.g. Hensen et al., 2004; Mau et al., 2007; Ranero et al., 2008; Kluesner et al., 2013; Riedinger et al., 2019), and identified a number of seep sites at which deep-sourced fluids might be sampled (e.g. Füri et al., 2010). As such, rather than having to develop new insights into the way seep systems work, we were able to use the existing information from Costa Rican seeps, supplemented with information from Hydrate Ridge offshore Oregon (e.g. Torres et al., 2009; Baumberger et al., 2018), and seep processes in general to guide our geologic strategy to help support the primary technology demonstration objectives. To pursue this strategy, we revisited known and previously studied seep sites (e.g., Bohrmann et al., 2002; Linke et al., 2005; Mau et al., 2006; Klaucke et al., 2008; Sahling et al., 2008) as well as documenting newly discovered seep sites.

METHODS

Ladder of Seeps

A Ladder of Seeps was constructed to provide a framework for relating data acquisition and interpretation to scientific objectives (**Figure 2**), and in our case identifying seeps with a higher likelihood of emitting deep-sourced fluids. The framework could be modified for alternative objectives, like searching for hydrothermal vents, cold seeps with microbial mats, or seep surveys to estimate fluid flux. While achieving the goal of identifying deep-sourced seeps with high confidence only from measurements above the sediment-ocean interface is unlikely because of fluid dilution effects, using the ladder can increase the likelihood of finding these seeps using low-resolution screening data, and thus improve the chances that deeper sediment cores taken at the seep sites will recover deep-sourced fluids. The ladder includes measurements common on marine geophysical vessels and conducted on the *R/V* Falkor expedition used to identify seafloor features common in seep environments such as carbonate crusts, mounds, seep biota, and bubbles. No single measurement is sufficient to identify a deep-sourced seep, but the ladder provides a framework to help an investigator determine which measurements to collect at each stage of analysis and understand the combination of measurements that increases the likelihood of identifying seeps with deep-sourced fluids.

The Ladder (**Figure 2**) assumes no initial knowledge of a given survey area. It presents a hierarchy of rungs that ascend from no knowledge to Possible Seep, on to Likely Seep, and then to Confirmed Seep, Hydrocarbon Seep (i.e. one with alkane gases), and Deep-Sourced Seep on the top rung. Note that, in general, the cost of data acquisition to ascend each rung increases. Each rung is achieved by the positive identification of a particular seep Feature and the corresponding measurement used to identify the feature. The target column indicates whether the measurement is made above the seafloor (*in situ*) or from subsurface fluid samples. The Likelihood column reflects an opinion about whether the specific measurement achieves the higher ladder rung (e.g. hydrocarbon seepage); note that aggregate measurements at a Possible Seep rung can increase Likelihood above that of any individual measurement. The Instrumental Criteria include assessments of whether the feature is quantifiable (detectable) with any particular measurement, at the physical and temporal scales of measurement (e.g., what chance does a passing ship have to observe a time-varying bubble flux?), whether the measurement is contamination-free (i.e. likelihood of false positive), and if it is repeatable. For example, magnetic anomalies are poor indicators of seeps because seep features are neither quantifiable (i.e. a seep must precipitate a magnetic mineral in sufficient volumes to rise above background noise) nor contamination-free (inversion of magnetic data allow multiple geologic scenarios). On the other hand, identification of a seep biologic consortium (e.g., microbial mats, tubeworms, clams, and mussels) is possible from photographs of the seafloor, and the chance of mis-identification (false positive) from photos is low.

The contextual criteria address how easy the sought-for feature is to recognize in the environment being analyzed and with the tool being used. Microbial mats, for example, are often detected by the color contrast between mats and surrounding sediments so detection will be better when the contrast is greater. Hydrocarbon plumes in the water column have variable survivability because of the time-varying nature of seeps and the ability of currents to disperse plumes. On the other hand, if a bubble plume is observed (reliable), confidence in the discovery of a seep is high. And bubble plumes are associated with few other marine geologic features (compatible), although some seep biota

[1]https://schmidtocean.org/technology/robotic-platforms/4500-m-remotely-operated-vehicle-rov/

RUNG		FEATURE	MEASUREMENT	TARGET	LIKELIHOOD	INSTRUMENTAL CRITERIA			CONTEXTUAL CRITERIA				
					Feature reflects active seepage	Quantifiable *Detectability*	Contamination-Free *Likelihood of false positive*	Repeatable	Detectable *Detectability*	Survivable *Likelihood of false negative*	Reliable *Ambiguity of feature*	Compatible *Specific to cold seeps*	Last-resort *Ambiguity of interpretation*
Active, Deep-sourced Seep	Deep-sourced Seep	Plumes of C2+ HC in water	Mass spec; MBES & SBEC bubbles	• In situ • Sample	High	Mod	Low	Depends upon properties of instrument used and the convergence of multiple feature observations collected simultaneously	Mod/High	Low/Mod	Low	High	Low
	HC Seep	Plumes of HC in water	Mass spec; MBES & SBEC bubbles	• In situ • Sample	High	Mod	Low		Mod/High	Low/Mod	Low	High	Low/Mod
	Seep	Seep biologic community	Photo ID	In situ	Mod/High	Mod/High	Low		Mod/High	Low/Mod	Low/Mod	Mod/High	Low/Mod
Possible Seep	Likely Seep	Carbonate hardground	Photo ID; MBES backscatter; SSS	In situ	Mod	Mod/High	Low/Mod		High	Low	Low/Mod	Mod/High	Low/Mod
		High MBES backscatter anomaly	MBES backscatter	In situ	Low/Mod	Mod/High	Mod/High		Mod/High	Low/Mod	Low/Mod	Mod	Low/Mod
		Geomorphic Form - strong	MBES morphology	In situ	Low/Mod	Mod/High	Low		Mod/High	Low/Mod	Low	Mod	Low/Mod
	Possible Seep	Seismic ampl anomaly	Seismic reflection data	In situ	Low/Mod	Mod/High	Low		Mod/High	Low/Mod	Low	Low/Mod	Mod
		Fluorimeter anomaly in water colulmn	Fluorescence above background	In situ	Mod	Low/Mod	Mod		Low/Mod	Low	Low	Mod	Mod/High
		Hydrate up-dip limit	Seismic reflection data	In situ	Low	Mod	Low		Mod	Low	Low/Mod	Low	Mod/High
		Geomorphic Form - weak	MBES morphology	In situ	Low	Mod/High	Low		Mod/High	Low/Mod	Low	Low	Mod/High
		Seafloor fault trace	Seismic reflection data	In situ	Low	Mod/High	Low		Mod/High	Low/Mod	Low	Low	Mod/High
		Magnetic anomaly	Incr magnetic intensity	In situ	Negligible	Low	Mod/High		Low	Mod/High	Mod/High	Low	High

FIGURE 2 | Ladder of Seeps. Conceptual framework for exploring for specific seep types. Lower part of table defines exploration progression from Possible to Likely Seep, and upper part describes different types of active seeps with each higher rung representing subset of seep type below. Table columns include type of feature observed in nature (Feature), what type of Measurement is made to detect feature, whether measurement is made above seafloor or below (Target), and Likelihood that proposed Feature describes Ladder Rung. Issues of Instrumental Criteria include whether proposed Feature is Quantifiable (Detectable), Contamination-Free (False Positive) and Repeatable. Contextual Criteria represent an explicit evaluation of scientific method by considering whether feature is Detectable, Survivable (False Negative), Reliable, Compatible (i.e. specific to natural cold seeps), and Last-Resort interpretation (i.e. does evidence refute all other possible hypotheses). Deep-sourced fluids are placed at top of ladder in this instance to identify locations for earthquake studies, but ladder could be modified for other scientific objectives.

are found in other environments (e.g., mats associated with organic-rich sediments or slumps). The final column (last-resort) aggregates all of the instrumental and contextual criteria used to identify a particular feature to evaluate the ambiguity of interpretation, or whether plausible alternative explanations for the measurement are permitted.

Bathymetric Mapping

Seafloor and acoustic backscatter mapping address the second rung of the ladder (Likely Seep; **Figure 2**). These data were collected with a 30 kHz Kongsberg EM302 MBES and a Kongsberg EM710 operating at 70 kHz on the *R/V* Falkor (Schmidt Ocean Institute cruise FK181210)[2]. While the survey covered 2,967 km^2 of seafloor in water depths from 225 to 3,616 m, the ship-track covered some areas multiple times as the ship was repositioned for AUG deployment/recovery and ROV operations.

The resulting seafloor map was created by oversampling the EM302 data; swaths on adjacent lines overlapped by ca. 20% in order to accommodate reasonable water column illumination. The EM710 was activated in water depths <1,000 m, but a ship-track dictated by EM302 data collection caused gaps between adjacent EM710 lines with a narrower beam footprint. Seafloor picks from both datasets were combined to create a bathymetric map gridded at 30 m even though local areas with EM710 data could allow a bathymetric grid at 15 m.

A seafloor backscatter map was constructed at a resolution of 15 m using standard methods in Qimera[3] (**Supplementary Material**). We applied a generic processing workflow in order to generate real-time backscatter maps for ROV operations planning and Spock analyses and recognize that further data processing might provide additional data insights. Maps were created in both geographic coordinates and projected onto UTM projection WGS 84 UTM Zone 16 N.

Water Column Analysis

Water column data, which address the fourth rung of the ladder (HC seep; **Figure 2**), were collected with both EM302 and EM710 MBES instruments, and water column anomalies were systematically identified with the Feature Detection algorithms

[2]https://www.rvdata.us/data

[3]https://www.qps.nl/qimera/

in FMMidwater[4] software. More detailed descriptions of filtering parameters applied and interpretation strategies employed are given in **Supplementary Material and Supplementary Table S1**.

Point Clusters defining water column anomalies were imported into Fledermaus and further filtered using the Clustering Algorithm tool to eliminate any remaining noise and to separate multiple anomalies contained within a single Point Cluster. Given the resulting character, shape, amplitude distribution, and position in the water column, each resulting anomaly was labeled a high, medium, or low confidence bubble plume (**Supplementary Table S8**). Low confidence anomalies were excluded from further analysis.

To aid in seafloor mapping, the source location of every water column anomaly was estimated with the Fledermaus Cluster Summary Object Tool by regressing a 3D line through the points and extrapolating that line to the seafloor. When poor or no regressions resulted, the seafloor source was manually estimated. For each resulting interpreted plume, we compiled a seafloor X, Y, Z location, recorded the number of points within the interpreted plume, defined the position of the base of the plume in the water column (Low, Moderate, or High), and interpreted a Low, Moderate, or High confidence in the final seafloor source interpretation.

AUG Water Column Mapping

The *Sentinel* AUG was deployed on two missions using an onboard adaptive mission controller, which enabled the AUG to transition autonomously from water column profiling in waters >1000 m deep, to a bottom-following behavior, wherein the AUG maintained an altitude band of between 5 and 50 m altitude above the seafloor. This behavior enabled the AUG's downward-looking 600 kHZ phased array Doppler velocity log (DVL) to interrogate both the water column and seafloor below the vehicle. Post-processing of acoustic ping ensembles (bin velocities and acoustic return intensities) for each of the four beams was merged with synchronized vehicle pose using a shear method process similar to that described by Visbeck (2002) to estimate water column velocities with 1 m vertical resolution. Thresholding of individual beam intensity while accounting for through-water acoustic attenuation and distance-dependent beam spreading enabled identification of seafloor contacts and water column acoustic anomalies attributable to bubble plumes (further details about method described in **Supplementary Material**, Sect. 2.7). Water column and seafloor (i.e., bottom lock) velocity estimates were then integrated with AUG dead-reckon navigation estimates to generate a DVL-odometry estimate of vehicle track which constrained vehicle position uncertainty to within approximately 15% of distance traveled. Using this DVL-odometry estimate, locations and intensities of seafloor and water column acoustic contacts were mapped to identify possible seep bubble plumes and carbonate hardgrounds. It is noteworthy that this AUG mapping process required only 20 J/m of linear survey, allowing for unattended mapping operations of up to weeks in duration before requiring AUG recharge or recovery.

Seep Target Identification

A series of automated algorithms formulated around Bayesian statistics, information theory, and multi-vehicle routing with time windows were developed and combined to identify cold seeps using bathymetric, acoustic backscatter, and water column data collected in real-time. These algorithms are collected into an application informally called Spock. Use of Spock was intended to plan ROV dives to increase the number of seeps visited during a dive (i.e. to advance sites from Possible Seeps to confirmed Seeps on the Ladder of Seeps). The success of predictions was tested by human observations from an ROV, and data obtained early in the cruise were used to update probabilities with the intent of improving prediction success on each subsequent ROV dive.

The operational significance of our approach is that newly acquired bathymetric, backscatter, and preliminary water column data were combined into ROV seep targets in an objective and reproducible manner in as little as 2 h, faster than analyses done by hand. The algorithmic approach identified novel candidate locations that may have otherwise been overlooked and was able to extract in a quantitative manner the relative strengths of evidence for seepage while at the same time evaluating sites without seeps, thereby strengthening the certainty of places to avoid.

Spock operates by using observation data and evidence of seep presence to learn the parameters of a Bayesian discrete undirected graphical model (Buntine, 1994) that correlates seep presence with local bathymetry and backscatter. Random samples of the model parameters that were consistent with the data were generated using the Metropolis Hastings algorithm (MacKay, 1998), which were then used to compute probabilities of seepage presence. Scores were assigned to visiting each site, which were computed according to Bayesian multi-armed bandit algorithms (Kaufmann et al., 2012; Lattimore and Szepesvári, 2020). The Bandit algorithms assigned a better score if a site had a high probability of seepage and if it displayed data signals that were uncommon in the data set. For example, pockmarks are uncommon in the Costa Rica data set so the influence of pockmarks on seepage probability was uncertain. Higher scores directed dives towards pockmarks so that posterior probabilities were better refined. Bandit algorithms describe how to select the relative weights of seep probability and uncertainty, and prove that these strategies result in more seeps found than only visiting the sites with the highest probability. A final stage solved for a connected track that maximized the cumulative score of all visited sites, limited by how far the ROV could travel over the time allotted to the dive (Desrosiers et al., 1995).

The initial Bayesian framework applied to the first dive was based on expert opinion trained on published data for cold seeps on the Costa Rica margin (Sahling et al., 2008). The Sahling et al. (2008) study identified 112 candidate seep sites associated with mounds, pockmarks, and faults visible in the bathymetry map, as well as high backscatter. The sites labeled with active seepage in the Sahling et al. (2008) data set were marked as seeps for

[4]https://confluence.qps.nl/fledermaus7/how-to-articles/how-to-fmmw/how-to-fmmidwater-feature-detection-in-fmmidwater

algorithm training. For the planned dives, sites with higher probability of seepage were identified based on the generated bathymetric and acoustic backscatter maps. Because prior studies indicated that seeps were frequently associated with mounds, pockmarks, faults visible in the bathymetry map, and high backscatter, locations with evidence of these bathymetric features and/or backscatter above background levels were identified from the map and used to build a candidate set of dive sites.

Bubble plumes identified from MBES water column data provided additional evidence for seepage, but few plumes were identified at the time of dive planning. Across all algorithmically planned dives, 19 plumes were available. When plumes were available, the location of the seafloor source was visually estimated from the base of the plume. The estimated source locations were added to the candidate site set if they did not align with candidates derived from bathymetry and acoustic backscatter.

Initial ROV dives were planned by hand, focused on seep areas defined by others, and took valuable time from other activities early in the expedition. Five subsequent ROV dives and two *Sentinel* AUG missions were planned with Spock's assistance. Every potential dive site was labeled in terms of features that were present, absent, or unmeasured, including mounds, pockmarks, high backscatter, and bubble plumes. The presence of high slope was hypothesized to be correlated with seepage and was also included because the Bayesian approach allows consideration of primitive hypotheses. Every possible combination of features was modeled as having a fixed probability of a seep being present. Over the course of the cruise, Spock learned the seep presence probabilities, and then used that information to identify the sites with the highest probability of seepage. Each dive selected 2–10 sites within close proximity to visit out of between 10 and 40 candidate sites that could be reached on a given dive. The Spock predictions were checked by hand to validate that dive targets were logical and of scientific interest.

Formulation of site selection as a multi-armed bandit problem balanced visiting sites that best improved seep presence probabilities against visiting sites with a high estimated probability of seepage. Multi-armed bandit algorithms produce

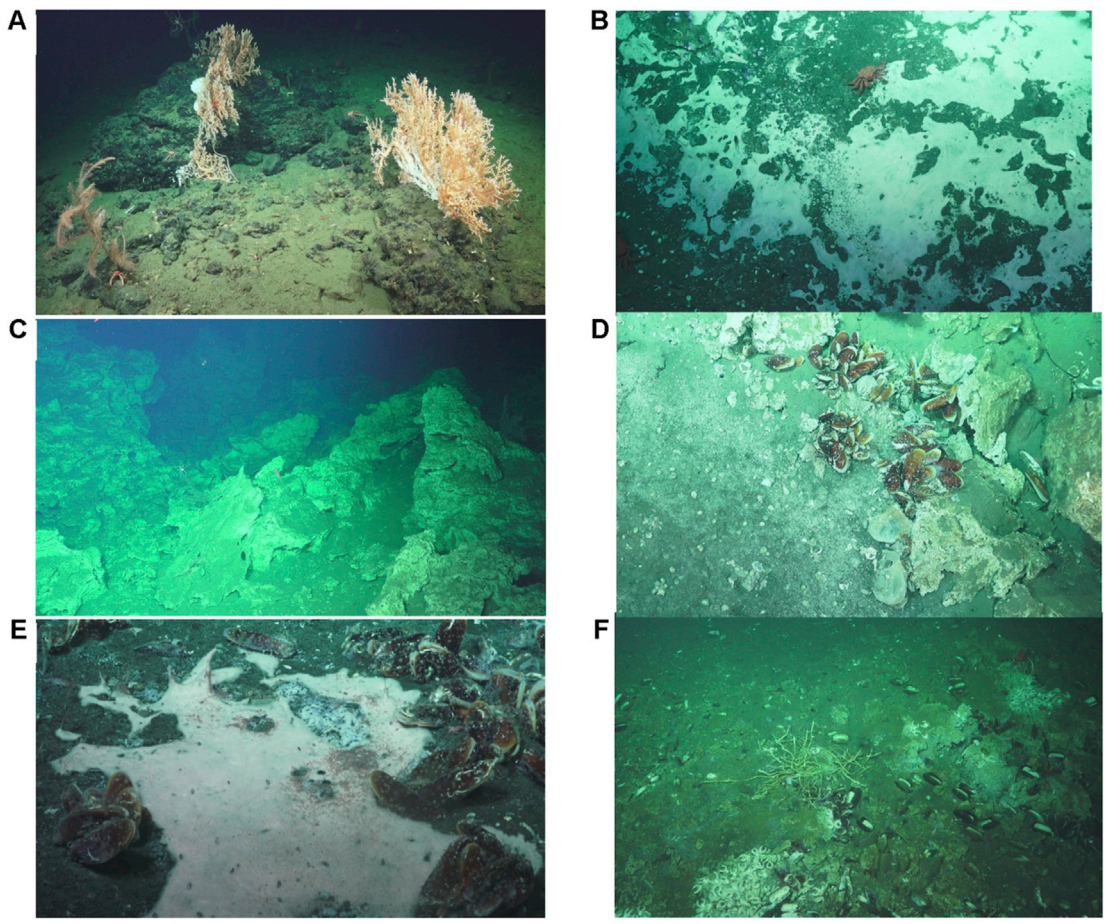

FIGURE 3 | Seep observations photographed by ROV. **(A)** Corals affixed to carbonate crust outcrops, Dive SO204 (SA4: Jaco); **(B)** Methane bubble stream rising out of edge of microbial mat, Dive SO206 (SA1: Pacuare); **(C)** Jagged carbonate crust outcrops, Dive SO204 (SA4: Jaco); **(D)** Clam colony nestled along edge of carbonate crust and adjacent thin microbial mat covered by snails, Dive SO204 (SA4: Jaco); **(E)** Thick microbial mat fringed by clams, Dive SO210 (SA2: Savegre); **(F)** Tubeworms growing from carbonate crust outcrop and flanked by clams, Dive SO208 (SA3: Mounds 11/12). Specific photo locations identified in **Supplementary Materials** (Seep_Array_Documentation.pdf).

strategies for sampling that maximize the expected reward drawn from unobserved probability distributions; in other words, when initial probabilities are based on global knowledge, how can that knowledge be refined in a given location to maximize success in finding seeps? In this case, the reward was 1 for a seep being present, and 0 otherwise, and the multi-armed bandit algorithm selected the combinations of features to visit to maximize expected reward. Among the many available multi-armed bandit algorithms, we used Information Directed Sampling (IDS; Russo and Van Roy, 2018). IDS provides a score for each possible site and directs that the site with the lowest score should be visited. By employing this approach, we sought to maximize opportunities for advancing on the Ladder of Seeps. IDS was chosen from a selection of bandit strategies because it is suitable for Bayesian problems, which allowed us to use priors drawn from previous observations in the area and model suspected correlations. Furthermore, IDS yields an explicit quantification of the relative contributions of seep likelihood and probability refinement towards score, making Spock's recommendations more interpretable. While IDS coupled with our conditional independence model gave scores for each dive, the choice of which sites to visit was still a combinatorial problem. Any number of sites could be visited if a path between them could be produced that was consistent with the average underwater speed of the vehicle and the time allotted for the dive. The optimal dive that minimized the IDS score was solved as a discrete search problem. Bounds on the score of any path that included a set of sites were computed, which allowed the optimal path to be found without explicitly evaluating all possible paths.

Seep Mapping

Ship-Based Mapping

The term "seep" is applied to phenomena at a range of scales from the area of an instrument placed on the seafloor to measure fluid flux (e.g., Tryon et al., 1999) to a km-scale map feature (e.g., Klaucke et al., 2008; Sahling et al., 2008). In order to test predictions of seep locations with Spock, a seep must be defined at a scale (50 m) that can be evaluated. To account for different spatial scales, a mapping hierarchy was defined and applied to data derived from bathymetry, acoustic backscatter, and interpreted seafloor sources of plumes. The smallest entity in the hierarchy is a Seep that is limited to a seafloor dimension of <5 m based on the size of seeps on land. Fluid flux from an individual seep is variable over multiple timescales (e.g., Tryon et al., 1999, Tryon et al., 2002). The scale of a seep is much smaller than mapping resolution.

Seeps occur in clusters on the seafloor rather than being randomly distributed, so individual seeps that occur near one another were collected into Seep Clusters. The scale of Seep Clusters is conditionally defined to lie between >5 m and <10 s to 100 s of meters based on observations of cold seeps on land (Gouveia and Friedmann, 2006; Barth and Chafetz, 2015) and includes multiple backscatter pixels. The boundary of a seep cluster occurs at a transition from a higher to lower seafloor backscatter value. To verify the significance of this boundary, the mean backscatter value is computed for each interpreted seep cluster and compared with the mean backscatter value of the surrounding region. Rather than use raw backscatter values, those values were binned and re-gridded at 50 m resolution in order to reduce the influence of data artifacts.

Seep Clusters similarly exist in groupings, designated as Seep Arrays. Seep Arrays sometimes occur around a clear bathymetric feature like the Jaco Scar (Seep Array 4; **Figure 1**), or sometimes in linear arrays that might reflect seepage along high-angle faults (Seep Array 2; **Figure 1**). The purpose of defining Seep Arrays is to help raise questions about sub-surface structure that might promote fluid flow. Costa Rican river and lake names were assigned to Seep Arrays to assist in communication. Given the desired relationship between Seep Arrays and geologic structures, dimensions of Seep Arrays are defined between 100 s of meters and 1–5 km.

ROV Mapping

Mapping Seeps

At sites visited by the ROV, geologic and biologic observations were compiled using Squidle+5 open-source software that allows real-time capture and annotation of ROV observations, coupled to flexible data storage for post-cruise analysis (e.g., Proctor et al., 2018). Squidle+ was expanded to include geologic observations like the state of the seafloor and structures observed (e.g., rubble). By using Squidle+, the geoscience participants generated consistent observations from site to site and between observers. The observations were captured within a classification scheme established and used by NOAA on the Okeanos Explorer (e.g., Gomes-Pereira et al., 2016), modified to include additional observations that help establish the position of each site on the Ladder of Seeps. **Figure 3** shows examples of the main seafloor features logged in Squidle+ during ROV dives. Biologic observations remain generic because of the geoscience expertise onboard, but the Squidle+ database allows more detailed interpretations. The classified ROV observations were captured in a geospatial mapping and analysis system and integrated with seafloor bathymetry and backscatter maps, MBES water column analyses, and sample data to build the spatially related Seep Clusters and Seep Cluster Arrays described above.

Mapping Seafloor Conditions and Dissolved Gases

Seafloor conditions were recorded by the CTD onboard the ROV. The ROV was also equipped with a double focusing membrane inlet mass spectrometer operating as payload to identify water column chemical anomalies in a functionally similar configuration to that described in Feseker et al. (2014), Camilli et al. (2010), and Camilli et al. (2009). A 6 mm diameter polyurethane sample introduction tube connected to the length of the manipulator arm and backed by a small impeller pump provided continuous sample introduction to the mass spectrometer's inlet. Analytes of interest included methane, ethane, hydrogen sulfide, propane, carbon dioxide, and benzene, which were observed in real-time as molecular ion peak and ratio signatures at m/z: 15, 27, 34:32, 43, 44, and 78, respectively. Ion peak height data were post-processed with a 10-

[5]https://squidle.org

min temporal "box" filter centered at ± 5 min to identify the onset and approximate magnitude of anomalously increased ion peak intensities above background levels.

Sample Analyses

Pore water and headspace gas samples were obtained from ROV push-cores using standard methods (**Supplementary Material**). Preserved pore water samples were analyzed for major and minor elements and oxygen and hydrogen isotope ratios at the University of Bremen. Methane concentrations were measured from headspace gas samples and from CTD water samples at the University of California, Santa Barbara by gas chromatography, and stable carbon isotope ratios of methane were measured at Woods Hole Oceanographic Institution. Because analytical precision is much greater than the precision required for the interpretations reached in this study, details of the methods used are documented in **Supplementary Material**.

RESULTS

Water Column Analysis

Water column anomalies that satisfy criteria of size, shape, amplitude distribution, and position in the water column are interpreted as bubble plumes (Anderson, 1950; Sullivan-Silva, 1989; Medwin and Clay, 1998) and offer the most substantive evidence for seafloor seeps from a sea-surface measurement. We recorded 209 unique bubble plumes that are tabulated in **Supplementary Table S2**. Information in those tables include the interpreted seafloor source of the bubble plume (X, Y, Z), the date and time it was observed, the number of points attributed to the bubble plume, our confidence that the water column anomaly is a bubble plume, and the MBES source of the observation. Some plumes were recorded by both MBES systems, and some plumes were recorded more than once.

The seeps are unevenly distributed in depth over the study area (**Figure 4**). Comparing plume occurrence with the distribution of bathymetry depth nodes suggests that there is no significant coverage bias in these results (i.e. ca. 5 × difference in number of depth nodes in survey area inside the upper and lower depth limits). In addition, small-moderate plumes are present at all depths, but the largest plumes are found where plumes are clustered in depth. A gap in plume occurrence is found between ca. 800–1000 m.

Water column anomalies identified in AUG sonar data correspond in space to anomalies identified with ship-based MBES data (**Figure 5**). While the data were collected at a

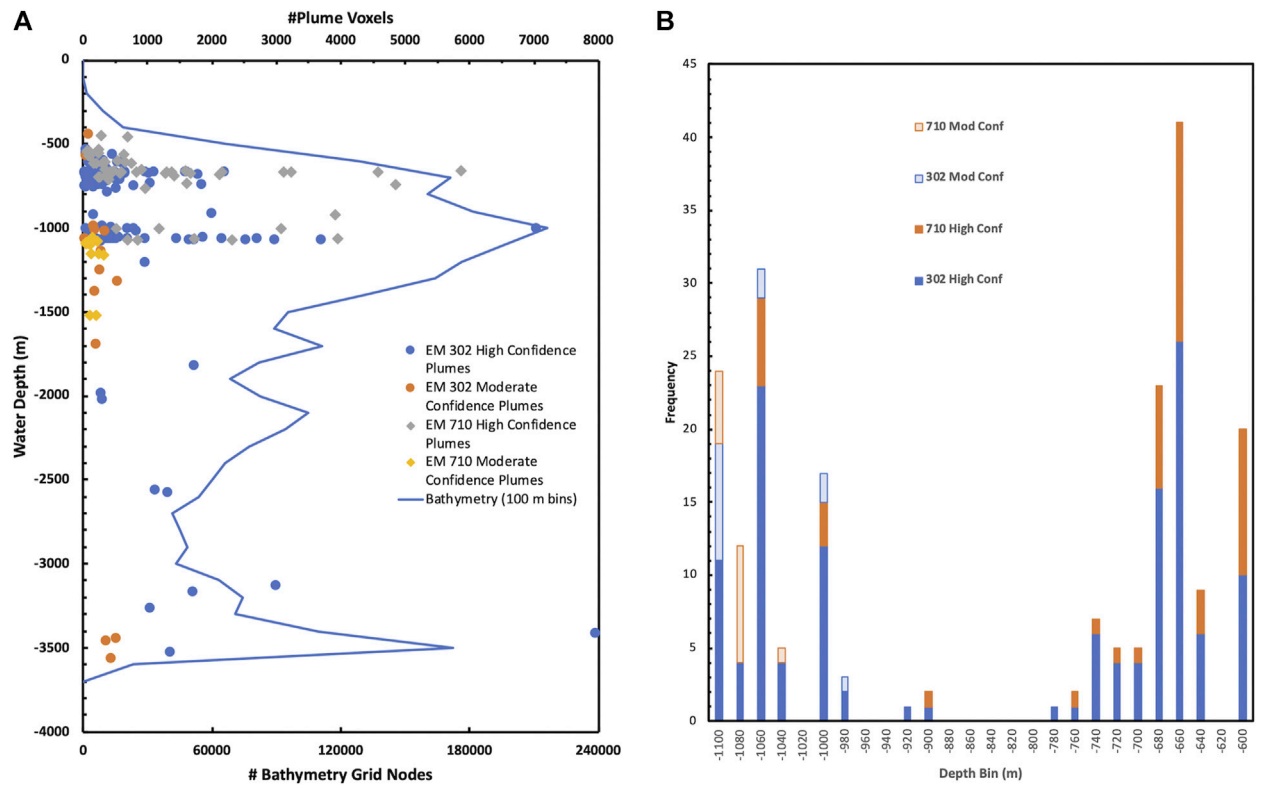

FIGURE 4 | Observed depth distribution of water column anomalies (bubble plumes) for EM302 and EM710 datasets. Note that EM710 sonar deactivated in water depths > ca. 1000 m. **(A)** Bubble plumes plotted as number of voxels (points) in final Fledermaus model vs. depth for High and Moderate Confidence plume interpretations. Bottom axis (blue curve) records number of bathymetry nodes in 100 m bins to test for possible coverage bias (e.g., between 800 and 1000 m where few plumes identified). **(B)** Histogram of EM302 and EM710 High and Moderate Confidence bubble plumes binned in 20 m increments. Note paucity of observations between 800 and 1000 m water depth.

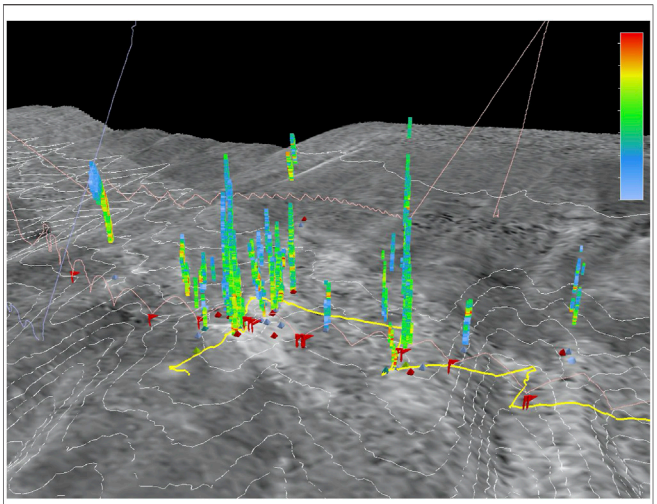

FIGURE 5 | AUG sonar observations of bubble plumes in SA1: Pacuare (red flags) compared with EM302 plume observations (pyramids represent seafloor source and blue-green-yellow-red colored stalks are bubble plumes with red colors indicating amplitudes of 3–10 dB and light blue amplitudes between –30 and –45 dB). Pink lines represent AUG flight path. Note that plumes identified at bottom of any flight cycle. Yellow line is ROV Dive 205/206 path. Closely spaced bathymetric contours in dive area at 10 m increments; shallowest depth contour at top of dive site is –660 m, and shallowest depth contour at top of image is –600 m. VE = 3x. View to NE. Note that given AUG navigation uncertainties, reasonable correspondence found between EM302 and AUG plume interpretations.

much higher acoustic frequency with vastly different spatial coverage and resolution, processed in a different way, and collected on different days than the ship recordings, the correspondence in seep source location between AUG and MBES data is remarkable.

Seep Mapping

Ship-Based Mapping

Application of the mapping hierarchy led to the identification of seven Seep Arrays from the combination of ship-based bathymetry, backscatter intensity, and water column anomalies (**Figure 1**). Four of the seven arrays occur in association with seafloor mounds, faults, and landslides identified by previous studies (Jaco, Quepos, Sierpe, and Mounds 11/12). A fifth array (SA2: Savegre) sits just outboard from a long, curved, steep slope that may coincide with a structural boundary. The remaining two arrays (Pacuare and Terraba), as well as several individual water column anomalies in the NW corner of the study area, occur at ~600–650 m water depth, near the intersection of the base gas hydrate stability zone with the seafloor.

Two to eight Seep Clusters have been mapped within each array. Cluster maps, high-resolution seafloor maps, raw and reclassified backscatter maps, and any additional data used to map the clusters are found in **Supplementary Material (Seep_Array_Documentation.pdf)**. The clusters range in area from 0.01 to ~1 km^2, although most are <0.1 km^2. Most clusters include all key mapping features: water column anomalies, relatively high backscatter intensities, and some seafloor bathymetric expression of a fluid pathway, e.g. mound, fault, break-in-slope, pockmark. A few clusters have no water column anomalies and were mapped from ROV observations (described below). Because Seep Clusters are smaller than Seep Arrays, the bathymetric morphology can change with the scale of the observation. For example, the clusters mapped in SA3: Mounds 11/12 consist of a SW plunging ridge, a gentle slope, and domes (mounds), while individual seeps are found on slopes, ridges, or mounds. **Figure 6** illustrates the mapping of two clusters that exemplify differences in attributes that may influence predictions made by Spock. SA1: Pacuare (**Figure 6A**) comprises six seep clusters ranging from 0.01 to 0.4 km^2, each with a minimum of 2–3 water column anomalies. At the scale of the array, each cluster occurs along a bathymetric ridge, although local topography around individual seeps may be flat. The mean backscatter class value for each cluster is above local background, although within standard deviation, particularly for the smaller clusters. In contrast, SA7: Sierpe (**Figure 6B**), in the southeast of the study area, contains just two seep clusters, ranging from 0.01 to 0.03 km^2. Both have water column anomalies, but backscatter intensity is similar to background. The high-resolution characteristics of these arrays are described in the next section (ROV Mapping).

In addition to Seep Clusters mapped within each of the arrays, we also identified individual clusters independent of the arrays. These clusters were defined in regions where two to three water column anomalies were identified within a few hundred meters to a kilometer of each other. The proximity of the seeps in these clusters suggests a broader geologic control, but that control was difficult to identify from the available data, hence they were given no formal Array designation (e.g. Seep Clusters Reventazon, and Tarcoles, adjacent to the trench; **Figure 1**).

ROV Mapping

Mapping Seeps

ROV mapping of individual dive sites provided the critical piece of information that allowed a target site to move from Likely Seep to Seep on the Ladder, based on observations of seep biologic communities and carbonate hardgrounds (**Figure 2**). The ROV dive sites visited during this expedition display the authigenic carbonates and associated biologic communities typical of seafloor seep environments and observed by previous expeditions to this region (e.g. Bohrmann et al., 2002; Mau et al., 2006; Klaucke et al., 2008; Sahling et al., 2008; Levin et al., 2015). Generic descriptions of the seep communities were sufficient to achieve the Ladder of Seeps objectives for this study, but the full expedition database is archived with the R2R repository[6] and can be revisited if a more detailed description of seep characteristics is warranted for future study. **Table 1** records observations of biologic communities and authigenic carbonates discovered at each ROV site. Complete tables of Squidle + annotations can be found in **Supplementary Material (Annotations-ROV Excel**

[6]https://www.rvdata.us/data

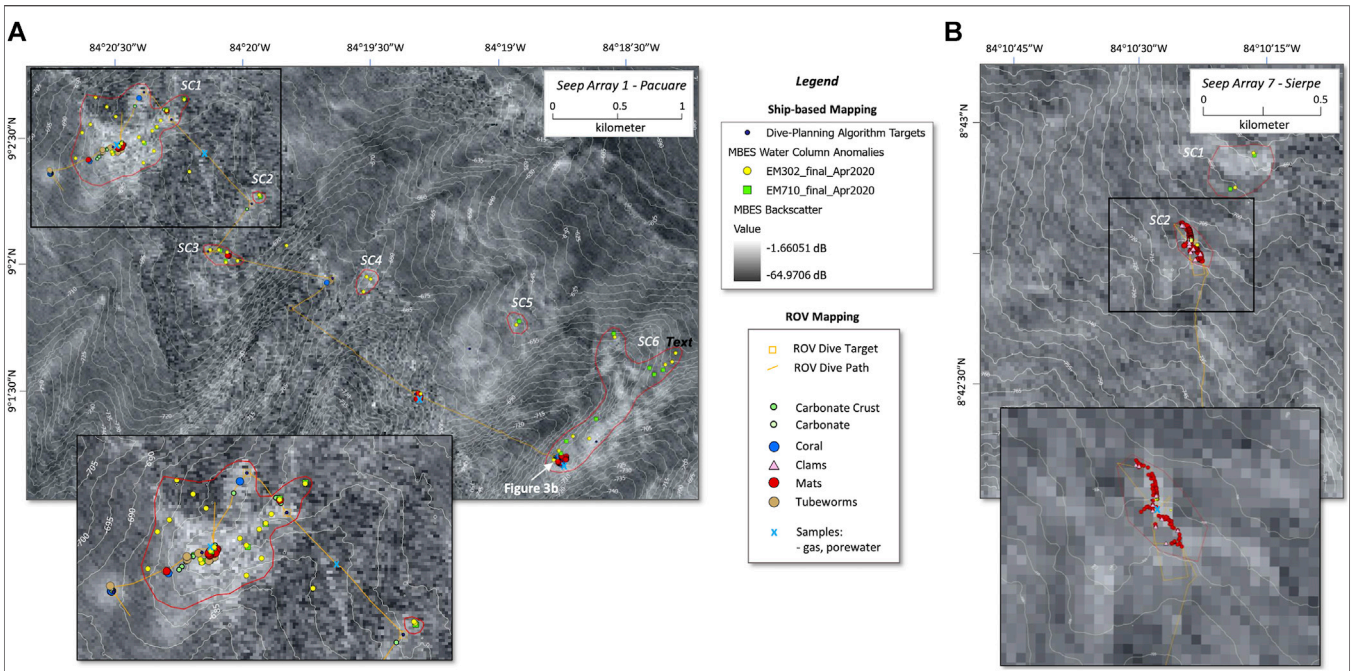

FIGURE 6 | ROV mapping of representative seep clusters. Maps illustrate MBES backscatter and bathymetric contours (meters) for two sites with different seep characteristics. Seep clusters defined from ship-based mapping are defined by red polygon outlines, labeled by Seep Cluster number. ROV observations annotated in Squidle + are superimposed. **(A)** Seep Array 1—Pacuare contains six clusters between 600 and 650 m water depth. Four clusters (SC1-3, SC6) were occupied during ROV dives SO205/SO206, and display heterogeneous distribution of carbonate crusts, corals, bacterial mats, and tubeworms that occur in regions of higher backscatter. SC1 characterized by mound-shaped geometry (inset map) while remaining clusters occur on topographic ridges, flats, and valleys. **(B)** Seep Array 7—Sierpe contains only two seep clusters between 690 and 720 m water depth, dominated by bacterial mats, with no carbonate crusts. Seafloor topography flat with backscatter values close to background (inset map).

files). The seep-related biologic communities observed in the study area included clusters of siboglinid tubeworms, abundant aggregations of vesicomyid clams, rare mussel beds, deepwater corals, and bacterial mats. Most are spatially associated with carbonate crusts, boulders, and mounds (**Figure 3**). Seep succession models (e.g. Cordes et al., 2008; Lessard-Pilon et al., 2010; Bowden et al., 2013; Guillon et al., 2017) suggest that bacterial mats are the earliest to develop at new seep sites. Subsequent precipitation of authigenic carbonate permits mussel colonization, and declining sulfide seepage allows tubeworm colonies to begin to dominate. Vesicomyid clams are prominent members of seep communities but tolerate a large range of chemical fluxes and concentrations, and as such, are less diagnostic for seep succession processes. They are, however, thought to enhance the anaerobic oxidation of methane, which can in turn accelerate the formation of the authigenic carbonates needed as substrates by other fauna (Guillon et al., 2017). Deepwater corals often grow on authigenic carbonates derived from hydrocarbon seepage, but their nutrition is considered to come from non-seep sources (Cordes et al., 2008) and may be concentrated in areas where seeps are no longer active.

Approximately 30 Seep Sites were documented during nine ROV dives (**Table 1**). Detailed maps of each dive site are included in **Supplementary Materials (Seep_Array_Documentation.pdf)**. **Figure 6** illustrates the key observations at two new sites with characteristics typical of those used to promote placement of a seep on the Ladder. SA1: Pacuare (ROV dives SO205/SO206; **Figure 6A**) comprises six individual seep clusters ranging from 0.01 to 0.4 square kilometers, each with a minimum of 2–3 water column anomalies. The seeps all occur at 652–695 m water depth (**Supplementary Table S2**), within 100 m of the intersection of the base gas-hydrate stability zone with the seafloor (Bohrmann et al., 2002, and *Mapping Seafloor Conditions*). At the scale of the array, the seeps occur along a series of dip-parallel topographic ridges, although local topography around individual seeps may be flat. The more well-developed clusters have mound-shaped topography and high backscatter intensity consistent with well-developed authigenic carbonates. Because additional seeps and seep clusters were identified by post-cruise comprehensive water column analyses, two seep clusters (SC4-5) lie beyond the ROV path. At the remaining four seep clusters (SC1-3; SC6), characteristic authigenic carbonates and seep biologic communities were observed (**Figure 6A**). SC1 is one of the largest seep clusters in the study area and consists of 19 individual seeps with an overall cluster diameter of ~1 km. The biologic communities suggest that the most active area of seepage is near the center; the edges of the cluster are dominated by authigenic carbonates and corals, whereas the central area contains abundant bacterial mats,

TABLE 1 | Summary of ROV seep observations.

ROV dive	Seep site	Seep array (*Cluster*)	Bathymetric shape	Lat (Dec degrees)	Long (dec degrees)	Predicted probability	MBES plume (#)	Carb	Bub	Mats	Clams	*Mus*	TW	Cor	Seep status
SO203	01	SA4: SC2	Valley	9.17367	–84.80383	0.678		M			m			M	D
	02a	SA4: SC1	Ridge	9.17346	–84.80020	0.678		m			m				AW
	02		Flat	9.17339	–84.79889	0.678		m		m	m			R	AW
SO204	01	SA4: SC3	High slope	9.14693	–84.81534	0.671								M	D
	02	SA4	High slope	9.14816	–84.81982	0.380		r							N/D
	03	SA4: SC5	Slope	9.15017	–84.81900	0.935		M				r		M	AW
	04	SA4: SC6	High slope	9.14975	–84.82160	0.380		m						M	D
	05	SA4: SC8	High slope	9.14905	–84.82977	0.380								M	D
SO205/	01		Flat	9.03937	–84.34600	0.316		m					r	M	D
206	01a	SA1: SC1	Mound	9.04030	–84.34359	0.204		m		r			r	R	AW
	02	SA1: SC1	Mound	9.04114	–84.34199	0.632	4	M	M	M			m		AS
	03	SA1: SC1	Mound	9.04468	–84.33996	0.204								R	D
	04a	SA1: SC1	Mound	9.04348	–84.33850	0.204	1	M	m	r					AW
	04	SA1: SC1	Mound	9.04291	–84.33815	0.204									N
	05	SA1: SC2	Flat	9.03746	–84.33288	0.699	2	r							AW
	06	SA1: SC3	Flat	9.03436	–84.33575	0.649	2		m	m					AW
	07		Flat	9.03261	–84.32759	0.316								R	D
	08		Valley	9.03069	–84.33032	0.316									N
	09		Ridge	9.02514	–84.32214	0.726			m	M				R	AS
	10	SA1: SC6	Ridge	9.02102	–84.31294	0.726	2	M	M	M				M	AS
SO207	01		Slope	8.91922	–84.30234	0.291									N
	01a	SA3: SC4	Mound	8.92010	–84.30300	0.332		M		M	m		M	M	AS
	02a	SA3: SC3	Mound	8.92171	–84.30435	0.332		M							D
	02		Mound	8.92286	–84.30542	0.332		m							D
		SA3: SC3	Mound	8.92292	–84.30379	0.332									D
			Mound	8.91948	–84.30367	0.045									N
SO208	01	SA3: SC2	Slope	8.93081	–84.30925	0.793	2	M							D
	01a	SA3: SC2	Slope	8.93094	–84.31067	0.793	2	M						M	D
	02a		Ridge	8.93060	–84.31183	0.793		m		M	m		m	m	AW
	02	SA3: SC1	Ridge	8.93057	–84.31293	0.793	12	m	m					m	AW
		SA3: SC2	Mound	8.93125	–84.31021	0.306	2	M						r	D
SO209		SA7-SC2	Flat	8.71290	–84.17338	0.724	2		m	M	M				AS
	01	SA7-SC2	Flat	8.71274	–84.17329	0.977	2		m	M	M				AS
SO210	01	SA2: SC2	Flat	9.04766	–84.39570	0.554									N
	02	SA2: SC2	Ridge	9.04920	–84.39359	0.979	5	m	M	M	r		m		AS
	03	SA2: SC2	Flat	9.04828	–84.39275	0.979	2		m	m					AS
	04		Flat	9.05042	–84.38972	0.554									N
	05		Flat	9.05855	–84.38414	0.737									N
SO211			Pockmark	9.02954	–85.38527	0.904									N

See text for description. Slope values: mean slope of target and four surrounding cells (30 m grid): Flat ≤3°; Mound/Ridge/Slope/Valley/Pockmark = 2–11°; High Slope ≥15°. Predicted Probability column indicates pre-dive probability of encountering seep at that location (Spock). ROV Observations: Carb: Carbonate crust, Bub: ROV-observed bubbles, Mats: Microbial Mats, Mus*: Mussels, TW: Tubeworms, Cor: Corals; Seep Status: M—Major, m—minor, r—rare, blank—absent. Seep Status: AS—Active/Strong, AW—Active/Weak, D—Dormant, N—Non-seep*

tubeworms, and authigenic carbonate crusts. Occasional observations of minor carbonates and/or mats along the dive pathway suggest the emergence of new seeps, but the features were likely too small to be identified as targets by Spock. SC2 and CS3 also display only rare carbonates and minor bacterial mats but do have water column anomalies. SC6 is another composite of individual seeps with 14 water column anomalies. The ROV path intersected only the southern portion of the cluster, where we found a heterogeneous mixture of carbonate crusts, bacterial mats, and minor corals, suggesting a complex distribution of seep activity.

In contrast to SA1: Pacuare, SA7: Sierpe (Dive SO209; **Figure 6B**) contains only two seep clusters at ~700 m water depth, ranging in area from 0.01 to 0.03 km^2. Water column anomalies were recognized during the initial shipboard processing of MBES data in this area. Those anomalies, coupled with published subsurface indicators of fluid flow (Kluesner et al., 2013), resulted in a strong pre-dive prediction of seep targets by Spock. Without those observations, the pre-dive prediction would have been much weaker, as neither the seafloor topography nor the backscatter intensity provided any strong indicators of seepage. The ROV dive identified abundant bacterial mats, and fields of vesicomyid clams, consistent with a robust seep in the relatively early stages of development. No carbonate crusts were observed.

A synthesis of ROV mapping at the dive sites confirms the presence of biologic communities that would designate a seep as Active (**Figure 2**) at approximately two-thirds of the sites (**Table 1**). At six of those sites, however, the communities

TABLE 2 | Inorganic pore water chemistry results.

Dive #-site	Sample ID	Vol (ml)	B	Ba (E^{-6})	Ca	Fe (E^{-3})	K	Li	Mg	Mn (E^{-6})	Na	P (E^{-3})	S	Si	Sr	Cl^-	Br^-	SO_4^{2-}	$\delta^{18}O$ (‰)	δD (‰)
SO204-03	SO204-04	7.8	0.503	706.3	9.92	3.743	13.52	0.027	64.9	145.6	581.6	41.293	25.78	0.275	0.093	554.3	0.844	23.30	0.18	0.14
SO205-02	SO205-02	6.0														549.0	0.825	31.38	–0.02	–1.68
SO205-BG	SO205-03	5.8	0.575	138.4	11.58	15.668	13.44	0.026	59.9	3585.9	553.7	19.274	32.78	0.348	0.096	535.8	0.826	27.49	0.02	0.53
SO206-10	SO206-04	14.9	0.499	51.0	4.52	0.233	11.08	0.024	48.9	0	471.1	1.421	6.99	0.160	0.061	547.4	0.835	1.20	–0.05	0.26
SO207-01a	SO207-02	11.4	0.627	502.4	6.41	0.430	12.61	0.024	50.6	36.4	496.3	7.974	6.82	0.241	0.072	523.6	0.820	15.40	–0.01	–0.28
SO208-02	SO208-01	7.4	0.582	152.9	11.06	0.681	13.22	0.024	53.6	1164.9	508.9	32.447	29.78	0.424	0.090	551.5	0.852	28.45	–0.02	0.15
SO208-02	SO208-04	3.6	0.659	684.5	8.61	9.670	13.87	0.026	55.4	163.8	535.0	20.372	16.15	0.323	0.082	587.9	0.900	7.48		
SO209-01	SO209-02	6.4	0.496	1776.7	5.16	2.758	11.80	0.021	53.6	36.4	507.6	14.851	0.55	0.269	0.071	566.3	0.867	1.56		
SO209-01	SO209-03	9.4	0.383	247.6	3.43	0.412	11.32	0.020	48.5	18.2	466.7	9.492	1.86	0.235	0.054	546.9	0.838	2.98	–0.02	0.38
SO210-02	SO210-01*u*	8.0	0.514	881.1	6.83	2.185	12.09	0.021	52.8	36.4	504.1	53.012	2.10	0.482	0.067	777.1	1.179	4.97		
SO210-02	SO210-01*l*	8.4	0.448	655.4	4.88	1.468	12.02	0.022	50.9	36.4	496.3	22.632	0.34	0.365	0.054	548.8	0.851	1.78	–0.18	–0.38
SO210-02	SO210-03 *u*	9.4	0.580	138.4	10.80	9.902	13.22	0.027	57.6	163.8	531.1	30.122	30.75	0.242	0.092	538.7	0.824	26.93	–0.02	0.07
SO210-02	SO210-03 *l*	7.8	0.678	152.9	11.67	0.286	15.25	0.031	67.0	36.4	622.4	25.602	33.69	0.289	0.100	538.8	0.829	26.46	–0.04	–0.09
SO210-03	SO210-06 *u*	8.9														694.0	1.066	17.84		
SO210-03	SO210-06*l*	9.0	0.508	2563.2	7.36	1.540	13.66	0.027	57.7	127.4	566.8	14.012	2.69	0.232	0.081	538.8	0.728	2.29	0.11	0.27
	Seawater		*0.420*	*152.9*	*10.3*	*0.609*	*10.2*	*0.026*	*52.7*	*7.281*	*469*	*2.841*	*28.9*	*0.1*	*0.089*	*547*	*0.84*	*28.9*		

Values given in mM/L. Seawater composition provided for reference. $\delta^{18}O$ and δD values reported with respect to SMOW.

were dominated by deepwater corals, suggesting that at those specific sites, seeps may be dormant.

Mapping Seafloor Conditions

Seafloor conditions were recorded by the CTD onboard the ROV, and the temperature and depth readings are used to document seafloor conditions (**Supplementary Table S3; Supplementary Figure S1**). While temperatures vary at water depths greater than 1000 m, there is good convergence in observations at 700 m. Combining these observations with a calculation of the hydrate stability field (Dickens and Quinby-Hunt, 1994) leads to an inference of the top of the hydrate layer at 580–600 mss, identical to the depth range reported by Bohrmann et al. (2002).

Porewater and Gas Analyses

The purpose of the porewater and gas analyses is to identify samples with possible deep fluid components, the top rung in the Ladder of Seeps, and to gather additional information about the longevity and frequency of individual seeps. Sample locations are recorded in **Supplementary Table S4**. We applied a process and fluid source framework developed in previous work (e.g., Whiticar, 1999; Chan and Kastner, 2000; Kopf et al., 2000; Silver et al., 2000; Grant and Whiticar, 2002; Lückge et al., 2002; Milucka et al., 2012) that include water modified by diagenesis and very low-grade metamorphic reactions (ultimate goal), water from deep compaction processes (>1 km), and hydrocarbon gas generated by thermal cracking of organic matter. Shallow fluid sources and processes that alter both shallow and deep fluids include water produced from shallow (<1 km) compaction, biogenic gas generated by microbial processes, bacterial methane oxidation, and hydrate formation and disassociation. Given these limited goals and the limited time and geoscience staff resources available on the ship, we only collected samples that were analyzed onshore and excluded ship-based analyses that might better define microbial processes (e.g., bicarbonate concentration). We also only took 1–2 samples in each core rather than the more conventional profiles because we collected short cores (ca. 25 cm) and had insufficient time for more sampling.

Porewater Samples

Most cores consist of only a single porewater analysis (**Table 2**), although samples SO210-01, -03, and -06 all include an upper and lower sample. In most cases, porewaters were extracted from a depth of 10–15 cm in the core. Ion concentrations are presented with respect to their concentration in seawater.

Major and Minor Element Analyses

The following cations are enriched in sampled pore waters with respect to seawater: B, Ba, Fe, K, Mn, Na, P, and Si (**Table 2**). Only one sample (SO209-03) has less B than seawater, and two samples (SO206-04 and SO-210-03) have less Ba than seawater (two samples have the same concentration of Ba as seawater). All samples have more Fe than seawater (up to 250 × enrichment), and all samples are enriched in Mn (up to 500 × enrichment) except for one sample (SO206-04); which has none. Extreme Fe and Mn enrichments occur in the same sample (SO-205-03). All

samples are enriched in P with an enrichment up to 15 × (SO204-04), except for SO206-04, which has half seawater concentration. K and Na are modestly enriched in all samples (up to 1.4 × for K and 1.3 × for Na), but sample SO209-03 has a slight Na depletion. Si is enriched in all samples up to a factor of ca. 5 × (SO210-01).

Ca is enriched in four samples with respect to seawater, like Na and K, but in most samples, Ca is depleted with as little as 1/3 the calcium of seawater (SO209-03). Li concentrations hover around seawater values (0.020–0.031 mM), and the same if found for Mg (48.9–67.0 mM) except that the number of depleted samples is smaller and enriched samples greater, and Mg enrichment > depletion. The average Sr concentration is less than seawater, but five samples out of 14 have more Sr than seawater.

There is more S in four samples than seawater, but in other samples S is depleted to such small concentrations (0.337 mM in SO210-01) that the average of S in all samples analyzed is half of seawater concentration. Those four samples also have similar SO_4^{2-} concentrations as seawater, and those samples with little total sulfur have SO_4^{2-} concentrations from half of seawater to as little as 4% of seawater sulfate (SO206-04). In general, there is strong sulfate depletion in the samples analyzed.

Analyzed samples also have both more and less Cl^- and Br^- than seawater. In general, depletion and enrichment of both species occur in the same samples. The lowest Cl^- (523.6 mM) and Br^- (0.820 mM) concentrations occur in the same sample (SO207-02), and the highest Cl^- (587.9 mM) and Br^- (0.900 mM) concentrations also occur in a single sample (SO208-04). Note that two samples (SO210-01*u* and SO210-06*u*) have much higher Cl^- (777.1 and 694.0 mM) and Br^- (1.179 and 1.066 mM) concentrations. Both have Cl/Br comparable to seawater (659 and 651, respectively; SW = 651). Sample SO210-06u was too small for cation analysis, and major cation (Na, Ca, and Mg) ratios with Cl are less than seawater, while all other samples have Na/Cl > seawater and Mg/Cl < seawater and much less than other samples. We consider these values suspicious because the anion concentrations are so far from seawater values and the adjacent, lower samples have values more in line with the rest of the sample set. These two samples are excluded from further analysis, but because there is no compelling evidence for how the samples may have been altered, the values are nevertheless reported.

TABLE 3 | Sediment headspace gas results.

Dive #-site	Sample ID	Vol (cc)	CH_4 (mM)	$\delta^{13}C$ (‰)	1σ (‰)	Repl	Gas detection			
							Ethane	Propane	Butane	Benzene
SO203-BG	SO203-04	3	0.06	ND						x
SO203-01	SO203-07a	3	0.03				x			x
SO203-01	SO203-07b	6	0.12	–50.62	0.04	2	x			x
SO203-02	SO203-03a	3	0.01					x		x
SO203-02	SO203-03b	6	0.03							x
SO204-03	SO204-04a	3	2.17	–49.60	0.14	2				x
SO204-03	SO204-04b	6	11.91	–70.15	0.04	2	x			x
SO205-02	SO205-02a	3	absent	ND						x
SO205-02	SO205-02b	6	0.08	ND						x
SO205-BG	SO205-03a	3	0.01	ND			x			x
SO205-BG	SO205-03b	6	0.09	ND						x
SO206-09	SO206-02a	3	14.52	–53.41	0.05	2	x			x
SO206-09	SO206-02b	6	9.21				x			x
SO206-10	SO206-04a	3	10.48				x			x
SO206-10	SO206-04b	6	11.22	–53.12	0.05	2	x		x	x
SO207-01a	SO207-02a	3	38.51	–47.76	0.26	3	x			x
SO207-01a	SO207-02b	6	0.88	–45.65	0.34	2	x			x
SO208-02	SO208-01a	3	0.11							x
SO208-02	SO208-01b	6	0.04				x	x		x
SO208-02	SO208-04a	3	1.01	–66.58	0.08	2				x
SO208-02	SO208-04b	6	1.06	–70.56	0.06	2	x			x
SO209-01	SO209-02a	3	12.09	–83.08	0.10	2	x			x
SO209-01	SO209-02b	6	7.84	–84.64	0.16	2	x			x
SO209-01	SO209-03a	3	19.66	–76.08	0.29	2	x			x
SO209-01	SO209-03b	6	17.62				x			x
SO210–02	SO210-01a	3	20.31	–60.78	0.35	2	x			x
SO210-02	SO210-01b	6	17.78	–61.98	0.28	2	x			x
SO210-02	SO210-03a	3	0.06	–53.82	0.17	2	x	x		x
SO210-02	SO210-03b	6	0.04							x
SO210-03	SO210-06a	3	28.21	–67.41	0.39	2	x			
SO210-03	SO210-06b	6	9.34	–70.40	0.01	2	x			x

Concentrations given in mM/L, and $\delta^{13}C$ values referenced to PDB standard. ND = Not Determined (too little gas for analysis). Repl column indicates number of replicate analyses of gas measured to achieve reported $\delta^{13}C$ value.

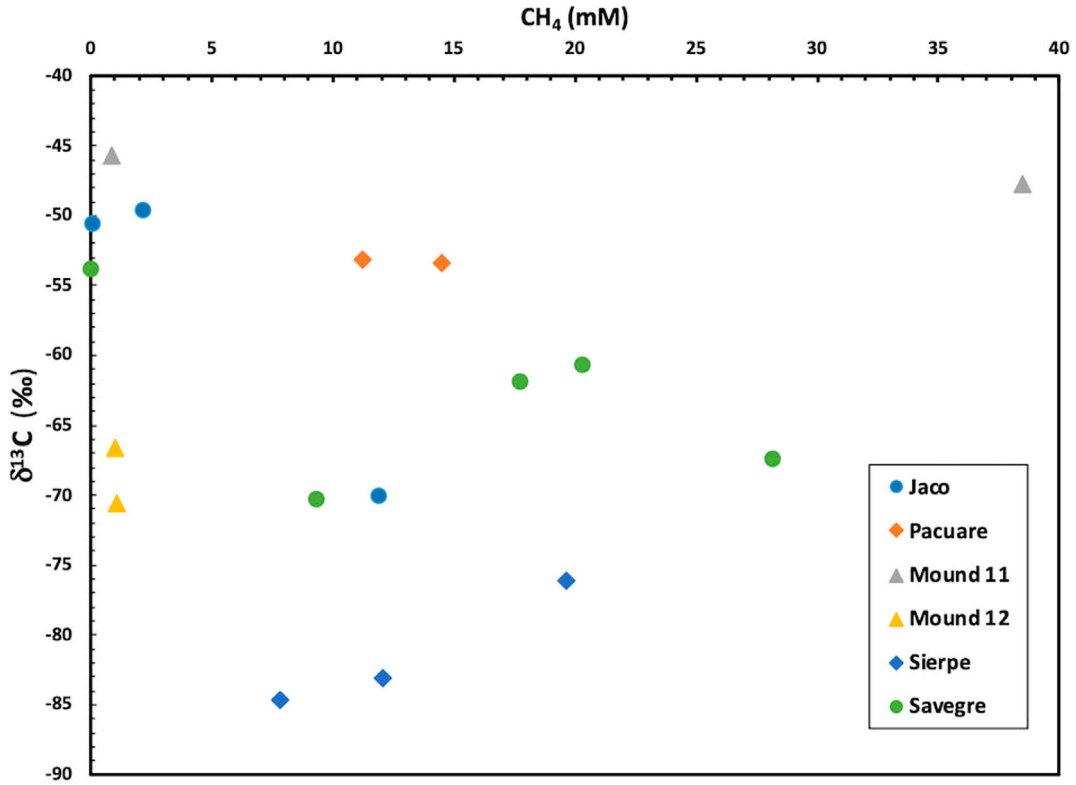

FIGURE 7 | Headspace methane gas concentration vs. carbon isotope ratio of methane. Methane gas concentration ranges from negligible to 38.5 mM, and carbon isotope ratios range from −45.7 to −84.6‰ PDB, covering spectrum from thermogenic to biogenic methane. Note that two samples from Mound 11 differ in methane concentration but yield similar carbon isotope ratios; these are two samples taken at different depths in same core and suggest recent influx of methane in order to create a large concentration gradient.

Stable Isotope Analyses

Oxygen and hydrogen isotope ratios of pore waters cluster around seawater values (**Table 2**). Oxygen isotope ratios are all within 0.2‰ of seawater, and hydrogen isotope ratios are within 2‰ of seawater. The greatest deviations from seawater are uncorrelated between oxygen and hydrogen isotope ratios.

Headspace Gas Samples

Methane Concentration and Ethane, Propane, and Benzene Detection

Methane gas concentrations range from negligible to absent up to 38.5 mM (**Table 3**). A cluster of samples with methane concentrations <1 mM (**Figure 7**) consist of samples taken as background samples and seep samples. A second cluster of samples range from 1 to 10 mM, and the biggest group of samples have methane concentrations between 10 and 40 mM. Local background values range from 0.5 to 2.0 nmol/L (Mau et al., 2006). Ethane is detected in most samples, especially those from Dives 206, 207, 208, 209, and 210, but propane is detected in only three samples. Benzene occurs in all but one sample.

Methane Isotope Ratios

Carbon isotope ratios of methane gas range in value from −45.7 to −84.6‰ (PDB; **Table 3**). Samples with the lowest methane concentrations (<5 mM) record isotopic ratios that range from −45.7 to −70.6‰ while samples with higher methane concentrations include the full spectrum of carbon isotope ratios (**Figure 5**). Two seep arrays show decreasing carbon isotope ratios with increasing methane concentration (Jaco and Savegre). Methane analyzed from Mound 11 has similar isotopic ratios but different gas concentrations, Pacuare also has similar isotopic ratios but for similar methane concentrations, Mound 12 records low methane concentrations and similar isotopic ratios, and Sierpe records an increase in carbon isotope ratio with increasing methane concentration (**Figure 7**).

CTD Water Samples

Two CTD water samples were collected in the middle of a gas plume sampled in april and May, 2002 and interpreted by Mau et al. (2006) to be sourced from a seep on the Jaco Scar (their CTD 7). We collected samples at 1780 and 1800 mss where Mau et al. (2007) encountered methane concentrations between 50 and >200 nmol/L with an average of 85.2 nmol/L.

We found methane concentrations with an average of 52.0 nmol/L with individual values as great as 72.6 nmol/L (**Supplementary Table S5**). While these values are on the low end of methane concentrations measured by Mau et al. (2007), they are still well above the concentrations measured by Mau et al. (2014)

outside the plume (7.1 nmol/L) and at offset background sites (1.9, 1.3, and 0.8 nmol/L). In addition, we measured C3 concentrations (average = 17.0 nmol/L) that are also above the methane background concentrations.

In Situ Mass Spectrometer Results

Water column chemical anomalies identified by the ROV's payload mass spectrometer (**Supplementary Table S6**) are a rare fraction of the *in-situ* measurement record (n = 3170) for methane, ethane, hydrogen sulfide, propane, carbon dioxide, and benzene (representing 1.5%, 0.88%, 0.28%, 1.1%, 1.8%, and 0.32%, of the sample record, respectively). Methane, carbon dioxide, and propane anomalies exhibit correlation across all ROV dives, but the relative magnitude of these water column anomalies appear to be independent of sediment headspace gas sample concentrations collected at neighboring locations. The relative magnitudes of propane anomalies are highest when the carbon isotope ratio of methane in an adjacent sample is less negative. Of the 46 methane anomalies recorded on Dives 204–210, 36 occurred within the limits of seep clusters previously mapped. CO_2 anomalies are the most abundant of the monitored analytes and had the highest discovery rate outside of seep clusters (8 of 58 anomalies). Ethane and propane anomalies are less common but were also detected on all dives, both species of anomalies occurring most often during Dives 204 and 210. All but 4 out of 28 (ethane) and 34 (propane) anomalies occur within mapped seep cluster boundaries, and the 4 exceptions are co-located with one another.

In contrast to the headspace gas samples, benzene was only detected during Dive 204 (9 anomalies) and 208 (1 anomaly). Seven occurrences of H_2S anomalies were recorded on Dive 204, and one each during Dive 208 and 210. All H_2S anomalies occur within seep clusters and are associated with seeps (including bubble plumes) on Dives 208 and 211.

An ROV data logging failure prevented simultaneous recording of analyte water stream temperature, precluding estimation of chemical species concentrations in absolute terms. If these anomalies are considered within the context of depth-dependent temperature records logged by same-day CTD casts, the ion peak data indicate mole fraction anomaly ranges above background of between: 10 ppb and 10 ppm for methane, 10 and 100 ppb for ethane and propane, and 1 and 10 ppb for benzene. Fragmentary temperature logs suggest that analyte fluids with elevated temperatures may have contributed to an amplification of ion intensity anomalies detected in the vicinity of the Jaco scar.

Mapping Synthesis and Seep Classification

Based on ship-based mapping, ROV observations, and sample analyses, we classified each seep location as (**Table 1**): 1) Active Strong, requiring the presence of microbial mats or clams, a headspace methane concentration >10 mM, and optional observation of bubble plume(s); 2) Active Weak with a seep biologic community but headspace methane concentration from 1 to 10 mM; 3) Dormant, where carbonate crusts and seep biota reflect past active seepage, but for which there is no evidence of methane in headspace gas samples and microbial mats and clams that require high methane flux are absent; and 4) Non-seep, where no biologic, chemical, or physical evidence of seepage is present. This classification is necessary for algorithmic seep predictions.

Predicted Seep Candidates and Outcomes

Spock was used to plan most ROV dives and two AUG missions incorporating new data collected during the expedition. Early Spock dive plans were compared with independent plans constructed by humans, and subsequent plans were only checked by humans, thereby freeing staff to devote more time to new data analysis and interpretation. Further details on Spock implementation are described in **Supplementary Material**.

Prior to the cruise, Spock was trained on bathymetric feature presence and backscatter data derived from previous cruises on the Costa Rican active margin (Sahling et al., 2008). Features that were absent from this training data were instantiated with priors that reflected their expected influence on seep probabilities (i.e. expert opinion).

Previously detected seepage at a site and high confidence evidence of bubbles were instantiated with strong positive priors so that sites with those features were more likely to show evidence of seepage (**Table 4**). Medium confidence bubble signatures were instantiated with a weaker positive prior. Low confidence bubbles and high slope were predicted to influence probability of seepage, but the impact, whether positive or negative, was unknown a priori. These features were instantiated with an uninformative prior that initially did not influence predictions. The effects of those features were learned through data gathered on the cruise.

Table 4 records predicted seep probabilities for the feature combinations visited by Spock alongside truth values for how many of those sites had seepage present. Prior probabilities are based on training data only, while posterior probabilities are based on both training data and data gathered during the cruise (**Table 1**; Active Strong and Active Weak seeps are counted as seeps present in this analysis, and Dormant or Non-seep results are seeps absent). Empirical probabilities with 1 standard deviation (1σ = 68%) confidence intervals are computed using the Wilson score interval for binomial events (Wilson, 1927; Wallis, 2013), but most feature combinations lacked sufficient information to compute meaningful average values.

Few sites were visited for each combination of features, and this introduces significant uncertainty into empirical measures of seep presence probability. The prior probabilities of elevated backscatter, mounds with elevated backscatter, and elevated backscatter with high confidence bubbles are within the 1σ confidence interval of the empirical seep probabilities. The predictions reflect the algorithm's belief that areas of high slope interpreted as normal fault scarps have a low probability of seepage, but high confidence bubbles are strongly associated with seeps, both of which held true throughout the cruise. Unmodeled bathymetric features, like flat seafloor, valleys, and ridges (**Table 1**), yielded no examples of seeps without further supporting indications (high backscatter or high confidence bubbles).

When observations from the cruise are included, modeled probabilities for seeps along high slopes and unmodeled bathymetric features drop and align better with empirical

TABLE 4 | Seep presence and probabilities—Spock results.

Features at site	Number with seep present/absent	Empirical seep probability	Prior seep probability	Posterior seep probability
Elevated backscatter	6/4	0.59 ± 0.15	0.678	0.639
Elevated backscatter, high slope	0/1	ID	0.674	0.368
Elevated backscatter, previously observed seepage	1/0	ID	0.906	0.928
High slope	0/3	0.13 ± 0.13	0.390	0.069
Unmodeled bathymetric features	0/4	0.10 ± 0.10	0.392	0.139
Mound, elevated backscatter, high confidence bubbles	1/0	ID	0.582	0.840
Mound, elevated backscatter	3/6	0.35 ± 0.15	0.225	0.212
Elevated backscatter, low confidence bubbles	1/0	ID	0.655	0.736
High confidence bubbles	2/0	ID	0.723	0.775
Mound	0/1	ID	0.079	0.022
Elevated backscatter, high confidence bubbles	3/0	0.88 ± 0.13	0.903	0.976
Mid confidence bubbles	0/2	ID	0.673	0.325
Elevated backscatter, pockmark	0/1	ID	0.847	0.738

Features column lists individual and combinations of features. Number column indicates observations of seeps present or absent. See text for explanation of different probabilities. ID = Insufficient Data (i.e. too few observations for meaningful calculation of mean probability).

probabilities, illustrating the benefit of expanded datasets. All predictions are within the empirical 1σ confidence interval, and the mean deviation from the maximum likelihood empirical estimate drops to 0.115. The greatest change in pre- and post-cruise probabilities, both increase and decrease, arise from feature combinations that were rare or absent from the training set (e.g., high slope presence and mid-confidence bubble signatures).

In addition to generating probabilities of seepage, Spock can extract a relative measure of the impact of each feature on the probability of seepage (**Table 5**). The algorithm produces an expected probability of seepage conditioned on the feature being present, and a probability conditioned on seepage being absent. If the former is larger, it indicates that seepage is more likely when the feature is present, so the feature has a positive impact. In the opposite case, seepage is more likely without that feature. If the two are identical, seepage is just as likely regardless of whether the feature is present, and so the feature has no impact. While the relative influence of most features remains unchanged, the ranking of individual features shifted with the cruise results.

DISCUSSION

We applied a series of new and established technologies to search for seeps on the Costa Rica accretionary margin:

1) Water column imaging from MBES and a novel AUG Doppler sonar survey
2) *In situ* mass spectrometry to identify hydrocarbons dissolved in ocean water that complement traditional core and CTD water analyses and help ascend a Ladder rung in our search for deep-sourced fluids
3) A decision-support system based on a Ladder of Seeps that helps define the data required to reach a specific scientific conclusion and Spock, a computer algorithm designed to use low resolution screening data and expert opinion to identify higher probability seep targets

Did these steps prove useful in improving operational efficiency and success rate in the search for higher probability, deep-sourced seep sites?

To evaluate the impact of our approach, the state of knowledge before the Falkor expedition must be defined. Sahling et al. (2008) conducted "a systematic search for methane-rich seeps at the seafloor" and documented >100 seeps. This compilation was based on 4 separate research cruises between 1999 and 2003, each cruise requiring approximately one month of ship time, plus additional bathymetric data collected earlier (Ranero et al., 2003). However, the resolution of the regional bathymetric map used for this analysis was only 100 m (von Huene et al., 2000; Ranero et al., 2008), which limited the scale of features that could be identified (>100 m). While this scale of observation was sufficient to detect the major seep clusters mapped in this study, some of the smaller seep clusters would have gone unrecognized (e.g., SC5 in SA1: Pacuare, **Supplementary Materials: Seep_Array_Documentation.pdf**). The Sahling et al. (2008) compilation contains a mixture of sites where seep biota confirm the need for fluid flux from below the seafloor, and sites where possible seep candidates are defined by seafloor morphology and acoustic backscatter. Subsequent Alvin dives (e.g., seeps 64 & 68; Sahling et al., 2008) demonstrated that

TABLE 5 | Relative impacts of individual features at beginning and end of cruise.

Feature	Prior impact	Posterior impact
Previous seepage	++ (1)	++ (2)
High confidence bubbles	++ (2)	++ (1)
Medium confidence bubbles	++ (3)	++ (3)
Elevated backscatter	+ (1)	+ (1)
Pockmarks	+ (2)	+ (3)
Low confidence bubbles	None (1)	+ (2)
High slope	None (2)	-- (1)
Mounds	--	-- (2)

++: Strong Positive, +: Weak Positive, None: No impact, -: Weak Negative, --: Strong Negative, (#): Numbers reflect order ranking within category.

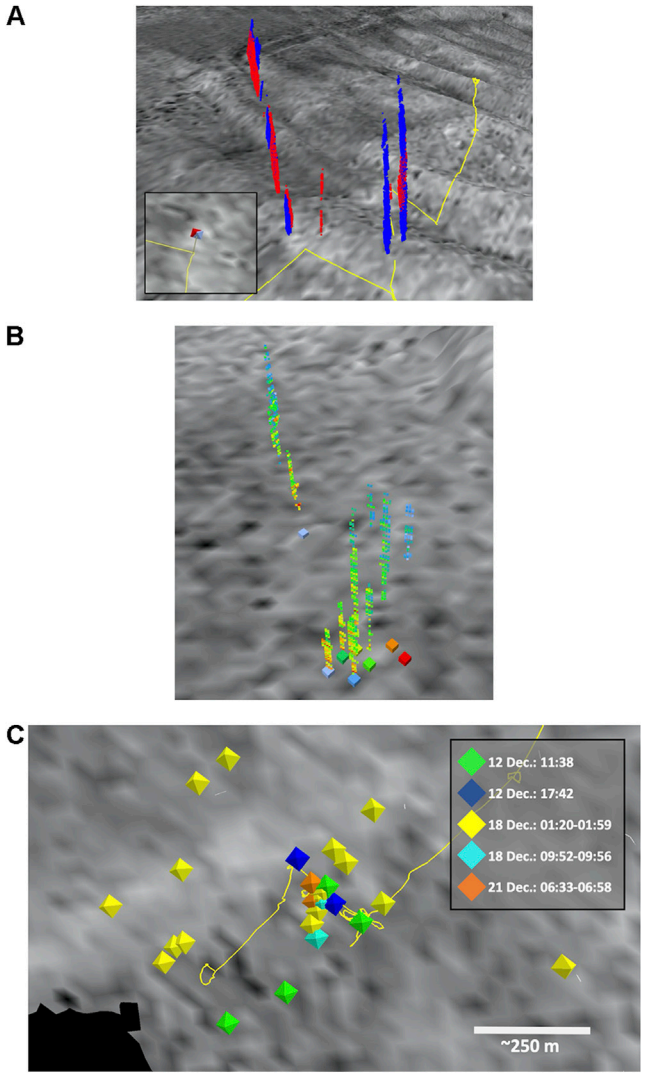

FIGURE 8 | (A) Comparison of EM302 (blue) and EM710 (red) bubble plumes in SA1: Pacuare. Excellent overlap of points recorded at same time supports interpretation that both sonars imaging same plumes. Plumes on left side near sharp corner in ROV path (yellow line) are SC2. Inset figure shows seafloor source of S1 (blue) and S2 (red). Distance along yellow ROV path between the two seep clusters ~450 m. **(B)** Moderate confidence anomalies identified on EM710, SA2: Savegre-SC3. No comparable anomalies are apparent on EM302 data, offering evidence of false negative in 30 kHz data. Colors in water column anomalies represent acoustic backscatter amplitude with red colors at +10 dB and light blue colors at –9 dB. Distance between main grouping of plumes and outlier plume ~380 m **(C)** Time series of EM302 data, SA2: Savegre-SC2. While anomalies were observed at all times, number of anomalies varies over 9-days timespan.

some of the seep candidates classified as seeps had no evidence of seepage. Using the Ladder of Seeps, this distinction includes Seeps (confirmed flux) and Possible Seeps. Moreover, seeps described by Sahling et al. (2008) include seep clusters and seep arrays from our mapping hierarchy, both of which contain multiple individual seeps.

In addition to testing our approach at established seeps, the Falkor expedition documented 24 seep clusters and numerous additional isolated seeps never before described with only a single 10-days cruise. Fourteen of the newly identified seep clusters occur in 3 seep arrays: SA1: Pacuare, SA2: Savegre, and SA5: Terraba, and these 3 seep arrays alone may account for a substantial fraction of the total subsurface fluid flux released into the ocean along this part of the margin.

Application of Modern Acoustic Methods

A significant contributor to our success was the use of modern MBES swath-mapping systems and collection and analysis of water column backscatter data unavailable during the previous *R/V Sonne* and *Meteor* expeditions. While the benefits of water column data to regional seep surveys is established (e.g., Skarke et al., 2014; Weber et al., 2014), this study further strengthens the value of collecting, processing, and interpreting water column data by documenting another successful example. The Falkor MBES systems resulted in a >3× improvement in seafloor resolution (30 m) and a continuous backscatter map (15 m), allowing a more detailed description of seafloor geomorphic forms and a better appreciation of nested geomorphic forms (e.g., Jasiewicz and Stepinski, 2013). However, as demonstrated by the Alvin dives referenced above, the use of bathymetric morphology and seafloor backscatter alone yields an incomplete picture of seep occurrence, including false negative interpretations.

The Ladder of Seeps requires a critical examination of each sonar system (**Supplementary Table S7**) and its ability to help ascend from a Likely Seep to Seep (**Figure 2**). One examination is based on a comparison of acoustic anomalies derived from each of the shipboard MBES systems (**Figure 8A**) because the data are collected at the same time, which reduces the uncertainty created by varying seep flux over time. This analysis documents fewer anomalies recorded by the 70 kHz data (**Supplementary Material**), which is attributed to a smaller swath width (i.e. less water column interrogated), higher frequency energy interacting with bubble plumes differently (i.e. bubble size distribution), and a lower signal-noise in the 70 kHz data. However, the 70 kHz data also identify anomalies unseen in the 30 kHz data (e.g., SA3: Savegre—SC3; **Figure 8B**).

The manner of multiple ship operations also provides a time record of bubble plumes with as many as five observations made over 9 days (**Figure 8C**). The details of this comparison are provided in **Supplementary Material**, but the complexities of varying seep flux, changing ocean current directions and magnitude, and uncertainty in seafloor source locations make comparison of specific seeps difficult to impossible. While a multitude of sonar issues (e.g., static offsets and ray-tracing errors) can affect the location of water column anomalies in space, we think the biggest potential error arises from the extrapolation of water column points, especially when the base is above the seafloor, back to its seafloor source. However, comparing seeps within a seep cluster is feasible (**Figure 8C**), and the spatial scale of clusters is comparable to the grid dimensions used by Spock (50 m), which minimizes the impact of small errors locating individual seeps. Within the 9-

days observation period most seep clusters remain active although the number of individual seeps will change. There are seep clusters (e.g., SA3: Savegre—SC3; **Figure 8B**) that are only observed at one time (two observations).

Acoustic anomalies recorded by the AUG sonar provide a novel contribution to the time history of seeps. The AUG sonar recorded acoustic anomalies near anomalies documented by EM302 and EM710 data (**Figure 5**), but additional anomalies are identified farther from established anomalies. These may be false positive results, or they could reflect lower bubble fluxes or smaller bubble sizes-further research is required to work out the limits of this new approach. Nevertheless, the potential for an AUG sonar to document a long-term time record of seeps identified by ship-based sonars is tremendous.

Long-Term Episodic Behavior of Seeps and Seep Durability

Because this is a well-studied margin and our cruise revisited documented seep locations, our results contribute to the record of decade-scale seep durability. However, previous authors apply the term seeps at a multitude of scales so some translation of previous results into our seep/seep cluster/seep array hierarchy is required. Comparison of individual seeps at a scale of 2–5 m—well below mapping resolution—is difficult to impossible so a more feasible objective is comparison of seep clusters and seep arrays.

The crest of the Jaco scar was identified as a site of active seepage (Sahling et al., 2008), and our expedition recovered CTD samples with methane well above background at the same sites sampled by Mau et al. (2014). Some of the seep clusters within SA4: Jaco (SC3, 4, 7, 8 in **Table 1**) contain well-developed deep-sea corals that would have used seep-related carbonates as a substrate. There was limited evidence along our ROV dive paths, however, for bacterial mats or other fauna that require a continuous, currently active source of methane, and no water column acoustic anomalies were observed, suggesting that at least some of the seeps are dormant. However, our Jaco seep sites visited by ROV are different than those studied by Mau et al. (2014) so even though they documented seep evolution on the year timescale with subsequent cruises, we can only confirm that the Jaco seep array maintains evidence of seepage on a 15- years timescale.

Previous expeditions to Mounds 11 and 12 collected methane flux observations between 2002 and 2009 (Linke et al., 2005; Mau et al., 2006; Füri et al., 2010; Tryon et al., 2010; Levin et al., 2015). All expeditions observed elevated methane concentrations near the seafloor. In 2005, the *R/V* Atlantis (AT-11-28) deployed submarine flux meters for 12 months (Füri et al., 2010). High-flux events were observed near the beginning and end of the deployment, as well as in late Sept-early Oct 2005, approximately midway through the deployment (Füri et al., 2010). Füri et al. (2010) also noted episodic free gas expulsions at Mounds 11 and 12 in the Spring of 2009 (RV Atlantis AT 15–44). Combining our observations with these previous data leads to the recognition that the Mound 11 seep system (our SA3: SC4) remains active on the days, weeks, months, year-long, and 15- years timescales, and the adjacent Mound 11 seep cluster (SA3: SC3) visited by Tryon et al. (2010), where they observed mats, may have become dormant (**Table 1**). Comparing our results for Mound 12 with previous work is complicated by the fact that Tryon et al. (2010) report no location information for their observations, but both of the seep clusters that we observed (SA3: SC1 and SC2) had either ROV-observed bubbles or mats (**Table 1**), consistent with the record of mats by Tryon et al. (2010) at Mound 12 and the observation of seep biota on the seafloor and methane in seawater above Mound 12 by Mau et al. (2006). On this basis, we conclude that Mound 12 has remained an active seep for 13 years or more. U/Th dates of the seep-derived carbonate at the two sites range from 3.4 to 10 ka (Kutterolf et al., 2008), reflecting a protracted history of seep processes during which shorter period processes wax and wane.

All of the observations regarding short- and long-term seep episodicity and durability suggest that the search for active seeps is best conducted at the scale of seep clusters and arrays, with a search duration of at least 1–2 weeks. Autonomous approaches such as AUG water column mapping coupled to Spock's decision-making capabilities constitute a possible breakthrough in our ability to identify and map these systems efficiently and at low-cost.

Seep Fluid Chemistry and Sources

The goal of this study is to improve the chances of finding seeps with deep-sourced fluids using a Ladder of Seeps framework. Inorganic fluid chemistry is critical to this effort as a means of gaining insights into silicate mineral reactions in seismogenic intervals (e.g., Moore and Vrolijk, 1992). Because fluid volumes at seismogenic depths (ca. 10–15 km) are small compared to the fluid volume in near-surface, porous sediments, extreme dilution of deep fluids is expected for shallow samples. Organic gases serve as a deep-fluid proxy if compounds are discovered that only form at elevated temperatures.

The characteristics of deep-sourced fluids along the Costa Rican margin, defined by ODP Leg 170 and IODP Expedition 334 samples and analyses, include lower salinity fluids (e.g., Silver et al., 2000), Li and Ca enrichment (Chan and Kastner, 2000; Kopf et al., 2000; Torres et al., 2014; Expedition 334 Scientists, 2011) and elevated B (Kopf et al., 2000). In addition, higher hydrocarbons are found in active subduction faults (Lückge et al., 2002), and ethane is interpreted as coming from a thermogenic source based on carbon isotope ratios.

We applied three methods to seek deep-sourced fluids. Two methods (CTD water samples and *in-situ* mass spectrometry; **Figure 2**, top Ladder rung) search for dissolved hydrocarbon gases in the ocean that reflect deep-sourced fluids. The final method, samples from sediment cores, yields more detailed information on proxy gases and inorganic chemistry. The mass spectrometer deployed on the ROV produces a larger dataset (ca. 3100 samples vs. 16 sediment and two CTD water samples) collected while undergoing other tasks, and it allows qualitative identification of anomalies in real-time. Sediment and CTD water samples require dedicated ship time to collect and the technical experience to choose the 'best' sample locations, but they provide more detailed information about concentrations and isotopic ratios as well as inorganic species. The benefits and limitations of each method are outlined in **Supplementary Table S7**, but our synthesis suggests that a combination of approaches

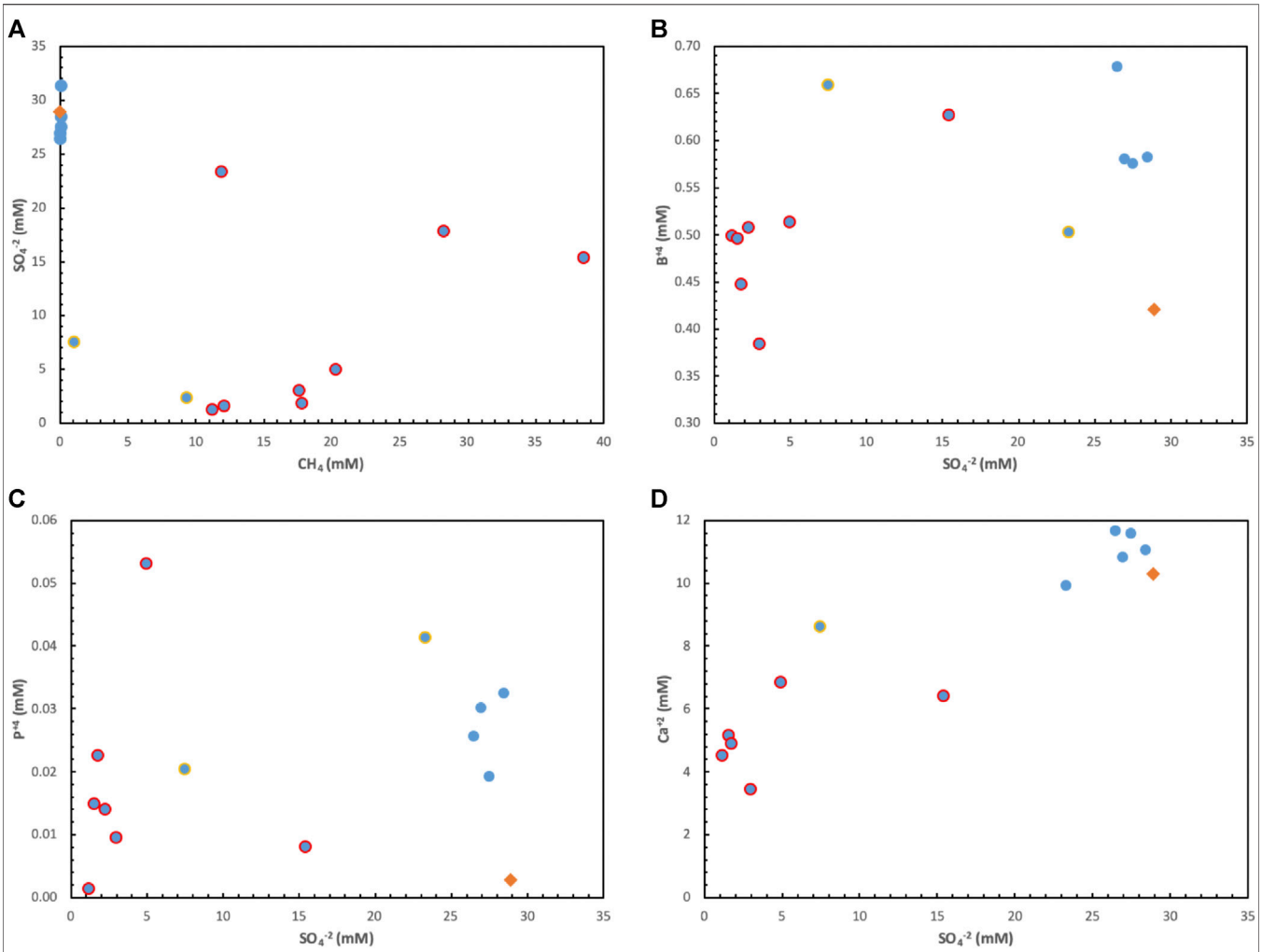

FIGURE 9 | Pore water summary graphs for methane alteration processes. In each plot orange diamond is seawater reference. Samples with >10 mM methane outlined in red, and 1–10 mM methane outlined in orange. Methane-poor samples (<1 mM) have no outline. **(A)** Head-space methane gas concentration vs. pore water sulfate concentration. Many methane-rich samples are depleted in sulfate. **(B)** Sulfate vs. boron concentration in pore waters. Methane-poor samples enriched in B with respect to seawater, reflecting organic matter degradation without sulfate reduction. Most methane-rich samples have B concentrations closer to seawater. **(C)** Sulfate vs. phosphorous concentration in pore waters. Methane-poor samples enriched in P with respect to seawater, reflecting organic matter degradation without sulfate reduction. Most methane-rich samples have P concentrations closer to seawater, but 2 methane-rich samples have high P concentration. **(D)** Sulfate vs. calcium concentration in pore waters. Methane-poor samples have sulfate and Ca concentrations near seawater but methane-rich samples have depleted sulfate and Ca from carbonate precipitation.

provides the greatest confidence in ascending the ladder to the top rung: confirmed deep-sourced fluids.

The inorganic geochemistry of pore waters offers no compelling evidence for deep-sourced fluids. While some measurements of Cl are below seawater values, as low as 524 mM/l, these values remain closer to seawater chlorinity than the values found in ODP drilling (Silver et al., 2000), and our samples' proximity to hydrate makes Cl variations from hydrate formation/disassociation difficult to exclude. Li concentrations (**Table 2**) are lower than seawater concentrations, consistent with the observations of Torres et al. (2014), and the one sample with more Li than seawater is well below the Li concentration inferred to reflect deep fluid sources (74 μM; Torres et al., 2014 and up to 148 μM, Kopf et al., 2000). Measured calcium concentrations are likely primarily affected by abundant carbonate crust formation, and indeed most values are below seawater concentration (**Table 3**). While some samples have B concentrations above seawater, these are interpreted as resulting from alteration of organic matter (see below).

Methane is one species that is found in high concentrations with respect to seawater. In **Figure 9A**, samples are divided into those with <1 mM concentration (blue border), 1–10 mM (orange border), and >10 mM (red border). Samples with no methane have near-seawater sulfate concentrations. In many methane-rich samples, sulfate is almost exhausted. Samples without methane have >2× B than seawater (**Figure 9B**), much more P than seawater (**Figure 9C**), and near-seawater

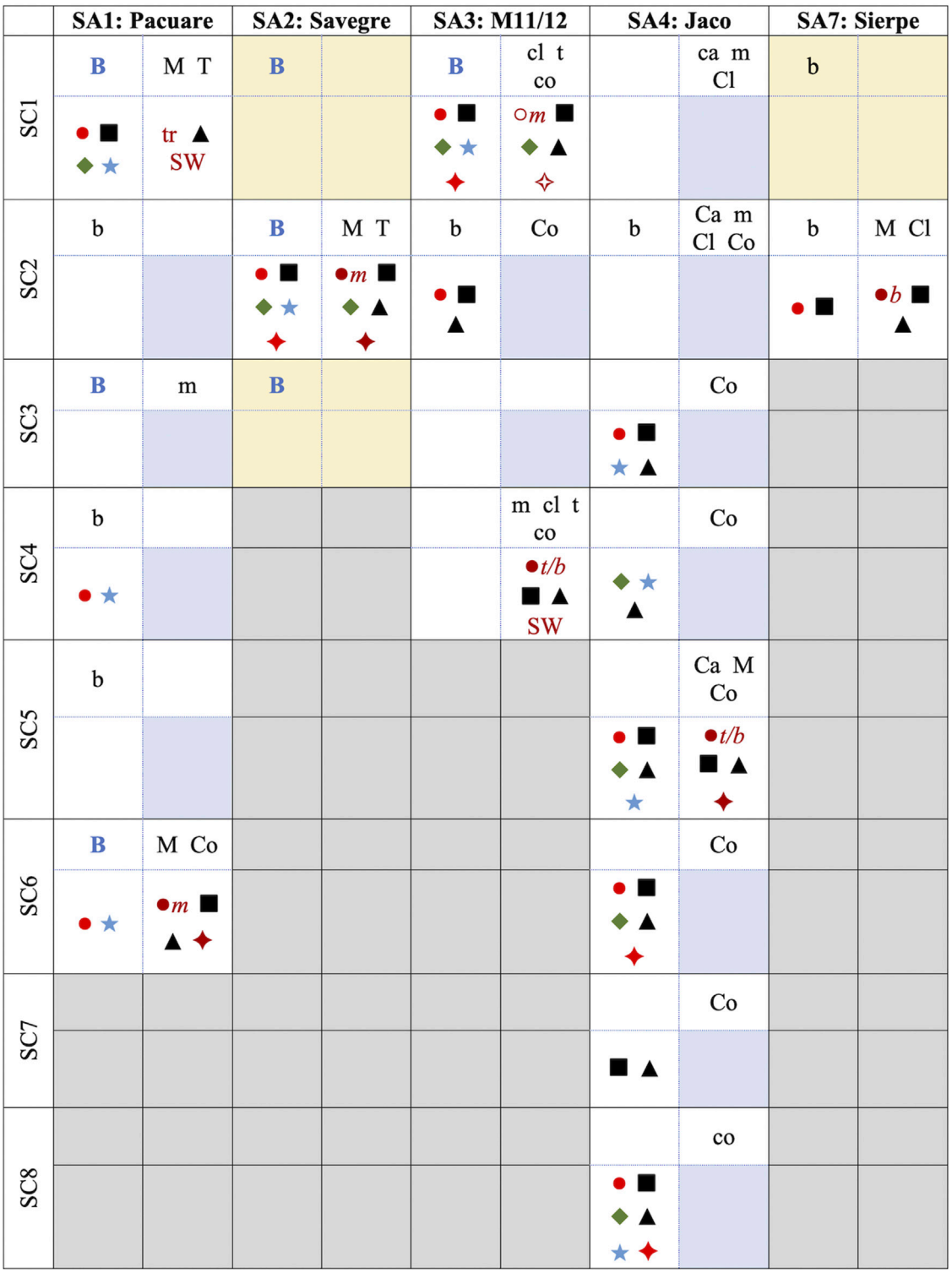

FIGURE 10 | Synthesis of seep results. Data arranged by seep array (columns) and cluster (rows); gray boxes indicate no seep cluster defined, orange boxes reflect seep clusters unvisited by ROV, and blue boxes visited by ROV but no samples obtained. Each seep cluster divided into 4 observation types: 1) acoustic anomalies/bubble plumes (upper left); **B**: 5 + plumes, b: <5 plumes, and blank = 0 plumes; 2) observed seep biota and substrate (upper right) where upper case indicates major component and lower case is minor component; M: mats; T: tubeworms; Cl: clams; Co: corals; Ca: carbonate; 3) mass spectrometer anomalies (lower left); ●: methane; ethane; ◆: propane; ▲: benzene; ★: carbon dioxide; ✦: hydrogen sulfide); 4) pore water and head-space gas results from push cores (lower right); ●: methane >20 mM; ○: methane = 1–10 mM; tr: methane <0.1 mM; ethane; ◆: propane; ▲: benzene; ✦: sulfate = 0–5 mM; ✧: sulfate = 2–20 mM; SW: sulfate = >20 mM; letters following methane symbols indicate $\delta^{13}C$ ratios: *t*: -40 to −50‰; m: −50 to −65‰; b: < −65‰.

Ca concentrations (**Figure 9D**). This pattern of concentrations is interpreted as alteration of organic matter contributing B and P species to porewaters without any calcite precipitation.

In contrast, the methane-rich samples have B and P concentrations much closer to seawater values, and calcium concentrations are half or less than seawater concentrations. For these samples the source of carbon is methane, which is consumed by Anaerobic Oxidation of Methane (AOM; e.g., Milucka et al., 2012), which results in no change in B or P concentrations. AOM reactions consume sulfate (Milucka et al., 2012), resulting in the near exhaustion of sulfate in methane-rich samples.

Carbon isotope ratios of methane show no clear pattern with methane concentration (**Figure 7**) but range from values around −50‰ that could reflect thermogenic methane and values as low as −84.6‰, which represent biogenic methane. Interpretation of thermogenic methane at Mound 11 (**Figure 7**) is consistent with more detailed analyses, as is the biogenic gas interpretation for Mound 12 (Schmidt et al., 2005; Füri et al., 2010; Krause et al., 2014).

In headspace gas samples, ethane, propane, and benzene are detected (**Table 3**), but the gas concentrations remain unquantified. Propane and benzene occurrences are especially critical because there is a high probability that they are only produced by thermal cracking of organic matter. Moreover, *in-situ* mass spectrometer measurements (**Figure 10**) indicate propane and benzene anomalies at just over half of the seep clusters visited, and in just over half of those sites they occur together. Even though carbon isotope ratios of methane samples indicate a large biogenic gas component in many samples, the presence of propane and benzene in samples suggests that seeps at all dive sites have some unquantified fraction of thermogenic gas.

While it is tempting to try to work out biogenic/thermogenic gas proportions based on carbon isotope ratios, the problem is further complicated by AOM processes that can increase the carbon isotopic value of residual methane if methane conversion is incomplete (e.g., Whiticar, 1999). Sulfate concentrations in pore water combined with flux inferences derived from seep biota (e.g., mats reflect high fluxes) could constrain AOM reaction progress, a necessary variable in the Rayleigh distillation problem arising from incomplete AOM consumption. Preliminary calculations suggest that our data suite remains too unconstrained to provide meaningful estimates of thermogenic gas proportion.

In summary, hydrocarbon gases offer good evidence for deep-sourced fluids, and on this basis, we confirm access to a deep fluid source at Mound 11 and suggest that most or all sites have received some component of thermogenic gas. While AOM complicates interpretation of a thermogenic gas from carbon isotope ratios, the presence of propane and benzene are proxy indicators of a thermogenic gas component. If Spock were expanded to rank the probability of sampling a higher concentration of deep-sourced fluids in subsurface samples (e.g., by scientific drilling) at each seep cluster, then an evolved approach that yields an improved estimate of the fraction of thermogenic gas is warranted.

Utility of Decision-Support Systems

Formal decision-support systems offer a number of benefits for documenting important decisions undertaken during scientific investigations and rendering them reproducible. These systems require a clear definition of what constitutes advancement and success, and the Ladder of Seeps was developed as a foundation for this purpose. A crucial aspect of decision-support systems is that they tolerate analytical uncertainty that may arise from processing and interpreting data quickly *if that uncertainty has no appreciable impact on the probability distributions used by Spock*. In other words, the use of a decision-support system specifies where back-of-the-envelope results are sufficient, and where results must be produced at a high precision. All of the data collection and analysis efforts in our study follow this principle (e.g., construction of a seafloor backscatter product using a generic processing workflow).

As deployed on this expedition, Spock was intended to improve the probability that visited sites could ascend to the 'Seep' rung in the Ladder of Seeps. Conceptually, this is performed by analyzing remote observations that allow a site to be identified as 'Possible Seep' or 'Likely Seep', and identifying combinations of observations that are more likely to be associated with fluid release. Because photographic identification is used to identify seep-dependent biota and confirm the acoustic bubble plume interpretation by verifying the flux of nutrients to the seafloor, visiting the site remains necessary to move up the ladder. Spock allows the associations between combinations of features and seepage probability to be learned quickly and balances the advantage of gathering new information against the benefits of visiting sites with high probability of seepage. Using Spock to perform dive planning resulted in significant time savings, allowed dives to make use of information from the most recent observations, and generated an objective record of why specific sites were chosen for investigation. A more detailed comparison between Spock and human-planned dives in terms of time and efficacy is presented in the **Supplementary Material**.

Even though our survey area was large and many seeps were visited, the number of unique observations remains small (**Table 4**), leading to some counter-intuitive conclusions. For example, the inference that high slope areas (normal fault scarps) are a good indicator that no seeps will be found (**Table 5**) arises from the Spock search for active seeps. Normal fault scarps are most common over the Jaco Scar, but the absence of water column anomalies and the abundance of deep-sea corals led us to consider this a dormant and weak-active (SA4: Jaco—SC5) seep array. The *in-situ* mass spectrometer data recorded a large number of anomalies for all species (**Figure 10**), but we think the number of anomalies is more affected by local data acquisition conditions than seep flux. How seeps are classified is critical for Spock's success, and this is an area that requires further research to reach a scientific consensus, which in turn will lead to modifications of the Ladder of Seeps. The Ladder is an explicit description of a community picture of seep systems. The Spock algorithms will benefit from a database of priors that incorporates more global information about seeps at different scales while

retaining the flexibility to adapt to local conditions. Moreover, the means to steer vehicles away from sites that have features without demonstrated seepage is an important benefit that probably exceeds human capabilities.

As an example, Spock inferred that mounds are considered good indicators that no seeps will be found. However, this inference arises because features are defined at a scale of 50 m, a dimension chosen to ensure a high probability of finding a seep at that location if there is one to be found. Others have described mounds as an important seep element in this region, but those descriptions are at the scale of a seep cluster (e.g., Klaucke et al., 2008, describe Mounds 11 and 12 as 600–1000 m across) that is too large for efficient seep surveys. Bathymetric morphologies defined at a multitude of scales may further help identify successful seep candidates. The observation also illustrates the importance of adding water column data to Spock's priors-high predicted probabilities for Dive nine sites (with no mound) depended on the availability of preliminary water column processing.

The Spock algorithms used observations from MBES and ROV dives to improve the planning and prediction model, resulting in shifts in the relative importance of different features (**Table 5**). The rate-limiting step in this work was the processing of raw MBES data and preliminary interpretation. Even simple tasks like identifying bathymetric morphology are daunting with large datasets, in particular if considering morphologic features at multiple scales of observation. Efficient, automated systems for aiding this analysis are available (e.g., Geomorphons; Jasiewicz and Stepinski, 2013) and could be added to the workflows. The presence of water column anomalies had the biggest impact on the success of finding seeps, but it was impossible to process the water column data during the cruise with the limited staff available. While the Feature Detection filters in FMMidwater are a benefit for finding anomalies, either more staff or faster filtering methods are needed to produce precise seafloor seep locations for Spock predictions in real-time.

The combined Ladder of Seeps and Spock approach could be modified to address other pressing questions, like estimating global fluxes of chemical species from seeps (e.g., Mau et al., 2006). Improved estimates probably derive from recognizing different seep types with different time-integrated fluxes. An analogous Ladder could be constructed to help define these seep types and the data needed to confirm any particular seeps as one type at a specified confidence level, and a Spock routine could be devised to efficiently collect the necessary data to achieve a confident extrapolation to all seep candidates.

SUMMARY

To address the question posed at the outset, the combined Ladder of Seeps and Spock approach provided us an effective and inexpensive means to identify seeps with the potential to yield deep-sourced fluids. Thirty seep sites were identified and visited with 9 ROV dives over the space of only 10 days, facilitated by the application of the Ladder framework within Spock's decision-making algorithms, coupled to historical data. High resolution bathymetry and backscatter data, coupled with water column anomalies allowed us to get from Possible to Likely Seep and helped us identify successful targets for ROV dives that collected observations allowing us to ascend to the highest confirmed seep rungs.

As a result of this short expedition, we identify SA3: Mound 11 and SA1: Pacuare as good candidates to pursue subsurface data collection studies to evaluate fluid migration pathways that could be sampled via cores taken hundreds of meters below the seafloor to obtain undiluted samples of deep-sourced fluids. A fair question is whether Spock would have brought us to Mound 11 in the absence of prior seep information and the absence of bubbles, but the proximity to Mound 12, the bathymetric morphology, and the high backscatter may have sufficed. In contrast, the decision to visit SA1: Pacuare was solely Spock's and is predicated based on the high number of bubble plumes, the close proximity of seep targets, and the bathymetric morphology and backscatter character. There is no prior indication of seeps at SA1: Pacuare. Seismic imaging of potential deep fluid-flow pathways at these seep clusters would reinforce the screening data collected during this study and provide a compelling reason for scientific drilling likely to result in a high probability of scientific success. Crutchley et al. (2014), in their study of the impact of fluid advection on gas hydrate stability at Mounds 11 and 12, used 2D and 3D seismic data to illustrate possible fault-related fluid-flow pathways for the gas in hydrates at those seep sites. A similar approach could be taken for SA1: Pacuare.

The use of Spock in this expedition contributed objectivity, repeatability, and time savings to the process of dive planning. Scoring all sites ensured that promising locations were not overlooked, while continuous data assimilation meant that sites were reconsidered under the most up-to-date understanding of the environment. Further, the algorithms provided a means to optimize probability of finding seepage against constraints on ROV dive time. This optimization was performed several hours faster than an equivalent dive could have been hand-designed and allowed the science team to focus instead on data interpretation.

From a broader perspective, our use of Spock also represents a step forward in the application of automated reasoning to intelligent exploration of the oceans and planetary bodies. Autonomous exploration vehicles must be able to learn from data and reason about the priorities of observations. Spock demonstrated this capability through the prediction of seep likelihoods and selection of dive sites to maximize probability of climbing the Ladder of Seeps. Deployment of such a system would lead to more thorough examination over a longer duration than has previously been possible, without the need for frequent communication and the risk and expense of manned exploration, or the need for frequent communication with remotely operated systems.

Our research expedition set out to apply and test new analytical and decision-support systems in the search for cold seeps in the Costa Rican accretionary margin. Existing

seep locations were visited to confirm the viability of our systems against existing knowledge, but additional seep locations were also discovered with our methods. A Ladder of Seeps was developed in the context of a specific scientific goal-identify seep sites with deep-sourced fluids-and it served as a foundation for Spock, which was used in ROV and AUG dive planning to collect additional data to further ascend the ladder. Many of the new seep sites discovered are attributed to MBES water column imaging methods, but the use of AUG sonar to identify water column anomalies shows the potential to collect additional information without the use of a dedicated surface ship. Data from an *in-situ* mass spectrometer deployed on the ROV complements data collected from traditional sediment sample methods. We think that the use of advanced data collection and decision-support technologies will elevate our understanding of how cold seep systems contribute to Earth systems.

DATA AVAILABILITY STATEMENT

The datasets generated for this study can be found in the R2R repository (https://www.rvdata.us/data).

AUTHOR CONTRIBUTIONS

RC was chief scientist for the *R/V* Falkor cruise, contributed processing and analysis of AUG sonar data, operated and processed *in-situ* mass spectrometer data, and led coordination of the diverse disciplinary tasks. PV, LS, and PN guided ROV dives and recorded observations, directed and processed samples on the ship, and interpreted new MBES bathymetry and backscatter data. PV processed water column data on the ship and post-cruise and took lead responsibility for writing this manuscript. LS compiled and integrated bathymetry, backscatter, bubble plume source, and Squidle+ data into maps and described those processes and results in this manuscript. BA executed missionplanning algorithms (Spock) on the ship and wrote up those processes and results here. AH collaborated on pore water chemistry analyses, FK measured methane concentrations in headspace gas and CTD water samples, and DV provided the laboratory resources for methane concentration analyses. SS contributed carbon isotope ratio measurements of methane from headspace gas samples.

FUNDING

Support for this research was provided through NASA PSTAR Grant #NNX16AL08G and National Science Foundation Navigating the New Arctic grant #1839063. Use of the *R/V* Falkor and ROV SuBastian were provided through a grant from the Schmidt Ocean Institute. The AUG Nemesis and the Aurora *in-situ* mass spectrometer was provided through in-kind support from Teledyne Webb Research and Navistry Corp, respectively.

ACKNOWLEDGMENTS

The authors wish to thank NASA, the National Science Foundation, Schmidt Ocean Institute, Teledyne Webb Research, and Navistry Corp for their generous support, as well as the country of Costa Rica for permitting operations in national waters. Additionally, the authors would like to recognize the valuable contributions of the entire FK181210 science team and especially Angelos Mallios and David Pingal for AUG support, Eric Timmons for computational support, and Ariell Friedman for Squidle + modifications and support. Bathymetry and acoustic backscatter maps were created by Marine Tech Deborah Smith (Schmidt Ocean Institute) and delivered to the scientific party as input to the seep-hunting analysis. Finally, the authors would like to thank the captain and crew of the *R/V* Falkor as well as the ROV *SuBastian* operations team for their skillful and friendly assistance.

SUPPLEMENTARY MATERIAL

The Supplementary Material for this article can be found online at: https://www.frontiersin.org/articles/10.3389/feart.2021.601019/full#supplementary-material

Data Sheet 1 | Seep_Array_Documentation.pdf

Data Sheet 2 | Supplementary Files (Annotations-ROV Excel files)

Data Sheet 3 | Supplementary Text

Data Sheet 4 | Supplementary Tables 1-9

Image 1 | Supplementary Figure 1

REFERENCES

Anderson, V. C. (1950). Sound scattering from a fluid sphere. *J. Acoust. Soc. Am.* 22 (4), 426–431. doi:10.1121/1.1906621

Barnes, P. M., Lamarche, G., Bialas, J., Henrys, S., Pecher, I., Netzeband, G. L., et al. (2010). Tectonic and geological framework for gas hydrates and cold seeps on the Hikurangi subduction margin, New Zealand. *Mar. Geol.* 272 (1–4), 26–48. doi:10.1016/j.margeo.2009.03.012

Barth, J. A., and Chafetz, H. S. (2015). Cool water geyser travertine: crystal geyser, utah, united states. *Sedimentology* 62 (3), 607–620. doi:10.1111/sed.12158

Baumberger, T., Embley, R. W., Merle, S. G., Lilley, M. D., Raineault, N. A., and Lupton, J. E. (2018). Mantle-derived helium and multiple methane sources in gas bubbles of cold seeps along the cascadia continental margin. *Geochem. Geophys. Geosyst.* 19 (11), 4476–4486. doi:10.1029/2018gc007859

Bohrmann, G., Heeschen, K., Jung, C., Weinrebe, W., Baranov, B., Cailleau, B., et al. (2002). Widespread fluid expulsion along the seafloor of the Costa Rica convergent margin. *Terra Nova* 14 (2), 69–79. doi:10.1046/j.1365-3121.2002.00400.x

Bowden, D. A., Rowden, A. A., Thurber, A. R., Baco, A. R., Levin, L. A., and Smith, C. R. (2013). Cold seep epifaunal communities on the Hikurangi Margin, New Zealand: composition, succession, and vulnerability to human activities. *PLoS One* 8 (10), e76869, doi:10.1371/journal.pone.0076869

Buntine, W. L. (1994). Operations for learning with graphical models. *JAIR* 2, 159–225. doi:10.1613/jair.62

Camilli, R., Bingham, B., Reddy, C. M., Nelson, R. K., and Duryea, A. N. (2009). Method for rapid localization of seafloor petroleum contamination using concurrent mass spectrometry and acoustic positioning. *Mar. Pollut. Bull.* 58 (10), 1505–1513. doi:10.1016/j.marpolbul.2009.05.016

Camilli, R., Reddy, C. M., Yoerger, D. R., Van Mooy, B. A., Jakuba, M. V., Kinsey, J. C., et al. (2010). Tracking hydrocarbon plume transport and biodegradation at deepwater horizon. *Science* 330 (6001), 201–204. doi:10.1126/science.1195223

Campbell, K. A., Farmer, J. D., and Des Marais, D. (2002). Ancient hydrocarbon seeps from the Mesozoic convergent margin of California: carbonate geochemistry, fluids and palaeoenvironments. *Geofluids* 2 (2), 63–94. doi:10.1046/j.1468-8123.2002.00022.x

Chan, L. H., and Kastner, M. (2000). Lithium isotopic compositions of pore fluids and sediments in the Costa Rica subduction zone: implications for fluid processes and sediment contribution to the arc volcanoes. *Earth Planet. Sci. Lett.* 183 (1, 2), 275–290. doi:10.1016/s0012-821x(00)00275-2

Cordes, E. E., McGinley, M. P., Podowski, E. L., Becker, E. L., Lessard-Pilon, S., Viada, S. T., et al. (2008). Coral communities of the deep Gulf of Mexico. *Deep Sea Res. Oceanogr. Res. Pap.* 55 (6), 777–787. doi:10.1016/j.dsr.2008.03.005

Crutchley, G. J., Klaeschen, D., Planert, L., Bialas, J., Berndt, C., Papenberg, C., et al. (2014). The impact of fluid advection on gas hydrate stability: Investigations at sites of methane seepage offshore Costa Rica. *Earth Planetary Sci Lett.* 401, 95–109. doi:10.1016/j.epsl.2014.05.045

Desrosiers, J., Dumas, Y., Solomon, M. M., and Soumis, F. (1995). Chapter 2 Time constrained routing and scheduling. *Handbooks Operat. Res. Manag. Sci.* 8, 35–139. doi:10.1016/s0927-0507(05)80106-9

Dickens, G. R., and Quinby-Hunt, M. S. (1994). Methane hydrate stability in seawater. *Geophys. Res. Lett.* 21 (19), 2115–2118. doi:10.1029/94gl01858

Duguid, Z., and Camilli, R. (2020). Improving resource management for unattended observation of the marginal ice zone using autonomous underwater gliders. *Front. Robot. AI* 7, 579256. doi:10.3389/frobt.2020.579256

Expedition 334 Scientists, (2011). Costa Rica Seismogenesis Project (CRISP): sampling and quantifying input to the seismogenic zone and fluid output. *IODP Prel. Rept.* 334, 114. doi:10.2204/iodp.pr.334.2011

Feseker, T., Boetius, A., Wenzhöfer, F., Blandin, J., Olu, K., Yoerger, D. R., et al. (2014). Eruption of a deep-sea mud volcano triggers rapid sediment movement. *Nat. Commun.* 5 (1), 5385–5388. doi:10.1038/ncomms6385

Füri, E., Hilton, D. R., Tryon, M. D., Brown, K. M., McMurtry, G. M., Brückmann, W., et al. (2010). Carbon release from submarine seeps at the Costa Rica fore arc: implications for the volatile cycle at the Central America convergent margin. *Geochem. Geophys. Geosyst.* 11 (4). doi:10.1029/2009gc002810

Gaschnig, J. (1982). in *Prospector: an expert system for mineral exploration*. Editor D. Michie, 47–64. New York: Gordon and Breach Science Publishers.

Gomes-Pereira, J. N., Auger, V., Beisiegel, K., Benjamin, R., Bergmann, M., Bowden, D., et al. (2016). Current and future trends in marine image annotation software. *Prog. Oceanogr.* 149, 106–120. doi:10.1016/j.pocean.2016.07.005

Gouveia, F. J., and Friedmann, S. J. (2006). Timing and prediction of CO2 eruptions from Crystal Geyser, UT *(No. UCRL-TR-221731)*. Livermore, CA (United States): Lawrence Livermore National Lab.(LLNL).

Grant, N. J., and Whiticar, M. J. (2002). Stable carbon isotopic evidence for methane oxidation in plumes above Hydrate Ridge, cascadia oregon margin. *Glob. Biogeochem. Cycles* 16 (4), 71–1. doi:10.1029/2001GB001851

Guillon, E., Menot, L., Decker, C., Krylova, E., and Olu, K. (2017). The vesicomyid bivalve habitat at cold seeps supports heterogeneous and dynamic macrofaunal assemblages. *Deep Sea Res. Part Oceanogr. Res. Pap.* 120, 1–13. doi:10.1016/j.dsr.2016.12.008

Hand, K. P., and German, C. R. (2018). Exploring ocean worlds on Earth and beyond. *Nat. Geosci.* 11 (1), 2–4. doi:10.1038/s41561-017-0045-9

Hensen, C., Wallmann, K., Schmidt, M., Ranero, C. R., and Suess, E. (2004). Fluid expulsion related to mud extrusion off Costa Rica-A window to the subducting slab. *Geology* 32 (3), 201–204. doi:10.1130/g20119.1

Jasiewicz, J., and Stepinski, T. F. (2013). Geomorphons - a pattern recognition approach to classification and mapping of landforms. *Geomorphology* 182, 147–156. doi:10.1016/j.geomorph.2012.11.005

Judd, A. G. (2004). Natural seabed gas seeps as sources of atmospheric methane. *Environ. Geol.* 46 (8), 988–996. doi:10.1007/s00254-004-1083-3

Judd, A., and Hovland, M. (2009). *Seabed fluid flow: the impact on geology, biology and the marine environment*. Cambridge: Cambridge University Press. doi:10.1017/CBO9780511535918

Kastner, M., Elderfield, H., and Martin, J. B. (1991). Fluids in convergent margins: what do we know about their composition, origin, role in diagenesis and importance for oceanic chemical fluxes?. *Philos. Trans. R. Soc. Lond. Ser. A Phys. Eng. Sci.* 335 (1638), 243–259. doi:10.1098/rsta.1991.0045

Kaufmann, E., Cappe, O., and Garivier, A. (2012). On Bayesian Upper Confidence Bounds for Bandit Problems, in: *Proceedings of the fifteenth international conference on artificial intelligence and statistics* La Palma, Canary Islands: MLResearchPress, in PMLR 22:592-600.

Klaucke, I., Masson, D. G., Petersen, C. J., Weinrebe, W., and Ranero, C. R. (2008). Multifrequency geoacoustic imaging of fluid escape structures offshore Costa Rica: implications for the quantification of seep processes. *Geochem. Geophys. Geosyst.* 9 (4), 708. doi:10.1029/2007gc001708

Kluesner, J. W., Silver, E. A., Bangs, N. L., McIntosh, K. D., Gibson, J., Orange, D., et al. (2013). High density of structurally controlled, shallow to deep water fluid seep indicators imaged offshore costa rica. *Geochem. Geophys. Geosyst.* 14 (3), 519–539. doi:10.1002/ggge.20058

Kopf, A., Deyhle, A., and Zuleger, E. (2000). Evidence for deep fluid circulation and gas hydrate dissociation using boron and boron isotopes of pore fluids in forearc sediments from costa rica (ODP Leg 170). *Mar. Geology* 167 (1, 2), 1–28. doi:10.1016/s0025-3227(00)00026-8

Krause, S., Steeb, P., Hensen, C., Liebetrau, V., Dale, A. W., Nuzzo, M., et al. (2014). Microbial activity and carbonate isotope signatures as a tool for identification of spatial differences in methane advection: a case study at the Pacific Costa Rican margin. *Biogeosciences* 11, 507–523. doi:10.5194/bg-11-507-2014

Kutterolf, S., Liebetrau, V., Mörz, T., Freundt, A., Hammerich, T., and Garbe-Schönberg, D. (2008). Lifetime and cyclicity of fluid venting at forearc mound structures determined by tephrostratigraphy and radiometric dating of authigenic carbonates. *Geology* 36 (9), 707–710. doi:10.1130/g24806a.1

Lattimore, T., and Szepesvári, C. (2020). *Bayesian bandits. Bandit algorithms*. Cambridge: Cambridge University Press, 438–457.

Leifer, I., Luyendyk, B. P., Boles, J., and Clark, J. F. (2006). Natural marine seepage blowout: contribution to atmospheric methane. *Glob. Biogeochem. Cycles* 20 (3), 268. doi:10.1029/2005gb002668

Lessard-Pilon, S., Porter, M. D., Cordes, E. E., MacDonald, I., and Fisher, C. R. (2010). Community composition and temporal change at deep Gulf of Mexico cold seeps. *Deep Sea Res. Part Topical Stud. Oceanogr.* 57 (21–23), 1891–1903. doi:10.1016/j.dsr2.2010.05.012

Levin, L. A., Mendoza, G. F., Grupe, B. M., Gonzalez, J. P., Jellison, B., Rouse, G., et al. (2015). Biodiversity on the rocks: macrofauna inhabiting authigenic carbonate at Costa Rica methane seeps. *PLoS One* 10 (7), e0131080. doi:10.1371/journal.pone.0131080

Levin, L. (2005). Ecology of cold seep sediments. *Oceanogr. Mar. Biol. Annu. Rev.* 43, 1–46. doi:10.1201/9781420037449.ch1

Lindsay, R. K., Buchanan, B. G., Feigenbaum, E. A., and Lederberg, J. (1993). DENDRAL: a case study of the first expert system for scientific hypothesis formation. *Artif. Intell.* 61 (2), 209–261. doi:10.1016/0004-3702(93)90068-m

Linke, P., Wallmann, K., Suess, E., Hensen, C., and Rehder, G. (2005). *In situ* benthic fluxes from an intermittently active mud volcano at the Costa Rica convergent margin. *Earth Planet. Sci. Lett.* 235 (1, 2), 79–95. doi:10.1016/j.epsl.2005.03.009

Lückge, A., Kastner, M., Littke, R., and Cramer, B. (2002). Hydrocarbon gas in the Costa Rica subduction zone: primary composition and post-genetic alteration. *Org. Geochem.* 33 (8), 933–943. doi:10.1016/s0146-6380(02)00063-3

MacKay, D. J. (1998). Introduction to Monte Carlo methods. *Learning in graphical models*. Dordrecht: Springer, 175–204. doi:10.1007/978-94-011-5014-9_7

Mau, S., Rehder, G., Arroyo, I. G., Gossler, J., and Suess, E. (2007). Indications of a link between seismotectonics and CH4 release from seeps off costa rica. *Geochem. Geophys. Geosystems* 8 (4). doi:10.1029/2006gc001326

Mau, S., Rehder, G., Sahling, H., Schleicher, T., and Linke, P. (2014). Seepage of methane at Jaco Scar, a slide caused by seamount subduction offshore costa rica. *Int. J. Earth Sci. (Geol Rundsch)* 103 (7), 1801–1815. doi:10.1007/s00531-012-0822-z

Mau, S., Sahling, H., Rehder, G., Suess, E., Linke, P., and Söding, E. (2006). Estimates of methane output from mud extrusions at the erosive convergent margin off costa rica. *Mar. Geol.* 225 (1–4), 129–144. doi:10.1016/j.margeo.2005.09.007

Medwin, H., and Clay, C. S. (1998). *Fundamentals of acoustical oceanography*, California. Academic Press. doi:10.1121/1.426950

Milucka, J., Ferdelman, T. G., Polerecky, L., Franzke, D., Wegener, G., Schmid, M., et al. (2012). Zero-valent sulphur is a key intermediate in marine methane oxidation. *Nature* 491 (7425), 541–546. doi:10.1038/nature11656

Mitchell, G. A., Orange, D. L., Gharib, J. J., and Kennedy, P. (2018). Improved detection and mapping of deepwater hydrocarbon seeps: optimizing multibeam echosounder seafloor backscatter acquisition and processing techniques. *Mar. Geophys. Res.* 39 (1, 2), 323–347. doi:10.1007/s11001-018-9345-8

Moore, J. C., and Vrolijk, P. (1992). Fluids in accretionary prisms. *Rev. Geophys.* 30 (2), 113–135. doi:10.1029/92rg00201

Neveu, M., Hays, L. E., Voytek, M. A., New, M. H., and Schulte, M. D. (2018). The ladder of life detection. *Astrobiology* 18 (11), 1375–1402. doi:10.1089/ast.2017.1773

Nikolopoulos, C. (1997). *Expert systems: introduction to first and second generation and hybrid knowledge based systems*, London: Marcel Dekker.

Peacock, S. A. (1990). Fluid processes in subduction zones. *Science* 248 (4953), 329–337. doi:10.1126/science.248.4953.329

Proctor, R., Langlois, T., Friedman, A., Mancini, S., Hoenner, X., and Davey, B. (2018). "Cloud-based national on-line services to annotate and analyse underwater imagery", in IMDIS 2018 International Conference on Marine Data and Information Systems, 05-07 November 2018, Barcelona, Spain. 59, 49, 2018 . Available at: https://imdis.seadatanet.org/content/download/121493/file/IMDIS2018_Proceedings.pdf.

Ranero, C. R., Grevemeyer, I., Sahling, H., Barckhausen, U., Hensen, C., Wallmann, K., et al. (2008). Hydrogeological system of erosional convergent margins and its influence on tectonics and interplate seismogenesis. *Geochem. Geophys. Geosyst.* 9 (3), 679. doi:10.1029/2007gc001679

Ranero, C. R., Weinrebe, W., Grevemeyer, I., Phipps Morgan, J., Vannucchi, P., and von Huene, R. (2003). *Tectonic structure of the Middle America pacific margin and incoming cocos plate from Costa Rica to Guatemala*, America. AGUFM, T52C–T0289.

Riedinger, N., Torres, M. E., Screaton, E., Solomon, E. A., Kutterolf, S., Schindlbeck-Belo, J., et al. (2019). Interplay of subduction tectonics, sedimentation, and carbon cycling. *Geochem. Geophys. Geosyst.* 20 (11), 4939–4955. doi:10.1029/2019gc008613

Russo, D., and Van Roy, B. (2018). Learning to optimize via information-directed sampling. *Operat. Res.* 66 (1), 230–252. doi:10.1287/opre.2017.1663

Sahling, H., Galkin, S. V., Salyuk, A., Greinert, J., Foerstel, H., Piepenburg, D., et al. (2003). Depth-related structure and ecological significance of cold-seep communities-a case study from the Sea of okhotsk. *Deep Sea Res. Part Oceanogr. Res. Pap.* 50 (12), 1391–1409. doi:10.1016/j.dsr.2003.08.004

Sahling, H., Masson, D. G., Ranero, C. R., Hühnerbach, V., Weinrebe, W., Klaucke, I., et al. (2008). Fluid seepage at the continental margin offshore Costa Rica and southern nicaragua. *Geochem. Geophys. Geosystems* 9 (5), 978. doi:10.1029/2008gc001978

Schmidt, M., Hensen, C., Mörz, T., Müller, C., Grevemeyer, I., Wallmann, K., et al. (2005). Methane hydrate accumulation in "Mound 11" mud volcano, Costa Rica forearc. *Mar. Geology* 216 (1, 2), 83–100. doi:10.1016/j.margeo.2005.01.001

Sibuet, M., and Olu, K. (1998). Biogeography, biodiversity and fluid dependence of deep-sea cold-seep communities at active and passive margins. *Deep Sea Res. Part Topical Stud. Oceanogr.* 45 (1), 517–567. doi:10.1016/s0967-0645(97)00074-x

Silver, E., Kastner, M., Fisher, A., Morris, J., McIntosh, K., and Saffer, D. (2000). Fluid flow paths in the Middle America Trench and Costa Rica margin. *Geology* 28 (8), 679–682. doi:10.1130/0091-7613(2000)28<679:FFPITM>2.0.CO;2

Skarke, A., Ruppel, C., Kodis, M., Brothers, D., and Lobecker, E. (2014). Widespread methane leakage from the sea floor on the northern US Atlantic margin. *Nat. Geosci.* 7 (9), 657–661. doi:10.1038/ngeo2232

Suess, E. (2018). in *Marine cold seeps: background and recent advances.* Hydrocarbons, Oils and lipids: diversity, origin, Chemistry and fate. Editor H. Wilkes (Cham: Springer International Publishing), 1–21.

Sullivan-Silva, K. B. (1989). *Underwater acoustic scattering from spherical particulates and bubbles*. London, Connecticut: Naval Underwater Systems Center Newport RI.

Torres, M. E., Embley, R. W., Merle, S. G., Trehu, A. M., Collier, R. W., Suess, E., et al. (2009). Methane sources feeding cold seeps on the shelf and upper continental slope off central Oregon, USA. *Geochem. Geophys. Geosyst.* 10 (11). doi:10.1029/2009gc002518

Torres, M. E., Muratli, J. M., and Solomon, E. A. (2014). "Data report: minor element concentrations in pore fluids from the CRISP-A transect drilled during Expedition 334," in *The expedition 334 scientists, proc. IODP*. Editors P. Vannucchi, K. Ujiie, N. Stroncik, and A. Malinverno (Tokyo: Integrated Ocean Drilling Program Management International, Inc.), 334. doi:10.2204/iodp.proc.334.201.2014

Tryon, M. D., Brown, K. M., and Torres, M. E. (2002). Fluid and chemical flux in and out of sediments hosting methane hydrate deposits on Hydrate Ridge, OR, II: H.ydrological processes. *Earth Planet. Sci. Lett.* 201 (3, 4), 541–557. doi:10.1016/s0012-821x(02)00732-x

Tryon, M. D., Brown, K. M., Torres, M. E., Tréhu, A. M., McManus, J., and Collier, R. W. (1999). Measurements of transience and downward fluid flow near episodic methane gas vents, hydrate ridge, cascadia. *Geology* 27 (12), 1075–1078. doi:10.1130/0091-7613(1999)027<1075:MOTADF>2.3.CO;2

Tryon, M. D., Wheat, C. G., and Hilton, D. R. (2010). Fluid sources and pathways of the Costa Rica erosional convergent margin. *Geochem. Geophys. Geosyst.* 11 (4), 818. doi:10.1029/2009gc002818

Visbeck, M. (2002). Deep velocity profiling using lowered acoustic Doppler current profilers: bottom track and inverse solutions. *J. Atmos. Ocean. Technol.* 19 (5), 794–807. doi:10.1175/1520-0426(2002)019<0794:DVPULA>2.0.CO;2

von Huene, R., Ranero, C. R., Weinrebe, W., and Hinz, K. (2000). Quaternary convergent margin tectonics of Costa Rica, segmentation of the Cocos Plate, and Central American volcanism. *Tectonics* 19 (2), 314–334. doi:10.1029/1999tc001143

Wallis, S. (2013). Binomial confidence intervals and contingency tests: mathematical fundamentals and the evaluation of alternative methods. *J. Quant. Linguist.* 20 (3), 178–208. doi:10.1080/09296174.2013.799918

Weber, T. C., Mayer, L., Jerram, K., Beaudoin, J., Rzhanov, Y., and Lovalvo, D. (2014). Acoustic estimates of methane gas flux from the seabed in a 6000 km2region in the northern gulf of mexico. *Geochem. Geophys. Geosyst.* 15 (5), 1911–1925. doi:10.1002/2014gc005271

Whiticar, M. J. (1999). Carbon and hydrogen isotope systematics of bacterial formation and oxidation of methane. *Chem. Geol.* 161 (1–3), 291–314. doi:10.1016/s0009-2541(99)00092-3

Wilson, E. B. (1927). Probable inference, the law of succession, and statistical inference. *J. Am. Stat. Assoc.* 22 (158), 209–212. doi:10.1080/01621459.1927.10502953

Conflict of Interest: The authors declare that the research was conducted in the absence of any commercial or financial relationships that could be construed as a potential conflict of interest.

frontiers in Earth Science

ORIGINAL RESEARCH
published: 28 July 2021
doi: 10.3389/feart.2021.626372

Inter-Comparison of the Spatial Distribution of Methane in the Water Column From Seafloor Emissions at Two Sites in the Western Black Sea Using a Multi-Technique Approach

Roberto Grilli[1], Dominique Birot[2], Mia Schumacher[3], Jean-Daniel Paris[4], Camille Blouzon[1], Jean Pierre Donval[2], Vivien Guyader[2], Helene Leau[2], Thomas Giunta[2], Marc Delmotte[4], Vlad Radulescu[5], Sorin Balan[5,6], Jens Greinert[3] and Livio Ruffine[2]*

[1]CNRS, Univ Grenoble Alpes, IRD, Grenoble INP, Grenoble, France, [2]Département Ressources Physiques et Ecosystèmes de Fond de Mer (REM), IFREMER, Plouzané, France, [3]GEOMAR Helmholtz Centre for Ocean Research, Kiel, Germany, [4]Laboratoire des Sciences du Climat et de l'Environnement, LSCE/IPSL, CEA-CNRS-UVSQ, Gif-sur-Yvette, France, [5]National Institute of Marine Geology and Geoecology–GeoEcoMar, Bucharest, Romania, [6]Faculty of Geology and Geophysics, Doctoral School of Geology, University of Bucharest, Bucharest, Romania

OPEN ACCESS

Edited by:
Martin Scherwath, University of Victoria, Canada

Reviewed by:
Xiaole Sun, Baltic Sea Centre, Stockholm University, Sweden
Thomas Pape, University of Bremen, Germany

***Correspondence:**
Roberto Grilli
roberto.grilli@cnrs.fr

Specialty section:
This article was submitted to Biogeoscience, a section of the journal Frontiers in Earth Science

Received: *05 November 2020*
Accepted: *06 July 2021*
Published: *28 July 2021*

Citation:
Grilli R, Birot D, Schumacher M, Paris J-D, Blouzon C, Donval JP, Guyader V, Leau H, Giunta T, Delmotte M, Radulescu V, Balan S, Greinert J and Ruffine L (2021) Inter-Comparison of the Spatial Distribution of Methane in the Water Column From Seafloor Emissions at Two Sites in the Western Black Sea Using a Multi-Technique Approach. Front. Earth Sci. 9:626372. doi: 10.3389/feart.2021.626372

Understanding the dynamics and fate of methane (CH_4) release from oceanic seepages on margins and shelves into the water column, and quantifying the budget of its total discharge at different spatial and temporal scales, currently represents a major scientific undertaking. Previous works on the fate of methane escaping from the seafloor underlined the challenge in both, estimating its concentration distribution and identifying gradients. In April 2019, the Envri Methane Cruise has been conducted onboard the R/V Mare Nigrum in the Western Black Sea to investigate two shallow methane seep sites at ~120 m and ~55 m water depth. Dissolved CH_4 measurements were conducted with two continuous *in-situ* sensors: a membrane inlet laser spectrometer (MILS) and a commercial methane sensor (METS) from Franatech GmbH. Additionally, discrete water samples were collected from CTD-Rosette deployment and standard laboratory methane analysis was performed by gas chromatography coupled with either purge-and-trap or headspace techniques. The resulting vertical profiles (from both *in situ* and discrete water sample measurements) of dissolved methane concentration follow an expected exponential dissolution function at both sites. At the deeper site, high dissolved methane concentrations are detected up to ~45 m from the seabed, while at the sea surface dissolved methane was in equilibrium with the atmospheric concentration. At the shallower site, sea surface CH_4 concentrations were four times higher than the expected equilibrium value. Our results seem to support that methane may be transferred from the sea to the atmosphere, depending on local water depths. In accordance with previous studies, the shallower the water, the more likely is a sea-to-atmosphere transport of methane. High spatial resolution surface data also support this hypothesis. Well localized methane enriched waters were found near the surface at both sites, but their locations appear to be decoupled with the ones of the seafloor seepages. This highlights the need of better understanding the processes responsible for the transport and transformation of the

dissolved methane in the water column, especially in stratified water masses like in the Black Sea.

Keywords: dissolved gas, methane, black sea, in situ measurements, gas seepages, instrumental inter-comparison

INTRODUCTION

Methane is a key climate-relevant trace gas widely encountered in seawater (Reeburgh, 2007; Etiope, 2012; Myhre et al., 2016; Saunois et al., 2017; Weber et al., 2019). Its distribution in the water column is highly heterogeneous, both horizontally and vertically. In the open ocean, dissolved methane concentrations are at level of nmol per litre (10^{-9} mol L^{-1}), and usually at higher concentrations within the near-surface most-ventilated and most-oxygenated water (Karl et al., 2008; Repeta et al., 2016). However, very high concentrations of methane can also be found in bottom waters at coastal, shelf and margin settings characterized by widespread gas seeps discharging fluids at the seafloor (e.g., Reeburgh et al., 1991; Borges et al., 2016; Mau et al., 2017; Ruffine et al., 2018). In such settings, the water column is considered as a sink for methane in which it is transported at short (meters) and medium (kilometers) distances, degraded or transferred into other earth compartments like the atmosphere. The dynamic of methane in the water column is complex and depends on the properties of the water mass: physical conditions such as currents, layer thickness, temperature, ventilation/exchange with the atmosphere, chemical conditions that control its redox state (e.g. hypoxic/anoxic conditions) and biological activity that might oxidize or even produce methane in the water column (Solomon et al., 2009; Shakhova et al., 2014; Weinstein et al., 2016; Garcia-Tigreros and Kessler, 2018). The multiple factors involved in methane transport and transformation explain why the fate of this compound in the dissolved state is still difficult to capture in the field. However, in a progressively warming climate, in-depth knowledge of the fate of methane is essential, as emissions are expected to increase, particularly from continental shelves and margins due to eutrophication, permafrost thaw and gas hydrate destabilization (Westbrook et al., 2009; Naqvi et al., 2010; James et al., 2016; Riboulot et al., 2018). Accordingly, campaigns of time series and worldwide measurements are indispensable to capture the time evolution of methane.

The methane concentration in seawater can be measured either in the laboratory from previously collected water samples or *in situ* using specific sensors and analyzers. Laboratory measurements consist of determining the methane concentration either by headspace (HS) or purge-and-trap (PT) methods coupled with gas chromatography (GC) (Lammers and Suess, 1994; Tsurushima et al., 1999; Donval and Guyader, 2017; Wilson et al., 2018). HS-GC is based on the analysis of the gas phase in equilibrium with the seawater sample; it is easy to perform and could also be implemented in the field. The PT-GC method requires a more sophisticated installation in which the originally dissolved methane is extracted by flowing a carrier gas throughout the seawater sample, followed by its entrapment in a cooled material, frequently active carbon or silica. The choice of method depends mainly on the methane concentration and the sample volume available. Although the PT-GC requires a larger volume of water than the HS-GC (>100 ml vs 5–20 ml), it provides a sub-nmol L^{-1} detection limit, whereas that of the HS technique is usually around few nmol L^{-1}.

Despite the reliability of laboratory measurements, *in situ* measurements are increasingly needed for both long-term monitoring through remote sensing and observatory, and high-resolution coverage of large areas of methane emissions. The most commonly encountered instruments for *in situ* methane concentration measurement are optical and chemical sensors (Marinaro et al., 2004; Faure et al., 2006; Krabbenhoeft et al., 2010; Schmidt et al., 2013), as well as optical spectrometers (e.g. Chua et al., 2016; Boulart et al., 2017; Grilli et al., 2018; Hartmann et al., 2018; Yuan et al., 2020). Their measurement range spans from few tens of nmol L^{-1} to hundreds of µmol L^{-1}, and they can be used up to hundreds of meters water depth.

Furthermore, anoxic environments receiving huge inputs of organic matter provide favourable conditions for the production and preservation of high concentrations of methane, and the Black Sea is well known for being a typical example (e.g. Kessler et al., 2006a; Pape et al., 2008; Reeburgh et al., 1991, 2006). Indeed, it represents the largest thick and permanently anoxic and sulfidic basin on earth, in which methane is discharged abundantly through seeps widely distributed on the shelf and slope, typically at the rim of the gas hydrate stability zone and from mud volcanoes in the deep basins (Artemov et al., 2019). In the anoxic waters below ~100 m water depth, methane concentrations can reach values of more than 10 µmol L^{-1} in contrast to the nmol L^{-1} level observed in the surface layer (e.g. Schmale et al., 2010).

The anoxic layer is successively superimposed by an intermediate suboxic- and an oxic-layer, leading to a distinct vertical stratification of the water column with limited chemical exchanges of redox-sensitive species (Capet et al., 2016; Özsoy and Ünlüata, 1997; Stanev et al., 2018, 2019). The total amount of dissolved methane stored in the Black Sea is estimated at ~96 Tg (Reeburgh et al., 1991) with the anoxic water layer being more charged (~72 Tg) than the others (Artemov et al., 2019).

Previous Black Sea methane studies have highlighted a variable vertical concentration distribution (McGinnis et al., 2006; Schmale et al., 2010; Sovga et al., 2008), with increasing values while going from the oxic into the anoxic water layer. So, methane concentrations up to 12 nmol L^{-1} were measured in the oxic layer, and in some areas, the sea surface was oversaturated in methane with respect to the atmosphere (Malakhova et al., 2010; Reeburgh et al., 1991). Concentrations reaching a few µmol L^{-1} were measured within the suboxic layer, and up to >10 µmol L^{-1} in the anoxic water mass (Kessler et al., 2006a; Reeburgh et al., 2006), where the concentration variations are much less pronounced.

Although today we are relatively confident that the methane originating from the Black Sea sediments is not a significant source accounting for the atmospheric CH_4 budget of the region, its transfer mechanisms from the seafloor through the three aforementioned water layers and seldom to the atmosphere still remain unknown and controversial in the scientific community (Schmale et al., 2005; McGinnis et al., 2006). Depending on the investigated area, different sources of discharged methane can be identified: deep hydrocarbon-reservoirs, gas-hydrate destabilization, shallow methanogenesis within the sediments, and even methanogenesis in the water column (Reeburgh et al., 1991; Kessler et al., 2006b). The contribution of these sources can be very asymmetric, and Kessler et al. (2006b) showed that the major methane inputs to the Black Sea water column are discharges from seeps and diagenesis within the sediments.

Despite several European and national Black Sea Projects (e.g., CRIMEA, METROL, MSM34 cruise by Geomar in 2013–2014 (EU project MIDAS), Ghass cruise by Ifremer in 2015 (ANR project Blame) and many other German research cruises with R/V Meteor and R/V Maria S. Merian), the distribution and fate of methane emissions in Romanian waters are still not fully constrained (Ghass, 2015; MSM34, 2014; Riboulot et al., 2018). The objective of this study is to present insights from the dissolved methane distribution in the water column from two shallow water emission sites (~55 m water depth, hereafter referred to as "shallower site" and ~120 m water depth, hereafter referred to as "deeper site") in the Romanian sector of the Black Sea using a multi-technique approach. High-resolution, horizontal and vertical profiles of dissolved methane concentration obtained from *in situ* measurements are reported and correlated to hydro-acoustic studies of gas bubbles. A detailed analysis of the results of the measurement systems is presented, and it emphasises the need to develop reliable and standardized protocols for *in situ* measurement of dissolved CH_4. The two sites are then compared and the dissolved methane distribution in the water column discussed.

MATERIALS AND METHODS

Recent previous studies on the distribution of dissolved CH_4 at a seepage site have highlighted the need for high-resolution methane concentration measurements to assess the extent of the influence area of a bubble plume and map the spatial concentration variability (Jansson et al., 2019b). In this respect, the fast response membrane inlet laser spectrometer (MILS) prototype (t_{90} < 30 s, Grilli et al., 2018) is well-suited. To better appreciate its performances, comparison was made with the Franatech METS sensor and against a standard method consisting of sampling with Niskin bottles followed by PT and HS analysis in the laboratory. This multi-technique approach identifies the advantages and drawbacks of the different methods, revealing weaknesses and possible artifacts in the measurements, while making the dataset more robust for the comparison between the two locations reported in the discussion section. It should be noticed here that, since the research vessel was not equipped with dynamic positioning, inter-comparisons on dissolved methane measurements remain challenging.

The Study Areas

The survey was performed on board of the R/V Mare Nigrum, operated by GeoEcoMar Romania, in April 2019 at two shallow sites in the Black Sea Romania territorial water. Over a period of 5 days (3–7 April), we surveyed an area of ~ 12.5 km^2 at the deeper site (44.233°N, 30.737°E, 100-km long survey), with water depths between 110 and 128 m, and ~ 3.5 km^2 at the shallower site (44.057°N, 29.491°E, 19-km long survey), with water depths between 53 and 58 m (**Figure 1**).

At the deeper site, water temperature and electrical conductivity were on average 9.5°C and 18.5 mS cm^{-1} at the sea surface, and 9.0°C and 20.5 mS cm^{-1} near the seafloor. At the shallower site, temperature and electrical conductivity were 9.5°C and 18 mS cm^{-1} at the sea surface and 8.0°C and 18.5 mS cm^{-1} at the seafloor. The deeper site showed an oxycline between 60 and 80 m water depth, while the concentration of dissolved oxygen near the seafloor at the shallower site was 17% lower than at the surface (360 mmol L^{-1}) (CTD, Conductivity, Temperature and Depth, data are reported in the **Supplementary Datasheet S1**).

Description of the Surveys

Two near-surface horizontal profile surveys (HP01, mean depth 5.2 m, min 0.4 m, max 18 m, and HP03, mean depth 4.2 m, min 1.5 m, max 9 m) on dissolved CH_4 were conducted. HP01 was performed for 11 h at the deeper site on April 4th and is composed of ten parallel ~5.5-km long lines spaced by ~260 m, for a total surface area of ~ 12.5 km^2. HP03 was a 2-h long survey at the shallower site performed on the April 6th, covering an area of ~3.5 km^2 (see **Figure 1**). During these two surveys, the MILS and METS sensors were deployed simultaneously. The MILS probe was configured to improve the sensitivity of the measurements, by minimizing the flow of carrier gas (see the method description below for further details). This decreased the dynamic range of the measurement, while increasing the precision at low concentrations, to the detriment of a slightly longer response time (t_{90} of 30 s, corresponding to 75 m resolution at the highest speed of 2.5 m s^{-1} reached during the surveys).

Vertical profiles (VPs) with the MILS and METS sensors were performed at different locations at the two sites. Because of the lacking in dynamical positioning, the vessel was located in the vicinity of a flare (hydroacoustic anomalies in echosounder records attributed to the presence of gas bubbles) or a cluster of flares, and down- and up-casts were performed. It should be noticed that because of the strong dependency of the METS sensor to dissolved oxygen content and change in hydrostatic pressure, the recorded vertical profiles are not reported in this work.

Hydro-casts (HYs) for discrete water sampling were conducted at different time with respect to *in situ* measurements. The locations should have been the same as the *in situ* measurements, but this has proven to be challenging due to the lack of dynamical positioning of the vessel.

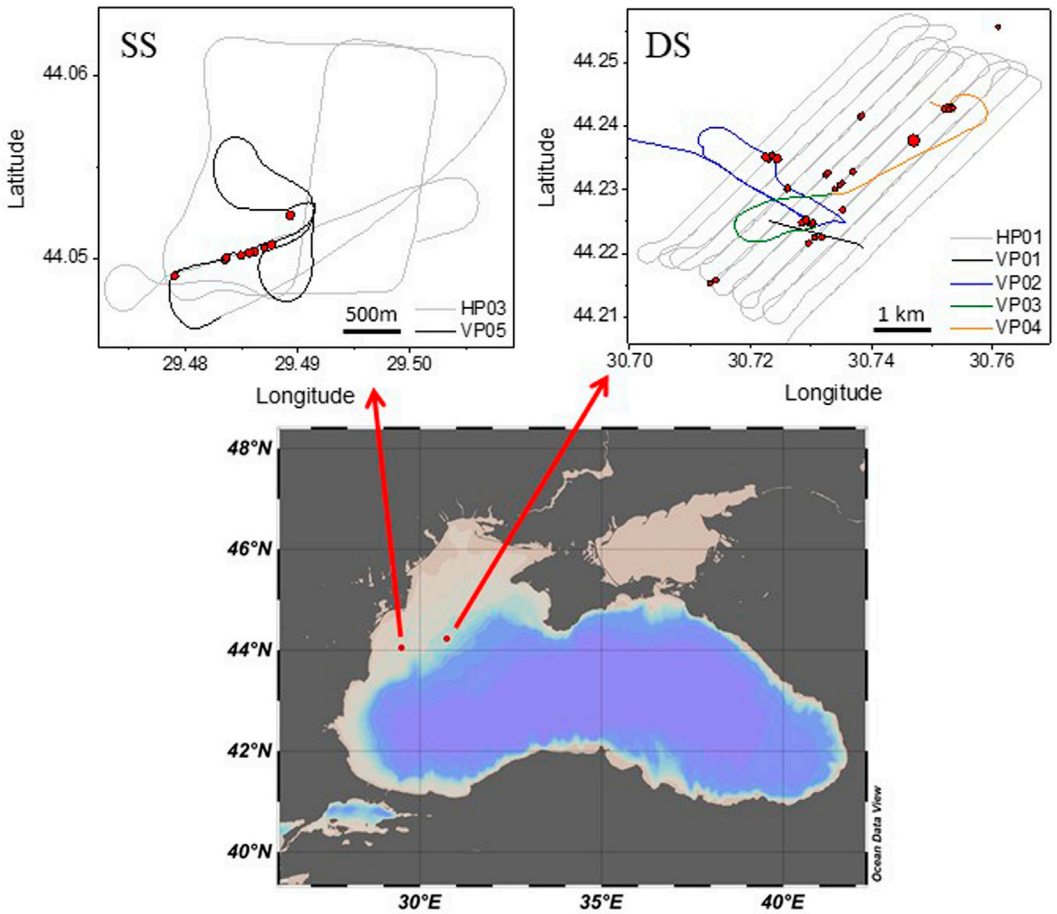

FIGURE 1 | Maps of the survey areas. At the bottom a large map of the Black Sea, and at the top two maps of the shallower site (SS, **left)** and deeper site (DS, **right)** with the trajectories of the vessel for the profiles of interest for this work. VP are vertical and HP are horizontal near-surface profiles in the water. During the vertical profiles the position of the vessel was drifting due to water current. Red dots are the locations of flares identified during the survey by the echosounder, with the size proportional to the strength estimated from the acoustic signature.

The Acoustic Method

During the cruise, a 70 kHz split beam echosounder (Simrad EK80 with ES70 transducer) was used to hydro-acoustically detect and locate bubble releasing methane seeps. With an opening angle of 18°, it has a footprint at the seabed of ~22 m and ~48 m diameter at 55 m and 120 m water depths, respectively. The pulse length was set to 0.256 ms over the entire cruise. This turned out to be suitable for the shallower site, while for the deeper site the noise level remained visibly higher. However, since this noise level was acceptable, for a better inter-comparability between the two study sites, the pulse length was unchanged for both surveys. At an average vessel speed of ~2 m s^{-1}, the distance between two pings was around 32 cm (14 cm) for 120 m (55 m) water depth at a ping rate of 0.16 s (0.07 s). To obtain precise backscatter values for the bubble quantification method, the echosounder was calibrated prior to the cruise with a 38.5 mm Tungsten sphere for the applied pulse length (MacLennan and Svellingen, 1989).

The idea to detect gas seepage locations using echo-sounding techniques was adopted from a series of former studies and has been accepted as an efficient approach to identify submarine gas flares. The method has been described in detail in e.g. Greinert et al. (2010) and Veloso et al. (2015).

The Membrane Inlet Laser Spectrometer *in situ* Sensor

A membrane inlet laser spectrometer (MILS) prototype allowing the combination of fast response and *in situ* dissolved methane measurements was used. The instrument relies on a patent-based membrane extraction system (Triest et al., 2017). It is described in detail in a previously published paper (Grilli et al., 2018), where a laboratory comparison with measurements of discrete water samples at different water temperatures and salinities was conducted. It was deployed successfully during two campaigns, over a methane seepage area in western Svalbard in 2015 (Jansson et al., 2019b), and at Lake Kivu in Rwanda in March 2018 (Grilli et al., 2020). The instrument allows a dynamic range from a few nmol L^{-1} up to a few µmol L^{-1}. The MILS was powered by a battery pack (SeaCell, STR Subsea Technology and Rentals) and

deployed together with a CTD SBE 911plus (Seabird) for measuring temperature, conductivity and water depth.

Because of the dynamic and fast profiling capability of the instrument, the spatial and temporal synchronization of measurements needs particular attention. For this, a first dynamic correction of the time-lag due to the flushing time (the time it takes the gas sample to go from the membrane extraction system into the measurement cell) was applied. By knowing the total gas flow (sum of the carrier gas plus the dry and wet gas permeating the membrane) and the volume of the gas line between the extraction system and the measurement cell, this time lag was calculated and varied between 15 and 60 s during the campaign (depending on the total gas flow). The instrument response time is related to the time necessary to replace the gas inside the measurement cell; it depends on the measurement cell volume (~20 cm^3 at standard temperature and pressure), the working pressure (20 mbar) and the total gas flow. This parameter can as well be calculated and it varied between 8 and 30 s during the campaign. Both time-lag and response time are affected by the total gas flow (Grilli et al., 2018). With the instrument towed behind the vessel, the distance between the instrument and the ship also varies as function of the ship speed and water depth of the sensor. Instrument location was therefore dynamically corrected simulating the mooring of our sensor using the "Mooring Design and Dynamics" matlab routine (Dewey, 1999). This dynamic correction allows to apply a time (and therefore a position) correction of the sensor which ranged from a few seconds and a few meters at the sea surface and at minimum speed, up to 100 s when the system was towed at 100 m water depth. This corresponds to maximum horizontal correction of ~80 m, since typical ship speed during vertical profiles was ~0.8 m/s. Water currents were neglected for this position correction. The vessel position was provided by a Garmin GPS 18x, with an accuracy of 15 m (1σ).

Measured concentrations are reported in mixing ratio with respect to the total dissolved gas pressure, which is assumed to be 1 atm for this setting. Therefore, a value of partial pressure, pCH_4, in the gas mixture can be retrieved, which is then converted into dissolved methane concentrations, C_{CH4}, expressed in mol per liter of water. This conversion is performed by considering the solubility of the gas in the water under given physical conditions as well as its fugacity. C_{CH4} is related to the pCH_4 through the following equation:

$$C_{CH_4} = K(T, S, P) pCH_4 \varphi_{CH_4}(T, P), \quad (1)$$

where φ_{CH4} is the fugacity coefficient (assumed to be one in this case) and K is the solubility coefficient, i.e. the ratio between the dissolved methane concentration and its fugacity. The solubility coefficient K (mol L^{-1} atm^{-1}) of CH_4 as a function of temperature T (K) and salinity S (g/kg) is calculated using the following equation:

$$\ln(K) = A_1 + A_2\left(\frac{100}{T}\right) + A_3 \ln\left(\frac{T}{100}\right) + S\left[B_1 + B_2\left(\frac{T}{100}\right) + B_3\left(\frac{T}{100}\right)^2\right], \quad (2)$$

Where A_i and B_i are empirical parameters from Wiesenburg and Guinasso. (1979).

The solubility coefficients need to be corrected for local pressure P (Pa) at the sampling water depth (sum of hydrostatic and atmospheric pressure), using the following equation (Weiss, 1974):

$$K(P) = Ke^{\left[\frac{(1-P)v_{CH_4}}{RT}\right]}, \quad (3)$$

where R = 8.31446 J mol^{-1} K^{-1} is the ideal gas constant, and v_{CH4} is the partial molar volume (cm^3 mol^{-1}) of CH_4 calculated from Rettich et al. (1981).

Calibration of the instrument was performed in the laboratory using the calibration system described in Grilli et al. (2018). Experiments were performed at atmospheric pressure for different water conditions (temperature from 5 to 25°C, and salinity from 0 to 30.5 g/kg) and at different concentrations of CH_4 (0–1,000 ppm). The gas mixtures were obtained using two mass flow controllers (Bronkhorst, EL-FLOW) and mixing zero air (ALPHAGAZ 2, Air Liquide) with synthetic air containing CH_4 (8920 Labline, 1,000 ppm of CH_4 in air, Messer).

The Commercial Sensor Franatech

A Franatech METS sensor was used to measure anomalies in a concentration of dissolved methane in water. The measurement principle is based on a SnO_2 semiconductor detector (Seiyama et al., 1962) working at ~500°C (Ippommatsu et al., 1990). Its principles can be summarized as follows: first, oxygen (O_2) is absorbed on the SnO_2, then, the dissolved CH_4 diffuses through a membrane to the measurement cell and interacts with O_2 molecules, causing their desorption and increasing the conductivity of the SnO_2 material. This technology is however known for its lack in gas selectivity and its dependency on the amount of O_2 present in the measured environment (Boulart et al., 2010; Chua et al., 2016). The METS sensor can be operated at water depths down to 4,000 m and temperature ranging between 2°C and 20°C. Prior to its deployment, the sensor was calibrated by the manufacturer (in February 2019) at atmospheric pressure and methane concentrations ranging between 100 nmol L^{-1} and 40 μmol L^{-1}. Although the sensor can be operated over a larger methane concentration range, the manufacturer calibrated the sensor in a narrower range in order to preserve its linear response (Franatech Pers. Comm.).

The Discrete Water Measurements

Discrete water sampling was conducted using a CTD-rosette with 16 Niskin sampling bottles (8 L), a SBE 911plus CTD (Seabird), an altimeter (Teledyne Benthos PSA 916), and an oxygen optode (Aanderaa Optode 4831F). The sensors were connected through telemetry for real-time monitoring of the water depth of the assembly. This allowed to adjust the sampling strategy during the profile according to the anomalies recorded by the echosounder. The Niskin bottles were sampled during the up-cast, and water subsampling was performed onboard for laboratory gas analysis (both PT and HS). For all the samples, a few mg of sodium azide (NaN_3) were added to the vials and glass bulbs before adding the water sample. Filled vials for HS analysis were then stored upside down.

The samples were analyzed by two different techniques: the purge and trap (PT) and the headspace (HS) techniques. These methods

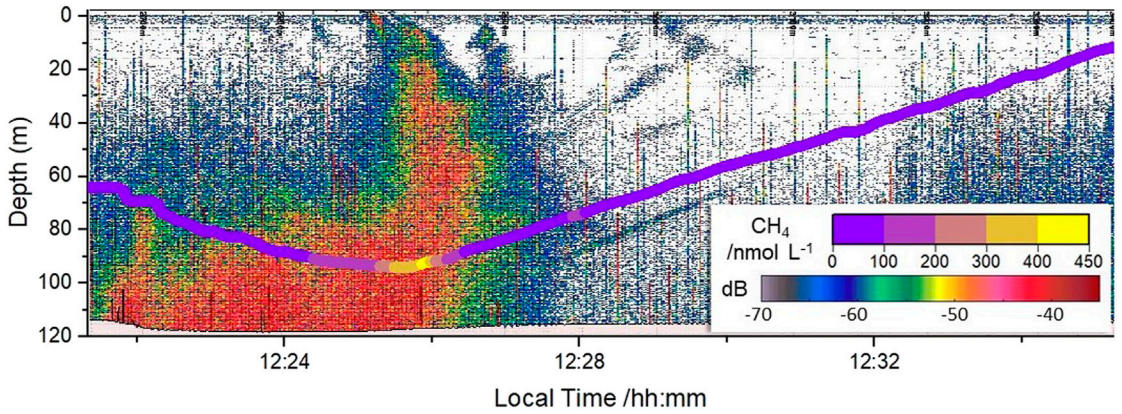

FIGURE 2 | Qualitative comparison between the time series from the continuous concentration of dissolved methane measured by MILS (colored line) and the acoustic signal from the echosounder (colored background). The data are plotted against local time. The data are from the VP03 profile performed on April 5th at the deeper site (44.224°N, 30.730°E).

have already been compared and validated in the laboratory (Donval and Guyader, 2017). The PT method used here is based on Swinnerton et al. (1968) and modified by Luc Charlou et al. (1988). Briefly, 125 ml glass bulbs devoted to the analysis of methane by PT method were used. The bulbs were overflowed with twice the volume of seawater. Particular care was taken to exclude air bubbles during sampling and avoid contamination. Once in the laboratory, CH_4 was stripped from seawater for 8 min using helium as carrier gas (quality 99.9995%), trapped on activated charcoal at −80°C, and detected and quantified with a flame ionization detector after separation on a packed column (GC Agilent 7890A/ column Porapak Q 2 m). The calibration was performed by injection of gas standards containing 108 ppm of CH_4 in air ±5% (Restek). The limit of detection was 0.03 nmol L^{-1}, the precision based on five replicates from the same rosette bottle was within ±2% (±1σ), while the accuracy corresponds to that of the gas standards (±5%). The HS method (Donval et al., 2008; Donval and Guyader, 2017) was performed on 10 ml vials by analyzing the composition of the headspace in equilibrium with the water. At the beginning of the cruise, the vials were flushed with zero air (Alphagaz 2, Air Liquide) to avoid introducing methane into the initial gas phase. With a gas tight syringe, 5 ml of seawater were transferred into the vial while a second needle was introduced to keep the pressure close to atmospheric pressure inside the vial. The analysis was performed by means of a headspace sampler connected to the same GC unit used for the PT method. The limit of detection was 5 nmol L^{-1} and the precision was ≤10% for concentrations below 100 nmol L^{-1}, and ≤5% for higher concentration (±1σ). Further details in the comparison between the results of two methods can be found in the **Supplementary Datasheet S1**.

RESULTS

Inter-Comparison Between the Techniques

In this section we compare results from different techniques with the aim of testing the reliability of the measurements, identifying possible artefacts or weaknesses of each technique used, and validating the finds on the dissolved methane distribution in the water column at the studied sites. This data validation is important for comparing the distribution of dissolved methane at the two locations as reported in the discussion section.

Qualitative Comparison of Echosounder Data and Membrane Inlet Laser Spectrometer

On the echogram, large areas of high backscatter (>−30 dB) of a flare-like shape have been identified as methane gas seeping areas (**Figure 2**, color-coded in orange to red). Broader high backscatter areas are related to vessel movement. In our case, the ship remained over the methane seep location for some time and as the echogram displays backscatter over time, the seepage area widens. During the cruise, 36 and 13 gas emissions in the deeper and shallower site, respectively, were identified from the 70 kHz echosounder data. The signal produced by the scattering of the acoustic wave by the gas bubbles provides only qualitative information about the distribution of dissolved CH_4 in the water column. This is due to the fact that gas bubbles shrink and change their chemical composition during their rise through the water column, and that free bubble-forming gas is mobile whereas dissolved methane is more stationary. Therefore, a quantitative analysis would require different assumptions on the initial bubble size distribution, the bubble rising speed and the gas exchange ratio between the two phases. Results from the quantitative analysis of the acoustic signal is beyond the scope of this paper, and will be the subject of another study. Here, an example of the qualitative comparison between the acoustic signal and the dissolved CH_4 concentrations from MILS is reported in **Figure 2** for the VP03 profile performed on April 5th at the deeper location (44.224° N, 30.730° E). The concentrations of dissolved methane determined by MILS were dynamically corrected for the position of the instrument with respect to the vessel. This correction allows to synchronize/match the two time-series, accounting for the fact that the echosounder passed over a

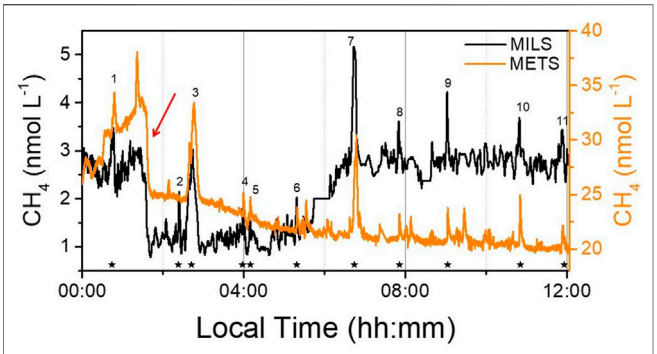

FIGURE 3 | Comparison between the dissolved methane measurements from the MILS and the METS sensor which were deployed simultaneously during the 12 h HP01 survey. The red arrow indicates a sharp concentration decrease observed by both instruments. Well localized peaks of dissolved CH_4 were observed by both instruments (main identified methane peaks are numbered and identified by the stars at the bottom).

target area prior to the towed MILS. A more detailed figure reporting original and synchronised data can be found in the **Supplementary Datasheet S1**.

In this inter-comparison, one should consider that the MILS probe is measuring a specific location behind the vessel, while acoustic data has a larger footprint on the seafloor as well as in the water column. This may induce discrepancy between the two signals, for instance in the case of a bubble plume located a few tens of meters on a side of the MILS instrument that would be spotted acoustically but not observed by the MILS (this could be the case for the signature at 12:22 local time in **Figure 2**, more visible in **Supplementary Figure S1-3**). The results may inverse if water enriched in CH_4 (by a bubble plume that is outside the acoustic lobe) is laterally transported by currents. This may be the case for the increase in dissolved CH_4 at 12:28 local time (visible in **Supplementary Figure S1-3**) that was observed by the MILS sensor without the corresponding acoustic signal.

Despite its evident limitations, this comparison allowed us to verify the qualitative agreements between these two datasets and validate the dynamic correction of the position of the MILS probe with respect to the vessel during the profiles.

Comparison Between the Two *in situ* Instruments

For comparison, the MILS and the METS sensor were deployed simultaneously during the vertical and horizontal profiles. However, due to dependency of the METS sensor to the hydrostatic pressure, salinity and oxygen (Newman et al., 2008), this comparison only focus on the 12-h long horizontal profile (HP01). The profile was conducted at ~5 m depth, and the water inlets of the two sensors were ~10 cm distance from each other. The resulting profiles used for comparison are reported in **Figure 3**. One can clearly see that most of the peaks in methane concentration for both instruments agree with each other. However, the methane concentrations measured by the METS are more than one order magnitude higher than the concentrations obtained with the MILS. Previous field studies have shown significant differences between measurements of discrete water samples of seawater methane concentration from well-proven laboratory methods and the METS outputs (Heeschen et al., 2005; Newman et al., 2008). This has led Heeschen et al. (2005) to interpret their METS *in situ* measurements in a qualitative way. Here, the differences observed between the MILS and the METS measurements may be explained by: 1) the fact that the METS sensor was used below the calibration range (100 nmol L^{-1}–40 µmol L^{-1} at atmospheric pressure) certified by the manufacturer and therefore it cannot provide reliable quantitative measurements at the sea surface; 2) the METS suffers from dependency to hydrostatic pressure, salinity and oxygen content (Newman et al., 2008), which makes near-surface horizontal profile also challenging. Moreover, the wide drifts observed during this 12 h continuous near-surface profile (**Figure 3**) can be explained by the fact that small height changes in near-surface depth lead to large relative changes in hydrostatic pressure that considerably affect the sensor response. Despite the large discrepancy on the methane concentration from the METS sensor, both *in situ* instruments agreed on the presence of highly localized peaks of CH_4 at the sea surface. The METS sensor, even when it is used outside the calibration range and under severe conditions (changing oxygen concentration that affect its detection system) can provide valuable qualitative information on the location of dissolved methane concentration spots. Further laboratory tests, together with deployment at deeper water depth within the anoxic layer, would be required to provide a thorough assessment of the sensor for quantitative and reliable dissolved methane measurements.

Eleven well localized dissolved CH_4 peaks (numerated and marked with stars in **Figure 3**) were identified during the horizontal profile HP01 and are discussed in the next section. Furthermore, the sharp concentration decrease recorded at 01:35 local time (highlighted in **Figure 3** by the red arrow and also visible in the 2D colored map graph of the dissolved methane concentrations measured by the MILS instrument and reported in **Figure 4**) that could have been associated with a possible instrumental (MILS) drift, was confirmed as a real signal since observed by both *in situ* sensors.

Membrane Inlet Laser Spectrometer Vs Measurements of Discrete Water Samples at the Deeper and Shallower Sites

Comparison on Vertical Profiles

The size of the MILS prototype did not allow to be mounted on the CTD for continuous *in situ* measurements simultaneous to discrete water sampling. For this reason, measurements with the MILS probe and discrete water samplings could not be conducted simultaneously. Moreover, because the research vessel was not equipped with dynamic positioning, inter-comparisons on dissolved methane measurements were challenging. As mentioned above, due to the high spatial variability of dissolved methane relative to the location and intensity of bubble streams, a few hundreds or even a few tens of meters could be significant for correctly reproducing the same spatial distribution of dissolved CH_4. However, we identified a few vertical profiles at the shallower

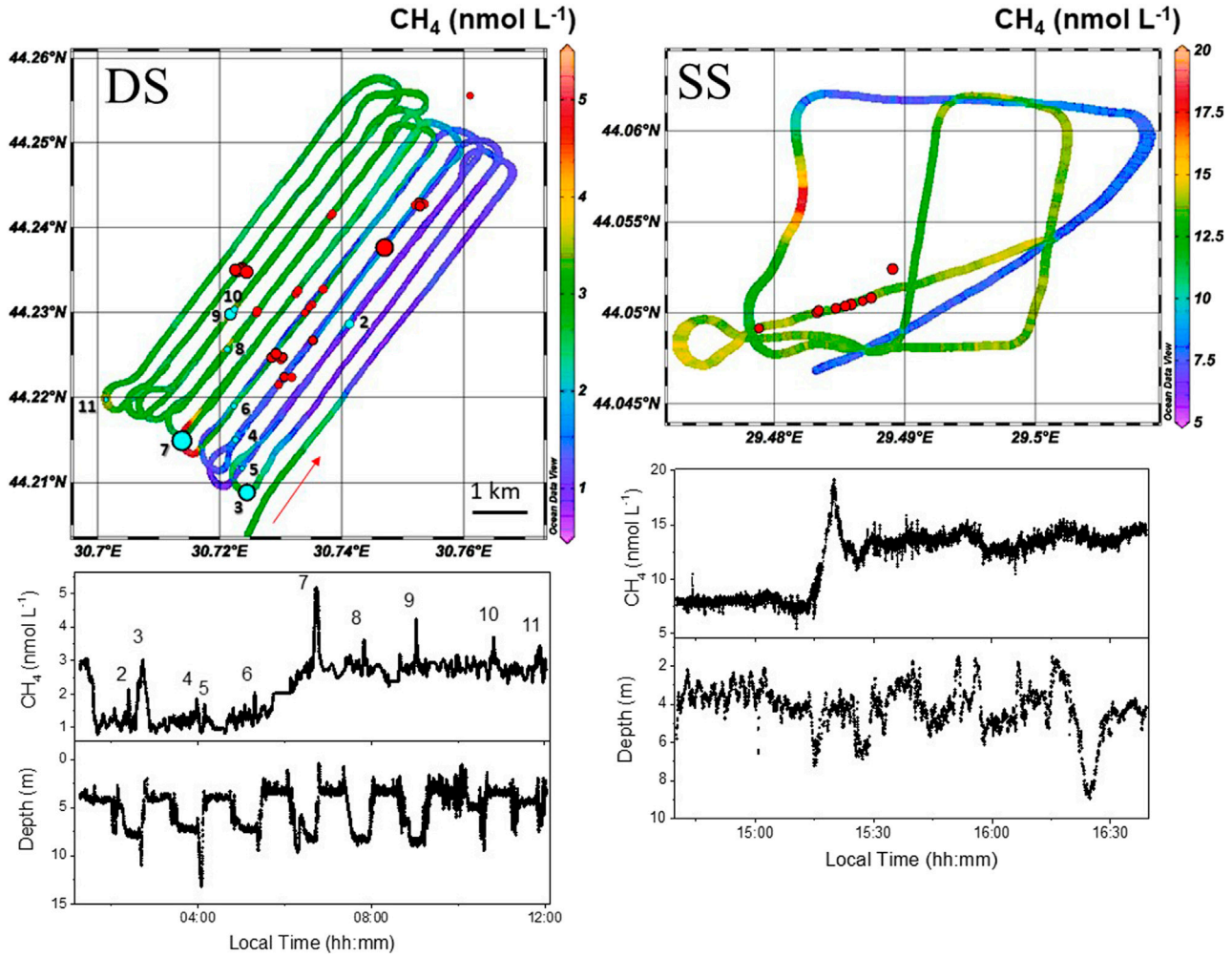

FIGURE 4 | 2D surface dissolved methane distribution (color map) at the deeper (DS, **left)** and shallower (SS, **right)** site. Both surveys were conducted near surface. The thickness of the color map (~60 m) was chosen accordingly to the 2σ accuracy of the GPS positioning. Red arrows indicate the time direction. Red and light-blue dots show the locations of the flares (echosounder) and surface dissolved CH_4 (MILS) peaks, respectively, both with the size proportional to the estimated intensity. Peak 1 is only visible in **Figure 6**, because it is located at a southern position with respect to the performed grid. At the bottom, the time series of the data together with the water depth information. Localized peaks of dissolved CH_4 were observed at certain locations, which seems uncorrelated with the flare locations.

and deeper sites, where the position of the MILS was relatively close to the hydro-casts (HYs) for discrete water sampling. These profiles are reported in **Figure 5**. The trajectories of the vessel during the measurements are shown in the inserts. The arrows indicate the time direction of the deployment, while the location of the bottom of the profile is indicated by green dots. The VP03 profile performed by the MILS sensor started with the probe at 60 m water depth, and it went first down to 93 m, and then back up to the surface. Red dots are the positions of the flares identified during the campaign. For discrete water sample measurements average values between the PT and HS analysis were used. Dissimilarities between the two techniques at the two sites ranged from 8 nmol L^{-1} (0–70 m water depth) to 86 nmol L^{-1} (>70 m water depth) at the deeper site, and from 8 nmol L^{-1} (0–25 m water depth) to 62 nmol L^{-1} (>25 m water depth) at the shallower site. At the shallower site, the MILS curves systematically show lower concentrations of dissolved CH_4 with respect to the measurement from discrete water sample analysis. This may be due to the strong spatial variability caused by the ascent of the multiple methane bubbles of variable size and trajectory within the water column, or by an unidentified bias in either the MILS or discrete sampling methods. Our results highlight the limitations of current *in situ* instrumentation and laboratory measurement techniques. Nevertheless, a larger number of measurements together with improved position maintaining or simultaneous deployment of the *in situ* instruments and Niskin bottle sampler would have been required for a finer comparison of the two methods. Further information on this comparison can be found in the **Supplementary Datasheet S1**.

Comparison on Near-Surface Measurements

MILS continuous sea-surface measurements were compared with the results from discrete water sampling performed during the

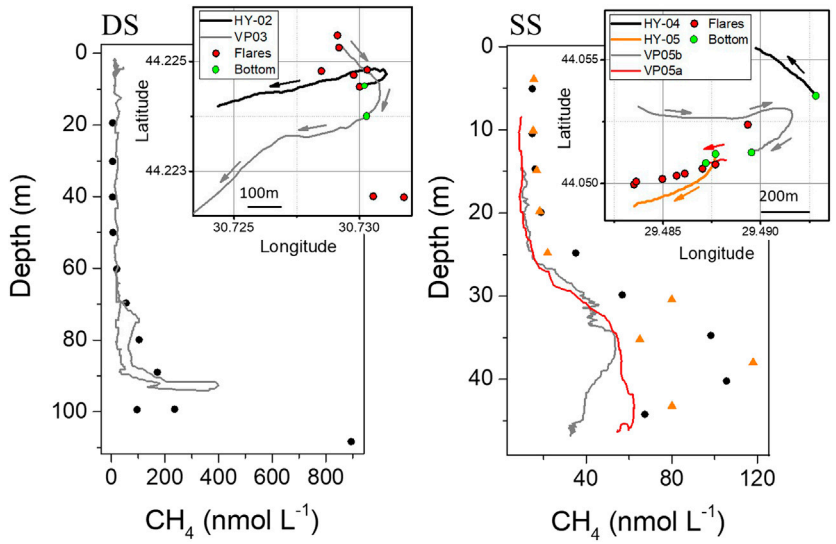

FIGURE 5 | Comparison between the dissolved methane measurements from MILS (VP) and discrete water sample (HY) techniques at the two sites (average concentrations between PT and HS methods are reported). The inserts show the trajectory of the vessel during the measurements, which were performed at different time and without dynamic positioning of the vessel. Red circles in the maps report the location of the flares identified from the acoustic survey. Arrows in the inserts represent the time direction of the measurement, and green dots the location of the bottom of the profile.

TABLE 1 | Data used in **Figure 6** for the deeper and shallower site. MILS (Membrane inlet laser spectrometer) data are an average from measurements which were closest to the discrete water sampling (HY) locations. HY data are averages between the PT and HS analysis. Water depths and estimated accuracies of the measurements are also reported.

—	—	MILS			HY		
—	—	Depth/m	CH_4/nmol L^{-1}	Accuracy (12%)	Depth/m	CH_4/nmol L^{-1}	Accuracy (5%)
Deeper site	HY-01	5.9	2.84	0.34	10.4	10.77	0.54
	HY-02	5.2	1.69	0.20	19.4	4.68	0.23
	HY-03	4.6	2.77	0.33	8.6	4.23	0.21
—	—	—	—	—	—	—	—
Shallower site	HY-04	5.0	12.70	1.52	5.0	14.59	0.73
	HY-05	3.6	13.50	1.62	3.9	15.52	0.78

HYs. The results from the shallowest measurements of the HY profiles were used (average concentrations between the PT and HS method; depths and accuracies of the measurements are reported in **Table 1**), and compared against the closest data from the MILS sensor. In the two maps of **Figure 6**, the trajectories during the MILS survey and the location of the near-surface discrete water sampling (HYs) are reported for the deeper and shallower site. The concentration of dissolved methane measured by MILS closest to the locations of the HYs were selected and highlighted with thick black lines. The selected MILS data were averaged at each location, and reported in the bar graph of **Figure 6** together with the results from the concentrations in dissolved methane by the analysis of discrete water samples.

The location of the HY-02 and HY-03 measurements lies between two horizontal profile lines, therefore data from both lines were selected and averaged. HY-05 was very close to the horizontal profile trajectories, while for HY-01 and HY-04 the closest dissolved CH_4 MILS data were 300 and 140 m away, respectively.

The comparison between MILS and measurements of discrete water samples at the shallower site (HY-04 and HY-05) shows a discrepancy of ~13% ($([CH_4]_{MILS} - [CH_4]_{HY})/[CH_4]_{HY}$), which lies within the accuracy of the measurements, as reported in **Table 1**. At the deeper site, the differences are larger, with 34% discrepancy for the HY-03 and even larger for HY-01 and HY-02. Different hypotheses can explain these discrepancies. As mentioned above, the measurements were not conducted at the same time. At the shallower location, HP03, HY-04, HY-05 were conducted on the same day (April 6th), while the measurements at the deeper site were spread over two and half days (April 3rd to 5th). Thus 1) The spatio-temporal variability of dissolved CH_4 at the sea surface can be affected by water currents producing different distribution patterns as well as meteorological conditions (change in wind direction or speed, humidity, water temperature, etc.) (Shakhova et al., 2014) that modify gas exchange/equilibration with the atmosphere and degassing activities at the seafloor. Although, this last hypothesis would require significant changes in meteorological

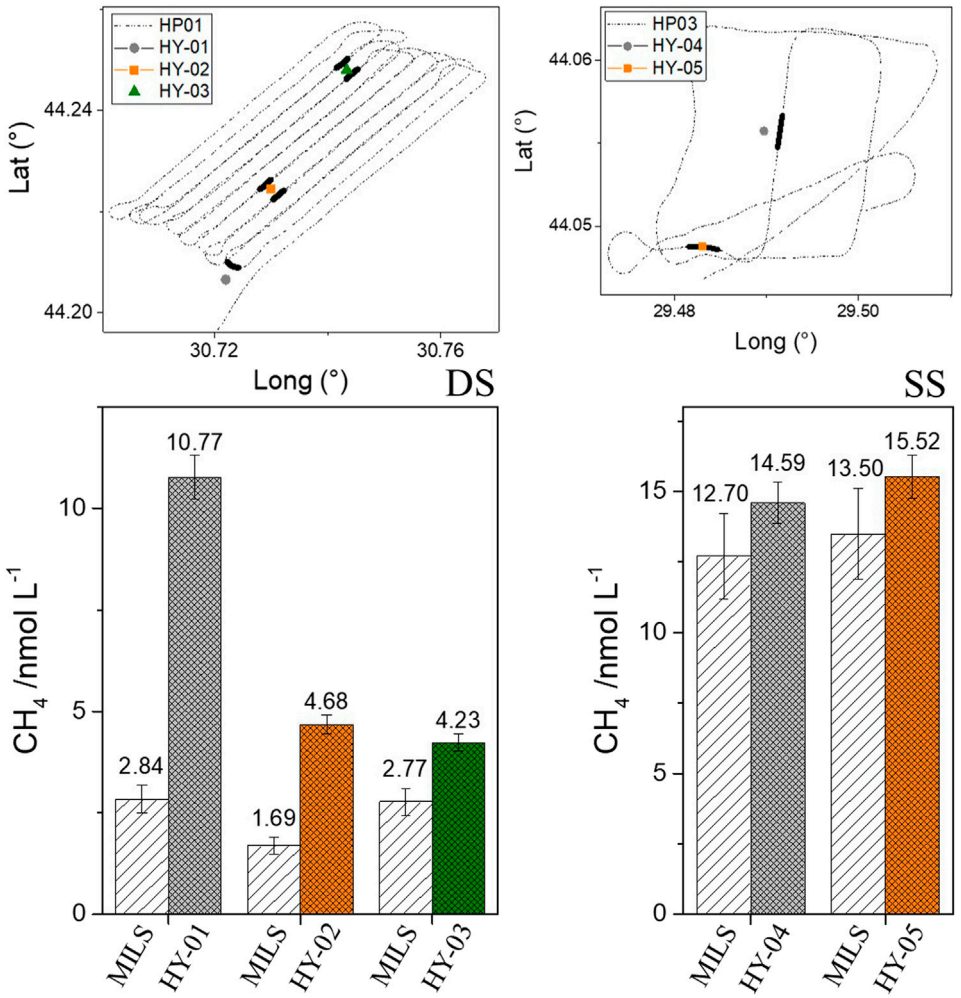

FIGURE 6 | Bottom: Comparison between near-surface water depth measurements made by the MILS sensor and the analysis of discrete samples (HY) at the deeper (DS, **left)** and shallower (SS, **right)** site. Data from discrete samples are reported as the average between the two analytical techniques used (PT and HS). Maps with locations are reported at the top, with the trajectories of the MILS surveys (dotted lines) and locations of the near sea surface sampling of the HYs. In thick black lines are the selected dissolved CH_4 MILS data closest to the discrete sampling locations which were averaged and used for the comparison.

conditions in order to explain the reported discrepancies; 2) the discrepancy could be due to the analytical techniques itself. The MILS measurements seem to be systematically lower than the measurements of discrete water samples. Apart from the HY-01 location where a 7.9 nmol L^{-1} difference was found, for the other locations the offset between the two techniques is ~2 nmol L^{-1}, which remains within the order of magnitude of the best precision one could expect today on dissolved CH_4 measurements in the ocean.

DISCUSSION: COMPARISON BETWEEN THE TWO SITES OF STUDY

Discussion on Vertical Profiles

The MILS vertical profiles recorded at the two sites during the campaign are reported by grey and orange dots in **Figures 7A,B**. For the deeper site, a total of four down- and up-casts (VP01, 02, 03, and 04) were used, whereas for the shallower location, the vertical profile VP05, composed of a series of seven down- and up-casts over the seepage area was used. The 2-m average curves are in black and blue for the deeper and shallower sites, respectively. Because the gas bubbles originate from the seafloor, the vertical profiles were compiled in distance from seabed (rather than in water depth), allowing a better comparison of the vertical distribution of the dissolved CH_4 within the two sites. For each datapoint, the distance from the seafloor was calculated using the depth of the seafloor measured by the echosounder and the water depth of the instrument provided by MILS-implemented CTD and the MILS instrument itself. The systematic decrease in dissolved CH_4 concentration near the seafloor may be due to the fact that the position of the vessel was not dynamically maintained. In most of the vertical profiles recorded, the instrument passed over the bubble plume either

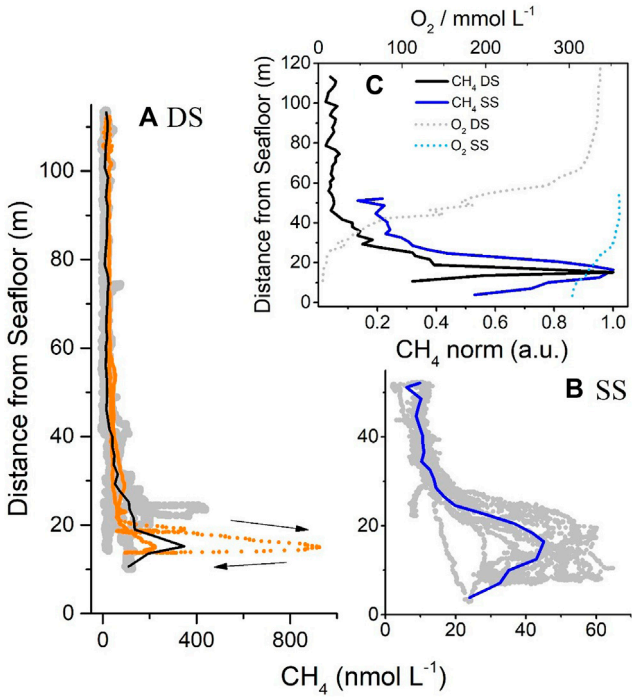

FIGURE 7 | (A) A compilation of vertical profiles acquired with the MILS probe at the deeper location (VP01, 02, 03 and 04 for a total of four down- and up-casts) and **(B)** at the shallower location (VP05 which is a series of seven down- and up-casts) (grey dots). The profile VP04 is represented with orange dots, highlighting the temporal evolution of the measurement during the descent and ascent (black arrows). Black and blue lines are 2-m average values. **(C)** the average curves of dissolved CH_4 (solid lines), normalized by the maximum concentration at each site, are plotted against the distance from the seafloor, showing a similar and expected exponential dissolution trend. While at the DS dissolved CH_4 concentrations reached background value at 50 m from the seafloor, at the SS, methane concentration at the sea surface was ~20% of the maximum of the average concentration measured at the sea bottom. The average variations in dissolved O_2 at both locations are also reported (dotted lines).

during its descent or ascent (this is visible in the time series reported in **Figure 2**). The MILS instrument was therefore within the uppermost part of the gas bubble plume most of the time a few tens of meters above the seafloor. For a finer visualization of this effect, the stronger profile recorded by the MILS at the deeper location (corresponding to the VP04) is reported in orange dots (**Figure 6A**). The two black arrows indicate the time direction during the descent. The maximum dissolved CH_4 concentration of 924.5 nmol L^{-1} was reached at 15 m from the seafloor (or 93 m water depth). Then, despite the probe continuing its descent, the concentration decreased, probably due to the fact that the probe was moving out of the bubble plume. Another possible reason for this trend may be directly related to bubble dissolution. The seafloor topography can influence bottom current (Weber et al., 2000; Stow et al., 2009), which in turn affect bubble trajectory in the water column and shape the plume morphology. Hence, the rim of the bubble plume is widened few meters above the seafloor, enhancing the spreading of dissolved CH_4 at this height, and placing the maximum level of dissolved methane concentration further above the seafloor. Lastly, note that the distance between the instrument and the ship was calculated by mooring simulation (as mentioned in the materials and methods section) which may add uncertainty on the position of the MILS sensor with respect to the one of the bubble plumes. From the maximum concentrations of the averaged curves, a difference in emission intensity of ~80 fold between the shallower and the deeper site was estimated.

In **Figure 6C**, all the vertical profiles were averaged producing one data point every 2 m water depth, and the concentration of dissolved CH_4 was normalized with respect to the maximum averaged dissolved CH_4 concentration. At both sites, an exponential trend was observed which follows the expected dissolution function of the bubbles into the water column (Jansson et al., 2019a). By fitting the exponential curves on the whole vertical profile, exponential time constants (corresponding to the distance from the seafloor required for decreasing the intensity by 1/e – e-folding – of the value at the sea bottom) of 6.8 and 6.3 m were obtained for the deeper and shallower sites, respectively. They are close, but the difference remains visible in **Figure 6C**, with a faster decreasing in concentration of the profile at the deeper site while moving away from the seafloor. This emphasizes the larger storage capability of dissolved CH_4 at the bottom water level of the deeper site (i.e. a better tendency of CH_4 to escape towards to the sea surface at the shallower site). The reason for this difference is likely a combination of factors, including: 1) the difference in hydrostatic pressure and bubble-size distribution, leading to a different bubble/water exchange (more precisely related to the difference between the buoyant rise time of the bubble and its diffusive equilibrium time (Leifer and Patro, 2002)); 2) decoupling between bottom and surface water at the deeper location marked by the presence of the oxycline, which prevents the rise of CH_4 towards the sea surface; 3) a possible local production of CH_4 in the anoxic water of the deeper site (Artemov et al., 2019), which would increase the concentration of dissolved CH_4 below the thermocline. Discriminating between the different scenarios would involve a more intensive investigation of methane distribution in all three water layers, combining a larger number of horizontal and vertical profiles, and both molecular and isotopic concentration measurements of CH_4; this was not performed during this campaign. From this analysis, we can conclude that at the deeper site, going from the seafloor towards the surface, the dissolved CH_4 rapidly decreases within the first 45 m (~7 times the exponential time constant), and remains uniform in the upper part. On the other hand, at the shallower site, dissolved CH_4 concentrations corresponding to ~20% of the maximum average dissolved CH_4 concentration on the water column are still present at the sea surface (at ~52 m from the seafloor).

Discussion on Horizontal Near-Surface Profiles

Two near-surface horizontal profiles were conducted during the cruise: HP01 at the deeper site and HP03 at the shallower site. The 2D distributions of dissolved CH_4 are reported in **Figure 4**. The average concentration at the deeper site was 2.23 ± 0.78 nmol L^{-1} (1σ, min 0.78, max 5.16 nmol L^{-1}). For the measured temperature and electrical conductivity of the surface water (9.5°C and

18 mS cm^{-1}), the atmospheric CH_4 concentration of 2 ppm (part per million) would correspond to an equilibrium dissolved CH_4 concentration of 3.5 nmol L^{-1} (calculated from **Equations 1**, **2** and **3**). This is slightly higher than the average concentration measured by the MILS, but it still lays within the range of the measurements made by the MILS sensor near the surface. On the other hand, from the comparison with measurements of discrete water samples (**Figure 6**), concentrations measured by the MILS seems to be systematically ~2 nmol L^{-1} lower. We can therefore conclude that at the deeper site, dissolved CH_4 in the water is close to equilibrium with the atmosphere. At the shallower site, the average dissolved CH_4 concentration was 5.6 times higher than observed at the deeper site (average concentration 12.5 ± 2.76 nmol L^{-1} 1σ; min 5.16, max 19.7 nmol L^{-1}) and almost four times higher than the expected concentration in equilibrium with the atmosphere. These concentrations are close to previously reported measurements by Amouroux et al. (2002) and Reeburgh et al. (1991) in north-western and central part of the Black sea, respectively. This, together with what we observed in the vertical profiles (i.e. the fact that, at the shallower site, 20% of the amount of dissolved CH_4 present at the bottom was found near the surface), confirms the occurrence of methane fluxes from the oxic layer to the atmosphere at shallow water depths, which is also in agreement with previous findings (Reeburgh et al., 1991; Schmale et al., 2005; McGinnis et al., 2006). The difference in dissolved CH_4 concentration at the sea surface of the two sites may support the hypothesis of an efficient vertical transport of dissolved methane from the seafloor up to the surface at shallow depths. Alternatively, other unidentified sources may be the cause of this oversaturation of the surface water, either through lateral diffusion or CH_4 generation in the upper water layer.

Average concentrations from measurements of discrete water samples (reported in **Table 1**) were obtained from only three data points at the deeper site and two at the shallower, with values of 6.6 and 15.1 nmol L^{-1}, respectively. This confirms the results of the *in situ* technique showing a generally higher concentration of methane at the shallower location.

From the near-surface dissolved CH_4 data of the deeper site, eleven isolated peaks were identified (light-blue dots in **Figure 4** corresponding to the peaks marked with stars in **Figure 3**, also numerated on both figures) with peak intensities ranging from 0.6 to 2.3 nmol L^{-1} and average width of ~500 m (full width at half maximum, FWHM). All the selected peaks were observed by both *in situ* instruments except for the second peak in the time series, which was recorded only by the MILS instrument but with a peak intensity of 1.26 nmol L^{-1} and therefore a relatively good signal to noise ratio. Peaks observed by the METS but not by the MILS sensor were disregarded, since they may be due to a measurement artefact because of the low selectivity of the sensor. The intensities were calculated after subtraction of the background concentration, by means of a Gaussian fit. The two stronger and larger peaks (FWHM of ~1,500 and ~640 m) are the N° 3 and 7, both located at the southern edge of the grid survey. These events at the sea surface are however difficult to correlate with the locations of the identified flares (red dots in **Figure 4**), and the mismatch suggests that: 1) the vertical transport of dissolved CH_4 from the seafloor up to the surface may strongly be affected by lateral transport of methane through currents; 2) other factors or other unidentified sources (i.e. microbial activities) may play a role in the occurrence spots of high methane concentration near the sea surface. Despite our achievements, we are still far from computing all the processes for conclusively assessing the fate of methane in the Black Sea water column. The fact that the shallower site has a higher dissolved CH_4 concentration at the sea surface with respect to the deeper site agrees with previous findings (Reeburgh et al., 1991; Amouroux et al., 2002). This reinforces the hypothesis of methane transport from the seafloor to the atmosphere at shallow sites, although contributions of other sources cannot be firmly discarded. This is further supported by the fact that the methane oxidation rate is lower in the oxic layer (Reeburgh et al., 1991), promoting its persistence in the water during the ascent. Our results agree with Schmale et al. who, in 2005, concluded that only shallow seeps (depths <100 m) seem to affect the methane concentration of surface water and direct local emissions into the atmosphere, while high-intensity seep sites below this boundary do not show regional influence on the surface layer. Greinert et al. (2010) highlighted how methane fluxes rapidly increase with increasing bubble size and decreasing water depth, underlining that shallow sites may represent a significant source of methane to the atmosphere. Other factors have been proposed to explain marine methane transfer to the atmosphere. Indeed, Shakhova et al., 2017 and Pohlman et al., 2017 also discussed the large release of CH_4 from the sediments at shallow sites in the Arctic regions and its potential impact on the climate. They claimed that upwelling and erosion are, for instance, possible mechanisms promoting gas transfer to the atmosphere.

CONCLUSION

We have presented a multi-technique approach (using acoustic, *in situ* and laboratory methods) capturing dissolved methane distribution in the water column at the Romanian sector of the Western Black Sea. The results from the cruise allowed the comparison of data from different sensors and techniques, highlighting the challenge for reliable dissolved gas measurements. Thanks to this multi-technique approach we have obtained new insights into the vertical and horizontal distribution of dissolved methane at two different sites.

Relatively good agreement between continuous, *in situ*, high resolution MILS measurements and discrete sampling followed by laboratory analysis (purge-and-trap and headspace technique followed by gas chromatography analysis) was found on vertical as well as horizontal profiles, despite the difficulties of the comparison due to the lack of dynamic positioning of the vessel. The METS sensor is compact, low-power and easy to use, and allowed to confirm the presence of localized sea surface 'hot spots' of dissolved methane observed by the MILS sensor. Nevertheless, it showed limitations for providing quantitative measurement on both vertical and horizontal surface profiles due to its low selectivity and strong dependency to changes in the physical conditions: hydrostatic pressure, water temperature, salinity and dissolved oxygen content. Concentrations of dissolved methane measured by MILS show good

agreement with the acoustic data (qualitatively) and measurements of discrete water samples (quantitatively), supporting the reliability of this *in situ* sensor.

The vertical profiles highlighted a similar distribution of the dissolved CH_4 that follows an expected dissolution function. Concentrations at the seafloor were on average ~80 times larger at the deeper site with respect to the shallower site. At the sea surface of the deeper location, dissolved CH_4 was present at a concentration close to that expected from equilibrium with the atmosphere, while it was four times higher at the shallower site. Localized peaks of dissolved CH_4 were observed at the sea surface, but a direct correlation with the position of flares at the seafloor was difficult to make. Due to the continuous decreasing trend (bottom to top) obtained from the dissolved methane concentration vertical profiles at the two investigated sites, we hypothesized that higher concentrations of dissolved methane near the surface at the shallower site can be explained by a methane transfer from the seafloor. However, we do not yet have undisputable evidence that would prove this transfer while methane may also be supplied from other sources. This underlines the need of further investigations for better understanding the methane dynamics in the Black Sea. For such a study, dynamic positioning of the vessel or a deployment using a Remotely Operated underwater Vehicle or a submersible will be crucial for accurately capturing the vertical distribution of CH_4 in the bubble plume. This would allow for easier comparison between different sensors and techniques, to better evaluate their accuracy, and eventually identify possible instrumental bias for future improvements. Furthermore, following the isotopic signature of methane together with its concentration variability in the water column would provide key information on the fate of methane released from the seafloor and eventually identify the processes mitigating or increasing its concentration at the different water layers of the Black Sea.

DATA AVAILABILITY STATEMENT

The raw data supporting the conclusions of this article will be made available by the authors, upon request.

AUTHOR CONTRIBUTIONS

All authors except JG participated in the cruise. LR was chief of the expedition, JP was the leader of the WP4 of the ENVRI + project. RG developed and calibrated the MILS sensor, and conceived and performed the experiments of deployments during the cruise. CB deployed the MILS. DB worked on the calibration and deployment of the METS sensor. JD and VG were in charge of the CTD-Rosette and sampled the seawater. JD performed the measurement of water samples in the laboratory. MS and HL installed the echosounder and performed the acoustic survey. MS performed the analysis of the acoustic data. RG and LR wrote the first draft, and all the authors contributed to the manuscript.

FUNDING

The research leading to these results has received funding from the ENVRIPlusH2020 project (call 597 Environment, project number 654182) the European Community's Seventh Framework Programme 598 ERC-2015-PoC under grant agreement no. 713619 (ERC OCEAN-IDs) and from the Agence 599 Nationale de la Recherche (ANR) under grant agreement ANR-18-CE04-0003-01.

ACKNOWLEDGMENTS

The authors would like to thank all members of the team who took part in the cruise, colleagues from INGV-Palermo for their fruitful discussions and exchanges during the cruise, the captain and staff of the R/V Mare Nigrum and all the logistic support from the Romanian GeoEcoMar.

SUPPLEMENTARY MATERIAL

The Supplementary Material for this article can be found online at: https://www.frontiersin.org/articles/10.3389/feart.2021.626372/full#supplementary-material

REFERENCES

Amouroux, D., Roberts, G., Rapsomanikis, S., and Andreae, M. O. (2002). Biogenic Gas (CH4, N2O, DMS) Emission to the Atmosphere from Near-Shore and Shelf Waters of the North-western Black Sea. *Estuarine Coastal Shelf Sci.* 54 (3), 575–587. doi:10.1006/ecss.2000.0666

Artemov, Y. G., Egorov, V. N., and Gulin, S. B. (2019). Influx of Streaming Methane into Anoxic Waters of the Black Sea Basin. *Oceanology* 59 (6), 860–870. doi:10.1134/S0001437019060018

Borges, A. V., Champenois, W., Gypens, N., Delille, B., and Harlay, J. (2016). Massive marine Methane Emissions from Near-Shore Shallow Coastal Areas. *Sci. Rep.* 6, 2–9. doi:10.1038/srep27908

Boulart, C., Briais, A., Chavagnac, V., Révillon, S., Ceuleneer, G., Donval, J.-P., et al. (2017). Contrasted Hydrothermal Activity along the South-East Indian Ridge (130°E-140°E): From Crustal to Ultramafic Circulation. *Geochem. Geophys. Geosyst.* 18 (7), 2446–2458. doi:10.1002/2016GC006683

Boulart, C., Connelly, D. P., and Mowlem, M. C. (2010). Sensors and Technologies for *In Situ* Dissolved Methane Measurements and Their Evaluation Using Technology Readiness Levels. *Trac - Trends Anal. Chem.* 29 (2), 186–195. doi:10.1016/j.trac.2009.12.001

Capet, A., Stanev, E. V., Beckers, J.-M., Murray, J. W., and Grégoire, M. (2016). Decline of the Black Sea Oxygen Inventory. *Biogeosciences* 13 (4), 1287–1297. doi:10.5194/bg-13-1287-2016

Chua, E. J., Savidge, W., Short, R. T., Cardenas-valencia, A. M., and Fulweiler, R. W. (2016). A Review of the Emerging Field of Underwater Mass Spectrometry. *Front. Mar. Sci.* 3 (209). doi:10.3389/fmars.2016.00209

Dewey, R. K. (1999). Mooring Design & Dynamics-A Matlab Package for Designing and Analyzing Oceanographic Moorings. *Mar. Models* 1 (1–4), 103–157. doi:10.1016/S1369-9350(00)00002-X

Donval, J. P., Charlou, J. L., and Lucas, L. (2008). Analysis of Light Hydrocarbons in marine Sediments by Headspace Technique: Optimization Using Design of Experiments. *Chemometrics Intell. Lab. Syst.* 94 (2), 89–94. doi:10.1016/j.chemolab.2008.06.010

Donval, J. P., and Guyader, V. (2017). Analysis of Hydrogen and Methane in Seawater by "Headspace" Method: Determination at Trace Level with an Automatic Headspace Sampler. *Talanta* 162, 408–414. doi:10.1016/j.talanta.2016.10.034

Etiope, G. (2012). Methane Uncovered. *Nat. Geosci.* 5 (6), 373–374. doi:10.1038/ngeo1483

Faure, K., Greinert, J., Pecher, I. A., Graham, I. J., Massoth, G. J., de Ronde, C. E. J., et al. (2006). Methane Seepage and its Relation to Slumping and Gas Hydrate at the Hikurangi Margin, New Zealand. *New Zealand J. Geology. Geophys.* 49 (4), 503–516. doi:10.1080/00288306.2006.9515184

Garcia-Tigreros, F., and Kessler, J. D. (2018). Limited Acute Influence of Aerobic Methane Oxidation on Ocean Carbon Dioxide and pH in Hudson Canyon, Northern U.S. Atlantic Margin. *J. Geophys. Res. Biogeosciences* 123 (7), 2135–2144. doi:10.1029/2018JG004384

Ghass (2015). Ghass. Available at: https://campagnes.flotteoceanographique.fr/campagnes/15000500/.

Greinert, J., McGinnis, D. F., Naudts, L., Linke, P., and De Batist, M. (2010). Atmospheric Methane Flux from Bubbling Seeps: Spatially Extrapolated Quantification from a Black Sea Shelf Area. *J. Geophys. Res.* 115 (1), 1–18. doi:10.1029/2009JC005381

Grilli, R., Darchambeau, F., Chappellaz, J., Mugisha, A., Triest, J., and Umutoni, A. (2020). Continuous *In Situ* Measurement of Dissolved Methane in Lake Kivu Using a Membrane Inlet Laser Spectrometer. *Geosci. Instrum. Method. Data Syst.* 9 (1), 141–151. doi:10.5194/gi-9-141-2020

Grilli, R., Triest, J., Chappellaz, J., Calzas, M., Desbois, T., Jansson, P., et al. (2018). Sub-Ocean: Subsea Dissolved Methane Measurements Using an Embedded Laser Spectrometer Technology. *Environ. Sci. Technol.* 52 (18), 10543–10551. doi:10.1021/acs.est.7b06171

Hartmann, J. F., Gentz, T., Schiller, A., Greule, M., Grossart, H.-P., Ionescu, D., et al. (2018). A Fast and Sensitive Method for the Continuous *In Situ* Determination of Dissolved Methane and its δ13C-isotope Ratio in Surface Waters. *Limnol. Oceanogr. Methods* 16 (5), 273–285. doi:10.1002/lom3.10244

Heeschen, K. U., Collier, R. W., de Angelis, M. A., Suess, E., Rehder, G., Linke, P., et al. (2005). Methane Sources, Distributions, and Fluxes from Cold Vent Sites at Hydrate Ridge, Cascadia Margin. *Glob. Biogeochem. Cycles* 19 (2), 1–19. doi:10.1029/2004GB002266

Ippommatsu, M., Sasaki, H., and Yanagida, H. (1990). Sensing Mechanism of SnO2 Gas Sensors. *J. Mater. Sci.* 25 (1), 259–262. doi:10.1007/BF00544217

James, R. H., Bousquet, P., Bussmann, I., Haeckel, M., Kipfer, R., Leifer, I., et al. (2016). Effects of Climate Change on Methane Emissions from Seafloor Sediments in the Arctic Ocean: A Review. *Limnol. Oceanogr.* 61, S283–S299. doi:10.1002/lno.10307

Jansson, P., Ferré, B., Silyakova, A., Dølven, K. O., and Omstedt, A. (2019a). A New Numerical Model for Understanding Free and Dissolved Gas Progression toward the Atmosphere in Aquatic Methane Seepage Systems. *Limnol. Oceanogr. Methods* 17 (3), 223–239. doi:10.1002/lom3.10307

Jansson, P., Triest, J., Grilli, R., Ferré, B., Silyakova, A., Mienert, J., et al. (2019b). High-resolution Underwater Laser Spectrometer Sensing Provides New Insights into Methane Distribution at an Arctic Seepage Site. *Ocean Sci.* 15 (4), 1055–1069. doi:10.5194/os-15-1055-2019

Karl, D. M., Beversdorf, L., Björkman, K. M., Church, M. J., Martinez, A., and Delong, E. F. (2008). Aerobic Production of Methane in the Sea. *Nat. Geosci.* 1 (7), 473–478. doi:10.1038/ngeo234

Kessler, J. D., Reeburgh, W. S., Southon, J., Seifert, R., Michaelis, W., and Tyler, S. C. (2006a). Basin-wide Estimates of the Input of Methane from Seeps and Clathrates to the Black Sea. *Earth Planet. Sci. Lett.* 243 (3–4), 366–375. doi:10.1016/j.epsl.2006.01.006

Kessler, J. D., Reeburgh, W. S., and Tyler, S. C. (2006b). Controls on Methane Concentration and Stable Isotope (δ2H-CH4andδ13C-CH4) Distributions in the Water Columns of the Black Sea and Cariaco Basin. *Glob. Biogeochem. Cycles* 20 (4), 1–13. doi:10.1029/2005GB002571

Krabbenhoeft, A., Netzeband, G. L., Bialas, J., and Papenberg, C. (2010). Episodic Methane Concentrations at Seep Sites on the Upper Slope Opouawe Bank, Southern Hikurangi Margin, New Zealand. *Mar. Geology* 272 (1–4), 71–78. doi:10.1016/j.margeo.2009.08.001

Lammers, S., and Suess, E. (1994). An Improved Head-Space Analysis Method for Methane in Seawater. *Mar. Chem.* 47 (2), 115–125. doi:10.1016/0304-4203(94)90103-1

Leifer, I., and Patro, R. K. (2002). The Bubble Mechanism for Methane Transport from the Shallow Sea Bed to the Surface: A Review and Sensitivity Study. *Continental Shelf Res.* 22 (16), 2409–2428. doi:10.1016/S0278-4343(02)00065-1

Luc Charlou, J., Dmitriev, L., Bougault, H., and Needham, H. D. (1988). Hydrothermal CH4 between 12°N and 15°N over the Mid-Atlantic Ridge. *Deep Sea Res. A. Oceanographic Res. Pap.* 35 (1), 121–131. doi:10.1016/0198-0149(88)90061-1

MacLennan, D. N., and Svellingen, I. (1989). Simple Calibration Technique for the Split-Beam echo-sounder. *Fiskdir. Skr. Ser. Havunders* 18 (9), 365–379.

Malakhova, L. V., Egorov, V. N., Malakhova, T. V., Gulin, S. B., and Artemov, Y. G. (2010). Methane in the Sevastopol Coastal Area, Black Sea. *Geo-Mar Lett.* 30 (3–4), 391–398. doi:10.1007/s00367-010-0198-7

Marinaro, G., Etiope, G., Gasparoni, F., Calore, D., Cenedese, S., Furlan, F., et al. (2004). GMM?a Gas Monitoring Module for Long-Term Detection of Methane Leakage from the Seafloor. *Env Geol.* 46 (8), 1053–1058. doi:10.1007/s00254-004-1092-2

Mau, S., Römer, M., Torres, M. E., Bussmann, I., Pape, T., Damm, E., et al. (2017). Widespread Methane Seepage along the continental Margin off Svalbard - from Bjørnøya to Kongsfjorden. *Sci. Rep.* 7, 1–13. doi:10.1038/srep42997

McGinnis, D. F., Greinert, J., Artemov, Y., Beaubien, S. E., and Wüest, a. (2006). Fate of Rising Methane Bubbles in Stratified Waters: How Much Methane Reaches the Atmosphere?. *J. Geophys. Res.* 111 (9), 1–15. doi:10.1029/2005JC003183

MSM34 (2014). MSM34. Available at: http://eprints.uni-kiel.de/29989/.

Myhre, C. L., Ferré, B., Platt, S. M., Silyakova, A., Hermansen, O., Allen, G., et al. (2016). Extensive Release of Methane from Arctic Seabed West of Svalbard during Summer 2014 Does Not Influence the Atmosphere. *Geophys. Res. Lett.* 43 (9), 4624–4631. doi:10.1002/2016GL068999

Naqvi, S. W. A., Bange, H. W., Farías, L., Monteiro, P. M. S., Scranton, M. I., and Zhang, J. (2010). Marine Hypoxia/anoxia as a Source of CH4 and N2O. *Biogeosciences* 7 (7), 2159–2190. doi:10.5194/bg-7-2159-2010

Newman, K. R., Cormier, M.-H., Weissel, J. K., Driscoll, N. W., Kastner, M., Solomon, E. A., et al. (2008). Active Methane Venting Observed at Giant Pockmarks along the U.S. Mid-Atlantic Shelf Break. *Earth Planet. Sci. Lett.* 267, 341–352. doi:10.1016/j.epsl.2007.11.053

Özsoy, E., and Ünlüata, Ü. (1997). Oceanography of the Black Sea: A Review of Some Recent Results. *Earth-Science Rev.* 42 (4), 231–272. doi:10.1016/S0012-8252(97)81859-4

Pape, T., Blumenberg, M., Seifert, R., Bohrmann, G., and Michaelis, W. (2008). "Marine Methane Biogeochemistry of the Black Sea: A Review," in *Links Between Geological Processes, Microbial Activitiese&Evolution of Life* (Dordrecht Netherlands: Springer), 281–311.

Pohlman, J. W., Greinert, J., Ruppel, C., Silyakova, A., Vielstädte, L., Casso, M., et al. (2017). Enhanced CO2 Uptake at a Shallow Arctic Ocean Seep Field Overwhelms the Positive Warming Potential of Emitted Methane. *Proc. Natl. Acad. Sci. USA* 114 (21), 5355–5360. doi:10.1073/pnas.1618926114

Reeburgh, W. S. (2007). Oceanic Methane Biogeochemistry. *Chem. Rev.* 107, 486–513. doi:10.1021/cr050362v

Reeburgh, W. S., Tyler, S. C., and Carroll, J. (2006). Stable Carbon and Hydrogen Isotope Measurements on Black Sea Water-Column Methane. *Deep Sea Res. Part Topical Stud. Oceanography* 53 (17–19), 1893–1900. doi:10.1016/j.dsr2.2006.03.018

Reeburgh, W. S., Ward, B. B., Whalen, S. C., Sandbeck, K. A., Kilpatrickt, K. A., and Kerkhof, L. J. (1991). Black Sea Methane Geochemistry. *Deep Sea Res. Part A. Oceanographic Res. Pap.* 38 (Suppl. 2), S1189–S1210. doi:10.1016/s0198-0149(10)80030-5

Repeta, D. J., Ferrón, S., Sosa, O. A., Johnson, C. G., Repeta, L. D., Acker, M., et al. (2016). Marine Methane Paradox Explained by Bacterial Degradation of Dissolved Organic Matter. *Nat. Geosci.* 9 (12), 884–887. doi:10.1038/ngeo2837

Rettich, T. R., Handa, Y. P., Battino, R., and Wilhelm, E. (1981). Solubility of Gases in Liquids. 13. High-Precision Determination of Henry's Constants for Methane and Ethane in Liquid Water at 275 to 328 K. *J. Phys. Chem.* 85 (22), 3230–3237. doi:10.1021/j150622a006

Riboulot, V., Ker, S., Sultan, N., Thomas, Y., Marsset, B., Scalabrin, C., et al. (2018). Freshwater lake to Salt-Water Sea Causing Widespread Hydrate Dissociation in the Black Sea. *Nat. Commun.* 9 (1), 1–8. doi:10.1038/s41467-017-02271-z

Ruffine, L., Donval, J.-P., Croguennec, C., Burnard, P., Lu, H., Germain, Y., et al. (2018). Multiple Gas Reservoirs Are Responsible for the Gas Emissions along the Marmara Fault Network. *Deep Sea Res. Part Topical Stud. Oceanography* 153, 48–60. doi:10.1016/j.dsr2.2017.11.011

Saunois, M., Bousquet, P., Poulter, B., Peregon, A., Ciais, P., Canadell, J. G., et al. (2017). Variability and Quasi-Decadal Changes in the Methane Budget over the Period 2000-2012. *Atmos. Chem. Phys.* 17 (18), 11135–11161. doi:10.5194/acp-17-11135-2017

Schmale, O., Beaubien, S. E., Rehder, G., Greinert, J., and Lombardi, S. (2010). Gas Seepage in the Dnepr Paleo-delta Area (NW-Black Sea) and its Regional Impact on the Water Column Methane Cycle. *J. Mar. Syst.* 80 (1–2), 90–100. doi:10.1016/j.jmarsys.2009.10.003

Schmale, O., Greinert, J., and Rehder, G. (2005). Methane Emission from High-Intensity marine Gas Seeps in the Black Sea into the Atmosphere. *Geophys. Res. Lett.* 32 (7), 1–4. doi:10.1029/2004GL021138

Schmidt, M., Linke, P., and Esser, D. (2013). Recent Development in IR Sensor Technology for Monitoring Subsea Methane Discharge. *Mar. Technol. Soc. J.* 47 (3), 27–36. doi:10.4031/mtsj.47.3.8

Seiyama, T., Kato, A., Fujiishi, K., and Nagatani, M. (1962). A New Detector for Gaseous Components Using Semiconductive Thin Films. *Anal. Chem.* 34 (11), 1502–1503. doi:10.1021/ac60191a001

Shakhova, N., Semiletov, I., Gustafsson, O., Sergienko, V., Lobkovsky, L., Dudarev, O., et al. (2017). Current Rates and Mechanisms of Subsea Permafrost Degradation in the East Siberian Arctic Shelf. *Nat. Commun.* 8 (1), 15872. doi:10.1038/ncomms15872

Shakhova, N., Semiletov, I., Leifer, I., Sergienko, V., Salyuk, A., Kosmach, D., et al. (2014). Ebullition and Storm-Induced Methane Release from the East Siberian Arctic Shelf. *Nat. Geosci.* 7 (1), 64–70. doi:10.1038/ngeo2007

Solomon, E. A., Kastner, M., MacDonald, I. R., and Leifer, I. (2009). Considerable Methane Fluxes to the Atmosphere from Hydrocarbon Seeps in the Gulf of Mexico. *Nat. Geosci.* 2 (8), 561–565. doi:10.1038/ngeo574

Sovga, E. E., Lyubartseva, S. P., and Lyubitsky, A. A. (2008). Investigation of the Biogeochemistry of Methane and Mechanisms of its Transfer in the Black Sea. *Phys. Oceanogr.* 18 (5), 272–287. doi:10.1007/s11110-009-9024-z

Stanev, E. V., Peneva, E., and Chtirkova, B. (2019). Climate Change and Regional Ocean Water Mass Disappearance: Case of the Black Sea. *J. Geophys. Res. Oceans* 124 (7), 4803–4819. doi:10.1029/2019JC015076

Stanev, E. V., Poulain, P. M., Grayek, S., Johnson, K. S., Claustre, H., and Murray, J. W. (2018). Understanding the Dynamics of the Oxic-Anoxic Interface in the Black Sea. *Geophys. Res. Lett.* 45 (2), 864–871. doi:10.1002/2017GL076206

Stow, D. A. V., Hernández-Molina, F. J., Llave, E., Sayago-Gil, M., Díaz del Río, V., and Branson, A. (2009). Bedform-velocity Matrix: The Estimation of Bottom Current Velocity from Bedform Observations. *Geology* 37 (4), 327–330. doi:10.1130/g25259a.1

Swinnerton, J. W., Linnenbom, V. J., and Cheek, C. H. (1968). A Sensitive Gas Chromatographic Method for Determining Carbon Monoxide in Seawater. *Limnol. Oceanogr.* 13 (1), 193–195. doi:10.4319/lo.1968.13.1.0193

Triest, J., Chappellaz, J., and Grilli, R. (2017). *Patent 08276-01: System for Fast and* In-Situ *Sampling of Dissolved Gases in the Ocean*. Grenoble FRANCE: CNRS.

Tsurushima, N., Watanabe, S., and Tsunogai, S. (1999). Determination of Light Hydrocarbons Dissolved in Seawater. *Talanta* 50 (3), 577–583. doi:10.1016/S0039-9140(99)00144-7

Veloso, M., Greinert, J., Mienert, J., and De Batist, M. (2015). A New Methodology for Quantifying Bubble Flow Rates in Deep Water Using Splitbeam Echosounders: Examples from the A Rctic Offshore NW- S Valbard. *Limnol. Oceanogr. Methods* 13 (6), 267–287. doi:10.1002/lom3.10024

Weber, M. E., von Stackelberg, U., Marchig, V., Wiedicke, M., and Grupe, B. (2000). Variability of Surface Sediments in the Peru basin : Dependence on Water Depth , Productivity , Bottom Water Flow , and Seafloor Topography. *Mar. Geol.* 163 (1–4), 163169–163184. doi:10.1016/s0025-3227(99)00103-6

Weber, T., Wiseman, N. A., and Kock, A. (2019). Global Ocean Methane Emissions Dominated by Shallow Coastal Waters. *Nat. Commun.* 10 (1), 1–10. doi:10.1038/s41467-019-12541-7

Weinstein, A., Navarrete, L., Ruppel, C., Weber, T. C., Leonte, M., Kellermann, M. Y., et al. (2016). Determining the Flux of Methane into Hudson Canyon at the Edge of Methane Clathrate Hydrate Stability. *Geochem. Geophys. Geosyst.* 17 (10), 3882–3892. doi:10.1002/2016GC006421

Weiss, R. F. (1974). Carbon Dioxide in Water and Seawater: the Solubility of a Non-ideal Gas. *Mar. Chem.* 2 (3), 203–215. doi:10.1016/0304-4203(74)90015-2

Westbrook, G. K., Thatcher, K. E., Rohling, E. J., Piotrowski, A. M., Pälike, H., Osborne, A. H., et al. (2009). Escape of Methane Gas from the Seabed along the West Spitsbergen continental Margin. *Geophys. Res. Lett.* 36 (15), 1–5. doi:10.1029/2009GL039191

Wiesenburg, D. A., and Guinasso, N. L. (1979). Equilibrium Solubilities of Methane, Carbon Monoxide, and Hydrogen in Water and Sea Water. *J. Chem. Eng. Data* 24 (4), 356–360. doi:10.1021/je60083a006

Wilson, S. T., Bange, H. W., Arévalo-Martínez, D. L., Barnes, J., Borges, A. V., Brown, I., et al. (2018). An Intercomparison of Oceanic Methane and Nitrous Oxide Measurements. *Biogeosciences* 15 (19), 5891–5907. doi:10.5194/bg-15-5891-2018

Yuan, F., Hu, M., He, Y., Chen, B., Yao, L., Xu, Z., et al. (2020). Development of an *In Situ* Analysis System for Methane Dissolved in Seawater Based on Cavity Ringdown Spectroscopy. *Rev. Scientific Instr.* 91, 083106. doi:10.1063/5.0004742

Conflict of Interest: The authors declare that the research was conducted in the absence of any commercial or financial relationships that could be construed as a potential conflict of interest.

The reviewer TP declared a past co-authorship with one of the authors LR to the handling editor.

Publisher's Note: All claims expressed in this article are solely those of the authors and do not necessarily represent those of their affiliated organizations, or those of the publisher, the editors and the reviewers. Any product that may be evaluated in this article, or claim that may be made by its manufacturer, is not guaranteed or endorsed by the publisher.

frontiers in Earth Science

ORIGINAL RESEARCH
published: 27 August 2021
doi: 10.3389/feart.2021.604930

Volumetric Mapping of Methane Concentrations at the Bush Hill Hydrocarbon Seep, Gulf of Mexico

William P. Meurer, John Blum and Greg Shipman*

Reservoir Systems, Research and Technology Development, ExxonMobil Upstream Research Company, Spring, TX, United States

The role of methane as a green-house gas is widely recognized and has sparked considerable efforts to quantify the contribution from natural methane sources including submarine seeps. A variety of techniques and approaches have been directed at quantifying methane fluxes from seeps from just below the sediment water interface all the way to the ocean atmosphere interface. However, there have been no systematic efforts to characterize the amount and distribution of dissolved methane around seeps. This is critical to understanding the fate of methane released from seeps and its role in the submarine environment. Here we summarize the findings of two field studies of the Bush Hill mud volcano (540 m water depth) located in the Gulf of Mexico. The studies were carried out using buoyancy driven gliders equipped with methane sensors for near real time *in situ* detection. One glider was equipped with an Acoustic Doppler Current Profiler (ADCP) for simultaneous measurement of currents and methane concentrations. Elevated methane concentrations in the water column were measured as far away as 2 km from the seep source and to a height of about 100 m above the seep. Maximum observed concentrations were ~400 n*M* near the seep source and decreased away steadily in all directions from the source. Weak and variable currents result in nearly radially symmetric dispersal of methane from the source. The persistent presence of significant methane concentrations in the water column points to a persistent methane seepage at the seafloor, that has implications for helping stabilize exposed methane hydrates. Elevated methane concentrations in the water column, at considerable distances away from seeps potentially support a much larger methane-promoted biological system than is widely appreciated.

Keywords: seep, methane, Bush Hill, *in situ* detection, volume mapping, ocean currents, near seafloor, temporal variation

OPEN ACCESS

Edited by:
Ira Leifer,
Bubbleology Research Intnl,
United States

Reviewed by:
Jeemin Rhim,
Dartmouth College, United States
Vitor Hugo Magalhaes,
Portuguese Institute for Sea and Atmosphere (IPMA), Portugal
Dong Feng,
Shanghai Ocean University, China

****Correspondence:***
William P. Meurer
william.p.meurer@exxonmobil.com

Specialty section:
This article was submitted to Biogeoscience, a section of the journal Frontiers in Earth Science

Received: *11 September 2020*
Accepted: *12 August 2021*
Published: *27 August 2021*

Citation:
Meurer WP, Blum J and Shipman G (2021) Volumetric Mapping of Methane Concentrations at the Bush Hill Hydrocarbon Seep, Gulf of Mexico. Front. Earth Sci. 9:604930. doi: 10.3389/feart.2021.604930

INTRODUCTION

The importance of methane, leaked from the seafloor at seeps, as a food source in the deep oceans supporting complex biological communities is well documented (e.g., Kennicutt et al., 1988a; MacDonald et al., 1989; Sibuet and Olu, 1998; Sibuet and Roy, 2002; Cordes et al., 2005; Levin, 2005; Girard et al., 2020). Studies of these seep communities typically focus on megafaunal communities and microbial mats found close to release points on the seafloor. Recent work suggests that even modest dissolved methane concentrations (~20 nM) can be important for

microbial methane oxidizers (Uhlig et al., 2018) and may help to support the benthic communities at large (Åström et al., 2017). However, the relationship between the distribution of dissolved methane around seeps and any associated biological communities is poorly documented; likely because of limited sampling.

The study of the release of methane from thermogenic and biogenic seeps in the world's oceans (and lakes) has expanded from simple recognition of the extent of the sources to efforts to characterize methane release mechanisms and quantify fluxes. These efforts include studies of: the exchange across the sediment water interface (Tryon and Brown, 2004; Kastner and MacDonald, 2006), bubble fluxes using bottom imaging (Leifer and MacDonald, 2003; Leifer, 2010; Thomanek et al., 2010; Römer et al., 2019; Di et al., 2020; Johansen et al., 2020), bubble fluxes using acoustic imaging (Weber et al., 2014), dissociation of hydrates (Lapham et al., 2010; Lapham et al., 2014), and inferred fluxes to the seafloor based on shallow thermal gradients (Smith et al., 2014). We now know that methane bubble release rates can vary on time scales of seconds, minutes, hours, and days (e.g., Greinert 2008; Leifer, 2019 (and references therein); Johansen et al., 2020). These flux variations can include times when no appreciable methane bubbles are released at all. The release point on the seafloor can also shift location on time scales of days (Razaz et al., 2020).

In contrast to the study of methane bubble releases, substantially less effort has been paid to understanding the distribution of dissolved hydrocarbons around seeps. Shipboard hydrocasts are commonly used to provide at most tens of samples of the water column around seeps. They provide point data in time and space and cannot effectively sample methane plumes without additional context. Manned submersibles and remotely operated vehicles have also been used to collect water-column samples. These are typically collected immediately adjacent to bubble plumes (e.g., Solomon et al., 2009). Such samples have the advantage of a clear context; they are sampling the volumes richest in methane. Unfortunately they provide little insight into how the concentrated methane is subsequently dispersed around the source in 3D.

The location and geological history of the Gulf of Mexico (GoM) have resulted in the accumulation of organic-rich sediments that, upon sufficient burial, generated hydrocarbon in the basin. The current configuration of the GoM is a product of the breakup of Pangaea and associated tectonics during the Mesozoic (Galloway, 2008; Hudec et al., 2013). Rifting and subsidence in the Mesozoic led to Middle Jurassic deposition of evaporites recording the influx of seawater into the basin. This evaporite layer, which forms the Louann Salt in the northern GoM, greatly influenced the subsequent development of the GoM (Salvador, 1991; Peel et al., 1995). Deposition in the Late Cretaceous was influenced by sea level change, and most deposits of this age in the GoM are marine (Sohl et al., 1991). Large volumes of clastic sediments were deposited in the Cenozoic adding more than 10,000 m of sediment to some areas of the northern GoM (Galloway et al., 1991; Salvador, 1991). Deposition in the Quaternary is characterized by thick, terrigenous sediments that can be more than 3,600 m thick under the present Texas-Louisiana continental shelf and 3,000 m deep in the GoM basin (Coleman et al., 1991). The deformation of the basal salt layer and its resulting structures is integral to the GoM's hydrocarbon systems. Sediment accumulation and tectonic activity caused migration of the salt resulting in much of the structure now seen in the northwestern and north-central GoM where salt movement has created salt-withdrawal minibasins and the related folds and faults focus hydrocarbon migration, create traps, and lead to focused seafloor seepage.

An area in the Green Canyon protraction polygon in the northern GoM, termed the Bush Hill area after the Bush Hill mud volcano in Green Canyon Lease Block 185 (or more simply GC185), is the focus of this study. The Bush Hill area includes the eastern part of GC184 and the western part of GC185 (**Figure 1**). Salt deformation and subsequent sediment loading in this area has focused hydrocarbon migration at and around Bush Hill.

Evidence of active seepage at the seafloor in the general study area is demonstrated through a variety of approaches. Multi-Beam Echo Sounder (MBES) surveys are typically conducted to acquire high-resolution bathymetry, but acoustic scattering off of bubble plumes, of sufficient bubble density, provides a means of locating active methane seepage (Weber et al., 2014). Oil droplets are not reliably imaged using MBES and so direct detection of seafloor oil seepage locations is commonly done via detection in sediments using drop cores or direct observation. The area surrounding Bush Hill has numerous seepage points (De Beukelaer, 2003; **Figure 1B**). The distribution of oil seepage (invariably associated with methane release) can also be assessed somewhat indirectly by examining oil slicks on the sea surface that are sourced from natural seeps.

The Bush Hill area is located below locations of persistent oil slicks imaged using Synthetic Aperture Radar (SAR) satellite imagery. The persistent nature of the seepage is demonstrated by the repeat observations (e.g., De Beukelaer, 2003). This relatively continuous seepage was one of the critical criteria for the experiment site selection. The SAR images also help to identify nearby discrete seepage points separated from Bush Hill by at least 750 m.

Bush Hill was one of the first submarine hydrocarbon seeps located on a continental slope to receive significant research attention (Brooks et al., 1984; Brooks et al., 1985; Brooks et al., 1986; Kennicutt et al., 1988b). Aspects of the Bush Hill setting that have received attention include: the hydrate deposits (Brooks et al., 1984; MacDonald et al., 1994; Sassen et al., 1998; Sassen et al., 1999; Vardaro et al., 2005; Kastner and MacDonald, 2006), the benthic chemosynthetic community (Kennicutt et al., 1988a; Brooks et al., 1989; MacDonald et al., 1989; Sager, 2002), and as a potential source of atmospheric methane (Solomon et al., 2009; MacDonald, 2011; Hu et al., 2012).

A detailed seafloor study was conducted prior to construction of the Jolliet Platform to the west of Bush Hill in GC184. The study found numerous areas of near seafloor carbonates, gas escape features, and hydrates (Kennicutt et al., 1988a). The mapping suggests that in addition to Bush Hill, some seepage has taken place over a considerable fraction of the area with one locus in the northern part of GC184 and another that is elongated

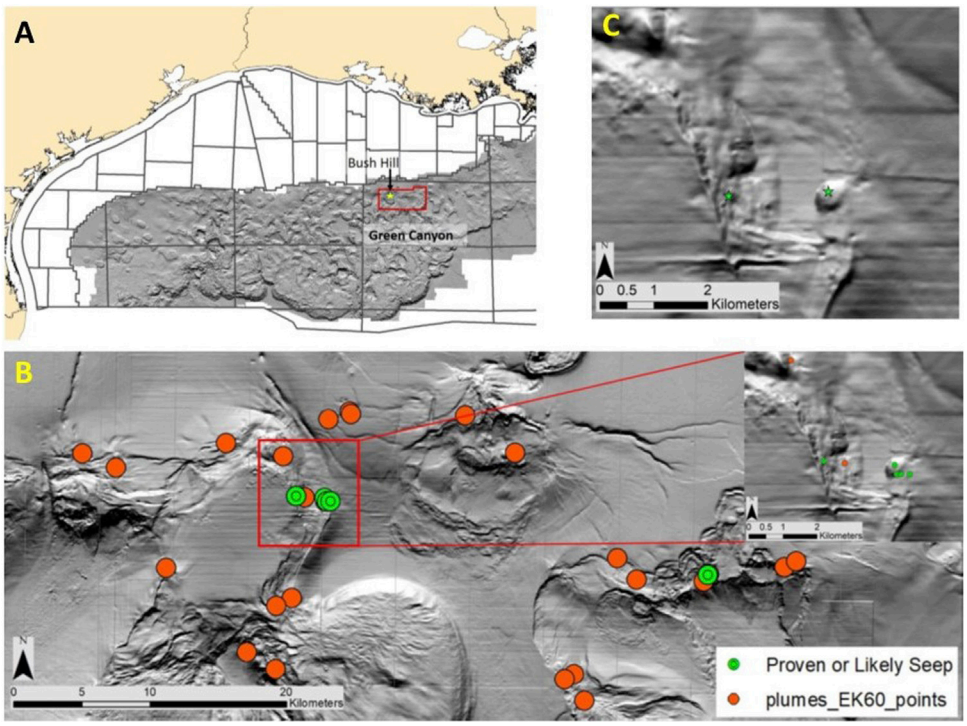

FIGURE 1 | General and more detailed location maps are provided in **(A–C)**. **(A)** Shows the outline of the area covered by our Bureau of Ocean Energy Management geological exploration permit in the context of the Texas-Louisiana coastline, protraction polygons, and slope bathymetry. The location of the Bush Hill mud volcano is indicated by a star. **(B)** Provides a detailed MBES (multibeam echo sounder) shaded map with the locations of oil-bearing dropcores and bubble plumes. There is an inset zoom of the area around Bush Hill. **(C)** Zoom of the Bush Hill area with stars indicating the location of the mud volcano and the seepage site on the slope to west of it.

N-S at the boundary between GC184 and GC185. To understand the source of hydrocarbons in the water it is therefore important to understand what parts of this general area actively seep significant volumes of hydrocarbons and which are relic, dormant, or low flux seepages. As an example we consider the potential seepage point ~1 km west of Bush Hill.

Side-scan sonar images of the Bush Hill area collected in 2001 (De Beukelaer et al., 2003) showed two bubble plumes, one originating from the crest of the mud volcano and the other from a point on the slope to the west. The plume to the west, located near a drop core hit (**Figure 1C**), was not observed a year later. The western bubble plume's location corresponds to an area with hydrate material at or near the seafloor and possible carbonates at the seafloor (Kennicutt et al., 1988b). The absence of a persistent bubble plume over the western area and the lack of surface slicks originating from that area in either 2001 or 2002 suggest that it has a lower average flux than Bush Hill and/or is only periodically active.

Aside from that just discussed, no bubble plumes have been imaged within >3 km of Bush Hill suggesting that any ongoing hydrocarbon seepage is relatively intermittent, low volume or dispersed. *In situ* analysis of dispersed flow at Bush Hill indicates that most venting is focused (Kastner and MacDonald, 2006). Measurements of background fluid fluxes reveal both up-flow and down-flow on the crest of the mud volcano (Tryon and Brown, 2004; Kastner and MacDonald, 2006). Although flow rates approaching 2 cm/day were measured in some locations for short durations, typical flow rates are less than 0.01 cm/day with some of the pore fluids escaping the seafloor being rich in dissolved methane. This average dispersed flow is insufficient to impact *in situ* measurements made greater than a few centimeters above the seafloor.

The current study provides a time-integrated 3D characterization of the dissolved methane distribution around Bush Hill. We present the result of two surveys that used *in situ* measurements to provide two separate and relatively complete snapshots of the dissolved methane plume around the seep. The inclusion of contemporaneous current data for one of the studies provides insight into how the methane is advected from the source. Together, these two studies provide a first attempt to understand the distribution of dissolved methane around an isolated natural source.

MATERIALS AND METHODS

This work is based on two field studies conducted in the spring and fall of 2018. Autonomous underwater gliders were used for *in situ* analyses in both studies. Uncertainty about the extent and concentration of dissolved methane around Bush Hill and the

nature of the near-bottom currents led us to deploy two distinct sampling strategies in the spring and fall. Time constraints did not permit us to modify the fall instrumentation packages based on the results of the spring study. We therefore opted for slightly different configurations of hardware as part of the experiment design. The spring results did provide insights that benefitted the operational execution of the fall study.

In the spring experiment, three Teledyne Slocum gliders were operated by Blue Ocean Monitoring (Australia). They were equipped with hybrid thrusters allowing them to travel at near constant elevation above the seafloor. The fall experiments used two Alseamar SeaExplorer gliders operated by Alseamar (France). The SeaExplorers relied solely on their buoyancy drive for thrust. They traverse the water column in "yos" that consist of a dive from a known position to near the bottom and then an ascent to the surface to reposition. They collected near bottom data using low amplitude mini-yos that generally kept the vehicle within ~25 m of the seafloor.

The sensor hardware used for the studies had two key differences. In the fall study Alseamar included a downward-looking ADCP on one of the two gliders. This provided collocated current and chemical measurements. The other major difference is that the sensitivities of the Franatech METS methane sensors differed with the spring study using ultra-high sensitivity and the fall using just high sensitivity sensors.

In the spring experiment the ultra-high sensitivity METS provided detection limits ~1 nM and non-linear performance at greater than 500 nM. The fall experiments used the high sensitivity METS with detection limit of ~20 nM and non-linear performance at greater than 1,000 nM. These are the theoretical quantitation limits, in practice the exact calibrations differ so an offset from the lower limit was defined to serve as a quantitation limit. For the data collected in the spring, with the more sensitive detectors, a conservative estimate of 10 times the environmental background is used for the quantitation limit (25 nM). Data from the fall experiments was corrected for a systematic baseline response difference and adjusted to two times the detection limit to yield quantitation values of 40 nM (glider SEA023) and 60 nM (glider SEA027).

The average sampling time frequency for the METS used in the spring study is every ~1 s. The fall survey METS sampled every ~1.5 s. The average horizontal speed of the gliders in the spring study was ~2.5 m/s and the in the fall study their horizontal speed was ~1.75 m/s. These combinations of sampling frequency and horizontal speed give similar lateral sampling of ~2.5 m for the spring study and ~2.6 m for the fall.

The capabilities of the METS senors were essential to this study. The high sensitivity allowed methane detection to background levels to define the extent of the methane plume. The *in situ* measurements provided extremely high spatial resolution and were reported from the gliders in near real time (allowing on-the-fly adjustments to operational plans). In total, more than 2 million near-bottom methane analyses were collected over Bush Hill during the spring and fall studies. The high density of data allows a much more confident understanding of the spatial and temporal characteristics of the methane distribution in the near and mid-field at Bush Hill.

A limitation of the METS sensor is its ability to provide a strictly quantitative methane determination because of its relatively significant uptake and washout delays. The T90 time of a sensor is the time required for it to register a concentration equivalent to 90% of the actual concentration present, reported as 1–30 min by Franatech for the METS. For example, if a clean sensor is exposed to a flow of solution with a methane concentration of 100 nM, the T90 time would correspond to how long it would take for the sensor to report a concentration of 90 nM. The greater the concentration difference of a new solution from that currently observed by the sensor the longer the T90 time. The delay associated with diffusion through the membrane and sorptive processes on the detector's semiconductor surface, both of which scale with the magnitude of the change, are responsible for a delay in sensor response. Both processes initially take place faster with high concentration gradients in the water and slow as the concentration gradients are minimized. This means that the METS will respond quickly to significant concentration changes but in a semi-quantitative way. The limited range of temperatures encountered near the seafloor (<1.5°C) and the limited impact of the pressure range on the detector window (from ~450 to 650 m depth) mean that the diffusion rates are essentially fixed throughout the study area. Hence the response performance of the sensor does not vary appreciably within the bounds of the study area.

Because of the signal delay inherent to the METS, the methane concentrations reported should be thought of as a kind of moving average. They are not strictly comparable to, for example, discrete seawater samples captured and analyzed in a lab. It is virtually certain that the T90 time for the sensor is never achieved because the glider is moving, the water is moving, and the methane concentration field is heterogeneous. This means the highest concentrations reported are lower than what the glider actually encountered and there is some degree of smoothing of both high and low concentration heterogeneities. However, understanding how the METS performs allowed us to interpret the data so as to generate appropriate concentration maps. The fact that the METS responds quickly to significant concentration gradients means that areas with limited concentration variations can be identified as can sharp concentration boundaries.

The best way to understand the data provided by the METS is to look at examples of data collected in different settings at Bush Hill (**Figure 2**). The figures shows the response characteristic of the METS associated with: moving into the plume (**Figure 2A**), moving inside the plume through a low concentration part (**Figure 2B**), moving through a high concentration area (**Figure 2C**), and leaving the methane plume (**Figure 2D**). Between dives the gliders spend 30 min or more at the surface reporting data. This assures that the METS detector has been cleared of methane to the background concentration. Therefore, during the descent, the upper limit of the methane plume can be readily identified (**Figure 2A**). During the early uptake of significantly higher methane concentrations, we observe a continuous and smooth point-to-point monotonically increasing signal in the highly resolved time series from the

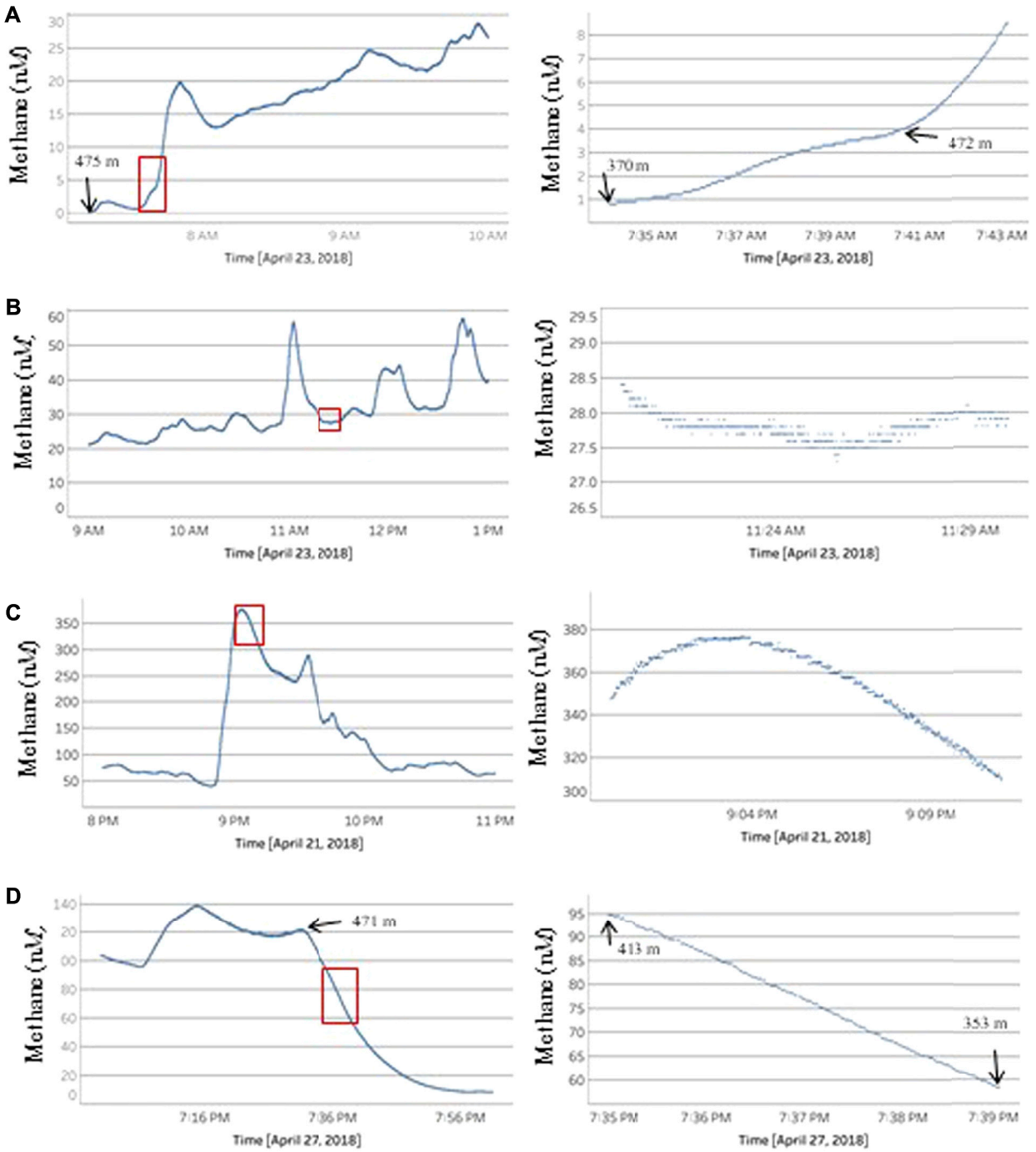

FIGURE 2 | Plots of methane-data time series for glider 187 resolved at hour and minute scales (sampling frequency is 1 Hz). For each longer period time series, an inset box shows the interval presented at the minute time scale on the right side. Key water depths are noted on the plots for descending part **(A)** and ascending part **(D)** paths. Water depth for traverse paths are near constant at ~475 m part **(B)** and ~550 m part **(C)**.

METS. When the glider is inside the methane plume in an area without abrupt concentration changes (**Figure 2B**), the short-term signal includes more variability on a point-to-point basis (i.e., contrast the monotonically increasing uptake data and the line defined by the plateau data that includes numerous increases and decreases about the mean trend). When the glider is traversing parts of the plume with relatively high methane concentrations, the same variability on a point-to-point basis is seen as at low concentrations (**Figure 2C**). When the gliders begin their ascent to the surface from the methane plume they quickly transit into background methane concentrations and this generates the signal characteristic seen during the initial uptake

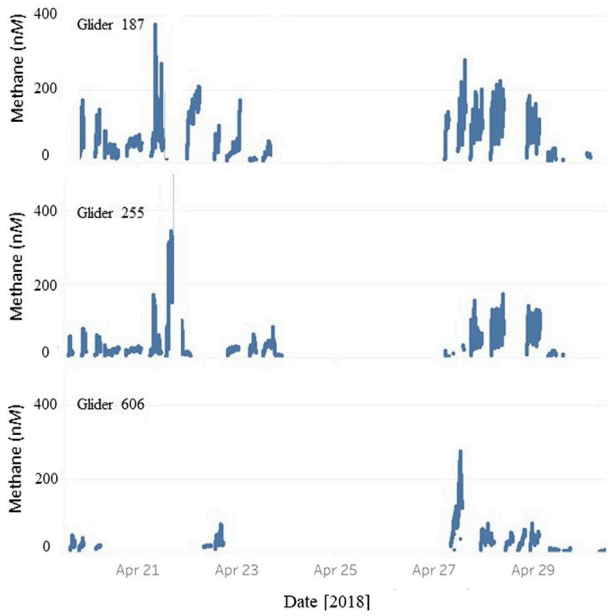

FIGURE 3 | Methane concentrations measured by each glider (187, 255, 606) during the spring study. Data has been filtered to eliminate measurements taken above 450 m below the sea surface.

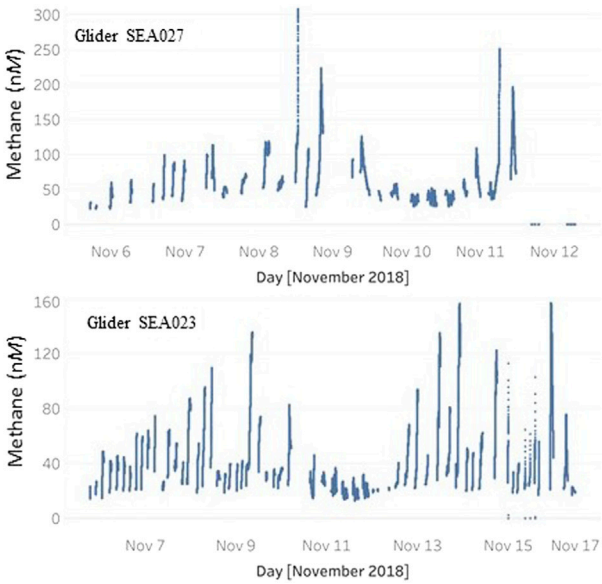

FIGURE 4 | Methane concentrations measured by gliders SEA023 and SEA027 during the fall study. Data has been filtered to eliminate measurements taken above 450 m below the sea surface.

except with a monotonic decrease (**Figure 2D**). By analyzing the METS data at fine temporal resolution and recognizing the signal characteristics of larger concentration contrasts, we are able to more clearly distinguish the structure and boundaries of the methane plume.

Current-velocity data were collected using a Nortek AD2CP Acoustic Doppler Current Profiler (ADCP) on every dive conducted by glider SEA027. SEA027 collected data from November 6th to the 11th inclusive but was damaged in a shark attack and no data were collected for the remainder of the survey (the glider was recovered). The ADCP data was processed in two ways depending on whether the ADCP detected the bottom. When the ADCP detected the bottom, the glider's motion was directly resolved and high temporal and spatial resolution data was collected (on the order of 10 s and 2 m). When the ADCP could not detect the bottom, the data were averaged over a much longer duration to compensate for the differential movement between the glider and the water. All raw ADCP data was processed by the equipment provider (Alseamar).

RESULTS

Methane Concentrations

The methane concentration provided by the METS are not strictly quantitative but are rather the smoothed values as described in the methods section. However, hereafter we discuss the measured methane concentrations as though the numerical values represent the actual concentrations present. This is done simply to reduce the number of qualifiers scattered throughout the text. We have examined all the data at high temporal resolution so that in all instances where we have found high contrasts in concentration values we can interpret their significance taking into account uptake and washout issues. We also note that while the maximum concentrations reported are assuredly lower than the maximum concentrations encountered, they are inferred to be lower by only ~30% based on the detailed time-series analysis.

Methane concentrations measured in the spring study found maximum methane concentrations of ~400 nM but most peak values were less than 200 nM (**Figure 3**). There is a systematic increase in the average concentrations measured as the study progressed. This is not interpreted to be related to an increase in flux from the seep, but rather simply reflects the progression of mapping from far to near with respect to the source. The gap in data centered on April 25th is an artifact related to bad weather and a shipboard equipment failure that required a return to port that resulted in a ~48 h gap in data collection.

On average, glider 187 measured higher concentrations than the other two gliders. Glider 606 was routinely flown at a higher elevation from the seafloor and so its measurements are not directly comparable with those of 187. Comparison of measurements of gliders 187 and 255 collected within 2–3 h of each other from the same location are consistent with the METS on glider 187 reporting higher methane concentrations. However, there is significant overlap in the concentrations measured by both gliders. So while we interpret glider 187 to have reported methane values ~10–25 nM higher than glider 255, no systematic correction could be applied.

Methane concentrations measured in the fall study found maximum methane concentrations of ~300 nM but most were less than 100 nM (**Figure 4**). As with the spring study, the higher average concentrations measured later in the study are related to

more traverses closer to the seep source. The low concentration measurements at the start of both gliders' records and on the November 10th for SEA027 and the 11th for SEA023 are data collected well away from Bush Hill (and any other hydrocarbon seepage sources) and are intended to measure background concentrations.

SEA027 measured four instances of methane concentrations at or above 200 nM in contrast to SEA023 which did not measure concentrations higher than 160 nM. Aside from these four high concentration dives, comparison of the remainder of the measurements from both gliders shows them to be comparable so we interpret the sensors to be consistently calibrated.

Segregating out far-field analyses from both studies, we find that the spring study found higher average concentrations relative to the fall study. Average concentrations measured in the spring were 109 (±38 at 1 SD) nM and those from the fall ~72 (±23 at 1 SD) nM. This difference could be explained by the different METS sensitivities used, although these concentrations are well within the detection range of both. The difference could also be explained by a 35% decrease in the methane flux from the spring to fall or by more effective removal of methane from the area by advection. That the lower average concentrations in the fall correspond with lower maximum concentrations is more consistent with a decrease in net flux.

Mapping of Methane Concentrations

Combining data from the two surveys along with the current observations allow the methane concentrations surrounding Bush Hill to be analyzed spatially, temporally, and in the context of the current directions. The simplest analysis is done by integrating the data from both field studies to constrain vertical variations and projecting them to a map view for lateral variations - discounting temporal variations in both cases. This analysis is perhaps the most useful approach for understanding how far away from the source methane concentrations are elevated above background. Localized temporal variations in methane concentrations can be examined by limiting analysis to locations that were revisited two or more times within a restricted amount of time. This approach has been applied to both field studies with a time restriction of 12 h. The impact of local variations in the near bottom currents on methane concentrations is assessed by examining the data from the fall deployment from the glider equipped with the ADCP (SEA027).

The aggregate methane measurements provide a sense of the vertical and lateral extent of the integrated methane plume. The data from the two studies are integrated using concentration distributions from both studies to define volumes appropriate for averaging and deriving average values from the spring study. The upper boundary for reliable methane detection around Bush Hill can be assessed looking at detection during glider descents, when no washout concerns exist. For the spring field study, the gliders operated using thrusters and so maintained a relatively constant height off the seafloor (aided by active bottom detection) and therefore made relatively few dives. In contrast, the gliders used in the fall field study relied on the buoyancy drive for thrust and so were constantly changing elevation. Because the fall study included more frequent water column transits it provides a more robust test of the depth of initial methane detection around Bush Hill.

Most of the dives in the fall study did not detect methane until the glider was navigating close to the seafloor, but 14 out of 78 dives detected methane on descent with a maximum detection height of 170 m and an average height of 100 m. A limitation of the data from the fall study is that most of the descents were displaced from the methane source. To further examine the vertical variability around the source we constructed 500 m thick smashes (orthogonal interval projections) of the data from the spring study onto N-S and E-W vertical planes centered on the mud volcano (**Figure 5**). The N-S smash indicates detection of methane at ~60 m above the mud volcano (540–480 m depth) while the E-W smash reveals ~90 m detection height (540–430 m). Both values should be taken as minimum detection heights as few or no background measurements are present above the mud volcano. Data from the constant elevation glider traverses (spring study) are therefore consistent with detectable methane concentrations being mostly restricted to less than ~100 m from the seafloor (with localized exceptions). In contrast, a significant number of background measurements can be found closer to the seafloor away from the mud volcano suggesting that the methane plume is domed above the source and thins vertically away from it and is concentrated near the seafloor.

Using a 450 m depth cutoff for filtering data for map-view projections (~90 m above the summit of Bush Hill) we can examine the general concentration profile away from the seepage source (**Figure 6**). Both studies show the highest concentrations closest to the methane source with concentrations dropping off significantly with distance. The area bounded by a radius of 500 m to the source has few non-detects and a significant number of high concentration measurements (**Figure 6**). For distances greater than 500 m from the source the fraction of non-detects increases significantly with increasing distance. Both studies suggest the effective radial limit of the methane plume around Bush Hill is 1,500–2,000 m.

Lateral variations of the methane plume are examined by projecting the data to the seafloor. Results from the spring experiment were split based on their elevation above the seafloor into 0–45 and 45–90 m (**Figure 7**). Both sets show high concentrations above the source with more background concentrations observed in the 45–90 m map and moving away from the source. Although limited to the south, the projected data reveal elevated methane concentrations can be detected at least 1.5 km (perhaps up to 2 km) from Bush Hill in all directions including up-slope to the west. This is consistent with the interpretation based on the vertical smashes. The data from the fall study includes, almost exclusively, data collected within 25 m of the seafloor during mini-yos (**Figure 8**). It shows similar spatial patterns as the spring study including lower concentrations to the east and southeast of the mud volcano summit. It is important to note that over the entire area mapped, even near the source, there is some fraction of the data that has

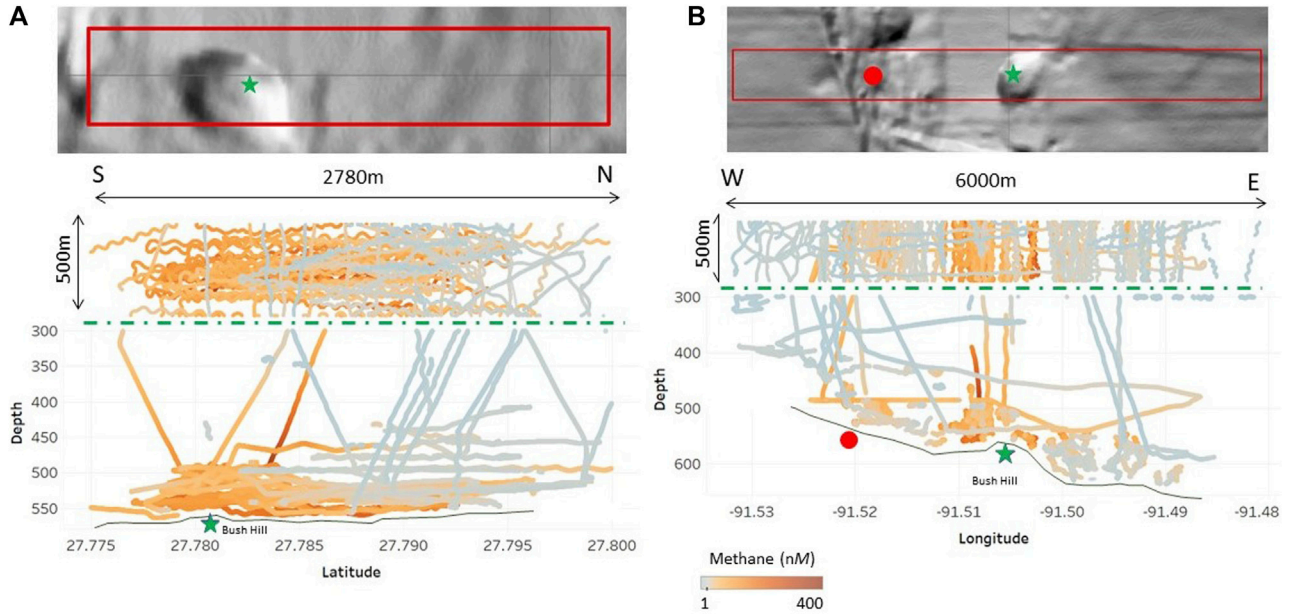

FIGURE 5 | Observed methane concentrations around Bush Hill during the spring study are depicted as color shading along the paths of the gliders. The upper images are detailed gray-shaded bathymetric relief maps of the area showing location boxes for data in middle and lower images. The location of Bush Hill is marked as a green star in each and the location of another potential methane source is noted as a red circle in the E-W shaded relief map (see **Figure 1C** for context). The middle images shows all glider data from 300 m down used to construct the vertical section smashed to a horizontal plane. The bottom images are S-N **(A)** and W-E **(B)** 500 m thick vertical data smashes onto a plane. The projected glider paths' color indicate the methane concentration (see scale) with orange colors indicating confident detections. The divergence of the methane scale is set at 10× the environmental background.

background concentrations. This strongly suggests that the methane plume around the seep source is not continuous in space, time, or both.

Documenting temporal variability relies on multiple visits to the same site. In this regard the spring survey provided many more instances of repeat visits within a 12 h time period. Twenty five locations as close as 0.25 km and as far as 1.75 km from around Bush Hill were selected to document the extent of any temporal variations (**Figure 9**). Five locations closest to Bush Hill (<0.75 km) did not include any measurements below 50 nM (**Figure 9**). However, all of these locations show significant variations in methane concentration. Most locations more than 0.75 km distance from the seeps include at least some measurements below 50 nM and half of these include measurements below 25 nM (interpreted as the quantitation limit for the spring study).

Collectively, the temporal variability data suggest that the dispersal pattern of methane around Bush Hill is highly variable in both time and space. The areas closest to the source (~0.75 km) appear to have concentrations that are almost always above detection limits, generally above 100 nmol, and with an average concentration of ~160 nM (spring study, ~100 nM for the fall study). At distances greater than ~0.75 km the methane concentrations are typically between 50 and 100 nM (fall study ~45–65 nM) and it is common for repeat sampling sites to include values both above and below quantitation limits. Based on the spring study concentrations, the general picture these observations generate is of an area surrounding the source (radius ~0.75 km) with persistently higher methane concentrations (~160 nM) but still occasionally having areas with little or no detectable methane. This central area is surrounded by a ~concentric region that extends another ~0.75 km and has concentrations around ~70 nM, and with some places varying above and below the detection threshold on time scales of tens of minutes to several hours.

Current Directions and Speeds

Comparison of currents resolved into East and North vector components shows that the water column can be subdivided into three parts (**Figure 10**). In the upper 100 m of the water column, the currents are generally less than 0.3 m/s and are skewed to a northern direction. These results are consistent with satellite surface current models over the study area that suggest the location was centered between two counter rotating eddies. There is no systematic temporal pattern to the measured currents on the scale of days with significant ranges in both directions and speed occurring. Within-day variations could be related to diurnal forces such as tides and/or changing wind conditions during day and night.

The depth range ~100–400 m shows a pronounced eastward directed current with speeds ranging between 0.15 and 0.3 m/s (**Figure 10**). This current is most pronounced at 250 m depth. Focusing on the magnitude of the east vector component of the current reveals an increasing trend from the 5th to the 10th of November, best seen between 200 and 300 m.

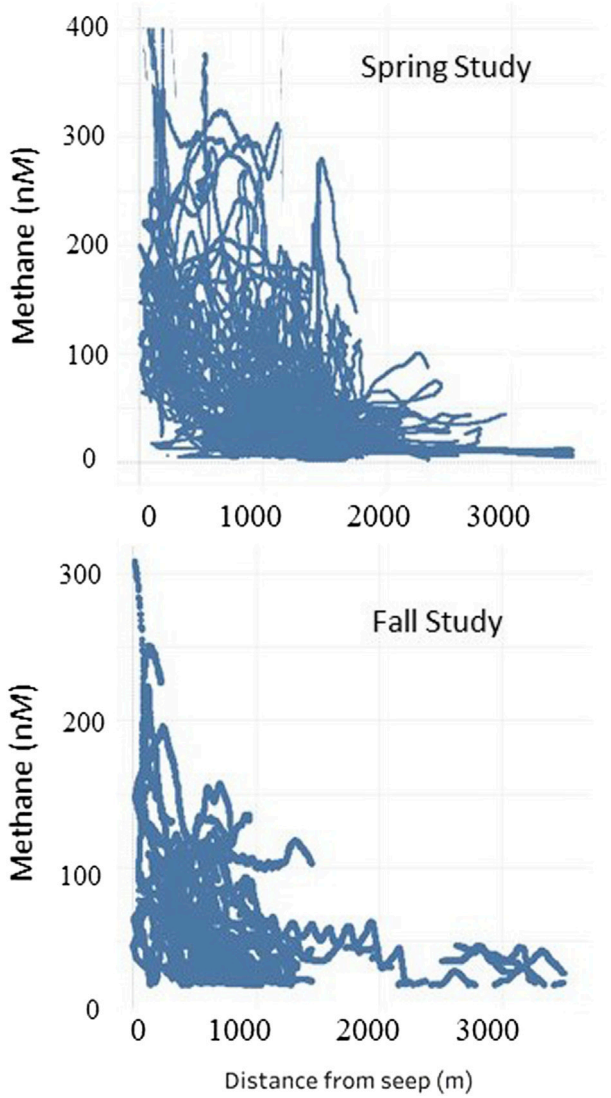

FIGURE 6 | Methane concentrations from all gliders are plotted against the horizontal distance from the seep where the data was collected. The data are filtered to include only measurements below 450 m water depth. The spring study data is at the top.

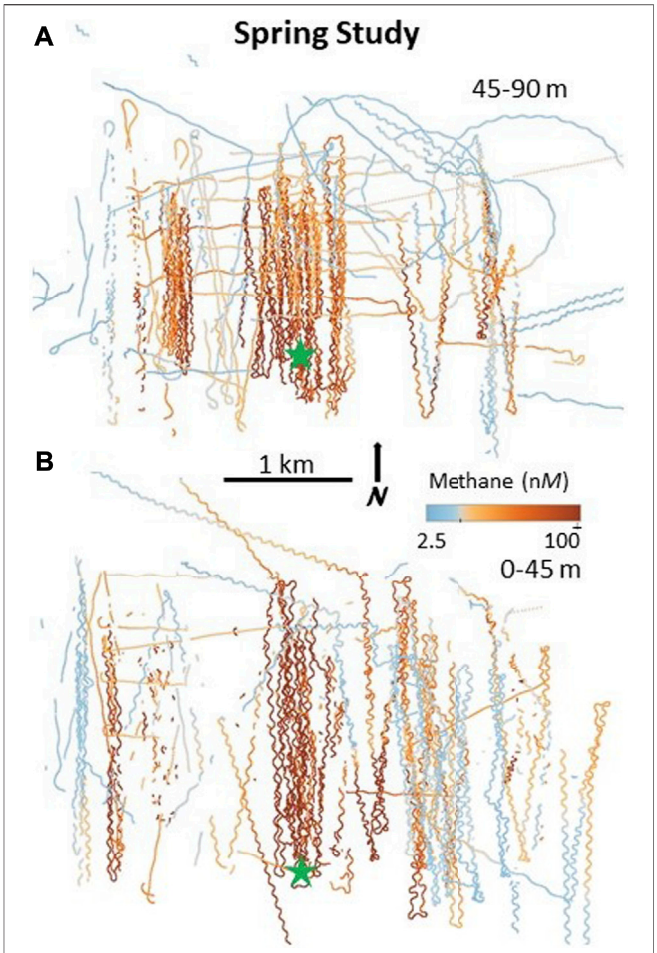

FIGURE 7 | Glider traverse maps for data collected in the spring study of the Bush Hill area (green star marks seep) color coded for methane concentration. **(A)** shows the data binned between 45 and 90 m and **(B)** 0–45 m above the seafloor. The divergence in the methane color coding corresponds to the 25 n*M* or 10× the environmental background with orange colors indicating confident methane detection.

For depths below 400 m, the current velocities are uniformly slower, generally less than 0.1 m/s, with no preferred orientation (**Figure 10**). In this depth range, there is no temporal pattern in the north-south component, but data from the 5th and 6th of November are modestly skewed to the east while results from the 9th and 10th are modestly skewed to the west.

Dives that approach within ~25 m of the seafloor allow the ADCP to achieve bottom-lock. This extra positioning data allows processing of the ADCP data that resolves the bottom-current structure at a much higher spatial and temporal resolution. For near-bottom studies, the gliders conducted mini-yos each consisting of an approach toward the seafloor and ascent away after achieving a depth of ~5 m from the seafloor. The bottom-water current data is analyzed initially by looking at the average current measured in each mini-yo. We then consider current variations within mini-yos that helps resolve the current structure on the scale of individual meters vertically and laterally and on time scales of 2–3 s.

Average mini-yo data shows a speed range from less than 0.03 to ~0.18 m/s (**Figure 11**). The aggregate data reveal no simple relations in terms of current orientations or speeds relative to the bathymetry around Bush Hill. The data collected contain direction reversals and changes in speed that span the observed range on time scales of less than 4 h.

Near-bottom dives on Nov. 6th traversed relatively short distances and had a limited number of mini-yos (**Figure 12**). These dives found bottom-water currents with low speeds and highly variable directions. Two mini-yos on the northern crest of Bush Hill found low speed currents (less than 0.06 m/s) that nearly reversed directions over ~3.5 h from WNW to ESE. Two dives on the southern flank of Bush Hill near the end of the Nov. 6th again found similar low current speeds

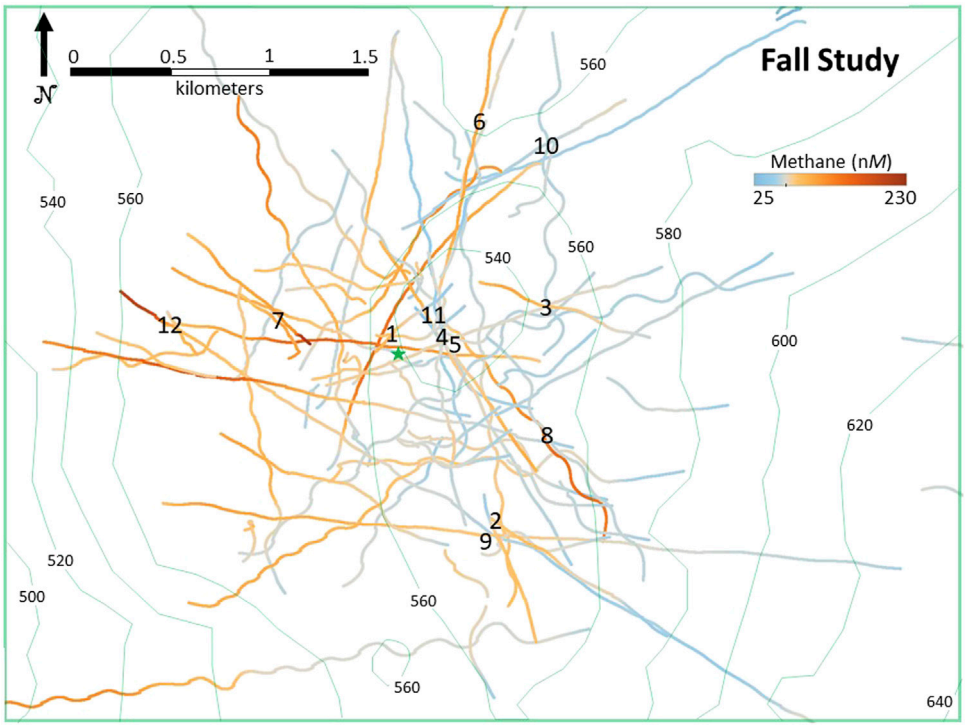

FIGURE 8 | Glider traverse maps for data collected in the fall study of the Bush Hill area (green star marks seep) color coded for methane concentration. The glider paths are overlain on the seafloor bathymetry contoured in meters below sea level (bathymetry from NOAA). The divergence in the methane color coding corresponds to the quantitation limit with orange colors indicating confident methane detection. The numbers correspond to a temporal analysis (see **Table 1**).

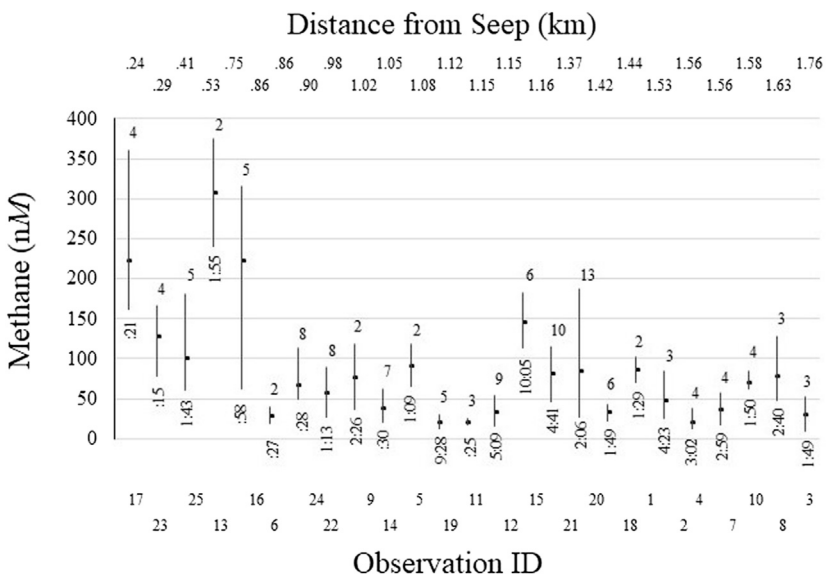

FIGURE 9 | The plot shows the temporal variation at 25 points of varying distance from the source during the spring study. The horizontal distance is not scaled in the figure see the upper axis label. Observations numbers are shown on the lower axis. The number of replicate observations is shown above the observed range. The duration of observations is shown below. The vertical lines represent the spread of the observed concentrations with the tick mark indicating the average for each set of measurements.

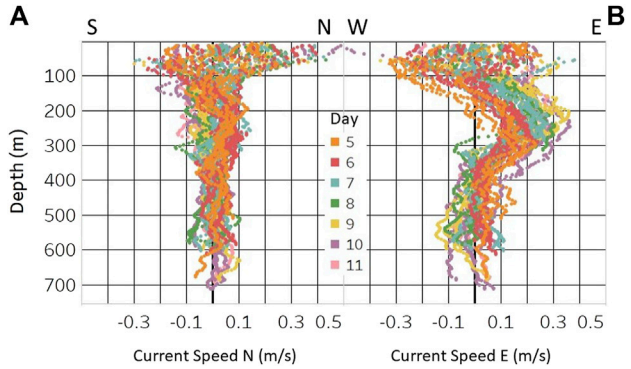

FIGURE 10 | Average current data for all dives showing how the north **(A)** and east **(B)** velocity components vary with depth (vertical axis). The data are color-coded by the date of the dive (November 2018).

and current directions that shifted by ~90° from to the W to the N in ~3.5 h.

Three near-bottom dives took place on Nov. 7th skewed to the east of, and crossing just over the top of the summit of Bush Hill (**Figure 12**). These dives found bottom-water currents with low to intermediate speeds and variable directions. Currents measured in the earlier part of the day to east of the summit flowed up slope with low speeds (less than 0.06 m/s). A traverse over the summit later in the day found directions varying around being directed due north, without regard to the bathymetry and with higher average speeds (0.03–0.09 m/s).

Five near-bottom dives took place on November 8th crossing over the summit of Bush Hill and extending significantly far to the north and west (**Figure 12**). These dives found bottom-water currents with speeds ranging over nearly the entire observed range (0.03–0.18 m/s) and with directions in every quadrant. Currents measured in the earlier part of the day from ~2:00 to 8:00 on the north side of the mud volcano found mostly high speed currents that shift from predominately eastward to southward directed over this time. Three dives later in the day (after 12:00) found a restricted range of speeds (0.03–0.06 m/s) with directions that varied from toward NNE to toward WSW.

A single near-bottom dive took place on Nov. 9th crossing from west to east over the southern extension of Bush Hill (**Figure 12**). This took just over 2 h and found bottom-water

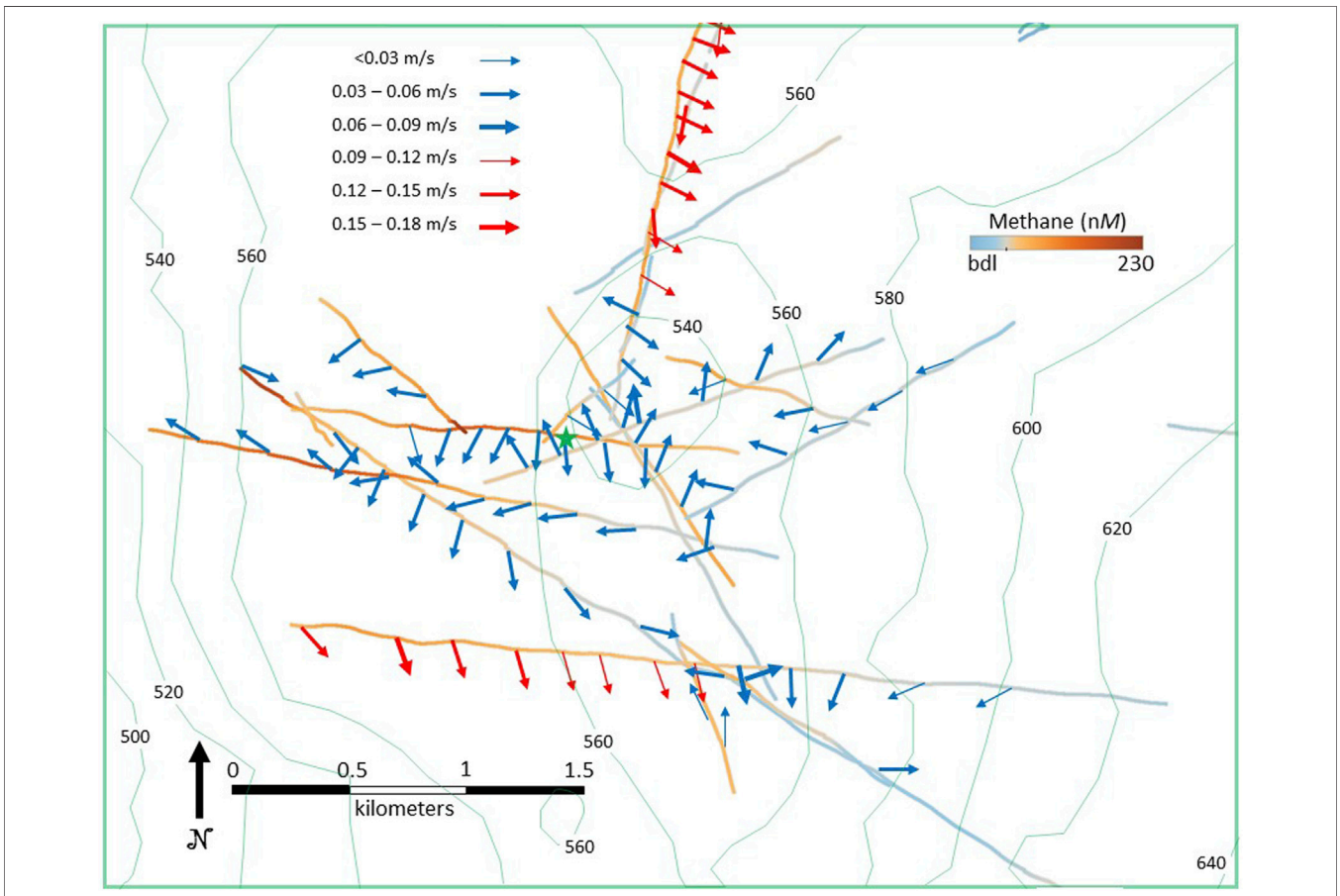

FIGURE 11 | Average near-bottom current measurements are shown as vectors (see legend). Each vector tail is located on the glider path for that data point. Glider paths are color coded to indicate the methane concentration with orange colors indicating confident detection (see e.g., **Figures 4**–**6**). The green star represents the venting location for Bush Hill (27.7811°N, 91.5082°W). Bathymetry shown is in meters below sea level.

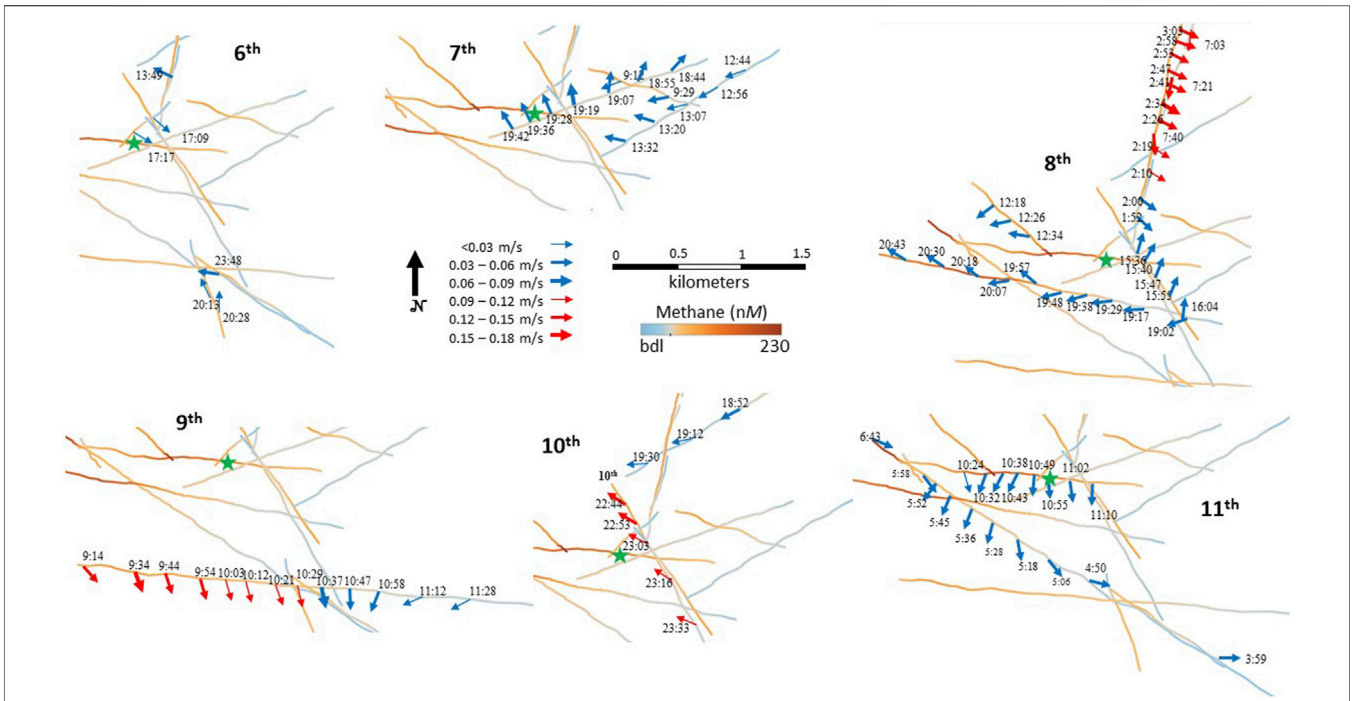

FIGURE 12 | Detailed daily average near-bottom current measurements. Data as per **Figure 10** but split out for each day with acquisition times indicated at the tail of each vector.

currents with directions predominately directed to the south but speeds ranging over the entire observed range. Current speeds were highest at the start of the dive to the west of Bush Hill (0.12–0.18 m/s) and dropped progressively as the glider went over the top of the elongate southern part of the mud volcano and traversed down the eastern slope (<0.03–0.09 m/s).

Three near-bottom dives took place on November 10th with one recording only a single mini-yo well to the east of Bush Hill and the other two traverses near/over the summit (**Figure 12**). Bottom-water currents were predominately to the west with a significant range of speeds (<0.03–0.15 m/s). The single average current measurement well to the east of Bush Hill, and nearly 100 m below its summit, is of a slow current (<0.03 m/s) flowing nearly due south. Similar low speed currents were measured just to the north of Bush Hill 13 h later directed to the ~SW. However, 3 h later on a traverse over the summit of Bush Hill currents with speeds up to 0.15 m/s were measured flowing to the NW.

Two near-bottom dives took place in the first half of November 11th with one being an exceptionally long traverse from the SE across the southern flank of Bush Hill and the other traversing from nearly due west near/over the summit and directly over the seep vent (**Figure 12**). Bottom-water currents were slow with a limited range of speeds (<0.03–0.06 m/s) and directions ranged over only slightly more than 90° from directed E to directed SSW. A traverse from the southeastern slope to well to the west of the summit took nearly 3 h to complete documenting little variation in current speed (0.03–0.06 m/s) and directions that sweep from directed nearly E to directed SW and then abruptly back to directed SE. The change in current direction from SW to SE is found between data points separated by ~100 m and ~6 min between average measurements. A traverse over the summit that took 50 min documented consistent current speeds (0.03–0.06 m/s) flowing ~S.

Analysis of the detailed current information contained in each mini-yo has the potential to reveal significant advection of methane near the seafloor. Each mini-yo resolves the 25 m above the seafloor into 2 m cubic bins. While most of the traverses did not image any significant structure to the bottom water currents, some revealed discrete higher velocity bottom water flows. Two examples of bottom water flows are shown from Nov. 8th and 9th. The traverse on the 8th starts on the lower slopes of the mud volcano on the north side and progresses away from the mud volcano up the slope to its north. The data reveal a much higher velocity flow in the bottom ~8 m of the seawater column (**Figure 13A**). The traverse is oriented perpendicular to the flow direction. The higher-velocity bottom-water current has a width of ~1 km and the southern and northern margins of the flow are elevated from the seafloor.

The traverse on the 9th starts to the west of the mud volcano and goes up and over its elongate southern flank. The glider traverse is perpendicular to the flow direction and samples a 1.5 km wide part of the flow (truncated on the western side). This flow has a variable height, ranging from ~6 to >14 m (**Figure 13B**). The higher-velocity flow is not restricted to the bottom and is decoupled from the seafloor both internally and at its eastern margin. The vertical extent of this flow is not constrained as higher velocity water is observed all the way to the top of some mini-yos.

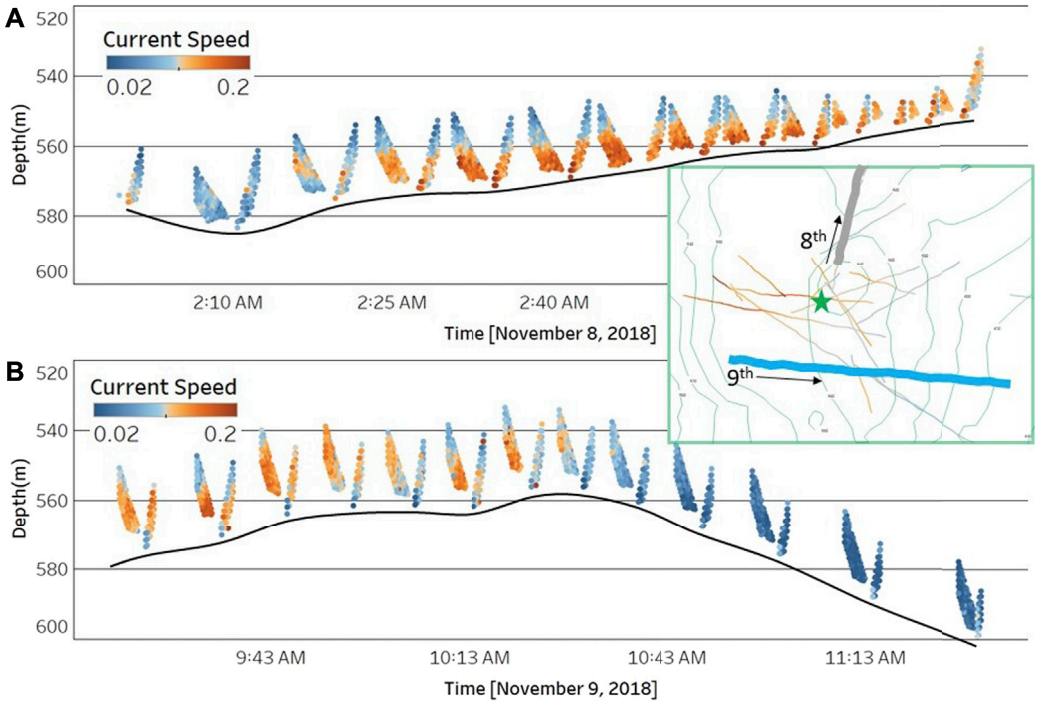

FIGURE 13 | Detailed on-bottom data showing strong near bottom currents. **(A)** shows data for the 8th of November and **(B)** for the 9th. The current speeds shown range from 0.02 to 0.2 m/s and the color scale diverges at 0.11. The horizontal axes indicate time of acquisition for each day. The inset map shows the locations of the traverses relative to Bush Hill and the local bathymetry (**Figure 10**). The current direction of the 8th is predominately to the east and on the 9th to the south (**Figure 11**) so in both cases the traverse is across the flow direction. The pairs of data points are collected on the descent and ascent of each mini-yo.

Methane Concentrations and Current Directions

The methane plume structure at Bush Hill is potentially dictated by several processes but the most important of these that we can constrain is current variations. Short term variations in flux, for example, could lead to spatial variations in concentration but we have no constraints on it during the field studies. Therefore in the analysis below we focus on spatial and temporal variations that can be ascribed to current variations. The analysis is necessarily restricted to the fall study data as there was no ADCP deployed in the spring.

Examination of the data from the SEA027 traverses on the 6th to the 11th of November should provide direct insight into methane advection from the source (**Figure 12**). All current measurements on the 6th and 7th have current directions moving toward the source, or nearly tangent to it, suggesting the measurements locations are upwind of the source. Despite being upcurrent, the measurements on these days are split nearly equally between those that detected methane and those that did not. The parts of traverses closest to the source detected methane on both the 6th and 7th, but methane was also detected on the 6th in locations ~1 km to the south despite northward directed currents. Traverses on the 8th and 9th found currents coming from the source or tangent to it, so they are mostly downcurrent of the source, and include some of the highest measured current velocities (**Figure 12**). Throughout most of the lengths of all these traverses methane is detected. Currents on the 10th are mostly oriented toward the source, upcurrent, with the traverse closest to the source measuring methane and the more distant traverse not detecting methane. Two traverses on the 11th include one that traveled over the source and another to the southwest that found current orientations from the source (downcurrent). Both traverses detected methane over most of their lengths except for the most distal part of the southwestern traverse.

The temporal variation of the currents can be examined by comparing repeat glider visits to a local area (less than 20 m radius) either by SEA027 (equipped with the ADCP) or where nearby ADCP at ~the same time (within an hour) is recorded. We identified 12 times in the data where these criteria were met (**Table 1**). To simplify the data interpretation we characterize the current direction as above with the vector orientation described as with respect to the source as observed from the data collection point. Thus, currents can generally be flowing: from the source (observation is downcurrent), toward the source (observation is upcurrent), or tangent to the source (defined as being at approximately a right angle to the line connected the observation to the source).

Two of the twelve repeat visits (7 and 9) have both observations with the current flowing from the source (**Figure 12** and **Table 1**). Observation 7 has the two highest measured concentrations (~100 nM) for all 24 measurement showing that high concentrations can persist locally for times of at least an hour. In contrast the first measurement at location 9 was below detection despite the current flowing from the source

TABLE 1 | Collocated observations with current data.

Obs	Date	Glider	Time	n*M*	Flow	Speed	Glider	Time	n*M*	Flow	Speed	Distance (m)
1	6	27	17:17	68	Toward	<0.03	23	19:38	60	Toward	<0.03	85
2	6	27	20:06	bdl	Toward	<0.03	27	23:58	59	Toward	0.03–0.06	890
3	7	27	09:15	70	Toward	<0.03	27	18:56	42	From	0.03–0.06	705
4	7	23	16:14	bdl	Toward	0.03–0.06	27	19:22	45	Tangent	0.06–0.09	245
5	7–8	23	15:58	41.7	Toward	0.03–0.06	27	01:49	43	Toward	0.03–0.06	260
6	8	27	02:24	87	Tangent	0.12–0.15	27	07:40	49	Toward	0.12–0.15	1,170
7	8	23	11:20	91	From	0.03–0.06	27	12:38	110	From	0.03–0.06	520
8	8	23	14:45	bdl	Tangent	0.03–0.06	27	18:52	bdl	Tangent	0.03–0.06	745
9	9	23	03:35	bdl	From	0.09–0.12	27	10:29	58	From	0.09–0.12	910
10	10	27	19:00	bdl	Tangent	<0.03	23	22:13	bdl	Tangent	<0.03	1,110
11	10	23	16:13	bdl	Toward	0.06–0.09	27	23:05	61	Toward	0.09–0.12	270
12	11	27	06:04	84	Toward	0.03–0.06	27	10:01	66	Tangent	<0.03	1,080

*Summary of 12 repeat observations captured within 20 m of each other during the fall experiment. Unique columns are as follows: Obs. = observation number (see **Figure 8**), Date = day of November 2018, and dist. (m) = the distance of each observation from the source. In between these columns are two sets of columns that give the glider making each measurement, time of day of the measurement, the observed concentration in nM, the flow direction of the current relative to the source (see text), and the speed of the current in m/s. Some concentration measurements are below detection limits (bdl).*

but ~7 h later the concentration had increased to ~70 nM. Two sets of observations (8 and 10) had both measurements below detection limits and in all four instances the current was tangent to the source. There are four examples of observations wherein the current was persistently flowing toward the source and these include examples of the methane concentration increasing, decreasing, and remaining the same on time scales from 2 to 7 h. There is a single example (observation 3) of the current direction reversing, initially flowing toward the source and ~10 h later flowing from the source. In this instance the concentration decreases from 70 to 40 nM between measurements.

DISCUSSION

Methane Distribution Around Bush Hill

Although the methane measurements and the fluid dynamics of the system indicate that it is not possible to image a static distribution of the methane concentrations around Bush Hill, a time averaged methane distribution pattern can be proposed. Toward this end we construct what we infer to be a 3D map of the time-averaged methane concentrations around Bush Hill beginning with the vertical distribution.

The descending dives place an effective ceiling for reliable methane detection over Bush Hill area at 100 m. This is consistent with prior hydrocast *ex situ* sampling (Solomon et al., 2009) and is typical for other *ex situ* sampling efforts above seeps releasing methane bubbles (e.g., Römer et al., 2019). However, the lateral glider operations in the spring study suggest that this result may reflect the methane detection height only near the source as dives more offset from the source, and lateral traverses, indicate lower maximum detection height (**Figure 5**). Intuitively it makes sense that ascending methane bubbles from the source would give rise to higher methane concentrations higher in the water column above the source. To uniformly define a bound for methane concentrations that are, on average, always above detection limits over the entire area we use an average detection concentration for methane of 25 nM (spring study) and require that methane be detected ~50% of the sampling times (a 25 nM isosurface). These criteria generate a boundary over the seep that has a domed structure and extends out to ~1,500–2,000 m.

The 25 n*M* isosurface surface defines a volume for the 3D map. To define concentration regions within that volume we use a combination of the map distributions for different depths (e.g., **Figure 7**) and smashes onto vertical planes (e.g., **Figure 5**). The 3D volume is not adequately sampled to robustly define lateral variations in all directions with confidence so we use a radially symmetric model. This allows us to define discrete volumes with average concentrations (**Figure 14**). The model honors the concentration patterns seen in both the spring and the fall but relies on the spring study for the concentrations.

There are very few studies, of which we are aware, that present spatial patterns for dissolved methane around seeps. Solomon et al. (2009) studied methane release from Bush Hill with a primary focus on methane transfer to the atmosphere. As part of that work they did *ex situ* sampling during three submersible dives and 5 hydrocasts. The data is presented as a sparse radial cross-section of methane concentrations in the water column. Their cross section suggests methane concentrations > 1,000 nM extend more than 300 m away from Bush Hill and up to 80 m elevation within the first 150 m. Concentrations this high would have been above the linear range for the detectors used in the spring study and at or slightly above those used in the fall study. However, no concentrations were measured that approached the non-linear portions in either study. It is important to note that the near source sampling by Solomon et al. was done via submersible and intentionally sampled near the bubble streams, creating a bias toward high concentrations.

The Impact of Currents on Methane Distribution

Even slow currents will move methane released from a seep three to four orders of magnitude faster than diffusion so advective transport explains the methane distribution around Bush Hill. Prior on-bottom work at Bush Hill (Tryon and Brown, 2004;

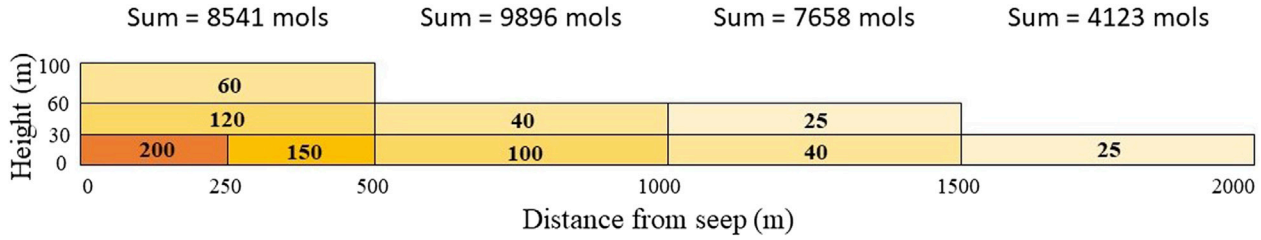

FIGURE 14 | Shown is a half space block model for the concentration variations around the Bush Hill seep site. The numbers in each block indicate average concentrations in nM. The sums above the model are the total number of moles of methane contained in each 500 m wide volume assuming radial symmetry.

Kastner and MacDonald, 2006) has found little evidence of a distributed source for methane so it is reasonable to consider it as a point source. Taking methane as a passive chemical tracer from a point source one might be inclined to draw an analogy with smoke from a chimney. Using this analogy, the currents are expected to carry the methane downwind away from the source and thereby create an asymmetric distribution. The combined collection of current and compositional data (**Figures 11**, **12**) allow us to test this model and find it lacking. We do observe some high concentrations downwind from the source but we also find high concentrations upwind of the source (**Table 1**). In general there is no clear relationship between the current direction relative to the source and the methane concentration observed.

Taking the near bottom average current data as a whole (**Figure 11**), there is no coherent direction in any area that persists over time. So in the analogy, the chimney is not located in a regular wind field that transports the smoke away; rather it is in an area with generally slow moving currents that change directions on time scales of hours. We suggest a better analogy is to think of the area surrounding Bush Hill as a smog basin with a central source. In this case the basin does not have any actual physical boundaries—there is higher bathymetry to the west and north but the seafloor slopes away to the east and south (**Figure 1**). Rather, the methane (smog) is retained around the source by the lack of any organized current to sweep it out of the area. The concentrations decrease vertically and laterally away from the source with progressive dilution.

Using a smog basin analogy, we can readily understand the lack of correlation between current and concentrations. The methane is being moved back and forth around the source so there is no particular significance to being upwind or downwind over the timescales of hours. The data from the spring and fall experiments define a similar sized detection radius – somewhat smaller in the fall. This could be an approximation of a quasi-steady-state environment around Bush Hill.

Temporal Aspects of Methane Distribution

Assuming the methane plume observed around Bush Hill is generally (always?) present, we can consider how its total methane content relates to that being released from the seep. On bottom characterization of the bubble flux from Bush Hill gives an output from the seep of ~5,390 mol/day (Leifer and MacDonald, 2003). Summing over the entire methane plume (**Figure 14**) gives a total of ~30,200 mol of methane or about 5.6 days equivalent of seeped methane. Similar calculations for the methane plume model proposed by Solomon et al. (2009) suggest 1.8 days equivalent. For the observed methane concentrations, these times are far too short to explain the marginal loss of methane via microbial oxidation (Pack et al., 2011). The upper boundary of the plume is interpreted to be controlled by more organized advective transport and dilution at higher levels in the water column (**Figure 11**); whereas the lateral margins simply reflect progressive dilution away from the source.

The presence of a persistent methane plume around the source could promote the stability of exposed methane hydrates (Kennicutt et al., 1988b). The initial growth of structure II or structure H hydrates (Sassen and MacDonald, 1994) at the depths of Bush Hill (>500 m) would be favored even at much higher water temperatures (at least up to 17°C) (Yin et al., 2018). In order to persist however, the exposed hydrates must maintain a methane concentration in the surrounding seawater that is at hydrate saturation—otherwise the hydrates would dissolve until the seawater was saturated. In the chimney analogy the saturated boundary layer around the hydrates would be continuously stripped away by the organized currents. In the smog basin analogy there should be a higher concentration plume of methane surrounding the hydrates so disruptions of the saturated boundary layer would not introduce "fresh" seawater but rather methane-rich seawater thereby minimizing the concentration gradient around the hydrates and reducing loses due to dissolution.

In their analyses of the hydrate dissociation Lapham et al. (2014) conclude that the observed long term stability of methane hydrates at Bush Hill is inconsistent with expected rates based on laboratory and *in situ* test measurements. They also conclude that the methane flux from below is insufficient to maintain the seafloor hydrates in a ~steady state condition. They infer that the long term stability of seafloor hydrates at Bush Hill and other GoM seepages site is related to having a protective sediment cover that limits dissociation by maintaining saturation methane concentrations in pore water adjacent to the hydrate. The sediment cover is required to shield the saturated boundary layer from being depleted by currents. Our findings suggest that low current speeds and locally high methane concentrations (within a few centimeters of the hydrate) can also help promote long-term hydrate stability.

We hypothesize that the stabilization of exposed seafloor hydrates at other seep sites is indicative of the long-term presence of elevated methane concentrations and the current structure that this requires. If true, then the presence/absence of seafloor hydrates might be used as a test for grouping areas to contrast the character of their biologic communities. In particular we expect methane-oxidizing microbes in the water column to be at higher concentrations and to occupy a significantly greater volume at seeps with exposed hydrates.

Using the Observed Methane Distribution to Better Understand Seepage

The distribution of dissolved methane around the Bush Hill mud volcano is governed by the flux of methane from the seep and subsequent distribution by near-bottom currents. The data are insufficient to allow us to draw hard conclusions about details of the methane release. A simplification that is implicit to some of the preceding interpretations is that the release of methane from Bush Hill can be fairly approximated as constant over time scales of at least 10–20 min and up to 1–2 h. This simplification allows us to makes sense of the repeat current and concentration data in **Table 1**, for example. If the methane flux from the source dropped substantially or stopped entirely between the measurements, then the relevance of currents moving toward or away from the source relative to observation point would be far more nebulas. The fairly regular radial distribution of methane around Bush Hill would be far more complicated to explain as a product of both a varying source flux and varying current patterns. In this case the flux and currents would have to co-vary to explain the methane distribution. Thus, while a quasi-steady state flux is not strictly required by the data; we interpret the system to behave in this way as it provides the simplest explanation of the observations.

The limited amount of data on the distribution of dissolved methane at seeps means that we cannot interpret our data by analogy; i.e., there is no basis to characterize the methane plume at Bush Hill as typical or unusual. The approach we used to collect the data is relatively low cost for ocean field-work and so could be used to survey other thermogenic and biogenic sources of methane seepage to develop a more general understanding. It is our hope that others will leverage these methods to provide a more complete understanding of dissolved methane around seepage sites.

There are a number of potential changes to the experimental design that could provide more detailed and better constrained results. For example, more gliders (four or five) all equipped with ADCPs could provide an understanding of current variability in both space and time. A laser-based methane detector could provide similar sensitivity to the METS and reduce or eliminate the smoothing effect on the quantitation imparted by it. Collecting contemporaneous water samples, either from the glider(s) or via hydrocasts, could validate *in situ* concentration measurements.

CONCLUSION

We present the findings of two *in situ* characterization studies of methane concentrations around the Bush Hill mud volcano conducted in the spring and fall of 2018. High spatial resolution (~5 m) mapping of methane concentrations as close as ~5–90 m above the seafloor allowed a 3D understanding of the methane plume. Maximum observed concentrations were ~400 nM, well below concentrations documented by *ex situ* samples captured via ROVs and submersibles at Bush Hill and other seep sites (which exceed 10,000 nM). On the other extreme, we found areas throughout the methane plume that had methane concentrations that were below detection limits. As might be expected, the frequency of non-detects increases away from the source. We interpret the concentration data to indicate the presence of a detectable methane plume within 30 m of the seafloor up to 2 km away from the source in all directions despite significant variations in the seafloor bathymetry.

Repeat sampling demonstrated significant variations in methane concentrations (and current directions) occur on time scales of 1–2 h. The majority (>90%) of the analyses conducted close to the source were above detection limits. At 750 m distance from the source, only about 65% of the analyses were above detection limits. This significant temporal and spatial variability presents a challenge for interpreting limited *ex situ* sampling. Comparison of the average results from the spring and fall studies suggests an overall decrease in the amount of methane present around the seep of ~35%. However, nearly all other characteristics of the methane plume were similar between both studies.

By coupling the concentration data with current data we are able to demonstrate that there is no pervasive transport of methane away from the seep source (i.e., as one might picture for a classic chimney plume). The dissolved methane associated with the seepage lingers in the area of the source because the near bottom currents vary in direction often enough that they provide no effective long-distance transport. Comparison of observed total methane in the plume with estimated flux from the seep suggests that an equivalent of about 6 days accumulated methane is found in the plume. Examples of relatively high velocity (up to 0.18 m/s) near bottom currents with limited lateral extents were documented by high resolution ADCP coverage. If these currents were to persist for as long as 5 h they have the potential to displace methane located in the lower ~20 m of the water column from the 2 km radius vicinity. Episodic occurrences of such currents may explain some of the significant temporal variations in concentration.

DATA AVAILABILITY STATEMENT

The datasets presented in this article are not readily available because Data release is limited by ExxonMobil. Requests to access the datasets should be directed to william.p.meurer@exxonmobil.com.

AUTHOR CONTRIBUTIONS

All authors contributed to the field effort with JB dealing with operations and planning, GS handling data ingestion and geodetic issues, and WM analyzing current and geochemical data. All three authors provided input into the ideas contained

in this manuscript. WM did most of the manuscript preparation drawing heavily from internal reports to which all three authors contributed significant blocks of text and analyses. All authors provided direct input into the final versions of text and figures.

FUNDING

ExxonMobil's Upstream Research Company provided all funding for the field work and subsequent data analysis.

ACKNOWLEDGMENTS

The field work presented here benefitted significantly from contributions from scientists associated with Alseamar especially in relation to analysis of the ADCP data and from Blue Ocean Monitoring. We also wish acknowledge significant contributions from other researchers at ExxonMobil. Lastly, we are thankful for ExxonMobil's Upstream Research Company financial support of this effort and their interest in publishing the results.

REFERENCES

Åström, E. K. L., Carroll, M. L., Ambrose, W. G., Jr., Sen, A., Silyakova, A., and Carroll, J. (2017). Methane Cold Seeps as Biological Oases in the High-Arctic Deep Sea. *Limnol. Oceanogr.* 63, S209–S231. doi:10.1002/lno.10732

Brooks, J. M., Cox, H. B., Bryant, W. R., Kennicutt, M. C., Mann, R. G., and McDonald, T. J. (1986). Association of Gas Hydrates and Oil Seepage in the Gulf of Mexico. *Org. Geochem.* 10, 221–234. doi:10.1016/0146-6380(86)90025-2

Brooks, J. M., Kennicutt, M. C., Fay, R. R., McDonald, T. J., and Sassen, R. (1984). Thermogenic Gas Hydrates in the Gulf of Mexico. *Science* 225, 409–411. doi:10.1126/science.225.4660.409

Brooks, J. M., Kennicutt, M. C., II, Macdonald, I. R., Wilkinson, D. L., Guinasso, N. L., Jr., and Bidigare, R. R. (1989). "Gulf of Mexico Hydrocarbon Seep Communities: Part IV - Description of Known Chemosynthetic Communities," in Proceedings of the 21st Offshore Technology Conference, OTC, Houston, TX, May 1989. 5954, 663–667.

Brooks, J. M., Kennicutt, M. C., II, Bidigare, R. R., and Fay, R. R. (1985). Hydrates, Oil Seepage, and Chemosynthetic Ecosystems on the Gulf of Mexico Slope. *Eos* 66, 105. doi:10.1029/eo066i010p00106-01

Coleman, J. M., Roberts, H. H., and Bryant, W. R. (1991). "Late Quaternary Sedimentation," in *The Gulf of Mexico Basin, The Geology of North America*. Editor A. Salvador (Boulder, CO: Geological Society of America).

Cordes, E., Hourdez, S., Predmore, B., Redding, M., and Fisher, C. (2005). Succession of Hydrocarbon Seep Communities Associated With the Long-Lived Foundation Species *Lamellibrachia luymesi*. *Mar. Ecol. Prog. Ser.* 305, 17–29. doi:10.3354/meps305017

De Beukelaer, S. M., MacDonald, I. R., Guinnasso, N. L., Jr., and Murray, J. A. (2003). Distinct Side-Scan Sonar, RADARSAT SAR, and Acoustic Profiler Signatures of Gas and Oil Seeps on the Gulf of Mexico Slope. *Geo-Mar Lett.* 23, 177–186. doi:10.1007/s00367-003-0139-9

De Beukelaer, S. M. (2003). Remote Sensing Analysis of Natural Oil and Gas Seeps on the Continental Slope of the Northern Gulf of Mexico. MSc thesis. Mexico: Texas A&M University, 117.

Di, P., Feng, D., Tao, J., and Chen, D. (2020). Using Time-Series Videos to Quantify Methane Bubbles Flux from Natural Cold Seeps in the South China Sea. *Minerals* 10 (3), 216. doi:10.3390/min10030216

Galloway, W. E., Bebout, D. G., Fisher, W. L., Dunlap, J. B. J., Cabrera-Castro, R., Lugo-Rivera, J. E., et al. (1991). *The Gulf of Mexico Basin: The Geology of North America*. Editor A. Salvador (Boulder, CO: Geological Society of America).

Galloway, W. E. (2008). "Depositional Evolution of the Gulf of Mexico Sedimentary Basin," in *The Sedimentary Basins of the United States and Canada: Sedimentary Basins of the World*. Editor A. D. Miall (Netherlands: Elsevier), 505–549.

Girard, F., Sarrazin, J., and Olu, K. (2020). Impacts of an Eruption on Cold-Seep Microbial and Faunal Dynamics at a Mud Volcano. *Front. Mar. Sci.* 7. doi:10.3389/fmars.2020.00241

Greinert, J. (2008). Monitoring Temporal Variability of Bubble Release at Seeps: The Hydroacoustic Swath System GasQuant. *J. Geophys. Res.* 113, C07048. doi:10.1029/2007jc004704

Hu, L., Yvon-Lewis, S. A., Kessler, J. D., and MacDonald, I. R. (2012). Methane Fluxes to the Atmosphere from Deepwater Hydrocarbon Seeps in the Northern Gulf of Mexico. *J. Geophys. Res.* 117, C01009–C01023. doi:10.1029/2011JC007208

Hudec, M. R., Norton, I. O., Jackson, M. P. A., and Peel, F. J. (2013). Jurassic Evolution of the Gulf of Mexico Salt Basin. *Bulletin* 97, 1683–1710. doi:10.1306/04011312073

Johansen, C., Macelloni, L., Natter, M., Silva, M., Woosley, M., Woolsey, A., et al. (2020). Hydrocarbon Migration Pathway and Methane Budget for a Gulf of Mexico Natural Seep Site: Green Canyon 600. *Earth Planet. Sci. Lett.* 545, 116411. doi:10.1016/j.epsl.2020.116411

Kastner, M., and MacDonald, I. (2006). Final Technical Report on: Controls on Gas Hydrate Formation and Dissociation, Gulf of Mexico: *In Situ* Field Study with Laboratory Characterizations of Exposed and Buried Gas Hydrates. DOE Report (DOE Award Number: DE-FC26-02NT41328), 31.

Kennicutt, M. C., Brooks, J. M., Brooks, G. J., and Denoux, G. J. (1988b). Leakage of Deep, Reservoired Petroleum to the Near Surface on the Gulf of Mexico Continental Slope. *Mar. Chem.* 24, 39–59. doi:10.1016/0304-4203(88)90005-9

Kennicutt, M. C., II, Brooks, J. M., Bidigare, R. R., and Denoux, G. J. (1988a). Gulf of Mexico Hydrocarbon Seep Communities-I. Regional Distribution of Hydrocarbon Seepage and Associated Fauna. *Deep Sea Res.* 35, 1639–1651. doi:10.1016/0198-0149(88)90107-0

Lapham, L. L., Chanton, J. P., Chapman, R., and Martens, C. S. (2010). Methane Under-Saturated Fluids in Deep-Sea Sediments: Implications for Gas Hydrate Stability And Rates of Dissolution. *Earth Planet. Sci. Lett.* 298, 275–285. doi:10.1016/j.epsl.2010.07.016

Lapham, L. L., Wilson, R. M., MacDonald, I. R., and Chanton, J. P. (2014). Gas Hydrate Dissolution Rates Quantified With Laboratory and Seafloor Experiments. *Geochim. Cosmochim. Acta* 125, 492–503. doi:10.1016/j.gca.2013.10.030

Leifer, I. (2019). A Synthesis Review of Emissions and Fates for the Coal Oil Point Marine Hydrocarbon Seep Field and California Marine Seepage. *Geofluids* 2019, 4724587. doi:10.1155/2019/4724587

Leifer, I. (2010). Characteristics and Scaling of Bubble Plumes from Marine Hydrocarbon Seepage in the Coal Oil Point Seep Field. *J. Geophys. Res.* 115, C11014. doi:10.1029/2009jc005844

Leifer, I., and MacDonald, I. (2003). Dynamics of the Gas Flux from Shallow Gas Hydrate Deposits: Interaction Between Oily Hydrate Bubbles and the Oceanic Environment. *Earth Plant Sci. Lett.* 210, 411–424.

Levin, L. (2005). "Ecology of Cold Seep Sediments: Interactions of Fauna With Flow, Chemistry and Microbes," in *Oceanography and Marine Biology: Annual Review*. Editors R. N. Gibson, R. J. A. Atkinson, and J. D. M. Gordon (Milton Park: Taylor & Francis), 1–46. doi:10.1201/9781420037449.ch1

MacDonald, I. R., Boland, G. S., Baker, J. S., Brooks, J. M., Kennicutt, M. C., II, and Bidigare, R. R. (1989). Gulf of Mexico Hydrocarbon Seep Communities. *Mar. Biol.* 101, 235–247. doi:10.1007/bf00391463

MacDonald, I. R., Guinasso, Jr., N. L., Jr., Sassen, R., Brooks, J. M., Lee, L., and Scott, K. T. (1994). Gas Hydrate that Breaches the Sea Floor on the Continental Slope of the Gulf of Mexico. *Geology* 22, 699–702. doi:10.1130/0091-7613(1994)022<0699:ghtbts>2.3.co;2

MacDonald, I. R. (2011). Remote Sensing and Sea-Truth Measurements of Methane Flux to the Atmosphere (HYFLUX Project). DOE Award No.: DE-NT0005638 Final Report. 164.

Pack, M. A., Heintz, M. B., Reeburgh, W. S., Trumbore, S. E., Valentine, D. L., Xu, X., et al. (2011). A Method for Measuring Methane Oxidation Rates Using

Lowlevels of 14C-Labeled Methane and Accelerator Mass Spectrometry. *Limnol. Oceanogr. Methods* 9, 245–260. doi:10.4319/lom.2011.9.245

Peel, F. J., Travis, C. J., and Hossack, J. R. (1995). "Genetic Structural Provinces and Salt Tectonics of the Cenozoic Offshore U.S. Gulf of Mexico," in *Salt Tectonics: A Global Perspective*. Editors Jackson, M. P., Roberts, D. G., and Snelson, S., 65, 153–175. doi:10.1306/m65604c7

Razaz, M., Di Iorio, D., Wang, B., Daneshgar Asl, S., and Thurnherr, A. M. (2020). Variability of a Natural Hydrocarbon Seep and its Connection to the Ocean Surface. *Sci. Rep.* 10, 12654. doi:10.1038/s41598-020-68807-4

Römer, M., Hsu, C.-W., Loher, M., MacDonald, I. R., dos Santos Ferreira, C., Pape, T., et al. (2019). Amount and Fate of Gas and Oil Discharged at 3400 m Water Depth from a Natural Seep Site in the Southern Gulf of Mexico. *Front. Mar. Sci.* 6, 700. doi:10.3389/fmars.2019.00700

Sager, W. W. (2002). "Geophysical Detection and Characterization of Chemosynthetic Organism Sites," in *Stability and Change in Gulf of Mexico Chemosynthetic Communities*. Editor I. R. MacDonald (New Orleans, LA: U.S. Department of the Interior), 456.

Salvador, A. (1991). "Triassic-Jurassic," in *The Gulf of Mexico Basin: The Geology of North America*. Editor A. Salvador (Boulder, CO: Geological Society of America).

Sassen, R., Joye, S., Sweet, S. T., deFreitas, D. A., Milkov, A. V., and MacDonald, I. R. (1999). Thermogenic Gas Hydrates and Hydrocarbon Gases in Complex Chemosynthetic Communities, Gulf of Mexico Continental Slope. *Org. Geochem.* 30, 485–497. doi:10.1016/s0146-6380(99)00050-9

Sassen, R., and MacDonald, I. R. (1994). Evidence of Structure H Hydrate, Gulf of Mexico Continental Slope. *Org. Geochem.* 22, 1029–1032. doi:10.1016/0146-6380(94)90036-1

Sassen, R., MacDonald, I. R., Guinasso, N. L., Joye, S., Requejo, A. G., Sweet, S. T., et al. (1998). Bacterial Methane Oxidation in Sea-Floor Gas Hydrate: Significance to Life in Extreme Environments. *Geology* 26, 851–854. doi:10.1130/0091-7613(1998)026<0851:bmoisf>2.3.co;2

Sibuet, M., and Olu, K. (1998). Biogeography, Biodiversity and Fluid Dependence of Deep-Sea Cold-Seep Communities at Active and Passive Margins. *Deep Sea Res. Part Topical Stud. Oceanogr.* 45, 517–567. doi:10.1016/S0967-0645(97)00074-X

Sibuet, M., and Roy, K. O.-L. (2002). "Cold Seep Communities on Continental Margins: Structure and Quantitative Distribution Relative to Geological and Fluid Venting Patterns," in *Ocean Margin Systems*. Editors G. Wefer, D. Billett, D. Hebbeln, B. B. Jørgensen, M. Schlüter, and T. C. E. van Weering (Berlin: Springer), 235–251. doi:10.1007/978-3-662-05127-6_15

Smith, A. J., Flemings, P. B., and Fulton, P. M. (2014). Hydrocarbon Flux from Natural Deepwater Gulf of Mexico Vents. *Earth Planet. Sci. Lett.* 395, 241–253. doi:10.1016/j.epsl.2014.03.055

Sohl, N. F., Martínez, E. R., Salmerón-Ureña, P., and Soto-Jaramillo, F. (1991). "Upper Cretaceous," in *The Gulf of Mexico Basin: The Geology of North America*. Editor A. Salvador (Boulder, CO: Geological Society of America).

Solomon, E. A., Kastner, M., MacDonald, I. R., and Leifer, I. (2009). Considerable Methane Fluxes to the Atmosphere from Hydrocarbon Seeps in the Gulf of Mexico. *Nat. Geosci.* 2, 561–565. doi:10.1038/ngeo574

Thomanek, K., Zielinski, O., Sahling, H., and Bohrmann, G. (2010). Automated Gas Bubble Imaging at Sea Floor - A New Method of *In Situ* Gas Flux Quantification. *Ocean Sci.* 6, 549–562. doi:10.5194/os-6-549-2010

Tryon, M. D., and Brown, K. M. (2004). Fluid and Chemical Cycling at Bush Hill: Implications for Gas- and Hydrate-Rich Environments. *Geochem. Geophys. Geosyst.* 5, a, n. doi:10.1029/2004GC000778

Uhlig, C., Kirkpatrick, J. B., D'Hondt, S., and Loose, B. (2018). Methane-Oxidizing Seawater Microbial Communities from an Arctic Shelf. *Biogeosciences* 15, 3311–3329. doi:10.5194/bg-15-3311-2018

Vardaro, M. F., MacDonald, I. R., Bender, L. C., and Guinasso, N. L., Jr. (2005). Dynamic Processes Observed at a Gas Hydrate Outcropping on the Continental Slope of the Gulf of Mexico. *Geo. Mar. Lett.* 26, 6–15. doi:10.1007/s00367-005-0010-2

Weber, T. C., Mayer, L., Jerram, K., Beaudoin, J., Rzhanov, Y., and Lovalvo, D. (2014). Acoustic Estimates of Methane Gas Flux from the Seabed in a 6000 km^2 Region in the Northern Gulf of Mexico. *Geochem. Geophys. Geosyst.* 15, 1911–1925. doi:10.1002/2014GC005271

Yin, Z., Khuranaa, M., Tan, H. K., and Linga, P. (2018). A Review of Gas Hydrate Growth Kinetic Models. *Chem. Eng. J.* 342, 9–29. doi:10.1016/j.cej.2018.01.120

Conflict of Interest: Authors WM, JB, and GS were employed by the company ExxonMobil Upstream Research Company during the period this research was conducted. ExxonMobil has never had working interest in GC blocks 184 and 185 (the Bush Hill area). The findings of this research have no bearing on any current development or production activities.

Publisher's Note: All claims expressed in this article are solely those of the authors and do not necessarily represent those of their affiliated organizations, or those of the publisher, the editors and the reviewers. Any product that may be evaluated in this article, or claim that may be made by its manufacturer, is not guaranteed or endorsed by the publisher.

frontiers in Earth Science

BRIEF RESEARCH REPORT
published: 06 October 2021
doi: 10.3389/feart.2021.589399

Proposed Methodology to Quantify the Amount of Methane Seepage by Understanding the Correlation Between Methane Plumes and Originating Seeps

Chiharu Aoyama and Nidomu Maeda*

Faculty of Marine Resources and Environment, Tokyo University of Marine Science and Technology, Minato, Japan

OPEN ACCESS

Edited by:
Ira Leifer,

Reviewed by:
Benjamin Phrampus,
United States Naval Research Laboratory, United States
Martin Scherwath,
University of Victoria, Canada

****Correspondence:***
Chiharu Aoyama
caoyam0@kaiyodai.ac.jp

Specialty section:
This article was submitted to Environmental Informatics and Remote Sensing, a section of the journal Frontiers in Earth Science

Received: *30 July 2020*
Accepted: *21 September 2021*
Published: *06 October 2021*

Citation:
Aoyama C and Maeda N (2021) Proposed Methodology to Quantify the Amount of Methane Seepage by Understanding the Correlation Between Methane Plumes and Originating Seeps. Front. Earth Sci. 9:589399. doi: 10.3389/feart.2021.589399

In recent years, discoveries of methane plumes (also called methane flares) have been reported in various sea areas around the world. Clusters of naturally seeping methane bubbles rising from the seafloor are visualized as methane plumes on the echograms of quantitative echo sounders and multibeam sonars. In order to determine if seeping methane can be used as energy resources and its environmental impact, it is necessary to estimate the amount of naturally seeping methane. From April, 2020, a 3-year project is being conducted in Japan to evaluate the amount of methane seepage from methane plumes. The authors propose the following steps to quantify the amount of methane seepage accurately. First of all, methane plumes in the Exclusive Economic Zone (EEZ) of Japan are mapped out using acoustic devices such as quantitative echo sounders and multibeam sonars. Secondly, methane bubbles of a few millimeters in diameter from methane seeps at seafloor are collected and sampled using a cone-shaped collector with 20 cm in diameter, operated by Remotely Operated Vehicle (ROV). If we can identify the number of seep mouths that form into one single plume, we will be able to quantify the methane seepage from one plume. Based on this result, calibration of the mean backscattering strength and the amount of seeping methane from methane plumes becomes possible and will be applied to the mapped plumes in order to estimate the methane seepage in the EEZ of Japan. Once this calibration is established, it can be applied to the methane plumes observed worldwide, and methane seepage can be quantified simply by acoustic observations of methane plumes. In this study, a method to verify the correlation between methane plumes and methane seeps is introduced, as well as a method to locate methane seeps effectively using the Target Position function of a quantitative echo sounder. The authors intend to use this as the basic data for establishing a method to estimate the amount of methane released from a methane plume by observing the methane plume acoustically.

Keywords: methane hydrate, methane plume, quantitative echo sounder, target position, beam width, footprint, methane seep mouth, multi beam sonar

1. INTRODUCTION

Recent offshore seismic surveys and logging have confirmed a wide distribution of methane hydrate in deep sea deposits (Shipley and Houston, 1979; Shipley and Didyk, 1982; Matsumoto, 2001). Investigations such as drilling and diving surveys are being conducted in methane hydrate bearing sea areas (Aoyama and Matsumoto, 2009).

Methane hydrate bearing conditions are categorized as either shallow type or pore-filling sand layer type. Shallow type methane hydrate refers to methane hydrate that is, generated and observed near seafloor surface in various forms such as plates, veins, and clumps (Ministry of Economy, Trade and Industry, 2016) on the seafloor surface in waters deeper than 500 m, and at about 100 m below seafloor in the sea area of Joetsu, Sea of Japan. Shallow type methane hydrate in the Sea of Japan is mostly confirmed in muddy sediments at 500–1,500 m depths, shallower than about 100 m below seafloor (National Institute of Advanced Industrial Science and Technology, 2021).

2. METHANE PLUME

A 3-year offshore investigation project of shallow type methane hydrate is being conducted in Japan from April 1, 2020. One of the purposes of this project is to establish a quantification method of methane plumes and utilize those results as an indicator to determine the potential of methane plume as a domestic natural resource and its environmental impacts (National Institute of Advanced Industrial Science and Technology, 2019).

Methane plumes, also called methane flares, are bubbles seeping from the seafloor which can be observed on the monitors of quantitative echo sounders and echogram of multibeam sonars onboard (Aoyama et al., 2009). Also, not all flares are continuously bubbling, often they switch on and off (Römer et al., 2016).

Based on the past investigations by Aoyama *et al.* (Aoyama and Matsumoto, 2009; Aoyama et al., 2009), shallow type methane hydrate is confirmed to exist in the subseafloor source of methane plumes and are used as indicators for shallow type methane hydrate investigations.

In recent studies, extensive observations of methane plumes have numerously been reported in areas such as offshore Spitsbergen (Mau et al., 2017), North Carolina (Skarke et al., 2014), northeastern Sakhalin (Young et al., 2011), as well as offshore Sado in the Sea of Japan (Niigata University, 2016), and offshore Shionomisaki in Wakayama, Japan (Aoyama and Mizukami, 2018). Methane plume observations from within methane hydrate stability zone is an indicator for the potential presence of methane hydrate, and quantification of these, including methane plumes, can reveal the potential use as an energy source.

One example from the past studies of methane flow quantification from ship's echo sounder data is the study by Thomas C. Weber et al. where they surveyed 357 natural seeps in 6000km2 using acoustic mapping techniques (Weber et al., 2014).

3. QUANTIFICATION OF METHANE PLUME SEEPAGE

One hypothesis made in this study is that all of the methane seeps are equal, but according to **Figure 2C**, they are not. However, this project will carry out an examination of many seeps so it will show the variability and uncertainty of this assumption. Also, whereas this study assumes that the methane flow rates from each plume to be constant, (Römer et al., 2016), for example, shows a strong correlation of methane flux with tides and also, longer timescale changes (weeks to months).

Future observations will help to indicate this variability and uncertainty. The methodology of Veloso et al. (2015) for quantifying bubble flow-rate using split-beam echo sounders has already been applied by Riedel et al. (2018) to estimate methane fluxes in Cascadia Margin. However, these types of studies are rare and have not been conducted in Japan, which is why the present methodology was proposed and is currently being implemented.

The following procedures are proposed to quantify methane seep rates.

① Assess methane plume mapping using acoustic devices such as quantitative echo sounders and multibeam sonars.
② Quantify methane seepage by collecting seeping methane with a cone-shaped container attached to an ROV. In this study, the author used a cone-shaped instrument with a diameter of 20 cm.
③ Determine the number of seep mouths of one single plume in order to quantify the methane seepage from a single plume.
④ Calibrate the mean backscattering strength of methane plume and the amount of methane seepage based on the result of ③.
⑤ By applying ④ to ①, the total amount of methane seepage in the surrounding sea areas of Japan will be estimated.

In this study, we consider a proposed methodology to understand ③ the correlation between methane plume and methane seeps accurately.

① Methane Plume Mapping

Methane plumes can be mapped by quantitative echo sounders and multibeam sonars. Observations have been conducted in offshore Joetsu in the Sea of Japan, northeast offshore Sado, and offshore Wakayama prefecture. Recently, this methodology has been used worldwide, including Spitsbergen (Mau et al., 2017) and North Carolina (Skarke et al., 2014).

② Quantification of Methane Seepage From Seafloor

In shallow type methane hydrate bearing sea areas, continuous seeping of methane bubbles with a diameter of 3–5 mm from seeps on seafloor surface are being confirmed. The diameter of these seep mouths is smaller than 1 cm and are often discovered at seafloor.

Seeping methane are immediately coated with methane hydrate film (hereinafter referred to as methane hydrate coated bubbles) under low temperature and high pressure (Matsui and Aoyama, 2019). Specific gravity of methane hydrate is approximately 0.9, and thus the methane hydrate coated bubbles to rise. This state can be observed real-time onboard the research vessels as images recorded with the Remotely Operated Vehicle (ROV) camera (Aoyama and Matsumoto, 2009). These methane hydrate coated bubbles are collected with a cone-shaped device with a 20 cm diameter, attached to the manipulator of an ROV. Methane seepage is quantified by analysis of the video from the ROV (Aoyama and Matsumoto, 2009).

Several studies have been reported on the amount of methane seepage (Hachikubo, 2009), and the amount collected in Umitaka Spur, offshore Joetsu in the Sea of Japan, using this device is estimated to be several tons a year (Aoyama and Matsumoto, 2020). As a specific example, 1,150 ml container was filled with bubbles in 481 s at the Natsushima voyage (NT07-20) in October, 2007. Assuming the constant methane seepage, 8,610 ml of hourly methane seepage can be estimated, with an annual seepage of 75.4 m^3.

③ – 1 Correlation Between Methane Plumes and Methane Seeps ~ Number of Seeps Within the footprint~

Seeping of methane bubbles are confirmed as methane plumes on the echogram of a quantitative echo sounder (Aoyama and Matsumoto, 2009). However, the correlation between the amount of methane seepage measured with a methane bubble collecting tool and methane plumes observed on the echogram is still yet to be known. If the number of seeps within the footprint and their locations are specified on the monitor of a quantitative echo sounder, the amount of methane seepage can be estimated simply by observations of methane plumes on a research vessel.

Methane Plumes Displayed on the Echogram of Quantitative Echo Sounders

Pulsed acoustic waves from the transducer of a quantitative echo sounder mounted beneath the research vessel scatter in various directions when these waves reflect off the objects underwater, such as methane hydrate coated bubbles. The decibel notation of the ratio between the intensity of reflected waves scattered back to the transducer and the intensity of incident waves is called volume backscattering strength (S_v), indicated as SV(= $10\log S_v$) (Furusawa, 1995). The intensity of SV is indicated in different colors and shades on the echogram. Clusters of rising methane hydrate coated bubbles are visualized on the echogram and referred to as methane plumes. **Figure 1** shows the echogram from the research cruise at Umitaka Spur in the Sea of Japan in June, 2019. Seafloor of about 900 m depth is marked in red line. Vertical axis indicates the depth with the sea surface on the top and the horizontal axis indicates the time lapse, with the recent data to the right. Echogram displays the images underwater, following the route of the research vessel. A candle flare-shaped image in the middle of **Figure 1** from the seafloor rising to 350 m depth is methane plume. Based on the analysis of the water samples, observations from the images of the ROV camera, and by a methane sensor, components of methane plume are confirmed to be clusters of methane hydrate coated bubbles.

Shapes of Methane Plumes

As shown in **Figure 1**, methane plumes appear in the shape of a candle flare on the display of an echogram, with a wider base towards the bottom. The 7° beam width of the acoustic waves from the transducer causes methane plume to appear in such figure with an apparently wider base towards the bottom. At seafloor of 1,000 m depth, the diameter of the beam width expands to about 120 m. The mean backscattering strength per unit volume within this range is shown on the echogram at 1000 m depth. Therefore, methane plume on the echogram becomes wider as it gets deeper. Methane seeps cannot be specifically located within the footprint range.

On the other hand, the amount of methane from seeps of about 1 cm in diameter can be quantified by seafloor observation using the ROV. Several studies (Aoyama and Matsumoto, 2009) (Hachikubo, 2009) have been reported and verification of the one-to-one correspondence between methane seeps and methane plume is discussed in detail in *Investigation of the Correlation Between Methane Plumes and Seeps Through Seafloor Experiments*. In the future, more observation data are necessary to estimate the amount of methane seepage precisely.

Investigation of the Correlation Between Methane Plumes and Seeps Through Seafloor Experiments

First efforts at correlating and sonar return were conducted on data collected during the cruise as presented at the AGU Fall Meeting 2019 by Maeda and Aoyama. Methane seeps were identified at seafloor of 1,000 m depth at Umitaka Spur, offshore Joetsu in the Sea of Japan within the diameter range of 120 m, which is equivalent to the footprint diameter with the beam width expansion of 7°. The ROV rotated the echosounder beam axis (200 kHz frequency) 360° in the horizontal plane. As a result, 4 seeps (June 11, 37°26.063′N,138°00.294′E, 880–885 m depth) and 8 seeps (June 12, 37°26.051′N,138°00.287′E, 880–885 m depth) were discovered within this range. Based on the quantitative echo sounder (38 kHz) onboard, the mean volume backscattering strength (mean SV) of the plume was −61.5 dB at 4 points and −60.53 dB at 8 points. In both cases, the average volumetric backscattering was obtained by integrating the data over a 60-min period at a height of 5 m above seafloor. Assuming the same amount of methane seepage from each source, the correlation between the number of seeps and the mean volume backscattering strength of methane plume becomes evident. Specifically, the fewer the seeps, the weaker the Sv.

③ – 2 Correlation Between Methane Plume and Methane Seeps ~ Identifying Methane Seepage Area Using Target Position function~

In order to determine the amount of naturally seeping methane from seafloor simply by acoustic observations of methane plume onboard a vessel, the authors investigated the Target Position function of a quantitative echo sounder, originally used to specify the location of fish, to locate methane plumes.

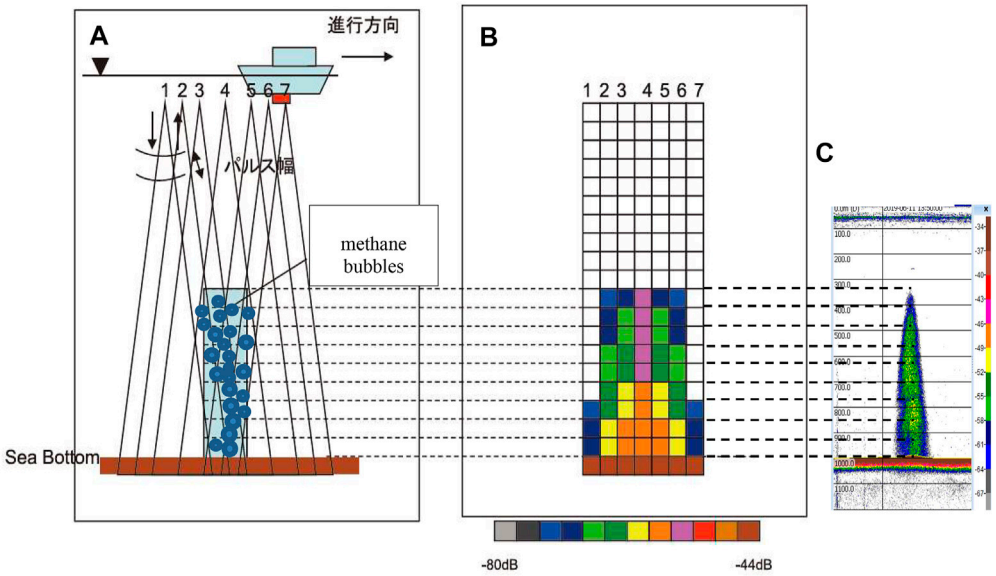

FIGURE 1 | Correlation between the movement of the beam axis and the actual location of methane plume, as well as the correlation of its images on the echogram is shown schematically. In **(A)**, the plume is first detected when the vessel is at position 1, so it appears as if the plume is directly below position 1, as shown in **(B)**. However, the plume is located on the seafloor directly underneath position 4, not under position 1. When the vessel is at position 7 in **(A)**, it appears as if methane is seeping directly under position 7, although the seep is not located directly underneath **(B)**. **(C)** is an example of an echogram display (methane plume observed by EA600 quantitative echo sounder onboard Kaiyo Maru No. 1 at 13:52:41 on June 11, 2019, at position 37-35.304N, 137-58.830E).

The diameter of the target position indicates the diameter of the footprint, which is 0 at the center and 5.0 on the circumference, with increments of 0.1, as shown in the orange circle in **Figure 2**. There is no unit of these values. Center is 0, left on the circumference (270°) −5.0, right (90°) +5.0, top (0°) +5.0, bottom (180°) −5.0. These values are set by the software for data acquisition. The length of the diameter is determined by the beam width and depth (**Figure 2A**). The range is set to measure the depth direction. In **Figure 2**, the depth is about 900 m to the seafloor (**Figure 2B**), so the width of 30 m is set between 855 and 885 m depth. (**Figure 2A**). The 30 m width does not come from the 900 m depth. Since the vertical observation width using a quantitative echo sounder attached to the ROV was 30 m when observing the seepage, the target position function was also aligned to 30 m. The minimum unit of width setting is 5 m. The diameter of the black circle becomes approximately 100 m because of the beam width of 7° and the depth of 870 m (the middle of the measurement width). The distance resolution at this point is approximately 1 m. The red circles indicate the footprint area (black circle) with strong backscattering strength (seeps) (**Figure 2C**).

The vessel location is accurately determined by GPS at the center of the circle. Given that the distance and direction from the vessel (center of the circle) are determined with the split beam, this allows the location (latitude and longitude) of seeps to be identified.

Ten methane seeps were located directly under the vessel, within 53 m × 9 m (**Figure 2C**, ③). Larger red circles indicate the location of seeps during the current transmission, and smaller red circle indicates the location during the previous transmission. A solid red dot indicates a single seep. However, because the distance resolution is 1 m, there may be multiple seeps within 1 m. Plumes ②, ③, and ④ were also identified in a similar method. Since living organisms were not confirmed during seafloor observation of methane seepage using the ROV camera, red dots were assumed to be methane seeps.

As a result of *in-situ* experiment using the Target Position function, the location of the methane seepage range could be determined with high accuracy, and a clear correlation can be seen between the number of seeps and mean SV. The amount of methane seepage can be estimated by measuring the amount of methane seepage from a single seep.

Calibration and Total Amount of Methane

④Based on the result of ③, the mean backscattering strength of methane plume and the amount of methane seepage is calibrated.

⑤Total amount of methane seepage in the surrounding sea areas of Japan can be obtained by applying ④ to ①. This result will be an indicator of whether methane plumes can be considered as a resource as well as its impact on the environment.

4. CONCLUSION

In this study, the correlation between methane plumes and methane seepage was examined. The results showed that multiple seeps exist within a single methane plume. Target Position function of a quantitative echo sounder is utilized to identify the precise locations of the methane seeps.

In the future, calibration of the mean back scattering strength and the amount of methane seepage need to be established to evaluate the

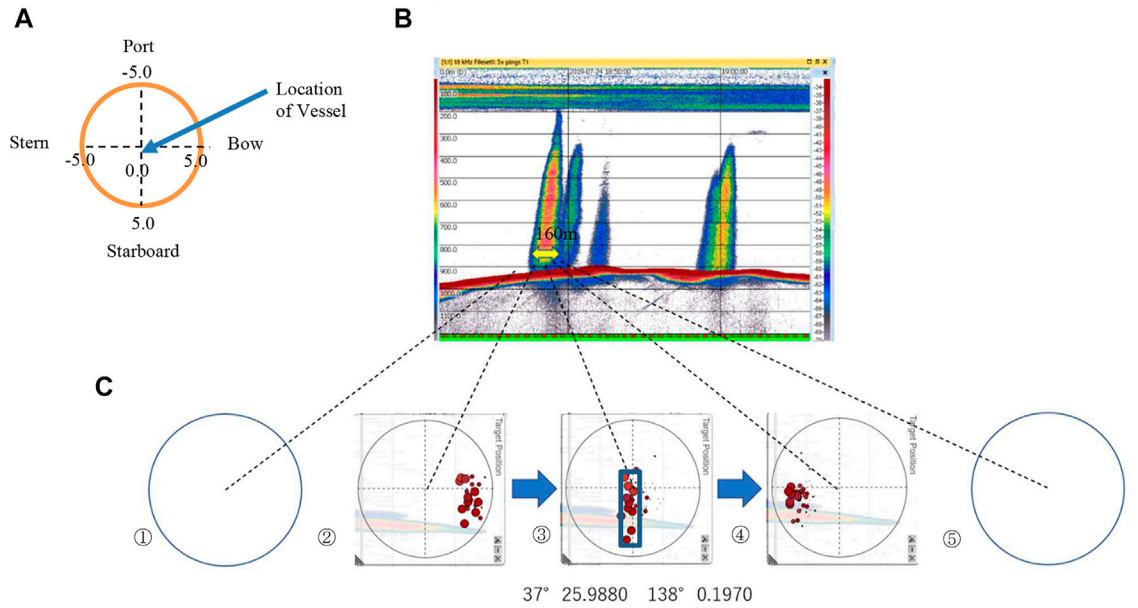

FIGURE 2 | Identification of methane seeps using Target Position function of quantitative echo sounder. **(A)** Display of Target Position function. **(B)** Echogram (observed on July 25, 2019 using EK80 quantitative echo sounder onboard Shinyo Maru) Vertical axis of the echogram indicates the water depth, with the water surface at the top and depth of the water at the bottom. Horizontal axis indicates the passage of time, with the right side being the latest. Each grid represents 10 min. Since the traveling speed of the research vessel is 3 knots, the distance in 10 min will be 926 m. **(C)** ①⑤ Footprint range where plumes are not detected on the echogram.②③④ Distribution of methane seep location within the footprint range on the echogram (855–885 m depth). ③ Blue box indicates 53 m × 9 m range.

total amount of methane seepage in Japan and to determine whether it can be used as a resource and its environmental impact.

Then the calibration can be applied to the methane plumes reported worldwide, and the amount of methane seepage can be estimated by simply observing the methane plumes acoustically.

DATA AVAILABILITY STATEMENT

The raw data supporting the conclusion of this article will be made available by the authors, without undue reservation.

AUTHOR CONTRIBUTIONS

NM performed the analysis of methane bubbles on echogram. CA organized the database, performed data analysis, wrote the manuscript, revision, read, and approved the submitted version.

FUNDING

We also thank Japan's Independent Institute for funding this research cruise.

ACKNOWLEDGMENTS

We are grateful for the data provided from the research cruise on Shinyo Maru (Tokyo University of Marine Science and Technology) in July 23–27, 2019 and on Kaiyo Maru No. 1 (KAIYO ENGINEERING CO., LTD.) in June 9–13, 2019. Additional support was provided by the crew members of Shinyo Maru and Kaiyo Maru No. 1.

REFERENCES

Aoyama, C., and Matsumoto, R. (2009). Acoustic Surveys of Methane Plumes by Quantitative Echo Sounder in Japan Sea and the Estimate of the Seeping Amount of the Methane Hydrate Bubbles. *J. Geogr.* 118 (1), 156–174. doi:10.5026/jgeography.118.156

Aoyama, C., Matsumoto, R., and Tomaru, H. (2009). Formation and Collapse of Gas Hydrate Deposits in High Methane Flux Area of the Joetsu Basin, Eastern Margin of Japan Sea. *J. Geogr.* 118 (1), 43–71. doi:10.5026/jgeography.118.43

Aoyama, C., and Matsumoto, R. (2020). Verifying Estimates of the Amount of Methane Carried by a Methane Plume in the Joetsu Basin. *East. Margin Sea Jpn.* 118 (1), 141–146. doi:10.5026/jgeography.129.141

Aoyama, C., and Mizukami, T. (2018). *MIS17-08: Plumes Observation in Offshore Shionomisaki of Wakayama Prefecture over the Past Five Years [Poster Presentation]*. Chiba, Japan: JpGU 2018.

Furusawa, M. (1995).Acoustic Survey Method for Marine Resources-Measuring Method and Quantitative Echo Sounder. *Mar. Acoust. Soc. Jpn.*, 79 152–161.

Hachikubo, A. (2009). Methane Hydrates and Plumes in the Sea of Okhotsk. *J. Geogr.* 118 (1), 175–193. doi:10.5026/jgeography.118.207

Matsui, K., and Aoyama, C. (2019). *OS43B-1707: Change of Phase Underwater Due to Change in the Depth of Methane Hydrate Particles [Poster Presentation]*. San Francisco, CA, United States: AGU Fall Meeting 2019.

Matsumoto, R. (2001). Distribution, Occurrence of Methane Hydrate and Amount of Methane. *Aquabiology* 23, 439–445.

Mau, S., Römer, M., Torres, M. E., Bussmann, I., Pape, T., Damm, E., et al. (2017). Widespread Methane Seepage along the continental Margin off Svalbard - from Bjørnøya to Kongsfjorden. *Sci. Rep.* 7, 42997. doi:10.1038/srep42997

Ministry of Economy, Trade and Industry (2016). Resource Quantity Assessment of Surface Type Methane Hydrate and Extraction Development Survey. (In Japanese). Available at: https://www.meti.go.jp/committee/summary/0004108/pdf/032_07_00.pdf (Accessed July 27, 2020).

National Institute of Advanced Industrial Science and Technology (2019). Action Plan for Research and Development of Surface Type Methane Hydrate (FY2019-2022). (In Japanese). Available at: https://www.meti.go.jp/shingikai/energy_environment/methane_hydrate/pdf/035_03_00.pdf (Accessed July 27, 2020).

National Institute of Advanced Industrial Science and Technology (2021). What Is Methane Hydrate. (In Japanese). Available at: https://unit.aist.go.jp/georesenv/topic/SMH/methane_hydrate.html (Accessed July 7, 2021).

Niigata University (2016). *FY2015 Gas Plume Investigation in Offshore Niigata Prefecture*. Niigata: Niigata Prefectural Office.

Riedel, M., Scherwath, M., Römer, M., Veloso, M., Heesemann, M., and Spence, G. D. (2018). Distributed Natural Gas Venting Offshore along the Cascadia Margin. *Nat. Commun.* 9 (1). doi:10.1038/s41467-018-05736-x

Römer, M., Riedel, M., Scherwath, M., Heesemann, M., and Spence, G. D. (2016). Tidally Controlled Gas Bubble Emissions: A Comprehensive Study Using Long-Term Monitoring Data from the NEPTUNE Cabled Observatory Offshore Vancouver Island. *Geochem. Geophys. Geosyst.* 17 (9), 3797–3814. doi:10.1002/2016gc006528

Shipley, T. H., and Didyk, B. M. (1982). Occurrence of Methane Hydrates Offshore Southern Mexico. Initial Reports. *Deep Sea Drilling Project* 66, 547–555. doi:10.2973/dsdp.proc.66.120.1982

Shipley, T. H., Houston, M. H., Richard, T., Buffler, F., Jeanne, S. J., et al. (1979). Seismic Reflection Evidence for the Widespread Occurrence of Possible Gas-Hydrate Horizons on continental Slopes and Rises. *Am. Assoc. Pet. Geologist Bull.* 63, 2204–2213. doi:10.1306/2f91890a-16ce-11d7-8645000102c1865d

Skarke, A., Ruppel, C., Kodis, M., Brothers, D., and Lobecker, E. (2014). Widespread Methane Leakage from the Sea Floor on the Northern US Atlantic Margin. *Nat. Geosci* 7, 657–661. doi:10.1038/ngeo2232

Veloso, M., Greinert, J., Mienert, J., and De Batist, M. (2015). A New Methodology for Quantifying Bubble Flow Rates in Deep Water Using Splitbeam Echosounders: Examples from the A Rctic Offshore NW- S Valbard. *Limnol. Oceanogr. Methods* 13, 267–287. doi:10.1002/lom3.10024

Weber, T. C., Mayer, L., Kevin, J., Beaudoin, J., Rzhanov, Y., and Lovalvo, D. (2014). Acoustic Estimates of Methane Gas Flux from the Seabed in a 6000 Km2region Inthe Northern Gulf of Mexico. Available at: https://agupubs.onlinelibrary.wiley.com/doi/full/10.1002/2014GC005271 (Accessed July 7, 2021).

Young, K., Kim, Y-G., Baranov, B., Shoji, H., and Obzhirov, A. (2011). Distribution and Expression of Gas Seeps in a Gas Hydrate Province of the Northeastern Sakhalin continental Slope, Sea of Okhotsk. *Mar. Pet. Geology.* 28 (10), 1844–1855. doi:10.1016/j.marpetgeo.2011.03.007

Conflict of Interest: The authors declare that the research was conducted in the absence of any commercial or financial relationships that could be construed as a potential conflict of interest.

Publisher's Note: All claims expressed in this article are solely those of the authors and do not necessarily represent those of their affiliated organizations, or those of the publisher, the editors and the reviewers. Any product that may be evaluated in this article, or claim that may be made by its manufacturer, is not guaranteed or endorsed by the publisher.

Advantages of publishing in Frontiers

OPEN ACCESS
Articles are free to read for greatest visibility and readership

FAST PUBLICATION
Around 90 days from submission to decision

HIGH QUALITY PEER-REVIEW
Rigorous, collaborative, and constructive peer-review

TRANSPARENT PEER-REVIEW
Editors and reviewers acknowledged by name on published articles

Frontiers
Avenue du Tribunal-Fédéral 34
1005 Lausanne | Switzerland

Visit us: www.frontiersin.org
Contact us: frontiersin.org/about/contact

REPRODUCIBILITY OF RESEARCH
Support open data and methods to enhance research reproducibility

DIGITAL PUBLISHING
Articles designed for optimal readership across devices

FOLLOW US
@frontiersin

IMPACT METRICS
Advanced article metrics track visibility across digital media

EXTENSIVE PROMOTION
Marketing and promotion of impactful research

LOOP RESEARCH NETWORK
Our network increases your article's readership